

Proceedings of the joint annual meeting of the
NORDIC and DACH Chapter
of the International Society for Magnetic Resonance in Medicine



Table of Content	1
Greetings	3
30 years of Medical Physics, 15 years of SBMI and MOINCC	8
Sponsors	9
Conference Locations – Getting there	10
Keynote Speakers	11
Preconference workshops – Open MR days	12
Conference Program	14
Postconference workshops	18
Gorter Awards - Abstracts	20
Oral Presentations – Abstracts (1 – 20)	45
Poster Presentations – Abstracts (1 – 61)	93
Poster Presenter List	222

Greetings from the conference president

Welcome to Kiel,
Welcome to SBMI,
Welcome to the joint meeting of the NORDIC & DACH chapters of ISMRM!

We are very happy to host, again, an ISMRM chapter meeting in Kiel, the city by the bay. I wish you an enticing time, lots of science, insights, friends and fun!

Your submissions have allowed us to put forward a fantastic program, covering topics from basic physics to clinical application, showcasing the breadth and quality of MR research in our region of this ever-changing world.

We're excited to open every session with an plenary talk - a real highlight. Many thanks to Prof. Matthias Günther, Prof. Inga Voges, Prof. Christoffer Laustsen, Prof. Jürgen Hennig and Prof. Martin Uecker! This year, we are thrilled to expand the program beyond the main conference:

- During the Open MR Days, leading experts will provide hands-on, cutting-edge insights into the future MR. A big thank you to Prof. Martin Uecker, Prof. Maxim Zaitsev, Prof. Matthias Günther and Siemens Healthineers!
- In the Advanced Magnetic Resonance Workshop, you have the chance of actually seeing SEOP, PHIP, DNP, and DMI in action – as far as we know, this is the only place where you can do this.

If you didn't get a spot this time, don't worry –we're planning to do it again. Stay tuned!

A very special highlight are our anniversaries: we are celebrating 30 years of medical physics in Kiel, 15 years of SBMI and 15 years of MOINCC. Join us for a special event at the water side on Monday evening.

But there is more to Kiel. Take a chance to stroll along the waterfront, visit the beaches and test the waters if you dare. There's a unique vibe here at the edge of land and sea, and we hope you'll experience it fully.

We're incredibly grateful to the Faculty of Medicine and our sponsors Siemens Healthineers, Skope, Merck, GE HealthCare, NVision Imaging Technologies, Pure Devices GmbH, Bruker and MR:Comp GmbH for their generous support. Be sure to stop by their booths to learn about the latest innovations and explore job opportunities. It's worth your time!

Last, and most importantly: a huge thank you to the amazing team of the Section Biomedical Imaging. Your dedication, energy and commitment made all of this happen. You are fantastic!

Enjoy the program and your time in Kiel. We're happy having you!
Prof. Jan Hövener

Conference President
Head of the Section Biomedical Imaging and MOIN CC



Greetings from the Dean of the Faculty of Medicine

Dear Participants,

It is with great pleasure and pride that I welcome you to the 27th Annual Meeting of the DACH Chapter of the International Society for Magnetic Resonance in Medicine (ISMRM), taking place here in Kiel. This year's event marks a historic milestone, as we are joined for the first time by the Nordic Chapter — bringing together researchers and clinicians from across Germany, Austria, Switzerland, Denmark, Finland, Sweden, Norway and The Netherlands and England as well.



We are especially delighted to host this significant gathering in Kiel for the second time under the leadership of Professor Hövener, whose commitment to advancing non-invasive imaging science has helped shape this vibrant program.

This year's conference is a celebration not only of scientific progress but also of enduring academic partnerships. We are proud to mark 15 years of MOIN CC and SBMI, as well as 30 years of medical physics in Kiel — three pillars of innovation in magnetic resonance and medical imaging.

The program offers a rich and diverse experience: from cutting-edge research presentations on topics such as metabolic imaging, lymphatic flow, and open MR, to interactive industry sessions, poster contributions, and hands-on workshops. We are also honored to welcome renowned international speakers, and to host the prestigious Gorter Prize competition, a highlight of the ISMRM calendar.

Beyond the conference halls, this event also showcases Kiel as a growing center for biomedical research. It strengthens our ties with leading institutions across Scandinavia.

On behalf of the Faculty of Medicine and Kiel University, I wish you a stimulating and rewarding conference — full of inspiration, exchange, and new ideas that will shape the future of magnetic resonance imaging.

Warm regards,
Prof. Dr. Joachim Thiery

Dean of the Faculty of Medicine at Kiel University (CAU)
Member of the Board of the University Hospital Schleswig-Holstein (UKSH)

Greetings from the Director of the Department of Radiology and Neuroradiology at UKSH

Dear colleagues,

It is my great pleasure to welcome you to Kiel for the first joint scientific meeting of the DACH and Nordic Chapters of the International Society for Magnetic Resonance in Medicine, hosted on September 16–17, 2025, by the Section Biomedical Imaging (SBMI) of the Department of Radiology and Neuroradiology at the Christian-Albrechts-University and the University Hospital Schleswig-Holstein.



Magnetic Resonance Imaging (MRI) has fundamentally transformed radiology and neuroradiology, and it continues to drive innovation in both scientific and clinical practice. Advances in MRI technology—whether in hardware development, pulse sequence design, or post-processing techniques—are enabling us to extract information at an unprecedented level of detail and specificity. For us as radiologists, these developments are not merely of academic interest; they shape how we diagnose, stratify, and treat our patients every day.

This meeting offers a unique platform for fostering translational research. Bringing together experts from physics, engineering, and clinical radiology allows us to ensure that groundbreaking MRI techniques are not confined to the laboratory but rapidly and effectively integrated into clinical workflows. It is precisely this interdisciplinary collaboration that accelerates the journey from innovation to patient benefit—making research tangible in daily clinical care.

The joint meeting of the DACH and Nordic Chapters symbolizes the strength of cross border scientific cooperation. By sharing knowledge, building networks, and encouraging dialogue between basic science and clinical practice, we create a fertile ground for future breakthroughs.

I warmly thank all organizers, speakers, and participants for their contributions to this meeting. I am confident that the discussions and insights exchanged here will inspire new ideas and collaborations, driving forward the field of MRI to the benefit of our patients.

Welcome to Kiel, and I wish you all an exciting and fruitful conference!

Prof. Dr. Olav Jansen

Director, Department of Radiology and Neuroradiology
Christian-Albrechts-University & University Hospital Schleswig-Holstein

Words of Welcome from the Lord Mayor and the City Council President

Dear conference participants,
Dear guests,

We warmly welcome you all to Kiel.Sailing.City and are delighted that our city is hosting the annual conference of the DACH section of ISMRM e.V. for the second time since 2019.



© LH Kiel – Gunnar Dethlefsen und Pepe Lange

Kiel has an excellent reputation as a center of science, and we are proud to offer a diverse and innovative research landscape. Kiel University and the numerous research institutions in our city are closely connected to the international scientific community and make important contributions across various disciplines. This is especially true for the Section for Biomedical Imaging within the Department of Radiology and Neuroradiology at UKSH and CAU.

This 27th Annual Meeting of the DACH-ISMRM is undoubtedly one of the highlights in Kiel's scientific calendar this year. We are impressed by the diversity of the program, which includes plenary lectures, presentations, workshops, and networking events.

A focus of this conference—the promotion of early-career researchers—is particularly close to our hearts. We fully support the goal of encouraging and inspiring young scientists in the field of magnetic resonance research, and we hope that all participants will gain valuable and memorable experiences during their time in Kiel.

We wish you all a successful and inspiring conference and hope that you will also have the opportunity to get to know our city. Kiel offers a unique blend of maritime atmosphere, cultural attractions, and scientific excellence— and we are confident that you will feel very welcome here.

Yours

Bettina Aust & Ulf Kämpfer
City Council President Lord Mayor

Greetings from the Minister of Education, Science, Research and Culture

Dear Guests,

it is a great honor to welcome you all to Kiel for this year's gathering of the DACH Chapter of the International Society for Magnetic Resonance in Medicine (ISMRM) — held for the first time in partnership with the Nordic Chapter.

This international collaboration brings together brilliant minds from across Central and Northern Europe, united by a shared commitment to advancing medical imaging. With more than 130 participants, this conference marks a new record and reflects the growing importance of magnetic resonance imaging in both research and clinical practice.

It also highlights Kiel's emergence as a hub for scientific innovation and cross-border cooperation.

This conference is another milestone and testament to the city's long-standing investment in science and healthcare. It offers a fantastic environment that combines state-of-the-art research, young talent development, and industry engagement. Workshops, panel discussions, and a vibrant exhibition space — featuring partners such as Siemens, Merck, GE, Bruker, and others — make this event both future-focused and grounded in real-world impact.

At the same time, Kiel's unique location by the sea adds to its appeal as a place to live, study, and work. The city is not only a center of innovation but also a place with high quality of life, offering a wide range of recreational opportunities, sports activities, and a welcoming environment for families. Whether it's sailing on the fjord, cycling along the coast, or enjoying cultural events — Kiel has much to offer beyond the lab and lecture hall.

I am confident that this joint DACH-NORDIC meeting will strengthen ties between researchers, institutions, and companies across borders. It also reinforces Kiel's role on the European map of medical innovation and contributes to making our region even more attractive for the next generation of scientists and healthcare leaders.

Thank you for being part of this outstanding event. I wish you productive days, valuable connections, and a memorable stay in Kiel.

With warm regards,
Dr. Dorit Stenke

Minister of Education, Science, Research and Culture of the State of Schleswig-Holstein



© Kaja Grope

30 year of Medical Physics, 15 years of SBMI and MOINCC

Dear Colleagues, Dear friends,

This year, we are celebrating **15 years of the Molecular Imaging North Competence Center (MOINCC)**, **15 years of the Section Biomedical Imaging (SBMI)**, and **30 years of Medical Physics** in Kiel.

30 years ago, the appointment of Claus Glüer as Professor marked the beginning of biomedical imaging physics research in the Medical Faculty of Kiel University.

Fifteen years later, Prof. Glüer, who retired in 2024, founded the section biomedical imaging (SBMI), the home of all imaging physics related research up to today. At the same time, the molecular imaging north competence center MOINCC was funded and founded as the core facility for preclinical imaging of Kiel University with the support of the European Union.

Today, both SBMI and MOINCC continue to thrive as active research centers known in the North and beyond, educating the next generation of scientists and contributing to shape the ever growing field of biomedical imaging.

Join us in celebrating this special occasion!

Yours

Prof. Jan Hövener & Prof. Em. Claus-C. Glüer



We thank our sponsors for their support of the Nordic+DACH-ISMRM conference 2025 in Kiel. The DACH-ISMRM (and thus indirectly the annual meeting) was financially supported in 2025 by the following sponsors: Medical Faculty of the CAU, Siemens Healthineers, Skope, Merck, GE HealthCare, NVision Imaging Technologies, Pure Devices GmbH, Bruker, and MR:comp GmbH. We thank the Medical Faculty of the Kiel University and the University Hospital Schleswig-Holstein for financial and logistic support of this conference.

Gold Sponsors



Silver Sponsors



skope

MERCK



GE HealthCare

Bronze Sponsors

NVISION 



Conference Locations – Getting there



Pre-conference workshop Sept. 14 and 15.

Rosalind-Franklin-Straße 9, 24105 Kiel (Quincke Forschungs - Zentrum, [google maps](#))

Fun & Games Social activities –Sept. 15

Kiellinie 61a, 24105 Kiel, (Reventlou meadow, next to MOBY, [google maps](#))

Icebreaker and Dinner –Sept. 15

Kiellinie 63, 24105 Kiel ([Jan&Klaas&Hein&Pit website](#), [google maps](#))

Conference Sept. 16-17

Olshausenstraße 75, 24118 Kiel (Hans-H.-Driftmann hall, [google maps](#))

Social Dinner –Sept. 16

Düvelsbeker Weg 46, 24105 Kiel ([Forstbaumschule Restaurant website](#), [google maps](#))

Post-conference workshop Sept. 18

Am Botanischen Garten 14, 24118 Kiel ([MOIN CC website](#), [google maps](#))

See also the conference website

<https://ismrm-dach-2025.moincc.de/>

Conference Keynote Speakers



Prof. Dr. rer. nat. Matthias Günther

Deputy Institute Director Fraunhofer Institute for Digital Medicine MEVIS, Bremen, Germany.

Matthias Günther studied Physics at the University Heidelberg and did his PhD at the Cancer Research Center in Heidelberg on Arterial Spin Labeling development and applications. After receiving his PhD he joined Advanced MRI Technology, a company founded by David Feinberg in California. Three years later he founded his own company in Heidelberg, mediri GmbH, offering (research) services for image-based clinical trials. He also continued his scientific career at the Universitätsmedizin Mannheim. After Habilitation in 2008, he became Professor at the University Bremen and joined Fraunhofer MEVIS in Bremen as part of the management board. He is now deputy institute director of Fraunhofer MEVIS with a joint professorship on MR-Physics. (Keywords: reconfigurable metamaterials to improve MRI, Arterial Spin Labeling, hemodynamics, blood brain barrier). (Plenary 1)



Prof. Dr. Med., Phd, Christoffer Laustsen

Department of Clinical Medicine – The MR Research Centre, Aarhus University, Aarhus, Denmark.

Christoffer Laustsen is a professor of translational MRI and the head of the MR research department at Aarhus University, Denmark. With over a decade of experience in X-nuclei NMR and MRI and in particular hyperpolarized ¹³C MRI and metabolic research. He has authored over 160 peer-reviewed publications and received notable accolades, such as the Lundbeck Young Investigator Award. (keywords: metabolic fingerprints of heart disease, hyperpolarized ¹³C MRI). (Plenary 2)



Prof. Dr. Dr. h.c. em. Jürgen Hennig

Medical Physics, Department of Radiology, University Medical Center Freiburg, Germany.

Development of new methods and technologies in Magnetic Resonance Imaging and Spectroscopy and their application in fundamental, preclinical, translational and clinical research and clinical applications. Key areas of applications are oncology, neuroscience and neurology, cardiovascular disease, metabolic disease. He studied chemistry in Stuttgart, London, Munich and Freiburg and obtained his doctorate in physical chemistry in 1980. After postdoctoral positions in Freiburg and Zurich, he was a research fellow in Freiburg from 1983 to 1992 and habilitated in medical physics in 1988. In 1993, he became a full professor at the Universität Freiburg and held various senior positions, including Research Director and Co-Chair of the Department of Radiology – Medical Physics. He retired in 2021. Prof. Hennig has received numerous awards, including the European Magnetic Resonance Award (1992), the Gold Medal of the Society of Magnetic Resonance (1994) and the Max Planck Prize (2003). He is an honorary member and honorary doctor of several international societies and universities. (Plenary 3)



Prof. Dr. med. Inga Voges

Clinic for Congenital Heart Defects and Pediatric Cardiology, University Hospital Schleswig-Holstein – Campus Kiel, Germany.

Inga Voges is a paediatric cardiologist and the lead of the cardiovascular magnetic resonance (CMR) group in the department of congenital heart disease and paediatric cardiology at UKSH Kiel. She has a long-standing clinical experience in CMR in paediatric cardiology and adults with congenital heart disease. Her research interests are focused on the use of CMR for the long-term follow up of patients with univentricular heart disease, 4D Flow and CMR reference values. (Plenary 4)



Prof. Dr. rer. nat. Martin Uecker

Institute of Biomedical Imaging, Graz University of Technology, Graz, Austria.

Martin Uecker is professor for biomedical imaging and the head of the Institute of Biomedical Imaging at the Graz University of Technology. He studied physics and mathematics in Göttingen and obtained his PhD at the Max-Planck-Institute for biophysical chemistry in Göttingen in 2009. He then had postdoctoral positions in Göttingen and at the University of California in Berkeley, before being appointed as an associate professor in the Department for Diagnostic and Interventional Radiology at the University Medical Center Göttingen in 2015. In 2021 he then became a full professor in Graz. His main research interest is the development of new computational imaging methods for MRI. He is the main author of the open-source BART toolbox. (Plenary 5)

Preconference workshops – Open MR days

Sunday Sept. 14 – Monday Sept. 15

Open MR days

Workshop – Sunday, September 14, 2025		
Time	Event	Lecturer/Topic
12:25	Registration & Coffee	
12:55	Welcome	Conference president Prof. Jan-B. Hövener
13:00	BART workshop	Prof. Martin Uecker, Daniel Mackner und Dr. Vitali Telezki
17:00	End day 1 of open MR days	

Workshop location: room 10.1, ground floor in the Quincke Forschungszentrum (QFZ), Rosalind-Franklin-Straße 9, 24105, Kiel

Workshops – Monday, September 15, 2025		
Time	Event	Lecturer/Topic
08:30	Registration & Coffee	
09:00	Welcome	Conference president Prof. Jan-B. Hövener
09:10	Teaser Session (1-4 each 10 min)	
09:10	gammaSTAR	Prof. Matthias Günther
09:20	Pulseq	Prof. Maxim Zaitsev
09:30	Siemens Healthineers Open Recon	Dr. Christian Eisen, Dr. Tobias Würfl
09:40	Q&A	
09:50	☛ Coffee Break 30 min	
10:20	Open Sequence Development, parallel workshops (each 2 h)	
10:20	gammaSTAR workshop	Prof. Matthias Günther
10:20	Pulseq workshop	Prof. Maxim Zaitsev
12:20	☘ Lunch Break 70 min	
13:30	Siemens Healthineers Open Recon workshop	Dr. Tobias Würfl, Dr. Frederik Testud, Dr. Florian Kümmel, Dr. Moritz Berger, Ali Ajouz, Dr. Lynn Frohwein, Dr. Christian Eisen
17:00	End of open MR days	

Workshop location: rooms 10.1-2, ground floor in the Quincke Forschungszentrum (QFZ), Rosalind-Franklin-Straße 9, 24105, Kiel

16:00	Fun & Games at Reventlou meadow – Kiellinie 61a, 24105 Kiel (near MOBY)
19:00	Icebreaker and Dinner at Jan&Klaas&Hein&Pit – Kiellinie 63, 24105 Kiel

Open MR days workshop content

workshop	Content
BART	<p>Sunday, Sept. 14, 1pm</p> <p>The Berkeley Advanced Reconstruction Toolbox (BART) is a free and open-source image-reconstruction framework for Computational Magnetic Resonance Imaging. Prof. Dr. Martin Uecker, Prof. Martin Uecker, Daniel Mackner und Dr. Vitali Telezki Institute of Biomedical Imaging, Graz University of Technology, Austria.</p>
PULSEQ	<p>Monday, Sept. 15, 9am</p> <p>Allows development and execution of MR pulse sequences for imaging and spectroscopy directly in Matlab, Octave or Python, and the export to the Pulseq file format which can be executed on real hardware. Prof. Dr. Maxim Zaitsev, Medical Physics, Department of Radiology, Medical Center – University of Freiburg, Germany.</p>
gammaSTAR	<p>Monday, Sept. 15, 9am</p> <p>gammaSTAR provides a hardware-agnostic, user-friendly platform for MR pulse sequence development that simplifies the transfer of research ideas to diverse MRI systems. The workshop will explore key features of gammaSTAR to create an MR pulse sequence based on a modular design concept, and highlight recent developments and applications. Prof. Dr. Matthias Günther, Deputy Institute Director Fraunhofer Institute for Digital Medicine MEVIS, Bremen, Germany.</p>
Siemens Healthineers „Open Recon“	<p>Monday, Sept. 15, 1.30pm</p> <p>Developing in the Open MAGNETOM Community puts you in control of cutting-edge MRI technology. Create, apply and scale your research - run your own reconstruction algorithms directly on the scanner (Siemens Healthineers, SHS).</p>

Time	Event	Lecturer/Topic
07:45	Registration & Coffee	
08:30	Welcome	Conference president Prof. Jan-B. Hövener
09:00	Plenary 1 Glymphatic Flow and Brain Self-Cleaning: An MR Physicist's Perspective	Prof. Matthias Günther (Fraunhofer Institute for Digital Medicine MEVIS, Bremen, Germany)
09:30	Scientific Session 1 (S1-4, each 9+3 min)	Flow & Diffusion MRI
09:30	S1: In-vitro and in-vivo comparison of accelerated dual-Venc 4D flow MRI using radial trajectories.	Adrian Duckert
09:42	S2: 3D distortion-free diffusion and T ₂ prepared reduced FOV imaging in the prostate at 3Tg	Yannik Ott
09:54	S3: Evaluation of flow modulating treatment response in intracranial aneurysms using black blood MRI signal changes.	Mariya Pravdivtseva
10:06	S4: Evaluation of the diffusion along perivascular spaces after subarachnoid hemorrhage	Patricia Ulloa
10:20	☕ Coffee Break 15 min	
10:35	Plenary 2 The Next Generation of Metabolic Imaging: Beyond the Radiotracer Paradigm	Prof. Christoffer Laustsen (Dept. of Clinical Medicine - The MR Research Centre, Aarhus University, Denmark)
11:05	Scientific Session 2 (S5-8, each 9+3 min)	Metabolic & Molecular MRI
11:05	S5: Integrating in situ parahydrogen hyperpolarization and ¹⁸ F-FDG-PET: toward high throughput single-device multimodal metabolic imaging	Henri de Maussin
11:17	S6: Characterization of Acute Kidney Injury (AKI) with combined Dynamic Contrast Enhanced (DCE) and Dynamic Glucose Enhanced (DGE) MRI	Chris Lippe
11:29	S7: Monitoring macaque brain organoid maturation using magnetic resonance imaging and spectroscopy	Tor Rasmus Memhave
11:41	S8: Developing Transportable Hyperpolarized 0.44 T Mouse MRI with Fast Anatomical Spectral CT Imaging	Josef Elsasser
11:55	🍽️ Lunch Break 50 min	
12:45	Gorter Session G1-3 (each 20+10 min)	
12:45	Gorter intro (10 min)	DACH-ISMRM e.V. chairs

Conference Program – Day 1, Tuesday, Sept. 16

12:55	G1: Assessment of tumor cell invasion and radiotherapy response in experimental glioma by MR Elastography	Hannah Fels-Palesandro
13:25	G2: Balanced Steady-State Free Precession Enables High-Resolution Dynamic 3D Deuterium Metabolic Imaging of the Human Brain at 7T	Sabina Frese
13:55	G3: From Blur to Dynamic Sharpness: Temporal Limits in Single-cell Tracking Time-lapse MRI	Dr. Enrica Wilken
14:25	☕ Coffee Break 20 min	
14:45	Gorter Session G4-6 (each 20+10 min)	
14:45	G4: Quantitative Sodium Magnetic Resonance Imaging of the Human Torso at 7 Tesla	Anna Scheipers
15:15	G5: MR-zero meets FLASH – Controlling the transient signal decay in gradient- and rf-spoiled gradient echo sequences	Simon Weinmüller
15:45	G6: Development of radiofrequency coils for magnetic resonance-guided particle therapy	Dr. Dietrich Kilian
16:20	Poster Flash Talks	20 presenters, each 2mins
17:00	Poster Party (drinks and posters)	Odd numbers 17:00 – 17:30, even numbers 17:30 – 18:00
18:00	End conference day 1	
19:00	Dinner at Forstbaumschule	(https://forstbaumschule.de)

Conference Program – Day 2, Wednesday, Sept. 17

Conference Day 2 – Wednesday, September 17, 2025		
Time	Event	Lecturer/Topic
08:30	☕ Coffee	
09:00	Plenary 3 50+ Years of MRI Development - Still going strong?!	Prof. Jürgen Hennig (Medical Physics, Dept. of Radiology, Uni. Medical Center Freiburg, Germany)
09:30	Scientific Session 3 (S9-12, each 9+3 min)	Low & High Field MRI
09:30	S9: Field-dependent ^{13}C and ^{15}N Relaxation Dispersion and T_1 Optimization Using CIDER	Josh Philipp Peters
09:42	S10: Correction of time-dependent phase fluctuations in diffusion-weighted MRS at very high b-values with an external phantom reference	Kristin Engel
09:54	S11: Pushing Boundaries in (Ultra) Low Field MRI: Towards an Adjustable Superconducting Magnet for the 1–200 mT Range	Pavel Povoloni
10:06	S12: Field-based spatial self-registration of multi-coil hardware for B_0 field control	Isabelle Zinghini
10:20	☕ Coffee Break – 15 min	
10:35	Plenary 4 Cardiovascular MRI: Fundamentals and Future Directions	Prof. Inga Voges (Clinic for Congenital Heart Defects and Pediatric Cardiology, UKSH Kiel, Germany)
11:05	Scientific Session 4 (S13-16, each 9+3 min)	Clinical application
11:05	S13: Can real-time phase contrast quantification of CSF flow predict shunt response in NPH patients?	Federica Calafiore
11:17	S14: ^{31}P -MRS saturation transfer to assess hepatic ATP synthesis at 3T in individuals with type-1-diabetes and control volunteers	Marc Jonuscheit
11:29	S15: Optimizing Quantitative MRI Protocols for Neurosurgery-Planning of Drug-Resistant Epilepsy Patients: A Multi-Site Traveling Heads Study	Jan Malte Oeschger
11:41	S16: Ex vivo and in vivo characterization of cystic kidneys in patients with ADPKD using ^{23}Na MRI at 7T	Judith Schirmer
12:00	Career Opportunities 60 min (Host: Jan-B. Hövener)	

13:00 ☕ Lunch Break 50 min

Conference Program – Day 2, Wednesday, Sept. 17

13:50	Plenary 5 Computational MRI: Sequences, Reconstruction, and Machine Learning	Prof. Martin Uecker (Institute of Biomedical Imaging, Graz Uni. of Technology, Austria)
14:20	Scientific Session 5 (S17-20, each 9+3 min)	Sequences, Reconstruction and AI
14:20	S17: The impact of the current-induced magnetic fields on the BOLD signal measured in concurrent tDCS-fMRI	Teresa Cunha
14:32	S18: QSM Beyond the Brain: Exploring Fat and Iron Effects	Simon Graf
14:44	S19: A Data Processing, Analysis and Quantification Pipeline for 1H-MRS in a Mouse Model of Pancreatic Ductal Adenocarcinoma	Diana Rotaru
14:56	S20: Validation of Model-Based Reconstruction for Joint Estimation of Multiple Quantitative Maps with Single-Shot IR Multi-Echo Radial FLASH using a Water-Fat-SPIO Phantom	Vitali Telezki
15:10	☕ Coffee Break – 15 min	
15:25	Chapters' Member Meeting	DACH-ISMRM, Nordic-ISMRM
16:25	Award ceremony	
16:45	Farewell	Conference president & Team
17:00	End conference day 2	

Postconference workshops – Thursday, Sept. 18

Post-Conference workshops

workshops	Thursday Sept. 18
High-field SABRE	<i>Participate in polarizing biomolecules like pyruvate at 9.4 T and measure J-couplings in exchanging systems. Charbel Assaf, Section Biomedical Imaging, MOINCC, University Hospital Schleswig-Holstein, Kiel University, Germany</i>
DNP	<i>Learn to operate the latest-generation DNP polarizer, the SPIN ALIGNER, in a pyruvate hyperpolarization experiment. MD Josh Peters, Section Biomedical Imaging, MOINCC, University Hospital Schleswig-Holstein, Kiel University, Germany</i>
PHIP-SAH	<i>Join experiments using our highly automated 0.5 T polarizers for PHIP-SAH of pyruvate. Yenal Gökpek, Section Biomedical Imaging, MOINCC, University Hospital Schleswig-Holstein, Kiel University, Germany</i>
SLIC-SABRE	<i>Experience ultra-fast polarization of pyruvate within seconds using our SLIC-SABRE polarizer. Martin Sandbrink, Section Biomedical Imaging, MOINCC, University Hospital Schleswig-Holstein, Kiel University, Germany</i>
CIDER / MFC	<i>Measure the field dependency of relaxation across 9 orders of magnitude and explore the fascinating effects of CIDER. MD Josh Peters & Charbel Assaf, Section Biomedical Imaging, MOINCC, University Hospital Schleswig-Holstein, Kiel University, Germany</i>
ALPS	<i>Measure the ALPS index in humans on the CIMAX system. Ali Ajouz, Siemens Healthineers and Section Biomedical Imaging, MOINCC, University Hospital Schleswig-Holstein, Kiel University, Germany</i>
Multi-nuclear MR	<i>Participate in measuring X-nuclei at a 3 T human system, including ^2H, ^{13}C, ^{23}Na, and ^{129}Xe. Ali Ajouz, Siemens Healthineers and Section Biomedical Imaging, MOINCC, University Hospital Schleswig-Holstein, Kiel University, Germany</i>
Deuterium MR	<i>Set up and measure DMI (Deuterium Metabolic Imaging) signals at 7 T. Aaron Diercks, Section Biomedical Imaging, MOINCC, University Hospital Schleswig-Holstein, Kiel University, Germany</i>

Gorter

Award Finalists' Abstracts

Die Deutsche Sektion der ISMRM e. V. zeichnet mit dem Gorter-Preis die beste aktuelle Arbeit auf dem Gebiet der biomedizinischen Magnetresonanz einer/eines jungen Wissenschaftlerin/Wissenschaftlers aus der Medizin oder einer anderen Naturwissenschaft aus.

Bewerben können sich Absolventen und Wissenschaftler bis maximal zwei Jahre nach Abschluss der Promotion mit einer erstklassigen Bachelor-, Master- oder Doktorarbeit oder als Erstautor einer hervorragenden Originalarbeit auf dem Gebiet der biomedizinischen Magnetresonanz. Die Bewerber müssen Mitglied der DACH-ISMRM sein. Eine Affiliation der/des Bewerberin/Bewerbers zu einer Institution in Deutschland, Österreich oder der Schweiz sollte gegeben sein. Außerdem muss die Arbeit zum Zeitpunkt der Bewerbung angenommen bzw. bestanden worden sein.

The German Section of ISMRM e.V. awards the Gorter Prize for the best current work in the field of biomedical magnetic resonance by a young scientist from medicine or another natural science discipline.

Eligible to apply are graduates and researchers up to a maximum of two years after completing their doctorate, who have submitted an outstanding bachelor's, master's, or doctoral thesis, or are first authors of an excellent original research paper in the field of biomedical magnetic resonance. Applicants must be members of DACH-ISMRM. They should also be affiliated with an institution in Germany, Austria, or Switzerland. Furthermore, the work must have been accepted or completed at the time of application.

Gorter Award Finalists

Hannah Fels-Palesandro (G1, 12:55)

Assessment of tumor cell invasion and radiotherapy response in experimental glioma by MR Elastography.

Sabina Frese (G2, 13:25)

Balanced Steady-State Free Precession Enables High-Resolution Dynamic 3D Deuterium Metabolic Imaging of the Human Brain at 7T.

Dr. Enrica Wilken (G3, 13:55)

From Blur to Dynamic Sharpness: Temporal Limits in Single-cell Tracking Time-lapse MRI.

Anna Scheipers (G4, 14:45)

Quantitative Sodium Magnetic Resonance Imaging of the Human Torso at 7 Tesla.

Simon Weinmüller (G5, 15:15)

MR-zero meets FLASH – Controlling the transient signal decay in gradient- and rf-spoiled gradient echo sequences.

Dr. Dietrich Kilian (G6, 15:45)

Development of radiofrequency coils for magnetic resonance-guided particle therapy.

Balanced Steady-State Free Precession Enables High-Resolution Dynamic 3D Deuterium Metabolic Imaging of the Human Brain at 7T

Sabina Frese 1*, Bernhard Strasser 1, Lukas Hingerl 1, Elton Montrazi 2, Lucio Frydman 2, Stanislav Motyka 1+3, Viola Bader 1, Anna Duguid 1, Aaron Osburg 1, Martin Krssak 4, Rupert Lanzenberger 5, Thomas Scherer 4, Wolfgang Bogner 1+3, Fabian Niess 1

1 High Field MR Center, Department of Biomedical Imaging and Image-Guided Therapy, Medical University of Vienna, Lazarettgasse 14, Vienna A-1090, Austria

2 Department of Chemical and Biological Physics, Weizmann Institute of Science, Rehovot, Israel

3 Christian Doppler Laboratory for MR Imaging Biomarkers (BIOMAK), Austria

4 Department of Medicine III, Division of Endocrinology and Metabolism, Medical University of Vienna, Austria

5 Department of Psychiatry and Psychotherapy, Comprehensive Center for Clinical Neurosciences and Mental Health (C3NMH), Medical University of Vienna, Austria.

* indicates presenter

Abstract: This study introduces a novel balanced steady-state free precession (bSSFP) acquisition combined with fast non-Cartesian sampling to enhance deuterium metabolic imaging (DMI) of the human brain at 7T. Six healthy subjects underwent dynamic DMI after oral administration of [6,6']-²H-glucose. Compared to conventional spoiled FID-CRT methods, the bSSFP-CRT approach tripled the signal-to-noise ratio, enabling a two-fold increase in spatial resolution. Significant correlations between brain and systemic glucose levels were observed using continuous glucose monitoring. This minimally invasive method enables high-resolution mapping of glucose uptake and metabolism, offering strong potential for clinical translation and improved understanding of brain metabolic dynamics.

Motivation: The mammalian brain primarily uses glucose (Glc) to fuel neuronal activity.[1,2] Many neurological conditions, including neurodegenerative diseases and brain tumors, are characterized by impaired brain Glc uptake and metabolism.[3–7] While [18F]-FDG-PET is the gold standard for imaging Glc uptake, it doesn't provide information on downstream metabolism.[8,9] Deuterium (²H) metabolic imaging (DMI) is a new magnetic resonance technique that non-invasively images Glc uptake and its downstream metabolism into neurotransmitters like glutamate+glutamine (Glx) or lactate (Lac). DMI uses ²H-labeled glucose solutions and benefits from spectral sparsity and the low natural abundance of ²H in water and lipids, eliminating the need for their suppression and simplifying water referencing.[10–13] However, clinical translation of DMI is hampered by its inherently low sensitivity and long acquisition times, which limit spatial resolution. While fast spatial-spectral k-space sampling with non-Cartesian trajectories has improved spatial resolution and differentiation between gray and white matter[14,15], further increases are still needed to detect smaller metabolic changes or lower concentrations. To enhance sensitivity and spatial

resolution, balanced steady-state free precession (bSSFP) acquisition schemes can be used.[16,17] Given deuterium's quadrupolar nature, DMI is well-suited for bSSFP, with preclinical studies showing up to four-fold signal-to-noise ratio (SNR) increases at 15.2T.[18-20] This study aimed to develop a bSSFP sequence combined with a concentric ring trajectory (CRT) readout to boost SNR, enabling dynamic, high-resolution, whole-brain DMI in humans at 7T.

Materials & Methods: Six healthy volunteers (27+/-2years, 4 male/2 female) participated after providing informed consent. Participants wore an MR-safe continuous glucose monitor (CGM, FreeStyle Libre®3)[21] for baseline glucose assessment. After overnight fasting, they orally consumed ²H-labeled glucose (0.8g/kg body weight) dissolved in water immediately before MRI measurements at a 7T MR system with a dual-tuned ²H/1H head coil.

A bSSFP acquisition scheme was combined with concentric ring trajectory (CRT) readout. This bSSFP-CRT sequence was optimized for detecting ²H-water, ²H-Glc, ²H-Glx, and ²H-Lac. Phantom measurements were conducted to assess SNR in bSSFP-CRT compared to conventional FID-CRT acquisitions for ²H-water, ²H-Glc, and ²H-Lac.

Dynamic in vivo DMI measurements were conducted over 80 minutes after oral ²H-Glc administration, acquiring 10 whole-brain datasets using FID-CRT (first and last) and bSSFP-CRT (second to ninth) sequences. Three participants were scanned at matched nominal spatial resolution (0.75 mL isotropic voxel volume), the other three at increased spatial resolution (0.36 mL isotropic voxel volume) using bSSFP-CRT. The protocol was complemented by a high-resolution 1H-B0 map[22] and a T1-weighted anatomical image.

Offline image reconstruction included B0-inhomogeneity correction. Spectral fitting for FID-CRT data used LCModel, while bSSFP-CRT data underwent metabolic separation with an adapted k-space IDEAL

algorithm. High-resolution T1-weighted images were used for segmentation of GM and WM. ^2H -Glc and ^2H -Glx concentrations were estimated using natural abundance ^2H -water signals as internal reference, accounting for relaxation times and fractional water content.[23,24] Linear mixed-effects models analyzed the relationship between brain ^2H -Glc concentrations and systemic glucose levels from CGM.

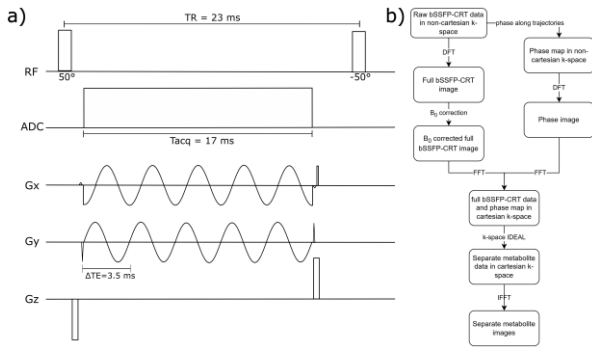


Fig. 1: a) Sequence diagram of novel balanced Steady State Free Precession (bSSFP) sequence combined with concentric ring trajectory (CRT) k-space readout. b) Image reconstruction and metabolite separation algorithm based on Iterative Decomposition algorithm with echo asymmetry and least-squares estimation (IDEAL).

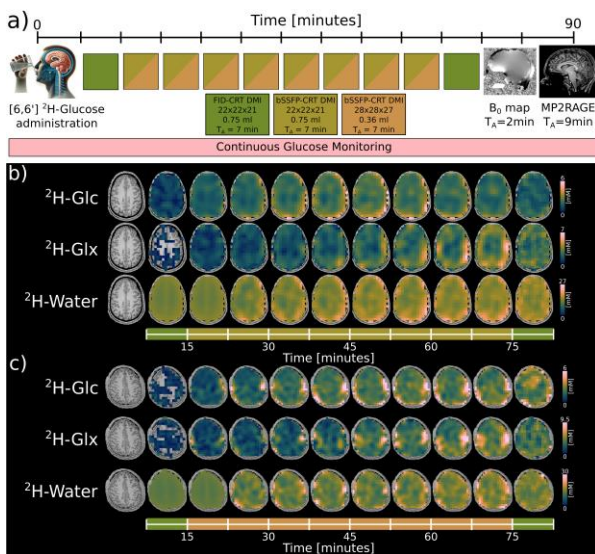


Fig. 2: a) Experimental protocol for dynamic DMI measurements in six healthy volunteers – three were scanned at matched spatial resolution (0.75ml isotropic), three with higher spatial resolution (0.36ml isotropic) in bSSFP-CRT acquisitions. Representative axial time courses at matched (b) and increased (c) spatial resolution show metabolite dynamics across acquisition schemes.

Results: In phantom studies, bSSFP-CRT DMI yielded higher SNRs for ^2H -water (~63) and ^2H -Glc (~40) compared to FID-CRT (^2H -water: ~23, ^2H -Glc: ~13). SNR for ^2H -Lac could not be reliably assessed due to B₀ inhomogeneities. This translated to SNR gains of 2.74 (^2H -water) and 3.07 (^2H -Glc) for bSSFP-CRT.

In vivo, dynamic brain DMI maps showed improved spatial resolution (0.36 ml vs 0.75 ml) with bSSFP-CRT. Data from six volunteers showed comparable regional concentrations of ^2H -Glc, ^2H -Glx, and ^2H -water across sequences. No significant differences in ^2H -Glc and ^2H -water concentrations were found between acquisition schemes. However, ^2H -Glx levels were significantly higher in GM and WM using bSSFP-CRT. GM consistently showed higher metabolite concentrations than WM across both methods. Intra-subject CoVs were similar between schemes, supporting measurement consistency. No ^2H -Lac+Lip analysis was done due to low ^2H -Lac signal in healthy volunteers.

Comparison to CGM revealed that interstitial glucose levels peaked ~48 min post-intake (9.21±1.65 mM) and decreased thereafter. Brain ^2H -Glc levels measured via DMI paralleled this trend, although delayed and blunted. Linear mixed models showed CGM significantly predicted brain glucose in GM ($\beta_1=0.47$, $p=0.01$) and WM ($\beta_1=0.36$, $p=0.03$). The ratio of brain to interstitial glucose AUC was 0.29±0.07.

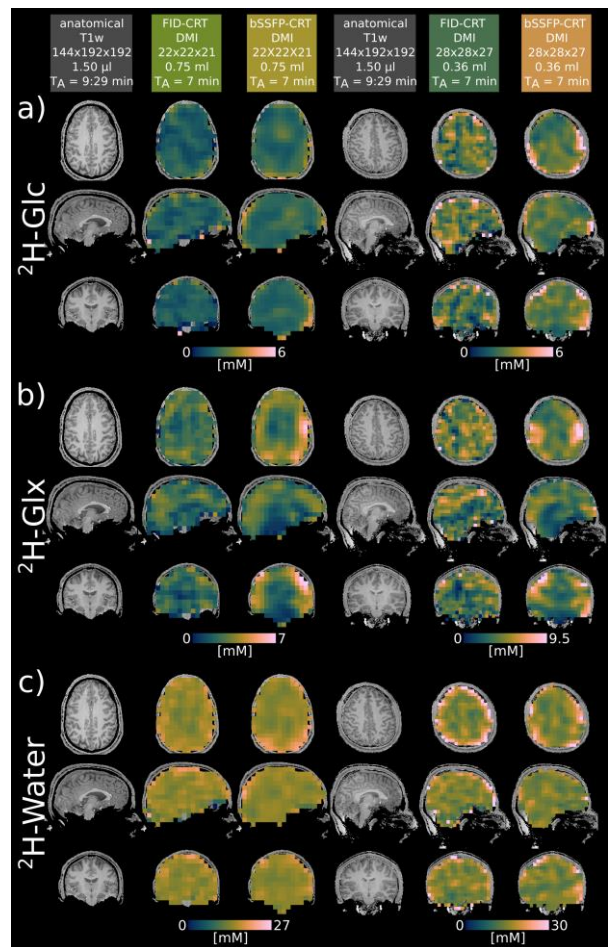


Fig. 3: Representative metabolic maps of ^2H -Glc (a), ^2H -Glx (b), and ^2H -water (c) of 2 subjects imaged with 0.75 mL (left 2 columns) and 0.36 mL (right 2 columns) isotropic spatial resolution with the 2 acquisition schemes, FID-CRT and bSSFP-CRT, >1 hour after oral administration of ^2H -Glc.

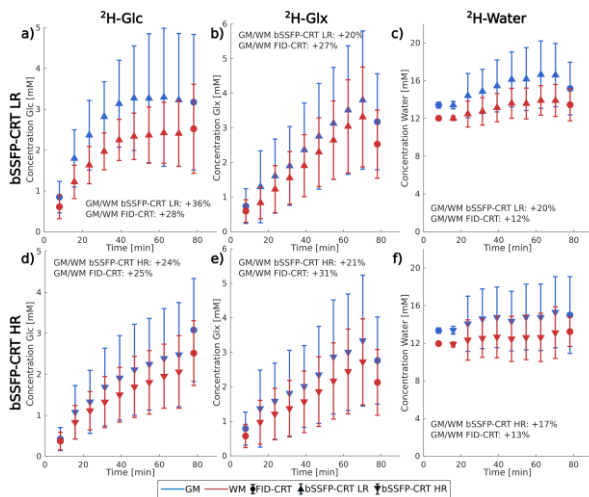


Fig. 4: Time courses of $^2\text{H-Glc}$ (a,d), $^2\text{H-Glx}$ (b,e), and $^2\text{H-water}$ (c,f) showed significant GM/WM contrasts across acquisition schemes and resolutions (top row matched 0.75mL isotropic, bottom row bSSFP-CRT 0.36mL, FID-CRT 0.75mL isotropic). bSSFP-CRT yielded higher $^2\text{H-Glx}$ concentrations than FID-CRT in GM and WM.

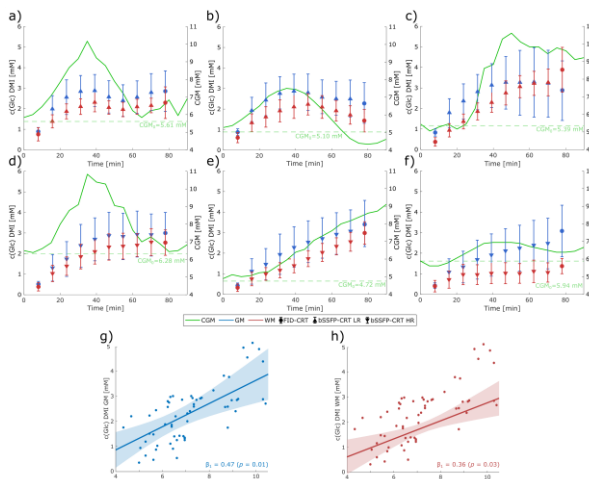


Fig. 5: Glc in GM and WM (DMI) and interstitial fluid (CGM) were tracked in six subjects (a-f). Significant correlations were found between CGM and DMI Glc (GM: $\beta=0.47$, $p=0.01$ (g); WM: $\beta=0.36$, $p=0.03$ (h)), indicating systemic glucose changes are reflected in brain metabolism.

Discussion: This study presents a novel bSSFP-CRT acquisition scheme for dynamic deuterium metabolic imaging (DMI) of the human brain at 7T, offering up to 3-fold SNR improvement over conventional FID-CRT methods. This enhancement enabled higher spatial resolution (0.36 ml vs. 0.75 ml isotropic) while maintaining comparable metabolite quantification of $^2\text{H-Glc}$, $^2\text{H-Glx}$ and $^2\text{H-water}$. The improved SNR of bSSFP-CRT allowed better delineation of small structures and quantification of low concentrations at the beginning of dynamic DMI experiments not feasible using FID-CRT acquisitions.

Dynamic mapping over 80 minutes post $^2\text{H-glucose}$ ingestion showed similar $^2\text{H-Glc}$ and $^2\text{H-water}$ concentrations between acquisition schemes, with slightly higher $^2\text{H-Glx}$ levels observed using bSSFP-CRT. Despite differences in T1-weighting, both methods yielded comparable GM/WM contrast for $^2\text{H-Glc}$, while $^2\text{H-Glx}$ contrast varied due to its longer T1.[24]

Brain DMI was complemented by MR-compatible CGM, offering a noninvasive reference of systemic glucose trends. CGM and brain $^2\text{H-Glc}$ time courses were significantly correlated, showing similar dynamics but with dampened amplitudes in brain. The CGM-to-DMI AUC ratio was consistent across subjects, though larger cohorts are needed for clinical interpretation.

Phantom studies confirmed SNR gains for $^2\text{H-Glc}$ and $^2\text{H-water}$ but not $^2\text{H-Lac}$, due to B_0 inhomogeneities. No reliable $^2\text{H-Lac}$ levels were detected in healthy brain tissue due to low lactate levels. Future improvements and measurements in tumors could enable reliable $^2\text{H-Lac}$ detection. While current DMI spatial resolution remains lower than FDG-PET, further post-processing (e.g., denoising) and bSSFP-CRT refinements may support clinical translation by improving resolution and reducing partial volume effects.

Conclusion: This study demonstrates the feasibility of dynamic deuterium metabolic imaging to noninvasively map whole-brain glucose metabolism with up to 3-fold increased signal-to-noise ratio and 2-fold increase of spatial resolution using a novel bSSFP pulse sequence combined with fast spatial-spectral k-space sampling at 7T. Dynamic brain glucose concentrations were complemented by simultaneously measuring systemic glucose levels in interstitial fluid minimally invasively using a continuous glucose monitoring sensor that is used in diabetes care. This suggests significant potential for clinical applications with improved characterization of local pathologic brain metabolism in conjunction with systemic metabolic aberrations in a minimally invasive way.

Acknowledgements: This work was supported by the National Institute of Health NIH R01EB031787, the Austrian Science Fund: WEAVE I 6037 & KLI 1106, the Christian Doppler Laboratory for MR Imaging Biomarkers (BIOMAK) and the European Union (ERC, GLUCO-SCAN, 101088351). The Weizmann coworkers were supported by the Israel Ministry of Health, and by the Israel Cancer Research Foundation. Conflicts of interest R. Lanzenberger received investigator-initiated research funding from Siemens Healthcare regarding

clinical research using PET/MR. He is a shareholder of the start-up company BM Health GmbH since 2019.

References:

1. Diemel GA. Brain Glucose Metabolism: Integration of Energetics with Function. *Physiol Rev.* 2019;99(1):949-1045.
2. Magistretti PJ, et al. A cellular perspective on brain energy metabolism and functional imaging. *Neuron.* 2015;86(4):883-901.
3. Koppenol WH, et al. Otto Warburg's contributions to current concepts of cancer metabolism. *Nature Reviews Cancer.* 2011;11(5):325-37.
4. Manji H, et al. Impaired mitochondrial function in psychiatric disorders. *Nature Reviews Neuroscience.* 2012;13(5):293-307.
5. Norat P, et al. Mitochondrial dysfunction in neurological disorders: Exploring mitochondrial transplantation. *npj Regenerative Medicine.* 2020;5(1):22.
6. Zhang S, et al. Cognitive dysfunction in diabetes: abnormal glucose metabolic regulation in the brain. *Front Endocrinol (Lausanne).* 2023;14:1192602.
7. Adamson PM, et al. Deuterium metabolic imaging for 3D mapping of glucose metabolism in humans with central nervous system lesions at 3T. *Magn Reson Med.* 2024;91(1):39-50.
8. Almuhaideb A, Papathanasiou N, Bomanji J. 18F-FDG PET/CT imaging in oncology. *Ann Saudi Med.* 2011;31(1):3-13.
9. Hahn A, et al. Quantification of Task-Specific Glucose Metabolism with Constant Infusion of 18F-FDG. *J Nucl Med.* 2016;57(12):1933-40.
10. De Feyter HM, et al. Deuterium metabolic imaging (DMI) for MRIbased 3D mapping of metabolism in vivo. *Science Advances.* 2018;4(8):eaat7314.
11. Lu M, et al. Quantitative assessment of brain glucose metabolic rates using in vivo deuterium magnetic resonance spectroscopy. *J Cereb Blood Flow Metab.* 2017;37(11):3518-30.
12. Ruhm L, et al. Deuterium metabolic imaging in the human brain at 9.4 Tesla with high spatial and temporal resolution. *Neuroimage.* 2021;244:118639.
13. Serés Roig E, et al. Deuterium metabolic imaging of the human brain in vivo at 7 T. *Magnetic Resonance in Medicine.* 2023;89(1):29-39.
14. Niess F, et al. Whole-brain deuterium metabolic imaging via concentric ring trajectory readout enables assessment of regional variations in neuronal glucose metabolism. *Human Brain Mapping.* 2024;45(6):e26686.
15. Nam KM, et al. Deuterium echo-planar spectroscopic imaging (EPSI) in the human liver in vivo at 7 T. *Magnetic Resonance in Medicine.* 2023;90(3):863-74.
16. Scheffler K, et al. Magnetization preparation during the steady state: Fatsaturated 3D TrueFISP. *Magnetic Resonance in Medicine.* 2001;45(6):1075-80.
17. Scheffler K, Lehnhardt S. Principles and applications of balanced SSFP techniques. *European Radiology.* 2003;13(11):2409-18.
18. Peters DC, et al. Improving deuterium metabolic imaging (DMI) signal-to-noise ratio by spectroscopic multi-echo bSSFP: A pancreatic cancer investigation. *Magnetic Resonance in Medicine.* 2021;86(5):2604-17.
19. Montrazi ET, et al. Deuterium imaging of the Warburg effect at sub-millimolar concentrations by joint processing of the kinetic and spectral dimensions. *NMR in Biomedicine.* 2023;36(11):e4995.
20. Montrazi ET, et al. High-sensitivity deuterium metabolic MRI differentiates acute pancreatitis from pancreatic cancers in murine models. *Scientific Reports.* 2023;13(1):19998.
21. Matievich W, Kiaie N, Dunn TC. Safety and Functional Integrity of Continuous Glucose Monitoring Sensors When Used During Radiologic Procedures Under High Exposure Conditions. *J Diabetes Sci Technol.* 2023;17(6):1634-43.
22. Eckstein K, et al. Computationally Efficient Combination of Multi-channel Phase Data From Multi-echo Acquisitions (ASPIRE). *Magnetic Resonance in Medicine.* 2018;79(6):2996-3006.
23. Gasparovic C, et al. Use of tissue water as a concentration reference for proton spectroscopic imaging. *Magnetic Resonance in Medicine.* 2006;55(6):1219-26.
24. Bader V, et al. Concentric Ring Trajectory Sampling With k-Space Reordering Enables Assessment of Tissue-Specific T(1) and T(2) Relaxation for (2)HLabeled Substrates in the Human Brain at 7 T. *NMR Biomed.* 2025;38(2):e5311.

Assessment of tumor cell invasion and radiotherapy response in experimental glioma by Magnetic Resonance Elastography

Hannah Fels-Palesandro 1+2*, Sophie Heuer 3+4, Berin Boztepe 1+6, Yannik Streibel 1, Johannes Ungermann 1, Chenchen Pan 3+4, Jonas G. Scheck 1+2, Manuel Fischer 1, Volker J. Sturm 1, Daniel D. Azorin 3+4+5, Kianush Karimian-Jazi 1, Giacomo Annio 7, Amir Abdollahi 2, Ina Weidenfeld 1+2, Wolfgang Wick 3+4, Varun Venkataramani 3+4, Sabine Heiland 1, Frank Winkler 3+4, Martin Bendszus 1, Ralph Sinkus 7+8, Michael O. Breckwoldt MD 1+6# and Katharina Schregel 1#

1 Department of Neuroradiology, Heidelberg University Hospital, Heidelberg, Germany

2 Clinical Cooperation Unit Translational Radiation Oncology, German Cancer Research Center (DKFZ), Heidelberg, Germany

3 Department of Neurology and National Center for Tumor disease (NCT), Heidelberg University Hospital, Heidelberg, Germany

4 Clinical Cooperation Unit Neurooncology, German Cancer Research Center (DKFZ), Heidelberg, Germany

5 Department of Biosystems Science and Engineering, ETH Zurich, Schanzenstrasse 44, 4056, Basel, Switzerland

6 Clinical Cooperation Unit Neuroimmunology and Brain Tumor Immunology, German Cancer Research Center (DKFZ), Heidelberg, Germany

7 INSERM UMRS1148 - Laboratory for Vascular Translational Science, University Paris, Paris, France

* presenter

shared senior authorship

Abstract: Although MRI is one of the main pillars in glioblastoma diagnosis and treatment monitoring, clinically-employed sequences have shortcomings regarding the detection of tumor invasion and therapy-associated parenchyma changes. The goal of this study was therefore to determine whether MRE and DTI could improve detection of tumor cell invasion and radiotherapy effects, as these sequences are sensitive to tissue microstructure. To this end, 23 tumor-bearing mice underwent MRI-scans for up to 16 weeks, with a subgroup undergoing additional radiotherapy. While MRE was the only metric sensitive to early tumor invasion, radiotherapy effects were better characterized by both MRE and the DTI-derived ADC.

Motivation: Glioblastoma is the most common primary malignant brain tumor, showing a highly invasive growth pattern as one of its key characteristics (1). While MRI is an essential tool for diagnosis and treatment monitoring, clinically-employed sequences fail to delineate tumor invasion and to differentiate therapy-induced tissue changes (1,2). Magnetic Resonance Elastography (MRE) is an imaging technique that quantifies biomechanical tissue properties, particularly “tissue stiffness” (IG*1), thereby delivering information on tissue microstructure (3–5). Diffusion Tensor Imaging (DTI) has already been investigated in neuro-oncological imaging, and the Apparent Diffusion Coefficient (ADC) and the Fractional Anisotropy (FA) have been proposed as markers of tumor cell density and infiltration, respectively (6).

We therefore evaluated in a preclinical invasive glioma model whether these advanced MRI-techniques can improve the delineation of tumor cell invasion and therapy-associated tissue changes. This was guided by the hypothesis that the brain parenchyma’s structural organization and its resulting biomechanical properties are affected differently by tumor invasion and

radiotherapy and thus amenable to microstructure-sensitive MRI-sequences.

Materials & Methods: Patient-derived S24-glioma cells were orthotopically implanted into the right striatum of 23 male NMRI mice. Thirteen mice (“radiotherapy group”) underwent tumor-focused radiotherapy (3x6 Gy) in week 9 after tumor implantation, the other 10 animals served as untreated, tumor-bearing controls (“treatment-controls”). Longitudinal imaging was performed on a 9.4T-MRI scanner (BioSpec 94/20USR, Bruker BioSpin GmbH, Ettlingen, Germany) in weeks 4, 8, and 12, with an additional scan at week 16 for a subset of irradiated animals (n=5). The imaging protocol included a 2D and 3D T2-weighted (T2w)-sequence, a DTI-sequence, and a MRE-sequence at 900Hz vibration frequency (sequence details provided in Table1/Fig.1A). Following their respective final imaging session, the mice were sacrificed and brains were harvested. Subsequently, they were prepared for tissue clearing followed by 3D-light sheet microscopy (LSM). Additionally, conventional histology (H&E and Alcian blue staining) was performed on a subset of samples (n=7).

All MRI data were analyzed using 3D Slicer (3D Slicer for Windows/macOS, versions 5.1.0&5.4.0, www.slicer.org) (7), MRE data were analyzed additionally with dedicated in-house software (ROOT environment, CERN, Meyrin, Switzerland) (5). For quantitative analysis, imaging data were co-registered, and the tumor core and corpus callosum were manually segmented on 2D T2w-sequences for all measurement time points. Mean values for IG*1, ADC, and FA were assessed and compared within these regions. An illustration of the experimental set-up is provided in Fig.1B. Statistical analysis was performed with paired and unpaired t-tests (Prism; GraphPad Software Inc, La Jolla, CA, USA), values are expressed as mean±standard error of mean, a p-value≤0.05 was considered significant.

Results: Tumor growth was visible on T2w-images as a faint hyperintensity that increased over time, with an exponential increase in volume between weeks 8 and 12 (Fig.1C).

A Table 1. Parameters of MRI and MRE sequences.

sequence	TR (ms)	TE (ms)	flip angle	averages	acquisition matrix	FOV (mm)	slice thickness (mm)	number of slices	duration
3D T2w TurboRARE	1800	72.5	90	1	200 x 200	20 x 10 x 12	0.1	120	10 min 48 s
2D T2w TurboRARE: axial	2500	33	90	2	256 x 256	20 x 20	0.7	20	2 min 40 s
2D EPI DTI: axial	3400	20	90	1	96 x 128	12 x 15	0.7	17	7 min 56 s
3D MSME MRE: 900 Hz vibration frequency; axial	1500	26.67	90	1	64 x 64	19.2 x 19.2	0.3	9	19 min 12 s

Abbreviations: DTI = diffusion tensor imaging, EPI = echo planar imaging, FOV = field of view, MRE = magnetic resonance elastography, MSME = multi-slice multi-echo, RARE = rapid acquisition with relaxation enhancement, TE = echo time, TR = repetition time.

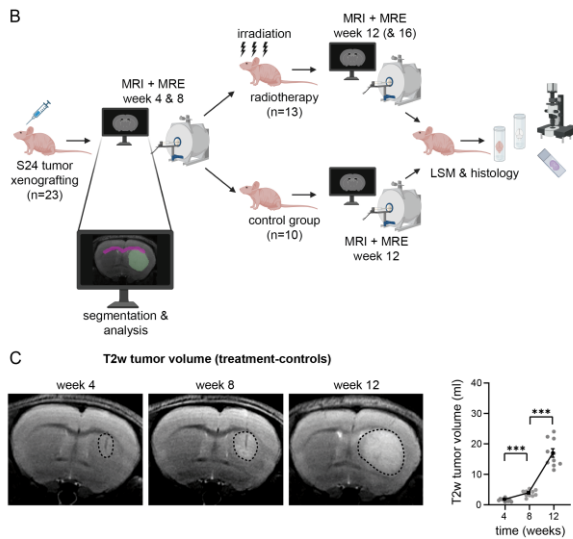


Fig. 1: In A the sequence parameters are provided. B illustrates the experimental set-up. In C the progressive growth of the tumor core in treatment-controls is shown and quantified. Dotted lines indicate the tumor core. Statistical analysis was performed with paired t-tests, *** signifies $p \leq 0.001$.

Tumor cell invasion of the corpus callosum was histologically confirmed by LSM in week 8 (Fig.2A) while remaining occult on T2w, ADC, and FA (Fig.2B,C). However, the callosal stiffness increased significantly from week 4 ($IG^*I = 4.44 \pm 0.22 \text{ kPa}$) to week 8 ($IG^*I = 5.31 \pm 0.29 \text{ kPa}$). Additionally, at later time points (weeks 12 and 16), a visual association between clusters of increased tissue stiffness and LSM-confirmed tumor cell invasion in the ipsi- and contralateral hemispheres could be established (Fig.2D).

The tumor core of treatment-controls showed – alongside with tumor growth – a significant ADC-increase from week 8 to week 12 (respective means 610.2 ± 12.27 and $711.2 \pm 13.42 \times 10^{-6} \text{ mm}^2/\text{s}$, Fig.3A) while its stiffness behavior was biphasic with an increase from week 4 to week 8 followed by a drop in week 12 (respective means $3.9 \pm 0.32 \text{ kPa}$, $5.51 \pm 0.30 \text{ kPa}$ and $4.24 \pm 0.29 \text{ kPa}$, Fig.3A), which correlated

histologically with a progressive increase in tumor cell density (Fig.3B) and a destruction of the extracellular matrix (ECM, Fig.3C).

Radiotherapy temporarily slowed tumor growth, resulting in significantly smaller tumor volumes ($10.96 \pm 1.04 \text{ mm}^3$) compared to treatment-controls ($16.88 \pm 1.40 \text{ mm}^3$) in week 12 (Fig.4A,B). This was accompanied by a decelerated ADC-increase and a delayed tumor core softening (Fig.4A). Histologically, the tumor cell density in week 12 was lower and the ECM was more preserved compared to treatment-controls (Fig.5A,B). However, radiotherapy did not stop tumor progression, as the tumor volume and ADC increased and its stiffness dropped in week 16.

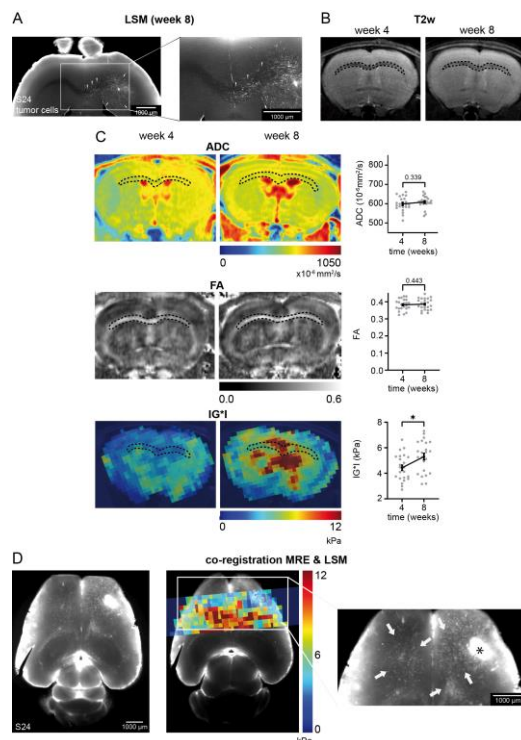


Fig. 2: A shows the callosal tumor invasion in LSM, which is not detectable on corresponding T2w (B). In C callosal ADC-, FA-, and IG^*I -values from week 4 to week 8 are visualized and quantified. D illustrates the visual association between stiffer clusters and tumor invasion at later time points (week 12 & 16). Statistical analysis was performed with paired t-tests, * signifies p -value ≤ 0.05 .

Discussion: While conventional MRI-sequences have known shortcomings in detecting tumor cell invasion (1,8), MRE is a promising tool that assesses microstructural changes by measuring tissue biomechanics (4). In this study, early tumor cell invasion into the corpus callosum was detected as significant stiffening on MRE, a finding that was completely invisible on T2w-images and not captured by DTI. This early stiffening is likely caused by the infiltration of progressively interconnected tumor cells that invade

along existing, still intact fiber tracts (9,10). The FA was insensitive to this early invasion, presumably because the invading cells aligned with the fiber tracts, thus preserving the callosal overall anisotropy (10).

Radiotherapy slowed but did not stop tumor progression as histology demonstrated and which was reflected by a delayed tumor core softening and a slower ADC-increase, suggesting that MRE and DTI can help to better characterize therapy-induced changes in the tumor's micro-architecture.

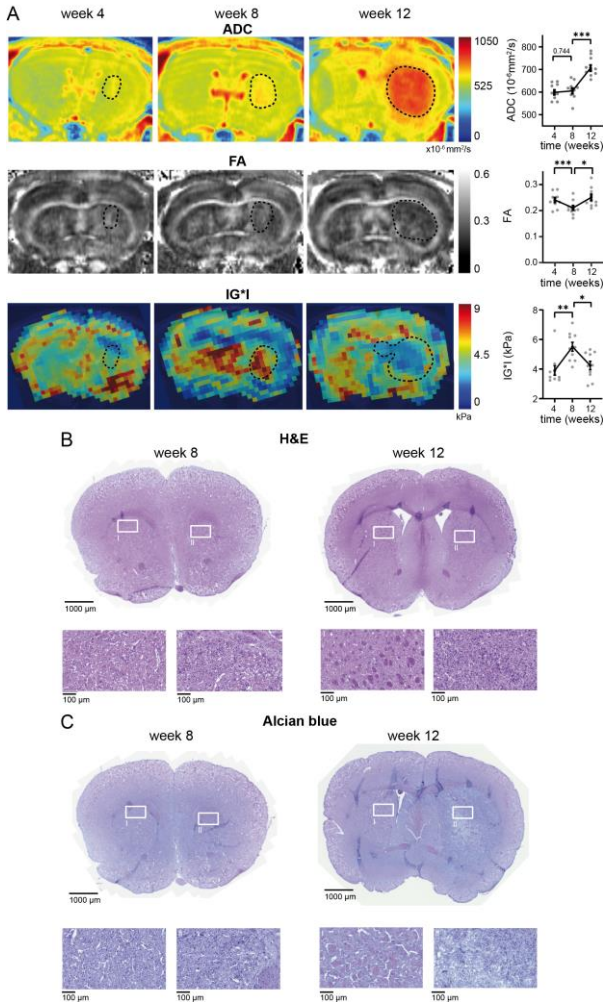


Fig. 3: A visualizes and quantifies the ADC-, FA-, and IG*1-values of the tumor core in treatment-controls. The H&E staining in B shows an increasing tumor cell density from week8 to week12 (magnifications II), the Alcian blue staining in C a progressively destroyed ECM (magnifications II). Statistical analysis was performed with paired t-tests, * signifies p-value≤0.05, **≤0.01 and ***≤0.001.

The biphasic evolution of tumor core stiffness—initial stiffening followed by significant softening—likely reflects the transition from organized cellular invasion to widespread destruction of the brain parenchyma. This later-stage softening aligns with findings from previous preclinical MRE-studies in which established gliomas were examined (11–13).

Given the large radii of S24-tumor cells (10µm) (14), the corresponding ADC-increase, contrary to typical clinical findings, likely stems from the strong gradients and short diffusion time of preclinical MRI-scanners, thus reflecting primarily intra- rather than extracellular diffusion processes (15).

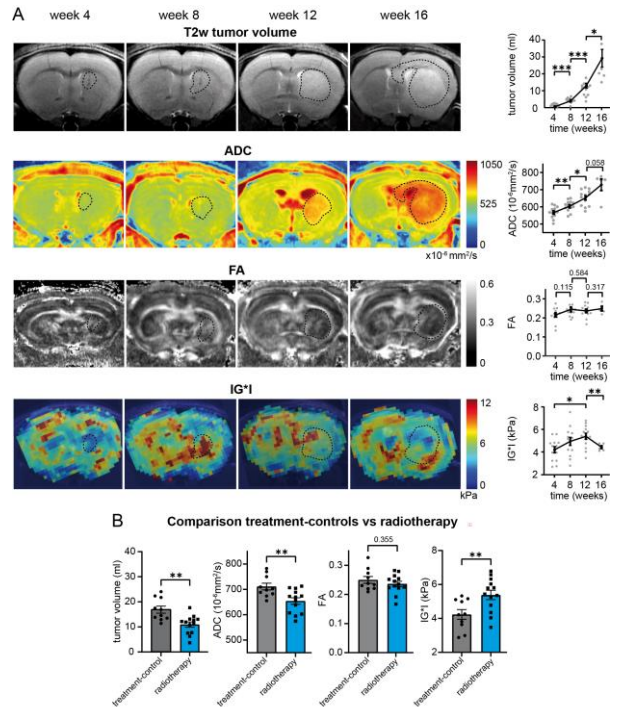


Fig. 4: A visualizes and quantifies the development of the tumor core volume, its ADC, FA and IG*1 under radiotherapy. A comparison between the treatment-controls and radiotherapy group in week 12 is shown in B. Statistical analysis was performed with paired and unpaired t-tests, * signifies p-value≤0.05, **≤0.01 and ***≤0.001.

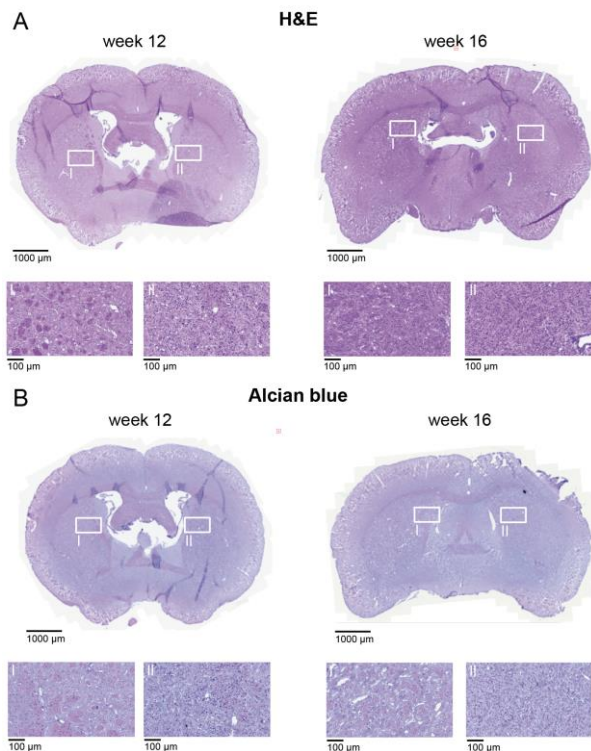


Fig. 5: A shows the H&E staining of the radiotherapy group in week12&16. When comparing to treatment-controls in week12 the tumor core cell density is lower while it increases drastically in week16. B shows the ECM-destruction within the tumor core which is (compared to treatment-controls) analogously lower in week12 and progresses markedly in week16.

Conclusion: In this study, MRE demonstrated high sensitivity to early, histologically-confirmed tumor cell infiltration, which was occult on conventional T2w-imaging and not detected by DTI-metrics.

Furthermore, the imaging characteristics derived from MRE and DTI could be directly related to histological findings of both progressive tumor growth and radiotherapy effects, thereby rendering valuable information complementary to clinically used MRI-sequences.

In conclusion, MRE is a highly promising tool for neuro-oncological imaging allowing for more precise delineation and detection of the tumor invasion zone as well as improved therapy monitoring.

References:

1. Sahn, F. et al. Addressing diffuse glioma as a systemic brain disease with single-cell analysis. *Arch. Neurol.* 69, 523–526 (2012).
2. Wen, P. Y. et al. RANO 2.0: Update to the Response Assessment in Neuro-Oncology Criteria for High- and Low-Grade Gliomas in Adults. *J. Clin. Oncol.* 41, 5187–5199 (2023).
3. Muthupillai, R. et al. Magnetic resonance elastography by direct visualization of propagating acoustic strain waves. *Science* 269, 1854–1857 (1995).
4. Sack, I., Jöhrens, K., Würfel, J. & Braun, J. Structure-sensitive elastography: on the viscoelastic powerlaw behavior of in vivo human tissue in health and disease. *Soft Matter* 9, 5672–5680 (2013).
5. Green, M. A., Bilston, L. E. & Sinkus, R. In vivo brain viscoelastic properties measured by magnetic resonance elastography. *NMR Biomed.* 21, 755–764 (2008).
6. Lu, S., Ahn, D., Johnson, G. & Cha, S. Peritumoral diffusion tensor imaging of high-grade gliomas and metastatic brain tumors. *AJNR Am. J. Neuroradiol.* 24, 937–941 (2003).
7. Fedorov, A. et al. 3D Slicer as an image computing platform for the Quantitative Imaging Network. *Magn. Reson. Imaging* 30, 1323–1341 (2012).
8. Ellingson, B. M., Chung, C., Pope, W. B., Boxerman, J. L. & Kaufmann, T. J. Pseudoprogression, radionecrosis, inflammation or true tumor progression? challenges associated with glioblastoma response assessment in an evolving therapeutic landscape. *J. Neurooncol.* 134, 495–504 (2017).
9. Venkataramani, V. et al. Glutamatergic synaptic input to glioma cells drives brain tumour progression. *Nature* 573, 532–538 (2019).
10. Schubert, M. C. et al. Deep intravital brain tumor imaging enabled by tailored three-photon microscopy and analysis. *Nat. Commun.* 15, 7383 (2024).
11. Schregel, K. et al. Magnetic Resonance Elastography reveals effects of anti-angiogenic glioblastoma treatment on tumor stiffness and captures progression in an orthotopic mouse model. *Cancer Imaging Off. Publ. Int. Cancer Imaging Soc.* 20, 35 (2020).
12. Jamin, Y. et al. Exploring the biomechanical properties of brain malignancies and their pathologic determinants in vivo with magnetic resonance elastography. *Cancer Res.* 75, 1216–1224 (2015).
13. Li, J. et al. Investigating the Contribution of Collagen to the Tumor Biomechanical Phenotype with Noninvasive Magnetic Resonance Elastography. *Cancer Res.* 79, 5874–5883 (2019).
14. Osswald, M. et al. Brain tumour cells interconnect to a functional and resistant network. *Nature* 528, 93–98 (2015).

Quantitative Sodium Magnetic Resonance Imaging of the Human Torso at 7 Tesla

Anna K. Scheipers 1+2

1 Medical Physics in Radiology, German Cancer Research Center (DKFZ) Heidelberg, Heidelberg, Germany,
2 Faculty of Physics and Astronomy, Heidelberg University, Heidelberg, Germany

Abstract: This study presents a noninvasive method for determining the apparent tissue sodium concentration (aTSC) across a large field-of-view in the human torso using ^{23}Na MRI at 7T. A reference vial setup together with T_1 , measured B_1^+ , and setup-specific simulated B_1^- corrections enabled accurate quantification, with errors under 3.4% in phantom measurements. Sliding window reconstructions captured renal aTSC changes during a water load event. Furthermore, a dual-nuclei setup enabled combined ^1H and quantitative ^{23}Na MRI over a $(400\text{mm})^3$ field-of-view in ≤ 47 minutes during free breathing. Mean aTSC values were measured for the liver $((36\pm 6)\text{mM})$, spleen $((30\pm 7)\text{mM})$, gallbladder $((139\pm 19)\text{mM})$, and other abdominal structures.

Motivation: Although hydrogen is typically used in MRI due to its strong signal, other nuclei, such as sodium, can provide additional physiological insights.¹⁻³ Sodium MRI is sensitive to changes in cell vitality and viability,⁴⁻⁵ because it is tied to the sodium-potassium ATPase and the gradient between intra- and extracellular sodium concentration.⁶ The volume-weighted average of both compartments is called the tissue sodium concentration (TSC).⁷

To account for unknown signal losses due to relaxation, pulse sequence characteristics, etc., the term apparent tissue sodium concentration (aTSC) was used for the determined in vivo sodium concentration values.⁸

Sodium MRI suffers from a low signal-to-noise ratio (SNR), resulting in lower resolution than proton MRI.⁹ Higher magnetic field strengths improve sodium MRI by increasing signal at least linearly.⁹ To enable anatomical segmentation in ^1H images, it is important to acquire sodium and proton images in the same position, especially for large fields-of-view (FOV) such as the torso.

However, at 7T, proton MRI suffers from wavelength-related interference due to the high resonance frequency, causing signal cancellations that can complicate segmentation. Thus, parallel transmit (pTx)¹⁰ and TIAMO¹¹ were used to enhance transmit field homogeneity in the presented work.

Knowledge of the aTSC in healthy subjects can help to distinguish normal physiological changes from disease-related changes.¹²⁻¹⁴ Since abdominal aTSC data is limited, this work investigates renal sodium changes

before, during, and after water consumption.¹⁵ Additionally, combined ^1H and quantitative ^{23}Na imaging at 7T is explored to simultaneously map the aTSC of multiple abdominal tissues in a large FOV.¹⁵

Materials & Methods: All measurements were performed on a 7T whole-body MR system¹⁶ with a custom-built ^{23}Na oval-shaped body coil¹⁷ for ^{23}Na imaging and a custom-built ^1H 32-channel pTx body coil¹⁸ placed behind the scanner bore for the combined measurements. A canister filled with 35mM NaCl solution served as a phantom. A self-developed reference vial setup¹⁵ was positioned below the phantom or volunteer's back to reduce motion artifacts and allow automatic segmentation for faster post-processing. Acquisition parameters and reconstruction settings are shown in Figure 1.

(a)

	^{23}Na B_1^+ map	Quantitative ^{23}Na image (long)	Quantitative ^{23}Na image (short)
T_E (ms)	1.65	1	1
T_R (ms)	150	100	100
Nominal FA (°)	45/90	61	61
Acquired isotropic nominal resolution (mm)	10	6	6
Number of projections	4100	36000	9000
Radial samples	256	256	256
Acquisition time (min:s)	10:15/10:15	60:00	15:00
Pulse duration (ms)	3	1.8	1.8
Readout duration (ms)	5	5	5
Acquired data points in k-space center	0	2	2
Zerofilling factor	3.34	2	2
Filter	Gauss ($\sigma=20\text{mm}$)	Hamming	Hamming
reconstructed FOV (mm ³)	$396 \times 396 \times 396$	$396 \times 396 \times 396$	$396 \times 396 \times 396$

(b)

	Quantitative ^{23}Na image	^{23}Na B_1^+ map (alternating excitation)	^1H 3D GRE-RPE static pTx
T_E (ms)	1	1.65	2.04
T_R (ms)	150	106/168 (alternating)	4.23
Nominal FA (°)	61	45/90 (alternating)	11
Acquired isotropic nominal resolution (mm)	5	20	1.25
Number of projections	10000	1020	-
Number of RPE lines	-	-	1536
Radial samples	256	256	-
Acquisition time (min:s)	25:00	4:39	17:20
Pulse duration (ms)	1.8	3	1
Readout duration (ms)	5	3.33	-
Bandwidth (Hz/Px)	-	-	1042
Acquired data points in k-space center	2	2	-
B_1^+ shim mode	-	-	TIAMO (2 modes)
Zerofilling factor	2	8	-
Filter	Hamming	Gauss ($\sigma=20\text{mm}$)	-
reconstructed FOV (mm ³)	$400 \times 400 \times 400$	$400 \times 400 \times 400$	$400 \times 400 \times 400$

Fig. 1: The acquisition parameters and reconstruction settings are shown for (a) the in vivo ^{23}Na water load measurements and (b) the different sequences employed for the phantom and in vivo ^{23}Na and ^1H MRI measurements (^{23}Na : DA-3DPR¹⁹ with GA projection distribution²⁰, B_1^+ : dual flip angle method²¹, ^1H : GRE-RPE²²).

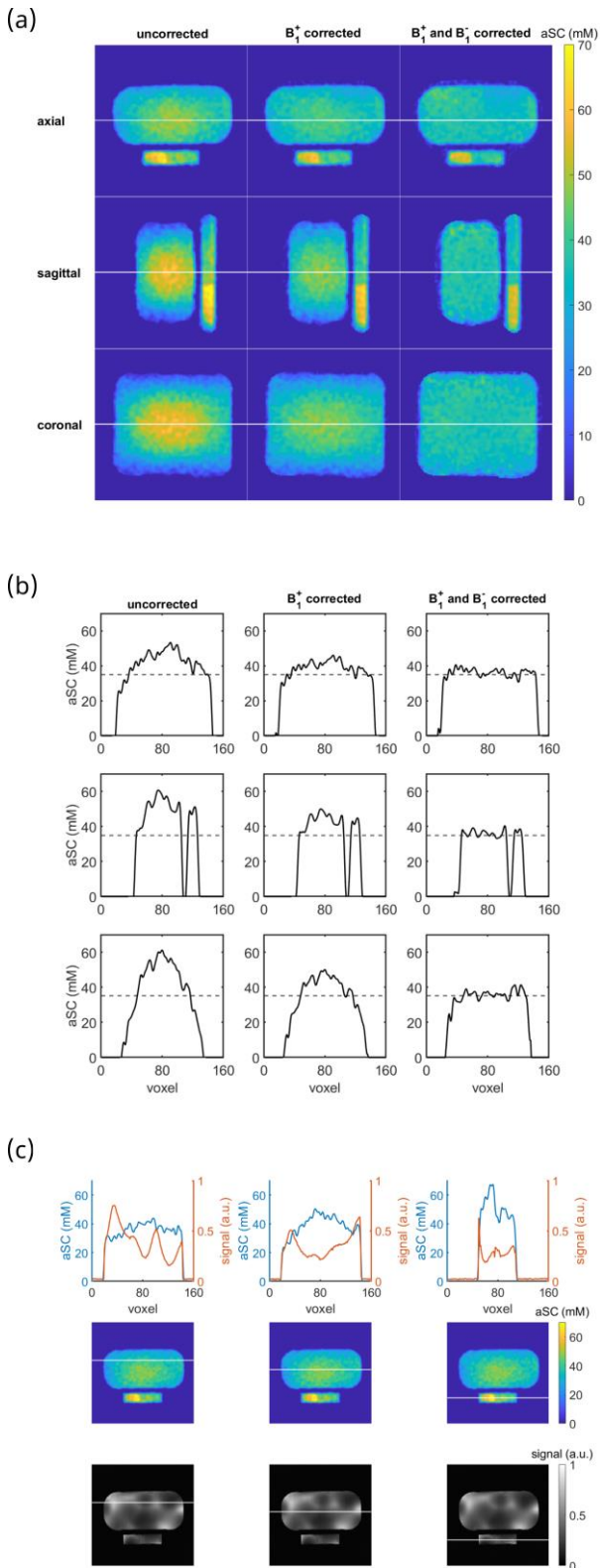


Fig. 2: Influence of the corrections in the phantom (a-b). (b) shows line plots along the lines plotted in (a). The dotted line depicts the 35mM ground truth. (c) shows the alignment of ^{23}Na and ^1H images, with the line plot displaying values along the lines in the second and third row.

^{23}Na T_1 relaxation effects in the reference vials and phantom were corrected according to the FLASH equation. Due to the chosen long repetition times, full relaxation was assumed for tissue.⁶

B_1^+ maps were acquired, and setup-specific B_1^- maps were simulated¹⁷⁺²³ in the phantom and in human voxel models²⁴⁻²⁵ scaled to subject anatomy using CST.²⁶

Quantitative ^{23}Na images were calculated by linear interpolation from reference signals.

Corrections were first evaluated in phantom measurements and then applied in vivo.

Subjects were positioned with their kidneys centered in the sodium coil and imaged during free breathing.

For the time resolved quantitative ^{23}Na MRI, two fasted healthy volunteers were scanned for one hour and fifteen minutes with water intake from a drinking bag 20min into the measurement. Renal aTSC changes were evaluated using sliding window reconstructions.

For the combined proton and sodium imaging, three fasted healthy volunteers were measured. Segmentation of various structures in the uninterpolated ^1H image was performed in MITK²⁷ Interpolated masks were then applied to the ^{23}Na images.

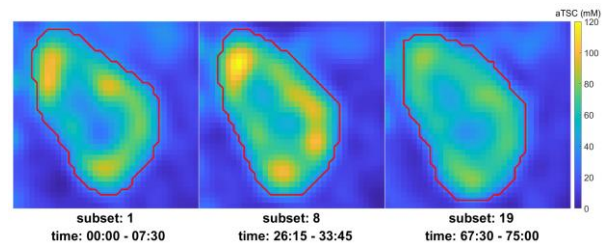


Fig. 3: Close up of the left kidney of volunteer one for water deprivation (subset 1), shortly after drinking (subset 8), and at the end of the measurement (subset 19), with the respective masks for the shown central slice. The 8th and 19th subset were shifted caudally by 2.1cm and 1.2cm, respectively.

Results: B_1^+ and B_1^- corrections reduced the signal over- and underestimations present in uncorrected phantom data (Figure 2a-b) and improved aTSC accuracy with a maximum deviation of 3.4% from the ground truth and a maximum standard deviation of 0.3mM across three measurements.

For the time-resolved quantitative ^{23}Na MRI, renal aTSC was determined in subsets of 4500 projections, corresponding to 7.5min. Since drinking caused visible kidney movement in the first volunteer, individual masks were used for each image subset. Figure 3 shows example masks for three different time points focused on the left kidney of volunteer one.

Furthermore, the medullary-to-cortical aTSC ratio was evaluated before, shortly after, and long after drinking. The ratios determined were 1.71, 2.08, and 1.43 for volunteer one, and 1.56, 1.89, and 1.69 for volunteer two.

Phantom measurements showed that ¹H and quantitative ²³Na MR images have the same large FOV (Figure 2c). aTSC values were determined for the liver, kidney, inferior vena cava, spleen, gallbladder, cerebrospinal fluid (CSF), and intervertebral discs (IVDs). Figure 4 shows examples of segmented structures from the quantitative ²³Na data overlaid with the ¹H data for volunteer two.

The mean aTSC values for the evaluated tissues were consistent across the three volunteers. These values are summarized alongside literature values at 3T and 7T, as well as values from other measurement modalities, in Figure 5.

Some IVD masks were only two to three voxels thick, resulting in small volumes evaluated after interpolating the ¹H images to the lower sodium resolution (see Figure 4).



Fig. 4: Exemplary visualization of the liver, kidneys and a subset of the intervertebral discs masks for volunteer two. The ¹H MR images are not displayed in the masked regions, which allows for a visual assessment of the aTSC for the depicted organs and IVDs.

Discussion: The presented setup enables simultaneous aTSC mapping across a large abdominal region. Comparing aTSC values across individual structures improves post-processing verifiability and provides a more comprehensive understanding of physiology.

Previous studies have limited insight into renal sodium changes during or immediately after water intake because volunteers drank outside the scanner.²⁸⁻³¹ This study's setup enables time-resolved sodium MRI during

drinking. This reveals a transient increase in the medulla-to-cortex sodium concentration ratio, which has not been reported previously.

These results demonstrate that time-resolved sodium MRI can track dynamic changes in aTSC in the kidney during hydration. However, since subjects showed varied physiological responses, more data are needed to better understand renal sodium handling. Ideally, future studies should include simultaneous proton MRI for anatomical segmentation.

(a)

evaluated VOI	measured aTSC (mM)	aTSC literature values		
		at 3 T (mM)	at 7 T (mM)	other modality (mM)
liver	36 ± 6	41 ± 10 ¹ 20.1 ± 0.9 ⁴	27 ± 5 ²	36.7 ± 3.4 ³
kidney (right)	65 ± 9	71 ± 10 ¹		
kidney (left)	66 ± 8	79 ± 15 ¹ 93 ± 9 ⁵		
renal cortex		58 ± 17 ⁶ 72 ± 6 ⁵	56 ± 2 ² 32.2 ± 5.6 ⁷	
renal medulla		99 ± 18 ⁶ 136 ± 7 ⁵	81 ± 3 ² 85.7 ± 16.0 ⁷	
IVC	74 ± 4	83 ± 21 ¹		80 ± 8 ⁸ 81 ± 7 ^{8b}
CSF	72 ± 8	94 ± 18 ¹ 135.2 ± 10.4 ¹⁰		150.6 ± 10.9 ⁹
spleen	30 ± 7	40 ± 9 ¹		31-34 ¹¹
gallbladder	139 ± 19	122 ± 42 ¹		122-164 ¹² 141-164 ¹³

¹ Birchall *et al.* (2024)
² Lott, Behl, *et al.* (2019)
³ Hooper *et al.* (1976) (flame photometry of rat livers)
⁴ James *et al.* (2015)
⁵ Grist *et al.* (2020) (volunteers drank 500 mL water before imaging)
⁶ Haneder, Kettner, *et al.* (2013) (no water or food intake restrictions)
⁷ Haneder, Juras, *et al.* (2014)
⁸ Lott (2020) (ex vivo blood samples at 7T)
^{8b} Lott (2020) (laboratory blood values)
⁹ Harrington *et al.* (2010) (chromatography)
¹⁰ Haneder, Konstantin, *et al.* (2011) (before water load, 135.5 ± 11.0 mM after)
¹¹ Graham *et al.* (1982) (bovine spleen)
¹² Furey (1966)
¹³ Liu *et al.* (2023)

(b)

evaluated VOI	measured aTSC (mM)	measured max. aTSC (mM)	aTSC literature values		other modality (mM)
			at 3 T (mM)	max. value at 7 T (mM)	
Th8 / Th9	64 ± 10	94			
Th9 / Th10	65 ± 12	106	208 ± 10 ¹		
Th10 / Th11	70 ± 14	120	237 ± 12 ¹		
Th11 / Th12	73 ± 14	124	259 ± 16 ¹	197 ²	
Th12 / L1	76 ± 15	131	297 ± 20 ¹	190 ²	
L1 / L2	87 ± 19	160	305 ± 26 ¹	200 ²	
L2 / L3	87 ± 19	164	342 ± 23 ¹	207 ²	
L3 / L4	92 ± 22	192	313 ± 19 ¹	235 ²	
L4 / L5			262 ± 14 ¹	218 ²	
L5 / S1			216 ± 12 ¹		
mean	77 ± 5	137	327 ± 53 ³		335 ⁴ 274.6 ± 18.9 ⁵

¹ Çavuşoğlu *et al.* (2022)
² Moon, Kim, *et al.* (2011)
³ Malzacher *et al.* (2016) (4 IVDs in the lumbar region)
⁴ Insko, Clayton, *et al.* (2002) (one volunteer at 4T)
⁵ Kamp *et al.* (2024) (ex vivo measurement of thompson grade 1 IVDs)

Fig. 5: Mean of the obtained aTSC in various abdominal structures (a) and mean and maximum aTSC of the IVDs (b) of three volunteers after corrections. Literature values are divided into in vivo measurements at 3T and 7T, and concentrations determined from other modalities. Sources are provided in footnotes for readability.

Liver aTSC values were consistent with existing literature. Comparing renal aTSC values across studies is more difficult due to the variability in hydration protocols and segmentation routines for this heterogeneous organ. Nevertheless, the measured values align with those reported at 3T. aTSC values for the inferior vena cava, spleen, and gallbladder also matched published results well. To the best of my knowledge, this is the first quantitative sodium MRI study investigating these abdominal structures at 7T.

Lower aTSC values were found for cerebrospinal fluid and IVDs, likely due to partial volume effects in small structures. Future studies applying partial volume correction could reduce this underestimation.

Conclusion: The presented workflow provides a basis for accurately measuring the aTSC in multiple abdominal structures simultaneously.

This enables to study the interplay between multiple organs or detect changes due to physiological processes in multiple regions of the body at the same time.

The first part of the presented work demonstrates that time-resolved sodium MRI can be used to investigate the renal aTSC before, during and after water loading.

The second part shows the feasibility of combining ^1H and quantitative ^{23}Na imaging at 7T in a large FOV of $(400\text{ mm})^3$ both under free breathing in ≤ 47 minutes.

References:

1. A. M. Nagel et al. *Investigative Radiology* (2011).
<https://doi.org/10.1097/RLI.0b013e31822836f6>
2. T. Gerhalter et al. *J. Magn. Reson. Imaging*. (2019).
<https://doi.org/10.1002/jmri.26681>
3. S. Regnery et al. *NeuroImage: Clinical* (2020).
<https://doi.org/10.1016/j.nicl.2020.102427>
4. L. V. Gast et al. *Prog. Nucl. Magn. Reson. Spectrosc.* (2023).
<https://doi.org/10.1016/j.pnmrs.2023.04.002>
5. G. Madelin et al. *Prog. Nucl. Magn. Reson. Spectrosc.* (2014).
<https://doi.org/10.1016/j.pnmrs.2014.02.001>
6. N. Maril, et al. *Kidney International* (2004).
<https://doi.org/10.1111/j.1523-1755.2004.00475.x>
7. A. Lu et al. *Magn. Reson. Med.* (2010).
<https://doi.org/10.1002/mrm.22381>
8. R. W. Stobbe et al. *NMR in Biomed.* (2016).
<https://doi.org/10.1002/nbm.3376>
9. M. E. Ladd et al. *Prog. Nucl. Magn. Reson. Spectrosc.* (2018).
<https://doi.org/10.1016/j.pnmrs.2018.06.001>
10. F. Padormo et al. *NMR in Biomed.* (2016).
<https://doi.org/10.1002/nbm.3313>
11. S. Orzada et al. *Magn. Reson. Med.* (2010).
<https://doi.org/10.1002/mrm.22527>
12. B. Kamp et al. *J. Magn. Reson. Imaging*. (2024).
<https://doi.org/10.1002/jmri.29521>
13. R. Ouwerkerk et al. *Radiology* (2008).
<https://doi.org/10.1148/radiol.2481071027>
14. A. J. Daniel et al. *Magn. Reson. Med.* (2021).
<https://doi.org/10.1002/mrm.28768>
15. A. K. Scheipers Dissertation Ruprecht-Karls-Universität Heidelberg (2025). <https://doi.org/10.11588/heidok.00036527>
16. MAGNETOM 7T, Siemens Healthcare GmbH, Erlangen, Germany
17. T. Platt et al. *Magn. Reson. Med.* (2018).
<https://doi.org/10.1002/mrm.27103>
18. S. Orzada et al. *Plos One* (2019).
<https://doi.org/10.1371/journal.pone.0222452>
19. A. M. Nagel et al. *Magn. Reson. Med.* (2009).
<https://doi.org/10.1002/mrm.22157>
20. R. W. Chan et al. *Magn. Reson. Med.* (2009).
<https://doi.org/10.1002/mrm.21837>
21. E. K. Insko, L. Bolinger, J. Magn. Reson. (1993).
<https://doi.org/10.1006/jmra.1993.1133>
22. S. Dietrich et al. *Magn. Reson. Med.* (2020).
<https://doi.org/10.1002/mrm.28602>
23. A. K. Scheipers et al. *ISMRM Workshop on Ultra-High Field MR* (2022). Poster: 64.
24. A. Christ et al. *Phys. Med. Biol.* (2010).
<https://doi.org/10.1088/0031-9155/55/2/N01>
25. S. Gabriel et al. *Phys. Med. Biol.* (1996).
<https://doi.org/10.1002/10.1088/0031-9155/41/11/001>
26. CST Studio Suite 2019/2020 (Dassault Systèmes, Vélizy-Villacoublay, France)
27. Snapshots/2024-10-25, German Cancer Research Center (DKFZ), Heidelberg, Germany
28. S. Haneder et al. *Radiology* (2011).
<https://doi.org/10.1148/radiol.11102263>
29. N. Maril et al. *Magn. Reson. Med.* (2006).
<https://doi.org/10.1002/mrm.21031>
30. A. Akbari et al. *Radiology* (2022).
<https://doi.org/10.1148/radiol.211238>
31. S. Haneder et al. *Eur. Radiol.* (2014).
<https://doi.org/10.1007/s00330-013-3032-6>

Development of radiofrequency coils for magnetic resonance-guided particle therapy

Kilian Dietrich

Department of Radiation Oncology, Heidelberg University Hospital, Heidelberg, Germany
Medical Physics in Radiology, German Cancer Research Center (DKFZ), Heidelberg, Germany

Abstract: This work presents the development, characterization, and integration of novel radiofrequency (RF) coils designed for magnetic resonance (MR)-guided particle therapy. On the one hand, a transmit/receive body coil was integrated into a rotatable patient capsule that is radiation-transparent for ion beams, enabling MR-based imaging and beam-angle optimization without compromising beam quality. On the other hand, receive-only coils for extremity imaging were also explored. RF and radiation performance were validated through simulations, phantom studies, and beam attenuation assessments. These developments mark a significant step toward adaptive, image-guided particle therapy with full angular access and high-quality MR imaging, ultimately enhancing treatment precision and patient outcomes in a clinical environment.

Motivation: Particle therapy, such as proton and carbon ion therapy, offers superior dose conformity compared to conventional photon-based radiotherapy[1,2]. However, its clinical accuracy is limited by uncertainties in patient positioning, organ motion, and anatomical changes during treatment. MRI offers exceptional soft-tissue contrast and treatment planning capabilities[3] without increasing the patient's dose exposure[4], making it a compelling imaging modality for particle therapy.

Despite its advantages, integrating MR systems with particle beam lines presents significant engineering and physical challenges. One example is the issue of radiation transparency of MR components. A key bottleneck lies in the radiofrequency (RF) coils, which are typically opaque to therapeutic ion beams and incompatible with patient rotation, both essential for multi-angle irradiation.

This work is motivated by the need to overcome these limitations through the development of RF coils that are not only MR-compatible and capable of high-quality imaging but also functionally transparent to therapeutic radiation. The integration of such coils into a rotatable patient capsule[5-7] enables complete angular flexibility during treatment, paving the way for MR-guided adaptive particle therapy. The goal is to improve treatment accuracy and allow for real-time monitoring and adaptation without compromising the beam

quality or patient comfort. This multidisciplinary innovation addresses a critical translational gap and represents a foundational step toward next-generation ion-beam treatment platforms.

Materials & Methods: The project involved the design, simulation, and experimental validation of multiple custom-built RF coils with supplementary electronics for MR-guided particle therapy, focusing on radiation transparency, mechanical integration, and MR imaging performance.

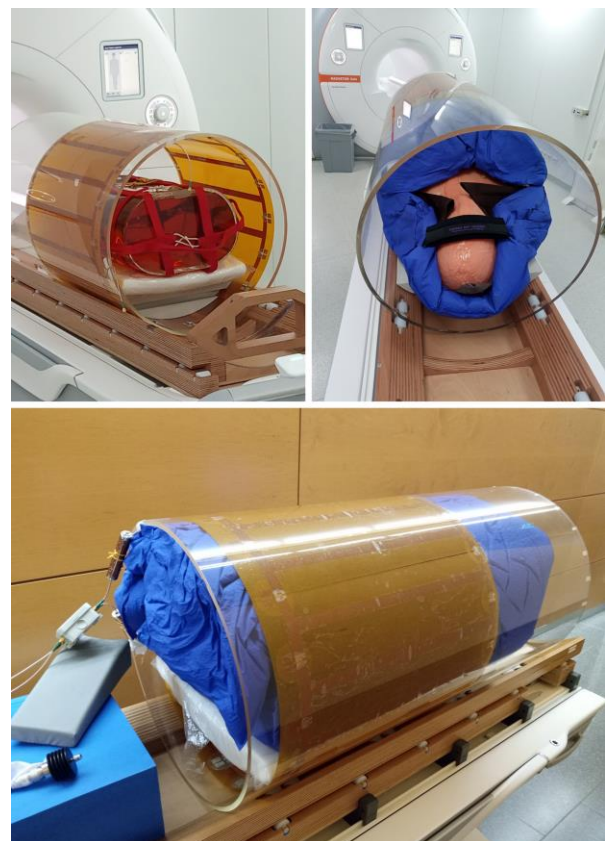


Fig. 1: The modular measurement setup of the RF body coil at a clinical 1.5T MR system. The radiation-transparent Tx/Rx coil is mounted on a rotatable PMMA patient capsule placed on a wooden table. Homogeneous or anthropomorphic phantoms were fixed with vacuum mattresses for multi-angle torso imaging.

The primary device was a birdcage-style[8,9] transmit/receive (Tx/Rx) body coil for a clinical 1.5 T MR system, constructed with ultra-thin (35 μm) copper, low-Z materials, and integrated into a rotatable patient

capsule (Figure 1). This design enabled in-bore rotation around the patient’s longitudinal axis while minimizing changes in the water-equivalent thickness (WET) across the RF coil to ensure beam transparency. A custom-built Tx/Rx switch and quadrature hybrid offered excellent transmit and receive characteristics for imaging[10]. The RF field distributions were simulated using the finite-integration-technique[11] (FIT) and compared to measurements.

Additionally, a receive-only extremity coil with adapted conductor geometry for homogeneous signal reception[12] including a custom-designed preamplifier was developed for a C-shaped 0.25 T open MR scanner. This design also uses ultra-thin conductors and a rotatable, radiation-transparent housing (Figure 2). The imaging performance of the developed RF coils was evaluated using phantoms, as well as in vivo testing for the extremity coil.

Evaluation criteria included SNR, transmit field (B_1) homogeneity, reflection coefficients (S11), and imaging performance under patient rotation in standard and anthropomorphic phantoms. Radiation tests were performed using carbon ion beams, with the coil materials placed in the beam path to measure attenuation and dose distribution impacts.

The developed coils were also compared with commercial RF coils in terms of imaging quality and RF field homogeneity.

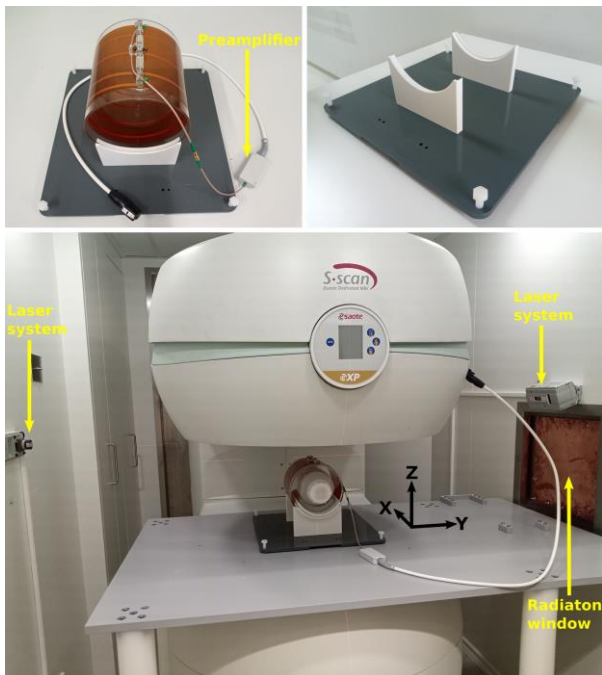


Fig. 2: Setup of the radiation-transparent extremity coil with the developed preamplifier at a C-shaped 0.25 T MR system with particle beam access. The holder enables full rotation around the coil’s X-axis and repositioning in 90° increments via its square base. Reproducible isocenter positioning is ensured with lasers marking the beam focus.

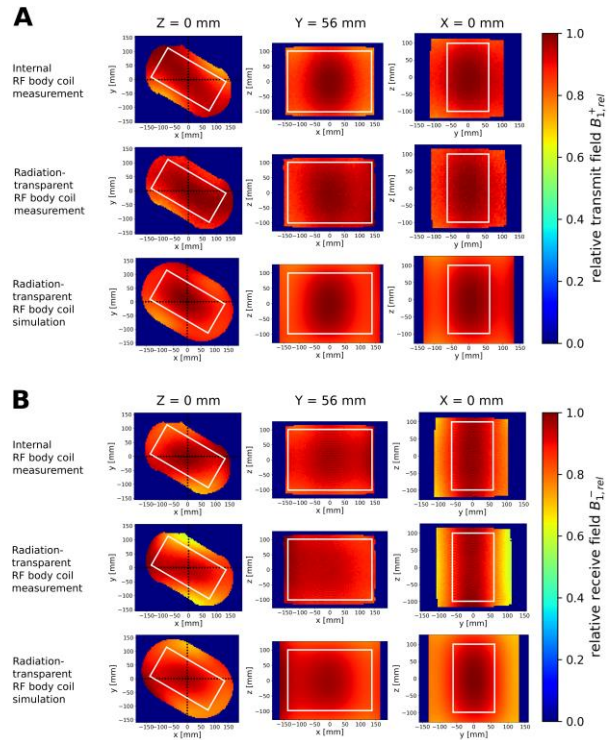


Fig. 3: Relative transmit (A) and receive (B) field maps for three orthogonal slices at the center of a rotated (30°) torso phantom, from both measurements and simulations using the radiation-transparent and internal body coils. Simulated maps ((4 mm)² pixels) were normalized to the maximum, measured maps to the 99th percentile.

Results: The developed RF coils demonstrated excellent compatibility with MR imaging and minimal interference with therapeutic ion beams. The materials of the rotatable body coil achieved a WET of ~420 μm with less than ~200 μm WET from the conductor, corresponding to negligible dose attenuation confirmed by in-beam measurements. This result signifies that the coil does not compromise the treatment beam quality.

Electromagnetic field simulations and imaging experiments with the rotatable Tx/Rx RF coil at

1.5 T (Figure 3) showed high B_1 field uniformity in a ROI of the phantom cross-section as well inside the complete phantom volume over a distance of 216 mm along the axial direction (Figure 4). The SNR performance exceeded that of the body coil in the commercial scanner, particularly in the central regions. Phantom studies confirmed the consistency and reproducibility of the transmit and receive field profiles for different rotation angles, indicating little distortion under coil rotation.

The extremity coil for the 0.25 T scanner demonstrated similarly strong MR performance (Figure 5), with high signal uniformity extending the application of RF coils with radiation-transparent materials to low-field MR

environments, which are more suitable for integration into treatment gantries.

Both coil designs functioned robustly during full 360° rotation, preserving image quality and electrical tuning parameters, even under simulated patient loads. In comparison to commercial RF coils, the developed coils outperformed conventional setups in terms of both MR imaging and radiation compatibility. This validates the concept of rotatable, radiation-transparent RF coil integration for adaptive MR-guided particle therapy systems.

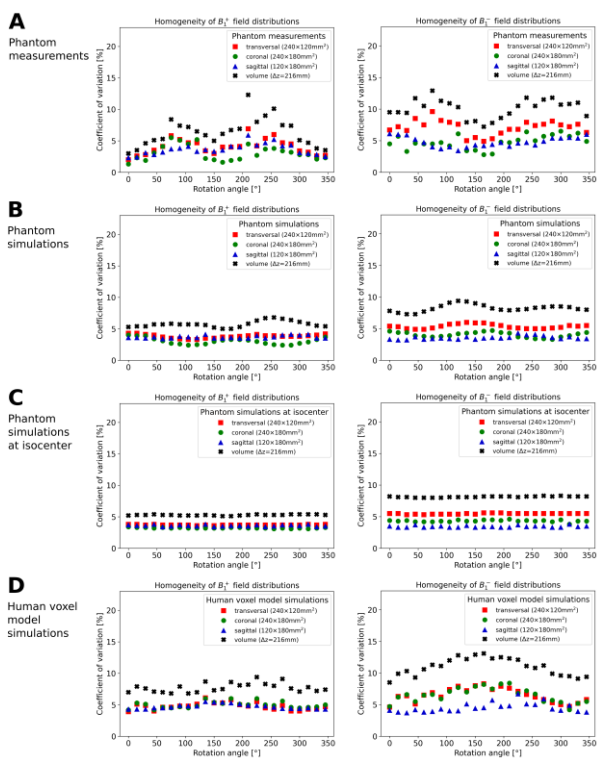


Fig. 4: Coefficients of variation (COV) for transmit/receive fields of the radiation-transparent body coil over a full rotation. Shown are results for measurements with a homogeneous phantom (A), corresponding simulations (B), ideal isocenter placement (C), and human voxel model simulations (D), with COVs calculated in central slices and the full volume.

Discussion: The presented RF coil systems represent a critical technological advancement toward the realization of MR-guided particle therapy. Their ultrathin design with a homogeneous distribution of low-Z materials across all angles enables full integration into rotating treatment platforms without compromising imaging quality or radiation delivery. This effectively addresses one of the central limitations of MR-beamline integration by minimizing beam perturbation while enabling high-performance MRI.

The body coil's high SNR and homogeneous B1 fields, combined with negligible WET, validate the concept of

embedding MR coils directly in the patient rotation system. Notably, the mechanical stability and RF field homogeneity remain consistent throughout full angular rotation, even with off-center rotation due to the elevated patient rotation system. This confirms its readiness for clinical workflows involving multi-angle beam delivery. Similarly, the extremity coil's excellent low-field imaging and high radiation transparency make it a suitable candidate for extremity-targeted particle therapy setups.

Future work could explore integration into more compact MR systems or combine these developments with motion management strategies, such as real-time tracking or gating to further elevate treatment accuracy. Limitations include the need for further clinical validation and testing across broader patient populations. Integration into real-time MR-guided therapy platforms also requires addressing workflow and image registration challenges. Nonetheless, these prototypes establish a robust foundation for future translation into clinical particle therapy systems.

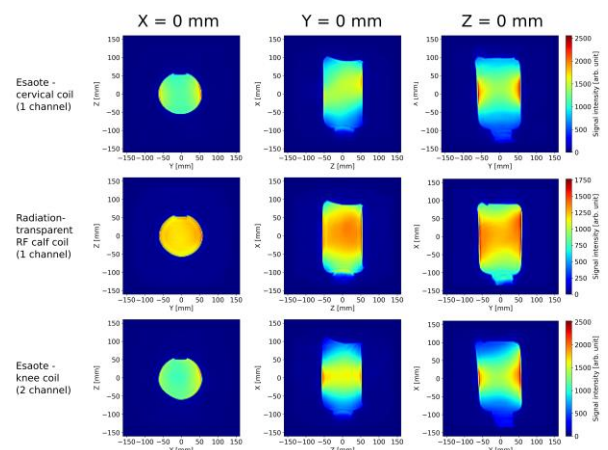


Fig. 5: Transverse, sagittal, and coronal MR images of a homogeneous calf phantom with the radiation-transparent extremity coil, cervical coil, and knee coil. The extremity coil shows better receive homogeneity. Images were individually scaled; SNR in phantom for X=0, Y=0, and Z=0: cervical coil (120,75,78), RF calf coil (183,90,117), knee coil (126,74,81).

Conclusion: This work demonstrates the feasibility and clinical potential of integrating radiation-transparent RF coils into MR-guided particle therapy platforms. The rotatable Tx/Rx body coil and extremity coil designs achieved high imaging quality, structural compatibility with patient rotation, and minimal ion beam perturbation. These systems allow for multi-angle treatment strategies with real-time MR imaging, which is an essential step toward adaptive, high-precision particle therapy. Their successful implementation paves the way for advanced imaging-guided protocols

that can dynamically adapt to patient-specific anatomical changes, ultimately improving treatment outcomes. Future clinical studies and workflow integration will further advance their readiness for widespread application in modern radiotherapy.

Acknowledgements: The author acknowledges the support of the German Cancer Research Center (DKFZ), Heidelberg University Hospital, and the Heidelberg Ion-Beam Therapy Center (HIT). Special thanks to Prof. Dr. Mark E. Ladd, Prof. Dr. Dr. Jürgen Debus, Dr. Sebastian Klüter, Dr. Stephan Orzada and Dr. Tanja Platt for their scientific guidance and mentorship. Additional gratitude is extended to the MR engineering and particle therapy teams for their technical support and collaborative spirit throughout the development and testing phases. This research was supported by funding (13GW0436) from the German Federal Ministry of Education and Research (BMBF).

References:

1. Pollard JM, Wen Z, Sadagopan R, Wang J, Ibbott GS, *The future of image-guided radiotherapy will be MR guided*, *Br J Radiol*
2. Hoffmann A, Oborn B, Moteabbed M, et al, *MR-guided proton therapy: a review and a preview*, *Radiation Oncology*
3. Gao Y, Zhou Z, Han F, et al, *Accelerated 3D bSSFP imaging for treatment planning on an MRI-guided radiotherapy system*, *Med Phys*
4. Dzierma Y, Mikulla K, Richter P, et al, *Imaging dose and secondary cancer risk in image-guided radiotherapy of pediatric patients*, *Radiat Oncol*
5. Whelan B, Liney GP, Dowling JA, et al, *An MRI-compatible patient rotation system — design, construction, and first organ deformation results*, *Med Phys*
6. Buckley JG, Rai R, Liney GP, et al, *Anatomical deformation due to horizontal rotation: towards gantry-free radiation therapy*, *Phys Med Biol*
7. Buckley JG, Dong B, Liney GP, *Imaging performance of a high-field in-line magnetic resonance imaging linear accelerator with a patient rotation system for fixed-gantry radiotherapy*, *Phys Imaging Radiat Oncol*
8. Tropp J, *The theory of the bird-cage resonator*, *J Magn Reson*
9. Hayes CE, Edelstein WA, Schenck JF, Mueller OM, Eash M, *An efficient, highly homogeneous radiofrequency coil for whole-body NMR imaging at 1.5T*, *Magn Reson Med*
10. Hoult DI, Chen CN, Sank VJ, *Quadrature detection in the laboratory frame*, *Magn Reson Med*
11. Clemens M, Weiland T, *Discrete Electromagnetism with the Finite Integration Technique*, *Progress In Electromagnetics Research*
12. Leifer MC, *RF Solenoid with Extended Equiripple Field Profile*, *Magnetic Resonance, Series A*

MR-zero meets FLASH – Controlling the transient signal decay in gradient- and rf-spoiled gradient echo sequences

Simon Weinmüller 1*, Jonathan Endres 1, Nam Dang 1, Rudolf Stollberger 2, Moritz Zaiss 1,3

1 Institute of Neuroradiology, University Clinic Erlangen, Erlangen, Germany

2 Institute of Bioimaging, Graz University of Technology, Graz, Austria

3 Department Artificial Intelligence in Biomedical Engineering, Friedrich-Alexander-Universität Erlangen-Nürnberg, Erlangen, Germany

Abstract: The complex signal decay during the transient FLASH MRI readout can lead to artifacts in magnitude and phase images. We show that target-driven optimization of individual RF flip angles and phases can realize near-ideal signal behavior and mitigate artifacts. The differentiable end-to-end optimization framework MR-zero is used to optimize RF trains of the FLASH sequence. We focus herein on minimizing deviations from the ideally spoiled signal by using a mono-exponential Look-Locker target. We were able to reproduce the complex substructure of the transient FLASH signal decay. Individual flip angle and RF phase optimization improves the transient signal decay of FLASH MRI sequences.

Motivation: A common problem in transient Fast Low-Angle Shot (FLASH) sequences is the decay of the magnetization which still affects quality of the image, as the decay in k-space acquisition leads to ringing or blurring artifacts. This decay can be described by the Look-Locker decay rate [1]:

$$(1) \quad S_{LL}(n \cdot TR) = (S_i - S_{SS}) \cdot \exp\left(-\frac{n \cdot TR}{T_{1,LL}}\right) + S_{SS}$$

$$(2) \quad \text{with } \frac{1}{T_{1,LL}} = \frac{1}{T_1} - \frac{\ln(\cos \alpha)}{TR}$$

Figure 1: Interestingly, this mono-exponential reflects an idealized description in the case of ideal spoiling. In real measurements the signal decay follows only coarsely this exponential function, but has complex substructure that depends, among other factors, on the rf-spoiling [2]. Herein, these deviations are reproduced and reduced using the end-to-end optimization MR-zero [3].

Materials & Methods:

Unencoded measurement (Phantom) - To visualize the substructures, FLASH sequence parameters as described by Epstein et al. [2] are employed for both, unencoded simulation and measurement: $\alpha = 10^\circ$, $TR = 10$ ms, $TE = 5$ ms, bandwidth = 217 Hz/pixel, FOV = 200 mm, slice thickness = 10 mm, matrix = 128 x 128, rf spoiling with a quadratic increment of $\psi = 117^\circ$ and $\psi =$

84° and gradient spoiler, saturation preparation with recovery time $TREC = 970$ ms. Parameters of a tube phantom ($T1 \approx 1.0$ s, $T2 \approx 0.17$ s, $D \approx 1.6e-3$ mm²/s) were set in a single voxel phantom for unencoded simulations and optimization.

Encoded measurement (Subject) - To make the existing signal fluctuations stronger visible in an image, we decreased TE and increase the flip angle. To achieve shorter TE and TR of $TE = 3.2$ ms and $TR = 6$ ms, the bandwidth was increased to 500 Hz/pixel. The excitation flip angle $\alpha = 19.5^\circ$ was increased and no preparation was used. For optimization task, again just one representative voxel was used with parameters matching the median of the in vitro phantom ($T1 \approx 1.5$ s, $T2 \approx 0.11$ s, $D \approx 0.84e-3$ mm²/s). All other parameters were chosen equally to the unencoded experiment. A centric reordering for acquisition was used. Encoded simulations were performed on a brain phantom built from the data provided by the BrainWeb Database [4].

Simulation and Optimization - For simulation and optimization the differentiable end-to-end optimization framework MR-zero [3] employing the with Phase Distribution Graph simulation [5] written in PyTorch [6] is used to optimize rf trains of the FLASH sequence using the ADAM optimizer [7]. We focus herein on minimizing deviations from the ideally spoiled signal SLL by using a mono-exponential Look-Locker target. As loss function we used the so-called perpendicular loss proposed for complex data by Terpstra et al. [8].

We first reproduce the transient FLASH signal decay substructure, and then minimize the deviation to the Look-Locker decay by optimizing the individual (i) flip angles (α), (ii) rf phases (ϕ) and (iii) flip angles and rf phases (α, ϕ). Comparison between measurement and simulation are performed using Pulseseq9,10 in 1D and 2D. The measurements were performed at a 3T MAGNETOM PRISMA scanner (Siemens Healthcare, Erlangen) on healthy subjects after written informed consent and approved by the local ethics committee.

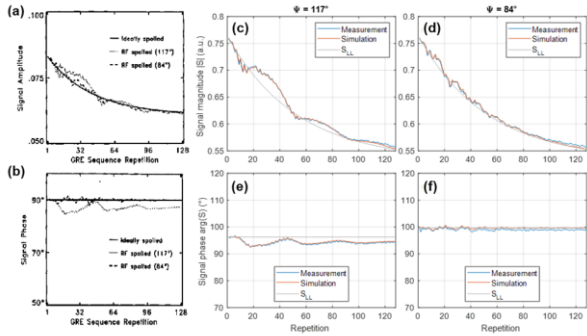


Fig. 2: Unencoded FLASH signal for $\alpha=10^\circ$, $TE=5ms$, $TR=10ms$, after one 90° preparation pulse with a recovery time of 970ms. (a) Simulated signal amplitude and (b) signal phase evolutions for a quadratic rf phase increment $\psi=84^\circ$ and $\psi=117^\circ$ and ideally spoiled magnetic prepared GRE, reproduced from Epstein et al.2. Measured and simulated signal magnitude (c,d) and signal phase (e,f). Additionally, the ideally spoiled signal S_{LL} is plotted (grey solid line). $T1 = 0.987 s$ and $T2 = 0.167 s$ were used in simulation.

Results: In Figure 2, we reproduce the finding of Epstein et al. [2] and find an excellent agreement between measurement and simulation in the unencoded experiment. The individual flip angles and rf phases for the three optimization tasks are visible in Figure 3. The overall result of Figure 3 is that for all tasks we get closer to the target signal upon optimization. Task 1 (α) leads to signal close to the target, but no constant phase. Task 2 (ϕ) leads to a constant phase while improving the signal with a RMSE similar to an rf cycling of $\psi = 84^\circ$. Task 3 (α, ϕ) leads to the best results regarding target signal and constant phase. The last task was initialized with the rf phases found in the second task, thus similar phases and only small flip angle variations are observed here. This can also be seen qualitatively in Table 4, where the RMSE of measurement and simulation was calculated.

The FLASH magnitude and phase images can be seen in Figure 5 for simulation (Figure 3A, B) and measurement (Figure 5C, D). The rf increment of 117° and 84° produce clear artefacts in the magnitude image, as well as in the phase image, clearly visible in the difference images. This is reduced especially by task 2 and 3, but not for task 1.

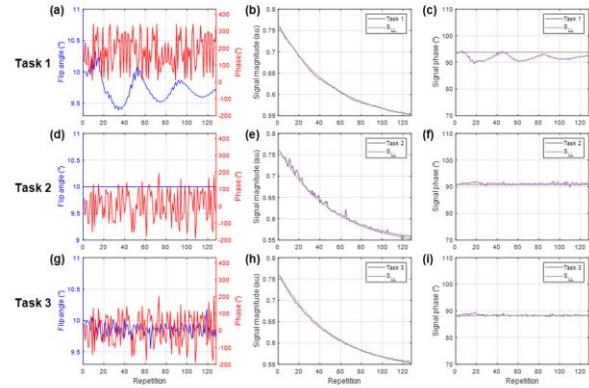


Fig. 3: The flip angles α and rf phases ψ are shown for the three optimization cases (a) task 1 (α), (d) task 2 (ϕ), and (g) task 3 (α, ϕ). The measured signal magnitude evaluations are shown in (b), (e) and (h), respectively for the three tasks. Additionally, the ideally spoiled signal S_{LL} is plotted (grey solid line). The same comparison is done in (c), (f) and (i) for the signal phase. Animated optimization process of Task 3 can be found here: <https://github.com/MRsources/FLASHzero/commit/c15b91b920d4c6b6a83e3e70950882226f196415>

Discussion: We revisited the problem of the transient FLASH signal decay using the end-to-end MR-zero framework. We showed that a general target-driven signal optimization is possible by optimization of each and every rf pulse angle and phase of the pulse sequence.

Interestingly, our rf phase cycling optimization challenges the often-used concept of quadratic phase cycling. Thus, we want to point out that a quadratic phase cycling ψ , most famous $\psi=117^\circ$, is derived using a steady-state argumentation, by finding the signal that is most close to the dynamic FLASH equation or Look-locker equation [11]. Despite the work of Epstein et al. [2] who already suggested the $\psi=84^\circ$ phase increment to be better in transient cases, in many transient state applications, even in vendor implementations.

	$\Psi = 117^\circ$		$\Psi = 84^\circ$		task 1 ($\bar{\alpha}$)		task 2 ($\bar{\phi}$)		task 3 ($\bar{\alpha}, \bar{\phi}$)	
	Magnitude	Phase	Magnitude	Phase	Magnitude	Phase	Magnitude	Phase	Magnitude	Phase
Meas	$12.0 \cdot 1e-3$	2.23°	$5.4 \cdot 1e-3$	0.68°	$2.6 \cdot 1e-3$	2.62°	$5.8 \cdot 1e-3$	0.35°	$3.0 \cdot 1e-3$	0.53°
Sim	$11.5 \cdot 1e-3$	2.62°	$5.5 \cdot 1e-3$	0.28°	$2.2 \cdot 1e-3$	1.89°	$5.2 \cdot 1e-3$	0.21°	$1 \cdot 1e-3$	0.12°

Fig. 4: (A) RMSE with regard to the ideally spoiled signal S_{LL} , calculated for measured (Meas) and simulated (Sim) signal magnitude (left value) and phase (right value) for $\psi=117^\circ$ and 84° , and the optimized rf trains of task 1-3. For the RMSE of the PSF just the absolute signal is considered for calculation. The underlying signals are shown in Figure 2 and Figure 3.

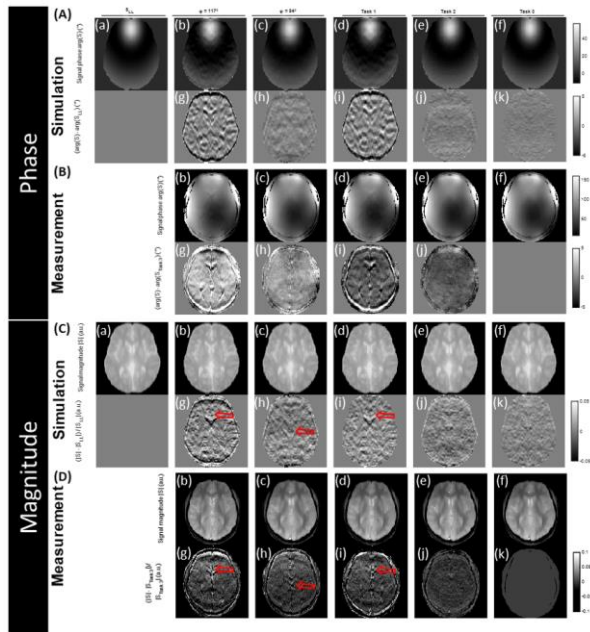


Fig. 5: Simulation (A,C) and measurement (B,D) of centric encoded FLASH readouts for typical rf increments of 117° (b) and 84° (c), and optimization task 1 (d) and task 2 (e) and task 3 (f). In simulation the ideal spoiled LL target was calculated as reference. Difference of signal magnitude (Cg-k) and phase (Ag-k) are calculated wrt. the LL target. For magnitude (Bb-f) and phase image (Db-f) task 3 is used as reference.

Conclusion: We propose a flexible method for improving the transient signal behavior of gradient- and rf-spoiled gradient echo sequences / FLASH-sequences, which was validated in vitro and in vivo. The proposed flip angle train and phase cycling can improve MPRAGE sequences as well as fast field map approaches.

References:

1. Look DC, Locker DR. Time Saving in Measurement of NMR and EPR Relaxation Times. *Review of Scientific Instruments*. 1970;41(2):250-251.
2. Epstein FH, Mugler JP, Brookeman JR. Spoiling of transverse magnetization in gradient-echo (GRE) imaging during the approach to steady state. *Magn Reson Med*. 1996;35(2):237-245.
3. Loktyushin A, Herz K, Dang N, et al. MRzero - Automated discovery of MRI sequences using supervised learning. *Magnetic Resonance in Med*. 2021;86(2):709-724.
4. BrainWeb: Simulated Brain Database. Accessed January 1, 2023. <https://brainweb.bic.mni.mcgill.ca/brainweb/>
5. Endres J, Weinmüller S, Dang HN, Zaiss M. Phase distribution graphs for fast, differentiable, and spatially encoded Bloch simulations of arbitrary MRI sequences. *Magnetic Resonance in Medicine*. Published online 2023.
6. Paszke A, Gross S, Massa F, et al. PyTorch: An Imperative Style, High-Performance Deep Learning Library. In: *Advances in Neural Information Processing Systems* 32. Curran Associates, Inc.; 2019:8024-8035. <http://papers.neurips.cc/paper/9015-pytorch-an-imperative-style-high-performance-deep-learning-library.pdf>
7. Kingma DP, Ba J. Adam: A Method for Stochastic Optimization. Published online 2014.
8. Terpstra M, Maspero M, Legendijk J, van den Berg CAT. Rethinking complex image reconstruction: L_1 -loss for improved complex image reconstruction with deep learning. In: ; 2021. <https://cds.ismrm.org/protected/21MPresentations/abstracts/1751.html>
9. Layton KJ, Kroboth S, Jia F, et al. Pulseq: A rapid and hardware-independent pulse sequence prototyping framework: Rapid Hardware-Independent Pulse Sequence Prototyping. *Magn Reson Med*. 2017;77(4):1544-1552.
10. Ravi K, Geethanath S, Vaughan J. PyPulseq: A Python Package for MRI Pulse Sequence Design. *JOSS*. 2019;4(42):1725.
11. Zur Y, Wood ML, Neuringer LJ. Spoiling of transverse magnetization in steady-state sequences. *Magnetic Resonance in Med*. 1991;21(2):251-263.

From Blur to Dynamic Sharpness: Temporal Limits in Single-cell Tracking Time-lapse MRI

Enrica Wilken 1*, Mark Armstrong 2, Asli Havlas 1, Felix Freppon 1, Max Masthoff 1, Clemens Diwok 3, Susann Boretius 4, Amir Moussavi 4, Dan Xiao 2, and Cornelius Faber 1

1 Clinic of Radiology, University of Münster, Münster, Germany.

2 Physics Department, University of Windsor, Windsor, Canada

3 Institute of Molecular Biosciences, University of Graz, Graz, Austria.

4 Functional Imaging Laboratory, German Primate Center, Leibniz Institute for Primate Research, Göttingen, Germany

Abstract: Time-lapse MRI enables single-cell tracking of iron-labeled immune cells by repetitive T2*-weighted imaging. Yet, the temporal resolution is limited, restricting tracking of fast-moving cells under inflammatory conditions. Here, we first performed contrast simulations and measured the detectable velocity range using a rotating phantom system. We then applied undersampling to Cartesian and radial sampling to accelerate data acquisition to a frame rate of less than 1 min and consequently reduce temporal blurring. Last, we employed bSSFP imaging, enabling time-lapse MRI at isotropic spatial resolution of (77 μm)³ and facilitating 3D single-cell tracking with whole-brain coverage.

Motivation: As the understanding of cell-based therapies and immune cell behavior deepens, the demand for reliable cell tracking methods is growing. Currently, only by using invasive intravital confocal microscopy, tracking of individual cells within the vasculature is possible. Here, various motion patterns of immune cells have been observed: fast bloodstream travel (>12 mm/min), and active migration as rolling in response to an inflammatory stimulus (~2.4 mm/min) or patrolling under healthy conditions (~0.012 mm/min), limited to one MRI voxel or extending beyond 100 μm . [1,2,3]

Time-lapse MRI provides a non-invasive imaging alternative: Labeling cells with iron-oxide nanoparticles makes them appear as hypointense spots in T2*-weighted images, and through repetitive imaging, individual immune cells inside the vascular system can be tracked. [2,3] However, temporal blurring limits detection of fast-moving cells and accelerated imaging is needed to gain greater insight into inflammatory processes by single-cell time-lapse MRI.

Here, we first evaluated the velocity range of cells detectable by time-lapse MRI through simulations and in vitro phantom studies with a T2*-weighted gradient echo (GRE) sequence [2,3]. A rotating phantom mimicked ultra-slow movement of cells to quantitatively measure the velocity detection limit.

To increase the temporal resolution, a variable density Cartesian sampling scheme was developed, permitting the reconstruction of fully sampled (FS) images and images at different acceleration factors simultaneously, using a dictionary learning (DL) compressed sensing (CS) reconstruction. Similarly, interleaved 2D radial acquisition was applied, enabling retrospective reconstruction of both FS and accelerated images with and without CS. Last, we employed bSSFP acquisition with both 2D Cartesian and interleaved 3D radial sampling. For all sequences, phantom measurements and in vivo experiments were performed to validate the approach.

Materials & Methods: Time-lapse MRI was performed at 9.4 T with cryogenic probe. Scan parameters for the different sequences were: Established Cartesian GRE sequence [2,3]: TE/TR=8.0/645 ms, spat.res.: 67x55 μm^2 , 38 slices of 300 μm , scan time/timeframe: 8:12 min; US Cartesian GRE: TE/TR=8.0/649 ms, spat.res.: 61x73 μm^2 , 38 slices of 300 μm , scan time/FS timeframe: 2:06 min; interleaved radial FLASH: TE/TR=11/400 ms, spat.res.: 59x59 μm^2 , 15 slices of 300 μm , scan time/FS timeframe: 5:12 min; 2D Cartesian bSSFP: TE/TR=6/12 ms, spat.res.: 59x59 μm^2 , 1 slice of 300 μm , scan time/timeframe: 1:42 min; Interleaved 3D radial bSSFP: TE/TR=0.9/4 ms, spat.res.: 77x77x77 μm^3 , scan time/per FS timeframe: 8:01 min. For US 2D Cartesian sampling, k-space-lines were grouped into bins depending on the highest acceleration factor. Images were then reconstructed from FS k-space data and at varying acceleration factors using DL low-rank reconstruction. Similarly, due to interleaved ordering in 2D and 3D radial sampling, spokes were divided into sequential subsets, then reconstructed with and without CS [4] using NUFFT.

Time-lapse contrast simulations were performed by stepwise increasing a signal voids position in a synthetic phantom and filling artificial k-space with fractions of the Fourier transforms of the individual images.

In vitro, agarose gel phantoms with MPIOs (diameter: 8.2 μm , 9.2 pg Fe/particle) imitated signal voids of iron-labeled cells. A custom, partly MR-safe rotating system

was built from acrylic glass and aluminum to hold the phantom and drive it via a stepper motor, enabling the quantitative measure of the velocity detection limit based on the change in contrast of particles in the static and the rotating phantom.

In vivo, mice intravenously received iron-based contrast agent 24 h before brain imaging. Hypointense cells were manually identified and categorized by patrolling behavior.

Results: Evaluating the velocity detection limit: Superpositions of simulated cells and real MRI data (Fig.1) show increasing blurring with faster cell movement. Phantom measurements using the rotating phantom system revealed a velocity detection limit between 0.12 and 0.18 mm/min for the Cartesian GRE sequence, dependent on contrast generated in the static position (Fig.2).

Accelerated time-lapse MRI: Cartesian and radial US in combination with CS reconstruction enable reconstruction of both FS images and US subframes from the same acquisition. Phantom measurements showed (Fig.3A,4A) decreased motion distortion, and additional fast-moving particles were recovered in US reconstructions. The fastest particle detectable using Cartesian CS had a velocity of 0.42 mm/min. Using the radial FLASH sequence, a velocity detection limit of 0.17-0.29 mm/min for FS, 0.31-0.61 mm/min for CS and 0.63-1.08 mm/min for US reconstruction was derived. Both k-space sampling patterns enabled in vivo detection of single cells with varying motion patterns in the mouse brain. Additional short-term patrolling cells, which were not visible in FS images, were identified in accelerated images (Fig.3B,4B). Using US radial sampling in vivo, severe streaking artifacts hindered cell detection (Fig.4B).

bSSFP time-lapse MRI: Single iron-labeled cells were successfully tracked in phantom and in vivo experiments using bSSFP acquisition (Fig.5). Decreased contrast and elongated shapes from temporal blurring was weaker using bSSFP than GRE in the rotating phantom (Fig.5A). A velocity detection limit of 0.6-0.8 mm/min for 2D Cartesian bSSFP, of 0.2-0.4 mm/min for FS and of 0.6-0.7 mm/min for CS 3D radial bSSFP was measured. In vivo, for 2D Cartesian sampling, N=38 cells detected in at least 2 timeframes had a mean velocity of 0.019 ± 0.002 mm/min. 3D radial sampling enabled 3D single-cell tracking in the whole brain at isotropic spatial resolution. CS decreased blurring effects, separating hypointensities in close proximity (Fig.5C).

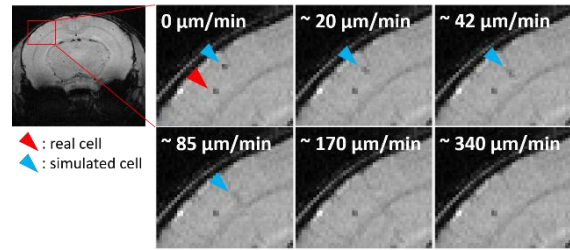


Fig. 1: Image details in the mouse brain cortex (red rectangle) present overlays of a representative in vivo time-lapse image and the contrast simulation for different cell motion velocities, showing a real, static (red arrowhead) and a simulated, moving (blue arrowhead) cell.

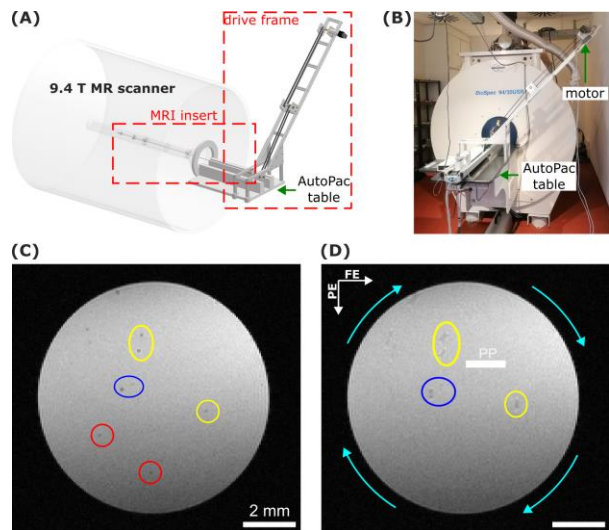


Fig. 2: (A) Design sketch and (B) photo of the rotating phantom system. In rotating phantom measurements (D) using the established GRE sequence particles close to the axis of rotation (blue) remained visible independent of the contrast in the static phantom (C). Faster-moving, low contrast particles disappeared (red), while high contrast features became blurred (yellow).

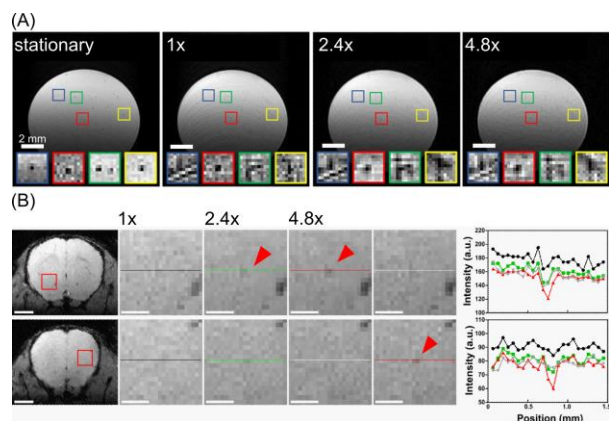


Fig. 3: Variable density 2D Cartesian US sampling scheme. (A) In rotating phantom experiments, single iron-particles can be detected as hypointensities for FS (1x), 2.4x, and 4.8x US images. Image details show examples of particles with varying velocities and contrast. (B) Image details of in vivo time-lapse MRI demonstrate examples of cells that were only resolved in accelerated CS images, but not in FS images where temporal blurring was too strong.

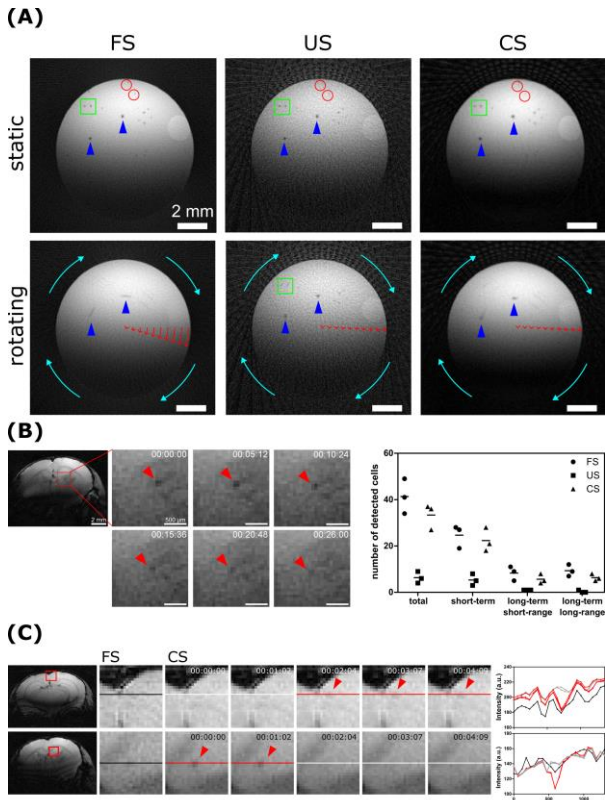


Fig. 4: Interleaved radial FLASH. (A) In rotating phantom measurements, particles are blurred (blue arrows) or fade (red circles). In US images, some particles are recovered (green square). (B) In vivo, image details show a single cell moving. Quantification revealed that in US images fewer cells than in FS images were detected, while in CS images most cells were recaptured. (C) Image details of FS and the corresponding CS images demonstrate examples of cells that were only resolved in accelerated images, but not in FS images.

Discussion: Superimposed images of simulated and real data account for noise and anatomical features and provide an estimate of the velocity detection limit. Phantom-based quantification showed that the original time-lapse sequence detected only velocities up to 0.18 mm/min. The detection limit could be improved by better contrast, indicating the need for efficient cell labeling.

In line with our overall aim to potentially capture rolling cells (~2.4 mm/min), accelerated imaging through Cartesian and radial US significantly improved the detection of fast-moving cells by increasing temporal resolution. Both in phantoms and in vivo detectability of single cells was improved, particularly by reduced temporal blurring. This enabled detection of faster-moving cells that were missed in conventional FS images. However, in vivo CS reconstruction was required to correct for streaking artifacts in radial sampling.

The application of bSSFP sequences offered higher velocity detection thresholds and reduced temporal

blurring compared to GRE. Despite the occurrence of banding artifacts, in vivo experiments confirmed bSSFP's potential for dynamic single-cell tracking. Hypointensities resembled those observed using spoiled GRE and exhibited patrolling behaviour. 2D Cartesian bSSFP allowed for high temporal resolution, however, was limited to a single slice, while 3D radial bSSFP enabled whole-brain volumetric tracking with high spatial resolution. Here, CS decreased blurring effects, consequently extending the velocity detection limit, outperforming the established GRE sequence.

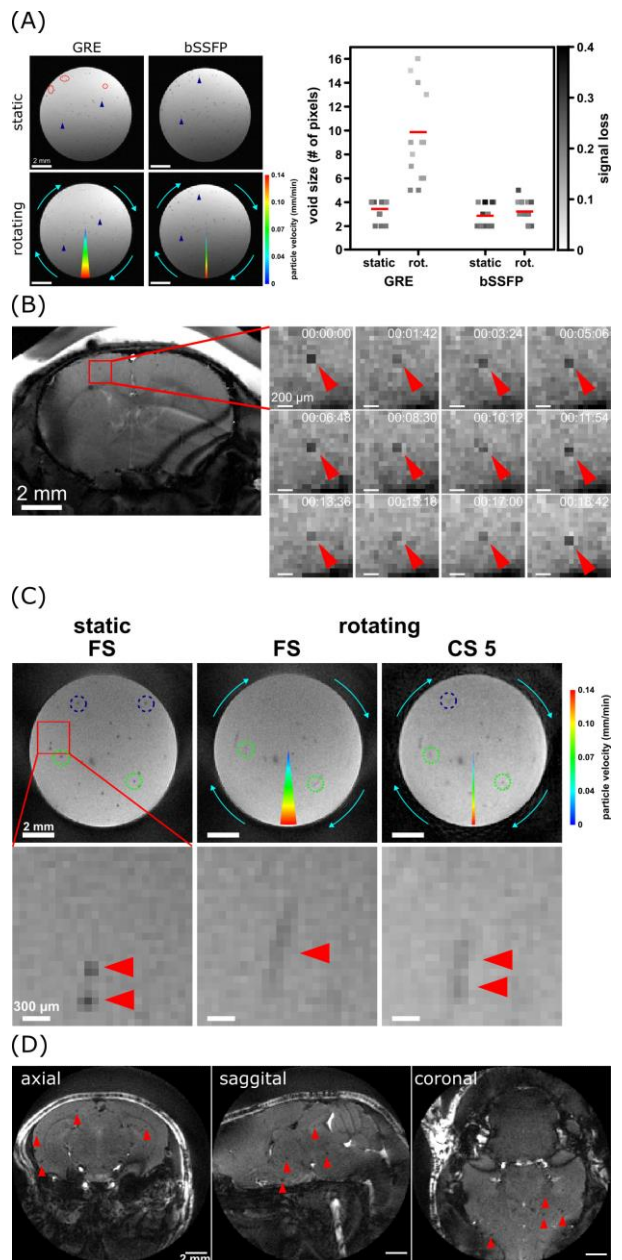


Fig. 5: bSSFP time-lapse MRI. In phantoms, temporal blurring was decreased using (A) 2D Cartesian bSSFP compared to GRE, quantified by void size and signal loss, and (C) using CS in 3D radial sampling. In vivo, single iron-labeled cells moving across several voxels in consecutive timeframes for (B) 2D Cartesian and in all three dimensions for (D) 3D radial sampling were detected.

Conclusion: Phantom measurements and in vivo time-lapse MRI indicate that single patrolling immune cells can be detected and followed dynamically. A variable density sampling scheme for 2D Cartesian as well as an interleaved radial sampling permit retrospective reconstruction of both fully sampled and accelerated images simultaneously. US enables single-cell tracking at higher temporal resolution, reduction of blurring effects, and recovery of cells that were blurred at lower temporal resolution. The custom-made rotating phantom system allowed to quantitatively measure the velocity detection limit of time-lapse MRI, which was pushed to up to 1.1 mm/min by 2D radial FLASH imaging. Additionally, bSSFP imaging in combination with 3D radial sampling facilitated the three-dimensional tracking of individual cells, offering whole-brain coverage at isotropic spatial resolution.

References:

1. Auffray C, Fogg D, Garfa M, et al. Monitoring of blood vessels and tissues by a population of monocytes with patrolling behavior. *Science*. 2007;317(5838):666-670.
2. Masthoff M, Gran S, Zhang X, et al. Temporal window for detection of inflammatory disease using dynamic cell tracking with time-lapse MRI. *Sci Rep*. 2018;8(1):9563.
3. Masthoff M, Freppon FN, Zondler L, et al. Resolving immune cells with patrolling behaviour by magnetic resonance time-lapse single cell tracking. *EBioMedicine*. 2021;73:103670.
4. Feng L, Grimm R, Block KT, et al. Golden-angle radial sparse parallel MRI: combination of compressed sensing, parallel imaging, and golden-angle radial sampling for fast and flexible dynamic volumetric MRI. *Magn Reson Med*. 2014;72:707-717.

Oral

Presenter's Abstracts

Can real-time phase contrast quantification of CSF flow predict shunt response in NPH patients?

Federica Calafiore 1*, Sara Hall 2, Mattis Jalakas 3, Nicola Spotorno 4, Danielle van Westen 5, Niklas Marklund 6, Johannes Töger 7 and Karin Markenroth Bloch 8

1 Medical Radiation Physics, Lund University - Lund - Sweden

2 Department of Clinical Sciences Malmö, Clinical Memory Research Unit, Lund University - Lund - Sweden / Memory Clinic, Skåne University Hospital - Malmö - Sweden

3 Department of Clinical Sciences Lund, Neurosurgery, Lund University and Skåne University Hospital - Lund - Sweden

4 Clinical Memory Research Unit, Department of Clinical Sciences Malmö, Lund University - Lund - Sweden

5 Department of Diagnostic Radiology, Clinical Sciences, Lund University and Skane University Hospital - Lund - Sweden

6 Department of Clinical Sciences Lund, Neurosurgery, Lund University and Lund University Hospital - Lund - Sweden

7 Clinical Physiology, Department of Clinical Sciences Lund, Lund University and Skåne University Hospital - Lund - Sweden

8 Lund University Bioimaging Center, Lund University - Lund - Sweden

Abstract: In this study, different flow parameters with the potential of predicting shunt response in patients with iNPH were analyzed using cardiac-gated and real-time 2D-PC techniques at 7T MR. In addition, RT flow measurements of young healthy volunteers served as controls. All iNPH patients underwent cognitive and motor function tests before and after shunt surgery. A percentage change score was used to derive a normalized improvement score (NIS). Flow parameters were then correlated to NIS, resulting in a positive significant correlation between NIS and RT net flow in iNPH patients. The relevance of this finding in a clinical setting will be further investigated by increasing the study size.

Motivation: Idiopathic normal pressure hydrocephalus (iNPH) is a possibly treatable but largely underdiagnosed neurological condition affecting 1.5% of 70-year-olds, with prevalence increasing with age [1]. It is characterised by gait and cognitive impairment as well as urinary incontinence. iNPH is primarily diagnosed through cognitive and motor function assessments and imaging. Symptoms can often be treated by surgically placing a shunt to remove excess cerebrospinal fluid (CSF) from the ventricular system [2]. However, prediction of shunt response is poor and studies investigating the use of cardiac-gated, through-plane phase contrast (CG 2D-PC) MRI for outcome prediction have been inconclusive [3-5]. iNPH patients typically exhibit wider cerebral aqueducts, faster CSF flow and larger net flow volumes than age matched controls, and that these parameters can be restored to normal values by interventions such as lumbar tap test and shunt placement [6-9]. Studies have also shown that respiration has a large influence on CSF flow in the aqueduct and spinal canal [10-13]. In contrast to CG PC, real-time phase-contrast (RT 2D-PC) preserves the respiratory effects on CSF flow dynamics. RT PC methods are mainly validated in healthy volunteers, and their utility in clinical settings is unknown. Recent findings using real-time CSF-flow measurements have shown promising potential to identify predictors for treatment responsiveness in patients with iNPH [14]. The aim of this study is to investigate whether CSF flow parameters measured with RT PC prior to shunt placement correlates with clinical outcome of surgically treated iNPH-patients.

Materials & Methods: Nineteen iNPH patients (mean age 75 years) underwent clinical tests prior- and post-shunting and a 7T MRI examination prior to surgery (Philips 7T Achieva). CSF flow in the cerebral aqueduct was measured using RT 2D-PC MRI with a golden-angle radial trajectory (Fig. 1) [15].

Moreover, CSF flow measurements were also acquired using a conventional CG 2D-PC MRI technique (Fig. 1). The RT data was reconstructed offline using MRecon (Gyrotools) and BART (v0.4.03) tools. Data analysis was performed in Segment (v4.1 R14708 Medviso [16]) with custom plugins for RT flow analysis (Fig. 2). Stroke volume (SV) for CG flow measurements was defined as the sum of the antegrade and retrograde flow volumes divided by two. For RT flow measurements, the CSF volume, meaning the mean volume passing through the aqueduct at a given scan time, was computed in the same way as SV. The net flow for both RT and CG flow measurements was defined as the difference between antegrade and retrograde flow volumes. Percentage change in clinical test scores from 12 months prior to 3 months post shunting was calculated. Positive values indicated improvement. A test-specific normative distribution of the percentage changes was created via bootstrapping, and thresholds were determined from the 95% confidence intervals (CI). Individual test results were classified as "Improved," "Worsened" or "Inconclusive" based on these thresholds. A normalized improvement score (NIS) was derived for each patient by subtracting the number of "Worsened" tests from the "Improved" ones and dividing the total number of tests.

Results: A statistically significant relationship was found between RT net flow and NIS ($p < 0.05$) (Fig. 3c). Patients who responded favourably to the surgery had RT net flow in the cranial direction (retrograde flow). In contrast, no statistically significant correlations were found between CSF volume and NIS (Fig. 3d). Similarly, no correlations were found while analysing CG net flow and SV with patients' response to treatment (Fig. 3a and Fig. 3b). A comparison of the iNPH RT net flow data with that of healthy volunteers (mean age 26 years) gave a statistically significant difference ($p < 0.05$). The longitudinal differences in test scores across all cognitive and motor function tests were investigated. A statistically significant difference was found for the motor function tests ($p < 0.01$).

Scan parameter	Cardiac-gated PC	Real-time PC
Acquisition mode	cartesian	golden angle radial
In-plane resolution (mm ²)	0.3 × 0.3	0.6 × 0.6
Slice thickness (mm)	5	
V _{enc} (cm/s)	15	
TR / TE / α (ms / ms / °)	15 / 4.8 / 7	11 / 5.1 / 7
Temporal resolution (ms)	60	168
Bandwidth (Hz)	312	202
Scan duration (mm:ss)	2:27	0:50

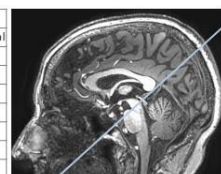


Fig. 1: Summary of the scan parameters for the cardiac-gated and real-time phase contrast scans (left), and an illustration of the placement of the flow measurement plane orthogonal to the cerebral aqueduct (right).

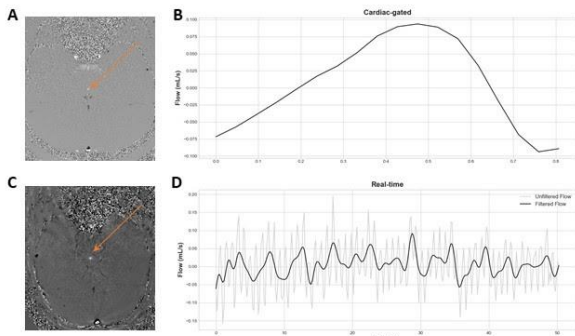


Fig. 2: The velocity image (A) and CSF flow curve (B) from the cardiac-gated scan, while (C) and (D) are from the real-time scan. In (D), the grey line shows the measured data with fast cardiac variations. The black line shows filtered data, isolating slow respiratory variations by removing high-frequency cardiac components.

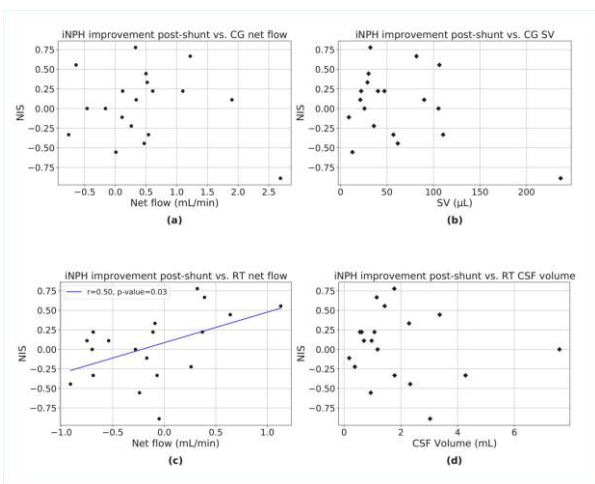


Fig. 3: Correlation between individual clinical improvement scores (NIS) in INPH patients and CSF dynamic parameters from both cardiac-gated and real-time scans. Net flow (a) and stroke volume (b) for cardiac-gated flow. Net flow (c) and CSF volume (d) for real-time flow.

Discussion: The higher resolution obtained in both RT and CG using a 7T MR enabled an accurate delineation of the aqueduct and quantification of CSF flow, effectively reducing partial volume effects (PVE) [17]. The temporal resolution for RT flow measurements was selected in the image reconstruction to investigate the slow variations in CSF flow. Study limitations include the small and heterogeneous cohort. For future studies, this number is being increased to improve statistics and provide a stronger basis to evaluate RT net flow as a possible shunt predictor for iNPH. Another limitation was that healthy volunteers and INPH patients were not age-matched. In the present study, it is unclear whether the statistically significant difference found between the two groups was due to the age difference or the neurological condition itself. In future analysis, other parameters such as velocity and the ratio of respiratory to cardiac frequency components will also be investigated. Moreover, both CG and RT flow measurements were studied under free-breathing conditions. Hence, the introduction of respiratory guided exercises could give a deeper understanding into how respiration influences CSF flow dynamics. A recent study investigates CSF flow in several anatomical locations in iNPH

patients using an EPI-based RT PC method, showing differences in patients and age-matched controls [14]. Notably, they suggest that disordered breathing may be a contributing factor in iNPH pathophysiology, supporting the use of RT PC over CG PC in this patient group.

Conclusion: This study findings suggest that RT PC measurements of net CSF flow in the cerebral aqueduct provide an indication of the outcome of shunting in patients with iNPH, with retrograde flow (cranial direction) correlating to clinical improvement. The clinical relevance of the method will be further assessed with the implementation of a larger study. A particular focus should be on motor function tests as they gave a statistically significant difference between prior-to post-shunt placement surgery.

Acknowledgements: The Swedish National 7T facility at Lund University Bioimaging Center is gratefully acknowledged for providing experimental resources.

References:

- Constantinescu, C., et al., "Prevalence of Possible Idiopathic Normal Pressure Hydrocephalus in Sweden: A Population-Based MRI Study in 791 70-Year-Old Participants", *Neurology*:102:e208037 (2024), DOI: 10.1212/wnl.0000000000208037
- Klinge, P et al. "One-year outcome in the European multicentre study on iNPH." *Acta Neurologica Scandinavica* vol. 126,3 (2012): 145-53. doi:10.1111/j.1600-0404.2012.01676.x
- Halperin, John J et al. "Practice guideline: Idiopathic normal pressure hydrocephalus: Response to shunting and predictors of response: Report of the Guideline Development, Dissemination, and Implementation Subcommittee of the American Academy of Neurology." *Neurology* vol. 85,23 (2015): 2063-71. doi:10.1212/WNL.0000000000002193
- Carlsen, Jonathan Frederik et al. "Can preoperative brain imaging features predict shunt response in idiopathic normal pressure hydrocephalus? A PRISMA review." *Neuroradiology* vol. 64,11 (2022): 2119-2133. doi:10.1007/s00234-022-03021-9
- Blitz, A M et al. "Does Phase-Contrast Imaging through the Cerebral Aqueduct Predict the Outcome of Lumbar CSF Drainage or Shunt Surgery in Patients with Suspected Adult Hydrocephalus?." *AJNR. American journal of neuroradiology* vol. 39,12 (2018): 2224-2230. doi:10.3174/ajnr.A5857
- Shanks, J et al. "Aqueductal CSF Stroke Volume Is Increased in Patients with Idiopathic Normal Pressure Hydrocephalus and Decreases after Shunt Surgery." *AJNR. American journal of neuroradiology* vol. 40,3 (2019): 453-459. doi:10.3174/ajnr.A5972
- Bradley, William G Jr. "Magnetic Resonance Imaging of Normal Pressure Hydrocephalus." *Seminars in ultrasound, CT, and MR* vol. 37,2 (2016): 120-8. doi:10.1053/j.sult.2016.01.005
- Qvarlander, S., et al. "Cerebrospinal fluid and blood flow patterns in idiopathic normal pressure hydrocephalus." *Acta Neurologica Scandinavica*:135:576 (2017), DOI: 10.1111/ane.12636
- Eide, Per Kristian et al. "Direction and magnitude of cerebrospinal fluid flow vary substantially across central nervous system diseases." *Fluids and barriers of the CNS* vol. 18,1 16. 1 Apr. 2021, doi:10.1186/s12987-021-00251-6
- Klose, U., et al. "Detection of a relation between respiration and CSF pulsation with an echoplanar technique". *Jmri-Journal of Magnetic Resonance Imaging*:11:438 (2000), DOI: 10.1002/(sici)1522-2586(200004)11:4<438::Aid-jmri12>3.0.Co;2-o
- Yildiz, Selda et al. "Quantifying the influence of respiration and cardiac pulsations on cerebrospinal fluid dynamics using real-time phase-contrast MRI." *Journal of magnetic resonance imaging : JMri* vol. 46,2 (2017): 431-439. doi:10.1002/jmri.25591
- Liu, Pan et al. "Cardiac and respiratory activities induce temporal changes in cerebral blood volume, balanced by a mirror CSF volume displacement in the spinal canal." *NeuroImage* vol. 305 (2025): 120988. doi:10.1016/j.neuroimage.2024.120988
- Dreha-Kulaczewski, Steffi et al. "Inspiration is the major regulator of human CSF flow." *The Journal of neuroscience : the official journal of the Society for Neuroscience* vol. 35,6 (2015): 2485-91. doi:10.1523/JNEUROSCI.3246-14.2015
- Karki, Pragati et al. "Real-Time 2D Phase-Contrast MRI to Assess Cardiac- and Respiratory-Driven CSF Movement in Normal Pressure Hydrocephalus." *Journal of neuroimaging : official journal of the American Society of Neuroimaging* vol. 35,1 (2025): e70000. doi:10.1111/jon.70000
- Töger, Johannes et al. "Real-time imaging of respiratory effects on cerebrospinal fluid flow in small diameter passageways." *Magnetic resonance in medicine* vol. 88,2 (2022): 770-786. doi:10.1002/mrm.29248
- Bidhult, Sebastian et al. "A new vessel segmentation algorithm for robust blood flow quantification from two-dimensional phase-contrast magnetic resonance images." *Clinical physiology and functional imaging* vol. 39,5 (2019): 327-338. doi:10.1111/cpf.12582
- Tang, C et al. "Accuracy of phase-contrast flow measurements in the presence of partial-volume effects." *Journal of magnetic resonance imaging : JMri* vol. 3,2 (1993): 377-85. doi:10.1002/jmri.1880030213

The impact of the current-induced magnetic fields on the BOLD signal measured in concurrent tDCS-fMRI

Teresa Cunha 1+2*, Miro Grundeis 3, Lars G. Hanson 1+2, Fróði Gregersen 1+2, Till Nierhaus 3, Felix Blankenburg 3, Axel Thielscher 1+2

1 Section for Magnetic Resonance, DTU Health Tech, Technical University of Denmark, Kgs Lyngby, Denmark

2 Danish Research Centre for Magnetic Resonance, Copenhagen University Hospital - Amager and Hvidovre, Copenhagen, Denmark

3 Free University of Berlin, Berlin, Germany

Abstract: fMRI is frequently used to assess brain activity modulation by transcranial electrical stimulation (tES). tES currents, especially those in the electrode cables, induce magnetic fields (ΔB_{zc}) that locally change the main field B_0 and distort the EPI images. The resulting intensity changes can be comparable to the blood-oxygen-level-dependent (BOLD) signal. The goal of this study was to identify and correct the main effects of ΔB_{zc} in typical fMRI EPI series. Concurrent tES-fMRI experiments were performed in a phantom and human brains, and the main artifacts characterized. A tailored acquisition and processing pipeline for mitigating ΔB_{zc} -induced artifacts was developed, which substantially reduced those undesired effects.

Motivation: EPI is the standard sequence for fMRI[1] due to its high temporal resolution, despite the well-known susceptibility to field inhomogeneities causing geometric distortions in the phase-encoding (PE) direction[2]. In tES-fMRI, the magnetic fields induced by the tES currents, ΔB_{zc} , add to the static field inhomogeneities. This issue has been demonstrated in subjects post-mortem[3], with signal changes comparable to BOLD effects. It is nevertheless commonly disregarded due to the weak brain currents typically applied in vivo, which induce negligible ΔB_{zc} . However, the effects of ΔB_{zc} from the currents in the electrode cables should also be considered. These are easily calculated using the Biot-Savart law and knowledge of the cable paths[4], which can be visualized using ultra-short echo time structural scans (e.g., PETRA[5]).

Heating from fast switching imaging gradients causes slow drifts of the scanner's center frequency over time. If this is not adjusted during an EPI series, the reconstructed images will appear to drift in the PE direction. The effect of ΔB_{zc} on the measurement and update of the center frequency should therefore be assessed. Finally, subject movement during long fMRI scans is expected, and rigid motion correction is commonly done. The sensitivity of these algorithms to the time-varying ΔB_{zc} artifacts is also worth an investigation. Here, we characterize the aforementioned artifacts and implement an acquisition and preprocessing pipeline to mitigate them. Because their severity and implications depend on specific experimental choices (e.g., cable configuration, paradigm, imaging parameters), this study can inform the design of more robust experiments.

Materials & Methods: An in-house built phantom and healthy volunteers were scanned at 3T (MAGNETOM Prisma, Siemens Healthcare, Erlangen, Germany) using a 64-channel head coil and the sequence "Multi-Band EPI C2P" from the Center for Magnetic Resonance Research (Minneapolis, USA). The following parameters were used: echo/repetition times TE/TR=36.8/1000 ms, echo spacing=0.54 ms, flip-angle=60°,

matrix size=110×110×10, 2×2×2 mm³ voxels, no RF-spoiling nor multislice/in-plane acceleration.

The current flow was either confined to a cable loop close to the head, or consisted of transcranial stimulation, with "injection" schemes varying across experiments. ΔB_{zc} was simulated by applying the Biot-Savart law to the current path. For the cable currents, this coincides with the cable paths which were imaged using a PETRA scan[4]. For the brain currents, their path was simulated using SimNIBS[6] 4.0.0. Two tES-fMRI pipelines were implemented: a conventional one using scanner-reconstructed images acquired with online center frequency updating and standard motion correction using SPM12[7]; an adapted one using images reconstructed from k-space with adapted offline frequency drift compensation, followed by adapted motion correction and correction of distortions caused by ΔB_{zc} from the cables. For frequency drift compensation, the global image shifts were estimated from the k-space center in the ghost correction lines. The current "injection" scheme was regressed out from the obtained time series, and the same was done to the series of motion parameters.

First-level fMRI analyses were conducted using FSL FEAT[8] without spatial smoothing, high-pass filter cutoff of 0.005 Hz, no prewhitening and the current scheme as regressor (all data acquired in resting state).

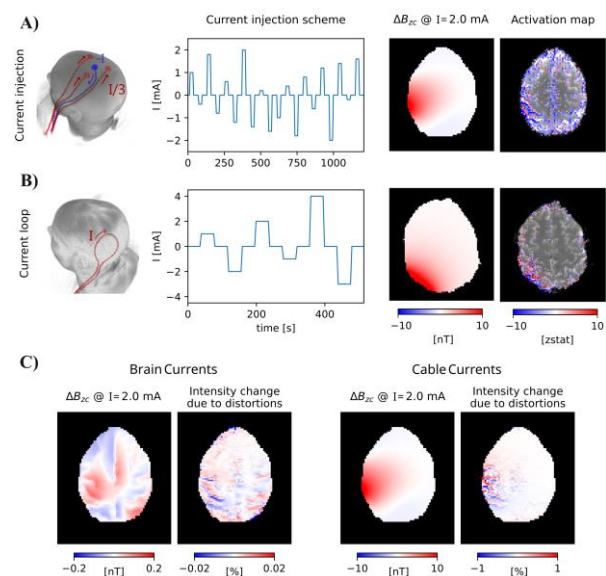


Fig. 1: tDCS-fMRI experiments with current injection and loop. A&B) Cable configuration, current (I) scheme, magnetic fields induced by cable currents (ΔB_{zc}), and z-statistics using I scheme as regressor of interest. C) ΔB_{zc} and expected intensity changes due to distortions, for simulated brain and cable currents, for the electrode montage in A.

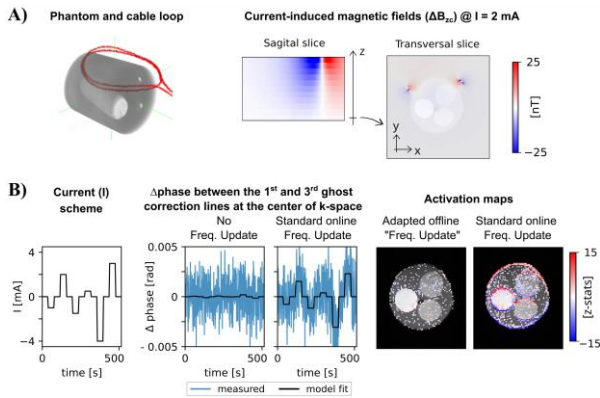


Fig. 2: Effect of ΔB_{zc} on central frequency, shown in a slice without/with online frequency updating. A) Cable configuration, and sagittal/transverse views of the resulting ΔB_{zc} . B) Current scheme, detrended phase differences between first and third ghost correction lines at the k-space center (blue) with fitted current scheme (black), and activation maps.

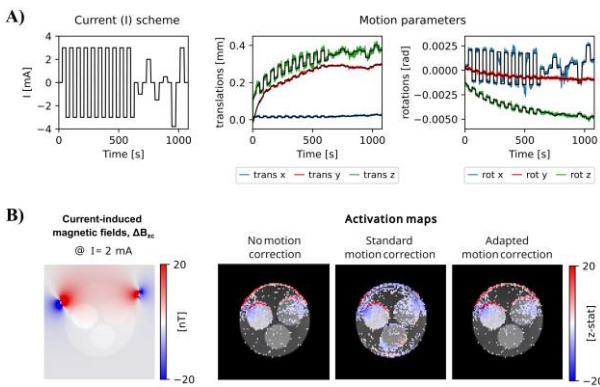


Fig. 3: Sensitivity of standard rigid motion correction to ΔB_{zc} -induced distortions (cable configuration in Figure 2-A). A) Current scheme and motion parameters (color). A model containing a 6th-order polynomial and the current scheme was fitted to each series (black). B) ΔB_{zc} and activations without/with standard/with adapted motion correction methods for example slice.

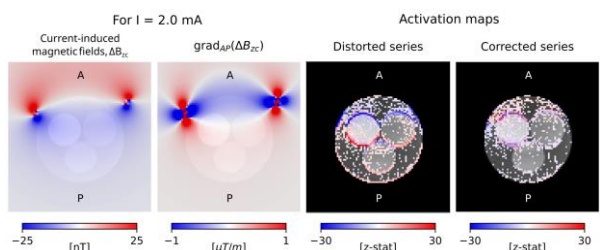


Fig. 4: Sensitivity of fMRI analysis to local current-induced distortions (phantom and cable configuration in Figure 2-A). Left to right: current-induced magnetic fields, ΔB_{zc} , their gradient in the phase-encoding direction, $grad\Delta B_{zc}$, and activations for original/distortion-corrected image series, for an example slice. The correction significantly reduced false positives around the inner compartments.

Results: Figures 1-A&B depict two resting state tDCS-fMRI experiments: during transcranial stimulation (A) or with currents confined to a cable loop (B). With a conventional pipeline, significant activations were found in both cases, and the activation pattern was strongly correlated with ΔB_{zc} from the cable currents. Some unexpected remote effects were also found. For the experiment with current injection, the simulated fields from the brain and cable currents are compared in Figure 1-C. The latter is estimated to induce 50 times stronger fields than the former. Figure 2 demonstrates, in a phantom experiment, the effect of ΔB_{zc} on the online

central frequency update. That is shown to cause remote effects – strong activations were seen in the lowest slice, despite the weak ΔB_{zc} . Those effects were largely mitigated with the adapted offline frequency drift compensation, which was used to produce the following results. Figure 3 reveals the sensitivity of a standard rigid motion correction method to the ΔB_{zc} -induced distortions. The current “injection” scheme was clearly visible in the motion parameters and, if not excluded, changed the well-understood local effects and induced unexpected remote ones. The adapted pipeline successfully avoided this. Finally, Figure 4 shows how the remaining activations were greatly reduced by correcting the time-varying geometric distortions caused by ΔB_{zc} and its gradients in the phase-encoding direction.

Discussion: In line with our previous findings[4], the simulations performed here show that the currents in the electrode cables, for being more concentrated than those inside the brain, create much stronger magnetic fields than the latter (Figure 1-C). Indeed, the strongest activations correlate well with ΔB_{zc} from the cables, both for the current injection and loop experiments (Figure 1-A&B). While these results support the common belief that the tES brain currents are too weak to cause in-vivo effects comparable to BOLD, they show that the effects of the cable currents may not be negligible. Another important finding is the sensitivity of the online center frequency updating to ΔB_{zc} . Unlike the local distortions caused by field inhomogeneity, the effects of ΔB_{zc} on the frequency updating are quite unpredictable: There is an averaging effect of ΔB_{zc} over the imaged volume, and the resulting shift affects all voxels equally. This causes signal changes far from the strongest ΔB_{zc} (Figure 2) and disturbs the well-understood local distortions. Lastly, standard rigid motion correction pipelines (rotations and translations only) were also shown to induce remote effects, while coarsely mitigating the non-linear local distortions (Figure 3). The proposed adapted pipeline substantially reduced the ΔB_{zc} -induced artifacts on a phantom (Figure 4). However, given its complexity, the feasibility of making it a standard procedure in real tES-fMRI human experiments remains to be assessed. These artifacts should preferably be avoided by design, through cable configurations that reduce the magnetic fields induced along z, and fMRI paradigms less sensitive to such artifacts.

Conclusion: In this study, we have shown that tES currents in the electrode cables can induce much stronger magnetic fields than the dispersed currents inside the brain. We have identified and characterized the local geometric distortions, center frequency update and rigid motion correction as the main mechanisms by which ΔB_{zc} induces artifacts in concurrent tES-fMRI data. We have adapted the data acquisition and processing pipeline to account for them and shown satisfactory results on a phantom. Given its complexity, the feasibility of correcting real tDCS-fMRI human data is still to be assessed. However, these artifacts should preferably be avoided by design, through cable configurations that reduce the magnetic fields induced along z, imaging parameters that reduce distortions, and fMRI paradigms less sensitive to such kind of artifacts.

References:

- [1] Glover G. H. (2011). Overview of functional magnetic resonance imaging. *Neurosurgery clinics of North America*, 22(2), 133–vii. <https://doi.org/10.1016/j.nec.2010.11.001>
- [2] Jezzard, P., & Balaban, R. S. (1995). Correction for geometric distortion in echo planar images from B0 field variations. *Magnetic resonance in medicine*, 34(1), 65–73. <https://doi.org/10.1002/mrm.1910340111>
- [3] Antal, A., Bikson, M., Datta, A., Lafon, B., Dechent, P., Parra, L. C., & Paulus, W. (2014). Imaging artifacts induced by electrical stimulation during conventional fMRI of the brain. *NeuroImage*, 85 Pt 3(0 3), 1040–1047. <https://doi.org/10.1016/j.neuroimage.2012.10.026>
- [4] Göksu, C., Scheffler, K., Siebner, H. R., Thielscher, A. & Hanson, L. G. (2019). The stray magnetic fields in Magnetic Resonance Current Density Imaging (MRCDI). *Physica Medica: European Journal of Medical Physics*, Volume 59, 142 – 150. <https://doi.org/10.1016/j.ejmp.2019.02.022>
- [5] Grodzki, D. M., Jakob, P. M., & Heismann, B. (2012). Ultrashort echo time imaging using pointwise encoding time reduction with radial acquisition (PETRA). *Magnetic resonance in medicine*, 67(2), 510–518. <https://doi.org/10.1002/mrm.23017>
- [6] Thielscher, A., Antunes, A., & Saturnino, G. B. (2015). Field modeling for transcranial magnetic stimulation: A useful tool to understand the physiological effects of TMS?. *IEEE Engineering in Medicine and Biology Society. Annual International Conference, 2015*, 222–225. <https://doi.org/10.1109/EMBC.2015.7318340>
- [7] <https://www.fil.ion.ucl.ac.uk/spm/software/spm12/>
- [8] https://web.mit.edu/fsl_v5.0.10/fsl/doc/wiki/FEAT.html

Integrating in situ parahydrogen hyperpolarization and 18F-FDG-PET: toward high throughput single-device multimodal metabolic imaging

Henri de Maissin[a,b], Obaid Mohiuddin[a], Isidora Kapor[a], Sergey Korchak[c,d], Theresa Hune[a,c,d], Justyna Platek[b,e], Denis Moll[c,d], Andreas Korzowski[b,e], Maxim Zaitsev[a], Stefan Glöggler[c,d], Prof. Dr. Matthias Eder[a], Andreas Schmidt[a,b]

[a] Division of Medical Physics, Department of Diagnostic and Interventional Radiology, University Medical Center Freiburg, Faculty of Medicine, University of Freiburg, 79106, Freiburg, Germany

[b] German Cancer Consortium (DKTK), partner site Freiburg, and German Cancer Research Center (DKFZ), Heidelberg 69120, Germany

[c] NMR Signal Enhancement Group, MaxPlanck Institute for Multidisciplinary Sciences, Am Fassberg 11, 37077 Göttingen, Germany

[d] Center for Biostructural Imaging of Neurodegeneration of the University Medical Center Göttingen, 37075 Göttingen, Germany

[e] Division of Medical Physics in Radiology, German Cancer Research Center (DKFZ), Heidelberg, Germany

Abstract: While 18F-FDG PET has revolutionized oncologic imaging, it remains limited by high cost, limited availability, and long scan times. Hyperpolarized 13C MRI offers high-throughput metabolic imaging without ionizing radiation and complementary information to FDG-PET but still requires external polarizers that can exceed cost and complexity of MRI scanners. In this pilot study, we implement Synthesis Amid the Magnet Bore Allows Dramatically Enhanced Nuclear Alignment (SAMBADENA) in a 3T sequential PET/MR system. Using hydrogenative parahydrogen (pH₂) induced polarization, we achieve over 20% 13C polarization of ethyl [1-13C]-pyruvate-d₆ in under 20 seconds. This represents a key step toward accessible, low-cost, high-throughput multimodal metabolic imaging.

Motivation: Metabolic imaging plays a central role in modern cancer diagnostics, complementing functional and anatomical imaging techniques. Positron emission tomography (PET), the current gold standard for metabolic imaging, has transformed oncology by offering an indirect measure of the Warburg effect via monitoring FDG uptake¹. However, it provides no chemical information for analysis of metabolic pathways and is often limited by operational costs, availability, and long examination durations. In contrast, hyperpolarized magnetic resonance imaging (HP-MRI) enables direct, quantitative assessment of tissue metabolism, with short scan times (<5 minutes)² and no ionizing radiation². Combining these two modalities offers synergies and promises to deepen our understanding of metabolic processes, also to further validate 13C-HP contrast agents. Prior work by Gutte *et al.* demonstrated the feasibility of simultaneous multi-modal metabolic imaging^{3,4}; still, their studies were constrained by complex workflows and low throughput, requiring over two hours per animal and relying on dissolution dynamic nuclear polarization (dDNP).

In this work, we propose a high-throughput, low-cost alternative using hydrogenative pH₂-induced polarization (PHIP)⁵. Unlike dDNP, PHIP enables rapid in situ generation of hyperpolarized [1-13C]-pyruvate-d₆ directly within the bore of the same MRI scanner used for acquisition. This integration minimizes system footprint, reduces preparation time, and enhances accessibility⁶. We present preliminary results toward the multimodal imaging application in tumor-bearing mice using a 3T sequential PET/MR system (Bruker, Ettlingen, Germany), for future side-by-side application of 13C pyruvate-to-lactate conversion with 18F-FDG uptake in mouse models.

Materials & Methods: General Setup: The general workflow is depicted in Figure 1: a preclinical sequential PET/MR 3T system (Bruker, Ettlingen, Germany) is envisioned to be used

to i) image the anatomy of an animal with proton-MRI, ii) image 18F-FDG-PET, iii) generate hyperpolarized [1-13C]-pyruvate-d₆ with RF-pulsed sequence, and iv) image the subsequent 13C HP-MRI signal.

Samples: pH₂ was enriched to ≈90% using a helium cryostat equipped with an iron-oxide catalyst⁷. The reaction solvent used was acetone-d₆ (400 μL per experiment). The hydrogenation catalyst was [Rh(dppb)(COD)]BF₄ (CAS: 79255-71-3), and either vinyl-[1-13C]-acetate-d₆ (VA, 1.1% naturally abundant 13C; CAS: 189765-98-8) or vinyl-[1-13C]-pyruvate-d₆ (VP, 100% 13C-labeled) were used as precursor.

Hyperpolarization: A 3D-printed NMR-tube holder was created to allow the solution to be placed at the iso-center while being surrounded by a 60°C water bath, ensuring prompt hydrogenation (see Figure 1). 8 bar pH₂ was guided through the sample for 20 s under continuous-gas-flow conditions. The proton polarization was then either made in-phase with Out-of-Phase Echo (OPE) pulse sequence for T₁ determination, or transferred to the 13C nucleus with a modified ESOTHERIC sequence described elsewhere⁸, for the evaluation of the polarization transfer efficiency.

Experiments: For proton T₁ determination, a train of low flip-angle pulses (5°) was played every 10 s, and a series of FIDs were acquired. For determination of 13C-hyperpolarization, the hyperpolarized 13C signal was detected at the end of the polarization transfer sequence and quantified by comparing it with the signal of a thermally-polarized reference solution (neat 17.4 M [1-13C]-acetic acid (CAS:1563-79-7)).

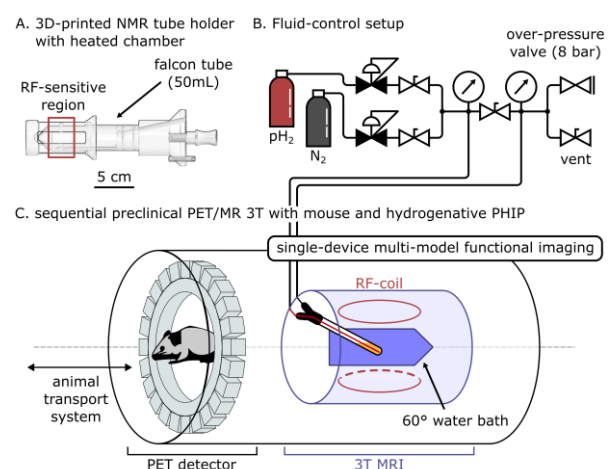


Fig. 1: General setup of the hydrogenative PHIP system integrated inside the PET/MR scanner. A. Custom NMR-tube holder with integrated heated chamber. B. Fluid-control setup for directing pH₂ through the reaction solution. C. Single-device multimodal metabolic imaging setup, including PET detector, MRI system, animal transport unit and polarizer.

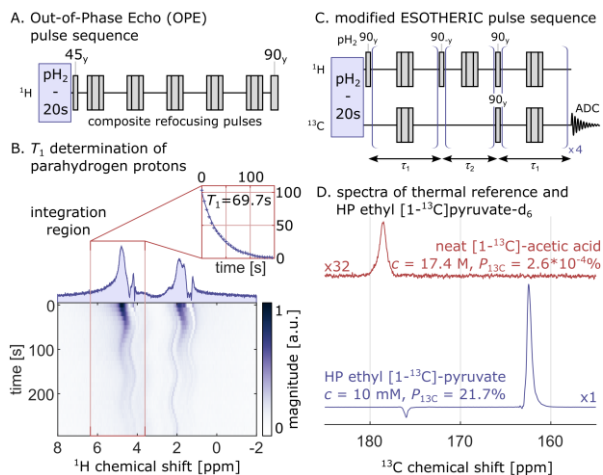


Fig. 2: A. Out-of-Phase Echo sequence⁹ with five composite refocusing pulses. B. Stacked spectra from low-flip angle acquisitions used for proton T_1 determination, along with the first spectrum of the series and its peak integration, with exponential fitting. C. Modified ESOTHERIC pulse sequence⁸. D. Spectra of hyperpolarized ethyl [1- 13 C]-pyruvate- d_6 and thermal reference.

Results: In the first series of experiments, we determined the T_1 relaxation time of the pH₂-derived protons in ethyl acetate- d_6 . Following hydrogenation of vinyl acetate- d_6 with pH₂, the Out-of-Phase Echo (OPE) sequence (see Figure 2)⁹ was used to convert the initial anti-phase signal into a longitudinal in-phase signal, enabling T_1 determination from a single experiment, using a train of low flip-angle RF pulses (5°). Despite the broad spectral lines caused by suboptimal magnetic field homogeneity inside the MRI bore, both hyperpolarized proton resonances were clearly detected. The resulting chemical shift spectrum exhibited a periodic oscillation with a ~2-minute period, attributed to heating effects from the shim iron components of the MRI. This oscillation did not interfere with peak integration. The T_1 of the pH₂-nascent protons in ethyl acetate- d_6 was determined to be 69.7 s.

In the second series of experiments, we evaluated the maximum achievable 13 C polarization using ethyl [1- 13 C]-pyruvate- d_6 . After 20 seconds of hydrogenation of vinyl [1- 13 C]-pyruvate- d_6 with pH₂, a modified ESOTHERIC pulse sequence was applied to transfer polarization from the nascent protons to the 13 C carboxylic site. By comparing the signal intensity to that of a thermally polarized reference sample, we reproducibly achieved a 13 C polarization level of 21.7% in ethyl [1- 13 C]-pyruvate- d_6 . The out-of-phase resonance line at 176.5 ppm is a side-product of the synthesis of the precursor.

Discussion: In this study, we optimized the experimental conditions of SAMBADENA to enhance polarization levels. Using an NMR tube as the hydrogenation vessel provides a more homogeneous magnetic field, while the surrounding heated water bath significantly accelerates the reaction kinetics by continuously heating the acetone solution. This configuration helps reduce polarization losses prior to the transfer step. Although the MRI bore typically poses challenges for pulsed sequences—due to B₀ inhomogeneity and suboptimal B₁₊ amplitude, we use the modified ESOTHERIC pulse sequence, which was shown to be resilient to the MRI limitations⁸, enabling improved polarization transfer efficiency. Achieving 21.7% polarization of ethyl [1- 13 C]-pyruvate- d_6 represents a significant milestone for preclinical applications, particularly as previous studies have reported 30-50% retention of initial polarization following

purification^{10,11}. Performing hyperpolarized 13 C MRI on a 3T preclinical PET/MR scanner is especially advantageous, as this field strength combines extended T_1 relaxation times with adequate chemical shift dispersion to resolve key metabolites spectrally¹². Moving forward, we aim to perform voxel-wise comparisons of 18F-FDG uptake and pyruvate-to-lactate conversion rates in the same subjects, across both healthy and tumor tissues. This correlation may yield deeper insights into the relationship between glucose uptake and the Warburg effect in cancer metabolism.

Conclusion: In this preliminary study, we have established Synthesis Amid the Magnet Bore Allows Dramatically Enhanced Nuclear Alignment (SAMBADENA) on a sequential PET/MR 3T system, paving the way toward high throughput multi-modal imaging. The proton T_1 of EA of 69.7 s and 21.7% 13 C polarization of EP are suitable for preclinical applications. By combining the compact PHIP setup inside the bore of the MRI, first pilot single-device multimodal metabolic imaging studies are on the horizon.

Acknowledgements: This work was supported by the German Cancer Consortium (DKTK) (A.B.S.), B.E.S.T. Fluidsysteme GmbH | Swagelok Stuttgart (A.B.S.), the German Research Foundation (DFG) grants: #SCHM 3694/1-1, #SCHM 3694/2-1, and #SFB1479 (A.B.S.), the German Federal Ministry of Education and Research (BMBF) in the funding program “Quantum Technologies—from Basic Research to Market” under the project “QuE-MRT” (contract number: 13N16448). The authors thank the Core Facility AMIRCF (DFG-Risources N° RI_00052) for support in this study. S.G. thanks the MaxPlanck Society, the Deutsche Forschungsgemeinschaft (DFG) for funding (grants 418416679, 426677227, and 450146057).

References:

1. A. Kjaer, A. Loft, I. Law, A. K. Berthelsen, L. Borgwardt, J. Löfgren, C. B. Johnbeck, A. E. Hansen, S. Keller, S. Holm and L. Højgaard, *PET/MRI in cancer patients: first experiences and vision from Copenhagen*, *Magn Reson Mater Phys*, 2013, 26, 37–47.
2. Z. J. Wang, M. A. Ohliger, P. E. Z. Larson, J. W. Gordon, R. A. Bok, J. Slater, J. E. Villanueva-Meyer, C. P. Hess, J. Kurhanewicz and D. B. Vigneron, *Hyperpolarized 13 C MRI: State of the Art and Future Directions*, *Radiology*, 2019, 291, 273–284.
3. H. Gutte, A. E. Hansen, M. M. E. Larsen, S. Rahbek, S. T. Henriksen, H. H. Johannesen, J. Ardenkjaer-Larsen, A. T. Kristensen, L. Højgaard and A. Kjaer, *Simultaneous Hyperpolarized 13 C-Pyruvate MRI and 18F-FDG PET (HyperPET) in 10 Dogs with Cancer*, *Journal of Nuclear Medicine*, 2015, 56, 1786–1792.
4. H. Gutte, A. E. Hansen, S. T. Henriksen, H. H. Johannesen, J. Ardenkjaer-Larsen, A. Vignoud, A. E. Hansen, B. Børresen, T. L. Klausen, A.-M. N. Wittekind, N. Gillings, A. T. Kristensen, A. Clemmensen, L. Højgaard and A. Kjaer, *Simultaneous hyperpolarized 13 C-pyruvate MRI and 18F-FDG-PET in cancer (hyperPET): feasibility of a new imaging concept using a clinical PET/MRI scanner*, *American Journal of Nuclear Medicine and Molecular Imaging*, 2014, 5, 38.
5. C. R. Bowers and D. P. Weitekamp, *Transformation of Symmetrization Order to Nuclear-Spin Magnetization by Chemical Reaction and Nuclear Magnetic Resonance*, *Phys. Rev. Lett.*, 1986, 57, 2645–2648.
6. A. B. Schmidt, S. Berner, W. Schimpf, C. Müller, T. Lickert, N. Schwaderlapp, S. Knecht, J. G. Skinner, A. Dost, P. Rovedo, J. Hennig, D. von Elverfeldt and J.-B. Hövener, *Liquid-state carbon-13 hyperpolarization generated in an MRI system for fast imaging*, *Nat Commun*, 2017, 8, 14535.
7. J.-B. Hövener, S. Bär, J. Leupold, K. Jenne, D. Leibfritz, J. Hennig, S. B. Duckett and D. von Elverfeldt, *A continuous-flow, high-throughput, high-pressure parahydrogen converter for hyperpolarization in a clinical setting*, *NMR Biomed*, 2013, 26, 124–131.
8. H. de Maissin, V. Ivantsov, O. Mohiuddin, S. Berner, D. von Elverfeldt, M. Zaitsev, V. Kiselev and A. B. Schmidt, *Overcoming the Challenges of Hyperpolarizing Substrates with Parahydrogen-Induced Polarization in an MRI System*, *Chemistry – A European Journal*, 2025, 31, e202402911.
9. A. N. Pravidtsev, J.-B. Hövener and A. B. Schmidt, *Frequency-Selective Manipulations of Spins allow Effective and Robust Transfer of Spin Order from Parahydrogen to Heteronuclei in Weakly-Coupled Spin Systems*, *ChemPhysChem*, 2022, 23, e202100721.
10. H. de Maissin, P. R. Groß, O. Mohiuddin, M. Weigt, L. Nagel, M. Herzog, Z. Wang, R. Willing, W. Reichardt, M. Pichotka, L. Heß, T. Reinheckel, H. J. Jessen, R. Zeiser, M. Bock, D. von Elverfeldt, M. Zaitsev, S. Korchak, S. Glöggler, J.-B. Hövener, E. Y. Chekmenev, F. Schilling, S. Knecht and A. B. Schmidt, *In Vivo Metabolic Imaging of [1- 13 C]Pyruvate- d_3 Hyperpolarized By Reversible Exchange With Parahydrogen*, *Angew Chem Int Ed Engl*, 2023, 62, e202306654.
11. T. Hune, S. Mamone, H. Schroeder, A. P. Jagtap, S. Sternkopf, G. Stevanato, S. Korchak, C. Fokken, C. A. Müller, A. B. Schmidt, D. Becker and S. Glöggler, *Metabolic Tumor Imaging with Rapidly Signal-Enhanced 1- 13 C-Pyruvate- d_3* , *ChemPhysChem*, 2023, 24, e202200615.
12. J. W. Gordon, H.-Y. Chen, N. Dwork, S. Tang and P. E. Z. Larson, *Fast Imaging for Hyperpolarized MR Metabolic Imaging*, *Journal of Magnetic Resonance Imaging*, 2021, 53, 686–702.

In-vitro and in-vivo comparison of accelerated dual-Venc 4D flow MRI using radial trajectories.

Adrian Duckert^{1,2*}, Susanne Schnell²⁺³, Ann-Christin Klemenz¹, Chris Lappe¹, Eiko Rathmann⁴, Ali El Ahmar², Marc-André Weber¹, Patrick Winter²⁺³

¹ Institute of Diagnostic and Interventional Radiology, Pediatric Radiology and Neuroradiology, University Medical Center Rostock, Germany

² Department of Medical Physics, University of Greifswald, Greifswald, Germany

³ Northwestern University, Chicago, USA

⁴ Institute for Diagnostic Radiology and Neuroradiology, University Medicine Greifswald, Greifswald, Germany

Abstract: Purpose: To evaluate radial undersampled trajectories for accelerated dual-VENC 4D-flow MRI in neurovascular applications. Methods: A radial 4D flow sequence with dual VENC was implemented using Stack-of-Stars and koosh-ball sampling and compared to a Cartesian PEAK-GRAPPA (R=5) reference. Experiments were performed in a healthy volunteer and an aneurysm phantom. Data was reconstructed using NUFFT and vessel-specific flow values were compared. Results: Similar median flow rates and peak velocities could be determined in-vitro. However, an underestimation of the flow with increasing acceleration was observed in-vivo. Conclusion: Radial dual-VENC 4D flow MRI is feasible for accelerated neurovascular imaging. However, future work needs to focus on advanced trajectories and reconstruction.

Motivation: Phase Contrast (PC) Magnetic Resonance Imaging (MRI) is a commonly used method to quantify hemodynamic parameters [1]. The dynamic range of measurable velocities is limited by the maximum encodable velocity (VENC). However, a higher Venc is also accompanied by more noise, thus slow velocities disappear in noise. In neurological measurements, however, both high flows (e.g., in the arteries, especially around stenoses) and slow flows (e.g., in the veins or in arterial aneurysms) occur. One way to increase the measurement range is to encode a second velocity (dual Venc), which increases the acquisition time. For a clinical application, it is therefore important to acquire two Vencs while reducing the measurement time and maintaining high spatial and temporal resolution [2]. Due to their intrinsic resistance to motion, radial measurements are a promising method to accelerate time-consuming flow measurements, also allowing for high spatio-temporal resolution [1]. However, the possible acceleration also depends on the choice of the sampling trajectory. The purpose of this study is to assess the effect of radial trajectories on the quantification of neurovascular flow parameters.

Materials & Methods: A radial 4D flow MRI sequence based on the Cartesian dual VENC (DV) sequence by S. Schnell [2] was developed. Cartesian DV-4D flow MRI with PEAK-GRAPPA (R=5) served as a reference. Cartesian, radial Stack of Stars (SoS) and koosh-ball measurements were performed in one healthy subject (25y/o, ethically approved) and in a phantom using a 3T MRI (MAGNETOM Vida) with an 18-channel ultra-flex coil (phantom) and a 20-channel head-neck coil (volunteer) (Siemens, Erlangen, Germany). The in-vitro koosh-ball acquisition was retrospectively down-sampled to 2000 spokes. All sequence parameters are given in Figure 1.

The flow phantom consisted of an aneurysm (Acandis, Germany) filled with blood-mimicking fluid (see Figure 2) [3]. Physiological pulsatile flow (25ml/s, 72BPM, carotid

waveform) was provided by a CompuFlow 1000-MR pump (Shelley Medical Imaging Technologies, London, Canada).

The radial measurements were reconstructed using an iterative density compensation [4] and a non-uniform Fourier transform (NUFFT) with MATLAB. The pre-processing, such as antialiasing, phase offset, and noise corrections, as well as the semi-automated segmentation and calculation of analysis planes, was done using in-house MATLAB tools [2,5].

For visualization, streamlines were determined to qualitatively compare overall flow pattern. For quantitative analysis, the median mean flow rates across the analysis planes along the tubes/vessels were calculated. In-vivo, the focus was limited to the middle cerebral arteries (MCA). Additionally, the inflow-outflow difference and the median peak velocity along the inflowing vessel I1 (see Figure 2) were determined in-vitro. The significance of differences between the measurements was determined using the Mann-Whitney-U-test.

Sequence	Voxel size	Slices	TE [ms]	TR [ms]	Temp. res. [cm/s]	Flip angle	# Spokes	Angle	VENC _{low} [cm/s]	VENC _{high} [cm/s]	Duration	R
Cartesian GRAPPA	1 mm isotropic	48	3	6	81	15°	-	-	40	80	12min 50s	5
Stack of Stars	1 mm isotropic	48	5	8	106	15°	144	Golden angle	50	100	49min 9s	1.7
Koosh-ball	1 mm isotropic	-	5	7	102	15°	5000/2000	Golden means*	50	100	35min 33s / 14min 13s	8 / 20
Cartesian GRAPPA	1 mm isotropic	40	3	6	83	15°	-	-	60	120	13min 24s	5
Stack of Stars	1 mm isotropic	48	5	7	101	15°	89	Golden angle	60	120	33min 48s	4.5
Koosh-ball	1 mm isotropic	-	4	7	97	15°	2000	Golden means*	60	120	14min 37s	50

Fig. 1: Parameter table of all measured sequences (top: phantom, bottom: in-vivo) and their duration with the acceleration factor R (*[7]).



Fig. 2: Aneurysm phantom inside a cylinder that was filled with Gd-doped transparent water beads (left) [3] and its segmentation with the inflowing tube I1 and the two outflowing tubes O1 and O2 (middle). On the right, the segmented Circle of Willis of the in-vivo acquisitions can be seen.

Results: Qualitative assessment: The streamlines follow the tubes/vessels anatomy in all cases (Figure 3 and 4). The Cartesian measurement exhibits the highest streamline density, while the koosh-ball acquisition with 2000 spokes resembles that with 5000 spokes but appears smoother. A lower streamline density in the radial measurements compared to the reference can also be seen in-vivo, especially in the peripheral arteries.

Quantitative assessment: For the Cartesian reference, the determined median flow rates (ml/s) along the tubes I1, O1 and O2 are $2.06(\pm 0.24)$, $0.52(\pm 0.06)$, and $1.22(\pm 0.09)$, respectively. Both the SoS measurement with $2.02(\pm 0.43)$, $0.51(\pm 0.14)$, and $1.07(\pm 0.17)$ and the 2000 spokes koosh-ball measurement with $1.96(\pm 0.35)$, $0.47(\pm 0.15)$, and $1.22(\pm 0.18)$ are similar to the Cartesian reference. The 5000 spokes koosh-ball measurement appears slightly higher with $2.32(\pm 0.26)$, $0.57(\pm 0.13)$, and $1.43(\pm 0.18)$ than the reference. The inflow-outflow difference yields 0.32ml/s for the Cartesian and 0.44ml/s for the SoS acquisition, while the 5000 and 2000 spokes koosh-ball acquisitions give 0.32ml/s and 0.27ml/s , respectively. The median peak velocity in tube I1 of the SoS measurement with 0.44m/s ($p=0.90$) and the 5000 spokes koosh-ball acquisition with 0.41m/s ($p=0.07$) are not significantly different from the reference with 0.46m/s . The 2000 spokes koosh-ball acquisition with 0.34m/s is lower than the reference ($p<0.001$). In the in-vivo measurements, the median mean flow rates (ml/s) of the left and right MCA were $3.42(\pm 0.57)$ and $3.71(\pm 0.27)$ in the Cartesian reference and $3.33(\pm 0.32)$ and $4.03(\pm 0.24)$ in the SoS acquisition. The determined values in the koosh-ball measurement with $2.13(\pm 0.34)$ and $3.31(\pm 0.19)$ were lower than the corresponding references (both $p<0.001$).

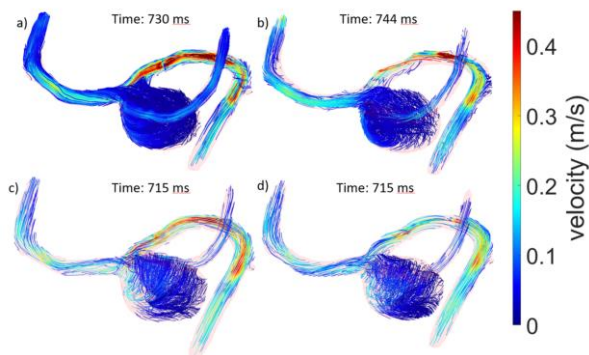


Fig. 3: Streamlines of the Cartesian (a), Stack of Stars (b) and koosh-ball with 5000 (c) and 2000 Spokes (d) measurement of the aneurysm phantom.

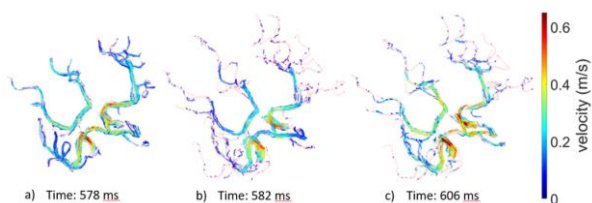


Fig. 4: Streamlines of the Cartesian (a), koosh-ball (b) and Stack of Stars (c) in-vivo measurements.

Discussion: We investigated the influence of different undersampled radial trajectories on the flow quantification. As the segmentation mask was created on the Cartesian datasets and co-registered to the radial dataset there are likely sub-voxel shifts between the mask and the actual vessels. Differences in the streamlines could be explained by the higher undersampling. The smoother streamlines in the retrospectively downsampled koosh-ball measurement may come from increased blurring when using a NUFFT reconstruction on undersampled data. This smoothing

combined with imperfect co-registration of the segmentation masks could also explain the underestimation of the flow rates in the radial in-vivo acquisitions and the observed difference between the flow rates of the left and right MCA in the koosh-ball measurement.

In-vitro, the flow rates in the tubes of the radial measurements were close to the Cartesian reference. The radial measurements agree with the reference for the peak flow velocities. The remaining difference between the inflow and the outflow in all cases may be due to the difference between the time the simulated pulse wave enters and leaves the phantom. Since the measurements were acquired using prospective gating, the measured surplus could leave the phantom between the last recorded frame and the next trigger.

In this preliminary study, we could show that an accelerated DV-4D Flow acquisition using radial trajectories is feasible. In future in-vivo and in-vitro studies, we will further investigate options for acceleration, reduction of TR/TE as well as, temporal resolution, for better comparability with the Cartesian reference.

Conclusion: The developed radial sequence returned similar flow measurements in-vitro and in-vivo as the Cartesian reference sequence. It could be shown that radial trajectories are a promising technique for DV-4D flow acquisitions. However, there is still a lot room for improvements, like using iterative reconstructions or trajectories adapted to an anisotropic FOV [6]. Thus, further experiments on volunteers and in flow phantoms warranted.

Acknowledgements: The author would like to thank the entire research group of the Department of Medical Physics at the University of Greifswald as well as the Radiology Department at the University Medical Center Rostock for their support.

References:

1. M. Markl et al., 4D flow MRI, *J. Magn. Reson. Imaging*
2. S. Schnell et al., Accelerated dual-venc 4D flow MRI for neurovascular applications, *J. Magn. Reson. Imaging*
3. A. El Ahmar et al., Using water beads as static tissue in a Circle of Willis flow phantom in 4D flow MRI, Abstract #1374 ISMRM 2025
4. N. R. Zwart et al., Efficient sample density estimation by combining gridding and an optimized kernel, *Magn Reson Med*.
5. J. Bock et al., Optimized pre-processing of time-resolved 2D and 3D Phase Contrast MRI data, In Proceedings of the 15th Annual Meeting of ISMRM 2007
6. P. Larson et al., Anisotropic field-of-views in radial imaging, *IEEE Trans Med Imaging*
7. R. W. Chan, Temporal stability of adaptive 3D radial MRI using multidimensional golden means, *Magn Reson Med*.

Developing Transportable Hyperpolarized 0.44 T Mouse MRI with Fast Anatomical Spectral CT Imaging

Josef Elsasser 1*, Stefan Petersen 1, Moritz Weigt 1, Zirun Wang 1, Gerd Strohmeier 3, Behnam Shamshiri 1+3, Sebastian Lucas 4, Stephan Knecht 4, Ilai Schwartz 4, Leif Schröder 5, Maxim Zaitsev 1, Dominik v. Elverfeldt 1, Markus Mützel 6, Michael Distler 6, Toni Driessle 6, Martin Pichotka 1, Andreas B. Schmidt 1+2

1 Division of Medical Physics, Department of Radiology, University Medical Center Freiburg, Faculty of Medicine, University of Freiburg, Germany

2 German Cancer Consortium (DKTK), partner site Freiburg and German Cancer Research Center (DKFZ), Germany

3 Scientific Workshop, Department of Neurology, University Medical Center Freiburg, Faculty of Medicine, University of Freiburg, Germany

4 NVision Imaging Technologies GmbH, Ulm, Germany

5 German Cancer Research Center (DKFZ), Germany

6 Pure Devices GmbH, Rimpar, Germany

Abstract: We present preliminary results towards a transportable platform for hyperpolarized (HP) metabolic MRI combined with fast anatomical μ -CT. The system is based on a low-field (0.44 T) permanent-magnet mouse MRI scanner. It includes a dual-resonant $1\text{H}/^{13}\text{C}$ coil, and radiation windows for μ -CT imaging using external hardware. We employ ^{13}C -HP contrast agents generated via Signal Amplification by Reversible Exchange (SABRE). Preliminary tests demonstrate the detection of HP-pyruvate ^{13}C signals, with sufficient sensitivity for imaging and spectroscopy, adequate spectral resolution for planned metabolic imaging, and rapid X-ray detection of an HP-pyruvate sample. These results show potential for affordable, high-throughput, and mobile imaging, broadening the scope and flexibility of future HP-MRI applications.

Motivation: Hyperpolarized (HP) contrast agents allow real-time observation of metabolic activity via time-resolved spectroscopy and chemical shift imaging. Their strong signal enhancement is especially advantageous to low-field MRI, where the thermal polarization and resulting signal are inherently lower.[1]

Here, we present a compact, transportable mouse MRI, operating at 0.44 T and based on permanent magnets used in conjunction with HP contrast agents and allowing future integration of μ -CT anatomical imaging. Whereas conventional small animal MRI often operates at 3-9.4 T, generated by superconducting coils that make the application expensive and strictly stationary, low-field MRI is less expensive, well transportable and consumes no cryogenics.[2,3] The reduced size and weight allow flexible deployment i.e. enabling preclinical imaging within specific-pathogen-free animal facilities. The low field additionally offers specific performance advantages such as longer T_1 relaxation times (advantageous for HP imaging) and increased resistance against susceptibility artifacts (relevant for imaging near air cavities or implants).[1]

The general disadvantage of low-field MRI—reduced thermal polarization and thus lower signal—is addressed by the application of HP contrast agents. This work uses the parahydrogen-based method Signal Amplification by Reversible Exchange (SABRE)[4]. The SABRE polarizer developed in this group is transportable and produces biocompatible doses of hyperpolarized pyruvate. Its application has recently been demonstrated for metabolic imaging of tumors in vivo.[5] By combining SABRE hyperpolarization with our low-field preclinical imaging platform, we aim to establish a flexible and economical approach for future mobile molecular imaging.

Materials & Methods: At the core of this work is a 3.5 cm bore diameter 0.44 T mouse-MRI (adapted from Magspec, Pure Devices GmbH) equipped with a $1\text{H}/^{13}\text{C}$ coil. It is controlled via an open, Matlab-based pulse programming environment that is shipped with common pulse sequences and offers a high degree of customizability. 1H -MRI was demonstrated on a Lego brick phantom (Bruker) using a FLASH sequence. The system further includes X-ray emission and detection windows for the additional acquisition of anatomical μ -CT images (Fig. 1a).

The hyperpolarized contrast agents are prepared using a home-built SABRE-polarizer as described previously (Fig. 1b).[5] A mixture of 5 mM $[1-^{13}\text{C}]$ - and 5 mM $[2-^{13}\text{C}]$ pyruvate- d_3 in 500 μL CD3OD held in a standard 5-mm NMR tube was hyperpolarized using Spin-Lock Induced Crossing (SLIC-SABRE) at 50 μT with 50% parahydrogen enrichment in a 5 mm NMR tube. Neat $[1-^{13}\text{C}]$ acetic acid (1 g, $\sim 17.5\text{ M}$) was used as a thermal reference. For ^{13}C -imaging, a single shot RARE sequence was used and unlocalized ^{13}C -spectra were acquired. For an X-ray projection of the sample, an X-ray handgun (EzRay Air P, Vatech) and a photon-counting detector (WidePIX MPX3 CdTe, ADVACAM) were used.

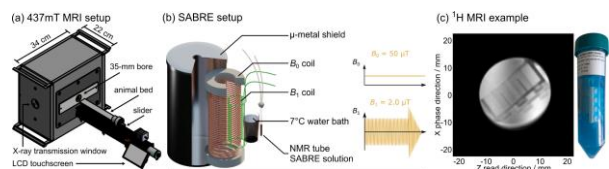


Fig. 1: Schematics of (a) the 0.44 T mouse MRI with animal positioning setup, and (b) the 50 μT SABRE polarizer; (c) 1H MRI of the pictured Lego brick phantom.

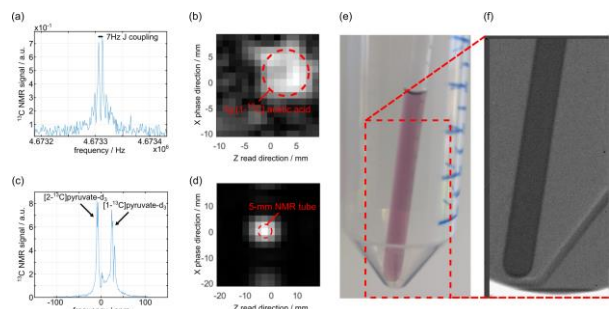


Fig. 2: (a) ^{13}C NMR spectrum and (b) ^{13}C MRI of $[1-^{13}\text{C}]$ acetic acid thermal reference; (c) ^{13}C NMR spectrum and (d) ^{13}C MRI of SABRE-hyperpolarized $[1-^{13}\text{C}]$ - and $[2-^{13}\text{C}]$ pyruvate; (e) photo and (f) X-ray projection of the SABRE sample recorded after the hyperpolarized ^{13}C -MRI.

Results: Preliminary tests were conducted to evaluate the imaging and spectroscopic capabilities of the low-field MRI and identify the development steps toward performing in vivo mouse studies.

Proton MR images of a Bruker standard phantom were successfully recorded using a FLASH sequence, showing the Lego brick in detail (128x128 matrix, 1 cm slice, ~5 min acquisition time, Fig. 1c). The field inhomogeneity has been measured to below 3ppm within a 3cm diameter spherical volume at the magnet's isocenter.

The NMR-spectrum of the reference shows the clearly resolved 7 Hz JHC-coupling (Fig. 2a). Notably, the [1-13C]pyruvate to [1-13C]lactate chemical shift difference at this field corresponds to >55 Hz (~12 ppm). Fast 13C MRI of the thermally polarized sample (8x8x1 matrix, 20x20x10 mm³, Fig. 2b) showed clearly visible signal but at low SNR.

The hyperpolarized 13C spectra – recorded without shimming – show strong and clearly distinguishable signals of the [1-13C]- and [2-13C]pyruvate (Fig. 2c). Hyperpolarized signal was visible in an axial MRI of the NMR tube (8x8x1 matrix, 35x35x10 mm³, Fig. 2d). An X-ray image was acquired as a spatial reference (Fig. 2e-f).

Conclusion: The aim of this project is to develop a fast and mobile platform for metabolic imaging in mice. The fundamental suitability for this purpose was demonstrated in this work. Especially, it has been shown that the spectral resolution is sufficient and, by the application of HP contrast agents, so is the sensitivity.

The proton imaging and 13C-spectroscopy are now to be demonstrated in vivo, with spectral μ -CT as a fast and accurate anatomical reference. The preliminary results presented here provide a solid foundation for the transition to in vivo experiments.

Acknowledgements: The research reported in this publication was supported by the German Cancer Consortium (DKTK INNOVATION-2023 HYPERBOLIC project, and DKTK INVEST-2024), the German Federal Ministry of Education and Research (BMBF) in the funding program "Quantum Technologies – from Basic Research to Market" under the project "QuE-MRT" (contract number: 13N16448), the Research Commission of the University Medical Center Freiburg, the German Research Foundation (DFG #SCHM 3694/1-1, #SCHM 3694/2-1, #SFB1479), and B.E.S.T. Fluidsysteme GmbH | Swagelok Stuttgart.

References:

1. J. Traechtler, M. Fuetterer, M. M. Albannay, T. Hoh, S. Kozerke, *Considerations for hyperpolarized 13C MR at reduced field: Comparing 1.5T versus 3T*, *Magn. Reson. Med.*
2. Y. Liu, A. T. L. Leong, Y. Zhao, L. Xiao, H. K. F. Mak, A. C. O. Tsang, G. K. K. Lau, G. K. K. Leung, E. X. Wu, *A low-cost and shielding-free ultra-low-field brain MRI scanner*, *Nat. Commun.*
3. H. de Maissin, P. R. Groß, O. Mohiuddin, M. Weigt, L. Nagel, M. Herzog, Z. Wang, R. Willing, W. Reichardt, M. Pichotka, L. Heß, T. Reinheckel, H. J. Jessen, R. Zeiser, M. Bock, D. von Elverfeldt, M. Zaitsev, S. Korchak, S. Glöggl, J.-B. Hövener, E. Y. Chekmenev, F. Schilling, S. Knecht, A. B. Schmidt, *In Vivo Metabolic Imaging of [1-13C]Pyruvate-d3 Hyperpolarized By Reversible Exchange With Parahydrogen*, *Angew. Chem. Int. Ed.*
4. R. W. Adams, J. A. Aguilar, K. D. Atkinson, M. J. Cowley, P. I. P. Elliott, S. B. Duckett, G. G. R. Green, I. G. Khazal, J. López-Serrano, D. C. Williamson, *Reversible Interactions with para-Hydrogen Enhance NMR Sensitivity by Polarization Transfer*, *Science*
5. S. Petersen, L. Nagel, P. R. Groß, H. De Maissin, R. Willing, L. Heß, J. Mitschke, N. Klemm, J. Treiber, C. A. Müller, S. Knecht, I. Schwartz, M. Weigt, M. Bock, D. Von Elverfeldt, M. Zaitsev, E. Y. Chekmenev, J.-B. Hövener, A. F. Martins, F. Schilling, T. Reinheckel, A. B. Schmidt, *In vivo molecular imaging of breast cancer metabolic heterogeneity using [1-13C]pyruvate-d3 hyperpolarized by reversible exchange with parahydrogen*, *Theranostics*

Correction of time-dependent phase fluctuations in diffusion-weighted MRS at very high b-values with an external phantom reference

Kristin Engel 1+2*, Vanessa Wiggermann 1, Itamar Ronen 3, Henrik Lundell 1+2

1 Hvidovre

2 Kongens Lyngby

3 Brighton

Abstract: High b-value diffusion-weighted MR spectroscopy (dMRS) suffers from strong eddy currents and field fluctuations that distort spectral line shapes, while conventional water reference scans often have insufficient SNR for effective correction. We present a simple, high-SNR silicone oil phantom reference for phase correction in 7 T dMRS. Field fluctuations were mapped and corrected in both simulations and in vivo brain data up to $b = 37 \text{ ms}/\mu\text{m}^2$. The phantom reference outperformed water scans in low-SNR conditions, offering robust phase information and comparable artifact correction in vivo. This approach reduces scan time and can improve data quality for high-b-value dMRS, supporting advanced microstructural investigations.

Motivation: Diffusion weighted MRS (dMRS) provides information on intracellular cell morphology by measuring the mobility of cell-specific metabolites 1 2. The strong diffusion encoding gradients needed for dMRS generate eddy currents and other field fluctuations like acoustic vibrations that can severely distort spectral line shapes. Therefore, experimental optimization and corrections with water reference scans are needed 3. However, in experiments with many and strong diffusion encoding conditions, such as powder-averaged acquisitions 4, water reference scans can be time-consuming and prone to noise 5. Other correction approaches require special mapping sequences or advanced field camera equipment that is less effective for the typical 10-100 Hz field oscillations created by diffusion encoding gradients 6.

In this study, we propose the use of a simple phantom measurement that provides high SNR phase reference data as an alternative to a conventional water reference to correct for the spatial characteristics of field fluctuations in a dMRS acquisition on a human 7T system. In simulations, we demonstrate the impact of noise in reference data for phase and frequency correction of low SNR dMRS data. Finally, we compare the performance of the phantom reference with a conventionally acquired water reference scan in a protocol with an exceptionally high b-value of $37 \text{ ms}/\mu\text{m}^2$.

Materials & Methods: Single voxel dMRS experiments were performed on a 7T Philips Achieva (Best, Netherlands) with a 32Rx/2Tx-channel head coil (Nova Medical, Wilmington, MA, USA) with a modified sLASER sequence (Figure 1). B-field fluctuations were mapped across the FOV to assess spatial and temporal stability using a high-viscosity (500 cSt) silicone oil phantom (Sigma-Aldrich, US). dMRS data were acquired at the isocenter, $\pm 25 \text{ mm}$ and $\pm 50 \text{ mm}$ along each gradient axis. Gradients were incrementally applied with both positive and negative gradient polarity.

Simulations to assess the relevance of noise were performed in Python, generating a free induction decay (FID) signal with three metabolite peaks, eddy currents, linear phase distortions, and complex Gaussian noise, with diffusion

weighting applied to each peak. Silicone oil and water reference were simulated with a single resonance at 4.7 ppm.

In vivo dMRS data were also acquired within parietal white matter from two healthy young volunteers (one female, mean age 26) using a 30 mm isotropic voxel in the first and a 15 mm isotropic voxel in the second volunteer. Six b-values ($b = [1.03, 4.10, 9.23, 16.41, 25.64, 36.93] \text{ ms}/\mu\text{m}^2$) and one direction were measured. (TR=4.9 s, TE=160 ms, repetitions per condition=48). Both ECC methods were applied, followed by data alignment, phasing and averaging for both simulated and in vivo data. In addition, metabolite levels were quantified for the in vivo data. All data processing was performed with the FSL-MRS toolbox 7.

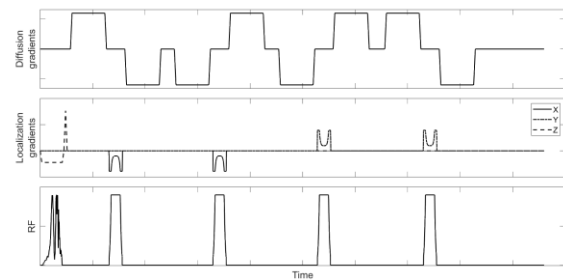


Fig. 1: Modified semi-LASER sequence. Gradient strength, duration and timings (TE and TR) were adapted to reach desired b-values.

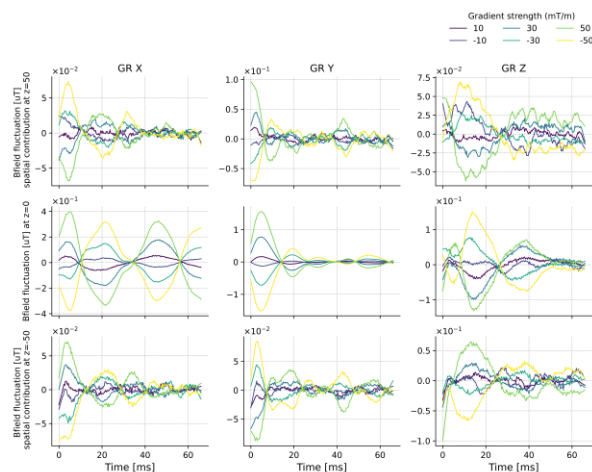


Fig. 2: Mapping of phase fluctuations along the z-axis (with $x=0, y=0$). Phase fluctuations are presented at three spatial positions: $z=0, z=+50 \text{ mm}$, and $z=-50 \text{ mm}$, across three gradient playout directions (1, 2, and 3). The isocenter ($z=0$) shows total measured phase fluctuations, while neighboring positions show only the spatially dependent phase components, isolated by subtracting isocenter phase data. The spatially independent fluctuations (same as in isocenter) are significantly larger than the additional phase variations that arise with increased distance from the isocenter.

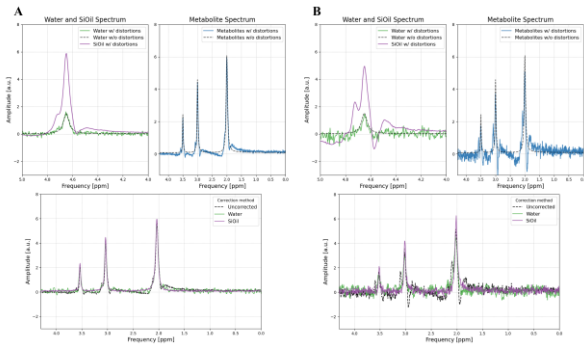


Fig. 3: The upper left plot shows simulations of the water reference and the silicone oil signal with high SNR in (A) and low SNR in (B). The corresponding distorted metabolite spectrum (upper right) is shown with same SNR conditions. For high SNR (A), both correction methods restore the line shape (lower plot). In the second scenario (B), the silicone oil signal remains largely unaffected as its phase information is preserved, while the noise significantly obscures the phase of the water reference. Thus, ECC using the water reference fails to restore the lineshape of the metabolite spectrum.

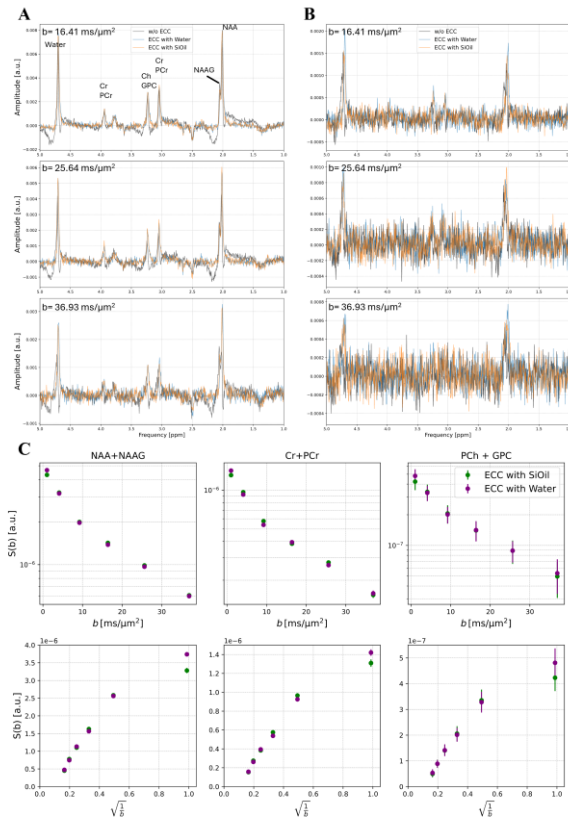


Fig. 4: In vivo spectra of subject 1 (A) and subject 1 (B) following correction with two ECC methods. The data was acquired with voxel sizes of 30 mm and 15 mm isotropic for subject 1 and 2, respectively. Each row represents increasing diffusion-weighting. Both ECC methods demonstrate similar performance in artifact correction, although residual phase distortions are evident across spectra. These results suggest that neither correction method completely eliminates phase distortions. (C) Fitting results and attenuation behaviors for data corrected with oil and with water reference.

Results: Figure 1 shows the modified semi-LASER sequence used for the mapping. We observed that spatially independent fluctuations (same as in isocenter) were significantly larger than the additional phase variations that arose with increased distance from the isocenter (Figure 2).

The simulations of Figure 3 show that while both ECC methods effectively restore the line shapes for high SNR conditions, low SNR conditions severely affect the phase of water reference data but not the phantom data.

Figure 4 shows the ECC of two in vivo data sets and results of the fitting for total N-acetylaspartate (NAA+NAAG) creatin (Cr+PCr) and choline (PCh+GPC). Similar performance in artifact correction was achieved for both ECC methods, with residual phase distortions evident across spectra for both methods.

Discussion: The simulations showed that in media with low diffusivity, the phase of the eddy currents remained stable even at high diffusion weighting values, which could open up new possibilities for investigating higher-order diffusion effects in human dMRS. Further, the in vivo data showed that even at very high b-values, sufficient water signal remained accessible for signal correction, which differed from previous simulations and observations 5. This suggests that the availability of the signal for correction may differ between brain regions. The extended b-value range suggest an asymptotic attenuation faster than $\sqrt{1/b}$ (lower row, fig 3C) indicating isotropic components from e.g. axonal diameter in contrast to earlier studies 4.

Conclusion: A silicone oil phantom provides robust reference data for line shape correction for dMRS data. Use of a reference phantom removes the need for potentially lengthy in vivo scans with many or strong diffusion weighting conditions, in particular in areas with limited water retention.

Future application could also be to resolve field fluctuations for lengthy diffusion weighted MRSI applications.

Acknowledgements: This project is supported by the European Research Council under the European Union’s Horizon 2020 research and innovation programme (grantnumber 804746).

References:

- Ronen, I. & Valette, J. Diffusion-weighted magnetic resonance spectroscopy, eMagRes
- Palombo, M., Shemesh, N., Ronen, I. & Valette, J. Insights into brain microstructure from in vivo DW-MRS, NeuroImage
- Weidlich, D., Zamskiy, M., Maeder, M., Ruschke, S., Marburg, S., & Karampinos, D. C. Reduction of vibration-induced signal loss by matching mechanical vibrational states: Application in high b-value diffusion-weighted MRS, Magn Reson Med
- Lundell, H., Ingo, C., Dyrby, T. B. & Ronen, I. Cytosolic diffusivity and microscopic anisotropy of N-acetyl aspartate in human white matter with diffusion-weighted MRS at 7 T, NMR Biomed
- Şimşek, K., Gallea, C., Genovese, G., Lehéry, S., Branzoli, F., & Palombo, M., Age-Trajectories of Higher-Order Diffusion Properties of Major Brain Metabolites in Cerebral and Cerebellar Gray Matter Using In Vivo Diffusion-Weighted MR Spectroscopy at 3T, Aging Cell
- van Gorkum, R. J. H., Guenther, C., Koethe, A., Stoek, C. T. & Kozerke, S. Characterization and correction of diffusion gradient-induced eddy currents in second-order motion-compensated echo-planar and spiral cardiac DTI, Magn Reson Med
- Clarke, W. T., Stagg, C. J. & Jbabdi, S. FSL-MRS: An end-to-end spectroscopy analysis package, Magn Reson Med

QSM Beyond the Brain: Exploring Fat and Iron Effects

Simon Graf 1+2*, Josefine Trapp 1, Maik Rothe 1+2, Alexander Gussev 1+2, Walter A. Wohlgenuth 1+2, Andreas Deistung 1+2

1 Halle MR Imaging Core Facility, Medical Faculty, Martin-Luther-University Halle-Wittenberg

2 University Clinic and Outpatient Clinic for Radiology, University Hospital Halle (Saale), Germany

Abstract: We present a dedicated spherical agar phantom designed to evaluate fat and iron effects on quantitative susceptibility mapping (QSM) in abdominal imaging. Nine small spheres with varying iron and fat concentrations were embedded in a larger agar matrix, enabling systematic analysis of chemical shift. Fat correction substantially altered susceptibility values, especially in regions combining fat and iron, and reduced high-frequency streaking artifacts. Repeated measurements over 14 months confirmed the phantom's long-term stability. Our results highlight the impact of fat on susceptibility maps, emphasize the importance of incorporating fat correction in QSM processing, and establish a stable phantom for benchmarking QSM processing strategies in non-brain applications.

Motivation: Quantitative susceptibility mapping (QSM), a post-processing technique that derives the magnetic susceptibility from the raw-phase of gradient-recalled echo sequences, demonstrated its use in terms of iron characterization in brain imaging. Employing QSM-processing in abdominal regions, such as the liver, offers the opportunity to estimate liver iron content (LIC) and may overcome current limitations of relaxometry-based LIC measurement. However, the presence of adipose tissue and high iron content complicate QSM processing, due to chemical shift artifacts and rapidly decaying signals, respectively. In order to systematically evaluate the influence of fat on susceptibility maps, and allow benchmarking of QSM processing strategies, we manufactured a dedicated agar-gel phantom mimicking both healthy and pathologic liver tissue in terms of effective transverse relaxation rates (R_2^*) and proton density fat fraction (PDFF), while also addressing QSM-specific prerequisites such as the removal of plastic barriers to prevent artificial susceptibility jumps.

Materials & Methods: Our spherical phantom contains nine small agar spheres, embedded within a large agar sphere (Fig.1). The small agar spheres (concentration c [%]: 2.0) were doped with varying concentrations of iron nano particles (c [mM]: 0.13, 0.19, 0.26) and peanut oil (c [%]: 4, 10, 20). Formaldehyde was incorporated to increase the small sphere's melting point. The agar base solution (concentration c [%]: 2.5) was spiked with Gadobutrol, modulating T1 relaxation. Sodium azide (c [%]: 0.1) was used to prevent phantom contamination. First, the small spheres were manufactured and sprayed with coating agent to prevent diffusion of water. The phantom's lower hemisphere was prepared, and after gelling and cooling, the small spheres were removed from their shells and placed on top.

Phantom measurements were conducted at two time-points on the same 3T MRI system (Siemens Vida), using the gradient-echo VIBE sequence (6 echoes, $TE_1/\Delta TE=1.17/1.71ms$) and 1H-STEAM spectroscopy (7 echoes, $TE=20,30,40,50,60,100,200ms$). Five measurements with tilts of approximately $\pm 60^\circ$ in $y \rightarrow z$ and $x \rightarrow z$ plane using the VIBE sequence were conducted for QSM gold-standard

COSMOS[1] processing. We performed 1H-spectroscopy to determine the phantom-specific fat spectrum for subsequent fat-correction (Fig.2D). The multi-lipid-peak signal model[2] was fitted using the VIBE-data to derive PDFF and R_2^* . The complex-valued VIBE data was processed with an iterative graph-cut approach for water-fat separation[3] (IGC) to obtain fat-corrected field maps. Each dataset (fat-corrected field maps were scaled to phase images at 9.72ms) underwent phase-unwrapping[4], scaling to field values, background field removal using SHARP[5] deriving the local field and field-to-susceptibility inversion with SDI[6], HEIDI[7] and COSMOS[1].

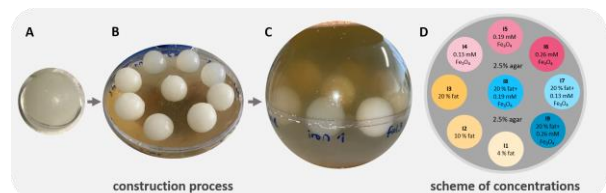


Fig. 1: Process of the phantom construction. The small spheres (A) are placed on the lower agar hemisphere (B) after removal of the plastic shells. The outer spherical shell is filled with agar (C) enclosing the small spheres containing varying concentrations of peanut oil and iron nano particles (D).

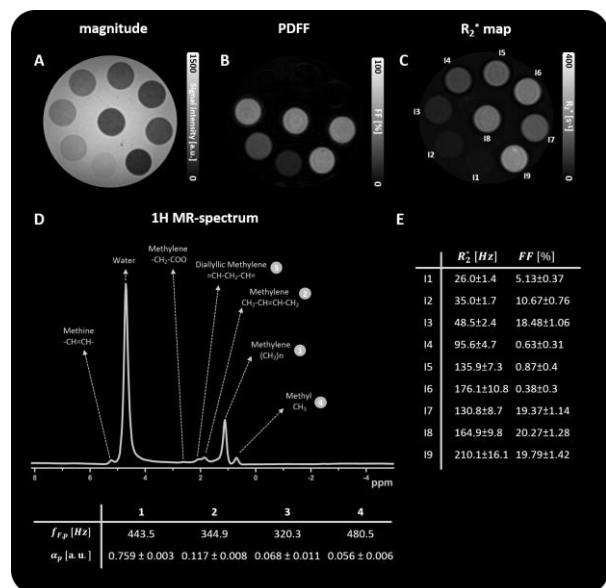


Fig. 2: The VIBE magnitude ($TE = 6.8 ms$) shows a homogenous agar background and nine spheres (A). A multi-lipid-peak signal model was fitted to obtain PDFF (B) and R_2^* maps (C). The 1H-MR spectrum (D) was used to determine the phantom-specific multi-lipid-peak model (E) with frequencies $f_{F,p}$ and relative amplitudes α_p .

Results: Figure 2A shows a largely homogenous agar sphere, with only a few air bubbles. PDFF and R_2^* increase with increasing fat and iron concentrations and correspond to the set concentrations during phantom construction (Fig. 2). The chemical shift influences susceptibility values markedly (Fig. 3), with the largest differences between fat-corrected and uncorrected maps being found in spheres that contain both

fat and iron (Fig. 3D–E, I7–I9). Fat-correction resulted in an increase of average susceptibilities (Fig. 3, turquoise circle) and a decrease of streaking artefacts around fat-containing spheres (Fig. 3, orange arrows). Overall, the susceptibility values increase with rising fat and iron concentration (Fig. 4). PDFF, $R2^*$ and the susceptibility obtained from the initial measurement and the two follow-up measurements 14 months later, exhibit comparable variations across the time intervals (Fig. 4). One-way ANOVA testing with repeated measurements yielded no statistical variations across the parameters and measurements ($p < 0.05$).

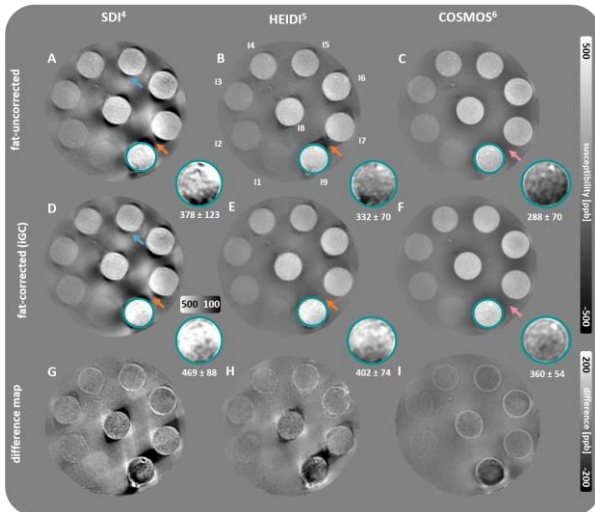


Fig. 3: Susceptibility maps computed with different inversion algorithms from fat-uncorrected (A–C) and fat-corrected (D–F) local field maps with a close-up of inclusion 19 (mean±SD in ppb). Arrows: reduced streaking after fat correction (orange); minimal effects of fat correction on streaking in COSMOS (pink) and iron-only spheres (blue).

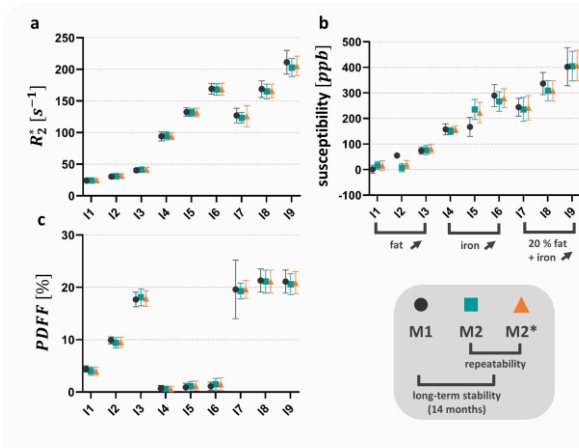


Fig. 4: Repeatability (scan-rescan) and long-term stability assessment 14 months after initial phantom construction. Average $R2^*$ (a), susceptibility (b) and PDFF (c) are plotted for each spherical inclusion, where error bars indicate the standard deviation. The susceptibilities were derived from a single-orientation susceptibility map reconstructed using HEIDI-based field-to-source inversion[7].

Discussion: Within this work, we propose a spherical agar phantom (Fig. 2) free of plastic boundaries—unlike conventional vial-based designs[8, 9]—thereby avoiding artificial susceptibility discontinuities[10]. The preset and measured $R2^*$ and PDFF values mimic those found in normal liver tissue and in pathologies such as non-alcoholic fatty liver

disease[11, 12]. Susceptibility values varied markedly with the post-processing technique, particularly in spheres that contained both iron nanoparticles and peanut oil (Fig. 3, I7–I9). In addition, high-frequency streaking artefacts decreased as the inversion complexity increases—progressing from SDI through HEIDI to COSMOS (Fig. 4, orange arrows). Among the methods, COSMOS is least prone to streaking artifacts due to the inherent oversampling provided by its multi-orientation acquisition, in contrast to single-orientation techniques like SDI and HEIDI. Repeated scans over 14 months yielded consistent quantitative parameters, confirming long-term phantom stability. Current limitations of the phantom are the range of iron and fat concentrations, as well as comparability with liver tissue, e.g. absence of fibrosis. Future versions may use surfactants to stabilize water-fat-agar emulsions beyond 20% fat and add nickel chloride to raise the longitudinal relaxation time ($T1$), thereby simulating fibrotic liver tissue[9].

Conclusion: This work introduces a long-term-stable, multi-purpose phantom for systematically assessing fat and iron effects in abdominal QSM and for benchmarking post-processing strategies. Our findings underscore the necessity of incorporating effective fat correction into the QSM processing pipeline, as both fat and iron substantially influence magnetic susceptibility.

Acknowledgements: This study was performed on a human research MR scanner funded by the German Research Foundation (DFG, Deutsche Forschungsgemeinschaft, INST 271/ 406-1 FUGG).

References:

- Liu, T., Spincemille, P., Rochefort, L. de, Kressler, B., Wang, Y.: Calculation of susceptibility through multiple orientation sampling (COSMOS): a method for conditioning the inverse problem from measured magnetic field map to susceptibility source image in MRI. *Magn Reson Med* (2009). <https://doi.org/10.1002/mrm.21828>
- Hernando, D., Kramer, J.H., Reeder, S.B.: Multiplex fat-corrected complex $R2^*$ relaxometry: Theory, optimization, and clinical validation. *Magn Reson Med* (2013). <https://doi.org/10.1002/mrm.24593>
- Hernando, D., Kellman, P., Haldar, J.P., Liang, Z.-P.: Robust water/fat separation in the presence of large field inhomogeneities using a graph cut algorithm. *Magn Reson Med* (2010). <https://doi.org/10.1002/mrm.22177>
- Abdul-Rahman, H.S., Gdeisat, M.A., Burton, D.R., Lalor, M.J., Lilley, F., Moore, C.J.: Fast and robust three-dimensional best path phase unwrapping algorithm. *Appl Opt* (2007). <https://doi.org/10.1364/ao.46.006623>
- Schweser, F., Deistung, A., Lehr, B.W., Reichenbach, J.R.: Quantitative imaging of intrinsic magnetic tissue properties using MRI signal phase: an approach to in vivo brain iron metabolism? *NeuroImage* (2011). <https://doi.org/10.1016/j.neuroimage.2010.10.070>
- Schweser, F., Deistung, A., Sommer, K., Reichenbach, J.R.: Toward online reconstruction of quantitative susceptibility maps: superfast dipole inversion. *Magn Reson Med* (2013). <https://doi.org/10.1002/mrm.24405>
- Schweser, F., Sommer, K., Deistung, A., Reichenbach, J.R.: Quantitative susceptibility mapping for investigating subtle susceptibility variations in the human brain. *NeuroImage* (2012). <https://doi.org/10.1016/j.neuroimage.2012.05.067>
- Li, J., Lin, H., Liu, T., Zhang, Z., Prince, M.R., Gillen, K., Yan, X., Song, Q., Hua, T., Zhao, X., Zhang, M., Zhao, Y., Li, G., Tang, G., Yang, G., Brittenham, G.M., Wang, Y.: Quantitative susceptibility mapping (QSM) minimizes interference from cellular pathology in $R2^*$ estimation of liver iron concentration. *J Magn Reson Imaging* (2018). <https://doi.org/10.1002/jmri.26019>
- Zhao, R., Hamilton, G., Brittain, J.H., Reeder, S.B., Hernando, D.: Design and evaluation of quantitative MRI phantoms to mimic the simultaneous presence of fat, iron, and fibrosis in the liver. *Magn Reson Med* (2021). <https://doi.org/10.1002/mrm.28452>
- Graf, S., Trapp, J., Rothe, M., Gussew, A., Wohlgemuth, W.A., Deistung, A.: A dedicated phantom for exploring the interplay of fat and paramagnetic substances in quantitative susceptibility mapping. *Magn Reson Mater Phys* (2025). <https://doi.org/10.1007/s10334-025-01261-3>
- Labranche, R., Gilbert, G., Cerny, M., Vu, K.-N., Soulières, D., Ollivié, D., Billiard, J.-S., Yokoo, T., Tang, A.: Liver Iron Quantification with MR Imaging: A Primer for Radiologists. *Radiographics* (2018). <https://doi.org/10.1148/rg.2018170079>
- Sberna, A.L., Bouillet, B., Rouland, A., Brindisi, M.C., Nguyen, A., Mouillot, T., Duvillard, L., Denimal, D., Loffroy, R., Vergès, B., Hillon, P., Petit, J.M.: European Association for the Study of the Liver (EASL), European Association for the Study of Diabetes (EASD) and European Association for the Study of Obesity (EASO) clinical practice recommendations for the management of non-alcoholic fatty liver disease: evaluation of their application in people with Type 2 diabetes. *Diabetic medicine: a journal of the British Diabetic Association* (2018). <https://doi.org/10.1111/dme.13565>

31P-MRS saturation transfer to assess hepatic ATP synthesis at 3T in individuals with type-1-diabetes and control volunteers

Marc Jonuscheit 1+2, Benedikt Korzekwa 1+2, Michael Schär 3, Julian Mevenkamp 4, Stefan Wierichs 1+2, Pavel Bobrov 2+5, Theresia Sarabhai 1+2+6, Sabine Kahl 1+2+6, Michael Roden 1+2+6 and Vera B. Schrauwen-Hinderling 1+2+4

1* Inst. for Clinical Diabetology, German Diabetes Center, Leibniz Center for Diabetes Research at Heinrich Heine University Düsseldorf, Germany.

2* German Center for Diabetes Research (DZD e.V.), Partner Düsseldorf, München-Neuherberg, Germany.

3 Division of Magnetic Resonance Research, Dept. of Radiology, Johns Hopkins University School of Medicine, Baltimore, United States of America.

4 Department of Radiology and Nuclear Medicine, Maastricht University Medical Center, Maastricht, The Netherlands.

5 Inst. for Biometrics and Epidemiology, German Diabetes Center, Leibniz Center for Diabetes Research at Heinrich Heine University Düsseldorf, Germany.

6 Dept. of Endocrinology and Diabetology, Medical Faculty and University Hospital Düsseldorf, Heinrich Heine University Düsseldorf, Germany.

Abstract: Motivation - 31P-MRS saturation transfer for detection of adenosine triphosphate (ATP) synthesis is currently almost exclusively performed at ultrahigh field. Goal - Establishing a method to robustly assess ATP synthesis in human liver using a clinical MRI system.

Approach - A 2D-ISIS sequence was used to assess the hepatic apparent spin-lattice relaxation time of inorganic phosphate ($T_{(1, \text{Pi})}^{\wedge}$), equilibrium forward rate constant (k_f) and forward ATP exchange flux (F_{ATP}) in healthy volunteers ($n=9$) and participants with type-1-diabetes (T1D) ($n=8$).

Results - Reproducibility measurements resulted in CVs of 7.1% and 21.3% for $T_{(1, \text{Pi})}^{\wedge}$ and k_f , respectively. Mean hepatic k_f and F_{ATP} were lower ($p=.001$ and $p=.0016$) in T1D vs. controls.

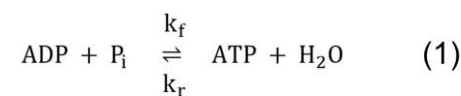
Motivation: Metabolic dysfunction-associated steatotic liver disease (MASLD) encompasses a spectrum of disease from simple liver steatosis to inflammation and cirrhosis. During progression from steatosis to steatohepatitis (MASH) mitochondrial function decreases, but currently, non-invasive methods are lacking. Saturation transfer (ST) magnetic resonance spectroscopy (MRS) provides insights into energy metabolism and is therefore a promising technique to monitor MASLD/MASH-associated changes. Using ST 31P-MRS, synthesis rate of adenosine triphosphate (ATP) can be obtained as a parameter characterizing mitochondrial metabolism by calculating the equilibrium forward exchange rate constant (k_f) between inorganic phosphate (Pi) and ATP. In liver, this technique has mainly been applied on research scanners at ultra-high field (7T) because clinical scanners suffer from a low signal-to-noise ratio combined with measurement times of ~2 hours due to the need for spatial localization^{1,2}. Moreover, data on reproducibility of the method at 3T are lacking. To make the technique more broadly available, we aimed to adapt the previously published TRiST method³ to robustly assess k_f at 3T, allowing a high degree of spatial localization within 90 minutes and determine reproducibility. Finally, the protocol was applied in people with type-1-diabetes (T1D) in order to determine whether the method can pick up differences that are expected for this pathology.

Materials & Methods: To assess k_f , a two-site model of chemical exchange between Pi and ATP is assumed (Fig. 1). During the ST experiment, γ -ATP is saturated by frequency-selective irradiation using a DANTE pulse train. The chemical exchange of Pi with the saturated γ -ATP pool leads to a reduction of both, equilibrium longitudinal magnetization (M_0) and spin-lattice relaxation time (T_1) of Pi from

$M_{(0, \text{Pi})}$ to $M_{(0, \text{Pi})}^{\wedge}$ and $T_{(1, \text{Pi})}$ to an apparent $T_{(1, \text{Pi})}^{\wedge}$, respectively.

The ST approach consists of the acquisition of four separate spectra: Three spectra at different repetition times ($[[\text{TR}]]_{\text{short}}$, $[[\text{TR}]]_{\text{center}}$ and $[[\text{TR}]]_{\text{long}}$) to determine $T_{(1, \text{Pi})}^{\wedge}$ and a fourth spectrum acquired with saturation mirrored around the Pi resonance ($[[\text{TR}]]_{\text{mirrored}}$) serves as control. Finally, k_f can be obtained according to Fig. 1.

For validation, we examined healthy individuals twice ($n=9$, age 25 ± 3 years; BMI 24 ± 2 kg/m²) on a clinical 3T MR system with a quadrature surface coil. All spectra were acquired using a 2D-ISIS sequence (VOI: 90mmx40mm) with a hyperbolic secant adiabatic pulse for excitation. Spectra were acquired at TR 0.7s, 2.7s and 1.7s with 1024, 548 and 768 averages for $[[\text{TR}]]_{\text{short}}$, $[[\text{TR}]]_{\text{long}}$, and $[[\text{TR}]]_{\text{center}}/[[\text{TR}]]_{\text{mirrored}}$, respectively. Shimming was performed using a dedicated shim-tool⁴. All spectra were analyzed with a custom-written MATLAB script. After validation, eight participants with T1D (age 42 ± 15 years; BMI 24 ± 3 kg/m²) were additionally measured. In order to calculate ATP synthesis rate (F_{ATP}), Pi concentration was assumed to be 1.73mM for healthy volunteers based on a previous publication, for T1D absolute quantification was performed as previously described⁵. For inter-group comparison ANOVA was performed with $\alpha=0.05$.



$$k_f = \frac{1}{T_{1, \text{Pi}}'} \left(1 - \frac{M_{0, \text{Pi}}'}{M_{0, \text{Pi}}} \right) \quad (2)$$

Fig. 1: (1) Two-site model of chemical exchange between Pi and ATP. (2) Calculation of the equilibrium forward exchange rate constant (k_f)

Results: Fig. 2 shows coil position and voxel placement. Full saturation of the γ -ATP resonance was achieved, while the absence of phosphocreatine signal indicates good localization to the liver and therefore no contamination by signal originating from muscle. Estimation of $T_{(1, \text{Pi})}^{\wedge}$ based on the acquisition of three spectra is shown in Fig. 3. The outcomes of the repeated measurements showed a coefficient of variation (CV) of 7.1%, 21.3% for $T_{(1, \text{Pi})}^{\wedge}$ and k_f , respectively. Individuals with T1D showed no difference in $T_{(1, \text{Pi})}^{\wedge}$ ($p=.35$), but lower values for k_f ($p=.0004$) and F_{ATP} ($p=.0016$) compared to healthy volunteers (Fig. 4).

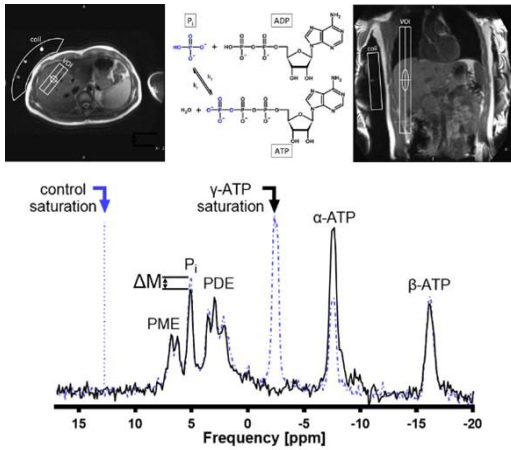


Fig. 2: Coil placement, planning and results of the ST 31P-MRS protocol. The black arrow indicates the frequency of the saturation pulse and the resulting spectrum is shown as solid black line. The spectrum of the mirrored experiment is shown in blue dotted line. Spectra are apodized by a 5Hz Gaussian filter.

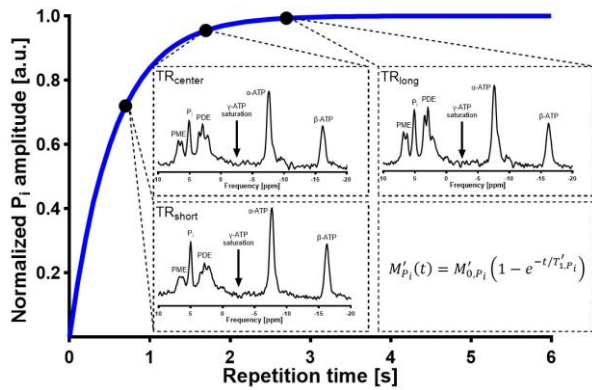


Fig. 3: Determination of the apparent spin-lattice relaxation time of Pi ($T_{1(Pi)}^{app}$) by a saturation recovery experiment. γ -ATP was saturated at three TRs (0.7 s, 1.7 s and 2.7 s) and $T_{1(Pi)}^{app}$ was obtained by fitting Pi amplitudes according to the displayed formula. Spectra are apodized by a 10 Hz Gaussian filter.

	Healthy controls	T1D	P-value
No. volunteers	9	8	
$T_{1(Pi)}^{app}$ [ms]	482 ± 22	517 ± 29	.35
ΔM [%]	15.9 ± 1.0	7.7 ± 1.4	<.001*
k_f [s ⁻¹]	0.34 ± 0.03	0.16 ± 0.03	.001*
F_{ATP} [mM/min]	35.3 ± 3.5	16.4 ± 4.4	.002*

Fig. 4: Determined 31P-MR spectroscopy parameters for the subgroups of healthy volunteers and type 1 diabetes (T1D). All values are reported as numbers of participants or mean ± SEM. ΔM = difference of Pi between saturating and control irradiation. * $p < .05$ indicates statistical significance

Discussion: This study demonstrates the feasibility and reproducibility of a ST method for assessing rates of hepatic ATP synthesis at clinical field strength within 90 minutes. This method provides faster assessment of $T_{1(Pi)}^{app}$ and better exclusion of muscle signals due to higher degree of spatial localization compared to previous approaches^{6,7}. The method showed the expected decrease in k_f and F_{ATP} in T1D. The values obtained for $T_{1(Pi)}^{app}$, k_f and F_{ATP} were in agreement with literature and show good-to-acceptable reproducibility.

Conclusion: Noninvasive methods to investigate hepatic energy metabolism are urgently needed to evaluate liver health while preventing unnecessary biopsies. For broad clinical applicability, the robustness shown by the proposed method at clinical field strength is crucial.

The proposed magnetic resonance spectroscopy method calculates hepatic ATP synthesis rates at clinical field strength.

The protocol shows acceptable reproducibility and spectra without contamination from muscle.

The method can detect differences between participants with type 1 diabetes and controls.

Acknowledgements: The authors thank all GDS participants and all physicians for their continued encouragement of their volunteers to participate in GDS.

References:

- Valkovič L, Gajdošik M, Traussnigg S, Wolf P, Chmelík M, Kienbacher C, Bogner W, Krebs M, Trauner M, Trattnig S, Krššák M. Application of localized ³¹P MRS saturation transfer at 7 T for measurement of ATP metabolism in the liver: reproducibility and initial clinical application in patients with non-alcoholic fatty liver disease. *Eur. Radio.* 2014;24(7):1602–9. doi:10.1007/s00330-014-3141-x
- Valkovič L, Bogner W, Gajdošik M, Považan M, Kukurová IJ, Krššák M, Gruber S, Frollo I, Trattnig S, Chmelík M. One-dimensional image-selected in vivo spectroscopy localized phosphorus saturation transfer at 7T. *Magn. Reson. Med.* 2014;72(6):1509–15. doi:10.1002/mrm.25058
- Schär M, El-Sharkawy A-MM, Weiss RG, Bottomley PA. Triple repetition time saturation transfer (TRiST) 31P spectroscopy for measuring human creatine kinase reaction kinetics. *Magn. Reson. Med.* 2010;63(6):1493–501. doi:10.1002/mrm.22347
- Schär M, Kozerke S, Fischer SE, Boesiger P. Cardiac SSFP imaging at 3 tesla. *Magn Reson Med.* 2004;51(4):799–806. doi:10.1002/mrm.20024
- Jonuscheit M, Wierichs S, Rothe M, Korzekwa B, Mevenkamp J, Bobrov P, Kupriyanova Y, Roden M, Schrauwen-Hinderling VB. Reproducibility of absolute quantification of adenosine triphosphate and inorganic phosphate in the liver with localized 31P-magnetic resonance spectroscopy at 3-T using different coils. *NMR Biomed.* 2024;37(8):e5120. doi:10.1002/nbm.5120
- Schmid AI, Chmelík M, Szendroedi J, Krššák M, Brehm A, Moser E, Roden M. Quantitative ATP synthesis in human liver measured by localized 31P spectroscopy using the magnetization transfer experiment. *NMR Biomed.* 2008;21(5):437–43. doi:10.1002/nbm.1207
- Buehler T, Kreis R, Boesch C. Comparison of 31P saturation and inversion magnetization transfer in human liver and skeletal muscle using a clinical MR system and surface coils. *NMR Biomed.* 2015;28(2):188–99. doi:10.1002/nbm.3242
- Wolf P, Fellinger P, Pfeleger L, Smajis S, Beiglböck H, Gajdošik M, Anderwald C-H, Trattnig S, Luger A, Winhofer Y, Krššák M, Krebs M. Reduced hepatocellular lipid accumulation and energy metabolism in patients with long standing type 1 diabetes mellitus. *Sci. Rep.* 2019;9(1):2576. doi:10.1038/s41598-019-39362-4

Characterization of Acute Kidney Injury (AKI) with combined Dynamic Contrast Enhanced (DCE) and Dynamic Glucose Enhanced (DGE) MRI

Chris Lippe 1*, Verena Hoerr 1+2

1 Clinic of Radiology, University of Münster, Münster, Germany

2 Heart Center Bonn, Department of Internal Medicine II, University Hospital Bonn, Bonn, Germany

Abstract: Acute kidney injury (AKI) was probed in a murine ischemia–reperfusion model using complementary dynamic contrast-enhanced (DCE) and dynamic glucose-enhanced (DGE) MRI at 9.4 T. Gadolinium kinetics revealed normal peak cortical delivery but markedly impaired wash-out in AKI, indicating reduced filtration. Glucose enhanced CEST readouts corroborated this deficit: AKI kidneys lacked the osmotic MT drop and showed minimal glucose-related asymmetry, implying hindered tubular transit and increased intracellular metabolization. Complementary DCE and DGE findings demonstrate their combined capacity to quantify hemodynamic and metabolic dysfunction, showing potential for precise, non-invasive AKI assessment.

Motivation: Acute kidney injury (AKI) represents a severe condition with high morbidity and mortality that is associated with rapid decline in kidney function. It compromises the kidney’s abilities to clear metabolic waste, regulate fluid and electrolyte balance, and maintain acid–base stability. It is usually recognized by diminished renal filtration capacity, a rise in serum creatinine, and reduced urine output. Early detection and targeted management are crucial to support recovery and minimize the risk of lasting kidney damage. [1]

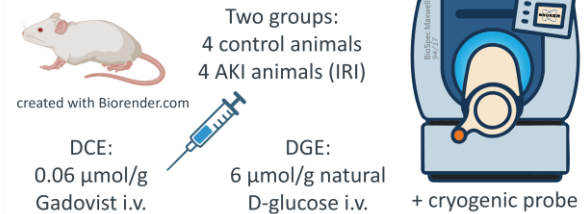
Dynamic Contrast Enhanced (DCE) and Dynamic Glucose Enhanced (DGE) MRI have great potential to improve the characterization of AKI by supplying complementary, noninvasive measures of renal function. In DCE-MRI, a gadolinium-based contrast agent is administered intravenously and serial T1-weighted images capture contrast kinetics, which can be used to derive renal perfusion and filtration metrics [2]. In DGE-MRI, natural D-glucose is infused and its accumulation is tracked via repeated chemical exchange saturation transfer (CEST) scans, providing maps of glucose filtration, tubular reabsorption and cellular uptake [3].

We previously developed reliable model-based quantification of glucose using CEST MRI which accounts for magnetization transfer (MT), relaxation effects, and field inhomogeneities while maintaining a sufficient temporal resolution [4]. In this study, we will apply this technique and cross-validate it with established DCE MRI protocols [5] to create a comprehensive suite of MRI techniques to assess kidney function.

Materials & Methods: Experiments were performed on a Bruker Biospec Maxwell 94/17 small animal MR system equipped with an 82 mm transmit-only volume resonator and a four-element receive-only cryogenic probe. One axial slice covering both kidneys was measured (96x60 matrix, 0.25x0.25 mm² resolution). Four control and four AKI (ischemia-reperfusion-injury model) mice were measured each. DCE MRI was performed using a FLASH sequence (TE = 1.66 ms, TR = 12.5 ms, 500 ms per slice, 1200 repetitions). A bolus of 0.06 μmol/g Gadovist (Bayer) i.v. was administered after 1 min. For DGE MRI, Spin-Lock preparation (B₁=6 μT, 0.2 s saturation, TR=1.5 s) was used, followed by a gradient-

echo snapshot for read-out. 31 offsets were measured for 60 repetitions with a temporal resolution of approximately 50 s per spectrum, with slight variations due to respiration triggering. A glucose bolus of 6 μmol/g was injected after 5 minutes. The model fitted to the Z-spectra is outlined in figure 1. R_{1,obs} was provided from an additionally measured T₁-map. B₀- and B₁-maps were obtained using WASABI [6].

Study design



Model fitted to Z-spectra:

$$R_{1\rho}(\Delta\omega) = \frac{\left(R_{1,obs} + \frac{f_{MT}}{1+f_{MT}} R_{1}^{MT}(\Delta\omega)\right) \cdot \Delta\omega^2 + (A \cdot \Delta\omega + B) \cdot \omega_1^2}{\Delta\omega^2 + \omega_1^2} \quad (\text{Eq. 1})$$

$$R_{1}^{MT}(\Delta\omega) = \frac{\omega_1^2 \cdot R_{2,MT}}{R_{2,MT}^2 + (\Delta\omega - \delta\omega_{MT})^2} \quad (\text{Eq. 2})$$

Fig. 1: Study design for combined Dynamic Contrast Enhanced (DCE) and Dynamic Glucose Enhanced (DGE) MRI in a murine model of acute kidney injury. Eight animals were divided into control (n=4) and AKI (ischemia–reperfusion injury, n=4) groups and imaged using a cryogenic probe. For DCE-MRI, 0.06 μmol/g of the gadolinium-based contrast agent Gadovist was administered intravenously; for DGE-MRI, 6 μmol/g of natural D-glucose was infused, exceeding the renal threshold. Z-spectra from both protocols were fitted to a model defined in equations 1 and 2 to quantify glucose concentration change.

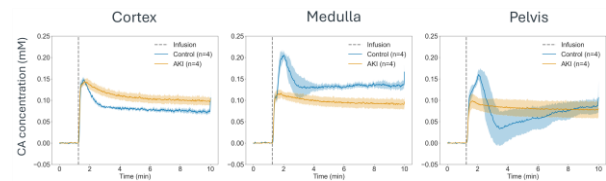


Fig. 2: Dynamic contrast-enhanced MRI time courses of gadolinium-based contrast agent (CA) concentration in the renal cortex, medulla and pelvis for control (blue, n = 4) and AKI (orange, n = 4) animals. Traces show the mean CA concentration over ten minutes and shaded bands represent the standard error of the mean. The vertical dashed line marks the start of intravenous CA infusion. The maximal CA concentration delivered to the kidney cortex was shared by both groups, however subsequent filtration dynamics were much suppressed in AKI animals.

Results: Figure 2 shows the dynamic contrast-enhanced MRI time courses of gadolinium concentration in cortex, medulla and pelvis. In both groups the cortical curve rose sharply after the bolus and reached a similar peak, yet the subsequent ten-minute profiles diverged: control animals exhibited a rapid decline and lower plateau values, whereas AKI animals maintained higher concentrations for the remainder of the scan. Comparable patterns were observed in the medulla. In

the pelvis, the control group displayed a pronounced peak followed by gradual wash-out, while the AKI curve remained relatively flat.

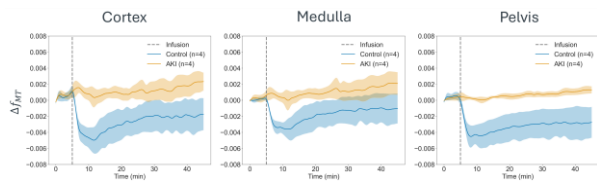


Fig. 3: Time courses of the change in magnetization transfer (MT) proton fraction (Δf_{MT}) following D-glucose infusion in the renal cortex, medulla and pelvis for control (blue, $n = 4$) and AKI (orange, $n = 4$) animals. Traces represent the mean Δf_{MT} and shaded regions denote the standard error of the mean. The vertical dashed line indicates the onset of glucose infusion. Control kidneys exhibited a marked drop in f_{MT} immediately after infusion that gradually returned toward baseline, whereas AKI kidneys remained mostly unchanged.

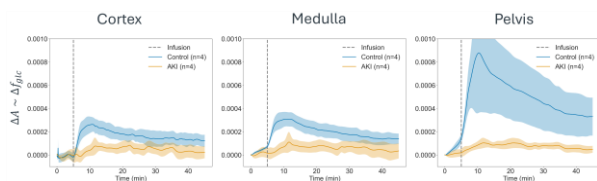


Fig. 4: Time courses of the DGE asymmetry parameter ΔA , which is proportional to the glucose proton fraction change, in the renal cortex, medulla and pelvis for control (blue, $n = 4$) and AKI (orange, $n = 4$) animals. Traces show mean ΔA over 45 minutes and shaded regions represent the standard error of the mean. The vertical dashed line marks the onset of D-glucose infusion. In control kidneys, a rapid rise in ΔA was observed in all regions, most prominently in the pelvis, followed by a gradual washout, whereas AKI kidneys exhibited a blunted increase in ΔA .

Figure 3 presents the magnetization-transfer proton-fraction change (Δf_{MT}) recorded for 45 minutes following intravenous D-glucose. In controls, Δf_{MT} dropped sharply in all renal zones immediately after infusion, reached a nadir within the first five minutes and then trended back toward baseline. AKI animals showed only a modest initial deflection and remained near baseline throughout the acquisition; the shapes of the curves were similar across cortex, medulla and pelvis.

Figure 4 depicts the DGE asymmetry parameter ΔA , which is proportional to the glucose proton-fraction change. Control kidneys demonstrated a rapid post-infusion rise in ΔA in every region, most prominent in the pelvis, followed by a gradual decay toward baseline. AKI animals exhibited a markedly smaller increase that stabilized at a low level for the full 45-minute period.

Discussion: The markedly suppressed wash-out of gadolinium in AKI kidneys (Fig. 2) confirms impaired filtration, and this deficit is mirrored in the glucose-based readouts. In control animals the osmotic load of glucose drives a transient expansion of the extracellular free-water pool, manifested as the acute drop in MT proton fraction (Fig. 3). AKI kidneys show almost no MT decrease. One plausible explanation could be that injured tubules metabolize higher amounts of glucose intracellularly, blunting both the osmotic dilution effect and the expected rise in free water [7].

Likewise, the minimal increase in the DGE asymmetry parameter in AKI (Fig. 4) suggests that little glucose reaches the pelvis despite the high infusion dose; this again points to hindered filtration. Therefore, DCE and DGE results show good agreement regarding the diagnosis of reduced filtration, while DGE can add complementary information about the macromolecular dynamics, as well as metabolic changes.

Conclusion: Combined DCE and DGE MRI offer a powerful multiparametric platform for non-invasive characterization of AKI. DCE detects perfusion and filtration deficits, while DGE captures macromolecular dynamics and aberrant glucose handling. Our findings demonstrate reductions in filtration and glucose transit in AKI, highlighting the value of DGE in revealing metabolic alterations not apparent with contrast enhancement alone. This integrated methodology holds promise for improved AKI diagnosis, phenotyping, and therapeutic monitoring.

Acknowledgements: This work was supported by the Deutsche Forschungsgemeinschaft (German Research Foundation, Project-ID 431460824).

References:

1. *Kidney Disease: Improving Global Outcomes (KDIGO) Acute Kidney Injury Work Group. KDIGO Clinical Practice Guideline for Acute Kidney Injury. Kidney Int Suppl. 2012;2(1):1–138.*
2. *Pedersen M, Irrera P, Dastrù W, et al. Dynamic Contrast Enhancement (DCE) MRI-Derived Renal Perfusion and Filtration: Basic Concepts. Methods Mol Biol. 2021;2216:205-227. doi:10.1007/978-1-0716-0978-1_12*
3. *Boyd PS, Breitling J, Zimmermann F, et al. Dynamic glucose-enhanced (DGE) MRI in the human brain at 7 T with reduced motion-induced artifacts based on quantitative R1ρ mapping. Magn Reson Med. 2020; 84: 182–191. https://doi.org/10.1002/mrm.28112*
4. *Lippe C, Hoerr V. Model-based Analysis of Renal Dynamic Glucose Enhanced (DGE) MRI. Proc. Intl. Soc. Mag. Reson. Med. 33 (2025), Program number: 2462*
5. *Pohlmann A, Niendorf T, editors. Preclinical MRI of the Kidney: Methods and Protocols. New York: Humana Press; 2021. doi: 10.1007/978-1-0716-0978-1*
6. *Schuenke P, Windschuh J, Roeloffs V, Ladd ME, Bachert P, Zaiss M. Simultaneous mapping of water shift and B1 (WASABI)-Application to field-Inhomogeneity correction of CEST MRI data. Magn Reson Med. 2017;77(2):571-580. doi:10.1002/mrm.26133*
7. *Schaub JA, Venkatachalam MA, Weinberg JM. Proximal Tubular Oxidative Metabolism in Acute Kidney Injury and the Transition to CKD. Kidney 360. 2020;2(2):355-364. Published 2020 Dec 22. doi:10.34067/KID.0004772020*

Monitoring macaque brain organoid maturation using magnetic resonance imaging and spectroscopy

Tor Rasmus Memhave 1*, Nesil Esiyok 1+2, Michael Heide 1, Susann Boretius 1+2

1 German Primate Center Göttingen, Germany

2 University of Göttingen, Germany

Abstract: Here, we present a novel MR-based approach to study organoid maturation non-invasively. Organoids are promising translational research models. The maturation of 8 rhesus macaque brain organoids was characterized at three time points. We observed profound morphological, microstructural, and metabolic alterations during organoid maturation. Notably, organoids were found to increase in size until 50 days post-seeding, after which they became smaller and more spherical. During maturation, the neurite density index and macromolecular content both increased. Taken together, our findings illustrate the potential of combining MR methods with advanced in vitro models.

Motivation: Organoids, 3D cell cultures derived from induced pluripotent stem cells, are complex in vitro models that have a high translational potential. They have been used to study and model complex metabolic and neurodevelopmental disorders^{1,2}. However, studying organoid maturation (and growth) with conventional optical imaging methods is often limited by low penetration depth. Histological techniques can overcome this limitation, but typically require tissue fixation or clearing, thereby preventing longitudinal studies. Recently, magnetic resonance imaging (MRI) has been successfully used to acquire structural and diffusion MRI^{3–6}. However, to date, no study has comprehensively characterized the morphological, microstructural, and metabolic maturation of organoids. Here, we used MRI and MR spectroscopy (MRS) to study the maturation of rhesus macaque brain organoids at three developmental time points. Our findings propose MRI/S as a complementary, non-invasive technique for studying the longitudinal development of brain organoids.

Materials & Methods: Eight rhesus macaque brain organoid was measured longitudinally on 30, 50, and 70 days post-seeding (dps). MR data was acquired using a preclinical 9.4T MRI system equipped with a custom-built, MR-compatible bioreactor. Structural MRI was acquired with a magnetization transfer gradient echo sequence at 100- μ m isotropic resolution and 20.5-min acquisition time. Diffusion-weighted images (echo planar imaging, 2 b-values, 30 directions, 17.3 min acquisition time) and relaxometry (multi-spin multi-echo sequence, 17.1 min acquisition time) were acquired at a 100 \times 100 \times 500 μ m³ resolution. MRS was performed using a stimulated echo acquisition mode with a 2.5 \times 2.5 \times 2.5 mm³ and 12.8 min acquisition time per organoid. The total protocol duration was approximately 4 hours. The culture medium in the bioreactor was exchanged halfway through the measurement before MRS and diffusion MRI.

Organoid volume and sphericity were calculated based on manual segmentations performed with ITK-SNAP on the anatomical MRI data. Diffusion tensor imaging (DTI) and neurite orientation dispersion and density imaging (NODDI)^{7,8} were reconstructed using in-house python scripts with the packages dipy⁹ and dmipy¹⁰. T2 maps were also

calculated using in-house python scripts. Diffusion images and relaxometry maps were analyzed using region of interest analysis. Spectroscopy data was analyzed using manual peak integration to calculate the concentration of myo-inositol, glucose, lactate, the combined amino acid peak (valine, leucine, and isoleucine), and macromolecules (peaks at 2.62, 1.2, 0.85 ppm). Statistics were performed using a one-way ANOVA and Tukey HSD for post-hoc testing ($\alpha=0.05$).

Results: The volume and surface area of the organoids were derived from manual segmentation of the anatomical MRI, fig. 1A. The brain organoids increased in volume by 19% from 30 to 50 dps, but decreased by 25% from 50 to 70 dps, fig. 1B. The trend in sphericity (measure of how close to organoid is to a perfect sphere) showed an opposite tendency with a small 2% decrease (n.s.) from 30 to 50 dps followed by a 5% increase (n.s.) from 50 to 70 dps, fig. 1C.

Using diffusion MRI, we probed the microstructural maturation of the organoids. Fractional anisotropy showed a non-significant increase from 30 to 50 dps, which, along with the decreased sphericity, may indicate early neuronal differentiation. However, overall fractional anisotropy decreased by 40% from 30 to 70 dps, fig. 2A, while the neurite density index and intracellular fraction increased by 18% and 13%, respectively, fig. 2B-C. The T2 relaxation time decreased by 7% after 50 dps, fig. 3, suggesting increased tissue density.

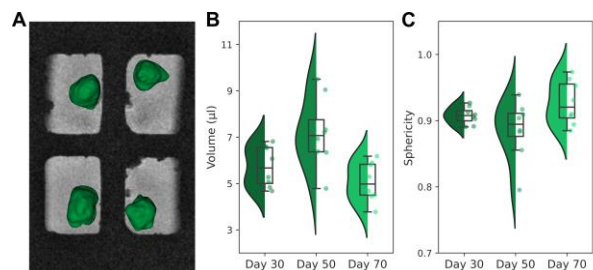


Fig. 1: Brain organoid morphological changes were measured using volume and sphericity, derived from the segmentation of each organoid, A. The organoid volume, B, increased from 30 to 50 dps and decreased from 50 to 70 dps. The sphericity, C, showed the opposite trend by first decreasing and then increasing.

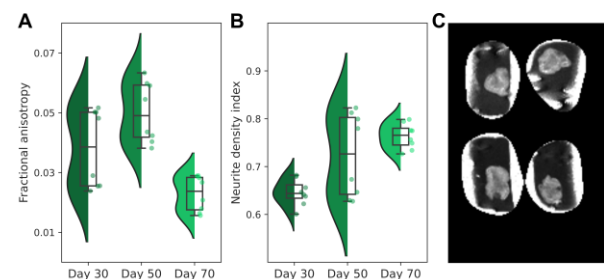


Fig. 2: Fractional anisotropy increased from 30 to 50 dps and decreased again at 70 dps, A. The neurite density index, B, and intracellular volume, example shown in C, increased at 70 dps. The diffusion results indicate a maturation of the cortical plate.

MRS was acquired with sufficient spectral quality for clear delineation of individual metabolites, fig. 4A. We observed a 52% increase in macromolecular content from day 30 to 70 dps, fig. 4B, however, the steady-state energy consumption peaked at 50 dps, fig. 4C., indicating that metabolic changes occur during organoid maturation.

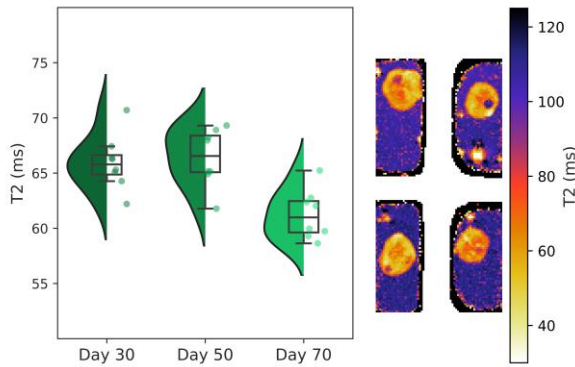


Fig. 3: The T2 time of the organoid decreased after 50 dps, left. From the calculated T2 maps, right, it is possible to distinguish cortical plate, core, and ventricles. The region of interest analysis was performed on the cortical plate.

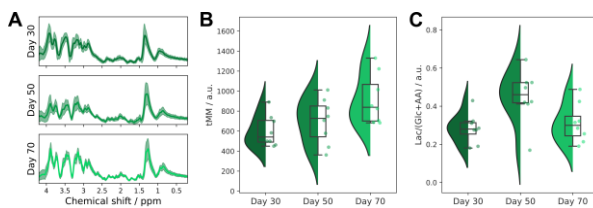


Fig. 4: Localized MRS was performed for each organoid at 30, 50, and 70 dps. The average spectra with standard deviation are shown in A. The macromolecular content increased during maturation, B. The energy turnover, lactate divided by glucose and amino acids, was highest at 50 dps.

Discussion: Our results suggest that the differentiation into neurons (30-50 dps) and subsequent maturation (50-70 dps) may be observable using MRI/S. Specifically, increased fractional anisotropy, decreased sphericity, and high energy turnover indicate that organoid expansion occurs up to 50 dps in rhesus brain macaques, followed by a potential pruning phase. These findings suggest that the observed MR parameters may be useful markers of organoid maturity. Furthermore, the decrease in T2 relaxation time as well as increase of neurite density index, intracellular volume, and macromolecular content indicate that the maturation of the cortical plate can also be detected using MRI/S. Taken together, our findings highlight the potential of MRI for longitudinal monitoring of key developmental stages in brain organoid maturation.

While previous studies have primarily focused on a single MR modality³ and usually only one time point^{4–6}, this study provides longitudinal, multi-modal characterization of organoid maturation. This represents the first comprehensive evidence that MRI can be used to assess morphological, microstructural, and metabolic changes that occur during organoid maturation. Furthermore, this is the first study to utilize nonhuman primate brain organoids, thereby paving the way for future research focused on cross-species brain development in an in vitro model using MRI.

Conclusion: We illustrate that MRI/S enables the longitudinal and non-invasive study of morphological, microstructural, and metabolic maturation in individual brain organoids. Interestingly, our findings indicate that rhesus macaque brain organoids expand until 50 dps, before undergoing a pruning process making them smaller and more spherical. Our MRS findings indicate that throughout their maturation, organoids show increased macromolecular content, potentially linked to increased cell density. As a complementary technique, longitudinal MRI/S of organoids may provide novel insights into disease progression and treatment response. This is of particular interest when combined with patient-derived organoids to provide a novel approach for personalized medicine.

Acknowledgements: The authors would like to thank Inwoo Kim for her technical assistance.

References:

1. Yan H, Chen S, Abdulla A, et al. Folic acid ameliorates high glucose–induced neurotoxicity in human forebrain organoids: Insights from proteomics. *Food Frontiers*.
2. Lu X, Yang J, Xiang Y. Modeling human neurodevelopmental diseases with brain organoids. *Cell Regen*.
3. Deininger L, Jung-Klawitter S, Mikut R, et al. An AI-based segmentation and analysis pipeline for high-field MR monitoring of cerebral organoids. *Sci Rep*.
4. Wu D, Lee HH, Ba R, et al. In vivo mapping of cellular resolution neuropathology in brain ischemia with diffusion MRI. *Sci Adv*.
5. Versace A, Hitchens TK, Wallace CT, Watkins SC, D’Aiuto L. 11.7T Diffusion Magnetic Resonance Imaging and Tractography to Probe Human Brain Organoid Microstructure. *Biological Psychiatry Global Open Science*.
6. Zur MK, Bhattacharya B, Dror SB, et al. Altered Extracellular Matrix Structure and Elevated Stiffness in a Brain Organoid Model for Disease. *Nature Communications*
7. Tariq M, Schneider T, Alexander DC, Gandini Wheeler-Kingshott CA, Zhang H. Bingham–NODDI: Mapping anisotropic orientation dispersion of neurites using diffusion MRI. *NeuroImage*.
8. Zhang H, Schneider T, Wheeler-Kingshott CA, Alexander DC. NODDI: Practical in vivo neurite orientation dispersion and density imaging of the human brain. *NeuroImage*.
9. Garyfallidis E, Brett M, Amirbekian B, et al. Dipy, a library for the analysis of diffusion MRI data. *Front Neuroinform*.
10. Fick RHJ, Wassermann D, Deriche R. The Dmipy Toolbox: Diffusion MRI Multi-Compartment Modeling and Microstructure Recovery Made Easy. *Front Neuroinform*.

Optimizing Quantitative MRI Protocols for Neurosurgery-Planning of Drug-Resistant Epilepsy Patients: A Multi-Site Traveling Heads Study

Jan Malte Oeschger* 1+2, Laurin Mordhorst 1+2, Nina Lüthi 1+2, Francisco J. Fritz 1+2+3, Difei Wang 4, Rüdiger Stirnberg 4, David Leitão 5, Philippa Bridgen 5+6, Zihan Ning 5, Shaihan Malik 5, David W. Carmichael 5, Tony Stöcker 4+7, Karsten Tabelow 11, Luke J. Edwards 3, Kerrin J. Pine 3, Nikolaus Weiskopf 3, Martina F. Callaghan 8, Markus Nilsson 9, Filip Szczepankiewicz 9, Arthur Chakwizira 9, Ileana Jelescu 10, Quentin Uhl 10, Siawoosh Mohammadi 1+2+3

1 Department of Neuroradiology, University of Lübeck, Lübeck, Germany

2 Institute of Systems Neuroscience, University Medical Center Hamburg-Eppendorf, Hamburg, Germany

3 Department of Neurophysics, Max Planck Institute for Human Cognitive and Brain Sciences, Leipzig, Germany

4 MR Physics, German Center for Neurodegenerative Diseases, Bonn, Germany

5 Imaging Physics & Engineering Research Dept., School of Biomedical Engineering and Imaging Sciences, King's College London, United Kingdom

6 Guy's and St. Thomas' NHS Foundation Trust, London, United Kingdom

7 Department of Physics and Astronomy, University of Bonn, Bonn, Germany

8 Functional Imaging Laboratory, Dept. of Imaging Neuroscience, UCL Queen Square Institute of Neurology, University College London, UK

9 Lund University, Clinical Sciences Lund, Department of Medical Radiation Physics, Lund, Sweden

10 Department of Radiology, Lausanne University Hospital, Lausanne, Switzerland

11 Weierstrass Institute for Applied Analysis and Stochastics, Berlin, Germany

Abstract: A multi-site traveling heads study evaluated quantitative MRI protocols intended to image drug-resistant temporal lobe epilepsy patients. The protocols encompassed MPMs (R1, R2, R2*, MTsat, PD) acquired using 3D-EPI and FLASH (or SSFP), and diffusion parameters using Q-space Trajectory Imaging. Variability measures guided protocol selection. For MPMs, 3D-EPI was faster than FLASH with similar variabilities but may have lower effective resolution. For QTI a protocol with shorter TE and higher SNR is preferable despite longer acquisition time to avoid critical imaging artifacts. These protocols were selected based on the presented findings:

- MPM: FLASH (cortical delineation)
- R2: MPR (faster, more sensitive to anatomy)
- QTI: Shorter-TE protocol (reduced artifacts)

Motivation: A multi-site, traveling heads study across multiple 3T MRI systems was conducted (Figure 1) to optimize time-constrained clinical imaging for future application in, e.g. drug-resistant temporal lobe epilepsy (TLE) patients, and planning of neurosurgery [1,9,16].

Implemented protocols included: (1) multi-parameter mapping (MPM) using 3D Echo-Planar Imaging (3D-EPI) [10] and FLASH [11], (2) transverse relaxation rate (R₂) mapping using 3D-EPI-based magnitude-phase-based relaxation (MPR) [3] and controlled saturation magnetization transfer with joint system relaxation (CSMT-JSR) using a combination of FLASH and SSFP sequences [4,5], and (3) Q-space Trajectory Imaging (QTI) [13,17] using two diffusion protocols with varying echo time and thus differing SNR and imaging artifacts. The MPM parameters included longitudinal and effective transverse relaxation rates (R1 and R2*), proton density (PD) and magnetization transfer saturation (MTsat).

For comparison, anatomical-, subject- and scan-rescan coefficients of variation (CoV) were quantified and presented in three separate ISMRM 2025 abstracts that are here joined together with the aim to choose a 1 hour protocol for imaging of TLE patients at the university clinic Hamburg-Eppendorf ("target site") as part of an ongoing ERC project.

Materials & Methods: Four healthy subjects, 3 male, 1 female, mean age ± standard deviation (SD) 36 ± 9 years, including one subject undergoing scan-rescan, were scanned at: UKE in Hamburg as well as the reference sites at DZNE in Bonn, MPI-CBS in Leipzig and the UCL and KCL in London, see Figure 1.

Variation in parameter estimates were quantified using inter-subject, inter-region and scan-rescan coefficients of variation (CoV) in gray matter regions of interest (ROI). Gray matter ROIs in subject space were created by combining conservatively thresholded gray matter segmentations [6,12] with liberally thresholded ROI priors from the Harvard-Oxford atlas [7].

- MPM Study: R1, R2*, PD, and MTsat were calculated using the hMRI toolbox [8].

- R₂ Mapping Study: We acquired MPR at the DZNE and UKE, CSMT-JSR at KCL and a simplified CSMT-JSR variant (JSR) at UKE; data were denoised and motion-corrected before R₂ mapping was performed [2,3,4,5].

- QTI Study: Pre-processing included: denoising [19], Rician bias correction [18], Gibbs-ringing [19], susceptibility distortion [18], eddy current and motion correction [14]. The QTI parameters microscopic fractional anisotropy (μFA), anisotropic kurtosis (MKA), and isotropic kurtosis (MKI) were estimated using this GitHub repository [15].

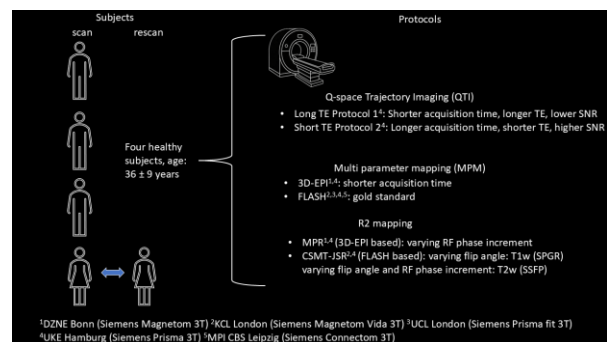


Fig. 1: Overview of the traveling heads study conducted at DZNE Bonn, KCL and UCL London, UKE Hamburg and MPI CBS Leipzig. For details on the MPM protocol, see ISMRM 2025 abstract 3547, for details on R₂ mapping, see ISMRM 2025 abstract 4472, for details on QTI, see ISMRM 2025 abstract 4205.

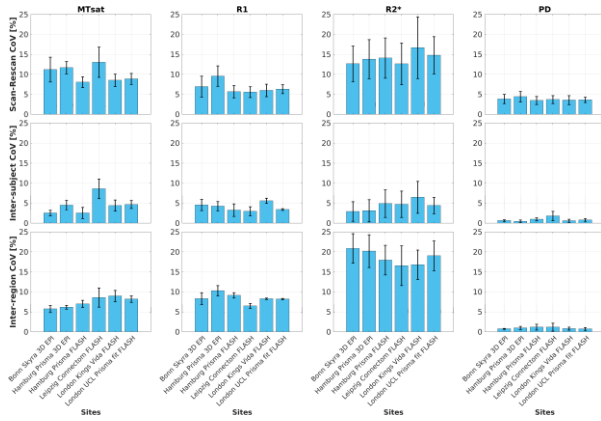


Fig. 2: Shown are (top to bottom) the Scan-Rescan, Inter-subject and Inter-region Coefficients of variation (CoV) of MTsat, R1, R2* and PD (left to right) for each site and MPM protocol.

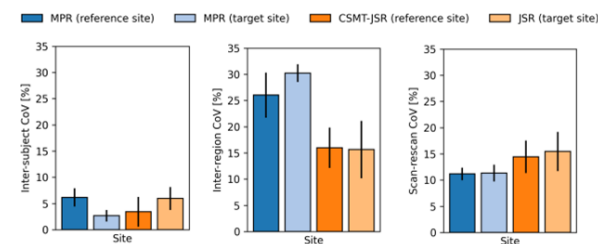


Fig. 3: R2 Coefficients of variation (CoV). The plots quantify R2 variability across subjects, regions and repeated scans. Left to right: Inter-subject (mean \pm SD across ROIs), inter-region (mean \pm SD across subjects) and Scan-rescan (mean \pm SD across ROIs) CoV.

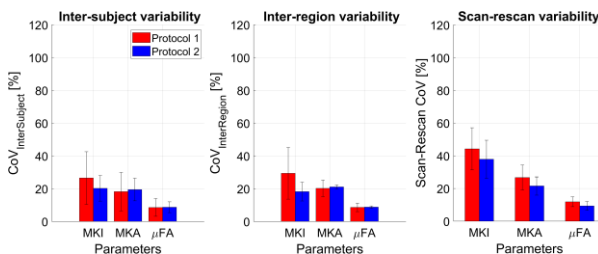


Fig. 4: Inter-subject, Inter-region and scan-rescan coefficients of variation (CoV) for MKI, MKA and μ FA. Bars show mean and lines show standard deviation (Inter-subject variability and Scan-rescan variability: across ROIs, Inter-region variability: across subjects)

Results: MPM Study:

- 3D-EPI reduced acquisition time “TA” (TA at target site: 6:38min) compared to FLASH (TA at target site: 14:09min) while maintaining comparable CoVs for MTsat, R1, PD and R2*.

- 3D-EPI exhibited possible reductions in effective resolution, which may limit its ability to detect subtle TLE abnormalities and impact CoV.

R₂ Mapping Study:

- Acquisition of the 3D-EPI-based MPR was three times as fast as (CSMT-)JSR (~4 min vs. ~13 min at target site) but required significantly longer post-processing time (MPR: ~15h vs. CSMT-JSR: ~10 min on a Ryzen 5800x, 8-core CPU).

- MPR demonstrated higher inter-region variability and lower scan-rescan variability. Inter-subject variability was comparable between both protocols.

- CSMT-JSR produced sharper images but was less effective at detecting anatomical variations between ROIs.

QTI Study:

- Protocol 2 (TA at target site: 7:34min), with shorter TE and higher SNR, showed consistently lower scan-rescan variability compared to Protocol 1 (TA at target site: 5:42min) with longer TE and lower SNR.

- Inter-subject and inter-region variabilities were similar between protocols.

- Protocol 2 avoided SNR-related (likely Rician bias) MKI hyperintensities (e.g., near the putamen), reducing the risk of false positives.

Discussion: For R1, PD, MT, and R2* mapping, 3D-EPI offers an acquisition time-efficient alternative to FLASH with comparable CoVs, with potentially lower effective resolution. In R₂ mapping, 3D-EPI based MPR balances speed and reliability and its higher inter-region CoV and lower scan-rescan CoV indicate superior and more reliable capture of anatomical differences, making MPR more suitable for TLE imaging than the FLASH based (CSMT-)JSR. MPR’s increased processing time may currently pose workflow challenges but speed increases via algorithm optimization are likely achievable.

Effective resolution is influenced by the sequence and its potential reduction in 3D-EPI requires further evaluation, especially since the epileptogenic zones requiring neurosurgical removal may in some patients’ MRI scans only be visible as small scleroses which might otherwise be missed. Here, FLASH offers an inherently isotropic resolution, independent of readout lengths or other features. In contrast, effective resolution of the current 3D-EPI protocol is reduced because of its image reconstruction method which can be improved by adjusting the partial Fourier factor at the cost of increased scan time. In an ongoing study we plan to investigate effective resolution using the cortical profile for known structures, such as the Line of Gennari, and compare, e.g., 3D-EPI and FLASH data with each other. As a gold standard, we will use 7T data from the same subjects.

In case of QTI, prioritizing higher SNR in the protocol choice turned out to be crucial for avoidance of image artifacts possibly leading to false positives, despite a ~2min longer acquisition time.

Conclusion: As a first outcome of this traveling heads study, the following protocols will be acquired on the TLE patients in our ERC project:

- QTI: Protocol 2 with shorter TE and higher SNR was chosen because it avoids SNR related image artifacts possibly causing false positives.

- MPMs: a 0.8 mm isotropic FLASH-based MPM sequence protocol was chosen despite the discussed 3D-EPI advantages, because of its better expected cortical delineation. To reduce the acquisition time, we will skip MTsat.

- R2: the 3D-EPI-based MPR protocol was chosen because of its drastically reduced acquisition time and increased anatomical sensitivity.

Acknowledgements: This work was supported by the German Research Foundation (DFG Priority Program 2041 “Computational Connectomics” (MO 2397/5-1, MO2397/5-2)), the Emmy Noether Stipend (MO 2397/4-1 and 2397/4-2), the BMBF (01EW1711A and B) in the framework of ERA-NET NEURON, and the ERC (Acronym: MRStain, Grant agreement ID: 101089218, DOI: 10.3030/101089218). Views and opinions expressed are, however, those of the authors only and do not necessarily reflect those of the European Union or the European Research Council Executive Agency. Neither the European Union nor the granting authority can be held responsible for them.

KCL received core funding from the Wellcome/EPSRC Centre for Medical Engineering [WT203148/Z/16/Z] and by the National Institute for Health and Care Research (NIHR) Clinical Research Facility (CRF) and HealthTech Research Centre in Cardiovascular and Respiratory Medicine (HRC) at Guy’s and St Thomas’ NHS Foundation Trust. The views expressed are those of the author(s) and not necessarily those of the NHS, the NIHR or the Department of Health and Social Care.

References:

[1] A. Bernasconi et al., “Recommendations for the use of structural magnetic resonance imaging in the care of patients with epilepsy: A consensus report from the International League Against Epilepsy Neuroimaging Task Force,” *Epilepsia*, vol. 60, no. 6, pp. 1054–1068, Jun. 2019, doi: 10.1111/epi.15612.

[2] D. Wang, P. Ehses, T. Stöcker, and R. Stirnberg, “Reproducibility of rapid multi-parameter mapping at 3T and 7T with highly segmented and accelerated 3D-EPI,” *Magn. Reson. Med.*, vol. 88, no. 5, pp. 2217–2232, 2022, doi: 10.1002/mrm.29383.

[3] D. Wang, R. Stirnberg, and T. Stöcker, “Improved gradient echo magnitude- and phase-based mapping of using multiple RF spoiling increments at 3T and 7T,” *Magn. Reson. Med.*, vol. 92, no. 6, pp. 2328–2342, 2024, doi: 10.1002/mrm.30217.

[4] R. P. A. G. Teixeira, S. J. Malik, and J. V. Hajnal, “Joint system relaxometry (JSR) and Crámer-Rao lower bound optimization of sequence parameters: A framework for enhanced precision of DESPOT T1 and T2 estimation,” *Magn. Reson. Med.*, vol. 79, no. 1, pp. 234–245, 2018, doi:10.1002/mrm.26670.

[5] R. P. A. G. Teixeira, S. J. Malik, and J. V. Hajnal, “Fast quantitative MRI using controlled saturation magnetization transfer,” *Magn. Reson. Med.*, vol. 81, no. 2, pp. 907–920, 2019, doi: 10.1002/mrm.27442.

[6] B. B. Avants, N. J. Tustison, J. Wu, P. A. Cook, and J. C. Gee, “An Open Source Multivariate Framework for n-Tissue Segmentation with Evaluation on Public Data,” *Neuroinformatics*, vol. 9, no. 4, p. 381, Dec. 2011, doi: 10.1007/s12021-011-9109-y.

[7] S. M. Smith et al., “Advances in functional and structural MR image analysis and implementation as FSL,” *Neuroimage*, vol. 23 Suppl 1, pp.S208–219, 2004, doi: 10.1016/j.neuroimage.2004.07.051.

[8] Tabelow K, Weiskopf N, Mohammadi S, et al. hMRI – A toolbox for quantitative MRI in neuroscience and clinical research. *NeuroImage*. 2019;194:191-210. doi: 10.1016/j.neuroimage.2019.01.029.

[9] Adler S, Lorio S, Jacques TS, Benova B, Gunny R, Cross JH, Baldeweg T, Carmichael DW. Towards in vivo focal cortical dysplasia phenotyping using quantitative MRI. *Neuroimage Clin*. 2017 Apr 20;15:95-105. doi: 10.1016/j.nicl.2017.04.017. PMID: 28491496; PMCID: PMC5413300.

[10] Wang D, Ehses P, Stöcker T, Stirnberg R. Reproducibility of rapid multi-parameter mapping at 3T and 7T with highly segmented and accelerated 3D-EPI. *Magn Reson Med*. 2022 Nov;88(5):2217-2232. doi: 10.1002/mrm.29383. Epub 2022 Jul 25. PMID: 35877781.

[11] Callaghan M, Lutti A, Ashburner J, Balteau E, Corbin N, Draganski B, Helms G, Kherif F, Leutritz T, Mohammadi S, Phillips C, Reimer E, Ruthotto L, Seif M, Tabelow K, Ziegler G, Weiskopf N. Example dataset for the hMRI toolbox. *Data in Brief*. 2019;25:104132. doi: 10.1016/j.dib.2019.104132.

[12] Friston K. Statistical parametric mapping. In: Friston K, Ashburner J, Kiebel S, Nichols T, Penny W, eds. *Statistical Parametric Mapping*. London: Academic Press; 2007. pp. 10–31. doi: 10.1016/B978-012372560-8/50002-4.

[13] F. Szczepankiewicz, J. Sjölund, F. Ståhlberg, J. Lätt, und M. Nilsson, „Tensor-valued diffusion encoding for diffusional variance decomposition (DIVIDE): Technical feasibility in clinical MRI systems“, *PLOS ONE*, Bd. 14, Nr. 3, S. e0214238, März 2019, doi: 10.1371/journal.pone.0214238.

[14]: <https://github.com/markus-nilsson/md-dmri/tree/master>

[15]: <https://github.com/bjeurissen/ciwlls/tree/master>

[16]: A. Bernasconi et al., “Recommendations for the use of structural magnetic resonance imaging in the care of patients with epilepsy: A consensus report from the International League Against Epilepsy Neuroimaging Task Force,” *Epilepsia*, vol. 60, no. 6, pp. 1054–1068, Jun. 2019, doi: 10.1111/epi.15612.

[17]: Morez J, Szczepankiewicz F, den Dekker AJ, Vanhevel F, Sijbers J, Jurissen B. Optimal experimental design and estimation for q-space trajectory imaging. *Hum Brain Mapp*. 2023;44: 1793–1809

[18]: G. David et al., „ACID: A comprehensive toolbox for image processing and modeling of brain, spinal cord, and ex vivo diffusion MRI data“, *Imaging Neuroscience*, Bd. 2, S. 1–34, Sep. 2024, doi: 10.1162/ima

3D distortion-free diffusion and T2 prepared reduced FOV imaging in the prostate at 3T

Yannik Ott 1+2*, Sarah McElroy 1+3, Raphael Tomi-Tricot 1+4, Carolyn Horst 5+6, Rahul Khamar 5+6, Omar Darwish 2, Vicky Goh 5+6, Radhouene Neji 1

1 Imaging Physics & Engineering Research Dept., School of Biomedical Engineering and Imaging Sciences, King's College London, United Kingdom,
 2 Research & Clinical Translation, Magnetic Resonance, Siemens Healthineers AG, Erlangen, Germany,
 3 MR Research Collaborations, Siemens Healthcare Ltd, Camberley, United Kingdom,
 4 Siemens Healthcare SAS, Courbevoie, France,
 5 Research Department of Cancer Imaging, School of Biomedical Engineering and Imaging Sciences, King's College London, United Kingdom,
 6 Department of Radiology, Guy's and St Thomas' NHS Foundation Trust, London, United Kingdom

Abstract: This work proposes a reduced FOV multi-shot sequence that yields natively co-registered 3D ADC and T2 maps. Slab-selective magnetization preparation modules that either employ diffusion or T2 preparation are applied before each shot that acquires one partition of the 3D volume using a GRE imaging readout. Inter-shot phase inconsistencies are captured by a 2D phase navigator. Constant timing between shots, together with dummy pulses following the T2-prepared shots, enables simple mono-exponential fitting of ADC and T2 maps. Quantitative evaluation in the prostate of 12 healthy volunteers showed that the proposed sequence yielded good agreement with reference acquisitions while no geometric distortions were observed.

Motivation: The current standard for reading prostate MRI (PI-RADS v2.1) still largely relies on qualitative visual assessment of diffusion- and T2-weighted, as well as dynamic contrast enhanced images [1]. However, it has been shown that additional quantitative information of apparent diffusion coefficient (ADC) [2], [3] and T2 relaxation [3], [4], [5] values can improve diagnostic performance. Thus, a joint ADC and T2 mapping sequence would be highly beneficial for prostate MRI. One major challenge is the geometric distortions inherent to the single-shot EPI (ssEPI) imaging readout, which is the gold-standard for clinical diffusion-weighted imaging (DWI). Diffusion preparation [6], [7], [8], [9] (DP) allows for distortion-free DWI and the combination with T2 preparation modules is straightforward [10], [11]. Previously proposed magnetic resonance fingerprinting [12] and multitasking [13] methods achieved joint quantification relying on high acceleration factors and complex reconstruction algorithms. In this work, we propose an extension of a previously proposed DP sequence that uses a reduced FOV (rFOV) approach for natural acceleration. By omitting the diffusion-sensitizing gradients, additional T2 prepared shots can be obtained that can be used to calculate naturally co-registered T2 maps.

Materials & Methods: The proposed sequence (Figure 1) extends the diffusion-prepared reduced FOV 3D GRE sequence by McElroy et al.[7] with additional T2 preparation (T2P) modules. Every partition is acquired within one shot, starting with a chemical shift-selective fat saturation pulse[14], followed by a magnetization preparation (DP or T2P) module, a 3D GRE imaging readout, and a 2D phase navigator without partition encoding. T2P modules start with a slab-selective tip-down pulse, apply twin-adiabatic refocusing pulses, magnitude stabilizer dephasing gradients, and a non-selective tip-up pulse followed by a spoiler gradient. Acquiring a shot without T2 preparation is not

feasible due to the rFOV approach. Therefore, a reduced version (T2P-min) without refocusing pulses is acquired. For diffusion preparation, additional diffusion-sensitizing gradients surrounding the refocusing pulses are applied. To ensure steady state for the longitudinal magnetization, the time between preparation modules remains constant throughout the shots.

To reconstruct the data, coil sensitivities are estimated on the T2P-min data set using ESPIRiT[15]. T2P images are obtained by applying the inverse Fourier transform followed by adaptive coil combination (ACC)[16]. For DP shots, the coil combined navigator data is used to correct the inter-shot phase inconsistencies [6]. Furthermore, multiple averages are combined based on the normalized squared navigator magnitude [9], [17]. Inverse Fourier transform and ACC [16] yield the final DP images. ADC and T2 maps are obtained using simple mono-exponential fitting.

The mean ADC and T2 values in the prostate of 12 healthy volunteers acquired at 3T (MAGNETOM Vida, Siemens Healthineers, Forchheim, Germany) were compared against reference sequences.

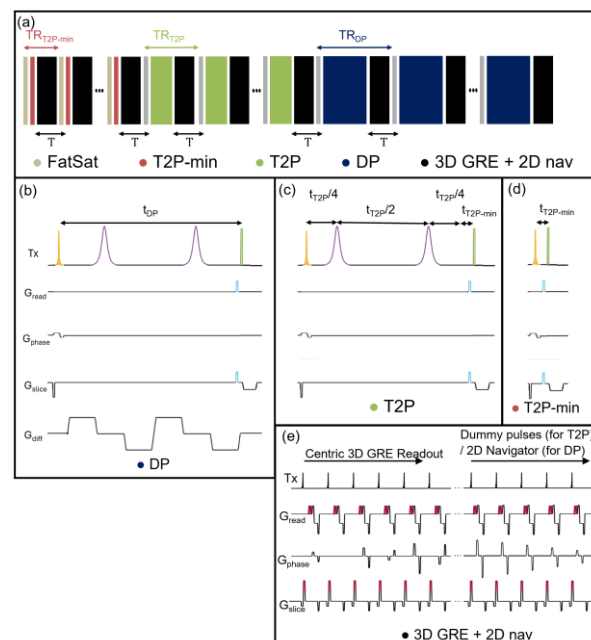


Fig. 1: Overview (subfigure a) of proposed multi-shot sequence. Either diffusion preparation (dark blue, subfigure b), T2 preparation (green, subfigure c), or a reduced version of T2 preparation (orange, subfigure d) are followed by a 3D GRE imaging readout and a 2D phase navigator (black, subfigure e).

Results: Figure 2 shows a Bland-Altman analysis of mean ADC (2a) and T2 (2b) values in the prostate gland. Subfigure 2a compares ADC values obtained by a rFOV ssEPI and the proposed sequence to reference values from a ssEPI acquisition. The proposed sequence yielded a non-significant ($p=0.91$) mean overestimation of $0.022 \times 10^{-3} \text{ mm}^2/\text{s}$ while the rFOV ssEPI yielded a statistically significant ($p<0.05$) underestimation of $0.040 \times 10^{-3} \text{ mm}^2/\text{s}$.

Reference T2 values were obtained using a multi echo spin-echo (meSE) sequence that excluded the first echo from the fitting (meSE-ref), as proposed by [18]. Figure 2b compares T2 values obtained by the meSE approach using all echoes as well as the proposed approach to the reference values. Values of both methods differed significantly from the reference ($p<0.05$). The mean bias of the meSE (using all echoes) and the proposed approach were 14.8 ms and -17.2 ms, respectively. Figure 3 shows all images and the resulting quantitative maps obtained by the proposed sequence. Figure 4 compares DWI images and ADC maps of the ssEPI, rFOV ssEPI, and the proposed sequence as well as the T2 maps from both meSE and the proposed approach. Red arrows indicate where geometric distortions are present in both EPI acquisitions but are not present in the proposed sequence.

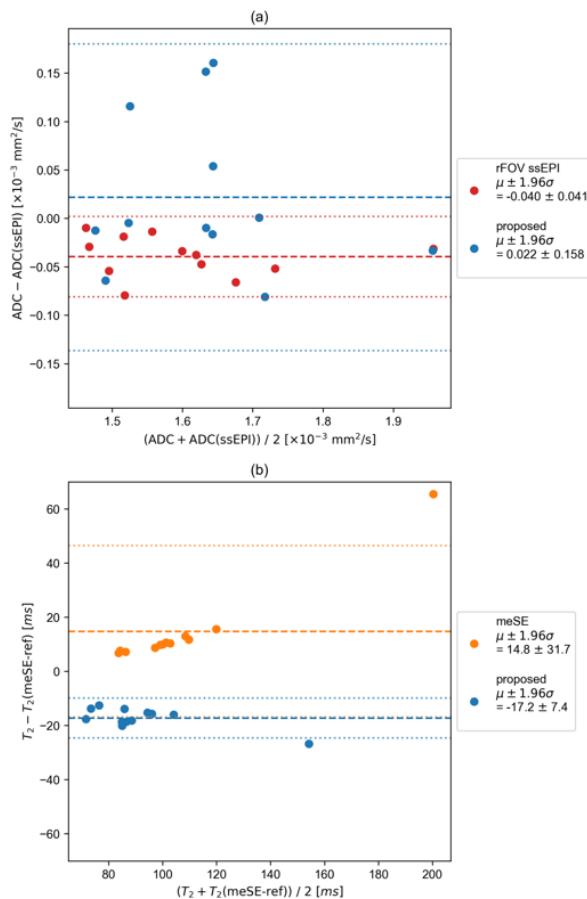


Fig. 2: Bland-Altman plots comparing ADC values (a) and T2 values (b) in vivo. In (a), the reference technique is ssEPI. In (b), the reference technique is meSE excluding the first echo from the fitting. Results are shown for the proposed technique (blue), rFOV ssEPI (red) and meSE including the first echo (orange).

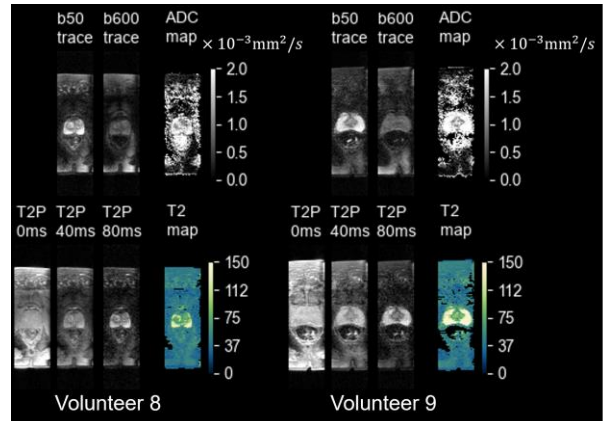


Fig. 3: Examples of obtained diffusion- and T2-prepared images as well as corresponding ADC and T2 maps for two representative volunteers.

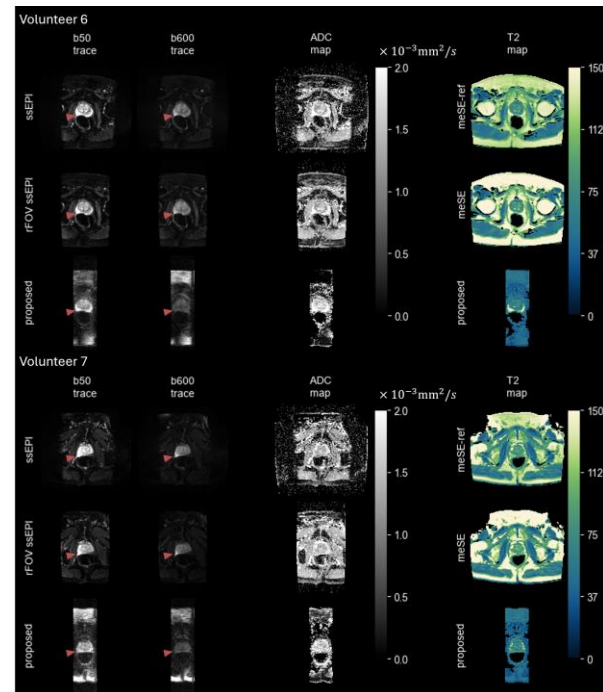


Fig. 4: Comparison of DWI images and ADC maps acquired using a ssEPI, rFOV ssEPI, and the proposed sequence as well as T2 maps that were obtained using meSE approaches, where one used all echoes for fitting (meSE), and one excluded the first (meSE-ref) and the proposed approach.

Discussion: We have proposed a 3D reduced FOV sequence to obtain natively co-registered non-distorted ADC and T2 maps in the prostate. The sequence is based on slab-selective tip-down pulses in the phase encoding direction applied in the T2 and diffusion preparation modules and maintains a steady state of the longitudinal magnetization prior to each tip-down pulse. This allows to use mono-exponential fitting for ADC and T2 estimation.

There was no significant difference between ADC values obtained by the proposed and the reference ssEPI sequence. However, 95% limits of agreement were wider than those of the rFOV ssEPI technique. Moreover, our sequence yielded a mean T2 estimation bias of -17.2 ms. It is worth noting that it was previously shown that meSE acquisitions are biased towards higher T2 values due to imperfect refocusing pulses and stimulated echo contributions [19].

Compared to EPI-based techniques for DWI or meSE sequences for T2 mapping, the proposed method suffers from low SNR efficiency due to the inherent 50% SNR penalty of stimulated echoes. [20] The current implementation of our sequence acquires the 2D phase navigator during T2P shots as dummy pulses, although phase correction is not required, to ensure constant time between tip-down and tip-up pulses. However, the time could be used more efficiently by acquiring additional imaging lines and increasing the resolution of the T2 maps.

Conclusion: This work proposes a 3D reduced FOV sequence for joint, distortion-free ADC and T2 mapping in the prostate, enabling the use of simple mono-exponential fitting to calculate ADC and T2 maps. In-vivo, the quantitative maps obtained using the proposed approach showed good agreement with reference acquisitions. Future work may include the application of deep learning methods to compensate the SNR penalty [21] or leverage redundancies between contrasts for accelerating the acquisition [22]. Moreover, the sequence could be extended using different delays between T2-prepared shots to enable saturation-recovery based T1 mapping. Finally, the approach has to be validated in patients.

Acknowledgements: The authors acknowledge financial support from Siemens Healthineers. This work was supported by core funding from the Wellcome/EPSRC Centre for Medical Engineering [WT203148/Z/17/Z] and by the National Institute for Health and Care Research (NIHR) Clinical Research Facility at Guy's and St Thomas' NHS Foundation Trust. The views expressed are those of the author(s) and not necessarily those of the NHS, the NIHR or the Department of Health and Social Care.

References:

- [1] O. T. Esengur, H. Stecko, E. Stevenson, and B. Turkbey, "Toward a refined PI-RADS: The feasibility and limitations of more informative metrics in reviewing MRI scans," *J. Magn. Reson. Imaging*, 2025.
- [2] H.-J. Meyer, A. Wienke, and A. Surov, "Discrimination between clinical significant and insignificant prostate cancer with apparent diffusion coefficient—a systematic review and meta analysis," *BMC Cancer*, vol. 20, pp. 1–11, 2020.
- [3] A. Panda et al., "MR fingerprinting and ADC mapping for characterization of lesions in the transition zone of the prostate gland," *Radiology*, vol. 292, no. 3, pp. 685–694, 2019.
- [4] C. H. Lee, M. Taupitz, P. Asbach, J. Lenk, and M. Haas, "Clinical utility of combined T2-weighted imaging and T2-mapping in the detection of prostate cancer: a multi-observer study," *Quant. Imaging Med. Surg.*, vol. 10, no. 9, p. 1811, 2020.
- [5] A. H. Dinh et al., "Characterization of prostate cancer using T2 mapping at 3 T: a multi-scanner study," *Diagn. Interv. Imaging*, vol. 96, no. 4, pp. 365–372, 2015.
- [6] H. Lee and R. R. Price, "Diffusion imaging with the MP-RAGE sequence," *J. Magn. Reson. Imaging*, vol. 4, no. 6, pp. 837–842, 1994.
- [7] S. McElroy et al., "3D distortion-free, reduced FOV diffusion-prepared gradient echo at 3 T," *Magn. Reson. Med.*, 2025.
- [8] P. K. Lee, J. J. Hess, A. A. Gomella, A. M. Loening, and B. A. Hargreaves, "A diffusion-prepared reduced FOV sequence for prostate MRI near metallic implants," *Magn. Reson. Med.*, 2024.
- [9] P. K. Lee, X. Zhou, and B. A. Hargreaves, "Diffusion-prepared imaging with amplitude navigation for correction of motion-induced signal loss," *Magn. Reson. Med.*, 2025.
- [10] T. Parrish and X. Hu, "A new T2 preparation technique for ultrafast gradient-echo sequence," *Magn. Reson. Med.*, vol. 32, no. 5, pp. 652–657, 1994.
- [11] J. H. Brittain, B. S. Hu, G. A. Wright, C. H. Meyer, A. Macovski, and D. G. Nishimura, "Coronary angiography with magnetization-prepared T2 contrast," *Magn. Reson. Med.*, vol. 33, no. 5, pp. 689–696, 1995.
- [12] X. Cao et al., "DTI-MR fingerprinting for rapid high-resolution whole-brain T1, T2, proton density, ADC, and fractional anisotropy mapping," *Magn. Reson. Med.*, vol. 91, no. 3, pp. 987–1001, 2024.
- [13] S. Ma et al., "Three-dimensional simultaneous brain T1, T2, and ADC mapping with MR multitasking," *Magn. Reson. Med.*, vol. 84, no. 1, pp. 72–88, 2020.
- [14] A. Haase, J. Frahm, W. Hancic, and D. Matthaei, "1H NMR chemical shift selective (CHESS) imaging," *Phys. Med. Biol.*, vol. 30, no. 4, p. 341, 1985.
- [15] M. Uecker et al., "ESPIRiT—an eigenvalue approach to autocalibrating parallel MRI: where SENSE meets GRAPPA," *Magn. Reson. Med.*, vol. 71, no. 3, pp. 990–1001, 2014.
- [16] D. O. Walsh, A. F. Gmitro, and M. W. Marcellin, "Adaptive reconstruction of phased array MR imagery," *Magn. Reson. Med. Off. J. Int. Soc. Magn. Reson. Med.*, vol. 43, no. 5, pp. 682–690, 2000.
- [17] K. L. Miller and J. M. Pauly, "Nonlinear phase correction for navigated diffusion imaging," *Magn. Reson. Med. Off. J. Int. Soc. Magn. Reson. Med.*, vol. 50, no. 2, pp. 343–353, 2003.
- [18] L. Biasioli, A. C. Lindsay, J. T. Chai, R. P. Choudhury, and M. D. Robson, "In-vivo quantitative T2 mapping of carotid arteries in atherosclerotic patients: segmentation and T2 measurement of plaque components," *J. Cardiovasc. Magn. Reson.*, vol. 15, no. 1, p. 69, 2013.
- [19] K. McPhee and A. Wilman, "Exponential T2 fitting with even echoes only or skipping the first echo: how well does it work," in *Proceedings of the 23rd annual meeting of ISMRM*, 2015, p. 1683.
- [20] J. Frahm, K.-D. Merboldt, W. Hänicke, and A. Haase, "Stimulated echo imaging," *J. Magn. Reson.* 1969, vol. 64, no. 1, pp. 81–93, 1985.
- [21] L. Pfaff et al., "Self-supervised MRI denoising: leveraging Stein's unbiased risk estimator and spatially resolved noise maps," *Sci. Rep.*, vol. 13, no. 1, p. 22629, 2023.
- [22] D. Polak et al., "Joint multi-contrast variational network reconstruction (jVN) with application to rapid 2D and 3D imaging," *Magn. Reson. Med.*, vol. 84, no. 3, pp. 1456–1469, 2020.

Field-dependent ¹³C and ¹⁵N Relaxation Dispersion and T1 Optimization Using CIDER

Josh P. Peters 1, Charbel D. Assaf 1, Arne Brahm 2, Kolja Them 1, Rainer Herges 2, Jan-Bernd Hövener 1, Andrey N. Pravdivtsev 1

1* Dept. of Radiology and Neuroradiology, Section Biomedical Imaging, University Hospital Schleswig-Holstein, Kiel University, Kiel, Germany, 2 Otto Diels Institute of Organic Chemistry, Otto-Hahn-Platz 4, 24098 Kiel, Germany

Abstract: This work aims to cumulate experimental data about the relaxation behavior of several ¹³C and ¹⁵N tracers. We explored approaches to extend the hyperpolarization lifetime. This is especially relevant for molecules like nicotinamide that have relaxation times in the range of 1 s to over 60 s, depending on conditions. T1 prolongation was achieved using chemically induced deceleration of nuclear spin relaxation (CIDER) and examined and optimized using magnetic field cycling between 7.8 μT and 9.4 T. CIDER significantly enhances the retained signal at the measuring site, which is necessary for successful *in vivo* applications.

Motivation: The hyperpolarization of nuclear spins boosts the MR signal of selected molecules and has enabled real-time metabolic imaging *in vivo* (Ref. 1). Still, hyperpolarized MR has not become a gold standard for metabolomics so far - partially because of the method's complexity and the lack of a diversified portfolio of disease-specific tracers which can be efficiently polarized.

Longitudinal magnetization dynamics is a key feature of magnetic resonance. T1-relaxation enables signal averaging, suppression, and anatomical contrast, therefore T1-shortening Gd-based agents are widely used. T1-prolonging agents, however, remain unexplored, with previous methods focusing on reducing relaxation sources (deuteration of solvent or molecule, chelating complexes). Long T1 maybe less useful for routine MRI than short T1, but it is essential e.g. for hyperpolarization experiments. Here, complete loss of polarization may occur in particular at low fields or certain pH (Ref. 2).



Fig. 1: A photo of the complete magnetic field cycling (MFC) device atop the spectrometer (NMR). The MFC enables the cycling of the NMR tubes from B0 magnetic field to the low magnetic field on top of the spectrometer. The MFC frame was mounted on a shelf positioned on top of the 400 MHz spectrometer.

Materials & Methods: ¹³C and ¹⁵N signals were acquired in the polarizer or after dissolution using a 1 T benchtop NMR, a 9.4 T WB NMR, and a 7 T MRI. dDNP was performed using a cryogen-free dDNP system (SpinAligner, POLARIZE) operating at ~1.4 K and 6.7 T. A microwave (MW) frequency between 187.07 and 187.19 GHz with 10 to 45 mW power was used for polarization.

20-50 mg samples with different compositions of the tracer with trityl radical (AH111501) in deionized water and trehalose were used for hyperpolarization.

A compact magnetic field cycling (MFC) system was constructed (Fig. 1). INEPT enhanced sequences were used for measuring the magnetic field cycling experiments and the sample's time at low field was varied to obtain the dispersion curves.

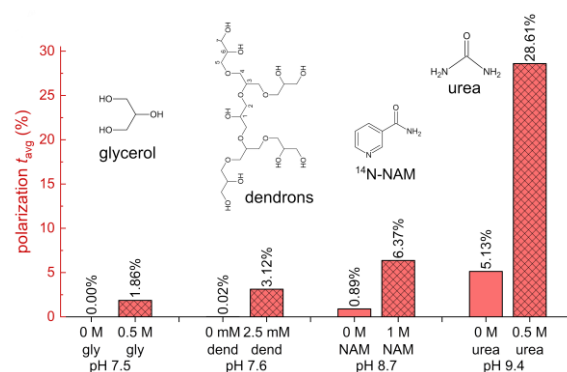


Fig. 2: CIDER-additives increase polarization and affect high-field T1. Adding NAM, urea, glycerol or dendrons to the dissolution medium in dDNP experiments increased the liquid state polarization of 1-¹⁵N-NAM drastically (detected after transfer through low fields). For example, the polarization increased from 5% to 30% when urea was added.

Results: We discovered hitherto unknown agents that prolong T1. Instead of reducing intra or inter molecular relaxation, these agents suppress exchange-driven relaxation, in particular at low fields, by several orders of magnitude (Fig. 2). This chemically induced deceleration of nuclear spin relaxation (CIDER) is very effective for molecules with pH-sensitive R1 relaxation (Ref. 3). The effect enabled us to polarize molecules with otherwise prohibitively short T1, and increasing polarization e.g. from 5% to 29% t=18s after polarization for 1-¹⁵N nicotinamide.

To examine this effect, we used a compact magnetic field cycling system for high-resolution NMR spectrometers (Ref. 4). The system enables the transfer of the sample from B0 field of 9.4 T to ~nT and all fields in between within 1 second. Utilizing a flexible gear rod made the shuttling system more compact, reducing the height to about the height required for filling liquid helium – hence, it can be installed in average-size NMR laboratories (the height of NMR with MFC is only 3.32 m).

Using the system, we uncovered the exact relaxation of the nicotinamide (Fig. 3) and pyruvate for common preclinical dDNP sample compositions, optimized these conditions and gave quantitative estimates for the retained polarization after sample transfer.

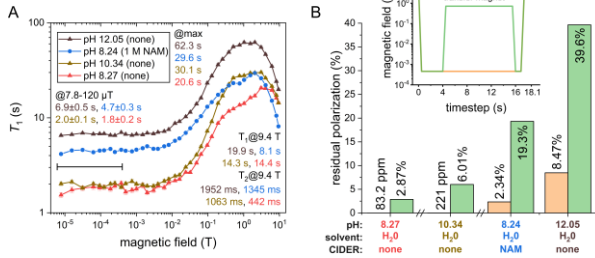


Fig. 3: Effect of pH and CIDER on T₁ of 1-15N-NAM at 10⁻⁵ – 9.4 T (A) and effect on polarization after 18 s transfer (B). MFC was conducted to measure T₁ 1-15N-NAM at pH 8.27 (red), pH 8.24 with 1 M NAM (blue), pH 10.34 (yellow), and pH 12.05 (brown).

Discussion: The impact on longitudinal relaxation is particularly effective in low magnetic fields and near pK_a where T₁ was tripled. The effect substantially reduces the polarization loss during transfer, so hitherto unsuitable, fast-relaxing molecules can be used now.

When the pH value is close to the pK_a of the protonated pyridine nitrogen, chemical exchange is rapid and can destroy magnetization at low fields most efficiently.

This chemically induced deceleration of nuclear spin relaxation (CIDER) effect was confirmed using magnetic-field-cycling experiments and has broad potential applications in hyperpolarized MR and beyond.

For pyruvate the buffer type and concentration affected relaxation at low and high fields, and optimized sample conditions are expected to increase retained polarization by up to 1.39 times.

Conclusion: This is the first report of relaxation agents that prolong T₁, which holds great potential e.g. for hyperpolarization.

Understanding the behavior aids the development of counterfeits to relaxation and the future employment of state of the art or novel tracers in vitro and in vivo. Our data strongly suggests the interplay of exchange at observed site and impurities in the DNP juice led to a drastic variation in observed polarization.

Using field cycling, we observed the relaxation and CIDER effect on pyruvate, NAM and other molecules at fields from a few μT to 9.4 T.

Acknowledgements: We acknowledge funding from the German Federal Ministry of Education and Research (BMBF, 03WIR6208A hyperquant), DFG (555951950, 527469039, 469366436, HO-4602/2-2, HO-4602/3, GRK2154-2019, EXC2167, FOR5042, TRR287). MOIN CC was founded by a grant from the European Regional Development Fund (ERDF) and the Zukunftsprogramm Wirtschaft of Schleswig-Holstein (Project no. 122-09-053). We acknowledge the financial support of Kiel University through validation funds and the assistance of the fabrication center “FabLab” for their support in the design and construction of the MFC, in particular, Jan Kirchner.

References:

1. Nelson, S. J. *et al.* Metabolic Imaging of Patients with Prostate Cancer Using Hyperpolarized [1-¹³C]Pyruvate. *Science Translational Medicine* 5, 198ra108-198ra108 (2013).
2. Peters, J. P. *et al.* Nitrogen-15 dynamic nuclear polarization of nicotinamide derivatives in biocompatible solutions. *Sci. Adv.* 9, eadd3643 (2023).
3. Peters, J. *et al.* Chemically induced deceleration of nuclear spin relaxation (CIDER) preserves hyperpolarization. Preprint at <https://doi.org/10.21203/rs.3.rs-4668036/v1> (2024).
4. Peters, J. P., Assaf, C. D., Hövener, J.-B. & Pravdivtsev, A. N. Compact magnetic field cycling system with the range from nT to 9.4 T exemplified with ¹³C relaxation dispersion and SABRE-SHEATH hyperpolarization. Preprint at <https://doi.org/10.48550/arXiv.2506.08711> (2025).

Pushing Boundaries in (Ultra) Low Field MRI: Towards an Adjustable Superconducting Magnet for the 1–200 mT Range

Pavel Povolni 1*, Kai Buckenmaier 1, Sergej Maltsev 1, Friedemann Bullinger 1, Nicolas Kempf 1, Judith Samlow 1, Georgiy A. Solomakha 1, Klaus Scheffler 1+2

1 High Field Magnetic Resonance, Max Planck Institute for Biological Cybernetics, Tübingen, Germany

2 Department of Biomedical Magnetic Resonance, University of Tübingen, Tübingen, Germany

Abstract: Permanent magnet based low-field-scanner (LFS) are easy manufacturable with limited performance due to field drift. We present our design of a novel LFS based on high-temperature superconductors. Due to the higher transition temperature, the cryostat can be more easily designed with a liquid nitrogen-based cooling system and solid insulators. However, the intrinsic noise of the superconductor must be considered in LFS. Initial studies show the feasibility of this magnet design. Increasing the poor SNR can be achieved utilizing Overhauser Dynamic Nuclear Polarization. First in-vivo investigations show promising results. In this unusual abstract, we provide an overview of the scanner design, initial prototypes and first measurements. Installation is expected in 2026.

Motivation: The popularity of low-field MRI scanners (LFS) continues to grow. Their affordability and ease of distribution are particularly advantageous[1]. Physically, the T1-value decreases at lower fields, resulting in increased tissue contrast for T1-weighted images[2,3], the impact of susceptibility differences between tissues is less significant and magnetic forces and SAR decrease, thereby enabling the use of implants (e.g., cochlear implants) in MRI[4], demonstrating that LFS is a valuable subject to explore further. The intrinsically lower SNR of LFS can be increased by a factor of up to 100 using Overhauser-enhanced MRI (OMRI)[5], resulting in signals comparable to those of high-field scanners (HFS). LFS also enables novel applications of electron paramagnetic resonance (EPR), which can be employed, for instance, in pO2 imaging during tumor examinations[6]. Permanent magnets (PM) appear to be the preferred option for LFS, though they are subject to substantial field drift and inhomogeneity[7]. Alternatively, electromagnets, as utilized in HFS, can be engineered to exhibit high levels of homogeneity and stability[8].

Here, we present the design, initial experiments and tools for a superconducting magnet based on a novel high-temperature superconductor (HTS, GdBaCuO) used at an adjustable field strength of 1-200mT while exhibiting a homogeneity <15ppm (Fig1). The integration of HTS led to a reduction in cooling requirements, which can now be met using liquid nitrogen (N2liq) and a vacuum-free cryostat. The primary objective of this LFS is to serve as a technological platform for improving LF-MRI by researching OMRI and developing of new sequence techniques (e.g., bSSFP).

Materials & Methods: B0-Magnet - The design of copper-based electromagnets is straightforward but is, however, limited to B0<10mT due to power loss[9]. Superconducting magnets may use low-temperature (LTS, niobium-based, liquid helium HeLiq) and high-temperature superconductors (HTS, cuprate-based, liquid nitrogen N2Liq), whereby HTS is preferable due to higher transition temperature and critical

current densities[10]. HTS (porous ceramic) is vapor-deposited onto a nickel-strip (width 4mm) and copper-coated, making it mechanically stable and protecting it against quenches. The tape is wound into radial coils ("Pancake"), with two of these coils forming a unit ("Double Pancake" DP). The windings are insulated enabling rapid B0-ramping. In contrast to HFS, LFS must consider the intrinsic noise of type-2 HTS, which accrues from the movement of quantized flux vortices[11]. Prior to magnet construction, the noise characteristics of HTS were evaluated using a SQUID-based setup[12] (Fig2).

Cryostat - Due to its higher transition temperature, N2Liq is used for cooling (alternatively small cold fingers) resulting in reduced insulation requirements (more headroom, latent heat of N2Liq 67x higher to HeLiq) and the possibility of using robust insulation materials based on silicates (aerogel), which have already been employed in cryo-applications[13]. A pressureless design allows for a metal-free construction using GFRP avoiding eddy-currents. In a preliminary study the insulation performance of aerogel at 77K is evaluated by examining the evaporation rate of a GFRP-cryostat prototype (Fig2).

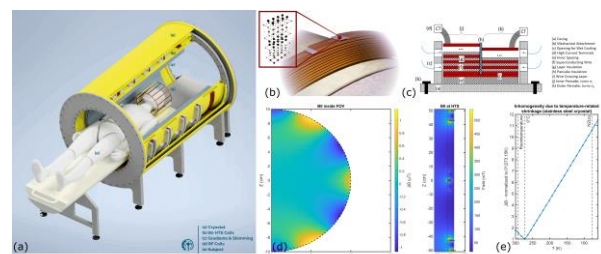


Fig. 1: Design of the new LFS. Position of the DP is fixed in the center and outside resulting in 13 parameters to be optimized (for positioning and winding pattern). (a) CAD rendering. (b) Pancake Coil. (c) Double Pancake (DP)-Coil. (d) B0-Simulation. (e) increasing inhomogeneity due to temperature-related shrinking.

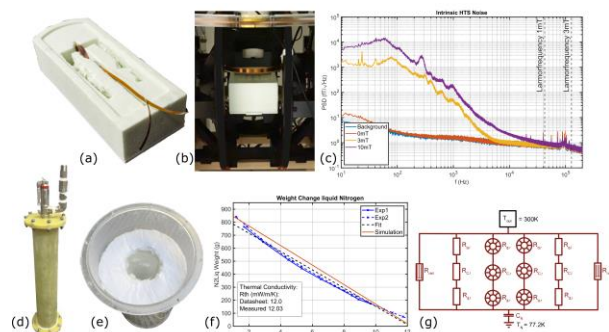


Fig. 2: Investigation of HTS noise and insulation. (a) Wound HTS sample in a N2Liq bath (green Styrodur). (b) Measurement setup (visible Helmholtz-coil magnetized the HTS)[16]. (c) Measured noise characteristic. (d) GFRP-based cryostat (cold side). (e) Image of aerogel-insulation. (f) Evaporation rate of N2liq, (g) thermal cryostat model.

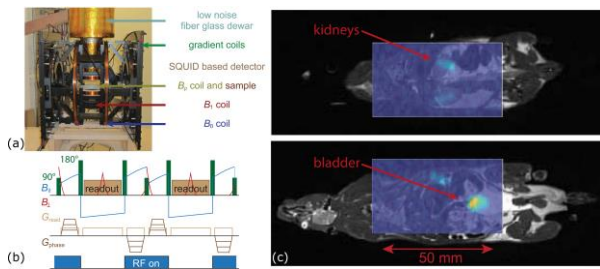


Fig. 3: In-vivo OMRI examination at 800µT. The radical used was Carboxy Proxyl (CP) (intravenous injection IV). (a) Used Ultra Low Field (ULF) Setup[16], (b) used modified bSSFP sequence[14], (c) OMRI (color) and 3T-MRI anatomy (grayscale). Bladder enhancement appeared 10–20min after IV injection. Continuous IV infusion enabled kidney imaging[14].

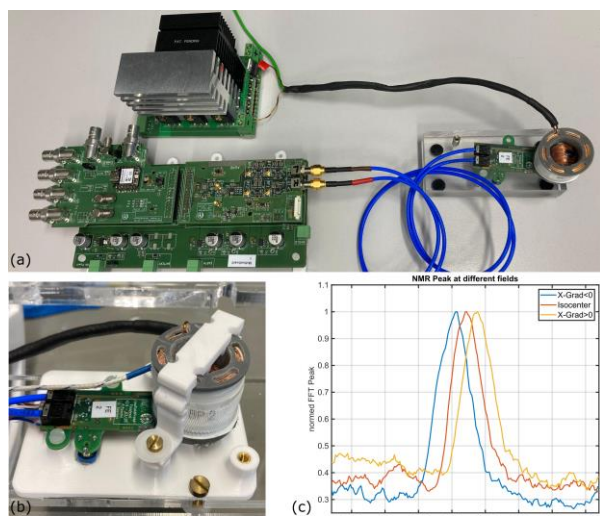


Fig. 4: Developed stand-alone low field probe for mapping LFS without apriori knowledge of the magnetic field. (a) Self-developed analog electronics for NMR measurements. (b) Sensor frontend with pre-polarization coil (>60mT) filled with a 1.2ml water sample surrounded by small Rx-Faraday coil. (c) Exemplary FID at 1mT (pre-polarization 60mT)

Hyperpolarization - Initial experiments were conducted to ascertain the feasibility of in-vivo-OMRI in rats in a self-built ULF-setup (800µT)[14]. A modified bSSFP-sequence was used[15]. Co-registration was performed using a 3T-MRI (Fig3).

Results: B0-Magnet - Numerical optimization is used to optimize the winding pattern and position of the DP (target: optimum homogeneity, boundary: critical current and field, cost minimization). For a human-size head magnet (shoulders within the magnetic field, bore $\varnothing=600\text{mm}$, FOV $\varnothing=200\text{mm}$) at 77K ($I=138\text{A}$, $B_{\text{crit}}<500\text{mT}$), 5911m HTS is required and 135mT at $\Delta B<14\text{ppm}$ is achieved. Pumping N2liq (380mbar/70K) increases the HTS-limits ($I=202\text{A}$, $B_{\text{crit}}<750\text{mT}$) reaching a B0 of 200mT.

HTS-Noise - In an MRI the magnet is cooled field-free and then driven to field using a current source in superconducting state. This field penetrates the HTS causing noise due to flux-vortex movement. In this experiment, however, the HTS was cooled with an external magnetic field applied so that the vortices freeze. After freezing, the 1/f-noise becomes evident.

Cryostat - A GFRP-cylinder ($\varnothing=70\text{mm}$, $l=400\text{mm}$) was filled with 1kg N2liq. The insulation consists of 90mm aerogel with the outer case made of Plexiglas. The N2liq-evaporation rate was determined by weight-measurements. The thermal

conductivity of the aerogel was determined using a thermal model of the prototype. The results are illustrated in Fig2.

Hyperpolarization - Fig3 show the successful in-vivo imaging of rat kidneys and bladder.

Tools (NMR-Sensor) - To maximize the performance of a superconducting magnet, a precise initial B0-mapping is necessary to shim for production-related tolerances. In HTS NMR-based field probes are used for this purpose. They cannot be used for LFS due to lower SNR and initial high inhomogeneity. To address this anticipated issue a novel stand-alone low-field probe employing a prepolarization phase (>60mT) was developed (Fig4).

Discussion: Demand - LF-MRI itself is promising and demonstrates its strengths especially in resource limited regions or as point-of-care-systems using PM-design[1] (where our LFS cannot be used). However, due to its superior field properties, experimental research, especially into OMRI and technology development, will benefit from the new LFS. To enable technology transfer, research should be integrated into widely used PM-systems as directly as possible.

Feasibility - This LFS shows a higher complexity than PM-systems, as reflected in total costs which are considered during conception.

Final Design - Given the high costs of HTS, its length must be minimized. Since HTS withstands higher critical currents and fields at lower temperatures, a hybrid design is sensible using N2liq for lower fields (<130mT) and slightly pumped N2liq for higher fields (<200mT). The same applies to active cooling using cold fingers: a less powerful/cheaper system (<130mT), supported by a more powerful system (<200mT).

Homogeneity is particularly sensitive to positioning of the outer coils, decreasing by approx. 47 ppm/ Δmm . Therefore, an adjustable positioning in the cold (shrunk) state is needed. In the event of quenching, only a small HTS part will become ohmic while current flow will be maintained by surrounding copper. When N2liq is used for cooling, only a small amount evaporates (approx. 55kJ stored in B0 evaporates less than 300g N2liq), resulting in fewer constraints for the quench pipe.

Hyperpolarization - In-vivo-OMRI shows promising organ imaging in ULF using the particularly sensitive bSSFP sequence. However, carboxy proxyl cannot be used in human experiments.

Conclusion: HTS is already used in HFS[8] and can easily be used in LFS. Disadvantageous is the high material cost resulting from a still low production volume. A GFRP-cryostat demonstrates its strengths when combined with solid insulation due to its simple design. Contrarily, it is a handcrafted individual piece and correspondingly complex to assemble.

Using OMRI in human-MRI still requires extensive in-situ and in-vivo studies in animals investigating biocompatible and non-toxic carrier molecules for nitroxide radicals. Promising initial results come from the molecules "human serum albumin" (HSA) or "tobacco mosaic virus" (TMV)[5]. If successful, OMRI-enhanced LFS can attain an SNR equivalent to HFS.

Due to this pending research on OMRI and associated unpredictability, the presented LFS will be built in a 50% scaled size enabling phantom and animal experiments while validating the presented design. The initial operation of the scaled LFS is expected by the end of 2026.

Acknowledgements: The authors would like to thank Ali Aghaeifar, Rahel Heule, Florian Birk, Felix Glang, Praveen Valsala, Dario Bosch, and the workshops led by Oliver Holder and Markus Scheu (all MPI for Biological Cybernetics) for their help in development. We would like to thank the team around A. Webb (Leiden University Medical Center) and Stefan Röhl (Neoscan GmbH, Magdeburg) for their valuable tips on the design of the scanner. Funding by European Research Council (ERC Advanced Grant No 834940, SpreadMRI), Deutsche Forschungsgemeinschaft (DFG BU 2694/6-1, BU 2694/9-1) and the Max-Planck-Gesellschaft is gratefully acknowledged

References:

1. Webb, Obungoloch. *Five steps to make MRI scanners more affordable to the world. Nature* 615, 391-393 (2023)
2. Escanye, Canet, Robert. *Frequency dependence of water proton longitudinal nuclear magnetic relaxation times in mouse tissues at 20°C. Biochimica et Biophysica Acta (BBA) - Molecular Cell Research* 721(3), 305-311 (1982)
3. Inglis, Buckenmaier, SanGiorgio, et. al. *MRI of the human brain at 130 microtesla. Proc Natl Acad Sci USA* 1108(48), 19194-19201 (2013)
4. Hori, Hagiwara, Goto, et. al. *Low-Field Magnetic Resonance Imaging. Investigative Radiology*. 56(11) (2021).
5. Fehling, Buckenmaier, Dobrynin, et al. *The effects of nitroxide structure upon ¹H Overhauser dynamic nuclear polarization efficacy at ultralow-field. The Journal of Chemical Physics*. 155(14) (2021)
6. Takakusagi, Kobayashi, Saito et al. *EPR and Related Magnetic Resonance Imaging Techniques in Cancer Research. Metabolites* 13(1) (2023)
7. Birk, Najac, O'Reilly, et. al. *Rapid multi-parametric relaxometry on a point-of-care 46 mT Halbach MRI scanner using balanced steady-state free precession imaging. ESMRMB* 2023, 19-20 (2023).
8. Li, Roel. *Key designs of a short-bore and cryogen-free high temperature superconducting magnet system for 14 T whole-body MRI. Supercond Sci Technol* 34, 125005 (2021)
9. Tsai, Mair, Rosen, et. al. *An open-access, very-low-field MRI system for posture-dependent ³He human lung imaging. JMRI* 193(2), 274-285 (2008)
10. Wimbush, Strickland. *A Public Database of High-Temperature Superconductor Critical Current Data. TASC* 27(4), 1-5, (2017)
11. Van Gorp. *Flux-Transport Noise in Type-II Superconductors. Phys Rev*. 166(2), 436-446 (1968)
12. Maltsev, Povolni, Schneider, et. al. *SQUID based Method of Evaluating Noise Characteristics of High Temperature Superconductors used in Novel Low Field MRI Scanner Designs. DACH-ISMRM 2024 Program & Proceedings*, 1-2 (2024)
13. Fesmire. *Aerogel-Based Insulation Materials for Cryogenic Applications. IOP Conf. Ser.: Mater. Sci. Eng.* 502, 012188 (2019)
14. Buckenmaier, Bullinger, Solomakha, et al. *In vivo Overhauser MRI at ultralow-fields. EUROMAR 2025*, 1 (2025).
15. Buckenmaier, Bullinger, Kempf, et al. *Imaging strategies for hyperpolarized contrast agents within the ultralow-field regime. EUROMAR 2024*, 271 (2024).
16. Buckenmaier, Rudolph, Fehling, et al. *Mutual benefit achieved by combining ultralow-field magnetic resonance and hyperpolarizing techniques. Rev. Sci. Instrum.* 89, 125103 (2018)

Evaluation of flow modulating treatment response in intracranial aneurysms using black blood MRI signal changes.

Mariya S. Pravdivtseva 1*, Hivnu Toraman 2, Jana Korte 3+4, Franziska Gaidzik 3+4, Alper Atici 1, Philipp Berg 3+5, Prasanth Velvaluri 6, Fritz Wodarg 2, Olav Jansen 2, Jan-Bernd Hövener 1, Naomi Larsen 2

1 Department of Radiology and Neuroradiology, Section Biomedical Imaging, University Hospital Schleswig-Holstein, Kiel University, Kiel, Germany

2 Department of Radiology and Neuroradiology, University Hospital Schleswig-Holstein, Kiel, Germany

3 Research Campus STIMULATE, University of Magdeburg, Magdeburg, Germany

4 Department of Fluid Dynamics and Technical Flows, University of Magdeburg, Magdeburg, Germany

5 Department of Medical Engineering, University of Magdeburg, Magdeburg, Germany

6 Chair of Inorganic Functional Materials, Kiel University, Kiel, Germany

Abstract: Flow modulating devices (FMDs) are a standard treatment for life-threatening intracranial aneurysms. However, delayed aneurysm rupture can still occur after treatment, highlighting the need for reliable methods to monitor treatment success. 4D flow MRI allows for measuring aneurysmal flow but suffers from metal artifacts from FMDs. Here, we investigated if spin-echo-based black-blood (SE BB) MRI may assess the flow reduction after treatment with FMDs. SE BB MRI is less susceptible to metal artefacts and offers a flow-dependent signal suppression. In 3D-printed aneurysm models, SE BB MRI showed increased signal in the aneurysm after FMD placement, indicating flow reduction. In vivo, increased SE BB signal was observed retrospectively in the aneurysm sacs of patients after FMD treatment, supporting BB MRI's potential for evaluating flow modulation.

Motivation: Intracranial aneurysms (IAs) are life-threatening vascular conditions that can be treated with flow-modulating devices (FMDs), which aim to reduce intra-aneurysmal blood flow. Despite overall successful treatment, some IAs may still rupture, highlighting the need for a reliable marker to evaluate and predict treatment success. Digital subtraction angiography (DSA) is currently the gold standard for assessing aneurysm occlusion status, but it is invasive. MRI might offer a promising non-invasive alternative. Flow MRI has been used to quantify flow reduction after FMD treatment [1] and to evaluate treatment success [2]. However, its accuracy and applicability are limited by metal-induced artifacts caused by the FMDs.

Spin-echo-based black-blood (SE BB) MRI is less sensitive to metal artifacts. The signal of SE BB MRI depends on the flow and increases with decreasing velocity [3]. Elevated SE BB signal in the aneurysm lumen has been associated with slow-flowing blood [4], which appears bright on the SE BB MR images. This finding suggests that SE BB MRI could potentially serve as a surrogate marker for flow inside the aneurysm, and thus for treatment evaluation.

In this study, we evaluated whether SE BB MRI signal changes after FMD placement and whether it can serve as a complementary tool to assess flow reduction. We conducted in vitro experiments using patient-derived 3D-printed IA models to measure flow velocities and SE BB MRI signal before and after FMD placement. Additionally, we retrospectively analysed SE BB MRI signal changes in a patient cohort treated with FMD.

Materials & Methods: In vitro MRI: 22 independent in vitro flow experiments were conducted using 20 IA models and two straight vessel models. The IA models were based on two

unique patient-specific anatomies—one from the basilar artery (BA) and one from the internal carotid artery (ICA) constructed as described before [5]. The BA model was modified four times to accommodate various FMD sizes. The BA and ICA models were 3D printed multiple times to enable comparison of different FMD designs under identical anatomical conditions. In total, 14 BA models and 6 ICA models were fabricated. Mimicking clinical treatment, FMDs were deployed in 15 models: five flow-diverting stents (FDs) in ICA models and ten intrasaccular flow-disrupting devices (IFDs) in BA models.

All models with (w.) and without (wo.) FMDs underwent 4D flow MRI and SE BB MRI on a 3T MRI system (Ingenia, Philips). 4D flow MRI was performed using a 3D T1w spoiled fast GRE sequence with three velocity encoding directions (echo time/repetition time (TE/TR): 5.0/8.3 msec; field-of-view (FOV): 110 × 110 × 40- 50 mm³; voxel size: 0.75 × 0.75 × 0.75 mm³; flip angle (FA): 8°). SE BB MRI was performed using a T1-w, black-blood, 3D variable refocusing flip angle turbo SE (Volume Isotropic Turbo spin echo Acquisition [VISTA]6, TE/TR: 29-35/700 msec; FOV: 200 × 250 × 160 mm³, voxel size: 0.65 × 0.55 × 0.65 mm³, echo train length: 55). Velocities and SE BB SI were calculated in the aneurysm sac and parent vessel, with 4D flow MRI verified by numerical simulations. A two-sided Wilcoxon test was used to evaluate the BB SI distributions.

In vivo MRI: Patients with IA (≥4 mm) treated with FMD were identified retrospectively from the patient database (n = 16). All patients underwent VISTA MRI before and after treatment, with follow-up imaging within 3–12 months. Regions of interest were manually segmented within the aneurysm lumen to assess pre- and post-treatment BB SI.

Results: The expected decrease of SE BB MRI signal with increasing flow rate was confirmed in straight vessels. In vitro, 4D flow MRI was successfully acquired of the IA models with and without FMDs. The intrasaccular devices caused strong metal artifacts at the aneurysm neck, while the intraluminal FMDs at the parental vessel. The artefacts were more pronounced on the 4D flow MRI compared to SE BB MRI (Fig. 1). FMDs reduced intra-aneurysmal flow (w.=2 vs. wo.=12.2 cm/s, p-value<0.01) while the parent vessel flow was maintained (w.=29.4 vs. wo.=28.4 cm/s, p-value = 0.18). Likewise, FMDs increased the intra-aneurysmal SE BB signal (w.=1.99 vs. wo.=0.1 a.u., p-value<0.01), but did not affect the signal in the parent vessel (w.=0.99 vs. wo.=0.86 a.u., p-value = 0.21). The increased BB signal was colocalized with reduced flow across all models.

In vivo, a preliminary qualitative assessment revealed an increased SE BB MRI signal within the aneurysm lumen following treatment with FMD, indicating a reduced intra-aneurysmal flow post-treatment. Quantitative analysis is ongoing.

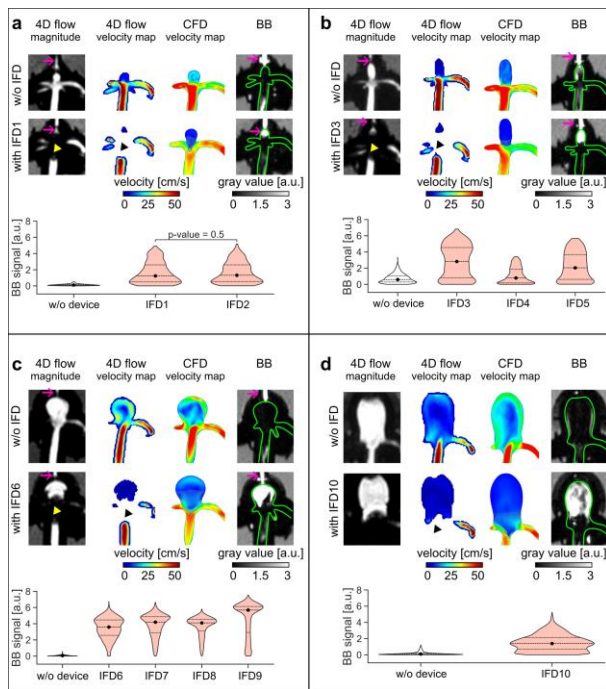


Fig. 1: Effect of IFDs on velocity (4D flow MRI, CFD) and BB MRI signal in BA models (a–d). Violin plots show the BB signal distribution within the aneurysm sac. IFDs caused metal artifacts (yellow/black arrowheads), reduced velocity, and increased BB signal. The pink arrow shows flow stagnation near the pressure sensor. Green lines outline the vessel lumen on the BB MRI.

Discussion: Consistent with our previous findings in untreated IA models [3], we now observed that treatment-induced flow reduction led to increased SE BB MRI signal within the aneurysm sac in IA models and a retrospective cohort. This likely reflects the limited suppression of slow flow by SE BB MRI, suggesting its potential utility for assessing intra-aneurysmal flow changes following device implantation.

While “failing” fluid suppression is usually considered an artifact of SE BB MRI, it may be valuable for monitoring aneurysm treatment, as it is more robust to metal artifacts than other angiographic techniques. Indeed, SE BB MRI enabled visualization of the aneurysm lumen even after coil implantation [7]. However, SE BB MRI is not quantitative, and care must be taken as different MRI sequence parameters will lead to different flow suppression. Further studies are needed to evaluate the clinical relevance and feasibility of SE BB MRI in assessing flow reduction and aneurysm treatment outcomes.

Conclusion: Intra-aneurysmal SE BB MRI signal increased after flow modulation in aneurysm models and a retrospective cohort. Compared to 4D flow MRI, SE BB MRI was less sensitive to metal artifacts. The observed signal increase in both in vitro models and treated patients supports the potential of BB MRI as a monitoring tool for evaluating the therapeutic efficacy of IA using FMDs.

Acknowledgements: We gratefully acknowledge the ongoing research support for MRI experiments from Philips Healthcare, Hamburg, Germany, and thank Kiel University and the Medical Faculty for their support of the SBMI 3D lab.

References:

1. Pereira VM, Brina O, Delattre BMA, et al. Assessment of intra-aneurysmal flow modification after flow diverter stent placement with four-dimensional flow MRI: a feasibility study. *J NeuroInterventional Surg.* 2015;7(12):913-919. doi:10.1136/neurintsurg-2014-011348
2. Brina O, Bouillot P, Reymond P, et al. How Flow Reduction Influences the Intracranial Aneurysm Occlusion: A Prospective 4D Phase-Contrast MRI Study. *Am J Neuroradiol.* 2019;40(12):2117-2123. doi:10.3174/ajnr.A6312
3. Henningsson M, Malik S, Botnar R, Castellanos D, Hussain T, Leiner T. Black-Blood Contrast in Cardiovascular MRI. *J Magn Reson Imaging.* n/a(n/a):e27399. doi:10.1002/jmri.27399
4. Pravdivtseva MS, Gaidzik F, Berg P, et al. Pseudo-Enhancement in Intracranial Aneurysms on Black-Blood MRI: Effects of Flow Rate, Spatial Resolution, and Additional Flow Suppression. *JMRI.* 2021;54(3):888-901. doi:10.1002/jmri.27587
5. Pravdivtseva MS, Peschke E, Lindner T, et al. 3D-printed, patient-specific intracranial aneurysm models: From clinical data to flow experiments with endovascular devices. *Med Phys.* 2021;48(4):1469-1484. doi:10.1002/mp.14714
6. Qiao Y, Steinman DA, Qin Q, et al. Intracranial arterial wall imaging using three-dimensional high isotropic resolution black blood MRI at 3.0 Tesla. *J Magn Reson Imaging.* 2011;34(1):22-30. doi:10.1002/jmri.22592
7. Larsen N, Flüh C, Madjidyar J, Synowitz M, Jansen O, Wodarg F. Visualization of Aneurysm Healing. *Clin Neuroradiol.* 2020;30(4):811-815. doi:10.1007/s00062-019-00854-5

A Data Processing, Analysis and Quantification Pipeline for 1H-MRS in a Mouse Model of Pancreatic Ductal Adenocarcinoma

Diana Rotaru 1+2*, Emma Van Praagh 1+2, Russell Posner 3, Yanping Sun 4, Stephen Sastra 4, Carmine Palermo 4, Michael Badgley 4, Daniel Ross 4, Kenneth Olive 4, and Christoph Juchem 1+2+3

1 Center for Medical Physics and Biomedical Engineering, Medical University of Vienna, Vienna, Austria,

2 Department of Biomedical Engineering, Columbia University, New York, NY, USA,

3 Department of Radiology, Columbia University, New York, NY, USA,

4 Oncology Precision Therapeutics and Imaging Core (OPTIC), Columbia University Medical Center, New York, NY, USA

Abstract: Technical limitations and lack of standardization led to an unmet need to characterize metabolic changes in the pancreas using *in vivo* 1H-MRS. The aim of this study is to establish a processing, analysis, and quantification pipeline for pancreas MRS data that aligns with current consensus guidelines and state-of-the-art methodology. A mouse model of pancreatic ductal adenocarcinoma treated with the targeted therapy cysteinase was used to test and validate this framework. The results of the proposed pipeline provide preliminary validation of its quantitative potential. Future studies can follow this approach to quantify metabolic changes associated with cancer, chronic disease, and metabolic disorders in the human and rodent pancreas.

Motivation: *In vivo* proton magnetic resonance spectroscopy (1H-MRS) can be utilized for the analysis of metabolic features of normal and cancerous tissue. Despite advancements in brain, muscle, breast, and liver MR spectroscopy, the implementation of *in vivo* 1H-MRS in the pancreas remains limited. From a clinical perspective, MRS may offer relevant insights in pancreatic ductal adenocarcinoma (PDAC), which accounts for ~90% of all pancreatic cancers [1]. PDAC is an aggressive malignancy with a poor prognosis and low 5-year survival rate [2]. Current 1H-MRS studies on PDAC have shown limited capabilities to a) acquire reliable data (due to poor SNR, water suppression and motion), b) quantify overlapping metabolites and lipids and c) comply with or complete MR experimental procedures due to illness severity [3,4,5,6,7]. Overall, due to technical limitations and lack of standardization, there is an unmet need to robustly characterize metabolic changes in the healthy and diseased pancreas using MRS.

The aim of this study is two-fold: a) to establish a processing, analysis, and quantification pipeline for MRS in the pancreas that aligns with current consensus guidelines and state-of-the-art methodology [8,9,10,11,12,13,14,15,16] and b) to test and validate the pipeline with MRS data acquired in a mouse model of PDAC treated with the targeted therapy cysteinase, that induces tumor-specific ferroptosis [17,18].

Materials & Methods: Acquisition. Data were collected on a 9.4T Bruker BioSpec 94/20 MR scanner with ParaVision.6.0.1 and a mouse whole-body 1-channel TX/RX coil. Eight KP172C mice (4F/4M, age 146±36 days, body weight 30.29±3.95 g) were scanned before and after (Day 0 and 10) receiving a vehicle (n=4) or cysteinase solution. Anesthesia was induced with isoflurane. The Institutional Animal Care and Use Committee at Columbia University in the City of New York approved all experiments. A localizer, B0 map, T2-weighted scan and water-suppressed and -unsuppressed spectra (PRESS, 16.3/1700 ms TE/TR, 2048 spectral points, 10 kHz bandwidth, VAPOR water-suppression) were acquired. The

MRS voxel was placed over a homogeneous cancerous area in the pancreas (Figure 1). Data processing, analysis, and quantification were achieved in the INSPECTOR software [19].

Processing. Repetitions were eddy-current corrected, frequency- and phase-aligned, and averaged [20]. The resulting spectrum was apodized, zero-filled to 8192 points and phase-corrected. Spectra were calibrated to the choline peak at 3.2 ppm. Residual water peak(s) were subtracted with Hankel singular value decomposition (HSVD) [21].

Analysis. Acquisition-tailored basis functions of metabolites and lipids were simulated in MARSS for linear combination modeling (LCM) analysis in INSPECTOR [19,22]. Lorentzian line-broadening, frequency-shifting, and zero-order phase correction were applied to basis functions. Polynomial baseline modeling was included.

Quantification. Concentration estimates of metabolites and lipids are reported as ratios of total lipid content. Errors are reported as Cramér-Rao Lower Bounds (CRLBs). Group differences (vehicle/cysteinase) were assessed with two-way ANOVA tests and Šidák's multiple-comparisons correction. Figure 2 presents the MRS pipeline summary.

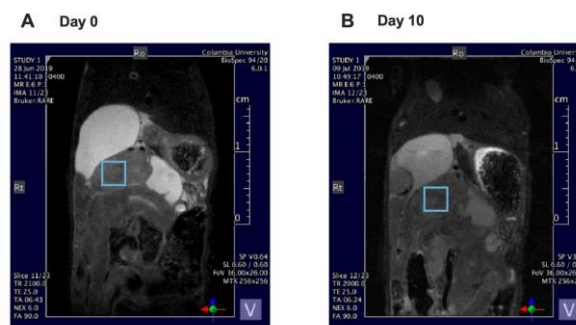


Fig. 1: Two representative MRS voxel placements (voxel size 3.0x3.0x3.0 mm³) over a cancerous tumor for each data acquisition time point: Day 0 (A) and Day 10 (B). The MRS voxel is shown as a blue square.

Results: Acquisition. Some data acquisition parameters (i.e., TR, TE, bandwidth) presented minor deviations from standard values (mentioned above). Therefore acquisition-matched basis sets were simulated for each combination of parameters. The induced spectral differences are expected to be negligible.

Processing. Figure 3 (A) illustrates representative processed spectra for each time point with corresponding compound annotations.

Analysis. The pancreatic metabolites identified at analysis were choline (Ch), creatine (Cr), glycerophosphocholine (GPC), glutathione (GSH), glucose (Glu), glycine (Gly), phosphocholine (PCh), phosphocreatine (PCr), and taurine

(Tau). Total choline (tCho=Ch+PCh+GPC) and total creatine (tCr=Cr+PCr) were also estimated. Lipid peaks were observed at 0.9, 1.3, 1.6, 2.02, 2.24, 2.75, 4.15, 4.3 and 5.3 ppm; the total lipid signal was calculated as totalLip=Lip09+Lip13+Lip16+Lip205+Lip22+Lip275+Lip415+Lip430+Lip53. Figure 3 (B) displays representative modeled and fitted spectra for both experimental time points; the individual basis functions, baseline and residuals are also included here.

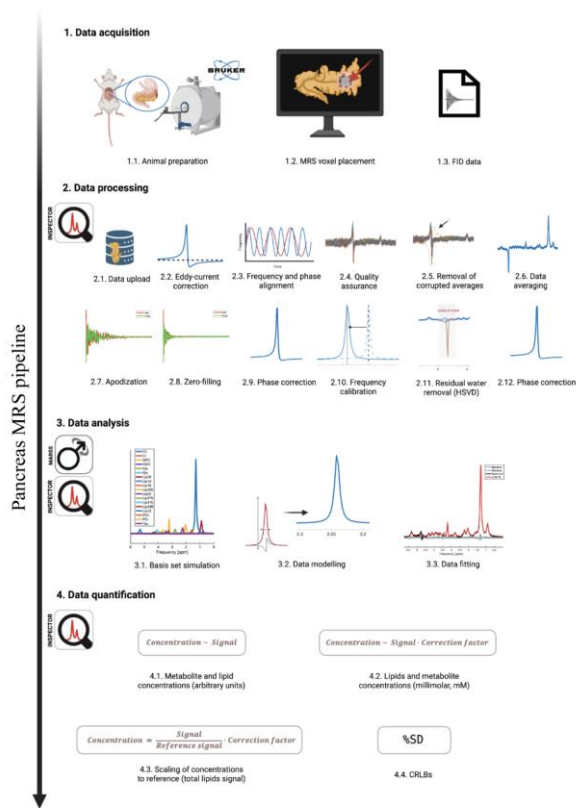


Fig. 2: The data acquisition, processing, analysis and quantification pipeline for pancreas MR spectra acquired in a mouse model of pancreatic ductal adenocarcinoma. Created in <https://BioRender.com>.

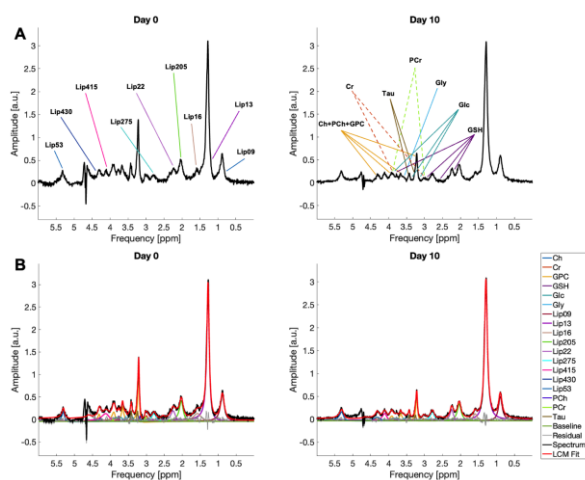


Fig. 3: Annotated processed (A) and modeled and fitted (B) spectra for each data acquisition time point (Day 0 [Left] & Day 10 [Right]). See legend for color-coded basis functions. Processed spectra are representative of overall data quality. Analyzed spectra are representative of overall modeling and fitting quality.

Quantification. Descriptive statistics (A) and graphical plots (B) of GSH, Glc, Gly, Tau, tCho, tCr, and all individual lipids are shown in Figure 4. The modelling and fitting of glycine and taurine did not succeed in one and three datasets, respectively. Lip430 was hindered by a residual water tail in four datasets. The pooled-groups (Day 0 + Day 10) average CRLBs for GSH, Tau, tCho, tCr and totalLip were 26.56%, 34.06%, 2.64%, 9.85%, and 0.28%, respectively. Individual lipid CRLBs were below 17.06%, except for Lip430 (53.54%). Tau/totalLip at Day 10 (*p<0.05) was significantly different between vehicle and cysteinase groups.

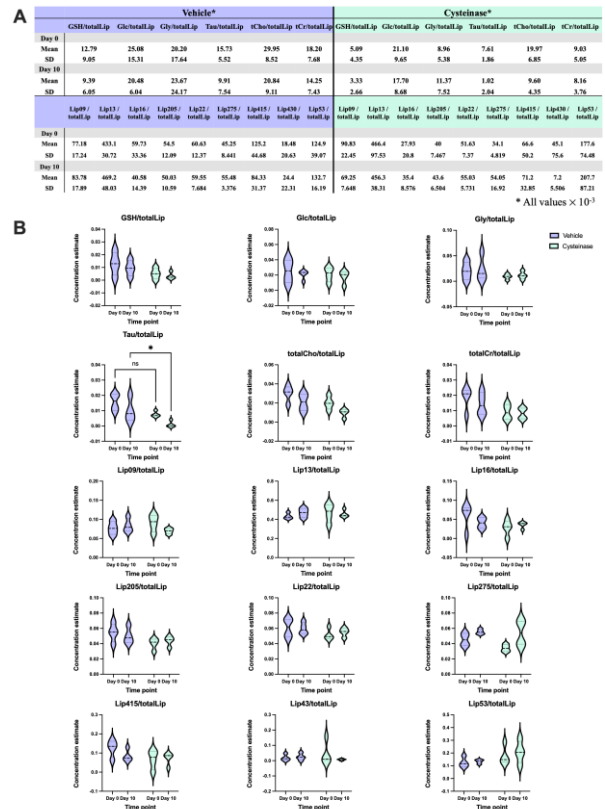


Fig. 4: Figure 4. Descriptive statistics (A) and graphical plots (B) are shown for all major compounds at both time points (Day 0 and Day 10). A scaling factor ($\times 1000$) was applied to values only in statistics tables. Purple and green color-code the vehicle and cysteinase animal groups.

Discussion: A consensus-aligned pipeline for processing, analysis, and quantification of MR spectra from the pancreas was piloted. Previous studies that investigated typical and altered pancreatic metabolism using 1H-MRS encountered difficulties related to poor data quality, lack of software/pipelines for data manipulation, and absent standardization of experiments [3,4,5,6,7]. To date, many pancreas MRS studies reported the use of built-in MR-vendors' analysis softwares, which have less robust options for processing operations essential to addressing sub-optimal data quality. Here, data processing, analysis and quantification were conducted in accordance with consensus guidelines [13,14,15]. Customizable signal handling and optimized modeling and fitting of basis functions, all needed to improve quantification accuracy, were achieved using processing and analysis tools in INSPECTOR.

The advantages of this framework include method robustness, replicability, transferability, speed and

applicability to pancreas MRS data from both healthy and diseased humans and animals. This pipeline also facilitates analysis of several data formats (i.e., Siemens, General Electric, Philips, Bruker, Varian, and DICOM). Limitations include reduced sample size, poor health of animals, variability of data acquisition parameters, and variable tumor size and locus. Another consideration is the effect of residual water tails on accurate modeling of neighboring metabolites (GSH) and lipids (Lip415, Lip430, Lip53) signals. No previous studies have identified a stable reference compound in the pancreas (i.e., metabolite, lipid or water content) [6,23]. Here, concentrations were normalized to total lipid content. Water is an alternative. Both approaches are limited given the changes in water content and lipid metabolism associated with aging and cancer [23,24].

Conclusion: A framework for pancreas MRS data processing, analysis and quantification was developed. MR spectra of pancreatic ductal adenocarcinoma were used to identify a protocol for optimal processing operations, data-tailored analysis parameters and quantification approaches that yield metabolite and lipid estimates in a reliable format.

The results of the proposed pancreas MRS pipeline provide a preliminary validation of the quantitative potential of this approach. Future studies can utilize this pipeline to quantify relative metabolic changes in healthy controls or associated with cancer, chronic disease, and metabolic disorders in the human and rodent pancreas.

Acknowledgements: The studies presented in this work were carried out in part in the MR Facility of the Oncology Precision Therapeutics and Imaging Core (OPTIC) Shared Resource, which is supported by funds from the Columbia University Medical Center - Cancer Center Support Grant (CCSG) and NIH grant #P30 CA013696 (National Cancer Institute). The authors would like to thank Karl Landheer for his support on basis set simulation and Martin Gajdošik for his meaningful contributions to prior knowledge and preliminary analysis of pancreas MRS.

References:

- [1] J. Kleff et al., "Pancreatic cancer," *Nat. Rev. Dis. Primer*, vol. 2, no. 1, p. 16022, Apr. 2016, doi: 10.1038/nrdp.2016.22.
- [2] E. M. Stoffel, R. E. Brand, and M. Goggins, "Pancreatic Cancer: Changing Epidemiology and New Approaches to Risk Assessment, Early Detection, and Prevention," *Gastroenterology*, vol. 164, no. 5, pp. 752–765, Apr. 2023, doi: 10.1053/j.gastro.2023.02.012.
- [3] C.-K. Chang et al., "Metabolic Alterations in Pancreatic Cancer Detected by In Vivo 1H-MR Spectroscopy: Correlation with Normal Pancreas, PET Metabolic Activity, Clinical Stages, and Survival Outcome," *Diagnostics*, vol. 11, no. 9, p. 1541, Aug. 2021, doi: 10.3390/diagnostics11091541.
- [4] M. Cui et al., "In vivo proton MR spectroscopy of pancreatic neuroendocrine tumors in a multiple endocrine neoplasia type 1 conditional knockout mouse model," *Magn. Reson. Med.*, vol. 74, no. 5, pp. 1221–1226, Nov. 2015, doi: 10.1002/mrm.25529.
- [5] T.-H. Su, E.-H. Jin, H. Shen, Y. Zhang, and W. He, "In vivo proton MRS of normal pancreas metabolites during breath-holding and free-breathing," *Clin. Radiol.*, vol. 67, no. 7, pp. 633–637, Jul. 2012, doi: 10.1016/j.crad.2011.05.018.

- [6] X. Ma et al., "The Metabolic Features of Normal Pancreas and Pancreatic Adenocarcinoma: Preliminary Result of In Vivo Proton Magnetic Resonance Spectroscopy at 3.0 T," *J. Comput. Assist. Tomogr.*, vol. 35, no. 5, pp. 539–543, Sep. 2011, doi: 10.1097/RCT.0b013e318227a545.
- [7] X. Yao, M. Zeng, H. Wang, S. Fei, S. Rao, and Y. Ji, "Metabolite detection of pancreatic carcinoma by in vivo proton MR spectroscopy at 3T: initial results," *Radiol. Med. (Torino)*, vol. 117, no. 5, pp. 780–788, Aug. 2012, doi: 10.1007/s11547-011-0757-7.
- [8] C. Cudalbu et al., "Contribution of macromolecules to brain 1H MR spectra: Experts' consensus recommendations," *NMR Biomed.*, vol. 34, no. 5, p. e4393, May 2021, doi: 10.1002/nbm.4393.
- [9] C. Juchem et al., "B0 shimming for in vivo magnetic resonance spectroscopy: Experts' consensus recommendations," *NMR Biomed.*, vol. 34, no. 5, p. e4350, May 2021, doi: 10.1002/nbm.4350.
- [10] R. Kreis et al., "Terminology and concepts for the characterization of in vivo MR spectroscopy methods and MR spectra: Background and experts' consensus recommendations," *NMR Biomed.*, vol. 34, no. 5, p. e4347, May 2021, doi: 10.1002/nbm.4347.
- [11] B. Lanz et al., "Magnetic resonance spectroscopy in the rodent brain: Experts' consensus recommendations," *NMR Biomed.*, vol. 34, no. 5, p. e4325, May 2021, doi: 10.1002/nbm.4325.
- [12] A. Lin et al., "Minimum Reporting Standards for in vivo Magnetic Resonance Spectroscopy (MRSinMRS): Experts' consensus recommendations," *NMR Biomed.*, vol. 34, no. 5, p. e4484, May 2021, doi: 10.1002/nbm.4484.
- [13] A. A. Maudsley et al., "Advanced magnetic resonance spectroscopic neuroimaging: Experts' consensus recommendations," *NMR Biomed.*, vol. 34, no. 5, p. e4309, May 2021, doi: 10.1002/nbm.4309.
- [14] J. Near et al., "Preprocessing, analysis and quantification in single-voxel magnetic resonance spectroscopy: experts' consensus recommendations," *NMR Biomed.*, vol. 34, no. 5, p. e4257, May 2021, doi: 10.1002/nbm.4257.
- [15] G. Öz et al., "Advanced single voxel 1H magnetic resonance spectroscopy techniques in humans: Experts' consensus recommendations," *NMR Biomed.*, vol. 34, no. 5, p. e4236, May 2021, doi: 10.1002/nbm.4236.
- [16] M. Wilson et al., "Methodological consensus on clinical proton MRS of the brain: Review and recommendations," *Magn. Reson. Med.*, vol. 82, no. 2, pp. 527–550, Aug. 2019, doi: 10.1002/mrm.27742.
- [17] M. A. Badgley et al., "Cysteine depletion induces pancreatic tumor ferroptosis in mice," *Science*, vol. 368, no. 6486, pp. 85–89, Apr. 2020, doi: 10.1126/science.aaw9872.
- [18] S. R. Hingorani et al., "Trp53R172H and KrasG12D cooperate to promote chromosomal instability and widely metastatic pancreatic ductal adenocarcinoma in mice," *Cancer Cell*, vol. 7, no. 5, pp. 469–483, May 2005, doi: 10.1016/j.ccr.2005.04.023.
- [19] M. Gajdošik, K. Landheer, K. M. Swanberg, and C. Juchem, "INSPECTOR: free

Ex vivo and in vivo characterization of cystic kidneys in patients with ADPKD using ²³Na MRI at 7T

Judith Schirmer 1*, Laurent Ruck 1, Katharina Tkotz 1, Jordan M. Höhn 1, Anke Dahlmann 2, Peter Linz 1 2, Michael Uder 1, Christoph Kopp 2, Armin M. Nagel 1+3

1 Institute of Radiology, University Hospital Erlangen, Friedrich-Alexander-Universität Erlangen-Nürnberg (FAU), Erlangen, Germany,
 2 Department of Nephrology and Hypertension, Friedrich-Alexander-University Erlangen-Nürnberg (FAU), Erlangen, Germany,
 3 Division of Medical Physics in Radiology, German Cancer Research Center (DKFZ) Heidelberg, Heidelberg, Germany

Abstract: In this study, ²³Na MRI at 7T was used to assess sodium signal of cysts ex vivo and in vivo in patients with autosomal dominant polycystic kidney disease (ADPKD). For ex vivo kidneys, several cysts were punctured and their sodium concentration was determined using laboratory analysis. These values were compared to sodium concentrations measured by ²³Na MRI. Both methods showed good agreement and enabled differentiation between cysts with high and low sodium concentration. In vivo imaging revealed cysts with varying sodium signal. These findings demonstrate the feasibility of ²³Na MRI to assess the sodium signal in ADPKD patients non-invasively, which could lead to a better understanding of cyst physiology.

Motivation: Autosomal dominant polycystic kidney disease (ADPKD) is the most common inherited cystic kidney disease with an incidence of 1 in 500 to 1 in 1000 people. It is characterized by progressive cyst formation in the kidneys over time, which might lead to kidney failure and the need for dialysis in an advanced stage of the disease. Ex vivo data suggests that in ADPKD patients kidney cysts may exhibit varying sodium concentrations,[1] but this has not yet been demonstrated in vivo. Sodium (²³Na) MRI enables non-invasive analysis of the tissue sodium concentration in vivo. To date only one publication has performed ²³Na MRI in vivo for ADPKD patients utilizing 3T MRI.[2] As ²³Na has a low MR sensitivity compared to protons, it greatly benefits from the increased signal-to-noise ratio (SNR) at ultra-high field (UHF) strengths such as 7T.[3] In this study, we investigate the reliability of characterizing kidney cysts based on the sodium content measured with ²³Na MRI at 7T.

Materials & Methods: Sodium MRI measurements were conducted at a 7T (MAGNETOM Terra.X). Four nephrectomized (i.e., ex vivo) ADPKD kidneys were scanned (Figure 1a). First a ²³Na image (resolution=(3mm)³) with a double-resonant ²³Na/³⁹K birdcage RF coil (Rapid Biomedical GmbH) followed by a coil change to a ¹H/³¹P RF birdcage coil (Rapid Biomedical GmbH) to acquire anatomical ¹H T1 FLASH images. A reference holder with known sodium concentrations ($c_{ref} = [30, 60, 90, 120, 150]$ mM) was used to retrospectively calibrate the sodium signal. Selected superficial cysts with high and low sodium signal were punctured and sodium concentrations were determined by our clinical laboratory. After the punctation diluted contrast agent (CA) was injected into the punctured cysts, to locate them in a subsequent measurement, to confirm the localization of the cysts.

Seventeen patients underwent two MRI scans. The first was conducted at the aforementioned 7T system using a ²³Na birdcage-coil combined with an 8Tx/16Rx ¹H array-coil (Rapid Biomedical GmbH, Rimpfing, Germany). Images were acquired

with an interleaved ²³Na/¹H[4] sequence under free breathing using a density-adapted 3D radial readout[5] and golden-angle acquisition[6] (resolution(¹H/²³Na)=(2/6mm)³).

To correct for B1+ of the ²³Na signal an actual flip-angle imaging (AFI)[7] scan was conducted. To acquire typical anatomical ¹H images the patients were additionally scanned at a 3T MRI system (MAGNETOM Vida).

²³Na and ¹H images were registered using elastix[8] with a rigid transformation (ex vivo ²³Na->¹H, in vivo ¹H(7T)->¹H(3T)). Segmentation of the cysts were performed on the ¹H image.

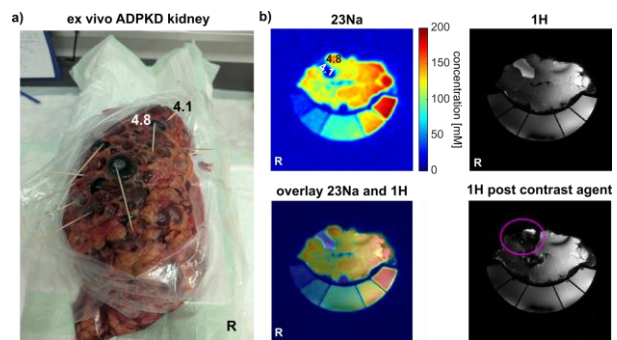


Fig. 1: a) Example ex vivo cystic kidney from measurement 4. The toothpicks mark punctuated cysts. b) ²³Na and ¹H image. The overlay shows good alignment of both images. Two cysts (4.1 and 4.8) are labeled in a) and b). The pink circle shows the area of the cysts post CA.

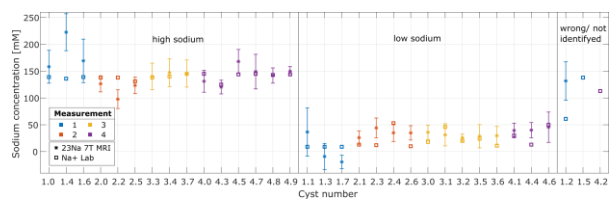


Fig. 2: Sodium signal from MRI measurement and lab from 33 cysts of four nephrectomized kidneys. Overall, the concentrations from the MRI measurement and the lab show very good agreement. Only one cyst was incorrectly classified by the MRI and two cysts could not be reliably identified in the MRI image

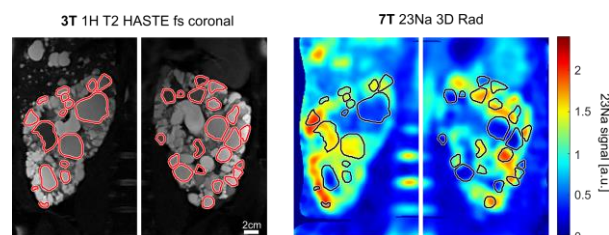


Fig. 3: Example images from one subject, with masks manually drawn on the 3T T2 haste image and overlayed onto ²³Na image. 3T and 7T images are co-registered for left and right kidney separately. High variation of the sodium signal across different cysts is visible.

Results: The exemplary overlay of ²³Na and 1H images of an ex vivo kidney in Figure 1 b) shows good alignment between ²³Na and 1H MRI. The pink circle marks the area of the punctuated cysts for the image post CA. While an enhancement of the signal intensity post CA is visible for cyst 4.8, a loss of signal was observed in cyst 4.1.

Figure 2 shows the sodium concentrations obtained ex vivo using ²³Na MRI at 7T and laboratory analysis for a total of 33 cysts. The error bars indicate the standard deviation of the mean ²³Na signal in the cyst mask. Cysts were classified as high- or low-sodium based on a threshold of >100mM in laboratory measurements. Overall, the concentrations obtained from ²³Na MRI and laboratory measurements are comparable for most of the assigned cysts. One cyst out of a total number of 33 was wrongly assigned, and two cysts could not be identified during the postprocessing.

For the in vivo data, cysts with high and low ²³Na MRI signal are visible as shown for one patient in Figure 3.

Discussion: The sodium concentrations determined by ²³Na MRI and laboratory analysis showed very good agreement, indicating that in nephrectomized ADPKD kidneys the sodium signal can be determined with high accuracy using the presented setup. High standard deviations of the mean sodium signal from MRI for some cysts may be caused by partial volume effects or inaccuracies in the registration process. Thus, for a more reliable quantification, partial volume effects have to be addressed to compensate for signal smearing at cyst boundaries.

In vivo, high and low sodium signal cysts could be identified. A quantitative analysis of the distribution of high and low sodium cysts might further help to understand the disease progression of patients at different stages of ADPKD. In the future, the aorta could be used as an internal reference to calibrate the ²³Na signal in vivo.

Due to the unknown size of the punctuated cysts, the dilution ratio of the contrast agent could not be precisely determined. This can explain the signal erasures for some cysts post CA. As

the cysts were also assigned according to the ²³Na image during the punctuation most of the cysts could be allocated except for two and one misaligned cysts.

Conclusion: This study demonstrates that ²³Na MRI at 7T enables non-invasive assessment of sodium concentrations of ex vivo cysts from ADPKD patients, and confirmed the occurrence of cysts with high and low sodium concentrations in ADPKD. The comparison between ²³Na MRI measurement and direct determination of Na⁺ by laboratory analysis for punctuated cysts from nephrectomized kidneys confirmed the reliability of MRI based sodium quantification ex vivo.

Acknowledgements: This project was funded by the Deutsche Forschungsgemeinschaft (DFG) under 509149993 (TR 374).

References:

1. Gardner, K. D. *et al.* On the probability that kidneys are different in autosomal dominant polycystic disease. *Kidney International* 42, 1199–1206 (1992).
2. Lemoine, S., Akbari, A. & McIntyre, C. W. ²³NaMRI Assessed Cyst Sodium Concentration in Polycystic Kidney Disease to Identify Cyst Metabolic Activity: A Proof of Concept Study. *Kidney Medicine* 6, 100820 (2024).
3. Gast, L. V., Platt, T., Nagel, A. M. & Gerhalter, T. Recent technical developments and clinical research applications of sodium (²³Na) MRI. *Progress in Nuclear Magnetic Resonance Spectroscopy* 138–139, 1–51 (2023).
4. Ruck, L. *et al.* Interleaved ²³Na / ¹H MRI of the human heart at 7T using a combined ²³Na / ¹H coil setup and ¹H parallel transmission. *Magnetic Resonance in Med* 94, 231–241 (2025).
5. Nagel, A. M. *et al.* Sodium MRI using a density-adapted 3D radial acquisition technique. *Magnetic Resonance in Med* 62, 1565–1573 (2009).
6. Chan, R. W., Ramsay, E. A., Cunningham, C. H. & Plewes, D. B. Temporal stability of adaptive 3D radial MRI using multidimensional golden means. *Magnetic Resonance in Med* 61, 354–363 (2009).
7. Yarnykh, V. L. Actual flip-angle imaging in the pulsed steady state: A method for rapid three-dimensional mapping of the transmitted radiofrequency field. *Magnetic Resonance in Med* 57, 192–200 (2007).
8. Klein, S., Staring, M., Murphy, K., Viergever, M. A. & Pluim, J. elastix: A Toolbox for Intensity-Based Medical Image Registration. *IEEE Trans. Med. Imaging* 29, 196–205 (2010).

Validation of Model-Based Reconstruction for Joint Estimation of Multiple Quantitative Maps with Single-Shot IR Multi-Echo Radial FLASH using a Water-Fat-SPIO Phantom

Vitali Telezki 1+2+3*, Daniel Mackner 4, Nick Scholand 2+4, Zhengguo Tan 5, Moritz Blumenthal 4, Philip Schaten 4, Xiaoqing Wang 6, Martin Uecker 1+3+4

1 Department of Interventional and Diagnostic Radiology, University Medical Center Göttingen, Germany

2 German Centre for Cardiovascular Research (DZHK), partner site Lower Saxony, Göttingen, Germany

3 Cluster of Excellence Multiscale Bioimaging: from Molecular Machines to Networks of Excitable Cells (MBExC2067), Uni. of Göttingen, Germany

4 Institute of Biomedical Imaging, Graz University of Technology, Graz, Austria

5 Michigan Institute for Imaging Technology and Translation (MIITT), Radiology, University of Michigan, Ann Arbor, Michigan, USA

6 Department of Radiology, Boston Children's Hospital, Harvard Medical School, Boston, Massachusetts, USA

Abstract: We designed and manufactured a quantitative water-fat-SPIO phantom covering a broad range of pathophysiological T_1 , R_2^* , and fat-fraction (FF) values with the aim of validating our method of joint estimation of water-specific T_1 , R_2^* , FF, and B_0 maps from a single acquisition. The goal was to design a quantitative MR phantom with high accuracy while keeping the manufacturing process simple. To acquire data within 4s, we use a single-shot inversion recovery (IR) multi-echo radial FLASH sequence. For joint estimation of these parameter maps directly from k-space data, we use a model-based reconstruction and formulate parameter estimation as a non-linear inverse problem.

Motivation: While quantitative water-specific T_1 , R_2^* , and FF mapping is of great interest in liver imaging [1,2], conventional methods are typically time-intensive, since they require individual data acquisition for each map. Instead, we apply here a fully non-linear model to reconstruct water-specific T_1 , R_2^* , and B_0 field maps directly from k-space data from a single acquisition [3].

Materials & Methods: For our phantom, we adopted manufacturing instructions of existing protocols [4,5]. It is comprised of 18 vials (18 mL) with varying designed fat volume percentages (0, 5, 10, 20, 40 and 100%), iron concentrations (0, 50, and 150 μ g/mL) and T_1 water values (800 and 1500ms). Similar to Hines et al. we chose peanut oil and super paramagnetic iron oxide (SPIO) particles (magnetite, 5nm, Sigma-Aldrich) to modulate fat concentration and R_2^* . Distilled water was doped with gadobutrol (Gadovist, Bayer Vital GmbH, Germany) to modulate T_1 values. For gelling, we added Agar (2.23%w/v) over heat while stirring. All vials were placed in a 1l cylindrical container in two sets (L1, L2). Background was filled with distilled water. For fast multi-parameter acquisition, we combined a single-shot IR sequence with continuous multi-echo radial FLASH readout. For improved k-space coverage, we incorporated blip gradients [6] (Fig. 1). To jointly estimate parameter maps directly from the acquired k-space data, we modelled the underlying physical signal and formulated parameter estimation as a non-linear inverse problem. Our model explicitly accounts for water and fat specific equilibrium and steady-state signal contributions and for their effective longitudinal relaxation rates. In addition, we considered the 6-peak fat spectrum [7] and field inhomogeneity. The forward model accounts for the radial sampling pattern, coil sensitivities and Fourier transform. The optimization problem is solved iteratively using IRGNM-FISTA [8-11] implemented and performed in BART [12], utilizing

Sobolev and l1-wavelet regularization. Phantom data was acquired at 3T (Siemens Magnetom Vida) equipped with a 20-channel head coil.

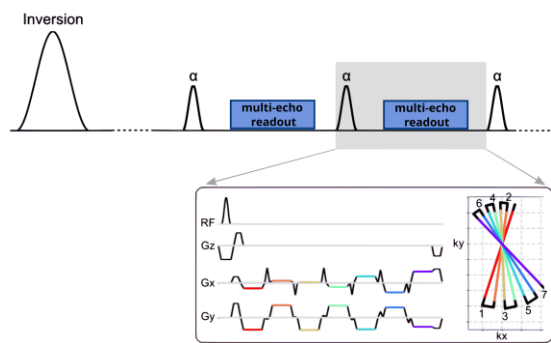


Fig. 1: Diagram of a radial single-shot inversion-recovery multi-echo FLASH sequence with corresponding trajectory in k-space. Spokes from several shots (TRs) and all echoes (colors) are distributed equally in one k-space. Each k-space is rotated by a small golden-ratio based angle after each multi-echo readout.

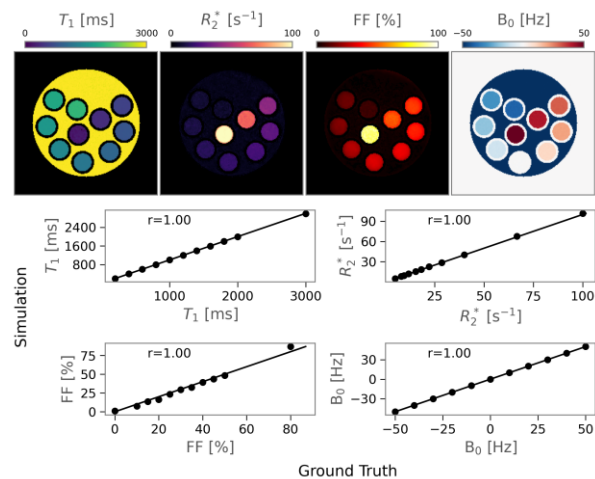


Fig. 2: Top: Reconstructed T_1 , R_2^* , FF, and B_0 maps from the numerical phantom study simulated with BART [12]. The phantom contains 11 ROIs (10 tubes + background), covering a wide range of parameter values. Bottom: Correlation plots comparing ROI-averaged simulation values to ground truth input values. Black line indicates identity.

Results: First, we validated the proposed model-based reconstruction on a numerical phantom (BART) (Fig. 2, top), covering a wide range of ground-truth values. Comparison of ROI-averaged simulated values to the ground truth shows perfect agreement, as indicated by Pearson correlation coefficient (Fig. 2, bottom).

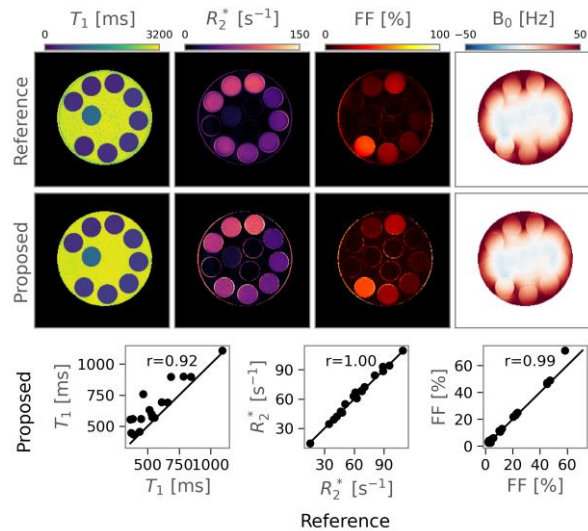


Fig. 3: Top: Reconstructed T_1 , R_2^* , FF, and B_0 maps from water-fat-SPIO (L1). Reference (top row) reconstructed from single-shot IR (T_1) and steady-state single-shot multi-echo acquisitions (R_2^* , FF, B_0). Joint reconstructions of the proposed single-shot IR multi-echo acquisition shown in bottom row. Bottom: Pearson correlation analysis between reference and proposed method. Black line indicates identity.

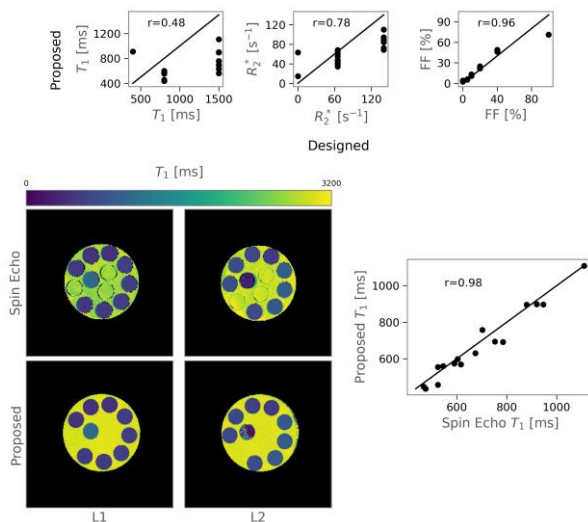


Fig. 4: Top: Pearson correlation analysis of values expected by phantom design and measured values by proposed method. Bottom: Gold-standard T_1 maps of both sets in comparison to maps obtained with proposed method with corresponding correlation analysis. Black line indicates identity.

In physical phantom studies, reference maps for R_2^* , FF, and B_0 were estimated using model-based reconstruction of steady-state multi-echo. For our phantom, we adopted manufacturing instructions of existing protocols [4,5]. It is comprised of 18 vials (18 mL) with varying designed fat volume percentages (0, 5, 10, 20, 40 and 100%), iron concentrations (0, 50, and $150\mu\text{g/mL}$) and T_1 water values (800 and 1500ms). Similar to Hines et al. we chose peanut oil and super paramagnetic iron oxide (SPIO) particles (magnetite, 5nm, Sigma-Aldrich) to modulate fat concentration and R_2^* . Distilled water was doped with gadobutrol (Gadovist, Bayer Vital GmbH, Germany) to modulate T_1 values. For gelling, we added Agar (2.23%w/v) over heat while stirring. All vials were placed in a 1l cylindrical container in two sets (L1, L2). Background was filled with distilled water. For fast multi-parameter acquisition, we

combined a single-shot IR sequence with continuous multi-echo radial FLASH readout. For improved k-space coverage, we incorporated blip gradients [6] (Fig. 1). To jointly estimate parameter maps directly from the acquired k-space data, we modelled the underlying physical signal and formulated parameter estimation as a non-linear inverse problem. Our model explicitly accounts for water and fat specific equilibrium and steady-state signal contributions and for their effective longitudinal relaxation rates. In addition, we considered the 6-peak fat spectrum [7] and field inhomogeneity. The forward model accounts for the radial sampling pattern, coil sensitivities and Fourier transform. The optimization problem is solved iteratively using IRGNM-FISTA [8-11] implemented and performed in BART [12], utilizing Sobolev and l1-wavelet regularization. Phantom data was acquired at 3T (Siemens Magnetom Vida) equipped with a 20-channel head coil. data ($0.8 \times 0.8 \times 5 \text{ mm}^3$) [13]. Steady-state data was extracted from the last 140 excitations of the same acquisition. T_1 references were estimated using single-shot IR FLASH with single-echo readout [11]. Figure 3 shows reconstructed maps from one set of vials. To assess accuracy, ROI averaged mean values of reference and the here proposed method were compared. Resulting maps of water-specific T_1 , R_2^* and FF are in excellent agreement, as indicated by Pearson correlation coefficient.

Discussion: To estimate manufacturing accuracy, we compared designed ground truth values to values obtained from our proposed method (Fig. 4, top). Although designed fat-fraction values were achieved adequately, we noticed deviations from the designed values in both R_2^* and T_1 . While deviations in R_2^* can be attributed to varying fat-fractions and its known effect on measured R_2^* values [5], discrepancy in T_1 values can only be explained by manufacturing inaccuracies at this point. To rule out acquisition errors, we additionally performed gold-standard T_1 mapping [14] using IR spin-echo water-only excitation acquisitions with varying T_1 s ($T_1 = 30, 280, 530, 780, 1030, 1280, 1530 \text{ ms}$). We can report excellent agreement between gold-standard T_1 maps and our proposed method (see Fig. 4, bottom).

Conclusion: We designed and manufactured a water-fat-SPIO phantom used to validating our new proposed method of joint multi-parameter estimation. In our proposed method, we combined a non-linear model-based reconstruction with radial IR multi-echo FLASH acquisition enabling joint estimation of water-specific T_1 , R_2^* , FF, and B_0 field maps from a single-shot acquisition of four seconds while maintaining high accuracy, as demonstrated with our reference measurements. Our developed method has the potential to improve patient comfort considerably and to add valuable diagnostic information while simultaneously rendering multi-parametric quantitative MRI more feasible for clinical applications.

Acknowledgements: This work was funded by the Deutsche Forschungsgemeinschaft (DFG, German Research Foundation) under grants UE 189/4-1 and TA 1473/2-1 and under Germany's Excellence Strategy - - EXC 2067/1-390729940. Supported by research grant from Else Kröner-Fresenius Foundation and by the DZHK (German Centre for Cardiovascular Research), funding code: 81Z0300115.

References:

1. Xia, T. et al. Association between Liver MRI Proton Density Fat Fraction and Liver Disease Risk. *Radiology* 309, e231007 (2023).
2. Margaret Cheng, H.-L., Stikov, N., Ghugre, N. R. & Wright, G. A. Practical medical applications of quantitative MR relaxometry. *Journal of Magnetic Resonance Imaging* 36, 805–824 (2012).
3. Wang, X. et al. Model-Based Reconstruction for Joint Estimation of T_1 , R_2^* and B_0 Field Maps Using Single-Shot Inversion-Recovery Multi-Echo Radial FLASH. Preprint at <https://doi.org/10.48550/arXiv.2402.05366> (2024).
4. Bush, E. C. et al. Fat-Water Phantoms for Magnetic Resonance Imaging Validation: A Flexible and Scalable Protocol. *J Vis Exp* 57704 (2018).
5. Hines, C. D. G. et al. T_1 independent, T_2^* corrected MRI with accurate spectral modeling for quantification of fat: Validation in a fat-water-SPIO phantom. *Journal of Magnetic Resonance Imaging* 30, 1215–1222 (2009).
6. Tan, Z., Voit, D., Kollmeier, J. M., Uecker, M. & Frahm, J. Dynamic water/fat separation and inhomogeneity mapping—joint estimation using undersampled triple-echo multi-spoke radial FLASH. *Magnetic Resonance in Medicine* 82, 1000–1011 (2019).
7. Yu, H. et al. Multiecho water-fat separation and simultaneous R estimation with multifrequency fat spectrum modeling. *Magnetic Resonance in Medicine* 60, 1122–1134 (2008).
8. Bakushinsky, A. B. & Kokurin, M. Y. *Iterative Methods for Approximate Solution of Inverse Problems*. (Springer Science & Business Media, 2005).
9. Engl, H. W., Hanke, M. & Neubauer, A. *Regularization of Inverse Problems*. (Springer Science & Business Media, 1996).
10. Beck, A. & Teboulle, M. A Fast Iterative Shrinkage-Thresholding Algorithm for Linear Inverse Problems. *SIAM J. Imaging Sci.* 2, 183–202 (2009).
11. Wang, X. et al. Model-based T_1 mapping with sparsity constraints using single-shot inversion-recovery radial FLASH. *Magnetic Resonance in Medicine* 79, 730–740 (2018).
12. Uecker, M. et al. Software toolbox and programming library for compressed sensing and parallel imaging. in *ISMRM Workshop on Data Sampling and Image Reconstruction* 41 (Sedona, 2013).
13. Tan, Z. et al. Free-Breathing Liver Fat, R_2^* and B_0 Field Mapping Using Multi-Echo Radial FLASH and Regularized Model-Based Reconstruction. *IEEE Transactions on Medical Imaging* 42, 1374–1387 (2023).
14. Barral, J. K. et al. A robust methodology for in vivo T_1 mapping. *Magnetic Resonance in Medicine* 64, 1057–1067 (2010).

Evaluation of the diffusion along perivascular spaces after subarachnoid hemorrhage

Patricia Ulloa 1, Justus C. Rudolf 1, Aileen Schmidt 1+2, Jan K uchler 3, Peter Schramm 1

1 Department of Neuroradiology, University Hospital Schleswig-Holstein (UKSH), Luebeck, Germany

2 Department of Diagnostic and Interventional Radiology, University Hospital Bonn, Bonn, Germany

3 Department of Neurosurgery, University Hospital Schleswig-Holstein (UKSH), Luebeck, Germany

Abstract: After subarachnoid hemorrhage (SAH), the accumulation of neurotoxic metabolites in the brain impairs the glymphatic system (GS) function. Here, we are using diffusion tensor imaging (DTI) along perivascular spaces (ALPS) index to indirectly evaluate GS performance in the context of SAH.

The interhemispheric ALPS index average was used to compare patients with HC, and we evaluated whether the index correlates with SAH severity as indicated by Hunt & Hess scores.

The ALPS index was lower in SAH patients than in HC. Additionally, in patients with severe symptoms the index was significantly lower than in the mild symptom group.

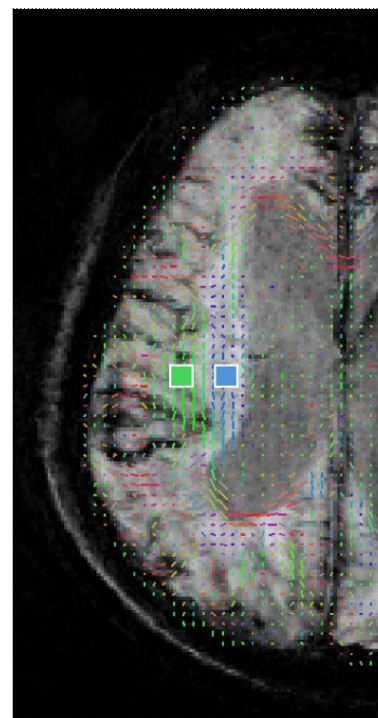
Motivation: The glymphatic system (GS) [1] is a potential pathway for removing toxic metabolic products, such as beta-amyloid and tau proteins. In subarachnoid hemorrhage (SAH), the accumulation of blood into the subarachnoid space (SAS) and toxic related metabolites change the cerebrospinal and interstitial fluid dynamics and composition². This results in an impaired GS function. Diffusion tensor imaging (DTI) along perivascular spaces (ALPS) index [3] offers a non-invasive way for indirectly assessing CSF dynamics in the human brain, whereby a large ALPS index may reflect efficient GS function, whereas a lower index could indicate system impairment. Previous studies have shown that in patients with cerebrovascular injury the ALPS index is lower than in healthy controls (HC) [4,5]. However, this has not been studied in SAH patients yet. Here, we determined the ALPS index in SAH patients and compared it with HC, and assessed the potential relationship with the initial Hunt & Hess (H&H) score.

Materials & Methods: Thirty-one patients with history of SAH were recruited at their annual follow-up at our institution (24 females, age: 57.8 ± 10 years). Eleven HC (7 females, age: 57.4 ± 10 years) were selected as sex- and age-matched controls. The study was approved by the local ethics committee.

All participants gave consent before undergoing MRI using a 3T scanner (MAGNETOM Vida, Siemens Healthineers, Germany) with a 20-channel head coil. For calculating the ALPS index, a 5-min DTI scan was added to the clinical protocol with the following parameters: TE/TR = 92/4400 ms, FOV = 200 x 200 mm², voxel size = 2 x 2 x 2 mm³, 70 slices, b-values = 0, and 1000 s/mm² with 64 diffusion directions.

DTI ALPS analysis [3] was done using DSI Studio, where a four-voxel squared region of interest (ROI) (volume = 32 mm³) was manually placed in the projection (proj) and association (assoc) areas (see Fig. 1). The ALPS index was calculated as $\frac{\text{mean}(D_{xx\text{proj}}, D_{xx\text{assoc}})}{\text{mean}(D_{yy\text{proj}}, D_{zz\text{assoc}})}$, where D_{xx} , D_{yy} , and D_{zz} correspond to the diagonal elements of the diffusion tensor matrix.

Statistical analysis was performed using Matlab R2022a (The MathWorks, Massachusetts, USA) with $\alpha = 0.05$. Wilcoxon signed-rank test was used to evaluate the difference between the ALPS index of patients and age- and sex-matched HCs. To assess the relationship between the ALPS index and H&H (Mann-Whitney U and Spearman's rank), SAH patients were classified into two subgroups, those with mild (H&H 1 to 3) and severe symptoms (H&H 4 to 5).



■ ROI association

■ ROI projection

Fig. 1: ROI placement for ALPS index calculation shown on a color-coded FA map overlaid on an SWI image of a 31-year-old male SAH patient, 1.3 years after left-hemisphere ACI aneurysm rupture (initial H&H grade 4).

Results: Significant differences were found between the ALPS index of SAH patients and the matched HC (Wilcoxon signed-rank, $p < .001$). Additionally, SAH patients with mild symptoms had a significantly larger ALPS index than those in the severe symptoms group (Mann-Whitney U, $p = 0.022$) (see Fig. 2). A possible, weak negative correlation with initial H&H classification and ALPS index (Spearman's, $\rho = -0.34$) might be considered.

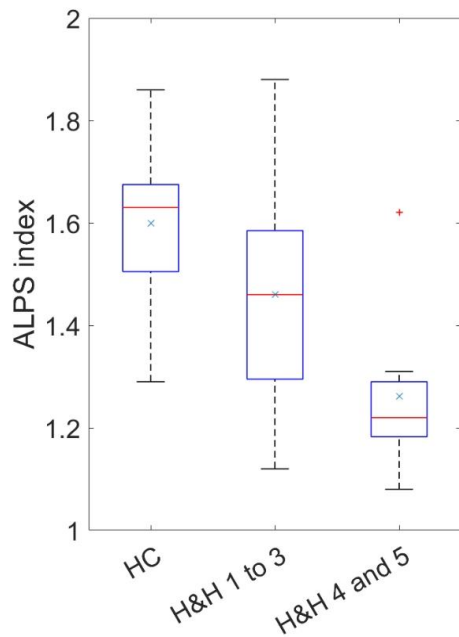


Fig. 2: ALPS index in SAH patients grouped by H&H into mild and severe symptoms. Box plots show the median (red line) and mean (x). Healthy controls exhibit higher ALPS values than patients, with a significant difference also observed between patients with mild and severe symptoms.

Discussion: Here, we found that the ALPS index was significantly lower in SAH patients than in HC and that, as a tendency, the ALPS index for SAH patients might negatively correlate with the initial H&H score. This is consistent with previous studies [3,6], where a lower ALPS index was related to increased functional impairment. However, a larger cohort is needed to determine the relationship between ALPS index and H&H grading.

Additionally, there are limitations inherent to the ALPS method, which is restricted to a very small area within deep white matter. This makes it difficult to interpret these results as reflecting whole-brain GS function. Additionally, pathological processes occurring in cortical brain areas cannot be assessed using the ALPS index. Therefore, the validity of the DTI ALPS index to draw definitive conclusions regarding the GS function only based on the diffusion in the periventricular area is questionable.

Conclusion: In summary, the lower ALPS index found in SAH patients compared to HC suggests a potential impairment of GS function following subarachnoid hemorrhage. This may result from the obstruction of perivascular pathways by blood degradation products and the disruption of AQP4 polarity, both of which can interfere with the normal clearance of interstitial fluid. This finding emphasizes the urgent need for further research in humans and to validate the ALPS method as a non-invasive biomarker for GS dysfunction. While the method appears promising, its validity remains uncertain, as microstructural changes in white matter may also influence the ALPS index, necessitating confirmation through complementary techniques [7].

Acknowledgements: Justus C. Rudolf received funding from the University of Luebeck in form of the Scholarship "Luebecker Exzellenzmedizin" during the winter semester 2023/2024.

References:

- [1] Iliff, J. J.; Nedergaard, M. Is There a Cerebral Lymphatic System? *Stroke* 2013, 44 (6_suppl_1), S93–S95. <https://doi.org/10.1161/STROKEAHA.112.678698>.
- [2] Chaudhary, N.; Pandey, A. S.; Gemmete, J. J.; Hua, Y.; Huang, Y.; Gu, Y.; Xi, G. Diffusion Tensor Imaging in Hemorrhagic Stroke. *Exp. Neurol.* 2015, 272, 88–96. <https://doi.org/10.1016/j.expneurol.2015.05.011>.
- [3] Taoka, T.; Masutani, Y.; Kawai, H.; Nakane, T.; Matsuoka, K.; Yasuno, F.; Kishimoto, T.; Naganawa, S. Evaluation of Glymphatic System Activity with the Diffusion MR Technique: Diffusion Tensor Image Analysis along the Perivascular Space (DTI-ALPS) in Alzheimer's Disease Cases. *Jpn. J. Radiol.* 2017, 35 (4), 172–178. <https://doi.org/10.1007/s11604-017-0617-z>.
- [4] Zhang, C.; Sha, J.; Cai, L.; Xia, Y.; Li, D.; Zhao, H.; Meng, C.; Xu, K. Evaluation of the Glymphatic System Using the DTI-ALPS Index in Patients with Spontaneous Intracerebral Haemorrhage. *Oxid. Med. Cell. Longev.* 2022, 2022, 2694316. <https://doi.org/10.1155/2022/2694316>.
- [5] Park, J. H.; Bae, Y. J.; Kim, J. S.; Jung, W. S.; Choi, J. W.; Roh, T. H.; You, N.; Kim, S.-H.; Han, M. Glymphatic System Evaluation Using Diffusion Tensor Imaging in Patients with Traumatic Brain Injury. *Neuroradiology* 2023, 65 (3), 551–557. <https://doi.org/10.1007/s00234-022-03073-x>.
- [6] Zeng, C.; Zhai, Y.; Ge, P.; Liu, C.; Yu, X.; Liu, W.; Li, J.; He, Q.; Liu, X.; Ye, X.; Zhang, Q.; Wang, R.; Zhang, Y.; Zhang, D.; Zhao, J. Glymphatic Impairment Associated with Neurocognitive Dysfunction in Moyamoya Disease. *Transl. Stroke Res.* 2024. <https://doi.org/10.1007/s12975-024-01250-z>.
- [7] Taoka, T.; Ito, R.; Nakamichi, R.; Nakane, T.; Kawai, H.; Naganawa, S. Diffusion Tensor Image Analysis Along the Perivascular Space (DTI-ALPS): Revisiting the Meaning and Significance of the Method. *Magn. Reson. Med. Sci.* 2024, rev.2023-0175. <https://doi.org/10.2463/mrms.rev.2023-0175>.

Field-based spatial self-registration of multi-coil hardware for B0 field control

Isabelle Zinghini* 1+2, Ian Macleod 2, Carlotta Ianniello 2, Sebastian Theilenberg 2, Christoph Juchem 1+2+3

1 High Field MR Center, Center for Medical Physics and Biomedical Engineering, Medical University of Vienna, Vienna, Austria

2 Department of Biomedical Engineering, Columbia University, New York, NY, USA

3 Department of Radiology, Columbia University, New York, NY, USA

Abstract: Introduction - Multi-coil (MC) shimming improves B0 homogeneity in MRI but is sensitive to hardware misplacement.

Methods - A field map-based self-registration algorithm can estimate transformations between calibrated and displaced MC positions by co-registering measured and expected B0 field maps.

Results - Monte Carlo simulations and scanner validation demonstrated sub-millimeter and sub-degree localization accuracy for SNR ≥ 10 . A genetic algorithm-optimized field yielded average errors of 0.20 mm and 0.11° across multiple displacements.

Discussion - The method enables robust localization without precise repositioning.

Conclusion - Field map-based registration improves MC shimming performance and supports practical, repeatable hardware use in MRI.

Motivation: Acquisition of robust Magnetic Resonance Imaging (MRI) data relies on homogeneous B0 field conditions, but magnetic susceptibility differences in vivo can create B0 distortions that lead to artifacts and signal dropout [1–3]. Multi-coil (MC) shimming systems use an array of individually-driven generic coils to homogenize the B0 field, and have been shown to outperform low-order spherical harmonic (SH) shimming in the brain [4–8].

Most MC setups are designed as temporary inserts for existing scanners, with high-quality basis maps [5, 7–9] (maps of the field produced per shim setting for each coil) acquired by a calibration process requiring multiple hours of scan and analysis time. Shim fields are calculated as a combination of calibrated basis maps for subsequent experiments. For an applied shim field to match the calculated field, it is therefore essential to either position the hardware in precisely the same location as in calibration or have knowledge of the exact position relative to the calibration scenario [5]. Degradations in B0 field control are observed even for millimeter-scale displacements (Figure 1). Our purpose is to reliably detect misplaced hardware using only a field map acquisition, ensuring optimal performance of MC inserts.

Materials & Methods: A hardware self-registration algorithm [10] in MATLAB (Mathworks, Inc., MA) co-registers two 3D field maps: an Expected Field, which is acquired at the Day 0 (i.e. calibration) position, and a Measured Field, which is the same field measured at Day N (Figure 2). The Expected Field is a mathematical combination of the calibration maps, and the Measured Field is measured after the hardware is replaced in the scanner. The algorithm calculates the translation and z-rotation needed to align the two fields in an eroded ROI through co-registration. Secondary rotations about the x- and y-axes were not considered in this proof-of-concept.

Three Expected Field shapes were tested: the shape of one MC element, a Four Lobe field generated by one ring of coils, and a GA Field optimized by a genetic algorithm (Figure 4). The latter two were selected for further validation.

A MC array comprising 6 rows of 8 coils was arranged on a cylindrical former to produce B0 distributions (Figure 3).

Monte Carlo simulations of 5,000 rigid transformation recoveries were used to calculate the average norm error of localization accuracy at ten SNR levels. Simulations were done for Simulated Basis Maps – generated from Biot-Savart simulations of the hardware – as well as the calibrated Experimental Basis Maps for the hardware.

The self-registration procedure was tested in the scanner by physically shifting the MC hardware a known distance. Scanner validation was performed at seven SNR levels for one hardware position, and then at one SNR level (19±1) for 10 hardware positions.

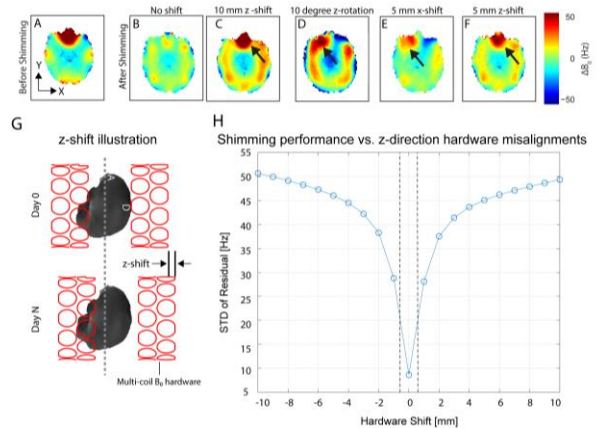


Fig. 1: B0 analysis in a brain after shimming with optimal and suboptimal hardware placement. A-F Transformations of hardware result in suboptimal shimming, including field asymmetries (D, E) and hotspots (C, F). The shift that produces C is illustrated in G. H) Analysis of residuals for z-translation of established MC hardware [5].

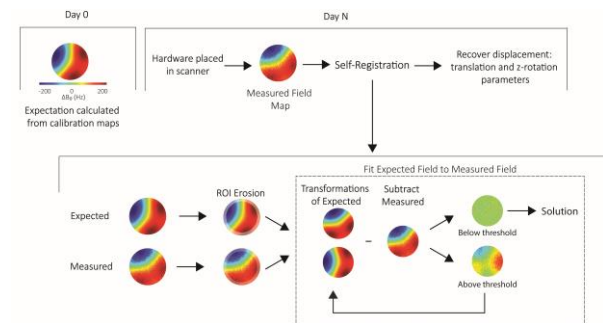


Fig. 2: Schematic of the self-registration procedure.

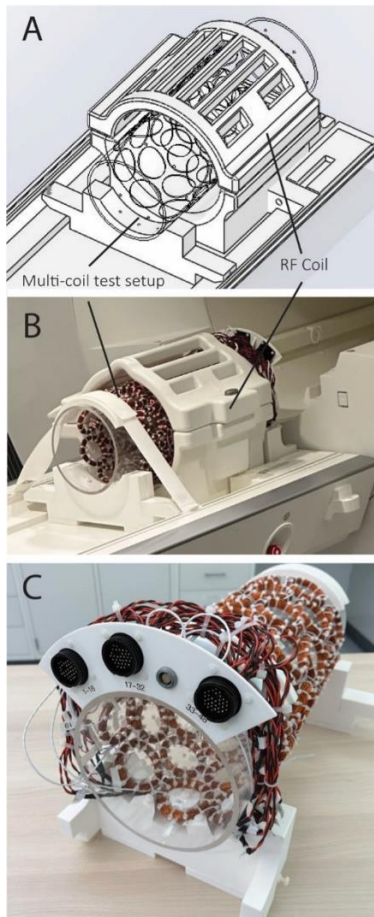


Fig. 3: Design of a MC prototype; application with a Siemens Prisma 3T scanner. The 6x8 array has 100 turns per coil of 70 mm diameter ($L = 880 \mu\text{H}$, $R = 717.7 \text{ m}\Omega$) on an acrylic former ($\text{OD} = 20.32 \text{ cm}$) and is driven by a multi-channel amplifier and controller [11].

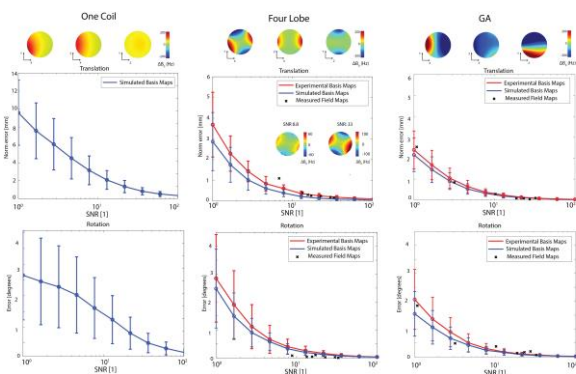


Fig. 4: Performance analysis of field-based self-registration algorithm. Signal in SNR was calculated as the maximum field value in the ROI, and noise was calculated as the standard deviation of the residual after 10th SH removal.

Results: The established framework enabled accurate hardware localization through application of unique field shapes (Figure 4). Localization accuracy with well below 1 mm and 1 degree errors was achieved irrespective of the applied test field shape with SNR of at least 10. In scanner validation, both Expected Fields had an average translation error below 1 mm for SNR levels above 4.6, and an average rotation error below 1 degree for SNR levels above 2.8 and 4.6 for the GA and Four Lobe fields, respectively. For all SNR levels, the Experimental Basis Maps had higher errors than Simulated Basis Maps.

Both Expected Fields were able to recover all 10 additional controlled hardware shifts within a norm translation error of under 0.44 mm, with an average error of 0.30 mm and 0.20 mm for the Four Lobe and GA Fields, respectively. All rotation errors were recovered within 0.17 degrees, with average errors of 0.13 and 0.11 for the Four Lobe and GA Fields.

Discussion: A field shape optimized with a genetic algorithm allows for an average localization accuracy of 0.2 mm and 0.11 degrees from a sub-1-minute B0 mapping experiment (SNR 20), allowing for improvement of B0 control and shimming potential of hardware inserts.

Simulated, Experimental, and Measured experiments showed excellent agreement across all SNR levels. Both Expected Fields could achieve error below 0.5 mm and 0.5 degrees for the 10 transformations – a reasonable threshold for success given the performance degradation curve in Figure 1 – but the GA Field had an overall lower error.

In the future, we plan to include x- and y- rotations, which cannot be accounted for by rigid transformations alone and require qualitative updates of the basis shapes themselves, and to test the self-registration method in vivo.

Conclusion: Here we have presented a method for field map-based hardware self-registration for MC inserts. This addresses the requirement of precise repositioning of MC hardware inserts, allowing for excellent shim capabilities of misplaced hardware.

Acknowledgements: This work was supported by the National Institute of Health under award number R01-EB030650.

References:

- Juchem C, de Graaf RA (2017) B0 magnetic field homogeneity and shimming for in vivo magnetic resonance spectroscopy. *Analytical Biochemistry* 529:17–29.
- Jezzard P, Clare S (1999) Sources of distortion in functional MRI data. *Hum Brain Mapp* 8:80–85.
- de Graaf RA, Juchem C (2016) B0 Shimming Technology. In: Webb AG (ed) *Magnetic Resonance Technology: Hardware and System Component Design*. The Royal Society of Chemistry, p 0
- Juchem C, Nixon TW, McIntyre S, Rothman DL, de Graaf RA (2010) Magnetic field homogenization of the human prefrontal cortex with a set of localized electrical coils. *Magn Reson Med* 63:171–180.
- Juchem C, Nixon TW, McIntyre S, Boer VO, Rothman DL, de Graaf RA (2011) Dynamic Multi-Coil Shimming of the Human Brain at 7 Tesla. *J Magn Reson* 212:280–288.
- Juchem C, Herman P, Sanganahalli BG, Brown PB, McIntyre S, Nixon TW, Green D, Hyder F, de Graaf RA (2014) Dynamic Multi-Coil Technique (DYNAMITE) Shimming of the Rat Brain at 11.7 Tesla. *NMR Biomed* 27:897–906.
- Stockmann JP, Witzel T, Keil B, Polimeni JR, Mareyam A, LaPierre C, Setsompop K, Wald LL (2016) A 32-channel combined RF and B0 shim array for 3T brain imaging. *Magnetic Resonance in Medicine* 75:441–451.
- Aghaeifar A, Mirkes C, Bause J, Steffen T, Avdievitch N, Henning A, Scheffler K (2018) Dynamic B0 shimming of the human brain at 9.4 T with a 16-channel multi-coil shim setup. *Magnetic Resonance in Medicine* 80:1714–1725.
- Ianniello C, Theilenberg S, Zinghini I, Vaughan Jr. JT, Juchem C (2024) Design and Construction of Integrated MC/RF Hardware for MRI of the Human Brain. *Proceedings of the ISMRM Annual Meeting, Singapore*, 1447.
- Zinghini I, Macleod I, Ianniello C, Theilenberg S, Juchem C (2024) Field-based spatial self-registration of multi-coil hardware for B0 field control. *Proceedings of the ISMRM Annual Meeting, Singapore*, 4944.
- Nixon TW, Juchem C, McIntyre S, Rothman DL, de Graaf RA (2010) Design and Implementation of a Real Time Multi-Coil Amplifier System. *Proceedings of the ISMRM-ESMRMB Joint Annual Meeting, Stockholm*, 1532.

Poster

Presenter's Abstracts

Multi nuclear MR imaging and spectroscopy using a whole body, 3T human MR system with 200 mT/m gradients

Ali Ajouz 1+2+3*, Maria Anikeeva 2, Olav Jansen 1, Lynn Johann Frohwein 3, Aaron Diercks 2 and Jan-Bernd Hövener 1+2

1 Department of Radiology and Neuroradiology, University Hospital Schleswig-Holstein, Kiel, Germany

2 Department of Radiology and Neuroradiology, Section Biomedical Imaging, University Hospital Schleswig-Holstein, Kiel University, Kiel, Germany

3 Siemens Healthineers AG, Forchheim, Germany

Abstract: We present our approach of using a state of the art, whole body 3T human MR system with strong gradients for multi-nuclear magnetic resonance imaging and spectroscopy.

Motivation: The power of conventional hydrogen (1H) MRI has made it the gold standard for soft tissue imaging in vivo. Imaging other nuclei, however, gives access to other information, which are not easily available to 1H MRI [1]. This includes metabolic imaging for 2H MRI and 13C MRI [2], physiological imaging for sodium MRI, energy metabolism for 31P or lung function with 129Xe MRI [3].

Here, both hyperpolarized and thermally polarized agents are being used, each with their distinct advantages and disadvantages [4]. Dominant factors for the signal to noise ratio are the gyromagnetic ratio, relaxation times and the tissue concentration of the MR active isotope. Here, long T1 relaxation is beneficial for hyperpolarized MR, where the magnetization is finite, and short relaxation times are beneficial for thermally polarized MR, where it is renewed.

However, X-nuclear MR is much less developed than 1H. Performing X-nuclei MR requires an upgrade of an ordinary MRI with respect to the transmit- and receive paths, coils, software and sequences. Because the gyromagnetic ratio is lower than that of 1H, stronger gradients are required to achieve similar frequency spread per voxel needed for spatial resolution (disregarding SNR considerations).

Here, we present our approach for implementing a platform for multi-nuclei human MRI with particularly strong gradients of 200 mT/m in research setting in a hospital.

Materials & Methods: MRI: Multinuclear MR experiments were conducted using a whole body 3 T MRI system with a maximum gradient amplitude of 200 mT/m and maximum slew rate of 200 T/m/s (MAGNETOM Cima.X, Siemens Healthineers AG, Forchheim). Enabling 2H required a special procedure guided by the manufacturer, all other nuclei were readily available as product.

Coils: 2H quadrature, transmit-receive (TxRx) head coil, 13C and 129Xe 4-legged quadrature birdcage (BC) TxRx with and without two four-channel receive arrays, 23Na TxRx quadrature head coil (all by Rapid Biomedical GmbH, Rimplar, Germany). 2H surface coils were also available (Stark, Erlangen, Germany).

Sequences: Free induction decay (FID) and 2D FLASH sequences were provided by the manufacturer natively (FID) or by disabling the frequency lock (FLASH, Figure 1 A, B).

Model solutions (MS):

2H (MS1): 50 ml 99% enriched D₂O in a 50 ml flacon tube (contains approx. 2.73 mol ²H, based on a density of 1.105 g/ml and molar mass of 20.03 g/mol).

13C (MS2): 1 l food-grade sunflower oil in product plastic bottle (approximately 3.2 Mol linoleic acid at molecular weight 280 g/mol, 59 Mol Carbon and 65 mMol 13C, assuming 100 % linoleic acid).

23Na (MS3): 500 ml saturated sodium chloride solution at room temperature in a plastic bottle (0.5 ml Coca Cola, contains approx. 3.08 Mol 23Na with 360 g/l NaCl at 58.5 g/mol).

129Xe (MS4): 200 mL hyperpolarized 129Xe in a polyvinylfluoride (PVF) bag at ambient pressure (Tedlar bag). This corresponds to approximately 8.3 mmol of xenon at 24.0 L/mol.

A

C#	Nuclei	Type	T / R	Anat	RP
1	² H/ ¹ H	1Ch Q BG	T&R	Head	120 V
2	¹³ C	1Ch Q BG	T&R	Torso	315 V *
3	¹³ C/ ¹ H	2x4 Ch AR	R	Torso	315 V *
4	²³ Na/ ¹ H	1Ch Q BG	T&R	Head	120 V
5	¹²⁹ Xe	1Ch Q BG	T&R	Torso	600 V
6	¹²⁹ Xe/ ¹ H	4x4 Ch AR	R	Torso	600 V

B

Nucleus	² H	¹³ C	²³ Na	¹²⁹ Xe
Coil No.	1	2, 3	4	5, 6
f [MHz]	18.910 206	30.974 732	32.583661	34.072363
FID				
TR (s)	1.74	3	2	1.5
TE (ms)	0.35	0.35	0.35	0.35
N	40	16	32	1
τ _{rect} (μs)	200	200	200	200
2D FLASH				
FOV (mm ²)	250 x 211	300 x 300	217 x 190	400 x 400
Matrix-size	96 x 80 x 8	64 x 64 x 1	96 x 82 x 19	80 x 80 x 8
ST (mm)	12	200	9	17
TR (ms)	782	33	404	11
TE (ms)	6.37	8.78	5.56	4.99
BW (Hz/Px)	210	70	210	170
τ _{gauss} (ms)	2.56	2.56	2.56	2.56

Fig. 1: A) Specifications of the coils used at the platform: Channels (Ch), quadrature (Q) polarization, birdcage (BG), array (AR) or surface coil (SC) geometry, anatomy designed for (Anat) and rough reference power (RP) provided by manufacturer or own calibration (*).

B) Sequence parameters for FID and 2D FLASH MR. Abbreviations: TR: repetition time; TE: echo time; N: averages; τ_{rect}: duration of block pulse; FOV: field of view; ST: slice thickness; BW: bandwidth; τ_{gauss}: duration of gauss pulse.

Hyperpolarization: Spin-exchange optical pumping (SEOP) was performed in a continuous-flow, human polarizer equipped with a 180W-laser diode array and 3.5-L optical borosilicate cell operating at 125 °C (PX-007, Polaris, Medical School of Sheffield, Great Britain). After flowing through the SEOP cell, ¹²⁹Xe frozen in a glass tube submerged in liquid nitrogen. Upon removal from the IN2, the gas was collected in a PVF bag and used for imaging within minutes.

Human MRI: A volunteer (co-author, m, 45) was positioned in the scanner where ¹H calibrations and MRI were performed. Upon inhalation of hyperpolarized ¹²⁹Xe gas, 2D FLASH was performed during a breath hold in 7 s.

Analysis: The spectral signals were phase-corrected, and Fourier transformed. Subsequently, only the real part of the spectrum was used for fitting and plotting. The full width at half maximum (FWHM) was determined as the width of the peak at half of its maximum height. The signal-to-noise ratio (SNR) was determined in the time domain by integrating the early FID signal (first 50 points) and dividing it by the standard deviation of the last 3900 points, which were assumed to represent noise [5].

An exponential function was applied to the signal to reduce high-frequency noise of the ¹³C spectrum.

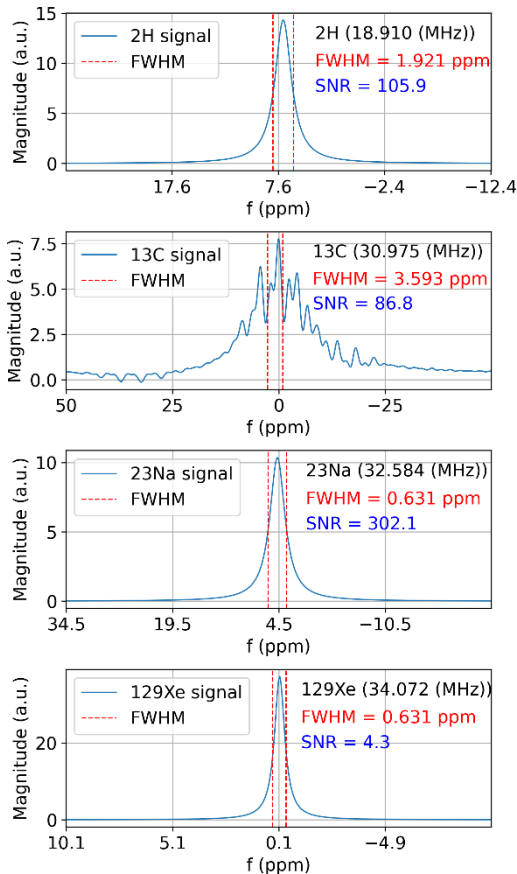


Fig. 2: In vitro ²H, ¹³C, ²³Na and ¹²⁹Xe phased real spectra of model solution MS1-4 acquired with pulse-acquisition sequences (Figure 1B). The FWHM varied between 0.6 and 3.6 ppm for 0.2 – 1 l solutions or gases in different containers. The SNR per excitation varied between 4 and 302. The frequency scale refers to the indicated frequency

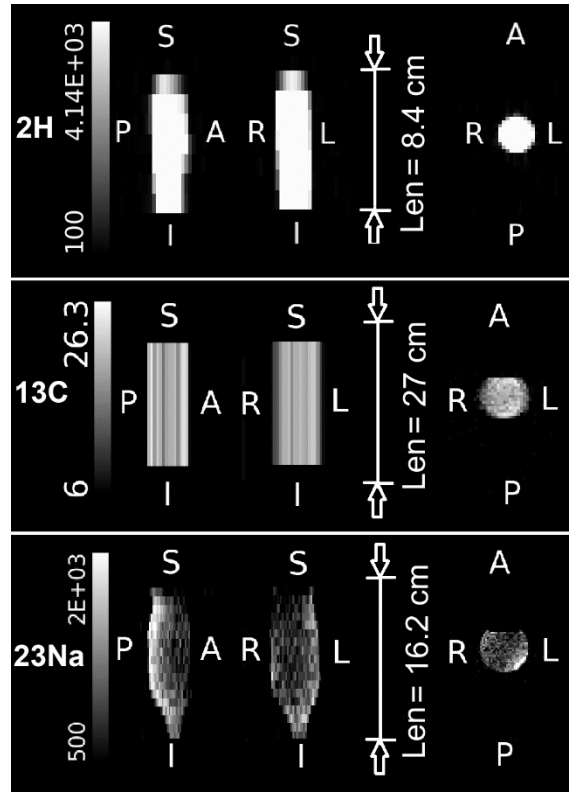


Fig. 3: Orthogonal reconstructions of ²H, ¹³C, and ²³Na FLASH MRI of thermally polarized models' solution MS1 – MS3. Len denotes the length of the phantom used. Note that the sequence parameters varied significantly (Figure 1B).

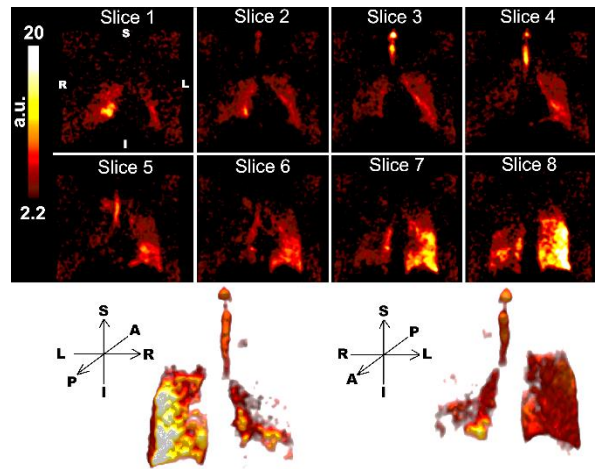


Fig. 4: In vivo MRI of hyperpolarized ¹²⁹Xe in the lung of a living human, individual slices and a front and back view of a 3D rendering, acquired with the transmit-receive birdcage coil (C5). For illustration, the data was smoothed with spline interpolation.

Results: MR spectra were successfully acquired for all nuclei (Figure 2). The full width at half maximum (FWHM) varied between 0.6 and 3.6 ppm for 0.2 – 1 l solutions or gases in different containers; all samples used the standard setting for the shimming (tune up).

The SNR per excitation was 106 for ²H (C1), 86 for ¹³C (C2 + C3), 302 for ²³Na (C4) and 4.3 for hyperpolarized ¹²⁹Xe (C5), assuming full excitation and disregarding T1 effects.

Using the manufacturer's tool for processing, visualizing and quantifying the spectra required installing custom post processing protocols.

Likewise, MRI of sodium, deuterium and carbon, was successfully acquired (Figure 3). Here, images were readily displayed on the device without further measures.

In vivo, the shape of the lungs was readily revealed by imaging hyperpolarized xenon in a single breath hold (Figure 4). The asymmetry of the signal intensity will have to be investigated. Because the 129Xe receive array C6 was not functional, the images were acquired with the large transmit-receive birdcage C5 only.

Discussion: In this contribution, we report on our first experiences of using a state of the art strong-gradient 3T human MRI as a platform for multi-X-nuclear MR imaging and spectroscopy.

Performing MNO MRI required the multi-nuclear option of the MRI system (hardware and software), unlocking the sequences for multi-nuclear use, integrating third party coils, configuring the spectroscopy tool as well as a special procedure for enabling 2H.

Problems occurred with one receive array (C6); some files needed for installing the coils and displaying the spectra on the scanner. All coils required to remove the proton spine array in the patient's bed, which is somewhat time consuming and a disadvantage for routine use.

The resonances were readily observed after the proton frequency calibration. Automated flip angle calibration is not available, and the pre-set value of the coil manufacturer was used; this will have to be verified manually and may depend on the coils loading. Shimming is not a problem for samples where the 1H signal available, and proton flip angle calibration may be used for scaling the x-nuclear reference power. Proton decoupling will be tested in the near future. A more quantitative assessment of the field homogeneity, measured by the linewidth of the spectra, will require similar containers such as spheres. Likewise, the SNR assessment will require accurate flip angle calibrations and sufficiently long repetition times. The inhomogeneous signal distribution on the 23Na and 129Xe MRI will have to be investigated, and a more standardized SNR study conducted.

Generally, all sequences installed on the scanner are set for a specific range of nuclei, typically only 1H, and only a few were natively available for other nuclei (like the FID). Using a command line tool, however, allowed us to undo the frequency lock so that all sequences were available for MNO, only limited by other constraints such as RF power and coil configuration (e.g. single – to multi-channel coils for parallel imaging).

Except for xenon, model solution for testing the nuclei were easily available. As a gas, a pressurized MR compatible container appears suited to hold enough xenon for thermal detection in reasonable time (with e.g. 20 for shortening T1).

The asymmetric distribution of xenon in the lung may be attributed to the low volume of the inhaled gas (200 ml whereas 500 ml are recommended) and low sensitivity of the large torso coil used.

Nominally, the power of the multi-nuclear transmitter was much less than the one for 1H. Whether or not the power is sufficient for demanding sequences such as bSSP and for exciting a sufficiently wide range of chemical shifts e.g. for 13C remains to be seen.

Conclusion: The presented setup enabled us to readily perform multinuclear MR imaging and spectroscopy of hyperpolarized and thermally polarized samples, paving the way for novel functional and metabolic imaging in humans.

References:

1. Niesporek SC, Nagel AM, Platt T. Multinuclear MRI at Ultrahigh Fields. *Topics in Magnetic Resonance Imaging*. 2019;28(3):173-188. doi:10.1097/rmr.0000000000000201
2. Cunningham CH, Lau JYC, Chen AP, et al. Hyperpolarized 13 C Metabolic MRI of the Human Heart: Initial Experience. *Circulation Research*. 2016;119(11):1177-1182. doi:10.1161/circresaha.116.309769
3. Marshall H, Stewart NJ, Chan HF, Rao M, Norquay G, Wild JM. In vivo methods and applications of xenon-129 magnetic resonance. *Progress in Nuclear Magnetic Resonance Spectroscopy*. 2021;122:42-62. doi:10.1016/j.pnmrs.2020.11.002
4. Hsieh CY, Lai YC, Lu KY, Lin G. Advancements, challenges, and future prospects in clinical hyperpolarized magnetic resonance imaging: A comprehensive review. *Biomedical Journal*. 2025;48(3):100802. doi:10.1016/j.bj.2024.100802
5. Xu J, Vaeggemose M, Schulte RF, et al. PyAMARES, an Open-Source Python Library for Fitting Magnetic Resonance Spectroscopy Data. *Diagnostics*. 2024;14(23):2668. doi:10.3390/diagnostics14232668

Comparison of the robustness of manual spectral line integration and automated spectral line fitting for deuterium-labeled metabolomics

Fatima Anum 1*, Marco Banzhaf 2, Meike Nienaber 2, Tom Ruge 2, Stephan Doerfel 2, Jan Bernd Hövener 1, Andrey Pravdivtsev 1

1 Department of Radiology and Neuroradiology, Section Biomedical Imaging, University Hospital Schleswig-Holstein, Kiel University, Kiel, Germany

2 University of Applied Sciences, Kiel University, Sokratesplatz 1, 24149 Kiel.

Abstract: Precise quantification of deuterium-labeled substrate and metabolite peaks is essential for kinetic modeling in deuterium magnetic resonance spectroscopy (DMRS) and imaging. However, manual integration is often time-consuming, user-dependent, and affected by spectral noise. We developed an automated, user-friendly pipeline applying Lorentzian fitting to NMR kinetics. We compared performance of this tool with manual integration (Mestre Nova/Origin) for analyzing ^2H spectra from *Saccharomyces cerevisiae*. Kinetic parameters were similar; however, automated pipeline showed 53% decrease in relative standard deviation of HDO reference spectrum, minimizing uncertainties in metabolic parameters evaluation. By standardizing baseline handling and eliminating operator bias, automated workflow improves reliability and efficiency of DMRS analysis, offering robust, scalable metabolic processing pipeline.

Motivation: Metabolism is essential for comprehending cellular function. Mass spectrometry (MS) and nuclear magnetic resonance (NMR) spectroscopy are key analytical modalities used to study metabolism. While MS is highly sensitive, it is invasive and needs processed samples to study metabolism. NMR, on the other hand, is a non-invasive technique that enables both static and dynamic metabolic monitoring. However, conventional ^1H NMR suffers from signal overlap in intact biological systems due to macromolecular interference, such as proteins and lipids.

DMRS offers a practical alternative. It has recently demonstrated both preclinical¹ and clinical relevance² and requires only a deuterium-compatible MR setup for metabolic flux analysis. Deuterium labeling is a safe and relatively straightforward process. Although ^2H suffers from inherently lower sensitivity due to its reduced gyromagnetic ratio, it exhibits favorable relaxation properties that permit extensive signal averaging and improved signal-to-noise (SNR) ratios in metabolic measurements.

Despite these benefits in acquisition, the post-processing of DMRS data, e.g., peak quantification, remains unaddressed. DMRS quantification relies heavily on manual processing, which is time-precise spectral peak fitting. Manual integration—though commonly used—is time-consuming, operator-dependent, and particularly error-prone when dealing with noisy ^2H spectra from dynamic biological systems. To address this limitation, we developed an automated application that uses Lorentzian fitting for reliable and efficient peak analysis. This study evaluates its performance against manual methods in quantifying deuterium-labeled biomolecules in *Saccharomyces cerevisiae*³, aiming to establish a standardized and scalable pipeline for metabolic flux studies using DMRS.

Materials & Methods: Yeast suspensions were analyzed using a Bruker Advance NEO (WB400) NMR spectrometer (9.4 T), following injection of deuterium-labeled compounds such as [2,3- $^2\text{H}_2$]fumarate (Fum-d2) and [3,3,3- $^2\text{H}_3$]pyruvate (Pyr-d3) to monitor metabolic flux (Figure 2). Free induction decays (FIDs) were acquired at defined time points using TopSpin software.

For HDO, 130 spectra were recorded every 140 s, with 8 signal averages per spectrum and repetition time (TR) of 17.5 s. For Fum-d2, 130 spectra were acquired every 92 s, with 8 scans and a TR of 11.5 s. The 4.7 ppm HDO resonance was used as an internal reference standard. All experiments were conducted in phosphate-buffered saline (PBS) at a concentration of 50 mM.

Mestre Nova was used in the manual workflow to correct baseline and integrate peak area of raw spectral data. The SNR/mM for HDO and Fum-d2 were 1.33 and 2.0 per scan, increasing to approximately 3.8 and 5.7 respectively, after 8 averages, indicating low concentrations required signal averaging. Integrated peak areas were then imported to Origin, where mono-exponential fitting was used to extract kinetic parameters.

The same spectra were used for the automated workflow and processed with developed software. This pipeline automatically reads data description files, spectral inputs, then aligns peak positions using HDO as reference, and applies optimized fitting for time-dependent DMRS spectra. Performance was evaluated by comparing HDO quantification variability via interquartile range (IQR), coefficient of variation (CV), and median absolute deviation (MAD). Kinetic parameters (rate constants) derived from Fum-d2 decay were compared between methods to assess agreement.

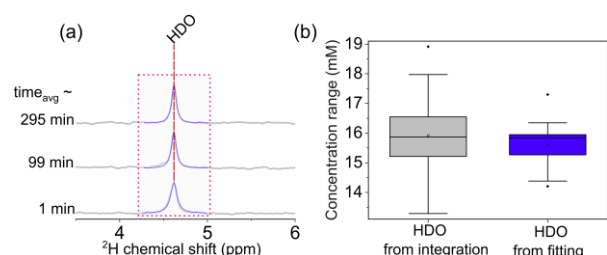


Fig. 1: Validation of automated line fitting using HDO reference signal. DMRS of HDO (grey) with Lorentzian fitting (purple) demonstrating reliable peak identification (a). Box plot compares [HDO] obtained from manual integration (grey) vs. automated fitting (blue) (b). The pink box in (a) is a region used for manual integration.

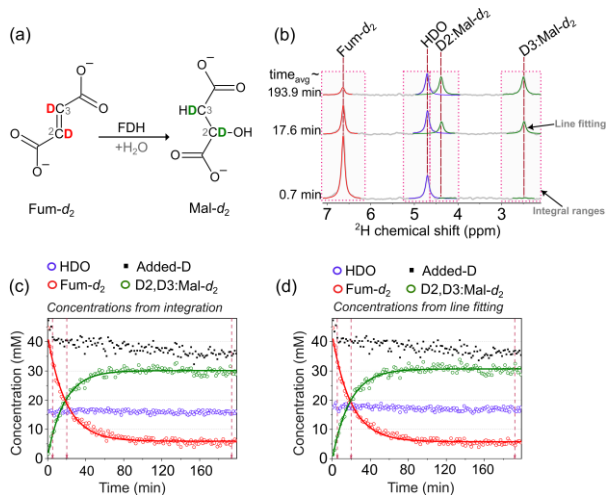


Fig. 2: [2,3-2H₂]fumarate (Fum-d₂) metabolism in *Saccharomyces cerevisiae*. Reaction pathway showing Fum-d₂ conversion into [2,3-2H₂]malate (Mal-d₂) (a). ^2H NMR spectra (grey) with automated fits of Fum-d₂ (red), HDO (purple), and Mal-d₂ (green) signals (b). Kinetics and mono-exponential fits derived from manual integration (c) and automated line fitting (d).

Results: Automated Lorentzian fitting significantly improved the consistency of quantification for the HDO internal reference signal compared to manual integration. The IQR of HDO concentrations decreased from 1.34 (manual) to 0.68 (automated), indicating a 49% reduction in variability. Additionally, the CV decreased from 22.6% to 10.5%, and the MAD was reduced by nearly 80%. These changes demonstrate that the automated workflow performs better in handling baseline noise and mitigating inconsistencies introduced by operators, thereby enhancing the reliability of spectral quantification (Figure 1).

For kinetic modeling, both workflows were used to analyze Fum-d₂ conversion to [2,3-2H₂]malate (Mal-d₂), a process complicated by overlapping peaks of HDO and malate, which the automated workflow efficiently resolved. Mono-exponential decay fitting yielded very similar rate constants: $k_{\text{fm}} = (0.0561 \pm 0.0017) \text{ min}^{-1}$ (manual) vs. $k_{\text{fm}} = (0.0539 \pm 0.0017) \text{ min}^{-1}$ (automated). This close agreement shows that the automated method for tracking metabolic dynamics is reliable in a quantitative way (Figure 2).

Discussion: The automated Lorentzian fitting method enhanced the robustness of the DMRS analysis by reducing errors, such as baseline-dependent errors and operator variability, which are commonly associated with the manual process. The decrease in variability matrices, such as IQR and CV, for HDO signal quantification indicates that automated

processing yields more precise and consistent results than the manual method.

For dynamic metabolic tracking (Fum-d₂), both workflows yielded nearly identical k_{fm} , indicating that the automated method maintains quantitative accuracy in modeling kinetic changes while reducing the time for the data analysis.

These results suggest that automated fitting works well with both stable and changing signals, even in cases of peak overlap, such as between Mal-d₂ and HDO. It simplifies the post-processing workflow, eliminates subjective handling, and facilitates standardized analysis across users and time points.

Overall, the pipeline is a strong alternative to manually integrating DMRS data. It supports reproducibility in metabolite quantification, making it possible to utilize it in larger metabolic flux analysis applications.

Conclusion: Automated Lorentzian fitting was a reliable and efficient method for analyzing our DMRS data. It made HDO quantification more consistent and gave kinetic parameters similar to those found by manual integration. One limitation of this study is that it employed a single model. In the future, tests should examine more general conditions, such as lower SNR and more complex spectra from other nuclei, such as ^{13}C and ^{15}N . Even so, the pipeline enhances spectral consistency, handles overlapping peaks, and reduces user bias, making it a suitable choice for high-throughput metabolic flux analysis with deuterium-labeled compounds.

Acknowledgements: We acknowledge our funding from German Federal Ministry of Education and Research (BMBF) with framework of e:Med research funding concept (01ZX1915C), BMBF hyperquant consortium (BlueHealthTech, 03WIR6208A9), DFG (555951950, 527469039, 469366436, HO-4602/3, EXC2167, FOR5042, TRR2879), Medical Faculty of Kiel University for financial support of the project, MOINCC was funded by the grant from the European Regional Development Fund (ERDF) and the Zukunftsprogramm Wirtschaft of Schleswig-Holstein (Project no. 122-09-053).

References:

- Dessau, H. *et al.* In vivo ^1H -MR spectroscopy and imaging of hepatic metabolic formation of trimethylamine-N-oxide. *Magn. Reson. Med.* doi:10.1002/mrm.30531 (2025).
- De Feyter, H. M. *et al.* Deuterium metabolic imaging (DMI) for MRI-based 3D mapping of metabolism in vivo. *Sci. Adv.* 4, eaat7314 (2018).
- Anum, F. *et al.* Probing intracellular yeast metabolism with deuterium magnetic resonance spectroscopy. Preprint at <https://doi.org/10.21203/rs.3.rs-5312977/v1> (2024).

Deep learning-based velocity anti-aliasing of 4D-flow MRI for intracranial vasculature

Lisa Artmann 1*, Socrates Gebremedhin 1*, Ngoc My Nguyen 1*, Roise Tomy 1*, Alper Atici 2, Alissa Saleh 2, Duygu Dengiz 3, Jan-Bernd Hövener 2, Olav Jansen 4, Naomi Larsen 4, Tillmann Schwörer 1, Stephan Doerfel 1, Mariya Pravdivtseva 2

1 Institute for Data Science, Kiel University of Applied Sciences, Kiel, Germany

2 Department of Radiology and Neuroradiology, Section Biomedical Imaging, University Hospital Schleswig-Holstein, Kiel University, Kiel, Germany

3 Institute for Materials Science, Faculty of Engineering, Kiel University, 24143 Kiel, Germany

4 Department of Radiology and Neuroradiology, University Hospital Schleswig-Holstein, Kiel, Germany

Abstract: 4D flow MRI enables in vivo assessment of blood flow but is often affected by artifacts such as velocity aliasing. Manually correcting these artifacts is time-consuming, and while automated algorithms exist, they often fail to detect all aliased regions. Recent deep learning approaches have shown success in correcting aliasing in the aorta. We propose a U-Net-based deep learning model trained on both in vivo and in vitro 4D flow MRI datasets with simulated aliasing. Our model generalizes beyond the aorta and outperforms state-of-the-art Laplacian-based algorithms, demonstrating that aliasing patterns can be effectively learned from 2D data. This approach offers a scalable solution for automated aliasing correction across diverse vascular regions.

Motivation: 4D flow MRI is a non-invasive imaging technique that provides comprehensive information on blood flow velocity [1]. To acquire 4D flow MRI data, the velocity encoding (venc) parameter must be set prior to the imaging. This parameter should not exceed the maximum expected velocity in the vessel to avoid velocity aliasing artifacts. However, maximum velocities are typically unknown in advance and vary substantially between individuals and vascular regions. The venc should be selected according to the expected maximum flow rate, because too high venc values result in misinterpretation of slower flowing particles, but too low venc values misinterpret fast particles.

This challenge is particularly relevant in pathologies such as intracranial aneurysms, where blood flow in the aneurysm sac is slow while flow in the parent vessel remains high. Using a moderate venc may minimize aliasing within the sac better but lead to aliasing in higher flow regions. Recent work has shown that deep learning approaches can successfully correct aliasing in large vessels like the aorta [2].

In this study, we investigate the potential of a machine learning-based method to correct velocity aliasing in 4D flow MRI of intracranial vasculature, aiming to improve the accuracy and reliability of hemodynamic assessments in cerebrovascular diseases.

Materials & Methods: The study included in total 40 in vitro 4D flow MRI datasets, comprising aneurysm models, straight tubes, and ventricular models, also 11 in vivo datasets from the brain, neck, and aorta. Some subjects and models were imaged multiple times using varying MRI parameters, such as venc, spatial and temporal resolution.

All 4D flow MRI scans were first segmented using the magnitude profile statistic values to estimate the far end tails for segmentation. Images were resized to incorporate the flow regions and minimize the noise areas. Each dataset was

manually inspected for velocity aliasing artifacts. Datasets without aliasing were used for training, while those exhibiting aliasing were excluded from training. Two 4D flow MRI scans were used exclusively for the test set, two for the validation set, and 20 for the training set. Ground truth for velocity aliasing was generated by lowering the venc. The voxels exceeding this lowered venc threshold were marked as aliased and saved in a binary mask. As a benchmark, 3D and 4D Laplacian-based unwrapping algorithms [3] were used.

A convolutional neural network, based on the U-Net [4] architecture, was trained using Dice Loss [5] and the Adam optimizer [6]. The training set was augmented with flips, rotations, zooming, translation, and shear. To balance the dataset, some non-aliased slices were excluded during training. Validation data were used for early stopping and overfitting monitoring. The test set was used exclusively post-training to evaluate generalizability. Performance of the U-Net and a Laplacian-based algorithm were assessed using Dice score, precision, and recall.

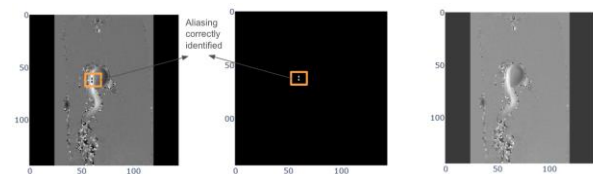


Fig. 1: Demonstration of U-Net performance on an in vitro 4D flow MRI dataset of intracranial aneurysm model. The original phase-contrast MRI image (left) shows regions with velocity aliasing (indicated by orange box). The middle panel displays the binary mask generated by the U-Net. The right panel shows the corrected phase image.

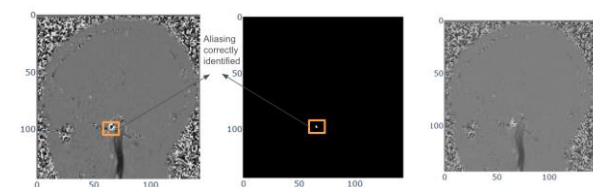


Fig. 2: Demonstration of U-Net performance on in vivo 4D flow MRI of the internal jugular vein. The original image (left) shows velocity aliasing (orange box), the middle panel shows the U-Net's binary mask, and the right panel shows the corrected image. Not all aliased voxels were identified by the network.

Test Scan / Filename	3D Laplacian-based	4D Laplacian-based	UNET
In vitro scan with venc 30	0.74	0.78	0.90
In vitro scan with venc 37	0.67	0.69	0.82
In vitro scan with venc 45	0.47	0.62	0.57
In vivo brain scan with venc 40	0.29	0.46	0.54
In vivo brain scan with venc 50	0.80	1.00	0.20

Fig. 3: Comparison of Dice scores. U-Net outperformed 3D and 4D Laplacian-based algorithms in three of five test scans, especially with high aliasing. The 4D Laplacian-based algorithm outperformed the 3D in all scans. One in vivo scan with venc 60 showed no aliasing and was excluded to avoid division by zero.

Results: The anti-aliasing model could identify aliased voxels. It performed better on in vitro test data (Fig. 1) than in vivo (Fig. 2), with notably higher Dice score (76% compared to 37%) and precision of 68% compared to 26%. The recall improved as well with in vitro values of 92% compared to 88% in vivo on flow patterns similar to the training set, while novel flow regions showed lower performance. Additionally, the model performed best in regions with low aliasing, achieving an average Dice score of 86%, precision 93% and recall 85%, while medium and high aliasing regions yielded progressively lower dice scores of 61%, precision 94%, recall 62% and dice score 40% precision 73%, recall 41%, respectively. Across three out of five datasets, the U-Net model demonstrated superior performance compared to the traditional Laplacian-based algorithm in terms of average Dice score (Fig. 3).

Discussion: The deep learning model performed better on unseen data with shapes similar to the predominantly in vitro training data, while performance on in vivo data—underrepresented in training—was lower. This limitation could likely be mitigated by incorporating a larger and more diverse dataset in future work.

Performance seemed to depend heavily on the segmentation algorithm. Several methods, such as the region growing algorithm [7], were implemented, some of which resulted in poor performance of the U-Net. The reasons for these differences in performance were not investigated further and could be examined in future research.

The Laplacian-based algorithm gave high precision scores but had lower scores for recall. The Laplacian-based algorithm is

a bit conservative i.e, it only flags the most obvious instances of aliasing, thus avoiding errors but likely missing subtle cases. It was reported previously that the Laplacian-based algorithm performs worse for smaller vessels, when aliasing occurs at vessel walls or when the wrapped area is too large and fills the entire vessel, or if the dataset has low resolution [3].

Conclusion: The U-Net framework successfully learned the spatial patterns from two-dimensional labelled data, which are complex and non-linear, with little to no assumptions on the structure or context. Generating labels using simulated masks provided the model pixel wise information that can be used to correctly identify relevant patterns and ignore irrelevant ones.

Results show promising applications of CNN networks to predict aliasing patterns as there is clear evidence of improved performance relative to Laplacian-based approaches, implying that these models can learn aliasing patterns even from a relatively small number of datasets. However, given limited variety in our training data, we do see non-generalization behaviours that could, however, be mitigated with more diverse datasets in future work.

Acknowledgements: We gratefully acknowledge the continued research support by Philips Healthcare, Hamburg, Germany, and Siemens Healthineers, Erlangen.

References:

1. Dyverfeldt P. 4D flow cardiovascular magnetic resonance consensus statement. *J Cardiovasc Magn Reson.* 2015:19.
2. Berhane H, Scott MB, Barker AJ, et al. Deep learning-based velocity antialiasing of 4D-flow MRI. *Magn Reson Med.* 2022;88(1):449-463
3. Loecher M, Schrauben E, Johnson KM, Wieben O. Phase unwrapping in 4D MR flow with a 4D single-step laplacian algorithm. *J Magn Reson Imaging JMRI.* 2016;43(4):833-842
4. Ronneberger O, Fischer P, Brox T. U-Net: Convolutional Networks for Biomedical Image Segmentation. In: Navab N, Hornegger J, Wells WM, Frangi AF, eds. *Medical Image Computing and Computer-Assisted Intervention – MICCAI 2015.* Cham: Springer International Publishing; 2015:234-241
5. Milletari F, Navab N, Ahmadi SA. V-Net: Fully Convolutional Neural Networks for Volumetric Medical Image Segmentation. In: *2016 Fourth International Conference on 3D Vision (3DV).* 2016:565-571
6. Kingma DP, Ba J. Adam: A Method for Stochastic Optimization. 2017.
7. Adams R, Bischof L. Seeded region growing. *IEEE Trans Pattern Anal Mach Intell.* 1994;16(6):641-647

J-coupling interactions and Hydrogen/Ligand Exchange in SABRE-pyruvate Systems

Charbel D. Assaf*¹, Oleg G. Salnikov², Vladimir Zhivonitko³, Anna P. Yi², Simon B. Duckett⁴, Eduard Chekmenev⁵, Igor V. Koptug², Jan-Bernd Hövener¹, Andrey N. Pravdivtsev¹

¹ Department of Radiology and Neuroradiology, Section Biomedical Imaging, University Hospital Schleswig-Holstein, Kiel University, Kiel, Germany
² International Tomography Center SB RAS, 3A Institutskaya St., 630090 Novosibirsk, Russia
³ NMR Research Unit, Faculty of Science, University of Oulu, P.O. Box 3000, Oulu, Finland
⁴ Centre for Hyperpolarization in Magnetic Resonance (CHyM), University of York, Heslington YO10 5NY, UK
⁵ Department of Chemistry, Integrative Biosciences, Karmanos Cancer Institute, Wayne State University, Detroit, MI 48202, US

Abstract: We present a study of chemical and physical interactions during SABRE hyperpolarization of pyruvate. Using frequency-selective SEPP-SPINEPT and an enhanced SEPP-SPINEPTplus-SABRE sequence, we probe specific 1H–13C interactions and the exchange dynamics between free and bound pyruvate. Our results reveal how DMSO (co-substrate) and temperature modulate intracomplex exchange, while pyruvate dissociation remains slow and largely unaffected by other variables. These findings, supported by high-field spin order transfer (SOT) experiments, offer key parameters for simulating and optimizing SABRE efficiency.

Motivation: Signal Amplification by Reversible Exchange (SABRE) is a nuclear spin polarization technique that enhances the signal of target substrates such as pyruvate (pyr) by exploiting the reversible interaction of parahydrogen (pH₂) and a substrate with an iridium-based polarization transfer catalyst. The hyperpolarization step is mediated by J-coupling interactions within this transient complex. By selectively exciting protons in the SABRE complex, we can probe directly the 1H–13C couplings that govern polarization transfer to pyruvate(1) and any exchange rates involved in this process(2,3); these are critical parameters for optimizing the efficiency and yield of SABRE hyperpolarization

Materials & Methods: Frequency-selective excitations can be used to refine this method to allow it to probe individual J-coupling interactions between specific protons and 13C nuclei within the SABRE complex. To disentangle these interactions, we therefore employ frequency-selective excitation of polarization using PASADENA (SEPP), followed by a frequency-selective spin order transfer INEPT sequence (SPINEPT), or a fully frequency-selective variant known as SEPP-INEPT (Fig. 1A). This approach enables selective polarization transfer to the carbon nuclei of bound pyruvate within the SABRE complex.

To extend this method, we introduce an additional 180° pulse to generate net polarization on both free and bound substrates, followed by two 90° pulses separated by a variable evolution delay t_e , allowing us to probe the exchange process between bound and free pyruvate. This enhanced sequence is referred to as SEPP-SPINEPTplus-SABRE (Fig. 1B).

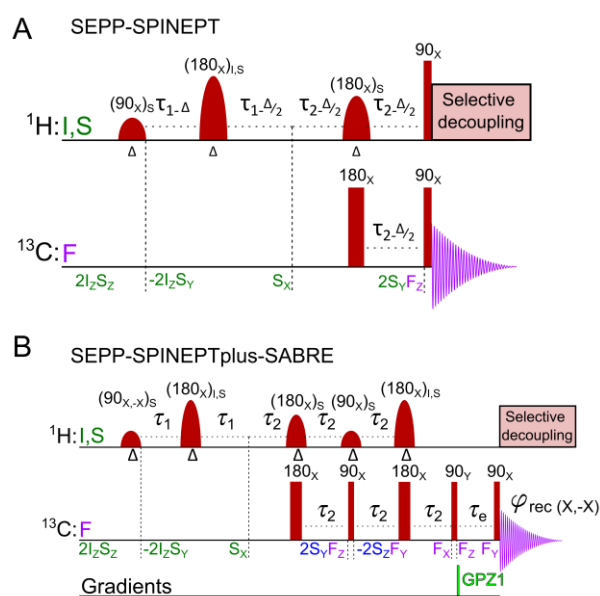


Fig. 1: (A) Scheme of 1H–13C selective spin order transfer SEPP-SPINEPT, and (B) SEPP-SPINEPTplus-SABRE sequences. In these sequences, we set the excitations such that no more than two spins are excited simultaneously, enabling us to probe interactions between two spins, 1H–13C J-couplings (A), and chemical exchange (B).

Results: By incorporating variable temperature analysis, we probe eight distinct 1H–13C J-coupling interactions (Fig. 2) that govern pyruvate-SABRE polarization. This enabled us to estimate exchange rates and determine the activation energies associated with pyruvate and H₂ binding and release. Additionally, we investigate the influence of [H₂], [DMSO], [pyruvate], and temperature on the chemical exchange pathway.

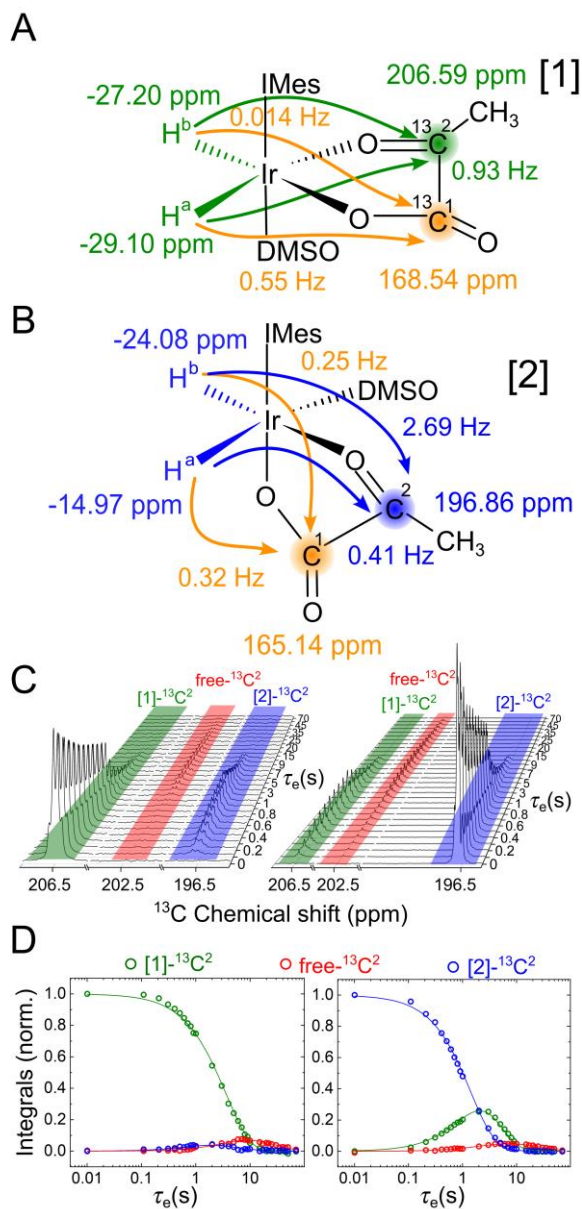


Fig. 2: Eight distinct ^1H - ^{13}C interactions that govern pyruvate-SABRE polarization in complexes [1] (A) and [2] (B). Corresponding ^{13}C NMR spectra at 265 K showing selective signal from $^{13}\text{C}_2$ carbon of complex [1] (C, left) and complex [2] (C, right). The associated kinetic profiles of signal integrals are shown in (D).

Discussion: So far, the best estimates for spin-spin interactions have been achieved by combining SOT measurements at ultra-low magnetic fields with DFT calculations. While our experimental methods enabled us to determine the magnitude of J-coupling interactions, their sign remains undetermined. Building on this, our study further sheds light on the exchange dynamics between pyruvate-bound forms in SABRE complexes. DMSO concentration and temperature strongly influence the transition between different binding modes, whereas hydrogen and pyruvate concentrations have minimal impact. At low [DMSO], the forward exchange rate is significantly slower than the reverse, but both rates converge, though at high [DMSO], supporting a kinetic role for DMSO in stabilizing specific complex structures. Pyruvate dissociation remains slower than internal exchange, underscoring the fact that complex rearrangements govern the dynamics. These insights help guide future optimization of polarization transfer in SABRE systems.

Conclusion: These insights advance the SABRE technique by enabling accurate simulations and experimental tuning of chemical exchange dynamics and spin-spin interactions. The parameters obtained in this study will be used to optimize SOT numerically, paving the way for even stronger hyperpolarization of pyruvate via SABRE. This method and its results will play a key role in facilitating the further development of SABRE as an emerging hyperpolarization technology

Acknowledgements: We acknowledge funding from the German Federal Ministry of Education and Research (BMBF) within the framework of the e: Med research and funding concept (01ZX1915C), DFG (555951950, 527469039, 469366436, HO-4602/2-2, HO-4602/3, GRK2154-2019, EXC2167, FOR5042, TRR287). MOIN CC was founded by a grant from the European Regional Development Fund (ERDF) and the Zukunftsprogramm Wirtschaft of Schleswig-Holstein (Project no. 122-09-053).

References:

1. Assaf et al, *J. Phys. Chem. Lett.* 2024, 10.1021/acs.jpcllett.3c02980.
2. Salnikov et al, *Anal. Chem.* 2024, 10.1021/acs.analchem.4c01374.
3. Assaf et al, *Commun. Chem.* 2024, 10.1038/s42004-024-01376-z.

Open-Source, Modular 4D-Flow MRI Pre-Processing Pipeline for research applications

Alper Atici 1, Alissa Saleh 1, Jan-Bernd Hövener 1, Olav Jansen 2, Naomi Larsen 2, Mariya Pravdivtseva 1

1 Department of Radiology and Neuroradiology, Section Biomedical Imaging, University Hospital Schleswig-Holstein, Kiel University, Kiel, Germany

2 Department of Radiology and Neuroradiology, University Hospital Schleswig-Holstein, Kiel, Germany

Abstract: We present a Python-based pre-processing pipeline for 4D flow MR imaging data. The pipeline supports multi-format data import (XMLREC, PARREC, DICOM, RAW), enabling metadata analysis and automated pre-processing. Preprocessing includes background correction via subtraction or polynomial fitting, static tissue and noise masking, and segmentation. Furthermore, the acquired data can be exported at each step as raw data or a data format compatible with 3D visualization softwares. The modular design facilitates integration into custom workflows and batch processing. This tool aims to streamline early-stage image analysis, ensuring automated reproducibility and flexibility across imaging modalities.

Motivation: 4D flow MRI is a powerful imaging technique that enables time-resolved, three-dimensional visualization of blood flow¹. It is routinely used in cardiovascular applications, offering insights into blood flow patterns that are not accessible with conventional imaging methods. Despite its potential, 4D flow MRI is not yet widely used in neurovascular clinical applications². Major barriers include the long examination times and the complex pre-processing required, such as correcting imaging artifacts like background phase errors, eddy currents, and velocity aliasing.

While commercial software solutions for 4D flow MRI pre-processing are available, they are often targeted at larger arteries like the aorta. Moreover, some of them are not compatible with various data formats or MRI system vendors, and do not allow for automated or customizable workflows. Additionally, the high cost of these tools can restrict access, particularly in resource-limited settings. Similarly,

currently available open-source solutions are also often lack support for multiple data types and MRI vendors³, or limited to a specific 4D flow MRI application.

To address these challenges, we aim to develop a modular, open-source pipeline for the pre-processing of 4D flow MRI data. This pipeline is designed to support flexible data import and customizable pre-processing steps. Crucially, it enables export in data formats used in other open-source software, making it suitable for integration with 3D visualization and analysis tools, such as ParaView. By focusing on reproducibility, adaptability, and accessibility, our tool seeks to bridge the gap between advanced imaging capabilities and practical research or clinical workflows.

Materials & Methods: The pipeline was implemented entirely in Python, utilizing established scientific libraries including NumPy, SciPy, Pydicom, and SimpleITK for numerical operations, signal processing, and image I/O. Custom modules were developed to support data import from multiple formats, including XMLREC, PARREC, DICOM, and RAW binary files. Metadata is automatically extracted using

format-specific parsers, and optional user-defined rules allow contextual filtering or batch-level parameter setting.

Background phase correction can be performed using two approaches: voxel-wise subtraction of the flow signal using a reference scan acquired without applied flow⁴, or by applying a plane-fitting method, where a polynomial function is fit to the static tissue signal and subtracted from each voxel⁵. The static tissue mask was created using thresholding of the velocity standard deviation and the 4D flow MRI magnitude signal. The segmentation was implemented using a seeded region-growing algorithm⁶.

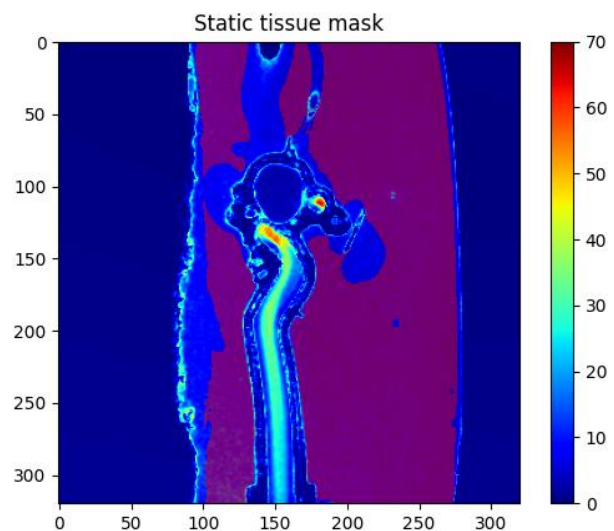


Fig. 1: Visualization of the static tissue mask (purple) overlaid on the measured average velocity.

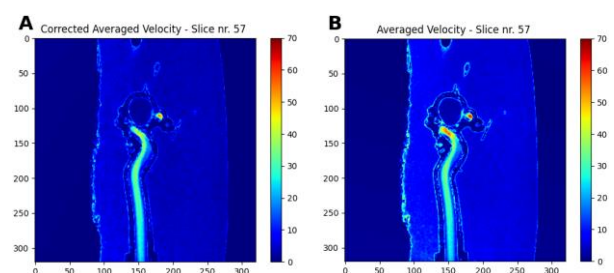


Fig. 2: Comparison of the corrected (A) and uncorrected (B) velocity volume of a given slice. The average velocity within the corrected slice is more homogeneous.

Results: The pipeline was implemented and tested on the following 4D flow MRI data formats: PARREC, DICOM, and XMLREC, acquired using Siemens Healthineers, Philips Healthcare, and Bruker MRI systems. It successfully imported and processed data across all supported formats, with

accurate metadata parsing and consistent file handling. After loading the data from a DICOM dataset, an exemplary slice was extracted, and the static tissue mask was applied (Fig. 1).

Through the voxels of the static tissue mask, a second-order polynomial function was fit, allowing the subtraction of the background correction phase from the dataset (Fig. 2).

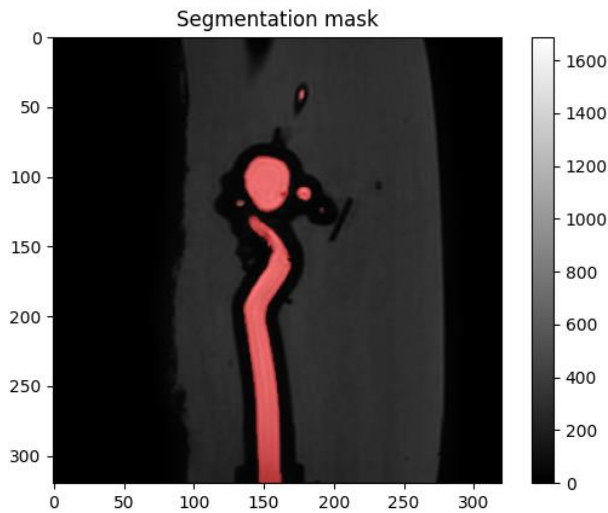


Fig. 3: Segmentation mask (red) visualized on the measured magnitude image.

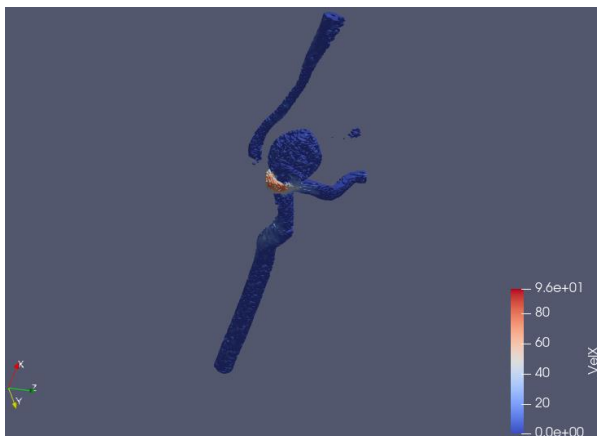


Fig. 4: Exemplary image of the pre-visualization within ParaView, using the exported VTK-File.

The preliminary result was exported as a raw data file, storing the numerical values, along with a corresponding JSON file that contained the data shape and type. After correction, the flow of interest was segmented (Fig. 3).

Afterwards, the results were exported to VTK (Visualization Toolkit) format for 3D visualization and flow analysis (Fig. 4).

VTK exports maintained spatial consistency and were compatible with common visualization tools, including ParaView and 3D Slicer. Exported data retained full image resolution and voxel dimensions, enabling downstream quantitative analysis. Furthermore, the preliminary result was imported back, potentially allowing the segmentation of another region of interest on the same corrected dataset.

Discussion: Both the segmentation and static tissue mask module demonstrated good and reliable results across datasets, as visually inspected. The static tissue mask calculation is highly efficient, as static tissue usually exhibits a low standard deviation within the measured velocity, but a high magnitude signal, compared to noise or similar background signals. However, the performance of the background correction needs to be evaluated in the future by implementing numerical comparisons of uncorrected and corrected data.

While the current segmentation module supports basic operations, future iterations could benefit from integration with AI-driven methods to enhance robustness and precision. Moreover, although VTK export works well for most downstream applications, supporting other standardized outputs (e.g., NIfTI, HDF5) would broaden the pipeline's utility. Additionally, the velocity anti-aliasing needs to be implemented, as it is a commonly occurring artifact in 4D flow MRI.

Compared to other solutions, the presented pipeline aims to support several data types and vendors, allowing unrestricted research. Furthermore, the modular structure encourages community-driven extension, and open-source release could facilitate collaboration and adoption. Moreover, the current adaptability ensures applicability in diverse 4D flow MRI contexts, from animal and human studies to in vitro research. In the future, logging and parameter documentation may further enhance reproducibility, helping users trace preprocessing steps for auditing or troubleshooting.

Conclusion: The development of this open-source pipeline marks a step toward more standardized and accessible pre-processing for 4D flow MRI. By enabling automated, flexible and reproducible workflows across diverse data formats, it supports more consistent image analysis and lowers the barrier to entry for researchers without access to expensive commercial tools. This promotes broader adoption of 4D flow MRI in research and facilitates translational efforts toward clinical use. With its open-source, modular design, the pipeline is well-positioned to evolve through community contributions and integration of advanced methods, ultimately fostering more reproducible and scalable imaging workflows in 4D flow MRI imaging.

Acknowledgements: We gratefully acknowledge the continued research support by Philips Healthcare, Hamburg, Germany, and Siemens Healthineers, Erlangen, Germany.

References:

1. Dyverfeldt, P. 4D flow cardiovascular magnetic resonance consensus statement. *J. Cardiovasc. Magn. Reson.* 19 (2015).
2. Schnell, S., Wu, C. & Ansari, S. A. 4D MRI flow examinations in cerebral and extracerebral vessels. Ready for clinical routine? *Curr. Opin. Neurol.* 29, 419–428 (2016).
3. Roberts, G. S. et al. Automated Hemodynamic Assessment for Cranial 4D Flow MRI. *Magn. Reson. Imaging* 97, 46–55 (2023).
4. Chernobelsky, A., Shubayev, O., Comeau, C. R. & Wolff, S. D. Baseline Correction of Phase Contrast Images Improves Quantification of Blood Flow in the Great Vessels. *J. Cardiovasc. Magn. Reson.* 9, 681–685 (2007).
5. Walker, P. G. et al. Semiautomated method for noise reduction and background phase error correction in MR phase velocity data. *J. Magn. Reson. Imaging* 3, 521–530 (1993).
6. Adams, R. & Bischof, L. Seeded region growing. *IEEE Trans. Pattern Anal. Mach. Intell.* 16, 641–647 (1994).

Implementation, and Assessment of Methods for Improved Temperature Mapping

Laura Bauer^{1*}, Mingming Wu¹, Valéry Ozenne², Max Seidensticker¹, Olaf Dietrich¹

¹ Department of Radiology, LMU University Hospital, LMU University, Munich, Germany

² Univ. Bordeaux, CNRS, CRMSB, UMR 5536, IHU Liryc, Bordeaux, France

Abstract: Magnetic resonance (MR) thermometry enables non-invasive, spatially resolved temperature monitoring during thermal therapies. However, its application for focal microwave tissue ablation can be challenged by heat-induced susceptibility artifacts that distort local magnetic fields. These artifacts produce misleading temperature maps, falsifying thermal dose calculations. To address this, we simulated susceptibility artifacts using a custom Python framework that integrates quantitative susceptibility mapping dipole convolutions and superimposes dipole fields to synthetic temperature data. The resulting data enables systematic study of temperature mapping and demonstrates the feasibility of artifact removal. This work lays the groundwork for developing robust real-time correction methods.

Motivation: Magnetic Resonance (MR) thermometry is a powerful non-invasive technique for monitoring temperature changes in biological tissues. It is well-established for applications like hyperthermia⁴, and is also used to monitor focal tissue ablation with interstitial microwave applicators.^{3,5} The possibility of MR thermometry to provide temporally and spatially resolved temperature maps makes it valuable for precise thermal dose delivery and real-time feedback during therapeutic interventions. However, the accuracy and reliability of MR thermometry can be significantly hampered by various artifacts. Of those, particularly heat-induced susceptibility artifacts pose a substantial challenge.⁶

Susceptibility artifacts arise from local variations in magnetic susceptibility, often due to gas or air bubbles generated by tissue vaporization during microwave ablation, leading to distortions in the magnetic field.⁶ These distortions result in phase differences in the MR data, which are misinterpreted as temperature changes. These temperature changes falsify the resulting temperature map and lead to incorrect calculations of the temperature field and the thermal dose. Typically, these artifacts manifest as characteristic dipole-shaped hot and cold regions aligned along the main magnetic field (B_0).

The primary motivation of simulating susceptibility artifacts in MR thermometry is to gain a comprehensive and controlled understanding of their origin and impact on temperature quantification. This should help in characterizing artifacts, understanding their origin and developing correction algorithms. An ultimate goal is developing a robust real-time correction method.

Materials & Methods: Real-time MR thermometry data was acquired on a 1.5-tesla clinical MR system (Magnetom SolaFit, Siemens Healthineers, Erlangen). Temperature mapping was performed using the proton resonance frequency (PRF) shift method, which uses the linear dependence of the proton resonance frequency on temperature. Data acquisition was performed with a single-shot gradient-echo echoplanar imaging pulse sequence (TE: 23 ms, TR: 1 respiratory cycle, matrix 128x128, 23 slices). During interventions, real-time temperature monitoring and visualization were performed

with a dedicated workstation (Certis Solution, Certis Therapeutics, Pessac, France), providing immediate thermal feedback at the target area.²

Post-treatment, the acquired DICOM image series, including magnitude and phase data, were exported for offline analysis. Custom scripts developed in Python were used for detailed temperature map reconstruction and artifact assessment (see Fig. 1).¹

After assessing multiple real data sets the emergence of susceptibility artefacts were documented. It became clear that it is necessary to simulate the artifacts for better and controlled understanding.

A custom Python tool was utilized to simulate these artifacts. Specifically, we generate a 4D phase array by simulating susceptibility artifacts via quantitative susceptibility mapping (QSM) dipole convolution to generate a 4D phase evolution array, producing synthetic phase images with realistic susceptibility-induced distortions. These were superimposed on simulated temperature data to create temperature maps containing the artifact. The original simulated heating can be seen in fig. 2.

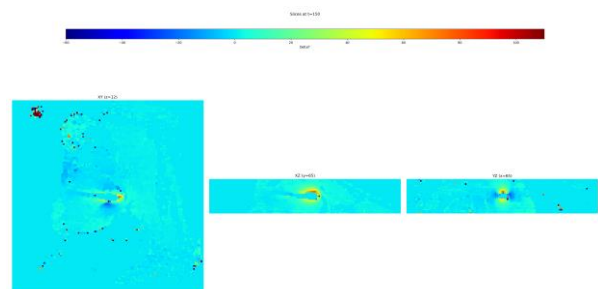


Fig. 1: MR thermometry data acquired on a 1.5-tesla clinical MR system (TE: 23 ms, TR: 1 respiratory cycle, matrix 128x128, 23 slices) - Temperature map reconstruction using the proton resonance frequency (PRF) shift method in custom Python scripts.

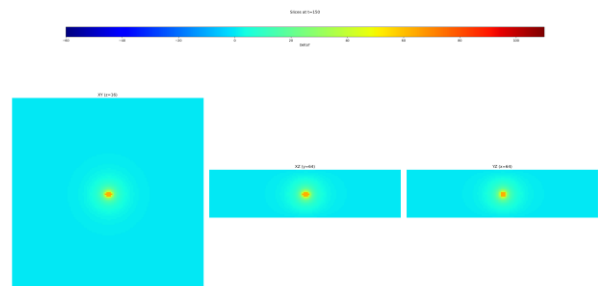


Fig. 2: Simple temperature simulation of microwave tumor ablation.

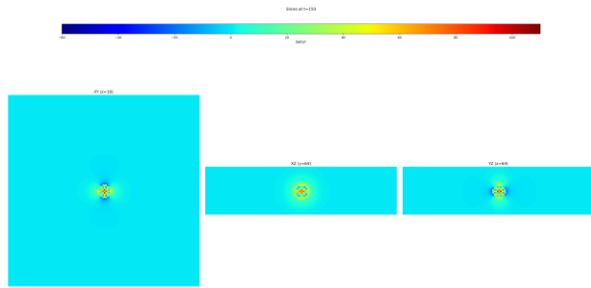


Fig. 3: Superimposed image from simple temperature simulation of microwave tumor ablation and artifact created from QSM dipole convolution.

Results: The simulation of susceptibility artifacts successfully reproduced susceptibility artifacts with the expected characteristic dipole patterns aligned along B_0 , closely matching observations in clinical data (see Fig. 3). This allowed for the creation of a comprehensive simulated temperature map that accurately incorporated the effects of susceptibility-induced field inhomogeneities.

Subsequent processing demonstrated the feasibility of artifact removal. By converting the simulated temperature map back into its unwrapped phase representation, the previously introduced susceptibility artifact could be removed, indicating the potential for robust correction strategies in real-world data.

Discussion: Future efforts will explore the use of the Laplacian boundary value (LBV) method to remove the artificial artifact. Another route to explore is using susceptibility artifacts of various gas bubble sizes and finding the best correction artifact to the simulated temperature map. Further investigations at different angles of the microwave applicator needle relative to B_0 can improve adjusting applicator

orientation and imaging planes to mitigate dipole effects in clinical datasets. The findings of these future steps will hopefully help mitigate artifacts in real data and possible even in real-time.

Conclusion: While this study is an early step, our simulation approach offers valuable insight into susceptibility artifacts in MR thermometry. It opens avenues for developing effective correction strategies, with the long-term goal of enhancing the accuracy of temperature monitoring during microwave ablation.

Acknowledgements: This project is supported by Deutsche Forschungsgemeinschaft (DFG) in course of the ANR/DFG partner project SMART-HEAT.

References:

1. Ozenne V, Bour P, Faller T, Desclides M, Denis de Senneville B, Öcal O, Lentini S, Seidensticker M, Dietrich O, Quesson B. Evaluation of a deformable image registration algorithm for image-guided thermal ablation of liver tumors on clinically acquired MR-temperature maps. *Med Phys*. 2025 Feb;52(2):722-736. doi: 10.1002/mp.17526.
2. Öcal O, Dietrich O, Lentini S, Bour P, Faller T, Ozenne V, Maier F, Fabritius MP, Pühr-Westerheide D, Schmidt VF, Öcal E, Seidensticker R, Wildgruber M, Ricke J, Seidensticker M. Predicting liver ablation volumes with real-time MRI thermometry. *JHEP Rep*. 2024 Aug 31;6(11):101199. doi: 10.1016/j.jhepr.2024.101199.
3. Dietrich O, Lentini S, Öcal O, Bour P, Faller TL, Ozenne V, Ricke J, Seidensticker M. Accuracy of 3D real-time MRI temperature mapping in gel phantoms during microwave heating. *Eur Radiol Exp*. 2024 Aug 14;8(1):92. doi: 10.1186/s41747-024-00479-5.
4. Wu, M. MR Thermometry for Monitoring mild Radio-Frequency Hyperthermia, Dissertation, TUM Munich School of Bioengineering. 2020
5. Lubner MG, Brace CL, Hinshaw JL, Lee FT Jr. Microwave tumor ablation: mechanism of action, clinical results, and devices. *J Vasc Interv Radiol*. 2010 Aug;21(8 Suppl):S192-203. doi: 10.1016/j.jvir.2010.04.007. PMID: 20656229; PMCID: PMC3065977.
6. Boehm C, Goeger-Neff M, Mulder HT, Zilles B, Lindner LH, van Rhoon GC, Karampinos DC, Wu M. Susceptibility artifact correction in MR thermometry for monitoring of mild radiofrequency hyperthermia using total field inversion. *Magn Reson Med*. 2022 Jul;88(1):120-132. doi: 10.1002/mrm.29191. Epub 2022 Mar 21. PMID: 35313384.

Evaluation of Various Cross-Linking Agents for Tunable MRI Relaxation Times in Multimodal Phantoms

Lucas Bolster 1+2, Manoj Jayaram Gowda 3, Alper Atici 1, Haoyi Qiu 3, Jan-Bernd Hövener 1, Olav Jansen 5, Leonard Siebert 3+4, Mariya Pravdivtseva 1

1 Department of Radiology and Neuroradiology, Section Biomedical Imaging, University Hospital Schleswig-Holstein, Kiel University, Kiel, Germany
2 University of Utah, Salt Lake City, USA
3 Functional Nanomaterials, Department of Materials Science, Kiel University, Germany
4 Kiel Nano, Surface and Interface Science (KINSIS), Kiel University, Germany
5 Department of Radiology and Neuroradiology, University Hospital Schleswig-Holstein, Kiel, Germany

Abstract: Multimodal imaging phantoms can improve the validation of medical imaging protocols and be a useful tool for clinicians to practice with, yet most lack MRI compatibility. This study investigates the use of gadolinium (Gd), nickel (Ni), and manganese (Mn) as cross-linking agents in hydrogel phantoms to independently tune MRI T1 and T2 relaxation times. MRI measurements on phantoms with varying concentrations revealed that Ni enables a broad, controllable range of T1 and T2 values, while Gd requires sub-1% concentrations for optimal results, and Mn is still under investigation. These findings pave the way for cost-effective, customizable multimodal phantoms.

Motivation: Most phantoms used in medical practice and research are designed to be suited for one modality and single purpose, e.g., ultrasound (US) or computed tomography (CT) imaging. Since all radiological procedures depict different aspects of the human body, multi-modality in phantoms is a necessary quality for process validation, training, and surgery practice. Recently, we developed cost-effective hydrogel phantoms with mechanically tunable properties, like density and elastic modulus, for use in multimodal ultrasound (US) and computed tomography (CT)1 imaging. Combining these with MRI would create versatile multimodal phantoms. However, tuneability of the hydrogel system for MRI contrast is not addressed yet.

This work seeks to build on existing fabrication methods used for CT and US phantoms to create a multimodal phantom that adds accurate and controllable MRI signal variations independent of the contrast in other imaging modalities. Previously, it was shown that ion doping in agarose gel-based phantoms can effectively alter T1 and T2 times², so this project aims to independently control relaxation times in hydrogel-based phantoms by incorporating these ions as cross-linking agents in the phantom fabrication process.

Materials & Methods: Hydrogel phantoms were fabricated using gadolinium (Gd), nickel (Ni), and manganese (Mn) as cross-linking agents to study their effect on MRI signal contrast. MRI experiments were performed on a 3T MRI system (Siemens Healthineers, Cima X) using a 64-ch head coil. In the first experiment, phantoms with Gd concentrations of 0% (pure hydrogel), 1%, and 10% were used in addition to two tubes of tap water. A spin echo (SE) sequence with varied repetition times ([TR], 15, 30, 70, 100, 300, 700, 1000, 3000, 7000, and 10000 ms) was acquired to calculate T1. A SE sequence with a TR of 3000 ms and varied echo times ([TE], 7, 10, 20, 30, 50, 70, 100, 300, 700, and 1000 ms) was measured to calculate T2.

In the second experiment, phantoms with Mn and Ni concentrations of 25%, 50%, and 100% were used in addition to one pure hydrogel, one water, and one oil phantom. An inversion recovery SE sequence with varied inversion times ([TI], 50, 100, 500, 1500, 2500, 5000 ms) was used to calculate T1. A SE sequence with varied echo times ([TE] 7.2, 8, 10, 15, 50, 100, 150, 300 ms) was used to calculate T2.

Acquired images were segmented using thresholding (Fig. 1), and the average signal in each phantom was evaluated against TR and TE for the Gd phantoms to calculate T1 and T2, respectively. Likewise, the average signal in each of the Mn and Ni phantoms was evaluated against TI and TE and pixel-wise T1 and T2 maps were created for all experiments.

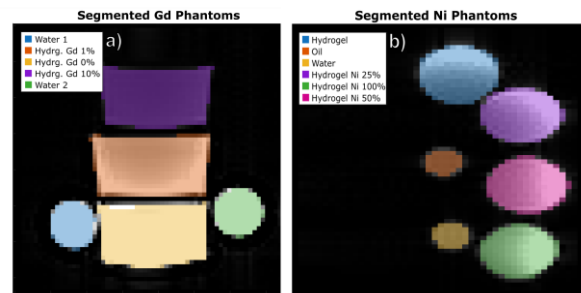


Fig. 1: Representative SE MRI images from the first (a) and second (b) experiments, showing hydrogel phantoms alongside water and oil vials. Note that in (b), the Mn-containing phantoms were placed in the imaging frame but did not produce any detectable signal. Binary masks outlining each phantom are overlaid on the images.

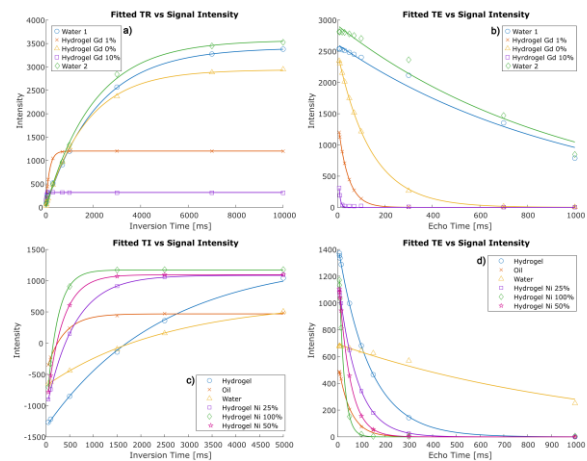


Fig. 2: Fitted relaxation curves calculated for each experiment: for the phantoms containing Gd, T1 recovery (a) and T2 decay curves (b) and for the phantoms containing Ni, T1 recovery (c) and T2 decay curves (d).

a)

	Water 1	Water 2	Pure Hydrogel	Hydrogel Gd 1%	Hydrogel Gd 10%
T1 [ms]	2165.44	2027.75	1760.67	151.83	18.93
T2 [ms]	998.96	976.27	139.87	42.86	6.21

b)

	Water	Oil	Pure Hydrogel	Hydrogel Ni 25%	Hydrogel Ni 50%	Hydrogel Ni 100%
T1 [ms]	2585.28	352.64	2453.63	740.57	330.65	225.39
T2 [ms]	1106.85	51.63	132.58	79.77	48.16	21.18

Fig. 3: Tables of T1 and T2 values resulting from the fitted recovery and decay curves in the phantoms containing Gd (a) and the phantoms containing Ni (b).

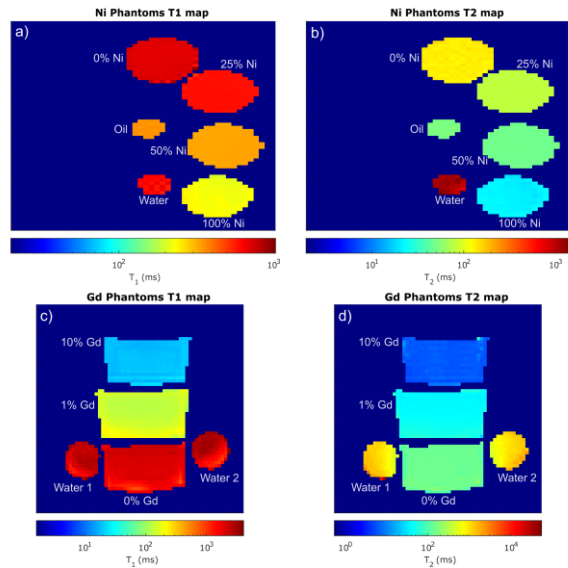


Fig. 4: T1 and T2 maps from the experiments: T1 (a) and T2 (b) for phantoms containing Ni, and T1 (c) and T2 (d) maps for phantoms containing Gd.

Results: The pure hydrogel phantom had a calculated T1 of 2165.44 ms and a T2 of 139.87 ms in the first experiment and a T1 of 2453.63 ms and a T2 of 132.58 ms in the second experiment. T1 and T2 times decreased substantially with the presence of all ions, as seen in the fitted signal curves (Fig. 2, Fig. 3) and T1 and T2 maps (Fig. 4). T1 and T2 times of Gd and Ni phantoms decreased with increasing concentration of the cross-linking agent. In the 1% Gd phantom, a maximum T1 of 151.83 ms and T2 of 42.86 ms was observed. In the Ni cross-linked phantoms, T1 values ranged from 225.39 and 740.57 ms with concentrations of 100% and 25%, respectively. T2 values ranged from 21.18 to 79.77 ms with concentrations of 100% and 25% respectively. None of the Mn phantoms present in the second experiment registered any signal in any variation of TI and TE, indicating T1 and T2 times less than the minimum TE time (7.2 ms) used in the experiments.

Discussion: Even small amounts of Gd had a significant effect on T1 and T2. 1% Gd for cross-linking resulted in a T1 of 151.83

ms and T2 of 42.86 ms which is lower than reported values³ at 3T for fat tissue around 350 and 100 ms, respectively, so concentrations of less than 1% Gd should still be tested. With relaxation times that are too short to give a substantial signal, hydrogel cross-linked with Mn should be tested with concentrations in the sub-1% range as well. Investigated concentrations of Ni covered a broader T1 value range of biological tissues, ranging from fat to white matter³. However, Gd and Mn may be more suitable candidates for multimodal phantoms, as even small amounts can significantly alter the MRI properties without noticeably affecting other key characteristics such as density and elasticity.

While the results of Ni and Gd phantoms were promising, further work is required to fully integrate this data with existing multimodal phantoms. First, lower concentrations of Gd and Mn should be tested to fit relaxation times to a range of biological values. So far, this has only been an investigation on the viability of different cross-linking agents. With this data, we can begin optimizing for specific T1 and T2 in a single phantom and casting geometries that mimic human anatomy. Additionally, Hydrogels cross-linked with Mn, Ni, and Gd should be mechanically characterized and evaluated using CT and US to ensure that new phantoms retain similar properties to previously developed hydrogel phantoms.

Conclusion: This work demonstrates that ion cross-linked hydrogels using Gd, Mn and Ni offer a promising approach to creating MRI-compatible multimodal phantoms. Future research should focus on refining Gd, Mn and Ni concentrations, characterizing mechanical and imaging properties across modalities, and developing anatomically realistic phantom geometries. These advances will support improved validation, calibration, and cross-platform imaging studies, ultimately enhancing both research capabilities and clinical imaging accuracy.

Acknowledgements: We gratefully acknowledge the continued research support by Siemens Healthineers, Erlangen, Germany.

References:

1. Qiu H, Nazarens J, Egeler B, Thode T, Osman F, Osmonov D, Bahr J, Kaps S, Siebert FA, Koch R, Lützen U, Adelung R, Siebert L. Hydrogel System with Independent Tailoring of Mechanics, CT, and US Contrasts for Affordable Medical Phantoms. *ACS Mater Lett.* 2024 Sep 26;6(10):4847-4853.
2. Kraft KA, Fatouros PP, Clarke GD, Kishore PR. An MRI phantom material for quantitative relaxometry. *Magn Reson Med.* 1987 Dec;5(6):555-62. doi: 10.1002/mrm.1910050606. PMID: 3437816.
3. Jorge Zavala Bojorquez, Stéphanie Bricq, Clement Acquitter, François Brunotte, Paul M. Walker, Alain Lalonde. What are normal relaxation times of tissues at 3 T? *Magn Reson Med.* 2017 Jan; Volume 35, Pages 69-80, ISSN 0730-725X.

The importance of RF-pulse-timing for B0- and B1-insensitivity in a T2-prep module

Lukas Bönsel 1+2*, Daniel Giese 1+2, Frederik Laun 2, Peter Speier 1

1 Research & Clinical Translation, Magnetic Resonance, Siemens Healthineers AG, Erlangen, Germany

2 Friedrich-Alexander-Universität Erlangen-Nürnberg, Institute of Radiology, Uniklinikum Erlangen, Erlangen, Germany

Abstract: T2-preparation is challenged by B0- and B1-inhomogeneities across field strengths. While composite and adiabatic pulses improve robustness, they increase SAR. This study investigates how the timing of excitation and flip-back pulses in a simple hard pulse T2-prep design affects robustness in three flip-back schemes: -90°_x , 270°_x , and a composite $270^\circ_x-[-360^\circ]_x$ variant. Bloch-simulations reveal that optimal pulse timing significantly enhances performance. Well-timed excitation and -90°_x flip-back pulses improve robustness by up to 152.1% over naive timing and even outperform the composite scheme with naive timing by 32.9%. These findings show that correct timing alone can match or even surpass the robustness of SAR-intensive designs, offering low-SAR alternatives for robust T2-preparation.

Motivation: Early detection of coronary artery disease (CAD) is critical, as lifestyle interventions for patients with prehypertension or stage I hypertension can reduce 10-year CAD risk by up to 14% [1]. Here, coronary MR angiography (MRA) may enable detection of CAD providing robust visualization of proximal and mid-coronary segments. However, imaging of distal and branching vessels benefits from the increased signal-to-noise ratio (SNR) available at higher field strengths [2]. T2-prepared MRA sequences enhance contrast between blood and myocardium without the high specific absorption rate (SAR) burden associated with magnetization transfer contrast (MTC). Standard T2-prep modules rely on an excitation pulse, one or more refocusing pulses and a final flip-back pulse [3]. Studies have demonstrated improved contrast-to-noise ratio (CNR) and visualization of the blood pool using T2-prep [4]. Especially at higher field strengths, B0- and B1-inhomogeneities - as well as cardiac wall motion and flow - pose challenges in achieving uniform magnetization preparation [5, 3]. While various T2-prep designs incorporating adiabatic excitation, composite pulses, and Malcolm-Levitt phase cycling (MLEV) have been proposed to increase robustness against these challenges, they typically incur an increased SAR [3]. To the best of our knowledge, the precise timing of the excitation and flip-back pulses relative to their respective virtual echoes has not been systematically addressed in the existing literature. This work therefore investigates the effect of different timings of the excitation and flip-back pulse on the B0-B1-robustness for three different flip-back pulse approaches.

Materials & Methods: A Bloch-simulation without considering relaxation was performed in C++ using rectangular hard pulses. The simulated T2-prep module was a Carr-Purcell-Meiboom-Gill (CPMG) sequence consisting of a 90°_x excitation pulse, two 180°_y refocusing pulses, and a flip-back pulse. Unlike Brittain et al. [5, 6], no MLEV or composite refocusing schemes were employed. All pulses were applied at a constant reference B1-amplitude ($\omega_{1,ref}=2\pi$). The period of free evolution between refocusing and echo formation was set to $13.02 \cdot t_{180}$ (t_{180}

= duration of a refocusing pulse) to match the inter-echo spacing in [5, 6]. Flip-back pulse variants included a -90°_x (original), a 270°_x , and a composite $270^\circ_x-[-360^\circ]_x$ (originally proposed by [7]) scheme. Corresponding timing tables are shown in Fig. 1. Simulations were performed across a range of off-resonances ($\pm 0.16 \cdot \omega_{1,ref}$, 1000 samples) and B1-amplitudes ($\omega_{1,ref}=[0.1,2.0] \cdot \omega_{1,ref}$, 190 samples). For each combination, the resulting normalized longitudinal magnetization M_z/M_{eq} was computed and visualized as a 2D heatmap. To assess the effect of pulse timing for the individual flip-back variants, simulations with temporal offsets to the naive timing, applied to both the excitation and flip-back pulses, were performed (using correction factors: $cF_{exc}, cF_{fb} = [-t_{90}, +t_{90}]$, t_{90} = duration of the excitation pulse). For each timing, the high-signal region ($M_z \geq 0.95 \cdot M_{eq}$) was identified. Robustness to B0- and B1-inhomogeneity was then quantified by computing the maximum extent along the off-resonance-axis and the minimum extent along the B1-axis of the high-signal region within the respective masks (Fig. 2c). The dimensions were multiplied, serving as a measurement for total B0-B1-robustness, specified as Insensitivity.

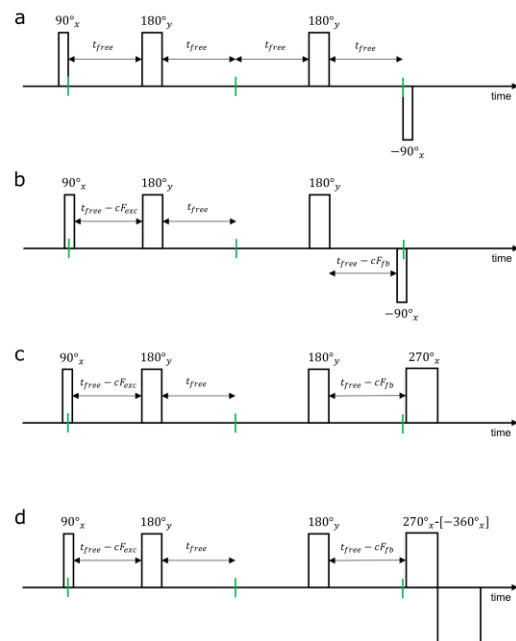


Fig. 1: Timing tables in case of naive timing for the -90°_x flip-back variant (a) and in case of optimal timing for -90°_x (b), 270°_x (c) and the composite $270^\circ_x-[-360^\circ]_x$ (d) scheme. Remark: 180°_y refocusing pulses are centred around the echo maxima (indicated by the green markers).

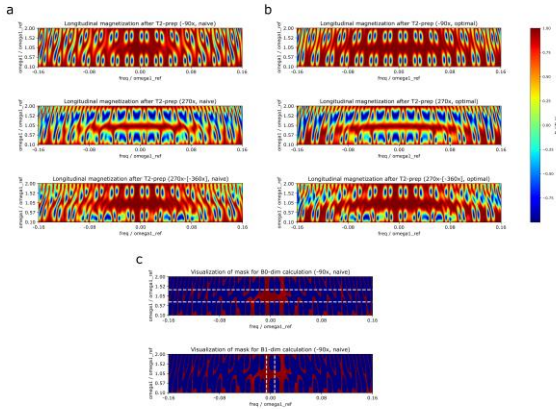


Fig. 2: Longitudinal magnetization after T2-prep across B0- and B1-inhomogeneities for naive timing (a) and optimal timing (b) for three flip-back approaches: -90°_x, 270°_x, 270°_x-[-360°_x] (top to bottom). (c) Visualization of a down-ramped heatmap including the masks (= areas in between the white dashed lines) for B0-dim (top) and B1-dim (bottom) determination.

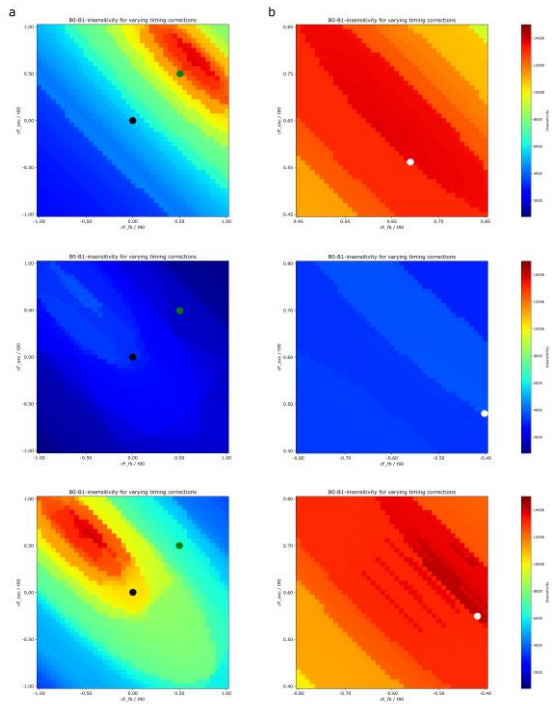


Fig. 3: Heatplots illustrating B0-B1-robustness over varying timing corrections within the range [-t₉₀, +t₉₀] (a) and within a zoomed-in range close to the respective optimal timing (b). From top to bottom: -90°_x, 270°_x, 270°_x-[-360°_x].

Flip-back variant	Timing (cF _{exc} , cF _{fb})	Insensitivity (B0-dim, B1-dim)	Gain with respect to naive timing (%)
-90° _x	naive	5445 (165, 33)	-
	cF = t ₉₀ /2	11319 (343, 33)	+107.9%
-90° _x	optimal	13728 (416, 33)	+152.1%
	(cF _{exc} = 0.56 · t ₉₀ , cF _{fb} = 0.69 · t ₉₀)		
270° _x	naive	3200 (320, 10)	-
270° _x	cF = t ₉₀ /2	1683 (187, 9)	-47.4%
270° _x	optimal	3740 (374, 10)	+16.9%
	(cF _{exc} = 0.48 · t ₉₀ , cF _{fb} = -0.40 · t ₉₀)		
270° _x -[-360° _x]	naive	10329 (313, 33)	-
270° _x -[-360° _x]	cF = t ₉₀ /2	6496 (203, 32)	-37.1%
270° _x -[-360° _x]	optimal	14256 (432, 33)	+38.0%
	(cF _{exc} = 0.55 · t ₉₀ , cF _{fb} = -0.42 · t ₉₀)		

Fig. 4: Insensitivities evaluated with the specified metric for all flip-back variants further distinguishing between different timings including naive timing, timing using a correction factor of cF=t₉₀/2 and the individually determined optimal timing.

Results: 2D heatmaps of the normalized longitudinal magnetization M_z/M_{eq} across B0- and B1-variations are illustrated in Fig. 2a-b for all three flip-back schemes for both naive timing and the calculated optimal timing conditions. For each flip-back approach the Insensitivity (as specified in Methods) over timing of the excitation and flip-back pulses is shown in Fig. 3a for a timing correction range of [-t₉₀, +t₉₀] and in Fig. 3b for a zoomed-in range close to the individual optimal timings. Insensitivities globally ranged between [2695, 13728] for the -90°_x flip-back pulse, [837, 3740] for the 270°_x flip-back pulse and [3500, 14256] for the composite flip-back variant, respectively. The Insensitivities for the different flip-back approaches in case of naive timing (black dots in Fig. 3a), optimal timing (white dots in Fig. 3b), and an alternative timing correction of cF_{exc}=cF_{fb}=0.50·t₉₀ (green dots in Fig. 3a) – a strategy potentially applied in prior studies – are listed in Fig. 4. Among all tested configurations, the composite flip-back 270°_x-[-360°_x] achieved the highest robustness under optimal timing (cF_{exc}=0.55·t₉₀, cF_{fb}=-0.42·t₉₀), closely followed by the optimally timed -90°_x variant (cF_{exc}=0.56·t₉₀, cF_{fb}=0.69·t₉₀). The 270°_x scheme performed worst, only reaching a maximum Insensitivity of 3740 despite timing correction (cF_{exc}=0.48·t₉₀, cF_{fb}=-0.40·t₉₀). Timing optimization improved robustness across all variants compared to the naive timing (Fig. 4). For a 90°_x excitation, -90°_x flip-back sequence design, centering both pulses on the virtual echoes (reflecting the described alternative timing correction) yielded an Insensitivity of 11319.

Discussion: Without timing correction, the composite flip-back scheme demonstrates superior robustness. This advantage over the -90°_x variant is consistent with the mechanism motivated in [6], arguing the identical effective B-field axis orientation during excitation and flip-back (initial 270°_x pulse) to facilitate a more accurate spin realignment along the longitudinal axis under off-resonance conditions - primarily enhancing B0-robustness. However, a pure 270°_x flip-back pulse amplifies B1-amplitude errors, resulting in poor B1-tolerance. In our simulations, this degradation outweighs the B0-related improvements, making the 270°_x variant the least robust overall. To mitigate this, literature proposes a composite 270°_x-[-360°_x] design, which improves robustness in off-resonance-direction without getting worse in B1-direction, as confirmed by our results. Timing optimization enhances robustness across all flip-back schemes, though to varying degrees. The -90°_x variant shows the largest improvement, with a 152.1% increase in Insensitivity compared to its uncorrected form. In contrast, the composite scheme shows a more modest gain of 38%. Ultimately, both timing corrected versions achieve comparable overall robustness (Fig. 2a-b, 4). Notably, the timing-optimized -90°_x variant outperforms the composite scheme using naive timing by 32.9%, indicating that precise pulse placement can not only recover but potentially exceed the robustness typically achieved by the SAR-intensive alternative. In case of the naive -90°_x scheme the high-signal region (central red area) in the down-ramped magnetization heatmaps (=0 if $M_z/M_{eq} < 0.95$) (Fig. 2c) closely resembles the 95% area illustrated in the isoline plots reported in [6], indicating that timing was likely not explicitly optimized in that and related studies, motivating our work.

Conclusion: This work demonstrates that precise timing of the excitation and flip-back pulses in T2-preparation modules significantly enhances robustness to B0- and B1-inhomogeneities. The SAR-efficient -90°_x flip-back variant, when properly timed, outperforms the naive implementation of the composite $270^\circ_x[-360^\circ_x]$ flip-back approach by up to 32.9% and even shows comparable performance to the respective timing-optimized $270^\circ_x[-360^\circ_x]$ scheme. Importantly, replacing the composite flip-back pulse with a standard -90°_x pulse significantly reduces RF-energy deposition by the deposition of three refocusing pulses, effectively halving the total flip angle and thus the required energy in our two-refocusing-pulse T2-prep design. It is shown that careful pulse timing can potentially yield high robustness to variations in B0 and B1 without relying on SAR-intensive methods. These findings highlight the importance of timing as a yet underexplored parameter in T2-prep design, offering the opportunity to improve uniformity in magnetization preparation, particularly in SAR-constrained high-field cardiac imaging.

Acknowledgements: The author gratefully acknowledges the technical support and valuable discussions provided by the

supervisors at Siemens Healthineers. Thanks also go to Prof. Laun at FAU for his academic supervision.

References:

- [1] Maruthur, N. M., Wang, N. Y., & Appel, L. J. (2009). Lifestyle interventions reduce coronary heart disease risk: results from the PREMIER Trial. *Circulation*, 119(15), 2026-2031.
- [2] Kim, W. Y., Danias, P. G., Stuber, M., Flamm, S. D., Plein, S., Nagel, E., ... & Manning, W. J. (2001). Coronary magnetic resonance angiography for the detection of coronary stenoses. *New England Journal of Medicine*, 345(26), 1863-1869.
- [3] Jenista, E. R., Rehwald, W. G., Chen, E. L., Kim, H. W., Klem, I., Parker, M. A., & Kim, R. J. (2013). Motion and flow insensitive adiabatic T2-preparation module for cardiac MR imaging at 3 Tesla. *Magnetic resonance in medicine*, 70(5), 1360-1368.
- [4] Botnar, R. M., Stuber, M., Danias, P. G., Kissinger, K. V., & Manning, W. J. (1999). Improved coronary artery definition with T2-weighted, free-breathing, three-dimensional coronary MRA. *Circulation*, 99(24), 3139-3148.
- [5] Nezafat, R., Stuber, M., Ouwerkerk, R., Gharib, A. M., Desai, M. Y., & Pettigrew, R. I. (2006). B1-insensitive T2 preparation for improved coronary magnetic resonance angiography at 3 T. *Magnetic Resonance in Medicine: An Official Journal of the International Society for Magnetic Resonance in Medicine*, 55(4), 858-864.
- [6] Brittain, J. H., Hu, B. S., Wright, G. A., Meyer, C. H., Macovski, A., & Nishimura, D. G. (1995). Coronary angiography with magnetization-prepared T2 contrast. *Magnetic resonance in medicine*, 33(5), 689-696.
- [7] Shaka, A. J., & Freeman, R. (1983). Composite pulses with dual compensation. *Journal of Magnetic Resonance* (1969), 55(3), 487-493.

Liberating pTx from Vendor Lock-in: Open-Source Cross-Vendor Parallel Transmit MRI Sequences by extending pTx-Pulseq to Siemens UHF Scanners

Dario Bosch 1+2+3*, Thomas Roos 4, and Klaus Scheffler 1+2

1 Department for Ultra-High Field MRI, Max Planck Institute for Biological Cybernetics, Tübingen, Germany

2 Institute for Biomedical Magnetic Resonance, University Hospital Tuebingen, Germany

3 Core Facility for Magnetic Resonance Imaging, Medical Faculty, University Hospital Tübingen, Germany

4 Department of Radiology, High Field MRI group, University Medical Center Utrecht, Utrecht, Netherlands

Abstract: We present an extension of the Pulseq environment to support parallel transmission (pTx) functionality on Siemens ultra-high field MRI scanners, addressing the lack of cross-vendor compatibility in MRI pulse sequences. Our modified Pulseq interpreter handles pTx pulses by converting them into Siemens' proprietary .ini format. Experimental validation was performed on Siemens 9.4T and 7T scanners, demonstrating successful integration of pTx pulses into Pulseq sequences. The results show identical B1+ maps compared to vendor-provided sequences and successful execution of arbitrary pTx RF waveforms. This advancement facilitates open-source, cross-vendor MRI sequence design, enhancing educational and research applications in MRI technology.

Motivation: Current MRI pulse sequences are often vendor-specific and limited to a single generation of scanners, hindering the development of open-source and cross-vendor compatible sequences. Pulseq [1] solves this problem by providing an open-source environment for cross-vendor sequence programming and execution. However, support for parallel transmission (pTx) functionality has been lacking in Pulseq, even though it is an invaluable technique required at ultra-high field (UHF). Solutions for pulse-specific RF shimming in Pulseq have been presented in the past [2], but they only supported a single manufacturer and generation of MRI scanner. Recently, Roos et al. presented an online full pTx extension for Pulseq that would run on Philips scanners. In this work, we adapt the approach and present a cross-platform version of pTx Pulseq, that allows to perform RF shimming and free waveform pTx on multiple generations of Siemens MRI scanners, while remaining compatible with the earlier solution for Philips scanners.

Materials & Methods: Pulseq uses vendor-specific interpreter software to execute pulse sequences on MRI scanners. We modified the Pulseq v1.4.3 interpreter for Siemens scanners to manage parallel transmit (pTx) pulses. Following Roos et al. [2], each pTx pulse's waveforms are concatenated into one long waveform. Siemens MRI systems require pTx pulses in a proprietary .ini format, so our interpreter converts these pulses automatically upon sequence loading. During execution, internal bookkeeping ensures correct RF waveforms for each pTx pulse, supporting numerous pTx pulses per sequence. For efficiency, pTx pulses describable by a single waveform and an RF shim are converted to that format. Helper functions for embedding pTx pulses are available for both Matlab and Python Pulseq toolboxes.

Experimental validation occurred on Siemens Magnetom Plus 9.4T and Terra.X 7T scanners with software versions "VE12U" and "XA70," respectively. Compatibility with the older "VB17a" version is experimental and untested. We acquired relative single-channel B1+ maps using a vendor-provided

GRE sequence and compared them to a Pulseq equivalent. A 3D pre-saturated Turboflash [3] sequence for absolute pTx B1+/B0 mapping was implemented in Pulseq. B1+ and B0 maps were reconstructed in Python, and FastPtx [4] calculated a free waveform pTx pulse for homogeneous excitation, used in a 3D gradient echo sequence.

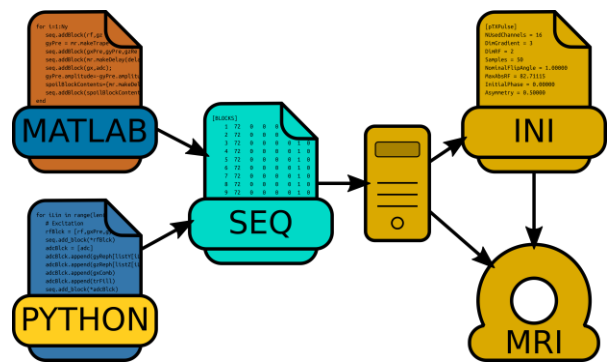


Fig. 1: The workflow of applying arbitrary pTx pulses in pulseq sequences on Siemens MRI scanners. Matlab or Python can be used to create the .seq file describing the sequence. The Pulseq interpreter on the scanner console reads the .seq file and converts the pTx pulse to a .ini file. The sequence can then play out the pTx pulse.

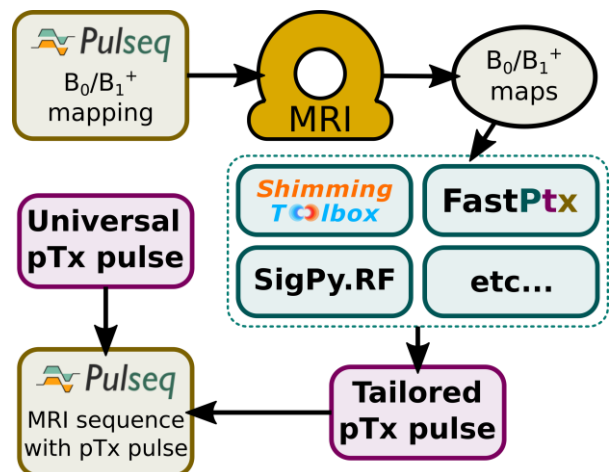


Fig. 2: An open-source pTx workflow, complete from B1 mapping to image acquisition. With pTx support in Pulseq, all steps can be implemented in an open-source cross-vendor compatible fashion, from B1/B0 mapping to imaging sequence.

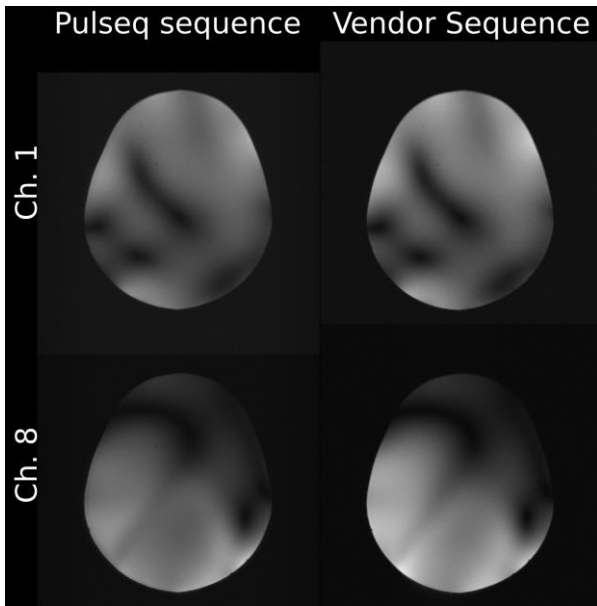


Fig. 3: Individual channel GRE images in a phantom, recorded with the Pulseq interpreter (left) and a vendor-provided sequence (right)

Results: Relative B1+ maps acquired with pulseq were compared to those acquired with the vendor-provided sequence and appeared identical (Fig. 3). Arbitrary pTx RF waveforms were successfully played out in a 3D GRE sequence with the excitation pattern looking as expected. Existing pTx pulse design tools could be seamlessly integrated into a measurement/pulse design workflow. When using our proposed pulseq interpreter, vendor specific pulse sequence programming for pTx use is no longer required. Thus, we were able to use pTx pulses in open-source cross-vendor compatible Pulseq sequences.

Discussion: We have demonstrated an extension to the Siemens Pulseq interpreter that allows for an arbitrary number of RF shims and free waveform pTx pulses in open

source sequence design. While many algorithms for pTx pulse design have been published as open-source, most sequences for the necessary B1+ mapping and for using the optimized pTx pulses have been closed source in vendor-specific frameworks. They can now be written in an easily interchangeable way. We have used this extension in several ongoing projects, allowing us to easily integrate pTx capabilities into new experimental sequences. In education, we have been able to provide students with the means to interface the pTx system after only a short learning process. Fig. 2 shows a pTx workflow like the one used in this work, which is completely open-source except for the MRI scanner itself. Optimizing pTx pulses in the given workflow still is a process that requires manual intervention on an external computer. It is, however, conceivable to fully integrate the open-source pTx optimization process with the Pulseq interpreter. This would allow for a fully automated one-click solution, similar to what some vendors are starting to offer in their proprietary systems.

Conclusion: With Pulseq now supporting pTx for MRI scanners from two major vendors, open and reproducible research can now also benefit from pTx technologies. The modified interpreter has proven to be reliable and useful in several occasions. Support for the new pulseq version v1.5.0 has been implemented recently. The modified interpreter for Siemens MRI scanners is available to Siemens customers upon request.

Acknowledgements: The authors want to thank the Pulseq team for providing their open-source software. Funding by the European Research Council (ERC Advanced Grant No 834940, SpreadMRI) is gratefully acknowledged.

References:

1. Layton et al., *MRM* (2017):1544-1552
2. Roos et al., *ISMRM*, 2024, #1149;
3. Bosch et al., *MRM* (2022):322-330
4. Bosch and Scheffler, *MAGMA* (2024):127-138

Measuring liver and kidney relaxation times at 7 T

Petr Bulanov¹⁺², Petr Mentshchikov¹, Johannes A. Grimm¹⁺², Niklas Himburg³⁺⁴, Simon Schmidt¹, Stephan Orzada¹, Mark E. Ladd¹⁺²⁺⁵ and Sebastian Schmitter¹⁺³⁺⁶

¹ Division of Medical Physics in Radiology, German Cancer Research Center (DKFZ), Heidelberg, Germany

² Faculty of Physics and Astronomy, Heidelberg University, Heidelberg, Germany

³ Medical Physics and Metrological Information Technology, Physikalisch-Technische Bundesanstalt (PTB), Braunschweig and Berlin, Germany

⁴ Technische Universität Berlin, Institut für Physik und Astronomie, Straße des 17. Juni 135, Berlin 10623, Germany

⁵ Faculty of Medicine, Heidelberg University, Heidelberg, Germany

⁶ Center for Magnetic Resonance Research, University of Minnesota, Minneapolis, Minnesota, USA

Abstract: Ultra-high field (UHF) MRI provides significant advantages for quantitative imaging such as T1 quantification – higher SNR could provide higher precision of the quantified parameters as well as higher spatial resolution. However, T1 mapping of the body faces several technical challenges: motion artifacts, strong B0/ B1+ inhomogeneities (including B1+ dropouts), and SAR restrictions. Moreover, most of the existing T1 mapping techniques exhibit a strong dependency on the B1+. In this study, we quantified the T1 relaxation times at 7 T for the liver, kidney cortex and kidney medulla. T1 maps were acquired using an optimized gradient-echo inversion recovery (GRE-IR) technique, which we have demonstrated to have low sensitivity to B1+ inhomogeneities. The mean T1 values across the group were as follows: 1378 ± 48 ms for the liver, 1829 ± 60 ms for the kidney cortex, and 2619 ± 83 ms for the kidney medulla. T1 values show low variability across all subjects, with coefficients of variation (COVs) of 3.5%, 3.3%, and 3.2%, respectively.

Motivation: Significant challenges, such as B1+ inhomogeneity, are key reasons for the limited availability of data on T1 values for abdominal organs at UHF. Only very few studies report renal and liver T1 values at 7 T [1-2]. However, reference T1 values are crucial for accurate simulations, T1 correction of multiple MRI contrasts (e.g., CEST), and for the development of T1 mapping techniques. The aim of this work was to demonstrate a workflow that enables robust T1 quantification in the liver and kidney at 7T.

Materials & Methods: T1 mapping data were acquired in five healthy volunteers (aged 27 ± 5 years) using a Magnetom 7T MRI system (Siemens Healthineers, Germany) equipped with a custom-built 8-channel Tx/Rx body coil. B1+ phase shimming was performed to maximize B1+ efficiency, i.e. B1+ magnitude per input power, locally within regions of interest (ROIs) in the liver and kidney [3]. GRE with an inversion pulse (GRE-IR) was used for T1 mapping. For each map, data were collected using 8 snapshot GRE-IR sequences during breath-holding with the following parameters: 3 shots per slice; TR = 7500 ms; TE = 3 ms; readout FA = 15°; res: $2 \times 2 \times 3$ mm³, TI = 300, 600, 1000, 2000, 3000, 4000, 5000, 6000 ms. Total acquisition time for whole T1 map was ~ 8 min including breath-hold instructions. Voxel-wise T1 values were calculated using model fitting as described in [4]: $S = a + b \cdot \exp(-TI/T1)$, where S – signal intensity from dicom data at different time points TI, a and b – real-valued parameters. To assess the inter-subject variability of the T1 values, the between-subject coefficient of variation (COV) was calculated within individual ROIs, defined as the ratio of the standard deviation to the absolute mean.

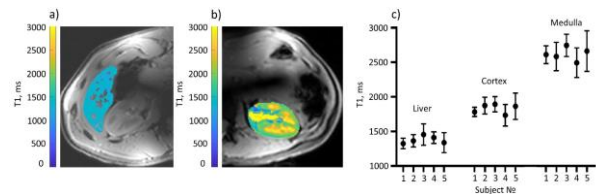


Fig. 1: T1 maps of the: a) liver b) kidney. c) Corresponding mean T1 with standard deviations for liver, kidney cortex and medulla.

Results: T1 maps demonstrate low variability of T1 values across the liver (Fig. 1a) as well as the expected contrast between the kidney cortex and medulla (Fig. 1b). The mean T1 values across the group were as follows: 1378 ± 48 ms for the liver, 1829 ± 60 ms for the kidney cortex, and 2619 ± 83 ms for the kidney medulla. T1 values show low variability across all subjects, with coefficients of variation (COVs) of 3.5%, 3.3%, and 3.2%, respectively.

Discussion: The application of static pTx effectively eliminates B1+ dropouts and allows for accurate quantification within the selected region. Estimated liver T1 values are comparable to those reported in the literature [1] (STEAM spectroscopy; 1362 ± 83 ms), but interestingly, cortical and medullary T1 values are significantly higher than those previously reported at 7T [2] (FSE-IR; 1661 ± 68 ms and 2094 ± 67 ms for the cortex and medulla, respectively). In the present study, we used a wide T1 range (300–6000 ms) compared to [2] (100–1200 ms) and an inversion efficiency-independent approximation model [4], which could have contributed to the differences in T1 values to [2]. The utilization of a straightforward GRE-IR technique yields robust, easily interpretable and processable results. However, it is time-consuming, which represents a limitation of the current methodology.

Conclusion: In this study, we have demonstrated the reliable acquisition of T1 maps for the liver and kidney in humans at 7 Tesla. The obtained T1 values can serve for the further development of faster and more advanced T1 mapping techniques.

References:

1. Gajdošík M, et al. *JMRI*. 40(6):1365-74. doi: 10.1002/jmri.24489.
2. Li X, et al. *NMR Biomed*. 28(1):63-9. doi: 10.1002/nbm.3195.
3. Metzger, G. J. et al. *MRM*. 59(2), 396–409. <https://doi.org/10.1002/MRM.21476>
4. Barral JK, et al. *MRM*. 64(4):1057-67. doi: 10.1002/mrm.22497.

Metabolic imaging with deuterated Glucose and Lactate

Aaron Diercks 1*, Jan-Bernd Hövener 1

1 Department of Radiology and Neuroradiology, Section Biomedical Imaging, University Hospital Schleswig-Holstein, Kiel University, Kiel, Germany

Abstract: This study explores the use of deuterated glucose and lactate for metabolic imaging. Using magnetic resonance imaging (MRI), including chemical shift imaging (CSI), the research investigates the metabolic fate of these labels in vitro. The findings demonstrate significant signals from deuterium-labeled glucose and lactate, suggesting potential for non-invasive monitoring of metabolic changes. This work aims to enhance early disease detection and personalized treatment through improved imaging modalities.

Motivation: Changes in metabolism are among the first indicators of disease and treatment response. These alterations occur earlier than macroscopic changes in tissue and anatomy, enabling early interventions, individually tailored treatment and improved welfare. As such, much research is focused on developing methods to measure or image metabolism. Undoubtedly, imaging the accumulation of ¹⁸F-labelled desoxyglucose with positron emission tomography has revolutionized cancer diagnostics and has become the standard of care since the 1990s. While radioisotopes provide information on the location of the label with superb sensitivity, however, there is no information on the labeled molecule itself. The magnetic resonance signal, in contrast, allows to identify the emitting molecule, but with much less sensitivity.

As a result, MR spectroscopy (MRS) has become a standard for analytical chemistry and is used in specialized cases in humans. It has not become, however, a widespread diagnostic standard. The reason for this is that the temporal, spatial and chemical resolution is usually limited to minutes, cubic centimeters, and milli-molar concentrations. There are only few applications where MRS is needed to make clinical decision that cannot be reached otherwise.

A new development promise to boost the bi-medical significance of MRS: metabolic imaging with deuterium-labelled molecules. The method allows to access and image the metabolism in living organisms non-invasively and in vivo by introducing a labelled nucleus into metabolic chains. In deuterium MRI (DMI), the low signal is partially compensated by averaging the signal (made possible by a short T1). Averages in range of a few hundreds to thousands is usual. DMI allow imaging the fate of the labels in metabolism over minutes to hours.

Because the physical properties of the DMI signal are different to that of conventional, thermally polarized proton MRI, specialized imaging methods are required to make optimal use of the signals.

In DMI, the challenge lies in obtaining the optimal SNR with ca. 0.5 ppm chemical shift resolution of a fast relaxing and recovering species (HDO at 4.7 ppm, glucose at 3.8 ppm and lactate at 1.2 ppm).

Here, we report our experiences in imaging and differentiating the metabolites Glucose-6,6-d₂ and Sodium L-Lactate-3,3,3-d₃ in the presence of Water (HDO).

Materials & Methods: A 7T animal MRI was used (Bruker Biospec 7/30, Avance Neo). For the proton images, a volume transmit-receive coil with 72 mm diameter from Bruker was installed. For the deuterium images, a volume transmit-receive coil with 32 mm diameter from Rapid was additionally installed.

Various sequences were used, including FID-based chemical shift imaging (CSI) and balanced steady state free precession (bSSFP) sequences with either a multi-echo1 or (gradient-free) FID readout2.

The phantoms are 5 mm NMR tubes with a volume of V=2.3 ml. The metabolites are solved in deuterium-depleted water (from Cambridge Isotope Laboratories) to avoid the natural abundance of deuterium in water. To calculate the mass *m* of the metabolites to get a certain concentration *c*, the formula

$$m = cMV$$

is used, where *M* is the molar mass.

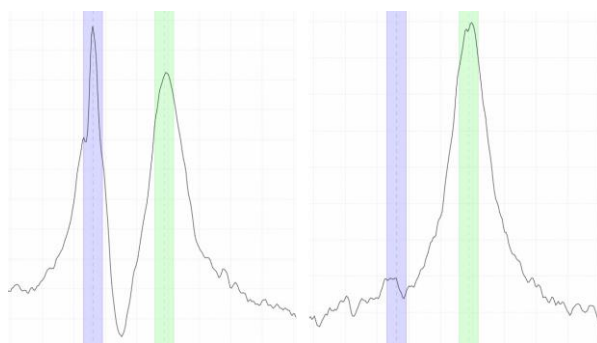


Fig. 1: Chemical Shift Image of Glucose (*c*=20 mM) in distilled water (left) and in depleted water (right). The blue marked area is the water-peak, the green marked area the glucose peak.

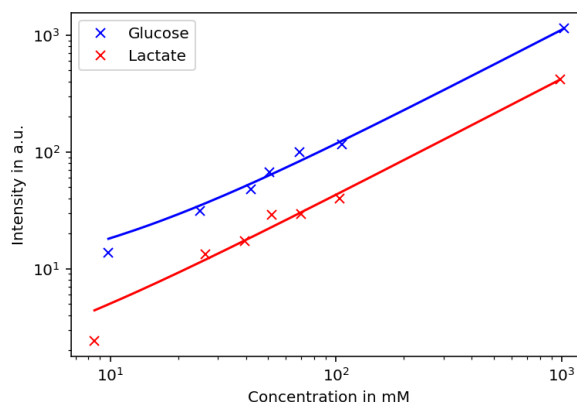


Fig. 2: Intensity of deuterated glucose and lactate over their concentration.

Results: There is a big difference between the deuterium-depleted water and distilled water as a solvent for the glucose and lactate. The distilled water has a natural abundance of 0.015 % deuterium, which resolves in a really high peak, as visible in Figure 1 in the left half. This water-peak vanishes completely for the depleted-water solution (right half of Figure 1).

We saw a linear growth between concentration and intensity of the metabolites over a wide range (10 mM to 1000 mM), as visible in Figure 2.

Conclusion: The depleted water is more than necessary. Otherwise, the water signal would be way too high to distinguish between the metabolites. The intensity of the phantoms is stable over several decades of concentration.

References:

1. Markovic S, Roussel T, et al. Deuterium MRSI characterizations of glucose metabolism in orthotopic pancreatic cancer mouse models. *NMR in Biomedicine*. 2021;34(9):e4569. doi:10.1002/nbm.4569
2. Montrazi ET, Sasson K, Agemy L, et al. High-sensitivity deuterium metabolic MRI differentiates acute pancreatitis from pancreatic cancers in murine models. *Sci Rep*. 2023;13(1):19998. doi:10.1038/s41598-023-47301-7

Feasibility of 4D Flow MRI for Flow Diverter Assessment Using a Custom-Built Phantom

Ali El Ahmar 1*, Patrick Winter 1, Adrian Duckert 1,3, Mark O. Wielpütz 4, Eiko Rathmann 4, Susanne Schnell 1,2

1 Department of Medical Physics, Faculty of Mathematics and Natural Sciences, University of Greifswald, Greifswald, Germany

2 Department of Radiology, Northwestern University, Feinberg School of Medicine, Chicago, IL, USA

3 Institute of Diagnostic and Interventional Radiology, Pediatric Radiology and Neuroradiology, University Medical Center Rostock, Rostock, Germany

4 Institute for Diagnostic Radiology and Neuroradiology, University Medicine Greifswald, Greifswald, Germany

Abstract: Flow diverter stents (FDSs) are used to treat complex intracranial aneurysms by redirecting blood flow and promoting thrombosis. Understanding their hemodynamic impact is essential for evaluating treatment success. This study investigates the feasibility of using four-dimensional (4D) flow MRI to assess flow changes caused by an FDS in a custom-built phantom. The phantom mimicked a cerebral artery under pulsatile flow conditions, with and without a Derivo® flow diverter. 4D flow MRI captured hemodynamic parameters across the cardiac cycle. Results showed localized artifacts near the stent and significant changes in flow during the systolic phases. These findings support the use of 4D flow MRI as a valuable tool for assessing flow diverters.

Motivation: Since the introduction of the Pipeline Embolization Device in 2008, flow diverter stents (FDSs) have gained widespread acceptance for treating complex intracranial aneurysms. By deploying an FDS within the parent artery, the dense, woven wire mesh alters intra-aneurysmal hemodynamics, promoting thrombosis and the eventual aneurysm occlusion(1).

Given the critical role of hemodynamics in aneurysm evolution and treatment response, it is important to understand the effect of FDSs on flow dynamics(1). Four-dimensional (4D) flow magnetic resonance imaging (MRI) is an advanced phase-contrast technique that enables comprehensive, volumetric, time-resolved blood flow visualization and quantification(2). It has been successfully applied to cerebrovascular studies, but its feasibility in assessing flow diverter stents remains largely unexplored.

This preliminary study aims to investigate the feasibility of using 4D flow MRI to visualize and quantify hemodynamic changes introduced by flow diverter stents, using a custom-built in vitro flow phantom. Specifically, we assessed whether 4D flow MRI can reliably capture flow alterations before and after stent deployment within a controlled phantom environment.

Materials & Methods: An in-vitro flow phantom was constructed to evaluate the feasibility of using 4D flow MRI for assessing flow diverter stents. The phantom consisted of a sealed cylindrical container (30 cm diameter, 20 cm length) filled with gadolinium-doped water beads and water to enhance MRI signal(3). A straight silicone tube with an inner diameter of 3 mm was embedded within the phantom to simulate a cerebral artery segment. To prevent overpressure during pulsatile flow, a parallel 6.4 mm diameter tube was connected externally (Figure 1).

The Derivo® Embolization Device (DED, Acandis, Germany), a second-generation flow diverter composed of 48 nitinol wires

with platinum cores, was used in this study (1). Two flow conditions were tested: one without a stent and one with the Derivo® device deployed inside the tube.

Pulsatile flow was provided by a CompuFlow 1000-MR pump (Shelley Medical Imaging Technologies, London, Canada) using the carotid waveform (peak flow=25 ml/s and 72 strokes per minute). A coaxial cable transmitted a TTL trigger signal from the pump to synchronize the cardiac-gated 4D flow MRI acquisition.

The flow circuit was filled with a blood-mimicking solution consisting of 60% water and 40% glycerol (viscosity: 0.003 kg·m⁻¹·s⁻¹; density: 1100 kg/m³). Gadovist (0.2% by volume, Bayer, Leverkusen, Germany) was added to enhance MRI signal(4).

Scans were performed on a Siemens 3T Vida MRI using an externally triggered, PEAK GRAPPA-accelerated, dual-VENC 4D flow MRI sequence (R = 5; VENC: 50/100 cm/sec, spatial resolution: 1mm isotropic, temporal resolution: 78.39ms, TR: ?ms, TE: 3.20ms)(2).

Data were processed and analyzed using in-house MATLAB software to compare flow patterns before and after stent deployment(2,5,6).



Fig. 1: (A) In-vitro flow phantom with embedded silicone tube (B) Image of the Derivo® flow diverter stent deployed inside an aneurysm phantom

Results: Figure 2A presents volume-rendered 4D flow MRI and magnitude images (Figure 2B) of the flow phantom. In the stented tube, two localized artifacts are observed at the proximal and distal edges of the stent (arrows), likely caused by susceptibility effects from the device's metallic structure. These artifacts were absent in the unstented case, where flow visualization remained artifact-free. The effect can also be seen in the 3D surface plot (Figure 2C), which shows flow reductions at the proximal and distal edges of the stented segment, mainly during systolic phases, corresponding to artifact regions.

Bland-Altman analysis was performed to assess agreement between flow measurements with and without the flow

diverter stent. For mean flow rate (Figure 3A), the bias was -0.01ml/s, with limits of agreement (LoA) of 0.36 and -0.38ml/s ($\pm 37\%$ of average flow rate). For peak velocity (Figure 3B), the bias was 0.02m/s, with LoA from 0.06 to -0.01m/s ($\pm 4.7\%$ of average peak velocity).

Figure 4A displays the transient flow waveforms across the cardiac cycle with and without the stent. The waveform with the diverter shows a slightly attenuated peak (~ 1.55 vs. ~ 1.65 ml/s) and a more gradual upstroke. Differences are most noticeable during phases 6-8 (systolic phases), while early diastolic phases (1-4) show little change. Paired t-tests revealed significant differences at phases 6 ($p=0.0046$) and 9 ($p=0.0206$).

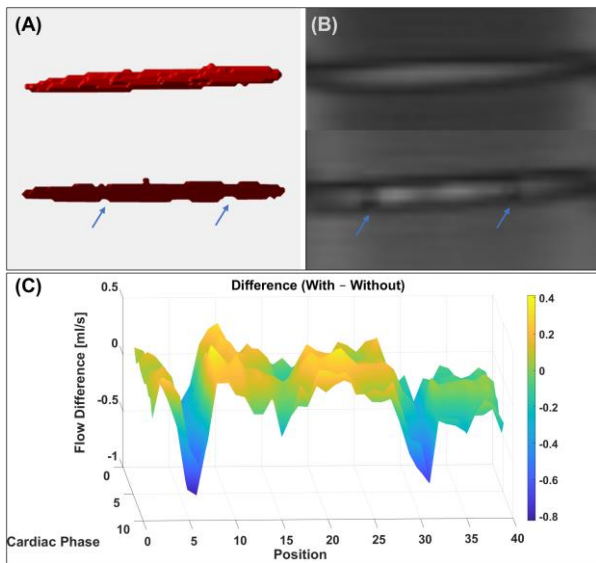


Fig. 2: (A) Volume-rendered vessel from 4D flow MRI acquisition and (B) magnitude images of 4D flow MRI showing artifacts at the proximal and distal stent edges (arrows). (C) 3D surface plot showing flow reductions at the same locations

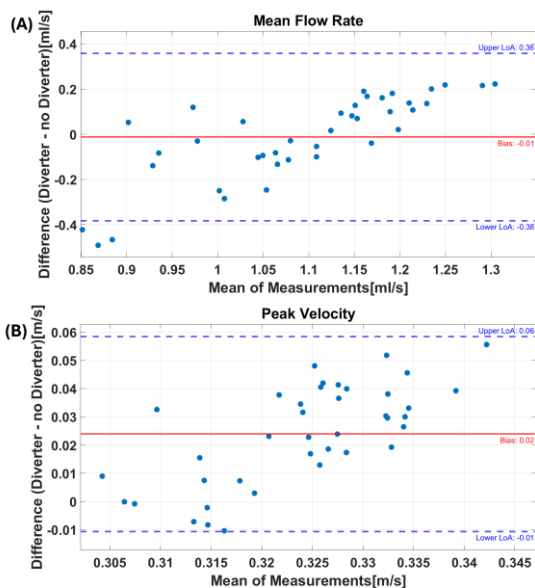


Fig. 3: Bland-Altman plots for (A) mean flow and (B) peak velocity comparing stented and unstented conditions. Each data point represents the time-averaged value at one of 39 measurement planes along the vessel.

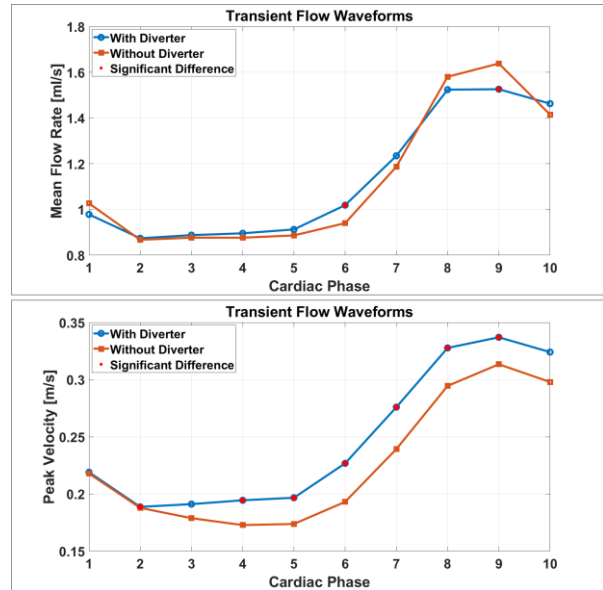


Fig. 4: (A) Mean flow waveforms across the cardiac cycle. (B) Peak velocity waveforms showing differences in systolic phases. Each point is the median across 39 planes for each cardiac phase

Figure 4B shows transient peak velocity waveforms. The stented configuration showed a lower peak (~ 0.72 vs. ~ 0.78 m/s) and smoother systolic rise. Significant differences were found at phases 2 and 4-9 ($p<0.05$). Paired t-tests revealed significant differences at phases 6 ($p=0.0046$) and 9 ($p=0.0206$).

Figure 4B shows the transient peak velocity waveforms. While overall shape was preserved, the stented configuration showed a lower peak (~ 0.72 vs. ~ 0.78 m/s) and smoother systolic rise. Significant differences were found at phases 2 and 4-9 ($p<0.05$).

Discussion: This study demonstrates the feasibility of using 4D flow MRI to assess hemodynamic changes introduced by a flow diverter stent in a controlled in-vitro setting. Our findings show that 4D flow MRI captures time-resolved flow alterations before and after stent deployment. However, susceptibility artifacts were observed at the proximal and distal ends of the stent, likely due to the device's metallic composition. The effect of these artifacts was also reflected in the 3D surface plots, which showed localized flow reductions at the proximal and distal edges of the stent, mainly during systolic phases. This suggests that artifacts may impact local flow measurements and should be interpreted with caution.

Bland-Altman analysis showed good agreement between stented and unstented conditions, with small biases and acceptable limits of agreement for both mean flow and peak velocity. These results suggest that 4D flow MRI provides reliable global flow metrics even in the presence of metallic implants.

Waveform analysis revealed stent-induced changes during the cardiac cycle, mostly at proximal and distal edges of the stent. The stented condition exhibited a dampened mean flow peak and a smoother systolic rise, with significant differences during high-flow phases. Similarly, peak velocity analysis showed reduced peak values and altered systolic profiles. Significant differences were observed across multiple phases (2 and 4-9), suggesting that the diverter affects

velocity patterns, especially during systolic acceleration and peak flow.

Conclusion: This study demonstrated the feasibility of using 4D flow MRI to assess hemodynamic changes caused by a flow diverter stent in a controlled in-vitro setting. The method successfully captured both mean flow and peak velocity waveforms across the cardiac cycle. While susceptibility artifacts were observed near the stent edges, flow measurements remained consistent in most regions, except for localized reductions near the artifacts.

Quantitative analysis showed that the stent affected the flow mainly during systolic phases, with significant differences in both flow rate and velocity.

In conclusion, 4D flow MRI appears to be a promising tool for evaluating the functional impact of flow diverters. Future studies should explore more complex geometries and in vivo validation .

Acknowledgements: The authors would like to thank the research group of the Department of Medical Physics at the University of Greifswald and the Department of Diagnostic Radiology and Neuroradiology at Universitätsmedizin Greifswald for their support.

References:

1. Fujimura S, Brehm A, Takao H, Uchiyama Y, Karagiozov K, Fukudome K, et al., Hemodynamic Characteristics and Clinical Outcome for Intracranial Aneurysms Treated with the Derivo Embolization Device, a Novel Second-Generation Flow Diverter, *World Neurosurg.*
2. Schnell S, Ansari SA, Wu C, Garcia J, Murphy IG, Rahman OA, et al., Accelerated dual-venic 4D flow MRI for neurovascular applications, *Journal of Magnetic Resonance Imaging.*
3. El Ahmar A, Winter P, König S, Duckert A, Kromrey M-L, Schnell S., Using water beads as static tissue in a Circle of Willis flow phantom in 4D flow MRI. In: ISMRM, Singapore; 2024.
4. Lorenz R, Bock J, Snyder J, Korvink JG, Jung BA, Markl M., Influence of eddy current, Maxwell and gradient field corrections on 3D flow visualization of 3D CINE PC-MRI data. Vol. 72, *Magnetic Resonance in Medicine.*
5. Bock J, Kreher BW, Hennig J, Markl M., Optimized pre-processing of time-resolved 2D and 3D phase contrast MRI data. IN: ISMRM, Berlin; 2007.
6. Vali A, Aristova M, Vakil P, Abdalla R, Prabhakaran S, Markl M, et al., Semi-automated analysis of 4D flow MRI to assess the hemodynamic impact of intracranial atherosclerotic disease., *Magn Reson Med.*

Quantitative MRI study of excised brain tissue in drug-resistant epilepsy patient: from in-vivo to ex-vivo

Francisco J. Fritz 1+3+9*, Noémie Sura 2, Nina Lüthi 3, Laurin Mordhorst 3, Jan Malte Oeschger 3, Laura Bogs 3, Rüdiger Stirnberg 4, José P. Marquez 5, Filip Szczepankiewicz 6, Ora Ohana 7, Markus Nilsson 8, Evgeniya Kirilina 9, Thomas Sauvigny 2, and Siawoosh Mohammadi 1+3.

1 Institute for Systems Neuroscience, University Medical Center Hamburg-Eppendorf, Hamburg, Germany

2 Department of Neurosurgery, University Medical Center Hamburg-Eppendorf, Hamburg, Germany

3 Institute of Neuroradiology, Advanced MRI section, Lübeck, Germany

4 Deutsches Zentrum für Neurodegenerative Erkrankungen: Bonn, Nordrhein-Westfalen, Germany

5 Donders Institute for Brain, Cognition and Behaviour, Centre for Cognitive Neuroimaging, Radboud University, Nijmegen, The Netherlands

6 Department of Medical Radiation Physics, Lund University, Lund, Sweden

7 Institute of Molecular and Cellular Cognition, University Medical Center Hamburg-Eppendorf, Hamburg, Germany

8 Department of Clinical Sciences Lund, Radiology, Lund University, Lund, Sweden.

9 Department of Neurophysics, Max Planck Institute for Human Cognitive and Brain Sciences, Stephanstraße 1a, 04103 Leipzig, Germany.

Abstract: Surgical resection for drug-resistant temporal lobe epilepsy (TLE) depends on accurate identification of epileptogenic tissue, yet "MRI-negative" cases pose challenges. Quantitative MRI (qMRI) offers detailed tissue contrasts, but its clinical application requires validation with histology. This study examines qMRI parameters across various tissue stages—unfixed, fixed, and hydrated—using high-resolution imaging of excised TLE tissue. Our results show dynamic changes in relaxometry, myelin water fraction (MWF), and diffusion parameters during tissue processing, with distinct patterns observed at high resolution. These findings underline the importance of understanding qMRI parameter evolution to improve diagnostic accuracy and surgical outcomes for MRI-negative TLE cases.

Motivation: Surgical resection remains a key therapeutic option for patients with drug-resistant temporal lobe epilepsy (TLE), but its success depends on accurately identifying epileptogenic tissue. Conventional MRI, while helpful, often presents challenges, particularly in "MRI-negative" cases where scans appear normal despite the presence of subtle abnormalities. This creates a major diagnostic hurdle, as microstructural changes may be too fine or spatially heterogeneous to detect with standard protocols. Quantitative MRI (qMRI) techniques offer a potential solution, providing parametric maps sensitive to underlying tissue properties such as myelin, iron, and axonal density [4]. However, the clinical interpretation of qMRI contrasts requires rigorous validation against histological data to ensure that these imaging biomarkers truly reflect the microstructure of the tissue[1,2].

While previous studies have compared in-vivo qMRI data to ex-vivo histology, the transition from living tissue to fixed samples introduces changes that are not yet fully understood. Additionally, differences in imaging resolutions further complicate the validation process. Our study extends previous work [3,4] by exploring a broader range of advanced qMRI markers and comparing these across different tissue stages—*in-vivo* and *ex-vivo* unfixed, fixed, and hydrated—at high resolutions. By addressing how qMRI parameters evolve through tissue processing, we aim to better align imaging techniques with histological gold standards, ultimately improving diagnostic accuracy and surgical outcomes, especially for MRI-negative TLE patients.

Materials & Methods: The study was acquired at the University Medical Center Hamburg-Eppendorf (ethics

committee approval: protocol PV5600). The MR techniques used for all measurements were multi-parametric mapping (MPM) [4], myelin water imaging (MWI) [5], magnitude-phase-based T2 mapping (MagPhT2) [6] and q-space trajectory imaging (QTI) [7]. Detailed information are in Fig. 1A.

In-vivo subject (pre-surgery): Two women (24 y and 56 y, hereafter tle003 and tle005) diagnosed with drug-resistant temporal lobe epilepsy (Fig. 2A) were measured with a 3T Prisma fit Siemens MR scanner and 64Ch head coil prior to undergoing hippocampal resection.

Ex-vivo specimen: A 16Ch wrist coil was used to measure the excised temporal poles (at room temperature) at three tissue stages: unfixed, fixed with a post-mortem interval of 45 min, and hydrated. The unfixed tissue was measured in glucose solution. Then, it was fixed with 4% paraformaldehyde (PFA) for 7 days (measured at the beginning and at the end of fixation). Later, the tissue was washed in phosphate buffered saline (PBS) solution for 2 days and measured in PBS + 0.1% Na₃N. Finally, the tissue was scanned again using the same and high resolution protocols. Protocol details are in Fig. 1A.

Pre-processing and analysis: Several relaxometry and diffusion analyses (Fig. 1B) were performed for all MR measurements (Fig. 2B). Next, we affine-registered and resampled all the masked *ex-vivo* MR images (from unfixed to hydrated high resolution) to the *in-vivo* MR image (Fig. 2C). However, the hydrated high resolution qMR parameters were not undersampled to *in-vivo* resolution.

Results: According to Fig. 3A to 3D, R1, R2*, R2, MWF and intra-axonal R2* (R2*-intra) increased after excision (*in-vivo* -> unfixed) and during fixation (fixed day 0 -> day 7), decreased after hydration (fixed day 7 -> hydrated), and preserved the cGM-WM contrast. Interestingly, myelin R2* (R2*-mye) behaves differently (Fig. 3F): it increases after excision and when fixation started (day 0), but drops at the end of fixation (day 7) and even further during hydration. At increasing resolution (HydratedHighRes), R1, R2*-intra and R2*-mye increased barely, R2* decreased, and R2 and MWF remained stable. These patterns were consistent across both subjects (dashed and dotted lines).

In Figure 4, MD (Fig. 4C) dropped by more than half after excision, increased slightly during fixation, and decreased again during hydration. Notably, its cGM-WM contrast increased across all states, by increasing in cGM and decreasing for WM. uFA and MKA (Fig. 4B and F) showed a trend similar to R2*-mye (Fig. 3F) while the trend of the noisy

MKI (Fig. 4D) was inconsistent. MKT (Fig. 4E), as a composite of MKI and MKA, followed the trends of its constituent parts. FA decreased in WM and increased in cGM after excision, then declined markedly in both during fixation. Hydration had no further impact. In high-resolution scans, GM-WM contrast was preserved, though absolute values shifted, presumably due to differences in protocol parameters. In contrast to the relaxometry parameters, these patterns on the diffusion parameters were not as consistent, except of MD and FA.

A

MR technique	In vivo	Unfixed	Fixed	Hydrated	High resolution	
MPM [4]	Resolution: 1.0 mm (t1e-003) / 0.8 mm (t1e-005) Epi: t1e-003: 2 signal-weighted FLASH sequences: T1w, PDw and M1w Epi: t1e-005: 2 signal-weighted FLASH sequences: T1w and PDw (acquired here) Both: studies with B0 and B1 calibration	Resolution: 1.0 mm (t1e-003) / 0.8 mm (t1e-005) TR: 20 ms TE: [2.32, 37.14, 15] FA's: 6° (PDw) and 11° (T1w) Acc: GRAPPA 2 (+ MB 2 only for in-vivo)	Resolution: 0.8 mm TR: 20 ms TE: [2.32, 37.14, 15] FA's: 6° (PDw) and 11° (T1w) Acc: GRAPPA 2 (+ MB 2 only for in-vivo)	Resolution: 0.6 mm (t1e-003) / 0.5 mm (t1e-005) TR: 35 ms TE: [2.14, 3.70, 31.74] ms Three repetitions per signal-weighting	Resolution: 0.3 mm TR: 40 ms TE: [3.33, 4.27, 27.24] ms FA's: 12° (PDw) and 40° (T1w) Three repetitions per signal-weighting	Resolution: 0.3 mm TR: 35 ms TE: [2.14, 3.70, 31.74] ms Two repetitions (but only one repetition was used for t1e-003 analysis)
MWI [5]	Resolution: 1.5 mm 3D FLASH sequences at 4 flip angles: 10°, 20°, 30° and 40° TR: 38.6 ms TE: [1.50, 3.88, 36.85] ms Acc: GRAPPA 2 x MB 2 (Capirinha)	Resolution: 1.0 mm TR: 38.6 ms TE: [1.50, 3.88, 36.85] ms Acc: GRAPPA 2 (Capirinha)	Resolution: 1.0 mm TR: 38.6 ms TE: [1.50, 3.88, 36.85] ms Acc: GRAPPA 2 (Capirinha)	Resolution: 0.6 mm (t1e-003) / 0.5 mm (t1e-005) TR: 35 ms TE: [2.14, 3.70, 31.74] ms Three repetitions per signal-weighting	Resolution: 0.3 mm TR: 35 ms TE: [2.14, 3.70, 31.74] ms Three repetitions per signal-weighting	Resolution: 0.3 mm TR: 35 ms TE: [2.14, 3.70, 31.74] ms Two repetitions (but only one repetition was used for t1e-003 analysis)
MagPhT2 [6]	Resolution: 1.0 mm Magnitudinal 3D GRE-EPI at 6 RF cycles: ±1°, ±15°, ±27°, ±37°, ±45° at FA 20° TR: 10.8 ms TE: 4.14 ms Acc: GRAPPA 2 (Capirinha) + PF-6/8 + (MB 2 only for in-vivo)	Resolution: 1.0 mm TR: 10.8 ms TE: 4.14 ms Acc: GRAPPA 2 (Capirinha)	Resolution: 1.0 mm TR: 10.8 ms TE: 4.14 ms Acc: GRAPPA 2 (Capirinha)	Resolution: 0.45 mm (t1e-003) / 0.5 mm (t1e-005) TR: 16.0 ms TE: 8.34 ms Two repetitions (but only one repetition was used for t1e-003 analysis)	Resolution: 0.45 mm (t1e-003) / 0.5 mm (t1e-005) TR: 16.0 ms TE: 8.34 ms Two repetitions (but only one repetition was used for t1e-003 analysis)	Resolution: 0.45 mm (t1e-003) / 0.5 mm (t1e-005) TR: 16.0 ms TE: 8.34 ms Two repetitions (but only one repetition was used for t1e-003 analysis)
QTI [7]	Resolution: 2.0 mm Multi-shell diffusion MRI with linear (LTE) and spherical (STE) diffusion vector encoding Acc: GRAPPA 2 + PF-7/8 + (MB 2 only for in-vivo)	Resolution: 2.0 mm TE: 98 ms (in-vivo); 88 ms (Ex-vivo) B-values: 2000 s/mm ² (LTE & STE) + 6-60 s at inverted phase encoding Acc: GRAPPA 2 + PF-7/8 + (MB 2 only for in-vivo)	Resolution: 2.0 mm TE: 98 ms (in-vivo); 88 ms (Ex-vivo) B-values: 2000 s/mm ² (LTE & STE) + 6-60 s at inverted phase encoding Acc: GRAPPA 2 + PF-7/8 + (MB 2 only for in-vivo)	Resolution: 1.0 mm TE: 112 ms B-values: 4000 s/mm ² (LTE & STE) [14] Two repetitions. Each repetition consisted in full dataset (LTE + STE) acquired twice with reversed phase encoding	Resolution: 1.0 mm TE: 112 ms B-values: 4000 s/mm ² (LTE & STE) [14] Two repetitions. Each repetition consisted in full dataset (LTE + STE) acquired twice with reversed phase encoding	Resolution: 1.0 mm TE: 112 ms B-values: 4000 s/mm ² (LTE & STE) [14] Two repetitions. Each repetition consisted in full dataset (LTE + STE) acquired twice with reversed phase encoding

B

MR technique	Data preparation	Preprocessing and analysis	Post-processing	Parameters
MPM [4]	1. K-space data reconstructed from MR console and off-line reconstructed using iso2mat [9] 2. Files named by BIDS standards	R ₁ and R ₂ * maps estimated using the MRI toolbox [10] with R ₁ and R ₂ images for calibration. M1 salt was also estimated when possible (for t1e-003)	R ₁ map used for performing registration and segmentation across different time points and contrasts. The registration steps are described as follows: 1. Estimate cortical gray and white matter masks using SPM [11]. The masks were obtained by using a threshold of 0.95 on the estimated T1w for cGM and WM. 2. Manually mask the tissue specimen per time-point in specimen space using ITKsnap [16]. 3. Manually align the masked R ₁ map for each time point to the in-vivo R ₁ map. The transformation affine matrix was used to transform all contrast and time points to in-vivo space. 4. All in-vivo time points (unfixed and hydrated) contrasts were resampled to their respective in-vivo counterparts, except for the high resolution images.	R ₁ : Longitudinal relaxation rate R ₂ *: Effective transverse relaxation rate
MWI [5]	1. DICOM images (both magnitude and phase) obtained directly from MR console 2. Images converted to NIFTI using iso2mat [9]	Data preprocessed using SEPIA toolbox [17] and analysed using the MCR-4 flip angle mode. For in-vivo analysis, CSF was used as a tissue reference for cGM estimation.	MWF: Myelin water fraction R ₂ *: Intra-axonal effective transverse relaxation rate R ₂ : Myelin effective transverse relaxation rate	
MagPhT2 [6]	2. Images converted to NIFTI using iso2mat [9]	Data preprocessed using a custom-optimized Python code [12] and analysed using the MagPhT2 code [18].	MD: Mean diffusivity FA: Fractional anisotropy uFA: Microscopic fractional anisotropy MK: Microscopic mean kurtosis MK _{iso} : Anisotropic mean kurtosis MK _T : Total mean kurtosis	
QTI [7]		Magnitude data denoised (denoise - MRB), digitized (mdeqbits - MRB), susceptibility (smap - FS) and eddy corrected with Eddy [15]. Preprocessed data analysed using the QTIv2 model Matlab code [15].		

Fig. 1: Table summary of the different MR techniques across different tissue stages (A) and the respective preprocessing, analysis and parameters used (B). Notice that t1e-003 had slightly different protocols in comparison to t1e-005.

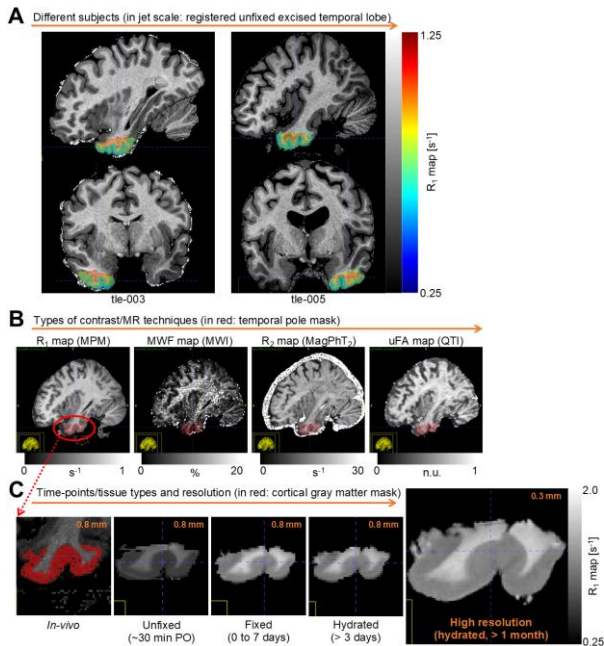


Fig. 2: Summary illustration of the analysis performed. We compare (A) different subjects with different diseased locations, (B) different MR techniques (see Figure 1) and (C) different tissue stages per contrast, exemplary illustrated for R1 here. The area studied is indicated shown in jet scale (A) and displayed as a mask in pale red (B). In this latter mask, we divided between cortical gray matter (solid red in C) and white matter. PO: post-operation.

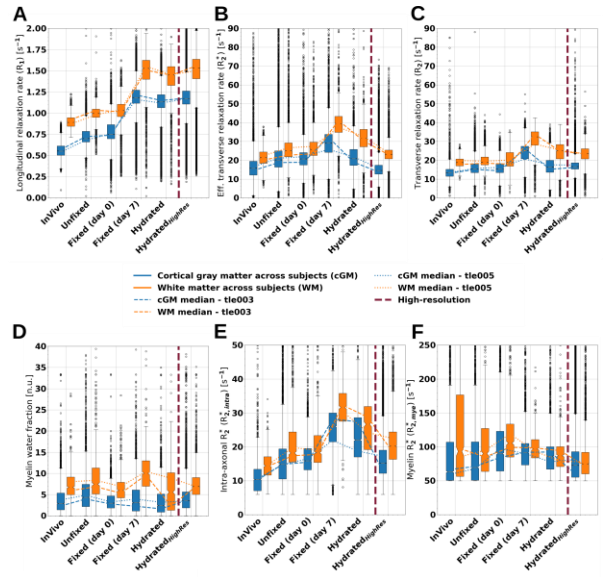


Fig. 3: Temporal evolution of the relaxometry parameters from MPM[5] (A-B), MagPhT2[6] (C) and MWI[5] (D-F) methods across subjects and tissue stages (Fig. 2). The blue and orange dotted lines join the median values for t1e003 and dashed lines for t1e005, while the carmine dotted line separates tissue stages from the high resolution comparison.

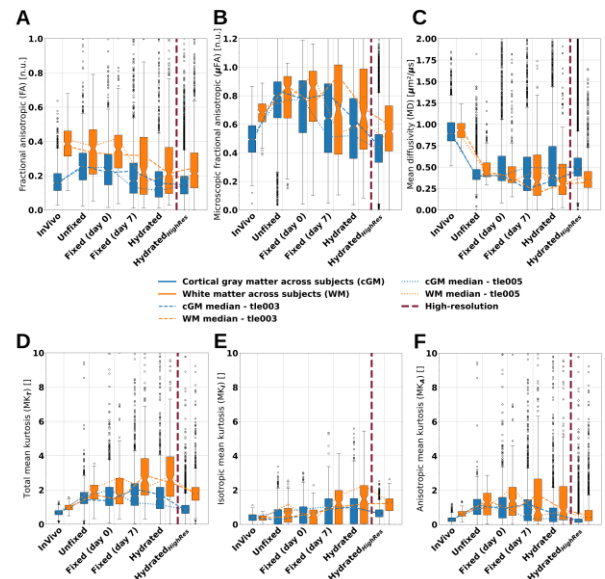


Fig. 4: Temporal evolution of the diffusion parameters from the QTI [8] model across across subjects and tissue stages (Fig. 2). The blue and orange dotted lines join the median values for t1e003 and dashed lines for t1e005, while the carmine dotted line separates tissue stages from the high resolution comparison.

Discussion: Our results confirm previous findings of how relaxometry, MWF, MD and FA change across tissue stages (e.g., [21,23]); we also found a new common trend across tissue stages between MKa, uFA and R2*-mye. From these observations, we speculate that there is a common mechanism driving MWF and relaxometry on one side, and uFA, MKa and R2*-mye on the other side. Well-known candidates for the observed changes in relaxometry and diffusion parameters are reduced temperature, loss of perfusion, cellular apoptosis, cross-linking of proteins due to fixative, and reduced para-vascular space compared to in-vivo

[20-23]. Finally, our high resolution results deviated from the low-resolution counterparts, some parameters more than others. This is probably due to deviations in the protocol parameters required to optimize image contrasts and signal-to-noise ratio. Limiting factors of our study are the sample size (two), the use of in-vivo MR protocols for the ex-vivo specimen, which could result in parameter-estimation bias and inaccuracies in registration between in-vivo and ex-vivo. Especially in this latter, diffusion MR dataset could be the most affected given the lower resolution (2.0 mm) and image deformation due to sequence technique (EPI vs FLASH).

Conclusion: Our comprehensive acquisition of qMRI parameters revealed that transferring findings from ex-vivo MRI to in-vivo requires a thorough characterisation of their changes across tissue stages. For that, it is necessary to improve the registration of the specimen across this time-frame, i.e. from in-vivo to hydrated fixed ex-vivo.

Acknowledgements: This work was supported by the German Research Foundation (DFG Priority Program 2041 "Computational Connectomics", [MO 2397/5-1, MO 2397/5-2, MO 2249/3-1, MO 2249/3-2], by the Emmy Noether Stipend: MO 2397/4-1; MO 2397/4-2).

Funded by the European Union. Views and opinions expressed are however those of the author(s) only and do not necessarily reflect those of the European Union or the European Research Council Executive Agency. Neither the European Union nor the granting authority can be held responsible for them. This work is supported by ERC grant (Acronym: MRStain, Grant agreement ID: 101089218, DOI: 10.3030/101089218).

References:

1. Stüber, C. et al. Myelin and iron concentration in the human brain: a quantitative study of MRI contrast. *Neuroimage*. 2014; 93:95-106.
2. West, K. et al. Myelin volume fraction imaging with MRI. *Neuroimage*, 2018; 182:511-521
3. Fritz, F.J. et al. Diffusion and relaxometry study of an excised temporal lobe from a drug-resistance epilepsy patient using in vivo and ex vivo MRI. Abstract #1260. *Proc. Intl. Soc. Mag. Reson. Med.* 31 (2023).
4. Weiskopf, N. et al. Quantitative multi-parameter mapping of R1, PD(*), MT, and R2(*) at 3T: a multi-center validation. *Front Neurosci* 2013; 7:95
5. Chang KS., et al. Multi-compartment relaxometry and diffusion informed myelin water imaging – Promises and challenges of new gradient echo myelin water imaging methods. *NeuroImage* 2020
6. Wang D, et al. Improved gradient echo magnitude- and phase-based mapping of using multiple RF spoiling increments at 3T and 7T. *Magn Reson Med.* 2024; 92: 2328-2342.
7. Westin CF, et al. Q-space trajectory imaging for multidimensional diffusion MRI of the human brain. *Neuroimage*. 2016 Jul 15;135:345-62.
8. <https://github.com/Donders-Institute/bidscoin>
9. <https://gitlab.gwdg.de/cbs-neurophy/image-recon>
10. Tabelow, K. et al. hMRI – A toolbox for quantitative MRI in neuroscience and clinical research. *NeuroImage* 2019; 194:191–210.
11. Friston, K., 2007. CHAPTER 2 - Statistical parametric mapping, in: FRISTON, K., ASHBURNER, J., KIEBEL, S., NICHOLS, T., PENNY, W. (Eds.), *Statistical Parametric Mapping*. Academic Press, London, pp. 10–31.
12. https://github.com/quantitative-mri-and-in-vivo-histology/t2_mapping_traveling_heads
13. Jenkinson, M. et al. FSL. *NeuroImage*, 2012; 62:782-90
14. Dyrby TB et al. An ex vivo imaging pipeline for producing high-quality and high-resolution diffusion-weighted imaging datasets. *Hum Brain Mapp.* 2011; 32(4):544-563.
15. https://github.com/filip-szczepankiewicz/Szczepankiewicz_DIB_2019
16. Paul A. Yushkevich, et al. User-guided 3D active contour segmentation of anatomical structures: Significantly improved efficiency and reliability. *Neuroimage* 2006 Jul 1;31(3):1116-28.
17. <https://github.com/kschan0214/sepia>
18. <https://github.com/mrphysics-bonn/MagPhsT2>
19. J.-D. Tournier, et al. MRtrix3: A fast, flexible and open software framework for medical image processing and visualisation. *NeuroImage*, 202 (2019), pp. 116–37
20. Berger, C. et al. Post mortem brain temperature and its influence on quantitative MRI of the brain. *Magn Reson Mater Phy* 2022; 35: 375–387
21. Raman MR, et al. Regional T1 relaxation time constants in Ex vivo human brain: Longitudinal effects of formalin exposure. *Magn Reson Med.* 2017 Feb;77(2):774-778.
22. Sepelband F. et al. Alzheimer's Disease Neuroimaging Initiative. Perivascular space fluid contributes to diffusion tensor imaging changes in white matter. *Neuroimage*. 2019; 197:243-254.
23. Shatil A., et al. Quantitative Ex Vivo MRI Changes due to Progressive Formalin Fixation in Whole Human Brain Specimens: Longitudinal Characterization of Diffusion, Relaxometry, and Myelin Water Fraction Measurements at 3T. *Front. Med.*, 2018. Volume 5.

Anatomy of neo-aorta can cause abnormal flow patterns related to dilatation

Gabbert DD 1*, Langnaese L 1, Schaffarczyk A 2, Michael Neidlin 3, Uebing A 1, Voges, I 1

1 Department of Congenital Heart Disease and Pediatric Cardiology, DZHK (German Center for Cardiovascular Research), partner site Hamburg/Kiel/Lübeck, University Hospital Schleswig-Holstein, Kiel, Germany

2 University of Applied Sciences, Kiel, Germany

3 Department of Cardiovascular engineering, Institute of Applied Medical Engineering, RWTH Aachen University

Abstract: Background: The aim of the present study was to investigate whether the abnormal shape of the aortic arch in patients with hypoplastic left heart may cause abnormal flow patterns in the descending aorta which promote dilatation.

Methods: CFD simulations were performed based on boundary conditions from 4DFlow MRI. Fluid-dynamics quantities circulation, wall-shear stress, and centrifugal pressure were evaluated.

Results: All fluid-dynamics quantities examined were significantly increased in anatomic models from patients with abnormal aortic arch anatomy.

Conclusion: This study demonstrated that the abnormal shape of the neo-aortic arch can directly cause abnormal flow patterns which may promote dilatation. Centrifugal pressure is proposed as novel fluid-dynamics marker.

Motivation: The descending aorta (DAo) in patients with hypoplastic left heart syndrome (HLHS) after Norwood procedure is frequently enlarged and exhibits increased stiffness. A recent study indicated that patients with DAo dilatation had caliber changes of more than 40% in the aortic arch and significantly increased rotational flow patterns in the DAo (1). The aim of the present study was to investigate whether the abnormal shape of the aortic arch may have a causative influence on rotational flow patterns and increased wall shear stress and thus may promote the development of dilatation in the DAo.

Materials & Methods: 11 CFD simulations were performed using OpenFOAM-v2406 with different anatomies and flow boundaries. Typical neo-aortic anatomies and velocity boundary conditions were extracted from the MRI examinations of two HLHS patients with caliber changes of more than 40% (a female patient, 2 yrs., 1 year after TCPC completion and a male patient, 19 yrs., 18 yrs after TCPC) and a control with normal cardiovascular anatomy (female, 11 yrs.). CFD simulations were performed with the three original anatomies and with two modified anatomies in which abnormal kinks and caliber changes of the neo-aorta were removed. In order to take into account that anatomic changes may influence flow conditions, in particular after removing fluid-dynamics obstacles due to caliber changes in the aortic arch, flow boundaries were varied with factors 0.9, 1.0, 1.1, 1.2. Fluid-dynamics quantities circulation, wall-shear stress, and centrifugal pressure were evaluated in a 10 cm long section of the descending aorta. Circulation and wall shear stress were evaluated as average over the full cardiac cycle. Centrifugal pressure was determined as pressure difference between the maximum (close to the wall) and minimum (close to the vessel center) pressures, averaged over diastole.

Validation of CFD was performed in the first HLHS patients by comparison with 4D flow MRI results.

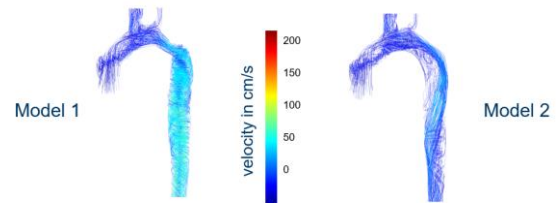


Fig. 1: Pathline visualization in the two models of the first HLHS patient in the diastole.

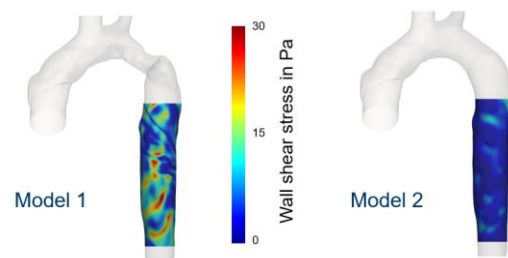


Fig. 2: Visualization of wall-shear-stress of the two models for the first patient.

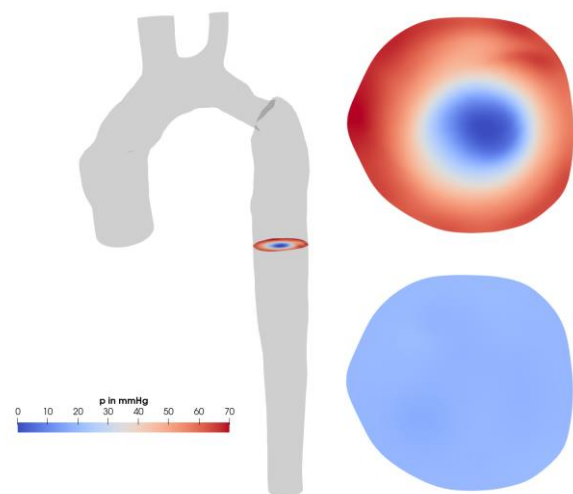


Fig. 3: Visualization of centrifugal pressure for the first patient.

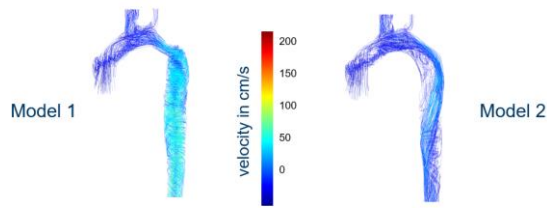


Fig. 4: Models used for simulation of first HLHS patient. Left: Model of the original neo-aorta. Right: Smooth model.

Results: For CFD simulations, unstructured, hexahedral meshes were prepared with 2.5 million cells which covered the aorta between neo-aortic valve and DAo at the diaphragm level. Visualization of pathlines revealed strong rotational velocities in both first original neo-aortic models in contrast to the second smooth models and in contrast with the control. 4D flow MRI differed from CFD results on circulation by $-7.1\% \pm 6.7\%$. Between CFD simulations with first and second models, circulation was reduced in average over the cardiac cycle by 78%-87% in patient 1 and 76%-85% in patient 2 depending on flow boundaries. Wall-shear stress in average over the cardiac cycle was reduced by 52%-63% in patient 1 and 26%-47% in patient 2 depending on the flow boundaries. Centrifugal pressure was reduced by 88%-92% in patient 1 and 58%-72% in patient 2 depending on the flow boundaries. Average circulation, wall-shear stress and centrifugal pressure in model 1 were significantly increased compared with simulations in model 2 for both HLHS patients and with the control simulation.

Discussion: This study demonstrated that the abnormal shape of the neo-aortic arch can directly cause increased circulation, wall shear stress and centrifugal pressure compared to a smooth anatomy. Increased wall shear stress has been associated with the development of dilatation (2). To the best of our knowledge, this is the first study to link centrifugal pressure to the development of dilatation.

Conclusion: This CFD study was able to establish a causal relationship between aortic anatomy and flow patterns which may promote the development of dilatation.

References:

1. Voges I, Scheewe J, Attmann T, Uebing A, Oechtering T, Gabbert D. Abnormal aortic arch shape and vortical flow patterns are associated with descending aortic dilatation in patients with hypoplastic left heart syndrome. *Int J Cardiol.* 2021 Jan 15;323:65-67.
2. Guala A, Dux-Santoy L, Teixido-Tura G, Ruiz-Muñoz A, Galian-Gay L, Servato ML, Valente F, Gutiérrez L, González-Alujas T, Johnson KM, Wieben O, Casas-Masnou G, Sao Avilés A, Fernandez-Galera R, Ferreira-Gonzalez I, Evangelista A, Rodríguez-Palomares JF. Wall Shear Stress Predicts Aortic Dilatation in Patients With Bicuspid Aortic Valve. *JACC Cardiovasc Imaging.* 2022 Jan;15(1):46-56.

A deep nonlinear subspace modelling and reconstruction for diffusion-weighted imaging using variational auto-encoder

Julius Glaser 1*, Zhengguo Tan 2, Annika Hofmann 3, Frederik Bernd Laun 1, Florian Knoll 3

1 Institute of Radiology, Uniklinikum Erlangen, Friedrich-Alexander-Universität Erlangen-Nürnberg, Erlangen, Germany

2 Michigan Institute for Imaging Technology and Translation (MIITT), Radiology, University of Michigan, Ann Arbor, Michigan, USA

3 Department Artificial Intelligence in Biomedical Engineering (AIBE), Friedrich-Alexander-Universität Erlangen-Nürnberg, Erlangen, Germany

Abstract: We present a novel reconstruction approach that leverages a variational autoencoder to learn a non-linear latent subspace from bio-physically simulated diffusion signals. The decoder of this network is then used in the forward operator of the image reconstruction process. The decoded latent images are scaled by the b_0 image, phase is added and processed as regular diffusion weighted imaging (DWI) images in the remaining forward operator. The proposed reconstruction is compared to the results of multiplexed sensitivity encoding (MUSE) [1] reconstruction and locally low rank (LLR) regularized reconstruction [2]. The proposed method shows strong noise suppression especially in the higher b-value domain (>1000 s/mm²) and outperforms MUSE and LLR reconstructions.

Motivation: High-resolution diffusion imaging suffers from long acquisition times and low SNR. The standard MUSE reconstruction often falls short in addressing these SNR issues. To decrease the noise level during reconstruction, LLR regularization can be used, though it can be limited by long reconstruction times

Mani et al. proposed the use of an auto-encoder (AE) as regularization functional during DWI reconstruction [3]. The AE was trained on simulated noisy diffusion signal curves, acting as prior knowledge to constrain the reconstruction and showed improved noise suppression in the reconstruction. The AE learned a compact latent representation and the corresponding subspace mapping of their training data in a nonlinear fashion. This mapping can also directly be used in the forward operator of an image reconstruction problem, increasing the model's influence to the reconstructed result. Since the AE's learned mapping is non-linear, it can lead to a more accurate representation of non-linear signals, potentially increasing reconstruction quality. This was first successfully shown by Arefeen et al. for T2 relaxometry [4], but has not been demonstrated for DWI yet.

We here present a combination of the standard reconstruction of multi-shot MRI data MUSE [1] with the approach presented in [4] to include the decoder part of an AE in the forward operator. Using a variational auto-encoder (VAE) [5] in training and converting the approach to DWI leads to the here proposed model-based reconstruction scheme.

Materials & Methods: First, the VAE was trained with simulated noisy diffusion data. Therefore, signal curves were simulated using the ball-and-stick model (BAS) [6]. The BAS model comprised two sticks to also capture crossing fibers. Sixty isotropically distributed tensor orientation were used, the remaining parameters for simulation were discretized in their according biophysical intervals. In the end, additional signal curves were generated by adding Gaussian noise of

different standard distributions to achieve a total number of 4,248,000 signals curves.

Second, the VAE was trained using the simulated signals. The VAE structure was 3 layers encoding and decoding depth, tanh activation function, and 11 latent variables.

The third step was to incorporate the decoder of the trained networks in the beginning of the reconstruction forward operator of multi-shot, multi-coil, multi-slice, k-q-undersampled reconstruction. Because the decoder output is normalized and absolute valued, scaling has to be done and phase added. Therefore, the output was scaled first with b_0 reconstructed images and the phase was reconstructed together with the latent images (see figure 1).

To evaluate the reconstruction, a brain scan with 126 diffusion encodings with 3 fold in-plane and 3 fold multislice acceleration was acquired with an interleaved EPI sequence in two shots with a nominal resolution of $1.0 \times 1.0 \times 2.0$ mm³.

The results of the reconstruction were compared qualitatively to the results of MUSE and LLR regularized reconstruction for certain diffusion encodings and for the colored fractional anisotropy maps (cFA). Additionally, fiber orientation distribution functions (fODFs) for a white matter crossing region were reconstructed and compared.

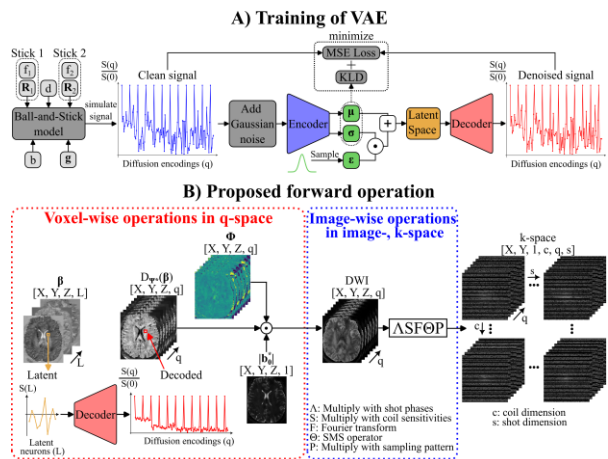


Fig. 1: Figure 1 (A) Depiction of the training process of the VAE model and (B) the forward operator of the proposed reconstruction scheme.

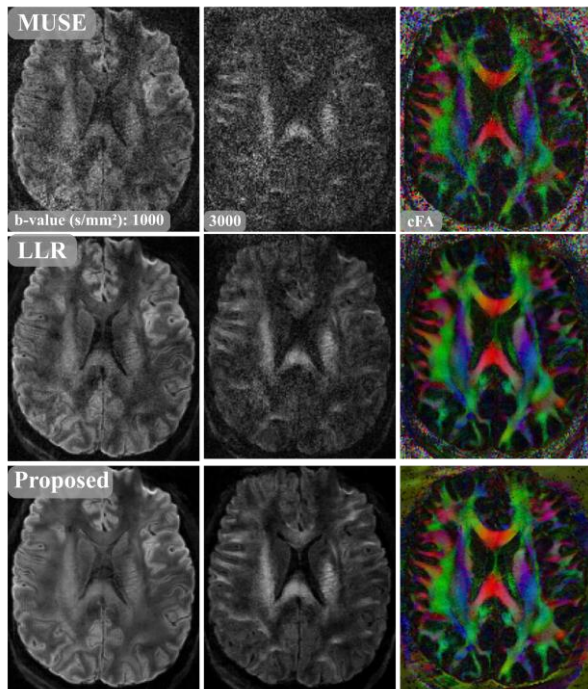


Fig. 2: Reconstructed diffusion-weighted images for one diffusion encoding direction with b-values 1000 and 3000 s/mm² and the resulting cFA map.

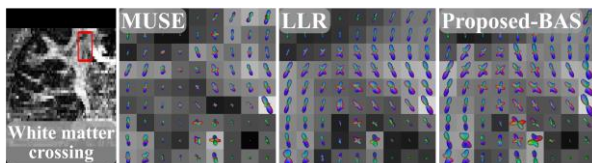


Fig. 3: fODFs of the reconstructions for a region of white matter crossing in a coronal slice are the same as in The fODFs are scaled by the general fractional anisotropy and FA.

Results: The reconstruction results of MUSE, LLR regularized, and the proposed method are shown in figure 2. MUSE reconstructions show substantial noise corruption at this acceleration rate, increasing with the b-value. The LLR-regularized reconstruction removes most of the noise at the cost of blurring, resulting in images with higher SNR compared to MUSE, but loss of details. The proposed reconstruction shows high noise suppression in the diffusion images and cFA, but higher degree of detail compared to LLR.

Figure 3 shows the fODF of a white matter crossing and the FA map in the background. The white matter crossing reveals that the MUSE fODFs show some amount of fiber crossing, but with outliers and noticeable variance in the fractional anisotropy map (FA). LLR regularization is able to remove the outliers in the fODFs by averaging them to the main direction, which seems more plausible anatomically. The proposed reconstruction shows similar fiber crossings and FA as LLR.

Discussion: We presented a novel DWI reconstruction approach, combining ideas of deep-learning, latent signal modelling, joint k-q-space reconstruction, and biophysical simulation for multi-shot, high resolution, DWI reconstruction.

The proposed k-q-space joint reconstruction with the VAE shows high noise reduction potential by simultaneously keeping a high degree of structural detail and good resolution of fiber crossings for the BAS-trained model. It outperforms other reconstructions in terms of noise suppression and detail preservation. The proposed method is applicable not only to the acquisition setting presented here. The decoding and scaling could be used in a plug-and-play manner for other diffusion acquisitions, if the network is appropriately trained with the used diffusion gradients.

In contrast to the q-model method by Mani et al [3], our approach used the trained model directly as part of the forward operator, leading to a model-based reconstruction. This increases the influence of the trained architecture on the reconstruction process, as the results are directly reconstructed from the model and not only loosely guided by it. In this regard, our proposed approach is more closely related to the work by Arefeen et al. [4], who proposed the use of a latent signal model for T2 mapping.

The main limitation of the method, which potentially reduces its performance and applicability, is the capability of the synthetic training data to represent signals observed in in-vivo acquisitions. A certain domain-shift between training and the reconstruction of the signals is present. This could lead to biased reconstruction results or limited accuracy, which requires further investigation.

Conclusion: The proposed DWI joint k-q-space reconstruction for multi-shot, high resolution data leverages the decoder of a VAE in the reconstruction forward operator. The decoder enables a nonlinear subspace mapping and denoising in the DWI reconstruction and leads to significant noise suppression, while retaining sharp structural details.

Acknowledgements: Funding by the German Research Foundation (DFG) is gratefully acknowledged (project 500888779 / RU5534 MR biosignatures at UHF) and the FAU HPC resources provided by Erlangen National High Performance Computing Center (NHR@FAU). Preliminary results were already presented at the 2025 ISMRM diffusion workshop in Kyoto.

References:

1. Chen et al. *NeuroImage*, 72:41–47, 2013
2. Tan et al. *Imaging Neuroscience*, 2:1–15, 2024
3. Mani et al. *MRM*, 86(2):835–851, 2021
4. Arefeen et al. *MRM*, 90(2):483–501, 2023
5. Kingma, *Willing arXiv*, 2022
6. Behrens et al. *NeuroImage*, 34(1):144–155, 2007

PHIP-SAH polarizer with increased sample volume and hydrogen diffuser

Yenal Gökpek 1*, Landon Colaresi 2, Jan-Bernd Hövener 1, Andrey N. Pravdivtsev 1

1 Department of Radiology and Neuroradiology, Section Biomedical Imaging, University Hospital Schleswig-Holstein, Kiel University, Kiel, Germany
2 Department of Physics, University of Wisconsin-Madison, Madison, WI 53706, USA

Abstract: We developed an automated PHIP-SAH setup capable of hyperpolarizing up to 2.2 mL of precursor solution using custom-engineered reactor vessels and hydrogen diffusers. The system operates on a 0.45 T 20 mm MRI platform with in situ temperature control (30–80 °C) and supports fully automated gas and liquid handling. Using vinyl acetate-d₆ as a test precursor and 50 mM acetate in acetone, we achieved up to 31.3% ¹H polarization out of 44.6% maximum theoretical limit. Multiport pressure caps made from PEEK and PEI enabled larger sample volumes, while diffusers improved pH₂ surface contact and hydrogenation rates. The effective field-of-view (FOV) of the setup allows polarization of (2.215 ± 0.014) mL precursor. The system delivers with a duty cycle of 80 s, producing 10 hyperpolarized samples in 15 minutes. Current efforts focus on optimizing spin order transfer, sidearm cleavage, and purification for preclinical tracer production using pyruvate.

Motivation: NMR relies on weak interactions between nuclear spins and the magnetic field to extract information about molecular structure and sample composition. Due to the inherently low nuclear spin polarization, its sensitivity is limited. Hydrogenative parahydrogen-induced polarization (PHIP) enhances sensitivity by reacting a molecule containing a C–C double or triple bond with parahydrogen (pH₂) in the presence of a catalyst. Biologically relevant tracers, such as pyruvate, are hyperpolarized using PHIP-suitable auxiliary sidearms (PHIP-SAH). The process involves: (i) hydrogenation of the sidearm, (ii) polarization transfer to the tracer, and (iii) sidearm cleavage followed by purification (1).

The small volume of conventional reactors and tedious purification routine limit the broader application of PHIP in vivo imaging. Most PHIP-SAH studies use 5 mm NMR tubes (~0.1–0.2 mL), which mechanically constrain hydrogenation and limit the precursor amount. Moreover, optimizing hydrogenation reactions could increase the reaction rate and hence polarization yield.

Materials & Methods: In this work, up to 2.2 mL of 50 mM acetate was hyperpolarized using various hydrogenation reactor vessels with or without pH₂ diffusers. Hyperpolarization was carried out on a 0.45 T 20 mm MRI setup (PureDevices) with an in situ temperature control unit (30–80 °C). All gas and liquid handling and injections were automated (2). Vinyl acetate-d₆ PHIP-SAH precursor (CDN ISOTOPES INC., D-4097) was used as a test system.

Results: We designed multiport pressure caps from engineering polymers such as polyetheretherketone (PEEK) and polyetherimide (PEI) for the accommodation of large sample volumes. We tested several diffusers generating smaller hydrogen bubbles to increase the pH₂ gas surface-to-volume ratio, accelerating hydrogenation. The MRIs of the designed reactors were obtained to determine the B0 and B1 homogeneity of the new 20 mm polarizer setup. The imaging

system provided a 20 mm field-of-view (FOV) height and a full width at half maximum (FWHM) of 2.492 ppm (Figure 1b). This FOV corresponds to a usable precursor volume of (2.215 ± 0.014) mL to be hyperpolarized (Figure 1a). Several hydrogen diffusers have also been designed and tested. We reached 31.3% ¹H polarization out of 44.6% maximum theoretical polarization for 50 mM of acetate in acetone starting with vinyl acetate-d₆ PHIP-SAH precursor. The automated duty cycle of hyperpolarization is 80 s, allowing for 10 hyperpolarized samples to be produced within 15 minutes with high accuracy (Figure 2). Ongoing work includes optimization of spin order transfer (SOT), sidearm cleavage, purification of the precursor for preclinical applications, and translation to pyruvate.

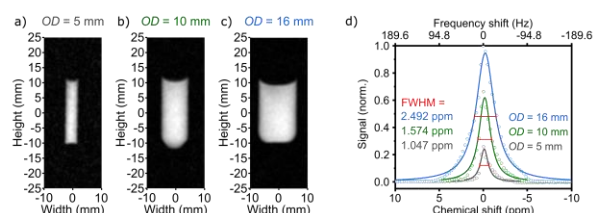


Fig. 1: Effect of sample size: (a) ¹H MRIs and (b) ¹H NMRs of 5 mm, 10 mm, and 16 mm reactors. The volumes of reactors are (0.265 ± 0.007) mL, (1.013 ± 0.023) mL, and (2.215 ± 0.023) mL, respectively

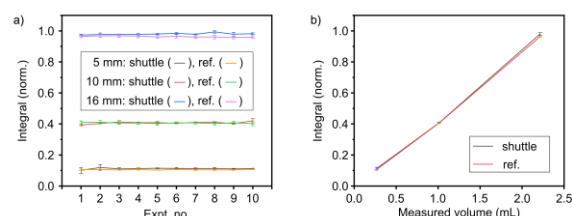


Fig. 2: Sample injection reproducibility. (a) Reproducibility of NMR signal integrals for reference and automatically shuttled samples for 5, 10, and 16 mm tubes. (b) The average integral of all spectra compared to the sample volume calculated from the measured sample weight.

Acknowledgements: We acknowledge support from the German Federal Ministry of Education and Research (BMBF) (03WIR6208A hyperquant), DFG (555951950, 527469039, 469366436, HO-4602/2-2, HO-4602/3, HO-4602/4, EXC2167, FOR5042, TRR287). MOIN CC was founded by a grant from the European Regional Development Fund (ERDF) and the Zukunftsprogramm Wirtschaft of Schleswig-Holstein (Project no. 122-09-053).

References:

- Reineri, F.; Boi, T.; Aime, S. ParaHydrogen Induced Polarization of ¹³C Carboxylate Resonance in Acetate and Pyruvate. *Nat Commun* 2015, 6 (1), 5858. <https://doi.org/10.1038/ncomms6858>.
- Ellermann, F.; Sirbu, A.; Brahms, A.; Assaf, C.; Herges, R.; Hövener, J.-B.; Pravdivtsev, A. N. Spying on Parahydrogen-Induced Polarization Transfer Using a Half-Tesla Benchtop MRI and Hyperpolarized Imaging Enabled by Automation. *Nat Commun* 2023, 14 (1), 4774. <https://doi.org/10.1038/s41467-023-40539-9>.

Tracing metabolic flux of hyperpolarized [1-¹³C]pyruvate in Escherichia coli K12

Farhad Haj Mohamad 1, Arianna Ferrari 1, Josh P. Peters 1, Maria Anikeeva 1, Charbel Assaf 1, Andrey N. Pravdivtsev 1, Jan-Bernd Hövener 1

1 Department of Radiology and Neuroradiology, Section Biomedical Imaging, University Hospital Schleswig-Holstein, Kiel University, Kiel, Germany

Abstract: A disturbed microbial ecosystem contributes to many diseases, ranging from infections to inflammatory bowel disease, characterized by altered metabolic pathways. Here, we present a protocol for utilizing hyperpolarized nuclear magnetic resonance (NMR) to non-invasively track Escherichia coli (E. coli K12) metabolic flux. With the help of dissolution dynamic nuclear polarization (dDNP) we hyperpolarized [1-¹³C]pyruvate, which was subsequently introduced into E. coli K12, enabling real-time detection of key pyruvate products - CO₂, bicarbonate, and lactate. Flux parameters of pyruvate conversion were quantified, demonstrating consistent lactate production, rapid pyruvate-CO₂ conversion, and CO₂/bicarbonate exchange. Our method offers a refined approach to studying bacterial metabolism with the potential for in vivo translation.

Motivation: Host-microbiota interactions are well studied and reveal a dynamic relationship that impacts metabolism, immunity, and general health. Disruption of this dynamic interaction can alter metabolic pathways, ultimately promoting the pro-inflammatory development and contributing to chronic inflammation as seen in inflammatory bowel disease. Unlike conventional NMR, dDNP-enhanced NMR is able to probe the enzymatic activity of key metabolic steps of a viable organism non-invasively and in real time [1]. E. coli K12 is a non-pathogenic strain widely studied and used as a model strain in microbiology, molecular biology, and biochemistry. Here, we report a method to dynamically investigate hyperpolarized pyruvate metabolism in E. coli K12, which we will further utilize in other strains and conditions.

Materials & Methods: E. coli K12 were grown under aerobic conditions to OD₆₀₀ of 0.8 in Lennox Luria-Bertani (LB) broth overnight (37°C, 250rpm), washed (40mM HEPES, pH 7.3), resuspended in 400 µL HEPES, and a total amount of 240 mg of the suspension was loaded to a Shigemi NMR tube. The tube with a 1/32" PTFE capillary was then placed in a 9.4T NMR spectrometer. dDNP hyperpolarized [1-¹³C]pyruvate (100 mM) was injected into the cells tube and imaged over time (5° pulses, 128 scans, TR 3 s) followed by thermal measurement. A parallel measurement of pyruvate hyperpolarization was conducted on a 1T NMR spectrometer and the thermal signal was measured subsequently. The obtained spectra were processed and integrated with Mnova software (V. 15.0.1). Resulting kinetics of substrate (pyruvate) and products (lactate, bicarbonate and CO₂) were fitted with an in-house python script to obtain the conversion rate constants of pyruvate to lactate (kPL), to bicarbonate (kPB), area under curve ratio of metabolite to pyruvate signal (AUC_{product/substrate}), and the time to the maximum signal (t_{max}) [2, 3].

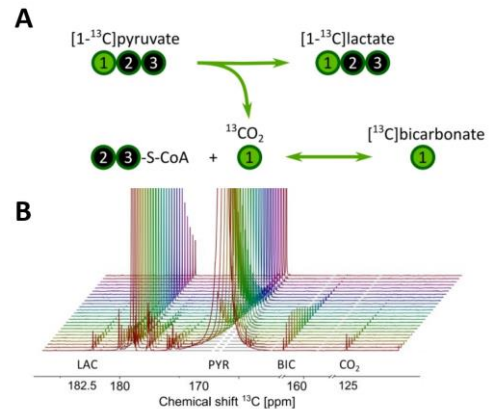


Fig. 1: A. The schematic of [1-¹³C]pyruvate metabolic pathways in E. coli K12, B. Stacked spectra of the dynamic-spectroscopy acquisition showing pyruvate (170 ppm), with lactate (182.5 ppm), bicarbonate (160 ppm), and CO₂ (124.5 ppm).

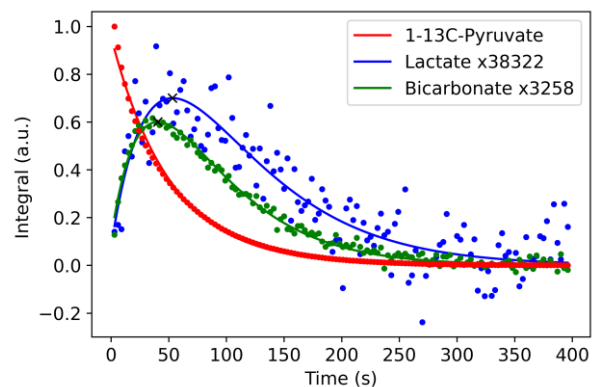


Fig. 2: Over time integrated NMR signals (indicators) and fit (lines) of pyruvate, lactate, and bicarbonate measured after adding hyperpolarized pyruvate solution to E. coli K12.

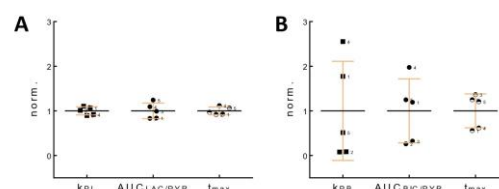


Fig. 3: Kinetics parameters, conversion rate constant, product-to-substrate area-under-the-curve ratio, and time-to-maximum (t_{max}), normalized to the mean of each parameter in A. lactate and B. bicarbonate. Individual data points are experiments, with mean and standard error overlaid.

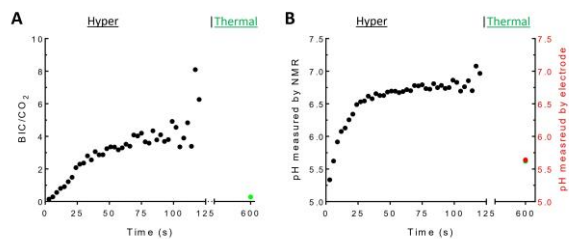


Fig. 4: A. Integrated NMR signal of the bicarbonate-to-CO₂ ratio. B. Measured pH: determined by NMR (hyperpolarized = black, thermal = green) and by pH electrode (red).

Results: The hyperpolarized pyruvate achieved a polarization level of 35.4±1.8% resulting in a strong initial signal that decayed over time due to T₁ relaxation. Simultaneously, pyruvate downstream metabolites were observed in the spectra, including CO₂, whose signal peaked after a few scans, followed by its signal diminishment. Additionally, bicarbonate was detected as a result of CO₂ dissolving in water. Due to the enzymatic activity of lactate dehydrogenase, pyruvate conversion to lactate resulted in a detectable amount of lactate signal in the spectra. Some impurity signals (not from pyruvate or its metabolic products) were also observed (Figure 1).

All metabolite signals exhibited a characteristic rise followed by a decay, reflecting the initial metabolite production and subsequent loss of hyperpolarized magnetization, which decayed faster than the rate of metabolite production (Figure 2). The kinetics values obtained include pyruvate-product conversion $k_{PL} = 8.1 \times 10^{-7} \pm 7.3 \times 10^{-8}$, $k_{PB} = 2.2 \times 10^{-5} \pm 2.44 \times 10^{-5}$; product-pyruvate ratio of area under the curve $AU_{CLAC}/PYR = 5.2 \times 10^{-5} \pm 9.1 \times 10^{-6}$, $AU_{BIC}/PYR = 4.2 \times 10^{-4} \pm 3 \times 10^{-6}$; and time to reach maximum signal: lactate $t_{max} = 52.1 \pm 4.6$ s, and bicarbonate $t_{max} = 36.3 \pm 13.8$ s (Figure 3).

Discussion: dDNP-enhanced signal intensity proved valuable to monitor the metabolism of pyruvate into its downstream metabolites: CO₂, bicarbonate, and lactate in K12 cells. CO₂ signal peaked early and rapidly declined, due to its conversion to bicarbonate in water; however, the decreased pH shifts the CO₂/bicarbonate equilibrium towards CO₂, influencing the observed dynamics. Thermal equilibrium spectrum measured after hyperpolarization decayed revealed [CO₂]/[bicarbonate] of about 3.5, corresponding to a pH of 5.62 (pK_a = 6.1 at 37°C, [4]), which closely matches the value of 5.64, measured independently by pH electrode (Figure 4). This indicates that the observed rapid decay of CO₂ can be attributed to its rapid relaxation, eliminating the possibility of CO₂ escaping into the atmosphere. In addition, the slow interconversion with bicarbonate is insufficient to replenish CO₂, and consequently, insufficient in sustaining the rapid signal decay.

The coefficient of variation (cv) of the pyruvate-to-lactate conversion rate (10%) was significantly lower than the bicarbonate-to-lactate rate (111%), showing higher consistency. As mentioned, bicarbonate is produced indirectly as a secondary byproduct of pyruvate metabolism, possibly explaining its large cv value. Due to CO₂ rapid production and conversion to bicarbonate, its kinetic parameters were difficult to obtain. Lowering K12 sample size or slowing pyruvate metabolism (e.g., by lowering the temperature below 37°C) could help mitigate this issue and improve data quality and reliability.

Conclusion: The enhanced signal strength provided by dDNP proved valuable, enabling the tracking of two pyruvate metabolic pathways and the detection of multiple metabolites produced under aerobic and nonaerobic conditions in real-time. Our study demonstrates the feasibility of utilizing this modality to study disease-relevant bacteria and map their metabolic profile, crucial for a better understanding of their role in disease progression, potentially assisting in the identification of novel therapeutic strategies. Our approach also provides the foundation for its translation into in vivo NMR, enabling tracking of bacteria within their hosts.

Acknowledgements: We acknowledge funding from the German Federal Ministry of Education and Research (BMBWF) within the framework of the e: Med research and funding concept (01ZX1915C), and hyperquant consortium (BlueHealthTech, 03WIR6208A9), DFG (555951950, 527469039, 469366436, HO-4602/2-2, HO-4602/3, GRK2154-2019, EXC2167, FOR5042, TRR287). MOIN CC was founded by a grant from the European Regional Development Fund (ERDF) and the Zukunftsprogramm Wirtschaft of Schleswig-Holstein (Project no. 122-09-053).

References:

1. Ferrari, A., Peters, J., Anikeeva, M. *et al.* Performance and reproducibility of ¹³C and ¹⁵N hyperpolarization using a cryogen-free DNP polarizer. *Sci Rep* 12 (2022).
2. Sriram R, Sun J, Villanueva-Meyer J, Mutch C, De Los Santos J, Peters J, Korenchan DE, Neumann K, Van Criekeing M, Kurhanewicz J, Rosenberg O, Wilson D, Ohliger MA. Detection of Bacteria-Specific Metabolism Using Hyperpolarized [2-¹³C]Pyruvate. *ACS Infect Dis.* (2018).
3. Peters JP, Assaf C, Haj Mohamad F, Beitz E, Tiwari S, Aden K, Hövener JB, Pravidtsev AN. Yeast Solutions and Hyperpolarization Enable Real-Time Observation of Metabolized Substrates Even at Natural Abundance. *Anal Chem.* (2024).
4. Ghosh RK, Kadlecsek SJ, Pourfathi M, Rizi RR. Efficient production of hyperpolarized bicarbonate by chemical reaction on a DNP precursor to measure pH. *Magn Reson Med.* (2015).

Characterizing reproducibility of fat/iron quantification in phantom across 0.55T, 1.5T, and 3T

Majd Helo 1,2, Marcel Dominik Nickel 2, Thomas Küstner 1, Stephan Kannengiesser 2

1 Medical Image and Data Analysis (MIDAS.lab), Department of Diagnostic and Interventional Radiology, University of Tuebingen, Tuebingen, Germany

2 Research & Clinical Translation, Magnetic Resonance, Siemens Healthineers AG, Erlangen, Germany

Abstract: Motivation - Phantoms are useful for validating fat/iron quantification but have different properties than human tissue. Exact properties are needed for cross-field-strength reproducibility investigations.

Goal - Identify and validate, for a commercially available phantom, fat signal model and field-strength-dependent intrinsic relaxivity and transverse relaxation enhancement.

Approach - Phantom measurements were taken using typical 3D multi-gradient-echo imaging at 0.55T, 1.5T, and 3T, with multiple echo times. Data were analyzed for phantom properties, their impact on quantification results (PDFF, R2*), and cross-field-strength reproducibility.

Results - Reproducibility was $\pm 1.6\%$ for PDFF and ± 7.1 s-1 for R2* or better. Using a human liver signal model produces misleading results.

Motivation: MR-based quantification of tissue fat and iron content is an important diagnostic tool. Fat/iron phantoms have proven useful in characterizing state-of-the-art algorithms that enable confounder-corrected, simultaneous estimation of proton density fat fraction (PDFF) and R2* as a measure of tissue iron content[1]. To obtain exact results, it is important to use a signal model tailored to the phantom's fat composition and temperature[2]. Once this is established, reproducibility of quantification results across acquisition details, scanner types, and field strengths can be investigated. In this work, a fat signal model, field-strength-dependent intrinsic relaxivity and transverse relaxation enhancement for a commercially available phantom were validated through measurements at 0.55T, 1.5T, and 3T using 3D multi-gradient-echo imaging. This study evaluates the phantom properties and their impact on the quantification results of PDFF and R2*, offering insights into the cross-field-strength reproducibility.

Materials & Methods: PDFF should not depend on field strength (B0). R2* values must be converted using the intrinsic relaxation rate Ri and the relaxation enhancement ER [3], where, for liver tissue, Ri was assumed constant, and ER was found to be almost perfectly proportional to B0

$$R2^*(B0) = (R2^*(1.5T) - Ri) \times ER(B0) + Ri$$

$$ER(B0) = 0.68 \times B0 - 0.0086$$

A commercially available fat/iron phantom consisting of vials with different nominal fat fractions and R2* in a spherical housing (s/n C0003450, Calimetrix LLC, Madison, WI, USA) was scanned on whole body scanners with 0.55T, 1.5T, and 3T (MAGNETOM Free.Star, MAGNETOM Sola, MAGNETOM Cima.X, Siemens Healthineers, Forchheim, Germany) using a regular 3D multi-gradient echo pulse sequence repeated with varying initial TE (TE1). Sequence parameters and nominal

phantom properties are listed in Table 1. Only phantom vials with R2* lower than 500 s-1 at 3T were considered, which is still comfortably quantifiable with the used TE range. At this point, only the first echoes of the first water/fat interference cycle were analyzed for maximum cross-B0 consistency (Table 1).

Data were processed offline using research tools written in Python with the NumPy, SciPy and Matplotlib libraries. Mean magnitude signal intensities (SI) of the central individual echo images over circular ROIs were fitted to the commonly used signal model.

$$SI = |M0 \times ((1 - PDFF) + PDFF \times c(TE)) \times \exp(-R2^* \times TE)|$$

M0 represents spin density, and c(TE) are the complex-valued fat dephasing factors calculated from the multi-peak spectrum of peanut oil, scaled according to B0 and spectrally shifted according to the phantom temperature[2].

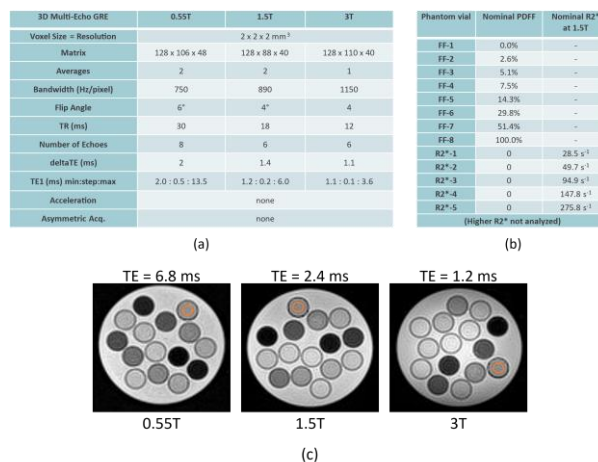


Fig. 1: a) Sequence parameters. b) Nominal phantom properties. Only vials <500s-1 at 3T were evaluated; only the first echoes (TE1) of the multi-echo acquisitions were analyzed at this point. c) Example individual echo images at the different field strengths and example ROIs drawn on the vial containing 100% fat.

Results: A linear regression of R2* values was performed. From this, Ri and ER values were calculated, and R2* values were converted to 1.5T (R2*_1.5T) (Figure 3). Bias and limits of agreement (LoA) for PDFF and R2*_1.5T across B0 were investigated with Bland-Altman analysis (Figure 4). To estimate the errors caused by a mismatched signal model, the comparisons were repeated using a standard human liver fat model, without temperature correction[4].

Exemplary individual echo images and ROIs are shown in Figure 1c. Measured SI from the 100% PDFF vial, corrected for R2*, agrees well with the peanut oil model (Figure 2). Linear regression analysis (Figure 3) yielded for the conversion of

$R2^*_{3T} \rightarrow 1.5T$ $Ri = 19.4$ s⁻¹ and $ER = 0.52 \times B0$, and for 0.55T $\rightarrow 1.5T$ $Ri = 14.3$ s⁻¹ and $ER = 1.0 \times B0$. There was no significant bias between the different $B0$ for PDFF, and the limits of agreement (LoA) were $\pm 1.6\%$ for PDFF and ± 7.1 s⁻¹ for $R2^*_{1.5T}$, or better (Figure 4). For PDFF <50%, these LoA were $\pm 1.0\%$. Using the (inappropriate) human liver signal model, the PDFF LoA worsened to as high as $\pm 4.8\%$ with significant bias (details not shown).

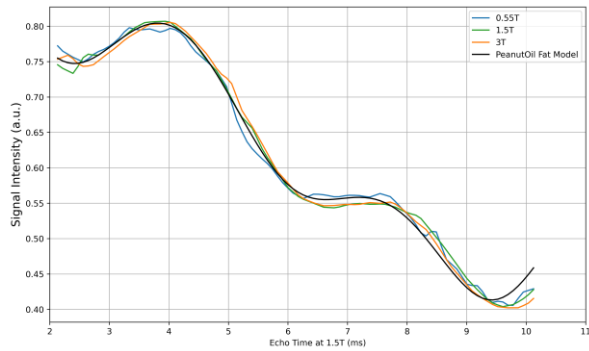


Fig. 2: Plot of the magnitude of the peanut oil fat dephasing factors $c(TE)$ vs. the signal intensities of the vial containing 100% fat at the different field strengths. The x-axis was scaled to equivalent echo times at 1.5T to show the same interference state.

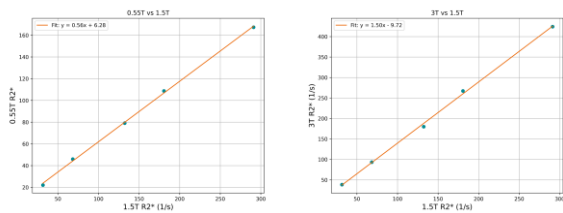


Fig. 3: Scatter plots and linear regression of $R2^*$ values across field strengths.

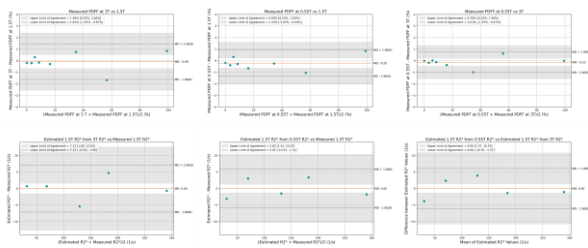


Fig. 4: Bland-Altman plots comparing PDFF and $R2^*_{1.5T}$ values across field strengths.

Discussion: PDFF and $R2^*_{1.5T}$ values showed good reproducibility across field strengths. However, the $R2^*$ conversion seems to be governed by unexpected mechanisms: Contrary to the liver case³, for the phantom, Ri is not constant, and ER is not proportional to $B0$.

As expected, large errors are being made if the human signal model is incorrectly applied to phantom data.

Further investigations will target clinical breath-hold protocols, which will necessarily contain a limited number of bipolar echoes and cover different numbers of the fat/water dephasing cycle with their TEs, which is expected to lead to larger deviations in PDFF and $R2^*$ estimations. Additionally, it needs to be confirmed that the current ROI-first fitting gives the same results as pixelwise fitting and ROI-analysis of the resulting maps, which is to be expected.

Conclusion: With appropriate parameterization of the fitting algorithm, fat/iron phantoms show good reproducibility of PDFF and $R2^*_{1.5T}$ across 0.55T, 1.5T, and 3T.

Acknowledgements: Daniel Amsel and Cornelius Jacob from Siemens Healthineers AG.

References:

1. Hernando D, Sharma SD, Aliyari Ghasabeh M, et al. Multisite, multivendor validation of the accuracy and reproducibility of proton-density fat-fraction quantification at 1.5T and 3T using a fat-water phantom. *Magn Reson Med.* 2017;77(4):1516-1524. <https://pubmed.ncbi.nlm.nih.gov/27080068/>
2. Hernando D, Sharma SD, Kramer H, and Reeder SB. On the confounding effect of temperature on chemical shift-encoded fat quantification. *Magn Reson Med.* 2014;72(2):464-70. <https://pubmed.ncbi.nlm.nih.gov/24123362/>
3. Ghugre NR, Doyle EK, Storey P, and Wood JC. Relaxivity-iron calibration in hepatic iron overload: Predictions of a Monte Carlo model. *Magn Reson Med.* 2015;74(3):879-83. <https://pubmed.ncbi.nlm.nih.gov/25242237/>
4. Hamilton G, Yokoo T, Bydder M, et al. In vivo characterization of the liver fat ¹H MR spectrum. *NMR Biomed.* 2011;24(7):784-90. <https://pubmed.ncbi.nlm.nih.gov/21834002/>

Hyperpolarized ¹³C metabolic MRI of tumor xenografts in fertilized chicken eggs with a tailored surface RF coil

Ruben Hernandez-Vega 1*, Miriam Kirst 1, Raphela A. Ranjan 2, Nadine Setzer 1, Sandra Sühnel 1, Geoffrey J. Topping 1, Maximilian Reichert 2, Franz Schilling 1+3

1 Department of Nuclear Medicine, TUM School of Medicine and Health, TUM University Hospital, Klinikum rechts der Isar, Technical University of Munich, Munich, Germany,

2 Clinic and Polyclinic for Internal Medicine II, TUM University Hospital, Klinikum rechts der Isar, Technical University of Munich, Munich, Germany,

3 Munich Institute of Biomedical Engineering, Technical University of Munich, Garching, Germany

Abstract: We established a protocol for hyperpolarized (HP) [1-¹³C]pyruvate-to-lactate metabolism detection in tumor xenografts on the chorioallantoic membrane (CAM) of fertilized chicken eggs. Different transplantation methods for murine T-cell lymphoma cells (EL4) and pancreatic ductal adenocarcinoma-patient derived organoids (PDAC-PDOs) were tested. A tailored surface RF coil was used for local ¹³C signal collection, and a water-heated egg bed was designed to keep the egg warm without drying out. EL4 tumors transplanted on three adjacent sites showed better metabolite ¹³C signal in slice-selective FIDs and 2D FID-CSI compared to the one-site method. Both EL4 and PDAC-PDO xenografts showed perfusion with Gd-DOTA, an essential property for HP metabolic MRI.

Motivation: Tumor xenografts on the chorioallantoic membrane (CAM) of fertilized chicken eggs have gained attention in preclinical research [1]. The Hen's Egg Test (HET) CAM model presents an environment that allows for the study of new tumor therapy strategies, such as drug efficiency, on tumor xenografts while being more cost- and time-efficient compared to rodent tumor models [1]. The effectiveness of these strategies could be assessed by measuring a change in the pyruvate-to-lactate metabolism of the tumors with hyperpolarized (HP) ¹³C metabolic MRI. However, this method has not yet been established on this model.

Our group has previously worked on establishing a protocol for HP [1-¹³C]pyruvate-to-lactate conversion of murine T-cell lymphoma EL4 using a self-built 7mm tunable passive ¹³C booster coil with inductive coupling to the volume resonator and passive decoupling during excitation. However, issues such as low metabolite signal intensity boosting and coil handling logistics problems prompted our group to acquire a surface RF coil designed specifically for local ¹³C signal collection in tumor xenografts on the CAM model.

In this study, our protocol was further refined by testing two different methods for transplantation of the EL4 cells and pancreatic ductal adenocarcinoma-patient derived organoids (PDAC-PDOs) to establish the optimal engraftment. The performance of the new surface RF coil was assessed on the EL4 xenografts.

Materials & Methods: On embryonic development day (EDD) 3, 5 ml albumin were removed [2] from the eggs and a small horizontal window was opened to add 0.5 ml Gibco™ Penicillin-Streptomycin (104 U/ml). On EDD7, the window was enlarged. On EDD9, silicon rings were placed on the CAM and EL4 cells with high glycolytic activity [3] (5×106/ring) or PDAC

PDOs B250/B339 (2.5×105/ring) were seeded as Matrigel droplets [4]. The eggs were scanned on EDD14-EDD16.

Eggs were catheterized through an extraembryonic vessel previously exposed (Fig. 1A). Intravenous injections applied subsequently included 0.75 mg/0.015 mg ketamine/midazolam in 100 µl saline for anesthesia, 230 µl of 80 mM HP [1-¹³C]pyruvate per HP ¹³C metabolic MRI, and 100 µl of 15 mM Gd-DOTA for DCE perfusion imaging. [1-¹³C]pyruvate was hyperpolarized using a HyperSense dNTP [5] polarizer.

Imaging was performed on a preclinical 7T MRI with a 72 mm 1H/¹³C volume resonator for 1H imaging and homogeneous ¹³C signal transmission. For local ¹³C signal reception, a 6 mm ¹³C surface coil containing crossed diodes for passive decoupling during excitation was mounted on a self-built holder (Fig. 1B). When possible, both slice-selective FIDs (during the first HP [1-¹³C]pyruvate injection) and single-shot 2D FID-CSI (28-35 s after the second HP [1-¹³C]pyruvate injection) were applied subsequently to measure the HP [1-¹³C]pyruvate-to-lactate conversion.

Initially, eggs were warmed using air (36-38°C) blown into the bore, and later using warm water (49-50°C) circulated through tubing wrapped around them with a self-built bed (Fig. 1E). Temperature probes placed next to the egg enabled temperature monitoring.

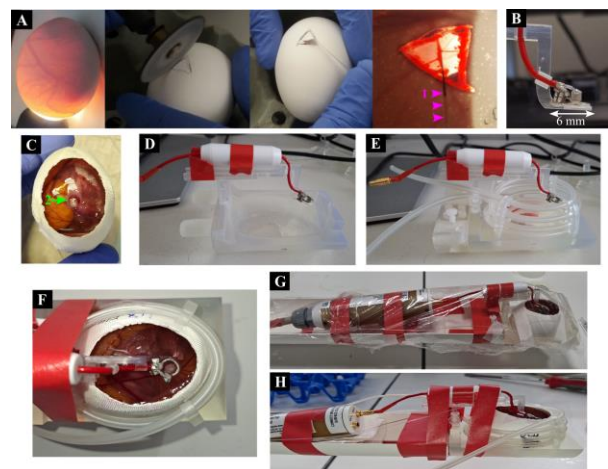


Fig. 1: Pre-scan protocol. A: Visualization of extraembryonic vascular system and catheterization. B: Receiver coil on self-designed holder. C: Exposed CAM, tumor in 5 mm silicon ring (2). Receiver coil and egg bed without (D) and with (E) water heating. F: Coil positioning. Complete setup without (G) and with (H) water heating.

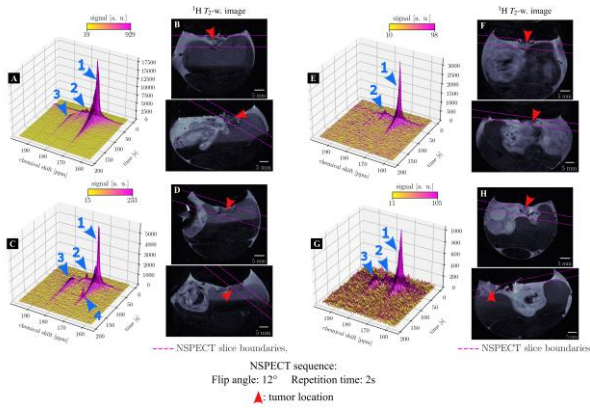


Fig. 2: Spectra from repeated slice-selective ¹³C FID measurements on three-sited (A/C) and one-sited (E/G) EL4 xenografts. HP [1-¹³C]pyruvate was injected at 23s. ¹H axial and sagittal images (B/D/F/H) show the selected slice. [1-¹³C]pyruvate (1), [1-¹³C]pyruvate hydrate (2), and [1-¹³C]lactate (3) peaks are highlighted. A repeated pyruvate peaking (4) indicates ineffective anesthesia.

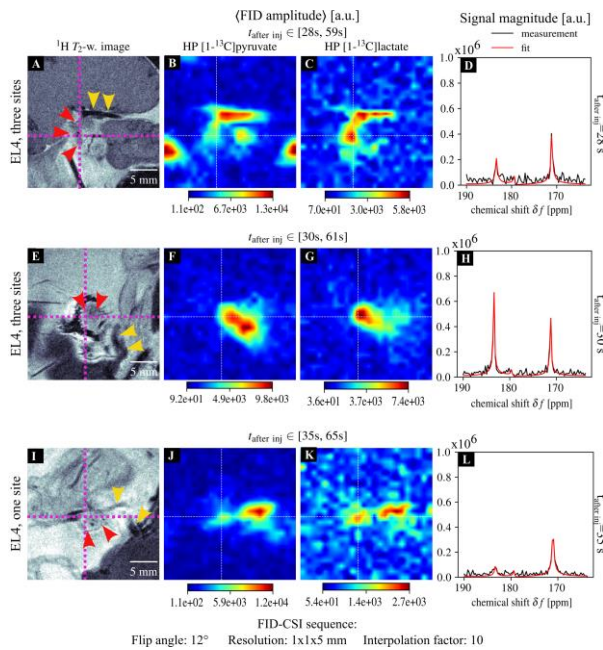


Fig. 3: Static 2D ¹³C FID-CSI of three CAM xenografts. Maps of HP [1-¹³C]pyruvate (B/F/J) and HP [1-¹³C]lactate (C/G/K) post intravenous injection of HP [1-¹³C]pyruvate show signal in tumor and blood vessels highlighted in the corresponding ¹H images (A/E/I) in red and yellow, respectively. D/H/L: ¹³C spectra of the dashed lines' intersection.

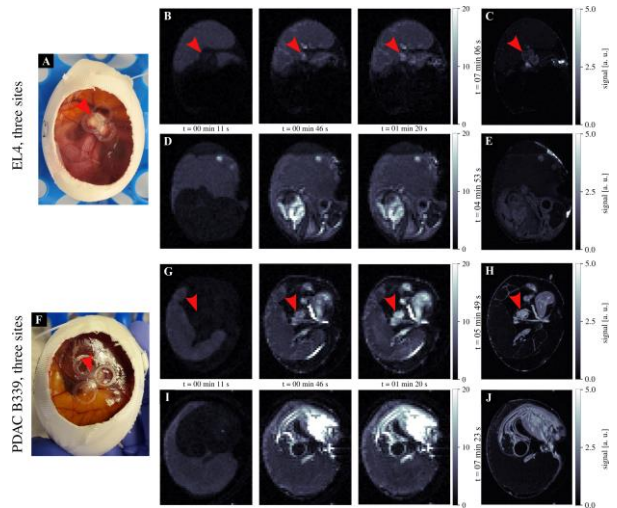


Fig. 4: DCE perfusion images of two eggs (Gd-DOTA injection at 10 s). A/F: Exposed CAM and tumor xenograft. DCE images of xenograft (B/G) and chick (D/I). High-resolution, contrast-enhanced FLASH images of xenograft (C/H) and chick (E/J) at corresponding time p.i. of Gd-DOTA. The red arrow points to the tumor.

Results: Fig. 1 shows the pre-scan protocol. The anesthetic was injected before anatomical scans and was effective almost until the end of the imaging protocol. The air flow setup (Fig. 1D/G) dried the CAM fast, potentially affecting perfusion. It was changed to the water-circulation heating system (Fig. 1E/H). Temperature measurements determined the ideal input water temperature of 49-50°C, which set the tube's temperature around the egg close to 40°C. A measured gradient (1°C between the tubes and the inner shell, 4°C between the inner shell and the CAM center) enabled keeping the inner egg between 35°C and 39°C.

[1-¹³C]Pyruvate-to-lactate conversion was observed in slice-selective FIDs for two EL4 xenografts (Fig. 2A/C/G) with a lactate/pyruvate Area Under the Curve Ratio (AUCR) of 0.14, 0.47, and 0.49, respectively. Repeated pyruvate peaking in Fig. 2C indicates previously unexcited [1-¹³C]pyruvate entering the slice due to chick motion, implying unsuccessful anesthesia.

Spatially resolved single-shot 2D FID-CSI 28 – 35 s p. i. of HP [1-¹³C]pyruvate on EL4 tumors showed both [1-¹³C]pyruvate (Fig. 3B/F/J) and [1-¹³C]lactate signal (Fig. 3C/G/K) in the tumor and surrounding blood vessels. Whereas the [1-¹³C]lactate signal in the tumor tissue is comparable to (Fig. 3C/K) or higher than (Fig. 3G) in the blood vessels, the corresponding [1-¹³C]pyruvate signal in the tumor is smaller compared to the blood vessels (Fig. 3B/F/J). This clearly isolates metabolic pyruvate-to-lactate conversion of the EL4 xenografts.

Fig. 4 shows Gd-DOTA perfusion for a three-sited EL4 and a PDAC-PDO B339 xenograft.

Discussion: The slice-selective FIDs and spatially-resolved FID-CSIs of the EL4 xenografts showed pyruvate-to-lactate conversion with lactate/pyruvate AUCRs of up to 0.49 (Fig. 2) and spatial correlation with tumor tissue and blood vessels (Fig. 3). The three-site EL4 (n=3) tumors enabled the clearest metabolic activity detection with registration with the tumor. In later egg measurements, the SNR of the slice-selective FIDs dropped drastically (easily observed in Fig. 2E/G), which was

found to be related to damage of the tailored surface coil. The PDAC-PDO xenografts were scanned with the damaged coil, potentially explaining the absence of HP [1-¹³C]pyruvate and HP [1-¹³C]lactate signal in the xenografts.

Gd-DOTA perfusion of the PDAC-PDO B339 xenografts (n=2, Fig. 4G) indicates that the detection of at least HP [1-¹³C]pyruvate in the tumor tissue should be possible. No Gd-DOTA perfusion could be measured in the PDAC-PDO B250 xenograft (n=1). This could have been caused either by suboptimal engraftment or by perfusion blockage due to the receiver coil being pushed down into the CAM. More scans are necessary to confirm these findings.

The water heating system (Fig. 1E) was able to reduce the moisture loss of the CAM during the scanning. However, the tube's location below the eggs increased the height where the receiver needed to be positioned, which caused problems fitting the apparatus into the volume coil, leading to the receiver being pressed into the CAM, potentially affecting tumor perfusion. A slight redesign of the holder will resolve this problem.

Conclusion: Overall, we established a protocol for metabolic imaging using hyperpolarized substrates in the HET-CAM model. The presented setup, transplantation method, and imaging protocol enabled the detection of metabolic activity in CAM EL4 tumor xenografts.

Both dynamics of pyruvate-to-lactate conversion as well as its spatial correlation to tumor tissue and blood vessels could be

detected with the tailored surface coil. The xenograft perfusion was verified with Gd-DOTA injections. Here, the PDAC-PDO B339 xenografts also showed perfusion in contrast to the PDAC-PDO B250 xenograft.

Future studies will focus on the detection of metabolic activity also in PDAC-PDO xenografts, with the presented Gd-DOTA perfusion data suggesting PDAC-PDO B339 as a promising candidate.

Acknowledgements: This work was supported by the German Federal Ministry of Research, Technology and Space (BMFTR) in the funding program "Quantum Technologies– from Basic Research to Market" under the project "QuE-MRT" (contract number: 13N16450).

References:

1. DeBord, L. C. *et al.* The chick chorioallantoic membrane (CAM) as a versatile patient-derived xenograft (PDX) platform for precision medicine and preclinical research. *American Journal of Cancer Research* 8, 1642 (2018).
2. Cárdenas, A. & Borrell, V. A protocol for *in ovo* electroporation of chicken and snake embryos to study forebrain development. *STAR protocols* 2, 100692 (2021).
3. Serrao, E. M. *et al.* Effects of fasting on serial measurements of hyperpolarized [1-¹³C] pyruvate metabolism in tumors. *NMR in Biomedicine* 29, 1048-1055 (2016).
4. Dantes, Z. *et al.* Implementing cell-free DNA of pancreatic cancer patient-derived organoids for personalized oncology. *Jci Insight* 5 (2020).
5. Ardenkjær-Larsen, J. H. *et al.* Increase in signal-to-noise ratio of > 10,000 times in liquid-state NMR. *Proceedings of the National Academy of Sciences* 100, 10158-10163 (2003).

Improving the Quantification Accuracy of Long T1 Times in Magnetic Resonance Fingerprinting

Niklas Himburg 1+2, Max Lutz 1, Sebastian Schmitter 1+3+4

1 Physikalisch-Technische Bundesanstalt, Braunschweig and Berlin, Germany
 2 Technische Universität Berlin, Institut für Physik und Astronomie, Straße des 17. Juni 135, Berlin 10623, Germany
 3 Medical Physics in Radiology, German Cancer research Center (DKFZ), Heidelberg, Germany
 4 Center for Magnetic Resonance Research, University of Minnesota, Minneapolis, MN, USA

Abstract: Magnetic resonance fingerprinting at ultra-high fields is a promising application for accurate quantification of T1 in the presence of inhomogeneous B1+ fields. An increase in field strength, however, leads to longer T1 times that require caution to not saturate the signal after inversion too quickly to sample the entire relaxation curve. The aim of this work is to investigate the influence of increased repetition times and the introduction of a pause in the flip angle pattern on the accuracy of MRF-based T1 quantification. Comparisons with a reference method confirm reduced underestimations of long T1 when using long TR or pause durations.

Motivation: Magnetic resonance fingerprinting (MRF) allows the acquisition of multiple quantitative parameter maps at the same time[1]. This reduces scan time but also allows to directly account for system imperfections that might influence the parameter maps. This is especially interesting for ultra-high fields (UHF) where this approach could be used to provide accurate relaxation time maps in the presence of B1+ field variations[2]. Attempts to measure T1 and B1+ together at UHF show good results in phantoms[2,3] and in the brain[4]. However, the T1 accuracy is often only validated in a range up to 1500ms[2,3]. As T1 increases with increasing field strength[5], T1 times exceeding this range might be found at UHF, e.g. for gray matter T1 in the range of 2100ms was found at 7T[6]. One approach to deal with long T1 values is the introduction of a pause in the flip angle (FA) pattern to allow relaxation of the longitudinal magnetization component[2]. Another way to achieve the same effect could be an increase in repetition time (TR). In this work, we investigate if and how these two measures influence the accuracy of MRF-T1 maps specifically in the case of long T1 values (>1500ms) at 3T.

Materials & Methods: All measurements were acquired at 3T (Cima.X, Siemens) using a 64-channel head coil. The FLASH based 2D radial MRF method presented by Lutz et al.[7] was modified by adding an adiabatic HS1 inversion pulse at the beginning of each FA pattern to enhance T1 sensitivity. Phantom experiments in a transversal orientation were conducted. The phantom consists of several tubes filled with either water and contrast agent (Tube 1-5, cf. Fig.2) or water and Polyvinylpyrrolidone (Tube 6-13, cf. Fig.2) in various concentrations to cover a wide T1 range of 400-3000ms. Measurements were acquired in two sets with TE=2.5ms and 2x2x5mm3 resolution as well as I) TR=5.0ms, 600 time frames (TF) per pattern and pause duration at the end of the FA pattern 0-2s in 0.2ms-steps II) no pause, TF=600 and TR=5.0-15.0ms in 1ms-steps. 13 repetitions of the FA pattern plus one dummy repetition were used for each measurement in all sets. This acquisition scheme is illustrated in Fig.1. MRF-T1 maps were reconstructed by dot product matching of the

measured fingerprint to a dictionary consisting of entries with T1=400-3400ms in 10ms-steps and FAs of 51°-69° in 1.2°-steps. Additionally, reference T1 values were acquired using an inversion recovery spin echo (IRSE) sequence with TR=8000ms and TI=25-6000ms.

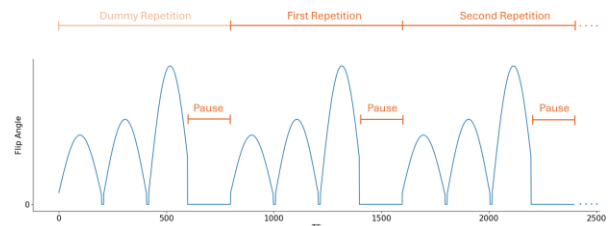


Fig. 1: Overview of the MRF acquisition. Every FA pattern has a length of 600 time frames (TF) and is followed by a pause. 13 repetitions of the pattern plus one dummy repetition were used for T1 map acquisition. The HS1 pulses at the beginning of each pattern are not shown.

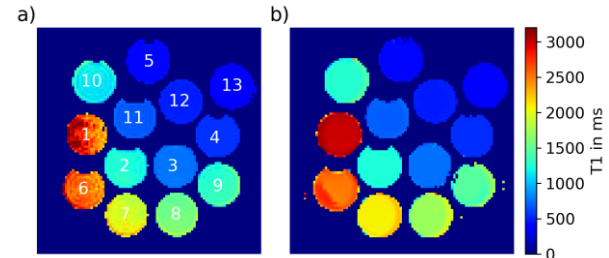


Fig. 2: Transverse T1 maps of several tubes filled with liquids with varying T1. T1 maps were acquired with a) the MRF method with a 1s-pause and TR=5ms and b) a reference inversion recovery method. Underestimations of T1 and increased inhomogeneity are found in tubes with T1 reference values above ~800ms.

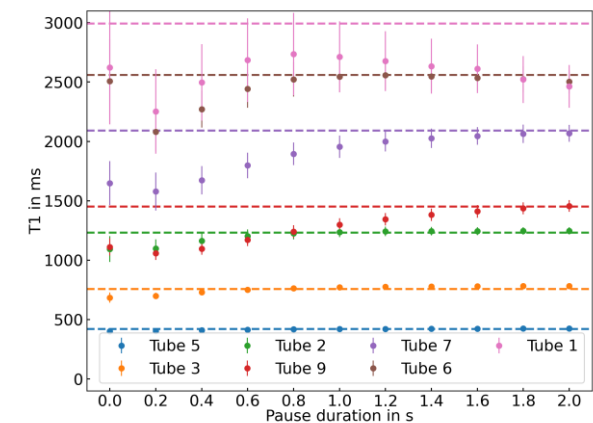


Fig. 3: MRF-T1 values of seven tubes acquired with varying pause durations. The dashed lines indicate the reference values from the T1 map in Fig.2b. Underestimations of T1 are found especially in tubes with T1>1200ms.

Underestimations as well as the standard deviation in each tube are reduced for increasing pause duration.

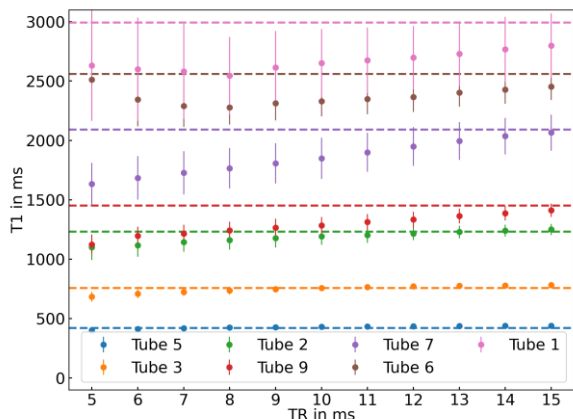


Fig. 4: MRF-T1 values of different tubes acquired with varying TR. The dashed lines indicate the reference values from the T1 map in Fig.2b. Similar to Fig.3, underestimations of T1 appear primarily in tubes with T1>1200ms and are reduced for increasing TR.

Results: Fig.2 shows the IRSE T1 map (Fig.2b) together with an exemplary MRF-T1 map acquired with a 1s-pause and TR=5.0ms (Fig.2a). The tube number is annotated in white (Fig.2a) and both subfigures share the same axis. The reference T1 map shows a homogenous T1 distribution in each tube and confirms the covered range of T1=400-3000ms. The T1 map acquired with MRF (Fig.2a) is comparable with the reference map for tubes with lower T1 values (tubes 3-5, 11-13). For high T1 tubes, however, the maps show increased T1 variations within the single tubes compared to the reference map that appear to be increasing with increasing T1 value. Additionally, the T1 values are underestimated in these tubes (e.g. tubes 8-10).

Fig.3 presents the mean T1 value and standard deviation in seven tubes for increasing pause durations. The reference values for each tube are shown as dashed lines. Generally, MRF results underestimate the reference values and increase with increasing pause durations except for tube 1 with the longest T1 (2993ms). Additionally, the standard deviation is increased for increasing T1 and decreases for increasing pause durations. Up to T1=1230ms (tube 2) the underestimation stays below 11%, even without a pause. For larger T1, underestimations of up to 25% (tube 7) were observed.

Fig.4 depicts the relation of matched T1 and TR for the same tubes that were shown in Fig.2 without a pause. Like Fig.3, the MRF results underestimate the reference values for long T1 times, but the deviation to them decreases with increasing TR.

Discussion: The results presented in Fig.3-4 confirm that both measures, long TR and the introduction of a pause at the end of the FA pattern, are suitable to improve T1 quantification for T1>500ms. The results also highlight the challenge of long T1 times at UHF. Accurate quantification of T1 times in the range of 0-1200ms, that covers a wide range of tissues at

3T[8], can be achieved with a short pause duration of 0.4s or a TR=9.0ms. For an increased T1 range up to 2500ms that is better suited for UHF applications, pause durations above 1.8s or TR>15ms are needed. For the 13 repetitions and TF=600 chosen here the introduction of a 1.8s-pause leads to a shorter TA=69s compared to an increase of the TR to 15ms (TA=168s). Additionally, the reduction in standard deviation found for increased pause durations indicates lower T1 variations in MRF-T1 maps that match better with the reference map in Fig.2b. Another advantage of the introduction of a pause at the end of the FA pattern is that it can be used for e.g. the acquisition of different slices during the pause[2]. Both options, increased TR and increased pause durations, lead to a longer TA which makes imaging in the presence of e.g. breathing movements more difficult. The increase in scan time could also be reduced by using less TFs also this might affect the matching process due to a shorter fingerprint. Additionally, the TA could be optimized by increasing the pause duration and TR together.

Conclusion: Acquisition of MRF-T1 maps revealed an increase in T1 accuracy for increased TR and increased pause durations. This allows accurate T1 quantification in the range of 0-2500ms that is necessary to cover the wide range of T1 times found at UHF[6]. An increase in pause duration instead of an increase in TR further increases the homogeneity of the T1 maps and leaves room for e.g. spoiling gradients or multi-slice approaches. Therefore, for an accurate quantification of long T1 times typically found in vivo at UHF, a pause of a few seconds should be included into the FA pattern. These findings might aid in the development of future quantitative MRF-based methods.

Acknowledgements: We gratefully acknowledge funding from the German Research Foundation (DFG) GRK2260, BIOQIC and SCHM 2677/4-1.

References:

1. Ma D, Gulani V, Seiberlich N, et al. Magnetic resonance fingerprinting. *Nature*. 2013;495(7440):187-192. doi:10.1038/nature11971
2. Cloos MA, Knoll F, Zhao T, et al. Multiparametric imaging with heterogeneous radiofrequency fields. *Nat Commun*. 2016;7(1):12445. doi:10.1038/ncomms12445
3. van Riel MHC, Yu Z, Hodono S, et al. Free-breathing abdominal T1 mapping using an optimized MR fingerprinting sequence. *NMR in Biomedicine*. 2021;34(7):e4531. doi:10.1002/nbm.4531
4. Buonincontri G, Schulte RF, Cosottini M, Tosetti M. Spiral MR fingerprinting at 7 T with simultaneous B1 estimation. *Magnetic Resonance Imaging*. 2017;41:1-6. doi:10.1016/j.mri.2017.04.003
5. Ladd ME. High-field-strength magnetic resonance: potential and limits. *Top Magn Reson Imaging*. 2007;18(2):139-152. doi:10.1097/RMR.0b013e3180f612b3
6. Rooney WD, Johnson G, Li X, et al. Magnetic field and tissue dependencies of human brain longitudinal 1H2O relaxation in vivo. *Magnetic Resonance in Medicine*. 2007;57(2):308-318. doi:10.1002/mrm.21122
7. Lutz M, Aigner CS, Flassbeck S, et al. B1-MRF: Large dynamic range MRF-based absolute mapping in the human body at 7T. *Magnetic Resonance in Medicine*. 2024;92(6):2473-2490. doi:10.1002/mrm.30242
8. Bojorquez JZ, Bricq S, Acquitier C, Brunotte F, Walker PM, Lalande A. What are normal relaxation times of tissues at 3 T? *Magnetic Resonance Imaging*. 2017;35:69-80. doi:10.1016/j.mri.2016.08.021

Assessing the Repeatability of SMS accelerated QTI Imaging at 7T

Annika Hofmann 1*, **Martin Freudensprung 2**, **Zijin Yang 3**, **Julius Glaser 4**, **Katharina Tkotz 4**, **Angelika Mennecke 2**, **Frederik B. Laun 4**, **Florian Knoll 1**
 1 Computational Imaging Lab, AIBE, Friedrich-Alexander-Universität Erlangen-Nürnberg, Erlangen, Germany
 2 Institute of Neuroradiology, Uniklinikum Erlangen, Friedrich-Alexander-Universität Erlangen-Nürnberg, Erlangen, Germany
 3 Pattern Recognition Lab, Friedrich-Alexander-Universität Erlangen-Nürnberg, Erlangen, Germany
 4 Institute of Radiology, Uniklinikum Erlangen, Friedrich-Alexander-University Erlangen-Nürnberg, Erlangen, Germany

Abstract: We present a scan-rescan repeatability study of a Q-space trajectory imaging (QTI) sequence accelerated using simultaneous multi-slice (SMS) acquisition at 7T. Twelve healthy volunteers were scanned twice using linear and planar b-tensor encoding. Repeatability was assessed using Bland-Altman analysis and tissue-type segmented comparisons. Most contrasts showed minimal bias and tight limits of agreement, with only minor deviations in a few slices. Differences between tissue types were consistently larger than scan-rescan or inter-subject variations. These results demonstrate good repeatability of the proposed SMS capable QTI-sequence for microstructure imaging.

Motivation: Diffusion MRI is used to study brain microstructure but suffers from partial volume effects due to limited resolution [1]. Q-space trajectory imaging (QTI) uses advanced acquisition and post-processing methods to improve microstructural contrast [2].

Imaging at 7 T offers improved signal to noise ratio but requires longer scan times [3]. QTI is routinely measured using single-shot acquisition [4]. We address these issues using simultaneous multi-slice (SMS) imaging to speed-up the acquisition.

To validate this new sequence, we assessed its scan-rescan repeatability. Repeatability is the consistency of quantitative results, when the same subject is measured repeatedly using the same scanning protocol at the same scanner in the same center [5].

Materials & Methods: Data acquisition was done using an SMS-capable, EPI-based sequence with generalized diffusion gradient waveforms. Two types of b-tensor encoding were used: linear and planar. Twelve healthy volunteers were scanned on a MAGNETOM Terra.X 7T MRI system (Siemens Healthineers, Erlangen, Germany) with a scan-rescan protocol at the same time of day, one or two days apart. The study was approved by the local IRB, and written informed consent was obtained prior to the exams. Imaging parameters were as follows: voxel size 1.4 x 1.4 x 2 mm³, parallel imaging acceleration factor = 6, 6/8 partial Fourier, TE = 80 ms, TR = 3000 ms, b = 0, 800, and 2000 s/mm² with 30 diffusion encoding directions each, total acquisition time: 6:36min.

QTI maps were computed using the QTI+ framework [6]. To assess repeatability, we generated histograms of intensity values for each QTI contrast, comparing their probability density distributions between scan and rescan sessions. This allowed us to evaluate scan-rescan similarity. We segmented the brain into white matter (wm), gray matter (gm) and cerebrospinal fluid (csf) to compute the mean and standard deviation, depending on tissue type. Additionally, to further assess agreement between measurements, we applied the Bland-Altman method, which evaluates agreement between

two measurements by analyzing bias and variability. Changes within the Limits of Agreement (LoA) are interpreted as variability due to patient related or imaging system related factors. Only changes outside this range indicate real change [7].

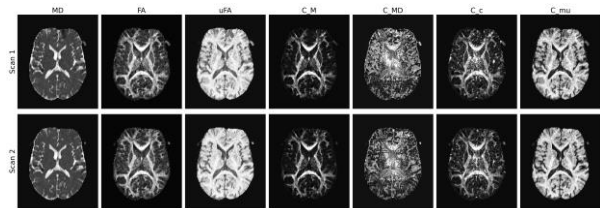


Fig. 1: Visual comparison of the scan-rescan images in subject 18. Fitted QTI maps from Scan 1 and Scan 2 are shown for selected contrasts (C_{MD}: normalized size variance of the tensors, C_{\mu}: microenvironment shape measure, C_M: macroscopic anisotropy measure, C_c: microscopic orientation coherence, FA: fractional anisotropy, MD: mean diffusivity, \mu FA: microscopic fractional anisotropy).

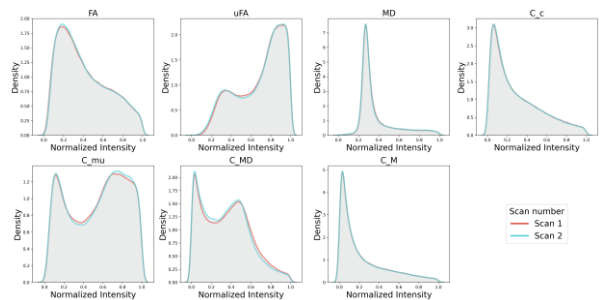


Fig. 2: Histogram of full brain volume pixel intensity value comparing Scan 1 (red) and Scan 2 (blue) for selected QTI contrasts (C_{MD}: normalized size variance of the tensors, C_{\mu}: microenvironment shape measure, C_M: macroscopic anisotropy measure, C_c: microscopic orientation coherence, FA: fractional anisotropy, MD: mean diffusivity, \mu FA: microscopic fractional anisotropy) for subject 18.

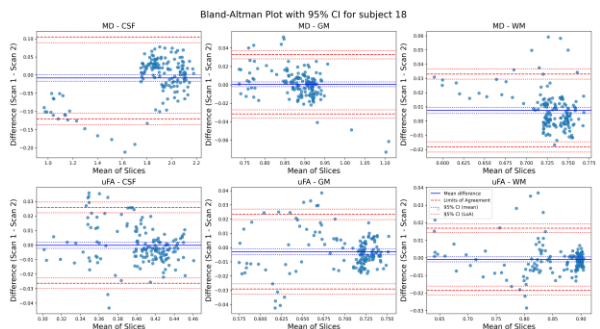


Fig. 3: Bland-Altman plots for three tissue types (CSF, GM, WM) showing Mean Diffusivity (MD) and microscopic Fractional Anisotropy (μ FA). The plots display slice-wise mean values along with the limits of agreement (LoA) and 95% confidence intervals for subject 18

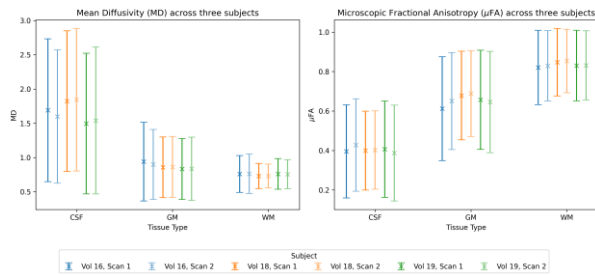


Fig. 4: Intrasubject comparison for three Volunteers (Vol) of mean values across tissue types. Mean values for cerebrospinal fluid (CSF), gray matter (GM), and white matter (WM) are shown for Mean Diffusivity (MD) and Microscopic Fractional Anisotropy (μ FA).

Results: We first performed a visual comparison of fitted parameter maps for a representative slice (Figure 1). Histogram comparisons of normalized voxel-wise values between scan one and scan two showed high overlap across most contrasts (Figure 2). Slight deviations were noted for the normalized size variance of the tensors ($C_{\{MD\}}$), and the microenvironment shape measure (C_{μ}).

Bland-Altman plots confirmed that most slice-wise differences remained within the LoA, with only isolated slices falling outside the expected range (Figure 3). Additionally, segmentation-based analyses of white matter, gray matter, and CSF in three volunteers showed that intra- and inter-subject variability are low for MD and micro-FA (Figure 4).

Discussion: We developed and tested a novel SMS-capable QTI sequence enabling faster acquisition by combining advanced diffusion encoding schemes with simultaneous multi slice imaging.

Our results showed high scan-rescan repeatability, with variations generally confined within expected error margins. The consistency of normalized values across subjects suggests robustness of the method.

Future studies will aim to include a larger cohort as well as different MRI contrasts, to enhance statistical power and investigate remaining inconsistencies.

Conclusion: Our developed QTI sequence with SMS acceleration demonstrates good repeatability in a 7 T scan-rescan setup.

Acknowledgements: Funding by the German Research Foundation (DFG) is gratefully acknowledged (project 500888779 / RU5534 MR biosignatures at UHF).

References:

1. Wang, Fuyixue, *Scientific data* vol. 8,1 122. 29 Apr. 2021, doi:10.1038/s41597-021-00904-z
2. Westin, Carl-Fredrik, *NeuroImage*, vol. 135 (2016): 345-62. doi:10.1016/j.neuroimage.2016.02.039
3. Le Ster C, Grant A, Van de Moortele PF, et al. Magnetic field strength dependent SNR gain at the center of a spherical phantom and up to 11.7T. *Magn Reson Med*. 2022;88(5):2131-2138. doi:10.1002/mrm.29391
4. Martin, Jan, *Zeitschrift für medizinische Physik* vol. 30,1 (2020): 4-16. doi:10.1016/j.zemedi.2019.01.003
5. Barnhart HX, Barboriak DP. Applications of the repeatability of quantitative imaging biomarkers: a review of statistical analysis of repeat data sets. *Transl Oncol*. 2009;2(4):231-235. doi:10.1593/tlo.09268
6. Herberthson M, Boito D, Haije TD, Feragen A, Westin CF, Özarlan E. Q-space trajectory imaging with positivity constraints (QTI+). *Neuroimage*. 2021;238:118198. doi:10.1016/j.neuroimage.2021.118198
7. Obuchowski NA. Interpreting Change in Quantitative Imaging Biomarkers. *Acad Radiol*. 2018;25(3):372-379. doi:10.1016/j.acra.2017.09.023

Impact of sequence parameters, parallel imaging and reduced FOW DWI techniques on ADC values

Ville Iso-Kouvola 1*, Harri Merisaari 2+3, Teija Sainio 1, Jani Saunavaara 1+4

1 Department of Medical Physics, University of Turku and Turku University Hospital, Turku, Finland

2 Department of Diagnostic Radiology, University of Turku, Turku, Finland

3 Turku Brain and Mind Centre, University of Turku and Turku University Hospital, Turku, Finland

4 Suomen Terveystalo Plc, Helsinki, Finland

Abstract: Magnetic resonance imaging (MRI) is an essential diagnostic tool. It has potential for producing clinically important quantitative information. Especially, in prostate MRI diffusion-weighted imaging (DWI) which allows calculation of apparent diffusion coefficient (ADC) values is key technology. However, variability in the results hinders their clinical use. Goal of this study was to investigate the impact of sequence parameters, parallel imaging and reduced field-of-view (FOV) DWI techniques on ADC values defined from DWI images.

Motivation: Magnetic resonance imaging is an essential tool in diagnosing cancer and guiding treatment decisions. Specially, in prostate MRI biparametric MRI protocols, which use T2-weighted and diffusion-weighted images, are key techniques [1,2]. ADC values defined from DWI data correlate with Gleason scores, adding in cancer classification [3]. A meta-analysis of 26 studies with 1633 findings showed significant differences in ADC values between clinically significant (Gleason score 7 or higher) and non-significant prostate cancers. Clinically significant tumors had an average ADC value of $860 \times 10^{-6} \text{ mm}^2/\text{s}$ [95% CI 0.83–0.90], while non-significant tumors averaged $1100 \times 10^{-6} \text{ mm}^2/\text{s}$ [95% CI 1.03–1.18]. There weren't any non-significant tumors that had ADC values below $750 \times 10^{-6} \text{ mm}^2/\text{s}$ [3].

Unfortunately, the reliability of ADC values is compromised by various factors, necessitating further standardization [4]. This study aims to evaluate the impact of sequence parameters, parallel imaging and reduced FOV DWI techniques on ADC values defined from DWI images.

Materials & Methods: This study was conducted using in total 11 different MRI scanners with 1.5 T and 3.0 T field strengths from two different well-known vendors (1 and 2).

Premium prostate phantom (CaliberMRI, Boulder, USA) was utilized to acquire DWI data from 11 different MRI scanners from two different well-known vendors (1 and 2). The phantom contains cylinders filled with aqueous PVP solutions at varying concentrations from 0% to 50% w/w, allowing accurate measurements of six different ADC values, traceable to NIST standards. Additionally, the phantom contains separate cylinders for sample temperature monitoring (1 °C steps), enabling correction for different scanner room temperatures.

The impact of parallel imaging techniques was studied by imaging the phantom with similar DWI sequences both with and without utilizing parallel imaging. For this part of the study seven different 1.5 T MRI scanners were used, out of which four were from vendor 1 and three from vendor 2.

The effect of reduced FOV techniques was studied similarly via imaging the phantom with and without reduced FOV techniques. Here four different MRI machines were utilized. One 1.5 T and 3.0 T scanners from vendor 1 and two 3.0 T scanners from vendor 2.

ADC maps were generated from the measurements. 40 mm² circular regions of interest (ROI) were drawn (Figure 1.) with an automatic tool that was created for ROI fitting and data analysis to ensure consistent measurements of ADC values from each sequence. Finally, the measured ADC values were compared to the standard values with temperature correction.

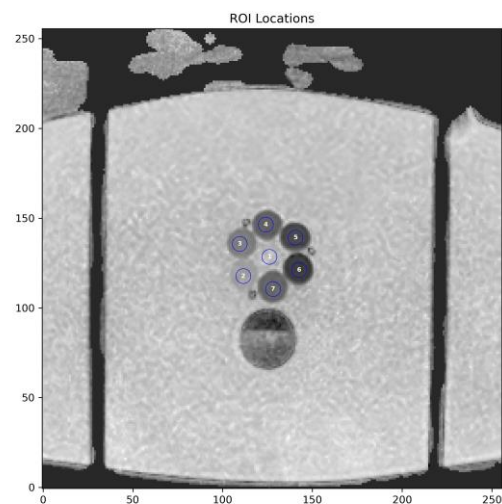


Fig. 1: ADC map of CaliberMRI Premium prostate phantom with 40 mm² ROIs drawn for each PVP solution cylinder.

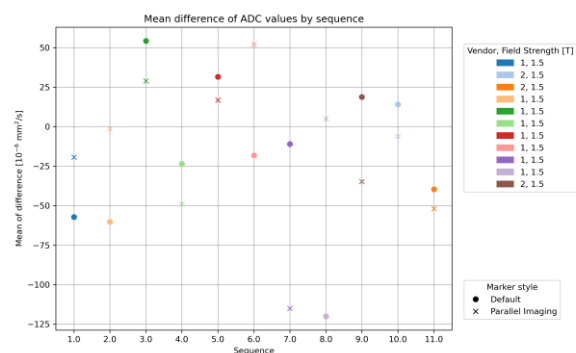


Fig. 2: Mean difference of ADC values compared to the standard ADC values plotted for sequences with and without parallel imaging.

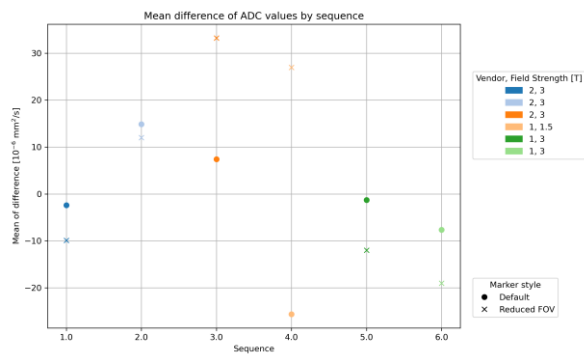


Fig. 3: Mean difference of ADC values compared to the standard ADC values plotted for sequences with and without reduced FOV techniques.

Results: The most important ADC values for prostate MRI are those between clinically non-significant and significant tumors ($850\text{--}1100 \times 10^{-6} \text{ mm}^2/\text{s}$). Two of the phantom's cylinders contain solutions with ADC close to this range, making them most interesting for this study.

With both sequences with and without parallel imaging the mean difference between the measured ADC values and the standard ADC values was less than $61 \times 10^{-6} \text{ mm}^2/\text{s}$ for most sequences (Figure 2.). Two outliers which were measured with the same vendor 1 scanner had higher differences. When comparing sequences and vendors the mean standard deviation of error of vendor 1 without the two outlier results was $(44 \pm 24) \times 10^{-6} \text{ mm}^2/\text{s}$ for sequences with parallel imaging and $(73 \pm 55) \times 10^{-6} \text{ mm}^2/\text{s}$ for sequences without parallel imaging. Respectively, for vendor 2 the results were (37 ± 35) and $(37 \pm 12) \times 10^{-6} \text{ mm}^2/\text{s}$.

When comparing impact of reduced FOV maximum mean difference between the measured ADC values and the standard ADC values was less than $34 \times 10^{-6} \text{ mm}^2/\text{s}$ for all compared sequences (Figure 3.). Again, comparing sequences and vendors the mean standard deviation of error of vendor 1 was $(77 \pm 11) \times 10^{-6} \text{ mm}^2/\text{s}$ for sequences with reduced FOV techniques and $(40 \pm 19) \times 10^{-6} \text{ mm}^2/\text{s}$ for sequences without reduced FOV techniques. Respectively, for vendor 2 the results were (24 ± 4) and $(24 \pm 2) \times 10^{-6} \text{ mm}^2/\text{s}$.

Discussion: Measured ADC values didn't differ significantly when parallel imaging was used. However, possibility of ghosting and other artifacts originating from parallel imaging techniques on diffusion-weighted images must be considered.

With reduced FOV techniques most of the time if voxel size of the default sequence and reduced FOV sequence were

similar, the measured ADC values were closer to the standard ADC values with reduced FOV sequence. However, default sequences had often higher voxel size which also leads to higher signal-to-noise ratio (SNR). While sequences with reduced FOV techniques were able to produce similar results with higher spatial resolution that is essential in clinical practice.

In addition, parallel imaging sequences had higher mean of difference and uncertainties than reduced FOV sequences. One factor is that mostly scanners with higher magnetic field strengths were considered for reduced FOV techniques, which leads usually into higher SNR and therefore to more accurate determination of ADC values. Typically, gradient strengths are also stronger in 3.0 T scanners than in 1.5 T scanners.

One of the largest sources of error in this study were the uncertainties in temperature measurements. Temperature of the phantom increased often for approximately 1°C during one scanning session. Already this change in temperature can lead to over $50 \times 10^{-6} \text{ mm}^2/\text{s}$ error in the measured ADC value at the lower PVP concentration cylinders of the phantom. The impact of phantom heating was minimized by comparing sequences that have been measured close to each other in time.

Conclusion: This study highlights the variability in ADC measurements across different MRI scanners and sequences, emphasizing the need for standardization in prostate MRI protocols and the value of calibration and quality control. The reliability of ADC values is compromised by various factors, necessitating further standardization [4]. In future, we aim to further evaluate the sources of errors and impact of acquisition parameters on measured ADC values on different MRI scanners.

Acknowledgements: The authors gratefully acknowledge funding support from the TYKS Foundation and the Lieto Savings Bank Foundation.

References:

- Merisaari H, Jambor I, Ettala O, et al. IMPROD biparametric MRI in men with a clinical suspicion of prostate cancer (IMPROD Trial): Sensitivity for prostate cancer detection in correlation with whole-mount prostatectomy sections and implications for focal therapy. *Journal of Magnetic Resonance Imaging* 50(5): 1641-1650 (2019).
- Jambor I, Verho J, Ettala O, et al. Validation of improd biparametric mri in men with clinically suspected prostate cancer: A prospective multi-institutional trial. *PLoS Medicine* 16 (6): e1002813 (1-14) (2019).
- Meyer H-J, Wienke A, Surov A. Discrimination between clinical significant and insignificant prostate cancer with apparent diffusion coefficient – a systematic review and meta analysis. *BMC Cancer* 20: 482 (2020).
- Giganti, F., Kirkham, A., Kasivisvanathan, V. et al. Understanding PI-QUAL for prostate MRI quality: a practical primer for radiologists. *Insights Imaging* 12, 59 (2021).

Accelerated Phase-Cycled bSSFP Imaging Joint Reconstruction with Improved Profile Estimation

Maryam Kargaran 1*, Anne Slawig 1, Oliver Speck 2, Volkert Roeloffs 3

1 University Clinic and Outpatient Clinic for Radiology, University Hospital Halle (Saale), Germany

2 Faculty of Natural Sciences, Otto-von-Guericke University, Magdeburg, Germany

3 Neoscan Solutions GmbH, Magdeburg, Germany

Abstract: Balanced steady-state free precession (bSSFP) offers high signal-to-noise ratios but is highly sensitive to field inhomogeneities, causing banding artifacts. Phase-cycling reduces these artifacts but increases the scan time. Accelerating bSSFP imaging is possible using parallel imaging principles by treating each phase-cycled acquisition as a virtual coil. However, accurate profile estimation remains challenging due to rapid intensity variations near banding regions. We introduce a physics-inspired approach that directly leverages off-resonance information from auto-calibration signals to improve profile accuracy. Phantom experiments at 1.5T demonstrated fewer aliasing artifacts, reduced noise amplification, and maintained image quality at high acceleration factors, achieving approximately 70% scan-time reduction.

Motivation: Balanced steady-state free precession (bSSFP) has gained popularity in clinical imaging due to its efficiency and high signal-to-noise ratios. However, its strong sensitivity to field inhomogeneity creates characteristic banding artifacts, limiting its clinical usability [1]. Phase-cycling reduces these artifacts by shifting artifacts across multiple acquisitions, so that their combination would result in a banding-free image. However, this significantly increases overall scan time [2]. To reduce acquisition time, methods inspired by parallel imaging have been introduced. These methods consider each phase-cycled acquisition as a "virtual coil," allowing for accelerated scanning [3, 4].

The critical challenge in this approach lies in accurately estimating the spatial modulation (profiles) induced by the bSSFP spectral response. While off-resonance itself typically varies smoothly, the bSSFP signal intensity can change sharply near spectral nulls. Conventional methods, which simply use the low-frequency information from auto-calibration signals can thus not fully represent these transitions and suffer from inaccuracies in the estimated profiles. We introduce a physics-inspired approach that leverages off-resonance information directly from auto-calibration signals. Thus, the bSSFP signal behavior is more accurately reflected which leads to an improvement in reconstruction quality, especially at high acceleration factors.

Materials & Methods: All experiments were conducted on a 1.5T scanner (neo315, Neoscan Solutions GmbH) using a multi-compartment phantom containing five tubes with varying concentrations of Polyvinylpyrrolidone (PVP) [5]. Image acquisition was performed using a 3D phase-cycled bSSFP sequence with eight evenly spaced RF phase increments. Other sequence parameters are: flip angle = 50°, TR/TE = 6/3 ms, and isotropic resolution of 1 mm³.

Two undersampling strategies were evaluated. First, prospective acceleration was applied using uniform 2- and 3-fold undersampling in both phase-encoding directions, with a

fully sampled 50×50 auto-calibration region (ACS). Second, retrospective undersampling was performed on a fully sampled dataset using 2D CAIPIRINHA and interleaved disjoint undersampling patterns (R=1×8) to ensure unique patterns across phase-cycled acquisitions (Figure 1) [6]. Reconstruction was then performed using CG-SENSE and the g-factor was calculated pixel-wise to assess quality [7].

The proposed physics-based method introduces an additional step in the reconstruction pipeline to account for rapid bSSFP signal variations. First, a low-resolution off-resonance map was estimated from the ACS using the PLANET method [8, 9]. Then, the map was interpolated to full imaging resolution and integrated into the analytical bSSFP signal model to simulate expected spatial modulations for each phase cycle (Figure 2). The updated profiles replaced conventional estimates in the standard CG-SENSE pipeline, without requiring further data acquisition or sequence modification.

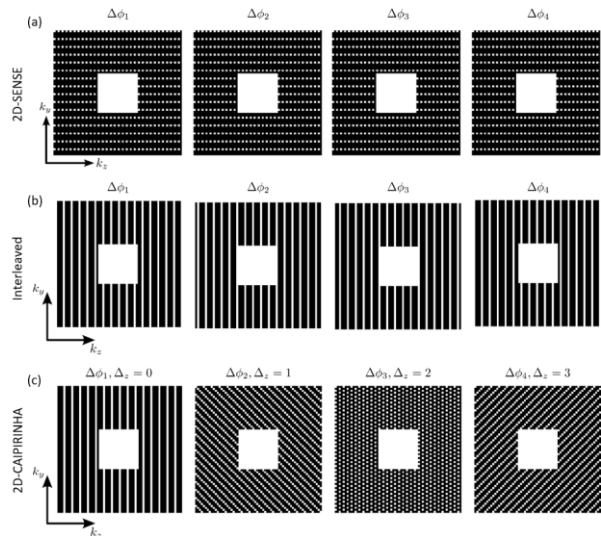


Fig. 1: Patterns for retrospective undersampling generated for the exemplary case of 4 different RF phase increments $\Delta\phi_n = 2\pi n/N, N=4$, (a) uniform undersampling (R=4x2), (b) interleaved method (R=1x4) and (c) 2D CAIPIRINHA (R=Ry×Rz=1x4, Δz ranging from 0, ..., R_Z-1).

Results: In the prospective experiments, the physics-based profile estimation led to improved image quality relative to the conventional method. As illustrated in Fig 3, the conventional method resulted in residual aliasing artifacts and increased noise amplification. The proposed method, however, reduced these effects so that reconstructions had fewer aliasing artifacts and showed improved signal uniformity.

Retrospective experiments highlighted the effect of sampling patterns on the final reconstruction (Figure 4). When the same undersampling pattern was applied to all phase-cycled images, aliasing artifacts remained coherent and difficult to resolve. In contrast, using different masks across acquisitions

- especially mutually exclusive sampling distributions - improved k-space coverage and subsequently the reconstruction quality.

G-factor analysis corroborated these findings, indicating lower noise amplification in the results from the proposed method. Additionally, the method did not introduce eddy current artifacts or disrupt the steady-state magnetization. No off-resonance-related distortions were observed. Finally, the results from the prospective experiments suggest that scan time reduction up to 70% is possible without affecting the image quality.

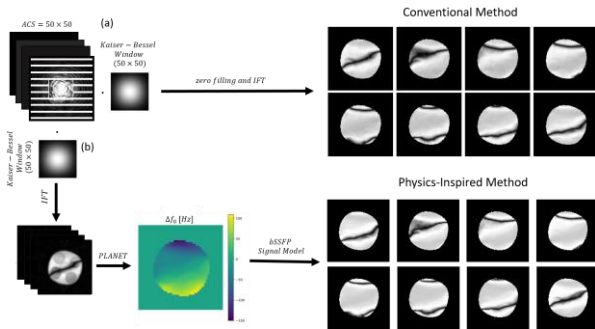


Fig. 2: Flowchart of the conventional (a) vs. proposed (b) profile estimation method. In the proposed method, low-resolution images from auto-calibration signals are used to calculate an off-resonance map using PLANET. The low-resolution off-resonance map is then interpolated, and the profile estimates are obtained using the bSSFP signal model.

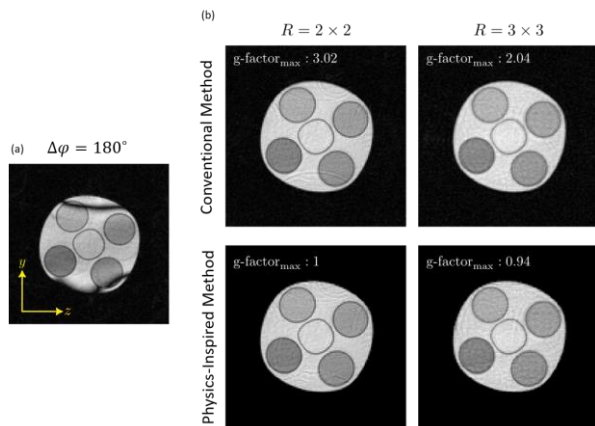


Fig. 3: (a) Fully-sampled bSSFP image acquired with an RF phase increment of 180-degree, showing banding artifacts. (b) Reconstruction results from prospectively undersampled data with shared sampling patterns across all acquisitions.

Discussion: The proposed profile estimation method improves reconstruction quality by introducing an additional computationally efficient step that requires no extra data acquisition. The estimated profiles provide a more precise representation of rapid signal variations occurring near bSSFP nulls, which are often missed by conventional low-resolution estimates. This improvement is especially beneficial at longer TRs or under specific T2/T1 and flip angle combinations. By incorporating off-resonance maps and the bSSFP signal model, our method outperforms the conventional approach, which relies solely on ACS data.

Observed g-factor values below one, as seen in Figure 3, result from regularization effects in the reconstruction algorithm,

which can improve apparent signal-to-noise ratios [10]. Additionally, the reduced maximum g-factor reflects improved handling of pixels previously affected by strong noise amplification.

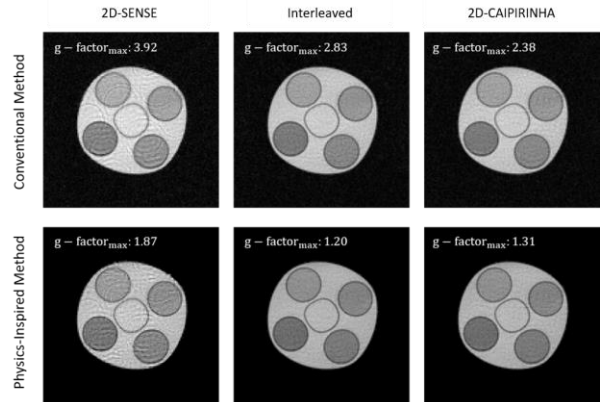


Fig. 4: Reconstruction results from retrospectively undersampled data using similar patterns as shown in Figure 1, with undersampling factors of $R=2 \times 4$ (2D-SENSE) and $R=1 \times 8$ (Interleaved/2D-CAIPI).

The sampling strategy also plays an important role in optimizing reconstruction quality. Using unique interleaved sampling patterns per phase-cycled acquisition enhances total k-space coverage, spreads aliasing artifacts, and creates a better-conditioned reconstruction problem, further amplifying the benefits of the physics-based profile estimation.

Conclusion: The proposed reconstruction framework enables substantial acceleration of phase-cycled bSSFP imaging while preserving image quality. The method achieves up to 70% scan time reduction without compromising reconstruction performance. These results highlight the potential for faster, more robust bSSFP imaging in clinical practice.

References:

- Klaus Scheffler and Stefan Lehnardt. Principles and applications of balanced SSFP techniques. *European Radiology* 13(11):2409-2418, August 2003.
- Yuval Zur, Saul Stokar, and Peter Bendel. An analysis of fast imaging sequences with steady-state transverse magnetization refocusing. *Magnetic Resonance in Medicine*, 6(2):175-193, February 1988.
- Michael Lustig, Juan Santos, and John M. Pauly. A super-fov method for rapid ssfp banding artifact reduction. In *Proceedings of the 13th Annual Meeting of the International Society for Magnetic Resonance in Medicine (ISMRM)*, page 504, 2005.
- Christian M. Holme, Nick Scholand, Sebastian Rosenzweig, Robin N. Wilke, and Martin Uecker. Banding-free reconstruction in frequency-modulated bSSFP using virtual coils with regularized non-linear inversion. In *Proceedings 27th Annual Meeting of ISMRM*, 2018.
- Ann-Kathrin Lehner. Diffusion weighted imaging on a pediatric MRI scanner: Comparison between TSE and EPI. Master's thesis, Otto-von-Guericke-University Magdeburg, 2024.
- Felix A. Breuer, Martin Blaimer, Matthias F. Mueller, Nicole Seiberlich, Robin M. Heidemann, Mark A. Griswold, and Peter M. Jakob. Controlled aliasing in volumetric parallel imaging (2d caipirinha). *Magnetic Resonance in Medicine*, 55(3):549-556, January 2006.
- Philip M. Robson, Aaron K. Grant, Ananth J. Madhuranthakam, Riccardo Lattanzi, Daniel K. Sodickson, and Charles A. McKenzie. Comprehensive quantification of signal-to-noise ratio and g-factor for image-based and k-space-based parallel imaging reconstructions. *Magnetic Resonance in Medicine*, 60(4):895-907, September 2008.
- Yulia Shcherbakova, Cornelis A.T. van den Berg, Chrit T.W. Moonen, and Lambertus W. Bartels. Planet: An ellipse fitting approach for simultaneous t1 and t2 mapping using phase-cycled balanced steady-state free precession. *Magnetic Resonance in Medicine*, 79(2):711-722, May 2017.
- Qing-San Xiang and Michael N. Hoff. Banding artifact removal for bSSFP imaging with an elliptical signal model. *Magnetic Resonance in Medicine*, 71(3):927-933, January 2014.
- Fa-Hsuan Lin, Kenneth K. Kwong, John W. Belliveau, and Lawrence L. Wald. Parallel imaging reconstruction using automatic regularization. *Magnetic Resonance in Medicine*, 51(3):559-567, February 2004. doi:10.1002/mrm.10718

Assessing scanner specific correction factors for calculation of fatty acid composition with 1H-MRS

B. Korzekwa 1+2, Y. Kupriyanova 1+2, J. Mevenkamp 3, V. Fritz 4, L. Rodehutsors 2+5, K. Bochinsky 6+7, H. Heise 6+7, M. Roden 8+1+2, J. Machann 2+4+5 and V.B. Schrauwen-Hinderling 3+1+2

1* Institute for Clinical Diabetology, German Diabetes Center, Leibniz Institute for Diabetes Research at Heinrich Heine University, Düsseldorf, Germany

2* German Center for Diabetes Research (DZD e.V.), München-Neuherberg, Germany

3 Department of Radiology and Nuclear Medicine, Maastricht University Medical Center, Maastricht, The Netherlands

4 Section on Experimental Radiology, Department of Diagnostic and Interventional Radiology, University Hospital Tübingen, Germany

5 Institute for Diabetes Research and Metabolic Diseases (IDM) of the Helmholtz Center Munich at the University of Tübingen, Tübingen, Germany

6 Institute of Biological Information Processing, Structural Biochemistry (IBI-7), Research Center Jülich, Germany

7 Institute of Physical Biology, Heinrich Heine University, Düsseldorf, Germany

8 Department of Endocrinology and Diabetology, Medical Faculty and University Hospital, Heinrich Heine University Düsseldorf, Germany

Abstract: Motivation: Earlier reports established a robust way to determine hepatic FAC, but scanner-specific factors may hamper implementation at other research sites.

Goal: Developing reliable and reproducible post-processing corrections for consistent calculation of hepatic FAC on different clinical MR-systems.

Approach: 1H-MRS was performed in oil-water emulsions with varying concentrations on MRI systems from two different vendors, to determine post-processing correction factors for PUFA and MUFA calculations, accounting for TE induced signal loss.

Results: Similar correction factors with 0.754 ± 0.005 and 0.682 ± 0.003 for PUFA calculation and 0.999 ± 0.002 and 0.907 ± 0.001 for MUFA calculation were achieved for both sites, respectively.

Motivation: Hepatic triglyceride accumulation is a key feature of metabolic dysfunction-associated liver disease (MASLD), but the role of fatty acid composition (FAC) remains unclear. Proton magnetic resonance spectroscopy (1H-MRS) at clinical field strength has been applied in liver and adipose tissue to measure fractions of saturated, mono- and polyunsaturated fatty acids (SFA, MUFA, and PUFA)^{1,2,3}. However, calculation of FAC in liver remains challenging due to strong water signal, motion, inherent microscopic magnetic field inhomogeneity due to iron/ferritin storage and therefore spectral overlap between α -carbonyl and allylic CH₂ resonances, especially at lower fields. A recent approach utilizing the ratio between the α -carbonyl and methyl resonances as prior knowledge robustly quantifies the α carbonyl and allylic CH₂ resonances even if they overlap¹. Due to unequal signal loss of the α -carbonyl and methyl resonances, additional correction factors (CPUFA and CMUFA), compensating for any other influence arising from different implementation of the STEAM sequence on individual MR-systems, need to be empirically determined at each site.

We performed phantom measurements at two sites with different MR-systems in various oil emulsions and optimized post-processing in order to determine CPUFA and CMUFA. This study provides valuable insight into the comparability of 1H-MRS for calculating FAC with foresight towards multicenter clinical studies for investigating metabolic disease such as MASLD.

Materials & Methods: 1H-MRS was performed in three different serial dilutions containing olive, safflower or peanut oil. Each phantom was prepared in 50 ml tubes with 8 different concentrations (1, 2, 3, 5, 10, 20, 40 and 100%) of the respective oil emulsified in water⁴. 1H-MRS measurements were performed on two clinical 3T MR systems: Achieva dStream (Philips, Best, The Netherlands) at site 1 and Magnetom Prismafit (Siemens Healthineers, Erlangen, Germany) for site 2. A spine array+16-channel torso coil and spine array+18-channel body array coil were used for acquisition of spectra for site 1 and 2, respectively. After scout imaging, a localized STEAM sequence with VAPOR water suppression was acquired. Sequence parameters were identical for both clinical systems with 25x15x15 mm³ voxel size, TR/TE 4500/20 ms, 2048 sample points, 2 kHz bandwidth. Number of averages were between 8 and 64, depending on lipid concentration. Spectra were analysed with a custom MATLAB script applying phase correction as well as mix of Gaussian and exponential filtering. Prior knowledge with appropriate starting values accounting for J-coupling, relative chemical shift, and T₂ estimates was implemented for fitting of resonances¹.

For the determination of CPUFA and CMUFA, ultra-high field nuclear magnetic resonance spectroscopy (UHF-NMR) was carried out on a 700 MHz Bruker scanner. A pulse-acquire sequence with 58.8 sec inter-pulse delay, 8 averages, 20166 sample points and 8.4 kHz bandwidth was acquired. UHF-NMR spectra were analyzed with MATLAB, calculating the integral of the resonances of interest and relating them to the amplitudes measured at clinical field strength.

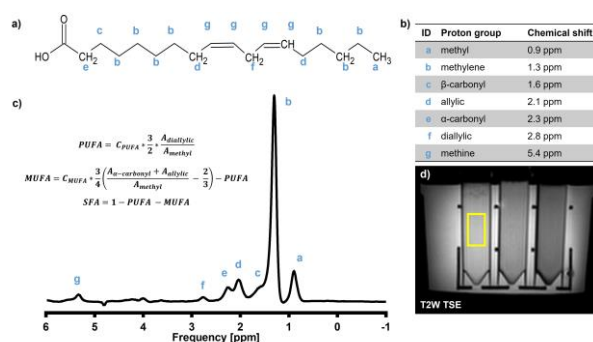


Fig. 1: Overview for 1H-MRS FAC phantom measurements. a) Exemplary structure of linoleic acid. b) Chemical shift of fatty acid resonances. c) Equations

for calculating PUFA, MUFA and SFA fractions and water suppressed spectrum for 20% peanut oil. d) Voxel planning in phantoms

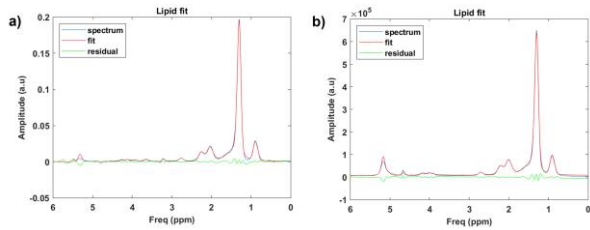


Fig. 2: Representative fitting results with MATLAB script for water suppressed lipid scans in 20% peanut oil. a) Results for site 1. b) Results for site 2.

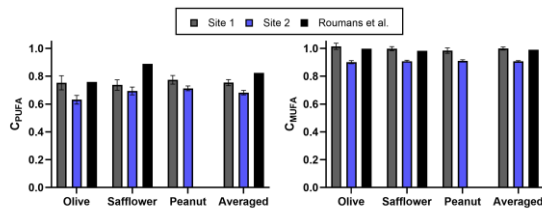


Fig. 3: Empirically determined correction factors CPUFA (left) and CMUFA (right) for both clinical scanners (Mean \pm SEM over all concentrations).

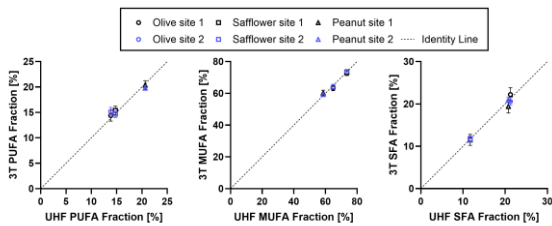


Fig. 4: PUFA, MUFA and SFA fractions for both clinical scanners after applying average correction factors (Mean \pm SEM over all concentrations).

Results: For 1H-MRS spectra, SNR, water suppression as well as spectral resolution were sufficient for fitting in all but one measurement with low lipid signal. Exemplary spectra with good quality and fits are shown for both sites in Figure 2. Next, correction factors for single oils and averaged for all oils were

calculated for both clinical scanners, based on the UHF-NMR results (Figure 3). Both, CPUFA and CMUFA presented low variation, independent of overall lipid content and oil type. The correction factors were close to values reported earlier¹. Using the experimentally determined correction factors, FAC ratios were individually calculated for each site over all oils and showed good agreement with the ground truth from UHF (Figure 4).

Discussion: Reported values for CPUFA and CMUFA agree with literature and only show small differences between sites, suggesting similar contribution of signal loss, independent on vendor specific sequence. Next steps include further validation for in vivo data with volunteers undergoing measurements consequently in both sites.

Conclusion: This study demonstrates the feasibility of calculating FAC as described by Roumans *et al.*¹ in other sites and highlights the feasibility of standardizing post-processing correction between different clinical MRI systems.

Acknowledgements: The study was supported by a collaborative grant of the German Center for Diabetes Research (DZD).

References:

- Roumans KHM, Lindeboom L, Veeraiah P, Remie CME, Phielix E, Havekes B, Bruls YMH, Brouwers MCGJ, Ståhlman M, Alsema M, Peters HPF, de Mutsert R, Staels B, Taskinen MR, Borén J, Schrauwen P, Schrauwen-Hinderling VB. Hepatic saturated fatty acid fraction is associated with de novo lipogenesis and hepatic insulin resistance. *Nat Commun.* 2020 Apr 20; 11(1):1891.
- Machann J, Stefan N, Wagner R, et al. Intra- and interindividual variability of fatty acid unsaturation in six different human adipose tissue compartments assessed by 1H-MRS in vivo at 3 T. *NMR in Biomedicine.* 2017; 30: e3744.
- Peterson P, Trinh L, Månsson S. Quantitative 1H MRI and MRS of fatty acid composition. *Magn Reson Med.* 2020; 85: 49–67.
- Fritz, V., Martirosian, P., Machann, J. et al. A comparison of emulsifiers for the formation of oil-in-water emulsions: stability of the emulsions within 9 h after production and MR signal properties. *Magn Reson Mater Phy* 35, 401–410 (2022).

Investigating Reproducibility Issues of the $1^3 3^1$ Excitation Pulse During wbNAA Sequence Implementation

Franziska Lohrengel 1*, Oded Gonen 2 and Jan-Bernd Hövener 1

1 Department of Radiology and Neuroradiology, Section Biomedical Imaging, University Hospital Schleswig-Holstein, Kiel University, Kiel, Germany
2 Center for Advanced Imaging Innovation and Research (CAI2R), Department of Radiology, New York University Grossman School of Medicine, New York, NY USA

Abstract: We attempted to implement a whole-brain NAA (wbNAA) spectroscopy sequence in a vendor-agnostic environment. During the 16 repeated acquisitions, we observed large fluctuations of the water signal exceeding 50%. It was demonstrated that these instabilities originate from the binomial $1^3 3^1$ excitation pulse. Ongoing work aims to identify the underlying cause of this behavior.

Motivation: Whole-brain magnetic resonance spectroscopy (wbMRS) enables non-invasive measurement of N-acetyl-L-aspartate (NAA), a key neuronal metabolite, across the entire brain volume. This approach is particularly valuable for studying diffuse or non-focal neurological conditions where localized spectroscopy is insufficient. To reliably detect low-concentration metabolites, such as NAA, the wbNAA sequence combines inversion recovery, water suppression, and binomial $1^3 3^1$ excitation pulses.

During the process of implementing a wbNAA sequence in Kiel, unexpected fluctuations of the water signal between repeated acquisitions were observed. These variations exceeded 50% and could compromise quantification accuracy and reproducibility. Preliminary observations suggested that the binomial $1^3 3^1$ excitation pulse might be particularly sensitive to magnetic field inhomogeneities.

To investigate this instability, the $1^3 3^1$ excitation pulse was isolated, measured, and analyzed. Clarifying the source and extent of this variability is essential for enabling robust whole-brain NAA quantification in clinical and research applications.

Materials & Methods: All measurements were performed on a whole-body 3T MRI system (Cima.X, Siemens Healthineers) equipped with a 64-channel head/neck coil. The wbNAA sequence included an adiabatic inversion pulse, WET water suppression, and a binomial $1^3 3^1$ excitation pulse, implemented in a vendor-agnostic framework (pulseseq) as described by Soher et al. To isolate the effect of the $1^3 3^1$ pulse, the same pulse was applied 16 times without other sequence elements and with a repetition time of $TR = 10s$. A spherical 1.4 L phantom containing brain metabolites (50 mM potassium phosphate monobasic, 5 mM sodium hydroxide, 12.5 mM N-acetyl-L-aspartic acid (NAA), 10 mM creatine hydrate, 3 mM choline chloride, 7.5 mM myo-inositol, 12.5 mM L-glutamic acid, 5 mM DL-lactic acid, 15mM sodium azide) was scanned using the wbNAA sequence and the single $1^3 3^1$ pulse. Data processing and visualization were performed in MATLAB R2022b.

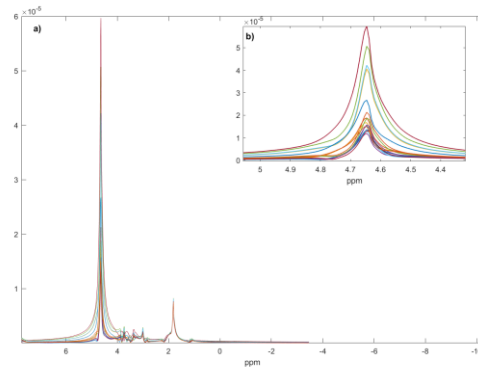


Fig. 1: Magnitude $1H$ MR spectra of the spherical model solution acquired with the wbNAA sequence: (a) full scale showing fluctuations between signal amplitudes exceeding 50% (b) zoomed view highlighting the distinct signal intensities of individual acquisitions

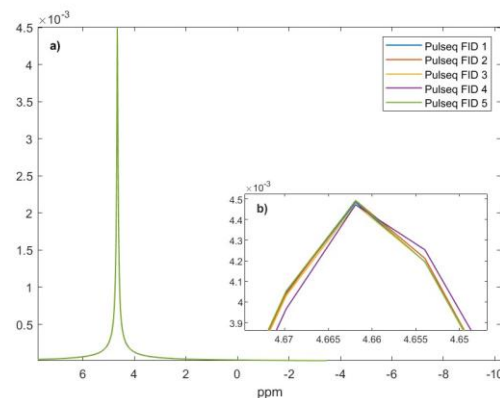


Fig. 2: Magnitude non-localized $1H$ MR spectra of the spherical model solution acquired with custom-written implementation of the FID sequence: (a) full scale demonstrating stable signal amplitudes with deviations below 1% (b) zoomed view confirming minimal variability across acquisitions

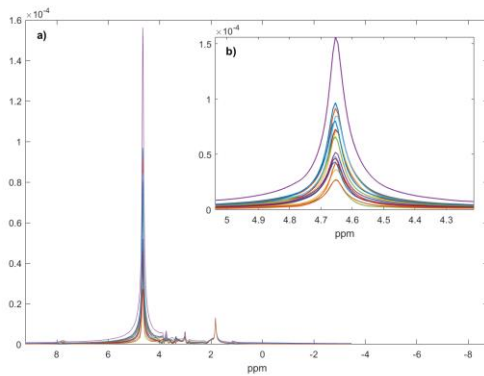


Fig. 3: Magnitude $1H$ MR spectra acquired with 16 sequential acquisitions using a single $1^3 3^{-1}$ binomial excitation pulse: (a) the repeated acquisitions reveal variability over 50% in signal amplitude (b) each spectrum shows notable differences in water peak amplitude

Results: The water signal measured over 16 repetitions of the complete wbNAA sequence showed pronounced fluctuations exceeding 60% (61.58%) relative to the mean.

To evaluate whether this variability was a general property of the implementation, we performed a conventional free induction decay (FID) sequence with a standard 90° excitation pulse programmed in pulseq. In this reference measurement, the water signal remained stable across repetitions with deviations below 1% (0.62%).

Finally, when the binomial $1^3 3^{-1}$ excitation pulse was executed 16 times in direct succession, a similarly high level of variability (50.46%) was again observed.

Discussion: The results clearly demonstrate that the wbNAA sequence exhibits substantial signal instability across repeated measurements, with fluctuations exceeding 60%. In contrast, the conventional FID sequence implemented in the same vendor-agnostic environment yielded highly reproducible water signals, showing deviations below 1%.

This observation indicates that the pulseq framework and the hardware setup themselves do not inherently introduce variability.

When the binomial $1^3 3^{-1}$ excitation pulse was applied in isolation, a similarly high level of fluctuation was observed, closely matching the variability seen in the complete wbNAA protocol. This finding strongly suggests that the $1^3 3^{-1}$ excitation pulse is the primary source of the observed instability.

Since this pulse is essential for suppressing water and lipid signals, its lack of reproducibility directly compromises the reliability of the entire wbNAA sequence. To enable robust whole-brain NAA quantification, it will be necessary to clarify the underlying cause of this effect and to develop strategies to mitigate it.

Conclusion: We demonstrated that the binomial $1^3 3^{-1}$ excitation pulse induces pronounced signal variability in repeated measurements, rendering the wbNAA sequence unstable under the tested conditions. Future work will focus on systematic investigations to identify the underlying mechanisms and to develop modifications that enable reproducible whole-brain NAA spectroscopy.

Acknowledgements: The author thanks Jan-Bernd Hövener for his support and guidance during this project.

References:

1. Gonen O, Viswanathan AK, Catalaa I, Babb J, Udupa J, Grossman RI. Total brain N-acetylaspartate concentration in normal, age-grouped females: Quantitation with non-echo proton NMR spectroscopy. *Magnetic resonance in medicine*. 1998;40(5):684-689.
2. Soher BJ, Wu WE, Tal A, et al. Automated whole-brain N-acetylaspartate proton MRS quantification. *NMR in Biomedicine*. 2014;27(11):1275-1284.
3. Layton KJ, Kroboth S, Jia F, et al. Pulseq: A rapid and hardware-independent pulse sequence prototyping framework. *Magnetic Resonance in Medicine*. 2017;77(4):1544-1552. doi:10.1002/mrm.26235

Dual Approach to Artifact Detection and Classification in High b-Value Breast DWI: A Deep Learning Perspective

Ameya Ajit Markale 1*, Luise Brock 1+2, Andrzej Liebert 1, Hannes Schreiter 1, Dominika Skwierawska 1, Ihor Horishnyi 1, Shirin Heidarikahkesh 1, Frederik B. Laun 1, Michael Uder 1, Lorenz A. Kapsner 1, Sabine Ohlmeyer 1, Sebastian Bickelhaupt 1

1 Institute of Radiology, Uniklinikum Erlangen, Friedrich-Alexander-Universität Erlangen-Nürnberg (FAU), Erlangen, Germany

2 Department of Artificial Intelligence in Biomedical Engineering (AIBE), Friedrich-Alexander-Universität Erlangen-Nürnberg (FAU), Erlangen, Germany

Abstract: In breast Magnetic Resonance Imaging (MRI), diffusion-weighted imaging (DWI) can aid lesion detection and characterization. However, high b-value breast DWI is prone to artifacts that can impair image assessment. This IRB-approved retrospective study used a university hospital's in-house dataset of n=1383 breast MRI examinations, and we evaluated three neural network architectures (DenseNet121, ResNet18, and SEResNet50) for binary classification of hyperintense and hypointense artifacts. The best performing model (DenseNet121) was applied to an independent holdout test set of n=24 high b-value DWI (b=1500 s/mm²) breast MRI examinations. The DenseNet121 achieved an AUC of 0.92 and 0.94 for identifying hyper- and hypointense artifacts in DWI single slice images.

Motivation: DWI is increasingly incorporated in breast MRI as it provides additional microstructural information by characterizing water diffusivity [1]. Especially high b-value images provide relevant information, aiding in identifying and characterizing malignant lesions [2]. However, these images can be prone to intensity-related artifacts that can obscure or mimic pathology and thereby compromise image quality and diagnostic confidence. Hyperintense artifacts can result from, e.g., patient motion, susceptibility effects, B0 field inhomogeneities, skin folding, or surface coil flare [1]. The factors contributing to hypointense artifacts occurrence are not yet well understood but are potentially associated, e.g., with vessel/heart pulsation phenomena.

To address this challenge of hyper – and hypointense artifacts in high b-value DWI images, our study proposes a deep learning-based solution using a convolutional neural network (CNN) to automatically detect hypointense and hyperintense artifacts in high b-value breast DWI at the slice level and to provide an explainable approach with bounding boxes for clear visualization.

Materials & Methods: This IRB-approved retrospective study included n=1383 female patients (mean age: 48 ± 12 years) who underwent clinically indicated multiparametric breast MRI examinations between 2022 and mid-2023, including high b-value DWI acquisition (b=1500 s/mm²).

Firstly, a reading was performed on the full dataset by two readers using Likert-like scales (where 1= no artifact to 5= highly severe artifact) on Maximum Intensity Projections (MIPs) to identify cases with moderate/severe artifacts in the high b-value DWI for further detailed evaluation [3]. This resulted in n=157 cases with moderate/severe artifacts, resulting in n=11890 slices separated into left and right breast (see Figure 1). These separated slices were then evaluated by three readers individually. 84 separated slices were excluded as they were blurry, resulting in n=11806 separated slices used for CNN training.

The data was stratified on the patient-level into training-, validation- and test dataset splits used for training different CNN (DenseNet121, ResNet18, and SEResNet50): training (hyperintense: n=8,164 slices, hypointense: n=8,164), validation (hyperintense: n=1,820 slices, hypointense: n=1,806), and test (hyperintense: n=1,822 slices, hypointense: n=1,836) sets for each artifact type [4], [5], [6]. Binary breast tissue masks, adapted from Liebert et al., were applied to the network inputs [7]. CNN performance was evaluated using the Area under Receiver Operating Characteristic curve (AUROC) and Area under Precision-Recall curve (AUPRC). Grad-CAM heatmaps based bounding boxes were generated and assessed on 50 randomly selected validation cases based on their performance to detect artifacts on a 5-point Likert-like scale [8]. The best-performing model was then applied to the test set.

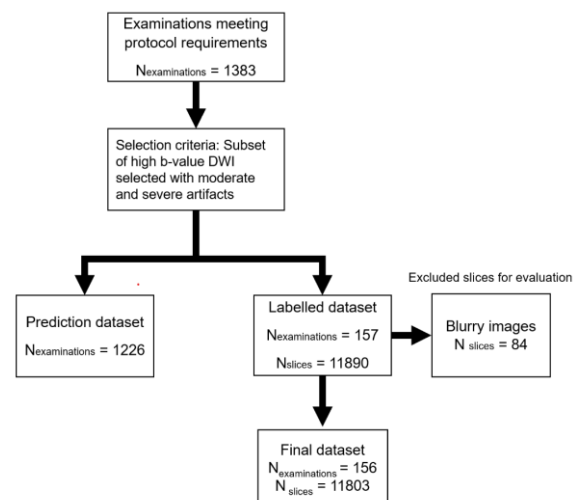


Fig. 1: Overview of the n=1383 MRI examinations included in the study.

Results: Based on the slice artifact reading, 19.33% of the slices exhibited hyperintense artifacts and 38.79% hypointense artifacts, with a mean score of 2 for hyperintense artifacts and 1 for hypointense artifacts. Among the three evaluated networks, DenseNet121 consistently outperformed ResNet18 and SEResNet50 in both detection accuracy and localization. For hyperintense artifact detection on the validation set, DenseNet121 achieved the highest AUROC (0.89) and AUPRC (0.73), followed by ResNet18 (AUROC: 0.87, AUPRC: 0.72) and SEResNet50 (AUROC: 0.84, AUPRC: 0.66). Performance improved on the test set, with DenseNet121 reaching an AUROC of 0.92 and AUPRC of 0.77 (see figures 2 and 4).

For hypointense artifacts, DenseNet121 outperformed ResNet18 (AUROC: 0.92, AUPRC: 0.87) and SResNet50 (AUROC: 0.90, AUPRC: 0.84) with validation AUROC and AUPRC of 0.92 and 0.88, respectively. On the test set, DenseNet121 reached 0.94 (AUROC) and 0.92 (AUPRC) (see figures 3 and 4).

Localization assessment on n=50 randomly selected cases of the validation dataset showed that for both artifacts, DenseNet121 effectively localized artifact regions with minimal inclusion of non-artifact areas, with ResNet18 generating tighter boxes but occasionally missing parts of artifacts or including lymph nodes in two cases for hypointense artifact detection. SResNet50 frequently misaligned with the artifact location. For hyperintense and hypointense artifacts, DenseNet121 and ResNet18 achieved a mean bounding box score of 4, while SResNet50 scored 3 and 2, respectively.

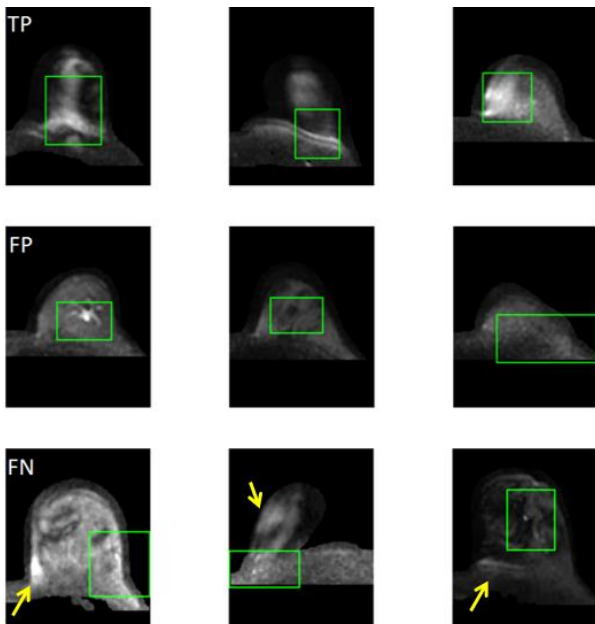


Fig. 2: The figure shows bounding box predictions for hyperintense artifact detection using DenseNet121 on the test set. The first row shows true positives (TP). The second shows false positives (FP), where artifacts are actually absent. The third shows false negatives (FN), where artifacts are not recognized and highlighted with yellow arrows.

Discussion: This study demonstrated the capability of CNNs to detect intensity-related artifacts on the slice level in high b-value breast DWI MRI.

Among the evaluated models, DenseNet121 achieved higher AUCs compared to ResNet18 and SResNet50 in both hyperintense and hypointense artifact classes for detection accuracy and localization. This might be associated with the DenseNet121's dense connectivity architecture, potentially preserving critical spatial features relevant for artifact detection [9]. On the independent test set, DenseNet121 detected both hyperintense (AUROC: 0.92, AUPRC: 0.77) and hypointense artifacts (AUROC: 0.94, AUPRC: 0.92) reliably.

Evaluation was performed using single slice level, opposite to previous AI-based assessments of artifacts in breast MRI, which were often based on MIPs. However, a single slice assessment might help to more specifically determine the relevance of artifacts for the diagnostic assessment, since

artifacts in some anatomical areas might be of less diagnostic relevance than in other areas.

To increase explainability, the generation of bounding boxes was introduced, which allows the readers to assess the CNN prediction and understand the decision-making process.

Limitations include the single centre dataset, although >10.000 individual slices were included in the assessment. Further, only a single MR vendor was included, and the assessment was focused on high b-value DWI only, whilst in other sites, only lower b-values might be acquired. Further, the impact on lesion detection of the individual artifacts was not explored. Thus, future research is necessary to explore the clinical relevance of artifact detection in DWI.

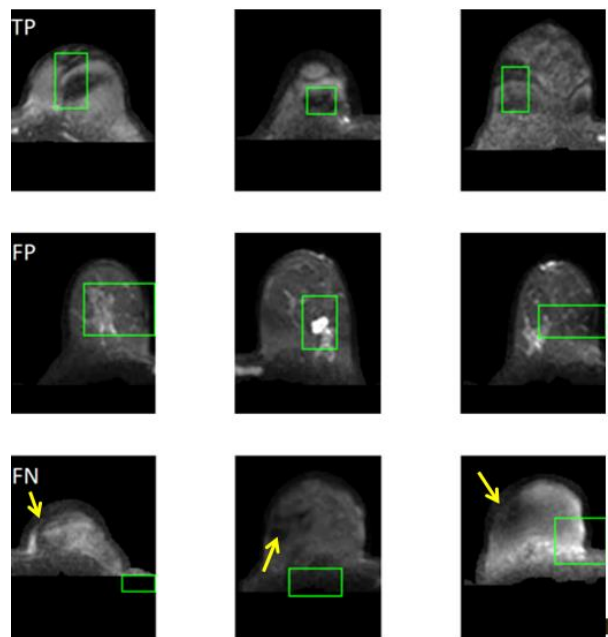


Fig. 3: The figure shows bounding box predictions for hypointense artifact detection using DenseNet121 on the test set. The first row shows true positives (TP). The second shows false positives (FP), where artifacts are actually absent. The third shows false negatives (FN), where artifacts are not recognized and highlighted with yellow arrows.

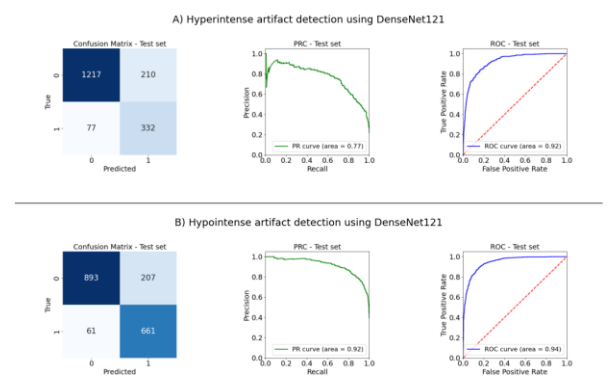


Fig. 4: Confusion matrix, AUROC curve, and AUPRC curve for DenseNet121 trained for binary classification and tested on the test set for hyperintense and hypointense artifact classification.

Conclusion: The goal of this study was to automatically detect the hyperintense and hypointense artifacts on the slice level in high b-value breast DWI. CNNs were able to reliably detect the hypointense and hyperintense artifacts, with DenseNet121 performing best at detection accuracy. For explainability localization, the generation of bounding boxes was introduced, regionally highlighting the artifact. Upon further study, this automated approach might assist clinicians and technicians in identifying artifact affected slices.

References:

1. Partridge, Savannah C., et al. "Diffusion-weighted breast MRI: Clinical applications and emerging techniques." *Journal of magnetic resonance imaging* 45.2 (2017): 337-355.
2. Wongkornchaovalit, Paween, et al. "Diffusion MRI With High to Ultrahigh b-Values: How It Will Benefit the Discovery of Brain Microstructure and Pathological Changes." *Investigative Magnetic Resonance Imaging* 26.4 (2022): 200-207.
3. Dickinson, Louise, et al. "Scoring systems used for the interpretation and reporting of multiparametric MRI for prostate cancer detection, localization, and characterization: could standardization lead to improved utilization of imaging within the diagnostic pathway?." *Journal of Magnetic Resonance Imaging* 37.1 (2013): 48-58.
4. Huang, Gao, et al. "Densely connected convolutional networks." *Proceedings of the IEEE conference on computer vision and pattern recognition*. 2017.
5. Hu, Jie, Li Shen, and Gang Sun. "Squeeze-and-excitation networks." *Proceedings of the IEEE conference on computer vision and pattern recognition*. 2018.
6. He, Kaiming, et al. "Deep residual learning for image recognition." *Proceedings of the IEEE conference on computer vision and pattern recognition*. 2016.
7. Liebert, Andrzej, et al. "Feasibility to virtually generate T2 fat-saturated breast MRI by convolutional neural networks." *medRxiv* (2024): 2024-06.
8. Selvaraju, Ramprasaath R., et al. "Grad-cam: Visual explanations from deep networks via gradient-based localization." *Proceedings of the IEEE international conference on computer vision*. 2017.
9. Meng, Mingzhu, et al. "Differentiation of breast lesions on dynamic contrast-enhanced magnetic resonance imaging (DCE-MRI) using deep transfer learning based on DenseNet201." *Medicine* 101.45 (2022): e31214.

Super-resolution in vitro 4D Flow MRI for intracranial aneurysms assessment

Kai Meinerz 1*, Jan-Bernd Hövener 2, Olav Jansen 3, Naomi Larsen 3, Mariya Pravdivtseva 2

1 Independent Researcher, Köln, Germany,

2 Department of Radiology and Neuroradiology, Section Biomedical Imaging, University Hospital Schleswig-Holstein, Kiel University, Kiel, Germany

3 Department of Radiology and Neuroradiology, University Hospital Schleswig-Holstein, Kiel, Germany

Abstract: This study investigates the application of machine learning to improve the spatial resolution of 4D flow MRI for evaluating intracranial aneurysms. A patient-specific aneurysm phantom was used for in vitro imaging at varying voxel sizes. A neural network, 4DFlowNet, is being adapted and evaluated against high-resolution ground truth and traditional interpolation methods. Early results indicate improved flow estimation and reduced noise, suggesting that machine learning could enhance the clinical viability of 4D flow MRI by enabling faster scans and more accurate diagnostics.

Motivation: 4D flow MRI is a non-invasive imaging modality that provides detailed information about blood flow velocity¹. It holds promise as a predictive tool for assessing the treatment effectiveness of intracranial aneurysm². If left untreated, such pathologies can lead to life-threatening hemorrhages. However, the clinical application of 4D flow MRI for intracranial use is currently limited by long acquisition times and insufficient spatial resolution³, which hinders accurate hemodynamic assessment.

In this work, we investigate the potential of machine learning to enhance the spatial resolution of 4D flow MRI, thereby reducing acquisition times and improving accuracy.

Materials & Methods: A patient-specific aneurysm model was designed and 3D printed using stereolithography (Form 3B, Formlabs)⁴. This model was integrated into a flow circuit, and 4D flow MRI was performed using 3 different voxel sizes (Ingenia, Philips, 3T, TE/TR: 5/8.4 ms; FOV: 200×132×55 mm³; acq. voxel sizes: 0.75mm³, 1.5mm³, and 3mm³; 20 temporal frames). 4DFlowNET, a neural network previously developed for cardiac⁵ and cerebrovascular applications⁶, was downloaded and initially evaluated using publicly available datasets provided by the authors (Fig 1). The trained model is being adapted to the in vitro 4D flow MRI datasets with voxel sizes of 3mm³ and 1.5mm³, and its outputs will be compared to the higher-resolution datasets (1.5mm³ and 0.75mm³) for validation.

Results: Following the adaptation of the model, the evaluation of the 4DFlowNet will be performed using the aneurysm model dataset with varying voxel sizes. The system's performance will be assessed using relative speed error, average flow rate, and divergence, with the results benchmarked against high-resolution ground truth. For comparison, the following interpolation methods will be included: linear, cubic spline, and SINC. The 4DFlowNet produced velocity fields that more closely matched the ground truth for the publicly available datasets while substantially reducing image noise. The evaluation of the network performance for the in-house in vitro datasets is ongoing.

Discussion: The current version of 4DFlowNET demonstrates the ability to improve spatial resolution and enhance the

accuracy of hemodynamic patterns of in vitro 4D flow MRI. Initial results suggest that machine learning can effectively bridge the gap between low-resolution and high-resolution 4D flow MRI data. However, to achieve optimal performance on in vitro datasets, retraining the network with more relevant examples is essential and is currently underway. Furthermore, we plan to adapt the model architecture from a conventional convolution neural network to an autoencoder-based design. This modification aims to satisfy better physical constraints, such as the Navier–Stokes equations, and improve generalizability across different anatomical regions and flow conditions in 4D flow MRI.

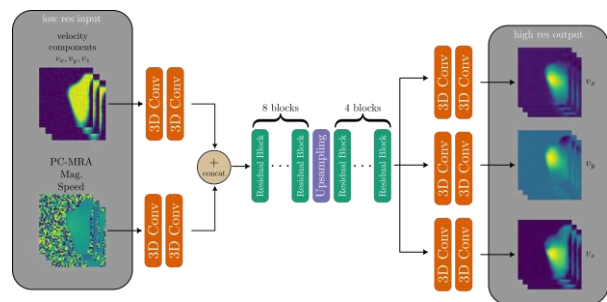


Fig. 1: Schematic illustration of 4DFlowNet architecture: The network receives two low-resolution 3D input blocks: one with velocity data and one with phase-contrast magnetic resonance angiography (PC-MRA) and the absolute values of the magnitude (mag) and velocity (speed). Both are processed through 3D convolutions, residual blocks, and an upsampling layer to reconstruct high-resolution velocity images.

Conclusion: Our initial findings suggest that machine learning has the potential to reduce acquisition times while preserving critical hemodynamic information, thereby enhancing the clinical utility of 4D flow MRI for neurovascular diagnostics. Future work will focus on expanding dataset diversity, as well as enforcing stronger adherence to physical constraints, to improve generalizability and clinical relevance.

Acknowledgements: We acknowledge Philips Healthcare for support in MRI experiments.

References:

- Dyverfeldt P. 4D flow cardiovascular magnetic resonance consensus statement. *J Cardiovasc Magn Reson*. 2015;19.
- Brina O, Bouillot P, Raymond P, et al. How Flow Reduction Influences the Intracranial Aneurysm Occlusion: A Prospective 4D Phase-Contrast MRI Study. *Am J Neuroradiol*. 2019;40(12):2117-2123. doi:10.3174/ajnr.A6312
- Schnell S, Wu C, Ansari SA. 4D MRI flow examinations in cerebral and extracerebral vessels. Ready for clinical routine? *Curr Opin Neurol*. 2016;29(4):419-428. doi:10.1097/WCO.0000000000000341
- Pravdivtseva MS, Peschke E, Lindner T, et al. 3D-printed, patient-specific intracranial aneurysm models: From clinical data to flow experiments with endovascular devices. *Med Phys*. 2021;48(4):1469-1484. doi:10.1002/mp.14714
- Ferdian E, Suinesiaputra A, Dubowitz DJ, et al. 4DFlowNet: Super-Resolution 4D Flow MRI Using Deep Learning and Computational Fluid Dynamics. *Front Phys*. 2020;8. doi:10.3389/fphy.2020.00138
- Ferdian E, Marlevi D, Schollenberger J, et al. Cerebrovascular super-resolution 4D Flow MRI – Sequential combination of resolution enhancement by deep learning and physics-informed image processing to non-invasively quantify intracranial velocity, flow, and relative pressure. *Med Image Anal*. 2023;88:102831. doi:10.1016/j.media.2023.102831

Assessing the microstructure of drug-resistant temporal lobe epilepsy patients using the fingerprint of in vivo histology MRI

Siawoosh Mohammadi^{1,2,3,5}, Noémie Camille Rachel Sura⁴, Laurin Mordhorst^{1,2}, Nina Lüthi^{1,2}, Jan Malte Oeschger^{1,2,3}, Björn Fricke^{1,2}, Ora Ohana⁴, Martina F. Callaghan⁶, Nikolaus Weiskopf^{3,6,14}, Ileana Jelescu⁷, Jürgen Finsterbusch², Filip Szczepankiewicz⁸, Arthur Chakwizira⁸, David Carmichael⁹, Difei Wang¹⁰, Rüdiger Stirnberg¹⁰, Tony Stöcker^{10,11}, Jose Marques¹², Markus Nilsson¹³, Thomas Sauvigny⁴, and Francisco J. Fritz^{2,1,3}

1 Department of Neuroradiology, Advanced MRI Research CBBM, Lübeck University, Lübeck, Germany

2 Department of Systems Neurosciences, University Medical Center Hamburg-Eppendorf, Hamburg, Germany,

3 Department of Neurophysics, Max Planck Institute for Human Cognitive and Brain Sciences, Leipzig, Germany

4 Department of Neurosurgery, University Medical Centre Hamburg-Eppendorf, Hamburg, Germany

5 Max Planck Research Group MR Physics, Max Planck Institute for Human Development, Berlin, Germany

6 Functional Imaging Laboratory, Department of Imaging Neuroscience, UCL Queen Square Institute of Neurology, University College London, UK

7 Department of Radiology, Lausanne University Hospital (CHUV), Lausanne, Switzerland

8 Department of Medical Radiation Physics, Clinical Sciences Lund, Lund University, Lund, Sweden

9 Imaging Physics & Engineering Research Department, School of Biomedical Engineering and Imaging Sciences, King's College London, UK

10 MR Physics, German Center for Neurodegenerative Diseases, Bonn, Germany

11 Department of Physics and Astronomy, University of Bonn, Bonn, Germany

12 Donders Institute for Brain, Cognition and Behaviour, Centre for Cognitive Neuroimaging, Radboud University, Nijmegen, The Netherlands

13 Department of Clinical Sciences Lund, Radiology, Lund University, Lund, Sweden

14 Felix Bloch Institute for Solid State Physics, Faculty of Physics and Earth System Sciences, Leipzig University, Germany

Abstract: Motivation: In drug-resistant temporal lobe epilepsy (dTLE), lesion detection via standard MRI supports surgical planning, but microstructural insights from in-vivo histology MRI (hMRI) remain unexplored.

Goal: To assess whether hMRI-Fingerprints reveal microstructural changes in neurosurgical target regions beyond standard MRI.

Approach: In three patients, we assessed interhemispheric differences between hMRI metrics in automatically identified dTLE-relevant target-regions for neurosurgery. We tested consistency of hMRI-metric-asymmetry-profiles (here: fingerprints) across patients.

Results: hMRI-Fingerprint shows significant correlations across patients in the target regions, with a stronger profile patient with smallest disease-onset time.

Conclusion: hMRI-Fingerprinting in automatically identified surgery-target regions provides an objective, non-invasive window into the microstructural underpinnings of dTLE and augments standard MRI.

Motivation: In surgical treatment of patients with drug-resistant temporal lobe epilepsy (dTLE) a clear-cut lesion on structural MRI is associated with favourable seizure outcome after surgery [1]. However, without confirmation via histopathology the microstructural underpinning of dTLE for individual patients cannot be determined. For example, for hippocampal sclerosis (HS), the “International League Against Epilepsy” (ILAE) types are determined by the histopathologist.

In vivo histology using MRI (hMRI) [2] is a non-invasively approach to improve our understanding of brain microstructure. However, hMRI has seldom been used in dTLE despite the fact that it can reveal microstructure information [3] and may contain microstructural fingerprints [4]. In this proof-of-principle study, we tested for four patients whether the profile of inter-hemispheric differences of hMRI metrics, henceforth the hMRI-Fingerprint, in the neurosurgery target region reveals information beyond standard clinical MRI. We also identified hMRI metrics with the highest inter-hemispheric effect size.

Materials & Methods: Subjects and MRI: Three patients with dTLE (ages 24, 28, 48, and 55 yrs) underwent a one-hour quantitative MRI protocol on a 3T Prisma-fit MR system (Siemens Healthineers) with approval from the University-Medical-Center-Hamburg-Eppendorf (ethic protocolPV5600). The site for surgical resection was identified via combined semiology, EEG video monitoring, MRI imaging and neuropsychological testing. Details about acquisition, pre-processing, parameter fitting are in Table 1.

Effect size and cross-correlation: Cohen's d was used to assess the effect size of each hMRI metric between hemispheres per subject: [1]

$$d = \frac{\langle x_L \rangle - \langle x_R \rangle}{s}$$

$$s = \sqrt{\frac{(n_L - 1)s_L^2 + (n_R - 1)s_R^2}{n_L + n_R - 2}}$$

where x_L and x_R are the left and right ROI averaged, s_L and s_R are the corresponding standard deviations, and n_L and n_R are the corresponding number of voxels. A positive $d_{x_L} > x_R$ and vice versa (Figure 1A). The cross-correlation was calculated between the hMRI-Cohen's d-profiles of pairs of patients (Figure 2A), with Bonferroni-corrected p-value for number-of-target-regions: $\alpha_{B*} = \frac{0.05}{3} \approx 0.017$.

Regions of interest (ROIs): We defined four ROIs per hemisphere: three clinically-identified areas for neurosurgical resection as “target”-ROIs: hippocampus, temporal pole, and amygdala; and a reference ROI: entire grey matter (GM). Hereby, we hypothesized that hemispheric differences within the entire GM are smaller than within target ROIs. To objectively identify target regions, we used labels from the Oxford-Harvard and SubfieldICBMspace atlases [5], [6], [7], transformed them into native space, thresholded (probability > 0.5) and multiplied them by the thresholded (probability > 0.9) tissue-probability map (TPM) of each individual. TPMs were estimated using multi-channel segmentation in SPM 12.

Whole brain measurements, resolution, and acquisition time	Sequences	Pre-processing	Estimated parameters
Multi parameter mapping (MPM) protocol ¹⁸ at 1.0 mm isotropic, 2x2 acceleration. TA: 19 min.	3-signal weighted FLASH: T1w, MTw and PDw + B0-B1 calibration + RF sensitivity head array per contrast. Flip angles: 21° (T1w), 6° (PDw and MTw) and 200°/2000 Hz MT saturation (MTw). Echo times (8 for PDw and T1w, 6 for MTw): 2.071; 9.8; 14.95 ms Repetition time: 25 ms	MPM maps estimation with B0 and B1 correction and RF sensitivity array per contrast using the hMRI toolbox ¹⁸ in SPM12 environment ¹⁹ .	Longitudinal relaxation rate (R ₁); effective transverse relaxation rate (R ₂); proton density (PD); and magnetization transfer saturation rate (MT _{sat})
Magnitude phase-based T2 relaxationometry (MPR) protocol ¹¹ at 1.0 mm isotropic, 2x2, x EPI factor 5 acceleration. TA: 5min	12 x 30-EPI with varying RF spoil phase increments: ±1, 1.5, 2, 3, 4, 5° Flip angle: 20° Echo time: 5.1 ms Repetition time: 13.7 ms	Flip angle map correction due to B0 inhomogeneities ¹⁴ , complex MPPCA denoising ¹⁵ , background phase subtraction ¹¹ .	R2 (R1+signal amplitude as rough estimates fitted simultaneously with R2)
Myelin water imaging (MWI) protocol ¹⁶ at 1.5 mm isotropic, 1x5 acceleration with free CAIPRRHHA. TA: 11 min and 16 s.	4-flip angle TFL measurements: 10°, 20°, 50° and 70° Repetition time: 38.6 ms Echo times (10): 1.93; 3.88; 36.85 ms	Magnitude and phase data were corrected by susceptibility and phase wrapping using SEPIA ¹⁵ . Analysis was performed using the MWI model ¹⁶ .	Myelin Water Fraction (MWF), free water longitudinal relaxation rate (R ₁); myelin-water transverse relaxation rate (R ₂); intra-axonal transverse relaxation rate (R ₂); exchange rate (Ex)
Standard DKI diffusion protocol ¹⁸ at 1.7 mm isotropic, 2x3 acceleration. TA: 7 min and 58 s	Spin-echo diffusion-weighted sequence: 2 multi-shell up to 2000 s/mm ² AP (bip-up) measurements and 1 b0 PA (bip-down) measurement. Repetition time: 3.1 s Echo time: 74.6 ms B-values (8 directions) in the AP measurements [s/mm ²]: b=0 (11); b=500 (7); b=1000 (29); b=2000 (64).	Diffusion data was corrected by noise, Gibbs rings, susceptibility and eddy currents. All corrections were performed using MRtrix and FSL through the dwifslpreproc command from MRtrix. Analysis was performed using the SMI model ¹⁷⁻¹⁹ .	Axonal water fraction (f), intra-axonal diffusivity (D), extra-axonal diffusivity parallel (D) and perpendicular (D _⊥), anisotropy (p), free water fraction (f _w)
Free waveform diffusion (FWF) protocol ¹⁶ at 2.0 mm isotropic, 2x2 acceleration. TA: 7 min and 34 s	Modified spin-echo diffusion-weighted sequence for free waveform diffusion: one spherical tensor encoding (STE), one linear tensor encoding (LTE), both multi-shell up to 2000 s/mm ² AP (bip-up) measurements and 1 b0 PA (bip-down) measurement. Repetition time: 4.5 s Echo time: 98 ms B-values (8 directions) for the STE/LTE: b=100, 700, 1400, 2000 s/mm ² shells with 6, 6, 10, 15/21 waveform rotations	FWF correction include: denoising; correction of Rician bias, Gibbs-ringing, susceptibility distortion using MRtrix and the ACID toolbox and eddy current and motion correction from [16]. Parameters were estimated using the QTI fit from [17].	Axial diffusivity (AD), radial diffusivity (RD), mean diffusivity (MD), fractional anisotropy (FA), micro FA (μFA), mean total kurtosis (Mk), mean isotropic kurtosis (Mk), mean anisotropic kurtosis (Mk _a)

Fig. 1: Summary of the hMRI datasets acquired for all patients, including the pre-processing, registration and segmentation. Notation and definitions: Depiction of echoes in multi-echo protocols: (first echo time : echo-time interval : final echo time); Abbreviations: TA = total acquisition time; PDw, T1w, MTw: proton-density, T1, and MT weighted; AP = anterior-posterior.

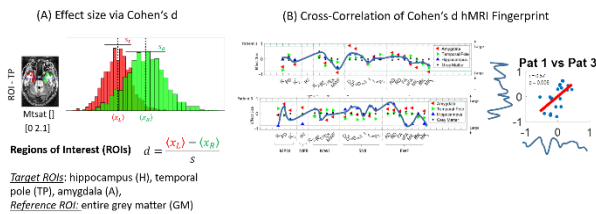


Fig. 2: Illustration of analyses in Figures 2 and 3 (A and B). (A) Cohen's d (Equation 1) in target region (here: temporal pole): subtraction of mean in left (red) and right (green) side, divided by joined standard deviation. (B) The cross-correlation between hMRI-Fingerprints of Patient 1 and 3 (blue line: hippocampus).

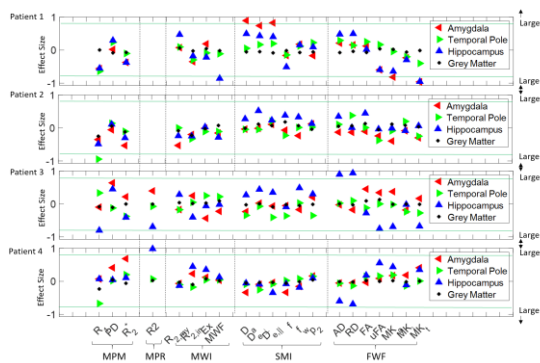


Fig. 3: Effect sizes of interhemispheric hMRI metric differences (patients 1–4, top to bottom) across 21 metrics. ROIs: amygdala (red), temporal pole (green), hippocampus (blue), and whole grey matter (black, reference). Green line indicates large effect size threshold (|d| > 0.8). See Table 1 for metric details.

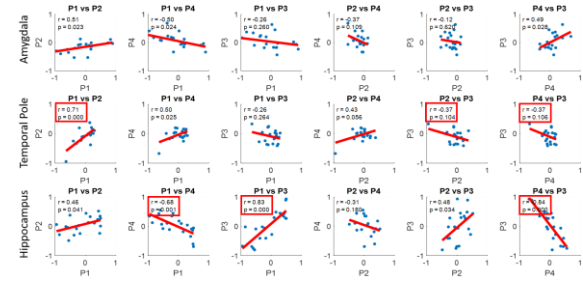


Fig. 4: Correlation of hMRI metric fingerprints between three patients (1-3) with the following clinical MRI patterns: (1) hyperintensities, (2) atrophic, and (3) hyperintensities and atrophic. Depicted are the scatter plot of the effect size across hMRI metrics (left to right): amygdala, temporal pole, hippocampus. Significant correlations are highlighted (red boxes).

Results: All patients had focal structural temporal lobe epilepsy, with seizure foci in the left hemisphere (patients 1–3) and right (patient 4). Patients 2, 3, and 4 had childhood-onset epilepsy (ages 6, 14, and 9) with long disease durations (15–41 years) and frequent seizures (3–16 episodes/month). Patient 1 had adult-onset epilepsy (age 45), shorter duration (3 years), but the highest seizure frequency (~30/month).

Clinical MRI (not shown) revealed hippocampal atrophy consistent with sclerosis in patients 2-4. Hyperintensities were observed in the amygdala, anterior hippocampus, and inferior temporal gyrus in patient 1, and in the hippocampus of patient 3. Histology confirmed HS in patients 2 (ILAE type 2), and 3 and 4 (both type 1). Reactive changes were found in the grey matter (patient 1), amygdala (patients 2 and 4), and temporal pole (patient 3).

hMRI metrics reflected these findings (Figure 2). Largest effect sizes (|d| > 0.8) matched MR-visible lesions: diffusion and MWF changes in the amygdala of patient 1, and R1/R2 increases in the hippocampus or temporal pole of patients 2–4. The smallest effect size was observed in the reference region (whole-hemispheric GM).

Cross-correlation of hMRI fingerprints across patients showed significant similarity in the hippocampus and temporal pole, but not in the amygdala (Figure 3). Notably, hippocampal correlations reflected lateralization: patient 4 (right focus) showed negative correlations with the left-focus patients (1-3). While Patient 1 showed significant cross-correlation with Patient 3 and 4 (type 1 HS) in the hippocampus, Patient 2 (type 2 HS) did not.

Discussion: Our proof-of-principle data show that inter-hemispheric hMRI-Fingerprints can noninvasively detect microstructural abnormalities in dTLE, aligning with surgical targets and providing greater insight than standard MRI. In all patients, the largest effect sizes (|d| > 0.8) localized to the epileptogenic zone—amygdala (patient 1), temporal pole (patient 2) and hippocampus (patients 1,3,4)—highlighting the sensitivity of quantitative metrics.

Patients 2–4, with visible atrophy, showed strong asymmetries in R1 and R2. In contrast, patient 1, without atrophy, exhibited marked asymmetry in myelin water fraction (MWF) and diffusion metrics (D_a, D_{e,||}, D_{e,⊥}, μFA, Mk), suggesting demyelination and possible inflammation. The elevated R2 may indicate iron-related pathology, though the biophysical basis of R1 and R2 increase remains unclear.

Cross-patient hMRI-Fingerprint correlations revealed subtype-specific patterns. Patients 3 and 4 (type 1 HS) correlated strongly in the hippocampus but not with patient 2 (type 2 HS), who also showed the smallest effect sizes. Interestingly, patient 1 (no HS) showed correlations with the other patients in the hippocampus (3,4) and temporal pole (2), suggesting overlapping microstructural changes despite differing pathology. The lack of correlation between type 1 and 2 patients together with the smallest effect size in the type-2 patient, points towards microstructural changes between subtypes that need to be better understood.

Limitations include the small sample size, absence of histological correlation with imaging, and potential inaccuracies in some hMRI metrics (e.g., SMI-model limitations in GM). ROI segmentation was based on MTsat maps, which may affect anatomical precision across contrasts, though no visual mismatches were observed.

Conclusion: In conclusion, inter-hemispheric hMRI-Fingerprinting in automatically identified surgery-target regions provides an objective, non-invasive window into the microstructural underpinnings of dTLE and augments standard MRI by quantifying microscopic tissue alterations. While metrics such as MWF and diffusion parameters show promise as sensitive biomarkers of epileptogenic tissue at the earlier disease stage, R1 and R2 seems to be a promising marker at later disease stages. However, more patients and comparison to ex-vivo histology and healthy controls are needed to assess clinical relevance.

Acknowledgements: This work was supported by the German Research Foundation (DFG Priority Program 2041 "Computational Connectomics", [MO 2397/5-1, MO 2397/5-2, MO 2249/3-1, MO 2249/3-2], by the Emmy Noether Stipend: MO 2397/4-1; MO 2397/4-2).

Funded by the European Union. Views and opinions expressed are however those of the author(s) only and do not necessarily reflect those of the European Union or the European Research Council Executive Agency. Neither the European Union nor the granting authority can be held responsible for them. This work is supported by ERC grant (Acronym: MRStain, Grant agreement ID: 101089218, DOI: 10.3030/101089218).

References:

1. Bernasconi, A. *u. a. Epilepsia* 60, 1054 (2019).
2. Weiskopf, N. *u. a. Nat Rev Phys* 3, 570 (2021).
3. Jackson, G.D. *u. a. Neurology* 43, 1793 (1993).
4. Lorio, S. *u. a. Epilepsia* 61, 433 (2020).
5. Smith, S.M. *u. a. Neuroimage* 23 Suppl 1, S208 (2004).
6. Saygin, Z.M. *u. a. Neuroimage* 155, 370 (2017).
7. Iglesias, J.E. *u. a. Neuroimage* 115, 117 (2015).
8. Callaghan, M.F. *u. a. Data in Brief* 25, 104132 (2019).
9. Tabelow, K. *u. a. NeuroImage* 194, 191 (2019).
10. Friston, K.J. *u. a. (Academic Press: London, 2006).*
11. Wang, D. *u. a. Magnetic Resonance in Medicine* 92, 2328 (2024).
12. Wang, F. *u. a. NeuroImage* 250, 118963 (2022).
13. Cordero-Grande, L. *u. a. Neuroimage* 200, 391 (2019).
14. Chan, K.-S. *u. a. NeuroImage* 266, 119824 (2023).
15. Chan, K.-S. *u. a. Neuroimage* 227, 117611 (2021).
16. Oeschger, J.M. *u. a. Magn Reson Med* 92, 69 (2024).
17. Reiser, M. *u. a. Neuroimage* 147, 964 (2017).
18. Novikov, D.S. *u. a. Neuroimage* 174, 518 (2018).
19. Coelho, S. *u. a. Neuroimage* 257, 119290 (2022).
20. Szczepankiewicz, F. *u. a. PLOS ONE* 14, e0214238 (2019).

Quantitative Susceptibility Mapping (QSM) of kidney stones: an ex-vivo investigation of the effect of masking the low-signal kidney stone regions

Lion H. Mücke 1*, Frederik B. Laun 1, Ruben de Figueiredo Cardoso 1, Guillaume Flé 1, Jennifer Lorenz 1, Alexander Fichte 2, Michael Uder 1, Nadine Bayerl 1†, and Jannis Hanspach 1†

1 Friedrich-Alexander-Universität Erlangen-Nürnberg, Institute of Radiology, Uniklinikum Erlangen, Erlangen, Germany

2 Friedrich-Alexander-Universität Erlangen-Nürnberg, Department of Urology and Pediatric Urology, Uniklinikum Erlangen, Erlangen, Germany

† shared last authorship

Abstract: To improve QSM reconstruction for susceptibility-based characterization of kidney stones, multi-echo gradient-echo data of three water-based Agar-Agar phantoms containing a total of 53 kidney stones of varying types were acquired at 3T. Conventionally reconstructed susceptibility maps were compared with maps obtained by setting signal void stone regions to zero during the dipole inversion step. All kidney stones were visualized using QSM, where mean susceptibility values ranged from -0.62 ppm to -1.61 ppm and -0.52 ppm to -1.50 ppm for the conventional and masked QSM reconstructions respectively. The masked QSM reconstruction successfully reduced noise inside stone regions, marking a crucial step towards radiation free in-vivo detection of kidney stones using MRI.

Motivation: In patients with flank pain and hydronephrosis detected on ultrasound, which strongly suggests urolithiasis, unenhanced CT with ionizing radiation is performed as the reference standard for kidney stone detection in routine clinical practice.[1] CT reliably visualizes most kidney stone types, including the five most common chemical compositions, which account for approximately 99% of all kidney stones: calcium oxalate (CaOx), calcium phosphate (CaP), uric acid (UA), cystine (CY) and struvite (ST).[1,2] While MRI produces no ionizing radiation and is particularly well-suited for soft tissue characterization, as well as vascular and functional imaging, kidney stones appear as hardly visible signal voids on conventional MRI contrasts, such as T1- or T2-weighted images, due to a lack of protons.[1,3]

In a recent renal MRI study, quantitative susceptibility mapping (QSM) has been shown to successfully visualize two kidney stones of unknown chemical composition in-vivo with diameters of 9 mm and 10 mm.[3] However, extended regions with low signal, such as large calcified plaques or hemorrhages, have been shown to present challenges for QSM reconstruction due to streaking or shadowing artifacts, as well as noise amplification.[4,5] It is therefore possible, that similar challenges might arise for kidney stones in QSM reconstructions.

The objective of this work was to i) visualize and characterize multiple kidney stones belonging to the five major types with known chemical compositions in three ex-vivo phantoms using susceptibility maps, and ii) improve the QSM reconstruction for kidney stones by reducing noise in signal void stone regions reconstructed from the acquired multi-echo gradient-echo data.

Materials & Methods: A total of 53 kidney stones were collected from 32 different patients (Table 1). Chemical analysis using infrared spectroscopy classified the samples as 3×CaP, 14×CaOx, 12×UA, 5×CY, 8×ST and 11×mixed stone type compositions.

Three phantoms were built using identical plastic cylinders and a water-based 2% Agar-Agar solution, with 0.5% NaCl (Figure 1).[6] Each phantom was created in four steps, allowing the placement of kidney stones atop hardened Agar-Agar layers, sealing in the stones without visible air pockets when pouring the next layer on top.

Multi-echo 3D gradient-echo data were acquired on a 3T MRI scanner (MAGNETOM Vida, Siemens Healthineers) using a 16-channel ankle-coil, with acquisition parameters: TE = 3.89/9.35/14.81/20.27 ms, $\Delta TE = 5.46$ ms, TR = 25 ms, voxel size = 0.94×0.94×0.94 mm³, flip angle = 13°, bandwidth = 250 Hz/px, no acceleration, 5 averages, acquisition time = 20:32 min.[5]

Susceptibility maps were reconstructed using the SEPIA toolbox (v1.2.1.1) and MATLAB. Phantom masks were created by thresholding the magnitude images, whereas the kidney stone regions were segmented manually. Phase unwrapping, background field removal and dipole inversion were performed using ROMEO, PDF and MEDI+0 algorithms respectively (“conventional QSM”).[5] In a second reconstruction approach, the field-map in kidney stone regions was set to zero before dipole inversion (“masked QSM”). Thus, only frequency variations induced by the stones and measured outside the stones contributed to susceptibility estimation, suppressing contributions of propagated phase noise caused by signal voids.

Susceptibility values of individual stones obtained from both QSM reconstructions were compared using the Agar-Agar substance as zero-reference.

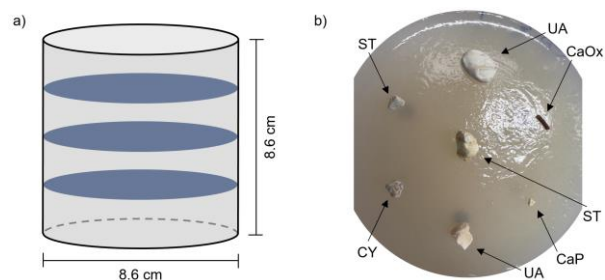


Fig. 1: Depiction of the Agar-Agar phantom design: a) A cylindrical plastic container (black), filled with four Agar-Agar layers (grey) and three embedded kidney stone layers (blue). b) Representative boundary layer image with 7 kidney stones atop hardened Agar-Agar substance, taken before sealing them in the next Agar-Agar layer.

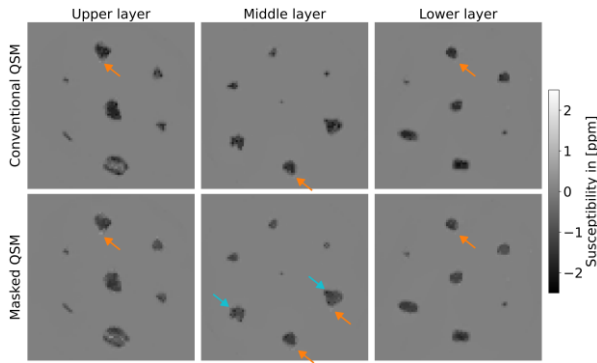


Fig. 2: Representative susceptibility maps of phantom 2 for the conventional (top) and the masked QSM reconstructions (bottom). Across three layers of seven kidney stones within the phantom, all stone types presented as diamagnetic regions. Arrows indicate remaining voxels with strongly diamagnetic values (blue) and paramagnetic artifacts at stone-agar-interfaces (orange).

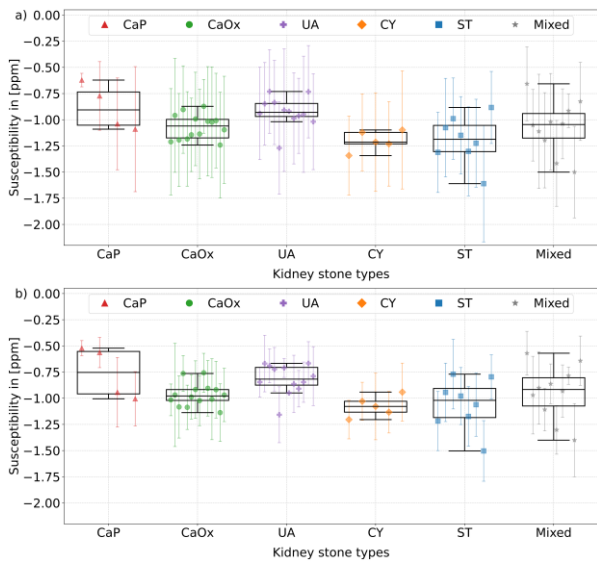


Fig. 3: Group comparisons of magnetic susceptibility between the five major kidney stone types and mixed stones for a) the conventional QSM reconstruction and b) the masked QSM reconstruction. Markers represent mean susceptibility values and SD of the 53 kidney stones, where different color and shape identify different stone types.

Kidney stone type	Number of stones	Diameter range [mm]	Mean susceptibility for conventional QSM [ppm]	Mean susceptibility for masked QSM [ppm]
CaP	3	3.9 to 5.0	-0.88 ± 0.11	-0.76 ± 0.13
CaOx	14	2.3 to 10.6	-1.07 ± 0.03	-0.97 ± 0.03
UA	12	2.3 to 10.1	-0.93 ± 0.04	-0.82 ± 0.04
CY	5	5.6 to 15.4	-1.20 ± 0.04	-1.08 ± 0.04
ST	8	2.3 to 16.4	-1.19 ± 0.08	-1.06 ± 0.09
Mixed	11	2.5 to 13.5	-1.07 ± 0.08	-0.95 ± 0.08

Fig. 4: Mean susceptibility values with standard errors of the investigated five major kidney stone types and mixed stones for the conventional QSM reconstruction and the masked QSM reconstruction. Also given are the respective number of individual stones per type and the range of stone diameters.

Results: All kidney stones were clearly visible in both QSM reconstructions, appearing as hypointense regions in the respective susceptibility maps (Figure 2). Setting stone regions to zero during dipole inversion visibly reduced noisy inhomogeneities within the diamagnetic kidney stones, but

occasional instances of singular strongly deviating diamagnetic voxels for stones with diameters of 5.0 mm and larger remained. Most stones with diameters below 3.4 mm exhibited partial volume effects in both the magnitude images and the susceptibility maps. Sporadic paramagnetic artifacts at interfaces between stones and Agar-Agar substance were less pronounced for the conventional QSM reconstruction.

Figure 3 shows group comparisons between different stone types for both QSM reconstructions, together with mean susceptibility values and standard deviations (SD) of all 53 individual stones. Mean susceptibility values of individual stones ranged from -0.62 ppm to -1.61 ppm for the conventional QSM reconstruction. In comparison, the masked QSM reconstruction yielded clearly reduced SD for individual stones. While this approach introduced a global offset of approximately +0.1 ppm, resulting in individual stone susceptibilities between -0.52 ppm and -1.50 ppm, the susceptibility differences between the individual stones remained similar. Most kidney stones of the type UA appeared less diamagnetic than CY stones in both QSM reconstructions, although no significance difference was observed due to the large SD.

The overall mean susceptibility values per stone type showed CY to be the most diamagnetic type for both QSM reconstructions (Table 1).

Discussion: By visualizing the five major kidney stone types as diamagnetic regions compared to water-based Agar-Agar substance in susceptibility maps, this study highlights QSM as reliable MRI technique for kidney stone imaging. Additionally, setting field-map values in stone regions to zero during dipole inversion effectively reduced noise inside signal void stone regions in the susceptibility maps at the cost of a global susceptibility offset of approximately +0.1 ppm.

A recently published in-vivo renal QSM study reported slightly more diamagnetic kidney stone susceptibilities of approximately -1.5 ppm, where discrepancies could result from different referencing or QSM reconstruction algorithms.[3] Excluding kidney stones with diameters below 3.4 mm would remove a bias introduced by partial volume effects, probably decreasing overall susceptibilities of the different stone types. Paramagnetic artifacts observed at interfaces between stones and Agar-Agar could probably be reduced by using more precise stone masks during dipole inversion or reconstruction algorithms optimized for a larger range of susceptibility values.[4,5] Similarly, a deep-learning based dipole inversion could improve QSM reconstruction in stone regions, since this approach considerably reduced artifacts caused by signal void air inclusions with high susceptibilities in prostate QSM.[7]

Future studies should include CT negative kidney stones, such as indinavir or pure matrix stones, and investigate a larger number of stone types CaP, CY and ST.[1] Furthermore, the dependency of stone susceptibilities on imaging parameters essential for QSM, such as selection of TE or field strength, as well as the repeatability of individual stone susceptibilities should be investigated.[5]

Conclusion: This study demonstrated, that modifying a conventional QSM reconstruction by setting the field-map to zero in kidney stone regions during dipole inversion step substantially reduces noise inside the stone regions in the

resulting susceptibility maps, thus improving the visualization of kidney stones belonging to the five most common chemical compositions CaOx, CaP, UA, CY, and ST in water-based surroundings using MRI. This marks a crucial step towards an MRI-based and radiation-free alternative to unenhanced CT for in-vivo imaging of patients with urolithiasis in clinical practice.

Acknowledgements: We would like to express our gratitude to Alexander K. Fichte senior for providing the kidney stone samples. This research was supported by DFG under project number 460333672 – SFB 1540 Y, and under ELAN project number P125. Preliminary results were already presented at the 2024 EMTP Joint Workshop on MR phase, magnetic susceptibility and electrical properties mapping in Chile.

References:

- [1] Cheng *et al.* (2012), "What the Radiologist Needs to Know About Urolithiasis: Part 1 - Pathogenesis, Types, Assessment, and Variant Anatomy", *AJR*, vol. 198, pp. W540-W547, doi: <https://doi.org/10.2214/AJR.10.7285>
- [2] Coe *et al.* (2005), "Kidney Stone Disease", *JCI*, vol. 115, pp. 2598-2608, doi: <https://doi.org/10.1172/JCI26662>
- [3] Schumacher *et al.* (2024), "Quantitative susceptibility mapping for detection of kidney stones, hemorrhage differentiation and cyst classification in ADPKD", *Abdom. Radiol.*, vol. 49, pp. 2285–2295, doi: <https://doi.org/10.1007/s00261-024-04243-6>
- [4] Dimov *et al.* (2023), "QSM Throughout the Body", *JMRI*, vol. 57.6, pp. 1621–1640, doi: <https://doi.org/10.1002/jmri.28624>
- [5] QSM Consensus Organization Committee *et al.* (2024), "Recommended implementation of quantitative susceptibility mapping for clinical research in the brain: A consensus of the ISMRM electro-magnetic tissue properties study group", *MRM*, vol. 91, pp. 1834-1862, doi: <https://doi.org/10.1002/mrm.30006>
- [6] Graf *et al.* (2025), "A dedicated phantom for exploring the interplay of fat and paramagnetic substances in quantitative susceptibility mapping", *MAGMA.*, pp. 1–16, doi: <https://doi.org/10.1007/s10334-025-01261-3>
- [7] Hanspach *et al.* (2022), "Deep learning-based quantitative susceptibility mapping (QSM) in the presence of fat using synthetically generated multi-echo phase training data", *Magn. Reson. Med.*, vol. 88.4, pp. 1548–1560, doi: <https://doi.org/10.1002/mrm.29265>

Phasor analysis enables unsupervised k-means-based metabolic segmentation of Hyperpolarized ¹³C-CSI data

Konstantin Müller 1+2*, Saar Székely 2, Josef Mayer 1+2, Christoph A. Müller 2, Nicolas Joudiou 3, Bénédicte Jordan 3, Ilai Schwartz 2, Timo Ropinski 1, Michael Götz 1, Pascal P. R. Ruetten 2

1 Ulm University, Germany

2 NVision Imaging Technologies GmbH, Ulm, Germany

3 UCLouvain, Belgium

Abstract: Spectral-phasor analysis showed promising results for image analysis in fluorescence lifetime imaging [1-3]. We adapted the phasor approach to separate metabolic signals in hyperpolarized ¹³C-MRI (HP-MRI). We applied the first Fourier harmonic to derive phasor coordinates, then used k-means clustering. Compared to a lactate-to-pyruvate ratio (LPR) threshold labeling voxels as mixed lactate and pyruvate, only lactate or noise, phasor clustering on a chemical shift imaging (CSI) data set of a mouse produced metabolic segmentations without pre-defined peak positions (Figure 3 d-f), whereas the threshold-based approach mislabelled peaks at the edge of the pre-defined cut off (Figure 4 c, f). Spectral-phasor analysis therefore offers a model-free, robust alternative for metabolic segmentation.

Motivation: HP-MRI enables real-time metabolic analysis of tumor tissue and other metabolic diseases [4, 5]. Segmentation of these datasets into regions of distinct metabolic activity conventionally relies on voxel-wise analysis, which requires manually chosen frequency windows or peak-fitting, which are sensitive to B₀ drift, linewidth heterogeneity, and signal-to-noise variations. Fixed thresholds fail to capture subtle shifts in resonance shapes and often require re-tuning for each acquisition [5]. The spectral-phasor concept treats the entire magnitude spectrum as a periodic signal and converts it into its normalized first Fourier coefficient, yielding a two-dimensional descriptor (g,s) of spectral shape (Figure 2). Voxels with similar profiles cluster naturally in phasor space, and because the transform is linear and shift-invariant, global frequency offsets merely rotate the phasor cloud while linewidth changes move points radially—providing intrinsic robustness to B₀ drifts and lineshape variations [2,3]. We hypothesized that k-means clustering in phasor space could discriminate between voxels of a different metabolic make-up without pre-defined parameters, yielding more reproducible metabolic maps than LPR-based thresholds.

Materials & Methods: A mouse was imaged on an 11.7 T small-animal scanner (Bruker) after bolus injection of hyperpolarised [1-¹³C]pyruvate. Data were acquired with a 5° flip-angle FID-CSI sequence (8×8 spatial matrix, 5 kHz spectral width, 469 spectral points, slice thickness 15mm) using a repetition time of 100 ms per acquisition; analysis focused solely on the 18-s time-point since it provided distinct metabolic shapes (Figure 1). Each voxel's spectrum was transformed into spectral-phasor coordinates (g, s) via the first Fourier harmonic, generating a compact representation of spectral shape (Figure 2). For segmentation, we assumed three distinct regions of interest, background, metabolically active region in the mouse, and an external lactate phantom.

This was used as input for k-means segmentation in phasor space for each voxel.

For comparison, a conventional LPR thresholding method was applied: we measured the highest spectral peak within ±20 Hz of the pyruvate resonance) and within ±20 Hz of the lactate resonance, known to be at around 171 ppm (pyruvate) and 183 ppm (lactate) for 11.7T ¹³C-MRI [6], which in our reconstructed frequency axis corresponds to peaks at roughly 0 Hz and 1.5 kHz. Voxels were classified based on the resonance showing either an LPR above one (lactate dominant representing the phantom region) or below (mixed-signal related to the metabolically active region), provided peaks surpassed a global pre-defined noise threshold set at the 80th percentile of the highest voxel peak intensities. Voxels not meeting this criterion were classified as noise. Hyperpolarized MR images were reconstructed using the NVision post-processing toolbox.

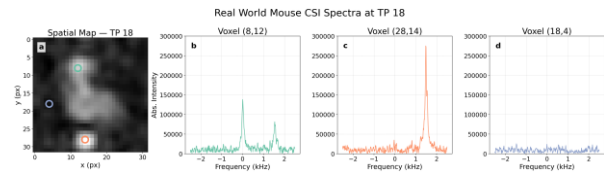


Fig. 1: Real-world CSI image, displaying the spatial map with sum of intensities. For each metabolic distinct region a highlighted voxel is displayed (a): metabolic active area in the mouse exhibiting pyruvate and lactate metabolism (b); a phantom with lactate only (c) and (d) noisy signal.

First-harmonic spectral phasor

$$g = \frac{1}{A} \sum_{k=0}^{N-1} \tilde{S}[k] \cos\left(\frac{2\pi k}{N}\right) \quad , \quad s = \frac{1}{A} \sum_{k=0}^{N-1} \tilde{S}[k] \sin\left(\frac{2\pi k}{N}\right)$$

N number of frequency points

$\tilde{S}[k]$ baseline-corrected magnitude at index k

$A = \sum_{k=0}^{N-1} \tilde{S}[k]$ total spectral area

g cosine (real) component

s sine (imaginary) component

Fig. 2: Formula for computing the g and s coordinates of the First harmonic spectra phasor.

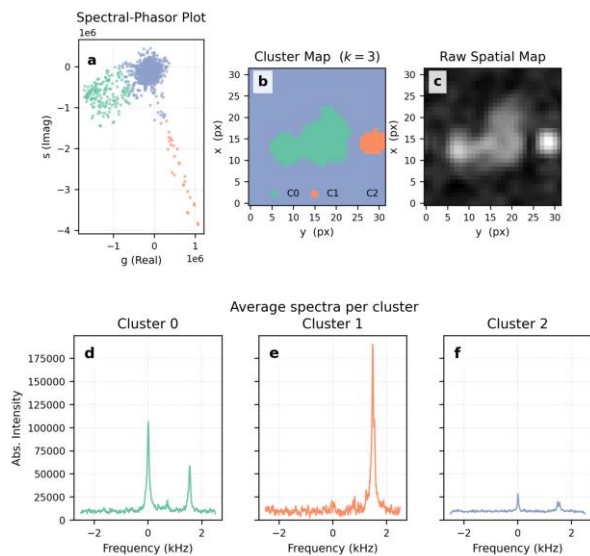


Fig. 3: Results of the phasor approach showing phasor space clustering with k -means (a) and reprojection to the spatial map (b), with comparison to the original spatial map (c). Each cluster segments three distinct metabolic regions: the metabolically active pyruvate and lactate region (d), a lactate-only phantom (e), and noise (f), respectively.

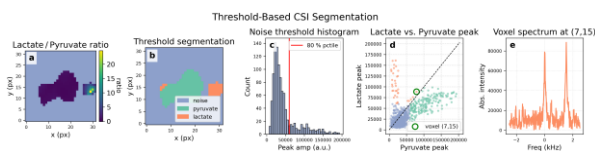


Fig. 4: Threshold-based segmentation: (a) noise-masked voxel-wise color-coded LPR map; (b) classification based on $LPR > 1$ (pyruvate and lactate), $LPR < 1$ (lactate), and noise; (c) noise presegmented via histogram of peak amplitudes at the 80th percentile; (d) lactate vs. pyruvate scatterplot with diagonal threshold and misclassified voxel; (e) spectrum of highlighted voxel.

Results: Phasor-based unsupervised k -means clustering identified three metabolically distinct tissue classes: mixed pyruvate-lactate metabolism, exclusively lactate-rich regions, and low-signal (noise-dominated) areas (Figure 3). Clustered spectra accurately represented the distinct metabolic resonances, clearly highlighting pyruvate at approximately 0 Hz and lactate at around 1538 Hz without baseline or linewidth artifacts. Spatially, the lactate-dominant clusters prominently formed a distinct circular core corresponding to a lactate phantom, whereas mixed lactate and pyruvate-rich voxels appeared localized in regions matching metabolically active areas in the mouse.

The LPR-based thresholding approach (Figure 4) generally corroborated the phasor method's findings; however, notable misclassifications emerged. Particularly, several voxels with clear visual evidence of pyruvate signal were incorrectly categorized as only lactate-dominated due to pre-defined ratio thresholds. These threshold-based misclassifications indicate lower robustness compared to the phasor-based segmentation, which better leverages the full spectral information and doesn't require pre-defined information such as thresholds or frequencies of peaks.

Discussion: A single Fourier harmonic suffices to encode the entire spectral fingerprint of each CSI voxel into a 2-D point, enabling unsupervised segmentation without prior knowledge of resonance positions. The threshold rule requires pre-defined parameters making it sometimes less robust, which was observed in the misclassification of some pixels as only lactate dominant while a clear pyruvate peak was still present. This highlights the method's dependence on careful a priori selection of threshold values. By contrast, phasor clustering relies only on relative spectral shape. Limitations include sensitivity to severe low SNR cases and the heuristic choice of k . In the next step, we aim to apply this to a larger dataset and show that we are able to distinguish between different types of metabolic activity. Future work will test clustering and longitudinal phasor trajectories over the full dynamic series of time points that are available in CSI and spectroscopy. Other advanced methods include combining phasor analysis with superresolution algorithms.

Conclusion: Spectral-phasor analysis provides a compact, rotation-invariant framework for hyperpolarized ¹³C-CSI data evaluation. In our mouse model it produced anatomically consistent pyruvate and lactate maps without manual threshold adjustments. Owing to its $O(N_{\text{vox}} \times N_{\text{freq}})$ computational efficiency and intuitive graphical representation, the phasor method can be readily incorporated into existing analysis pipelines. It demonstrates robustness to B_0 drift, linewidth variability, and baseline fluctuations, while effectively suppressing noise-dominated voxels. These attributes facilitate reproducible, real-time metabolic segmentation and quantitative assessment. Collectively, our findings support the spectral-phasor approach as a promising front-end for automated metabolic segmentation in both preclinical research and future clinical ¹³C-MRI applications.

Acknowledgements: We gratefully acknowledge the NEST imaging platform at UC Louvain.

References:

- Bianchetti G, Ciccarone F, Ciriolo MR, De Spirito M, Pani G, Maulucci G. Label-free metabolic clustering through unsupervised pixel classification of multiparametric fluorescent images. *Anal Chim Acta*. 2021 Mar 1;1148:238173.
- Bianchetti G, Spirito M, Maulucci G. Unsupervised clustering of multiparametric fluorescent images extends the spectrum of detectable cell membrane phases with sub-micrometric resolution. *Biomed Opt Express*. 2020 Sep 21;11(10):5728-5744.
- Vallmitjana A, Torrado B, Gratton E. Phasor-based image segmentation: machine learning clustering techniques. *Biomed Opt Express*. 2021 May 17;12(6):3410-3422.
- Chaumeil MM, Bankson JA, Brindle KM, Epstein S, Gallagher FA, Grashei M, Guglielmetti C, Kaggie JD, Keshari KR, Knecht S, Laustsen C, Schmidt AB, Vigneron D, Yen YF, Schilling F. New Horizons in Hyperpolarized ¹³C MRI. *Mol Imaging Biol*. 2024 Apr;26(2):222-232.
- Hsieh CY, Lai YC, Lu KY, Lin G. Advancements, challenges, and future prospects in clinical hyperpolarized magnetic resonance imaging: A comprehensive review. *Biomed J*. 2024 Oct 21;48(3):100802.
- Takado Y, Cheng T, Bastiaansen JAM, Yoshihara HAI, Lanz B, Mishkovsky M, Lengacher S, Comment A. Hyperpolarized ¹³C Magnetic Resonance Spectroscopy Reveals the Rate-Limiting Role of the Blood-Brain Barrier in the Cerebral Uptake and Metabolism of L-Lactate in Vivo. *ACS Chem Neurosci*. 2018 Nov 21;9(11):2554-2562.

Age-Related Changes in Myelin and Iron on MR Parameters Through Cortical Layers at 9.4T.

Angela Osenberg 1*, Jonas Bause 1, Pascal Martin 3, Klaus Scheffler 1 + 2, Gisela E. Hagberg 1 + 2

1 High Field Magnetic Resonance; Max Planck Institute for Biological Cybernetics; Tübingen, Germany

2 Biomedical Magnetic Resonance; University Hospital Tübingen, Germany

3 Department of Neurology and Epileptology, Hertie Institute for Clinical Brain Research

Abstract: We investigated age-related changes in myelin and iron within cortical and SWM layers using quantitative MR parameters (R1, R2*, and QSM) at 9.4T, aiming for more detailed, layer-specific vulnerabilities towards age due to increased SNR. Our findings confirm that R1 decreases in white matter with age, as an indication for myelin loss, but unexpectedly increases in deeper cortical gray matter, indicating late myelination of the cortical grey. R2* shows an age-related increase throughout cortical layers and the first layer of SWM. Accordingly, QSM depth profiles confirm a paramagnetic peak in SWM, especially in late-myelinating sulci with stronger paramagnetic effects in central regions, suggesting iron accumulation in SWM through aging.

Motivation: Recent advancements in ultra-high field (UHF) MRI, particularly at 9.4T, have enabled high-resolution investigations of age-related microstructural changes in the brain due to improved signal-to-noise ratio and spatial resolution [1, 2, 3]. Emerging evidence shows that alterations in myelin and iron are not uniformly distributed but follow layer- and region-specific patterns across the cortex and superficial white matter (SWM) [4, 5, 6]. However, further studies are needed to characterize these changes across a wider age range investigating layer-specific changes of myelin and iron. Therefore, this work aimed to map cortical and SWM alterations with aging using quantitative MRI parameters R1, R2*, and QSM in 28 participants aged 19–74 years. Based on previous work [4, 7, 6], we hypothesized an age-related increase in R2* within mid-cortical layers (particularly layer 5), reflecting iron accumulation. In contrast, R1 is expected to increase in layers near the white matter boundary, especially in late-myelinating association cortices like the middle frontal gyrus, consistent with ongoing or late myelination [8]. Further, we investigated age-related effects in the superficial white matter SWM, building on recent findings showing distinct age-related patterns in these regions [9, 6]. Additional analysis of depth profiles of R1, R2*, and QSM included comparisons of QSM with R2* to improve sensitivity to iron, and with R1 to enhance myelin specificity [5, 6]. Given the differentiation into early and late myelinating regions, ROIs were chosen based on previous literature [6, 9], indicating early and late myelination and higher U-fiber density [6, 9].

Materials & Methods: 39 participants underwent anatomical imaging at a 9.4T whole body MR scanner with MP2RAGE, T11/T12 = 900/3500ms; flipangles, FA = 4/6; TR = 6ms; TE = 2.3ms; TR = 9s; and 0.8mm isotropic voxel size. Grey-White Matter Segmentation was performed using FreeSurfer (v.6.0 and v.7.4.0). For 28 of the subjects (19-74, M = 42.1, SD = 18.75), quantitative maps of R1, R2*, and QSM were acquired at 9.4 T (Siemens Medical Solutions, Erlangen, Germany) with whole-body gradients, 16-channel, dual-row, transmit array in circularly polarized mode, and a 31-channel receive array [10]. R1 maps were obtained after correction for flip angle and

inversion efficiency deviations [11]. For R2* and QSM mapping, mono-polar multi-echo 3D gradient echo images with 5 echoes at 6, 12, 18, 24 and 30ms; TR=35ms; FA=11°; voxelsize 375x375x800µm [12]. R2* maps were obtained by non-linear fitting of a monoexponential decay function based on 5 echoes [12]. QSM was obtained from the third echo image [12]: correction of the receiver, Laplacian unwrapping, phase-based tissue masking that included voxels at the brain surface, RESHARP background correction (1.6mm kernel, Tikhonov regularization: 10-12) and the iLSQ algorithm from STI-suite v. 3 for dipole inversion (STI-Suite <https://people.eecs.berkeley.edu/~chunlei.liu/software.html>; v. 3.0, dated 201905). Cortical layers were sampled at 10 percent intervals of cortical thickness within FreeSurfer. ROIs were extracted using Destrieux atlas parcellation [13, 14]. Finally, an LME-model was used to predict the effect of age on R1 and R2*. Significant main effects and interactions were corrected for multiple comparison using Benjamini-Hochberg method [15].

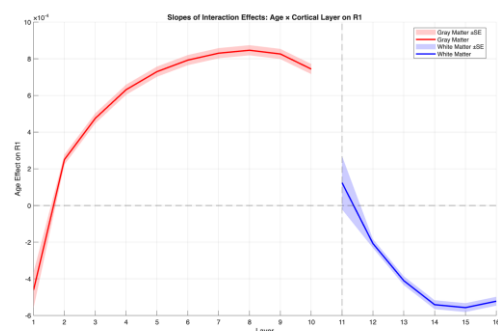


Fig. 1: Slope values of the Interaction Effects (Age x Layer) on R1. The strongest positive effect on R1 was found in layer 8 ($\beta = 0.00122$, $t = 22.73$, $p < .0001$). In SWM, the strongest effect was found in layer 15 ($\beta = -0.00074$, $t = -19.25$, $p < .0001$).

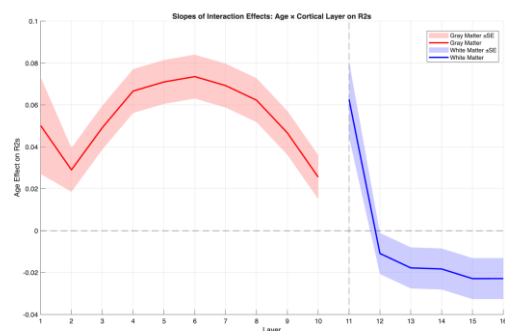


Fig. 2: Age-by-layer interactions showed increasing R2* with depth, peaking in Layer 6 ($\beta = 0.074$, $t = 7.02$, $p < 0.0001$). In SWM, the strongest effect was found in layer 15 ($\beta = -0.00074$, $t = -19.25$, $p < .0001$). Interactions were significant in Layers 15 and 16 ($p < 0.05$), indicating negative age effects in the deepest white matter.

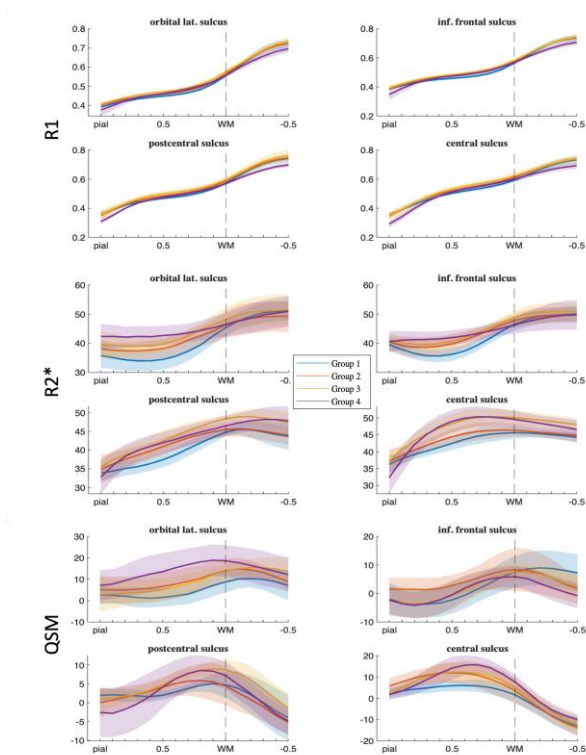


Fig. 3: Depth profiles of R1, R2*, and QSM across 4 age groups of increasing age (N=7 per group) for two early- and late-myelinating regions. QSM shows a paramagnetic peak in SWM of the two frontal regions.

Results: A linear mixed-effects model was used to examine age and cortical depth effects on R1 in gray matter. A significant negative main effect of age on R1 was observed driven by the most superficial layer ($\beta = -0.00084$, SE = 0.00012, $t(6140) = -7.04$, $p < .0001$). Age-by-layer interaction effects were significant, showing a depth-dependent increase in R1 with age, peaking in Layer 8 ($\beta = 0.00122$, SE = 0.00005, $t = 22.73$, $p < .0001$; Fig.1). A vertex-wise GLM confirmed clusters in lateral orbitofrontal, superior frontal, middle and superior temporal, precentral, and postcentral regions. In superficial white matter, R1 increased with depth. Age-by-layer interactions revealed significant decreases in R1 with age, with the strongest effect in Layer 15 ($\beta = -0.00074$, SE = 0.00005, $t = -19.25$, $p < .0001$). For R2*, a significant positive main effect of age was found in gray matter ($\beta = 0.050$, SE = 0.023, $t = 2.17$, $p = .030$). Age-by-layer interactions showed increasing R2* with depth, peaking in Layer 6 ($\beta = 0.074$, SE = 0.011, $t = 7.02$, $p < .0001$; Fig.2). Significant clusters emerged in frontal and parietal areas. In white matter, age was positively associated with R2* ($\beta = 0.063$, SE = 0.018, $t = 3.47$, $p < .001$). Age-by-layer interactions were significant in Layers 15 and 16 ($p < .05$), indicating negative age effects in the deepest white matter. Significant clusters were found at WM border of medial and lateral orbitofrontal cortex.

Discussion: While iron accumulation with age is well established [16–18], recent layer-specific analyses highlight the importance of mapping iron and myelin across cortical depth as markers of late myelination [9, 6] or neurodegeneration [19, 20]. We investigated how these parameters vary with age from superficial cortical layers into SWM. As expected, R1 increased with cortical depth [7, 5].

Superficially, R1 decreased with age, particularly in frontal and temporal regions, mirroring cortical thinning patterns in supramarginal, rostral middle frontal, inferior/middle temporal, and precentral regions. In contrast, deeper layers showed increasing R1 with age, especially in lateral orbitofrontal, superior frontal, middle/superior temporal, and central regions. These findings suggest late intracortical myelination in these regions, consistent with histological reports of myelin maturation into the third decade [21]. White matter R1 decreased with age, in line with prior findings of myelin loss during healthy aging [22]. For R2*, widespread increases with age were observed, especially in deeper gray matter, in frontal (medial/lateral orbitofrontal, rostral middle frontal, pars triangularis, precentral) and parietal areas, consistent with age-related iron accumulation. In SWM, R2* increases were age-related but plateaued at greater depths. This supports prior findings [9, 6, 19, 20] showing peak iron in late-myelinating, U-fiber-rich regions like the middle frontal, lateral orbitofrontal, and inferior frontal sulci [6]. Our findings confirm age-related iron accumulation in the first SWM layer of orbitofrontal cortex, aligned with QSM-confirmed paramagnetic peaks (Fig.3). These results extend previous work [9, 6] by demonstrating depth-dependent R1 and R2* aging effects across gray and white matter.

Conclusion: This study highlights the importance of layer-wise analysis, revealing microstructural differences in vulnerability to age-related changes in MR parameters. We replicated established findings of myelin decline in white matter with aging, a robust hallmark of healthy aging. Additionally, we found an increase of myelin in the innermost cortical gray matter layers, suggesting ongoing late myelination up to 74 years, potentially supporting functional preservation. Further, we demonstrated an age-related iron accumulation (validated by QSM) in the first layer of superficial white matter, followed by a significant decrease of iron in deeper white matter. These findings extend prior work [9, 6] confirming age-dependent effects on iron in the SWM.

Acknowledgements: I would like to thank all co-authors for their valuable contributions to this study and their efforts in data collection. I am especially grateful to Prof. Gisela Hagberg for the opportunity to work on this project. Her supervision, expertise, and insightful discussions were essential in shaping the direction and quality of this work.

References:

- [1] Deistung, A., Schweser, F., and Reichenbach, J. R. (2017). Overview of quantitative susceptibility mapping. *NMR in Biomedicine*, 30(4):e3569.
- [2] Möller, H. E. et al. (2019). Iron, myelin, and the brain: neuroimaging meets neurobiology. *Trends in Neurosciences*, 42(6):384–401.
- [3] Weiskopf, N., Suckling, J., Williams, G., Correia, M. M., Inkster, B., Tait, R., Ooi, C., Bullmore, E. T., and Lutti, A. (2013). Quantitative multi-parameter mapping of r1, pd*, mt, and r2* at 3t: a multi-center validation. *Frontiers in neuroscience*, 7:95.
- [4] Northall, A. et al. (2023). Layer-specific vulnerability is a mechanism of topographic map aging. *Neurobiology of Aging*, 128:17–32.
- [5] Carey, D., Caprini, F., Allen, M., Lutti, A., Weiskopf, N., Rees, G., Callaghan, M. F., and Dick, F. (2018). Quantitative mri provides markers of intra-, inter-regional, and age-related differences in young adult cortical microstructure. *Neuroimage*, 182:429–440.
- [6] Lee, S., Shin, H.-G., Kim, M., and Lee, J. (2023). Depth-wise profiles of iron and myelin in the cortex and white matter using χ -separation: A preliminary study. *NeuroImage*, 273:120058.
- [7] Marques, J. P., Khabipova, D., and Gruetter, R. (2017). Studying cyto and myeloarchitecture of the human cortex at ultra-high field with

- quantitative imaging: R_1 , r_2^* and magnetic susceptibility. *NeuroImage*, 147:152–163.
- [8] Sereno, M. I., Lutti, A., Weiskopf, N., and Dick, F. (2013). Mapping the human cortical surface by combining quantitative t_1 with retinotopy. *Cerebral cortex*, 23(9):2261–2268.
- [9] Kirilina, E. et al. (2020). Superficial white matter imaging: Contrast mechanisms and whole-brain in vivo mapping. *Science Advances*, 6(41):eaaz9281.
- [10] Shajan, G., Kozlov, M., Hoffmann, J., Turner, R., Scheffler, K., and Pohmann, R. (2014). A 16-channel dual-row transmit array in combination with a 31-element receive array for human brain imaging at 9.4t. *Magnetic resonance in medicine*, 71(2):870–879.
- [11] Hagberg, G. E., Bause, J., Ethofer, T., Ehses, P., Dresler, T., Herbert, C., Pohmann, R., Shajan, G., Fallgatter, A., Pavlova, M., et al. (2017). Whole brain mp2rage-based mapping of the longitudinal relaxation time at 9.4 t. *Neuroimage*, 144:203–216.
- [12] Hagberg, G. E., Eckstein, K., Tuzzi, E., Zhou, J., Robinson, S., and Scheffler, K. (2022). Phase-based masking for quantitative susceptibility mapping of the human brain at 9.4t. *Magnetic resonance in medicine*, 88(5):2267–2276.
- [13] Destrieux, C., Fischl, B., Dale, A., and Halgren, E. (2010). Automatic parcellation of human cortical gyri and sulci using standard anatomical nomenclature. *Neuroimage*, 53(1):1–15.
- [14] Fischl, B., Van Der Kouwe, A., Destrieux, C., Halgren, E., Ségonne, F., Salat, D. H., Busa, E., Seidman, L. J., Goldstein, J., Kennedy, D., et al. (2004). Automatically parcellating the human cerebral cortex. *Cerebral cortex*, 14(1):11–22.
- [15] Benjamini, Y., & Hochberg, Y. (1995). Controlling the false discovery rate: a practical and powerful approach to multiple testing. *Journal of the Royal statistical society: series B (Methodological)*, 57(1), 289–300.
- [16] Ward, R. J., Zucca, F. A., Duyn, J. H., Crichton, R. R., and Zecca, L. (2014). The role of iron in brain ageing and neurodegenerative disorders. *The Lancet Neurology*, 13(10):1045–1060.
- [17] Sedlacik, J. et al. (2014). Reversible, irreversible and effective transverse relaxation rates in normal aging brain at 3 t. *Neuroimage*, 84:1032–1041.
- [18] Möller, H. E. et al. (2019). Iron, myelin, and the brain: neuroimaging meets neurobiology. *Trends in Neurosciences*, 42(6):384–401.
- [19] Ayton, S., Fazlollahi, A., Bourgeat, P., Raniga, P., Ng, A., Lim, Y. Y., Diouf, I., Farquharson, S., Fripp, J., Ames, D., et al. (2017). Cerebral quantitative susceptibility mapping predicts amyloid- β -related cognitive decline. *Brain*, 140(8):2112–2119.
- [20] Ghadery, C., Pirpamer, L., Hofer, E., Langkammer, C., Petrovic, K., Loitfelder, M., Schwingenschuh, P., Seiler, S., Duering, M., Jouvent, E., et al. (2015). R_2^* mapping for brain iron: associations with cognition in normal aging. *Neurobiology of Aging*, 36(2):92

Scaling Up SABRE: Development of a Hyperpolarizer for Large-Animal Studies and Human-Dose Production

Stefan Petersen 1, Behnam Shamshiri 1+2, Sebastian Lucas 3, Stephan Knecht 3, Maxim Zaitsev 1, Dominik v. Elverfeldt 1, Andreas B. Schmidt 1+4
1 Division of Medical Physics, Department of Radiology, University Medical Center Freiburg, Faculty of Medicine, University of Freiburg, Germany
2 Scientific Workshop, Department of Neurology, University Medical Center Freiburg, Faculty of Medicine, University of Freiburg, Germany
3 NVision Imaging Technologies GmbH, Ulm, Germany
4 German Cancer Consortium (DKTK), partner site Freiburg and German Cancer Research Center (DKFZ), Germany

Abstract: Signal Amplification by Reversible Exchange (SABRE) is a fast, versatile, and cost-efficient hyperpolarization technique that has shown strong potential for preclinical imaging applications.[1,2] However, current implementations are typically performed using 5mm NMR tubes and thus limited to sub-milliliter volumes, restricting their use to small-animal studies. We report the development of a scalable SABRE polarizer based on a 200 ml Buechiglas reactor, featuring an automated pressure-driven transfer system. The setup operates within a Twinleaf MS-2 μ -metal shield, providing active time-resolved control over both B0 and B1 fields. The system enables the production of several milliliters of hyperpolarized solutions, marking a significant step toward larger animal studies and future clinical translation of the SABRE technology.

Motivation: SABRE hyperpolarization offers a rapid, low-cost alternative to hyperpolarization techniques like DNP or PHIP, with potential for widespread biomedical use. However, current implementations typically rely on NMR tubes, restricting the active volume to $\sim 250 \mu\text{l}$ —adequate only for in vitro or small-animal experiments.

To transition SABRE into a more versatile method for preclinical and clinical research, it is essential to scale up the production of hyperpolarized contrast agents. This requires not only larger reactor volumes but also tailored magnetic environments, efficient handling of gaseous parahydrogen, and improved purification workflows.

The two common SABRE techniques are SABRE-SHEATH (Shield Enables Alignment Transfer to Heteronuclei), a robust low-field method well-suited for initial tests with inexpensive, protonated substrates;[3] and SLIC-SABRE (Spin-Lock Induced Crossing), a pulse-based technique that currently yields the highest polarization levels—especially with deuterated substrates—yet demands higher magnetic field homogeneity and RF control.[4]

The aim of this project is to develop a scalable, automatable SABRE polarizer capable of producing milliliter-scale quantities suitable for larger animal models, ultimately paving the way for clinical translation.

Materials & Methods: An actively water-cooled 200 ml glass reactor (Buechiglas) served as the central polarization chamber for large-volume SABRE hyperpolarization. The entire setup was housed within a Twinleaf MS-2 μ -metal shield equipped with integrated B0 and B1 coils. These coils were driven by a precision power supply (B0). More complex, programmable RF pulse shapes and magnetic field profiles can be generated via a custom Python control interface and a digital-to-analog converter. Gradient coils embedded in the μ -metal shield enabled manual shimming for improved field homogeneity.

Parahydrogen was introduced through biocompatible solvent-resistant filters ($20\mu\text{m}$) to ensure clean and consistent bubbling. A custom-built, pressure-driven valve control module enabled automated shuttling of the hyperpolarized solution to adjacent compartments.

Initial polarization tests were conducted using 10 mM sodium pyruvate dissolved in 50 ml methanol. For small-scale reference measurements, $600\mu\text{l}$ of this solution was hyperpolarized in standard 5-mm NMR tubes using 9.5 bar parahydrogen. In contrast, the large reactor was operated at a reduced pressure of 6 bar, due to current pressure limitations. The ^{13}C polarization was quantified using a 1T benchtop NMR system.

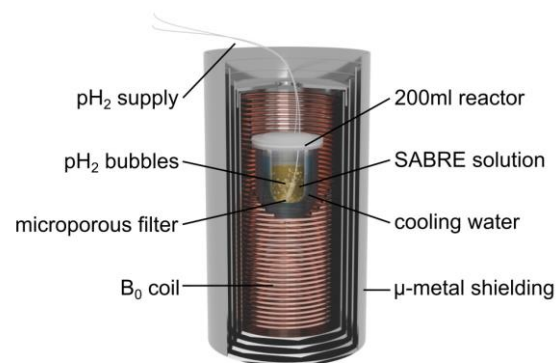


Fig. 1: Experimental setup for large-scale SABRE hyperpolarization. The system includes a four-layer μ -metal shield equipped with a B₀ coil for magnetic field control, a 200 ml glass reactor with active water cooling, and an integrated parahydrogen (pH_2) delivery system via a microporous filter for continuous gas flow into the SABRE solution.

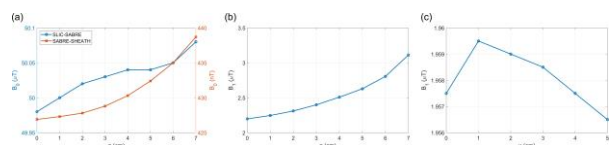


Fig. 2: B₀ and B₁ homogeneities in z- and x-directions. (a) B₀ homogeneities for SLIC-SABRE (blue) and SABRE-SHEATH (orange) fields in z-direction. (b) B₁ homogeneity in z-direction. (c) B₁ homogeneity in x-direction.

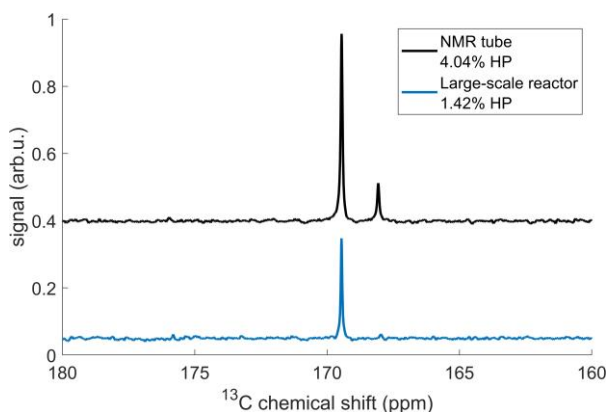


Fig. 3: ^{13}C NMR spectra of SABRE-SHEATH pyruvate hyperpolarized using a 5 mm NMR tube (black) and in the large-scale reactor (blue).

Results: Magnetic field homogeneity within the reactor volume was characterized at relevant SABRE operating fields. At the SABRE-SHEATH field (0.42 μT) and the SLIC-SABRE field (50 μT), the B_0 field deviation in z-direction remained below 1%, see figure 2a. However, B_1 field distribution—critical for the performance of SLIC-SABRE—showed significant inhomogeneity along the z-axis, see figure 2b.

In initial SABRE-SHEATH experiments, the large-scale reactor yielded a ^{13}C polarization of 1.42 %, corresponding to roughly one-third of the polarization achieved in the 5 mm NMR reference (4.04 %), under reduced hydrogen pressure (6 bar compared to 9.5 bar). In the large-scale NMR spectrum, figure 3, the bound-pyruvate peak at ~ 168 ppm is nearly absent, whereas it remains clearly visible in the 5 mm NMR tube reference.

Discussion: Scaling SABRE hyperpolarization to milliliter volumes introduces technical challenges, particularly in maintaining the magnetic field homogeneity and sufficient parahydrogen delivery to the large volume. While RF-based polarization transfer methods such as SLIC-SABRE have demonstrated the highest polarization values in small-scale studies—especially when using deuterated substrates—they are highly sensitive to B_0 inhomogeneities and thus more difficult to implement in larger systems. In contrast, SABRE-SHEATH is more tolerant of magnetic field variations and better suited for cost-effective, protonated compounds, making it a practical choice for scalable applications.

To preserve magnetic field homogeneity, the construction of the pressure-resistant reactor must avoid metallic materials that disturb the magnetic field. For safety reasons, the reactor has therefore been operated at only 6 bar, instead of the 10 bar vendor-specified for the glass reactor. Moreover, achieving uniform hydrogen distribution is more challenging in the larger, less elongated reactor geometry compared to a standard NMR tube. In this setup, microporous solvent filters were employed to facilitate efficient gas dispersion. Both factors are known to restrict the polarization build-up and will be improved in future work.

The disappearance of the bound pyruvate signal in the large-scale spectrum likely reflects longer transfer times between the polarization reactor and the NMR spectrometer, during which bound pyruvate undergoes rapid relaxation. This underlines the need for faster or more optimized solution shuttling in future designs.

Conclusion: We successfully developed a scalable SABRE hyperpolarizer capable of producing milliliter-scale volumes of hyperpolarized pyruvate, addressing a key bottleneck in translating SABRE from bench-scale to preclinical applications beyond mice studies. The modular design and automation offer a robust and adaptable platform for ongoing development.

Recent advancements such as Ace-SABRE[5] – a SLIC-SABRE implementation in water-acetone mixtures - are promising for improving biocompatibility and efficient purification workflows. These developments are fully compatible with our reactor setup, which can be readily adapted to chemically and thermally robust materials such as PEEK, as recently demonstrated in a PHIP setup.[6]

Future work will focus on increasing polarization transfer efficiency, extending substrate compatibility, improving purification strategies at scale, and preparing the system for biomedical validation and ensuring regulatory compatibility for biomedical applications.

Acknowledgements: The research reported in this publication was supported by the German Cancer Consortium (DKTK INNOVATION-2023 HYPERBOLIC project, and DKTK INVEST-2024), the German Federal Ministry of Education and Research (BMBF) in the funding program “Quantum Technologies – from Basic Research to Market” under the project “QuE-MRT” (contract number: 13N16448), the Research Commission of the University Medical Center Freiburg, the German Research Foundation (DFG #SCHM 3694/1-1, #SCHM 3694/2-1, #SFB1479), and B.E.S.T. Fluidsysteme GmbH | Swagelok Stuttgart.

References:

1. de Maissin, H. *et al.* In Vivo Metabolic Imaging of $[1-^{13}\text{C}]$ Pyruvate-d3 Hyperpolarized By Reversible Exchange With Parahydrogen**. *Angew. Chem. Int. Ed.* 62, e202306654 (2023).
2. Petersen, S. *et al.* In vivo molecular imaging of breast cancer metabolic heterogeneity using $[1-^{13}\text{C}]$ pyruvate-d3 hyperpolarized by reversible exchange with parahydrogen. *Theranostics* 15, 3714–3723 (2025).
3. Adams, R. W. *et al.* Reversible Interactions with para-Hydrogen Enhance NMR Sensitivity by Polarization Transfer. *Science* 323, 1708–1711 (2009).
4. Schmidt, A. B. *et al.* Over 20% Carbon-13 Polarization of Perdeuterated Pyruvate Using Reversible Exchange with Parahydrogen and Spin-Lock Induced Crossing at 50 μT . *J. Phys. Chem. Lett.* 14, 5305–5309 (2023).
5. McBride, S. J. *et al.* Scalable Hyperpolarized MRI Enabled by Ace-SABRE of $[1-^{13}\text{C}]$ Pyruvate. *Angew. Chem. Int. Ed.* n/a, e202501231.
6. Mohiuddin, O. *et al.* Rapid in situ carbon-13 hyperpolarization and imaging of acetate and pyruvate esters without external polarizer. *Commun. Chem.* 7, 240 (2024).

Assessment of structural response of FRP bore liner for a high-count UHF transmission array

Andrea Pino 1+2*, Mark E. Ladd 1+2+3, Stephan Orzada 1.

1 German Cancer Research Center (DKFZ), Heidelberg, Germany
2 Faculty of Medicine, Heidelberg University, Heidelberg, Germany
3 Faculty of Physics, Heidelberg University, Heidelberg, Germany

Abstract: Compact gradient coils in next-generation 7T MRI systems introduce tight spatial constraints, limiting integration of high-channel-count transmit arrays. The previously implemented 32-channel array is no longer compatible with the reduced dimensions of newer Siemens models.

This study investigates structural adaptations to the fiber-reinforced plastic (FRP) bore liner to accommodate the array while maintaining RF performance and patient comfort. Finite element analysis (FEA) is employed using total deformation (TD), reflecting combined material displacements under stress, along with two well-established failure criteria to evaluate the mechanical behavior of composite FRPs. The analysis confirms that the proposed modifications preserve mechanical integrity, identifying critical load-bearing regions and introducing targeted changes to reduce stress concentrations.

Motivation: The introduction of compact gradient coils (SC72) in next-generation 7 T Siemens MRI systems compromises the implementation and performance of high channel-count integrated RF transmit arrays for managing excitation homogeneity at ultra-high field strengths^{1,2}. Accommodating a custom 32-channel transmit array³ in newer systems, requires structural adaptation of the bore liner, as the installation space is reduced to nearly one third of earlier models. The decreased distance between transmit elements and the RF shield affects magnetic field strength, which depends on conductor height above the shield⁴, impacting SAR, power efficiency, and mutual coupling.

This study focuses on a structural optimization of the modified bore liner, constructed from FRP (E-glass), which exhibits brittle and ductile responses. Finite element analysis (FEA) was conducted to assess structural viability under loads exceeding standard operating conditions. TD, representing the magnitude of structural distortion ($TD = \sqrt{X^2+Y^2+Z^2}$), is particularly useful in applied structural analysis, as it encompasses both elastic and plastic deformation under applied loads⁵.

Mechanical failure was further evaluated using maximum principal stress (MPS) and von Mises equivalent stress (SvM), both well-established failure criteria⁶ for composite integrity assessment under complex stress states⁷. Results from MPS and SvM analyses have provided initial support to ensure the structural robustness of the modified bore liner. These combined methods add further support to identify critical stress zones while enabling safe integration of the 32-channel array without compromising transmission performance or space within the bore liner for the patient and additional components such as receive-only coils.

Materials & Methods: The modelling and finite element analysis (FEA) structural simulations were done with ANSYS Mechanical (ANSYS, Inc., Canonsburg, PA, USA) using a bore liner model from Siemens Magnetom 7T system (Siemens Healthineers, Erlangen, Germany). The bore liner material pro-

perties were provided by Maschinenfabrik Reinhausen GmbH (Reinhausen, Regensburg, Germany). The bore liner consists of E-glass/epoxy (roving, 79.5 wt.-% glass), with mechanical limits defined by IEC 61462: 60 MPa axial and 120 MPa tangential stress. E-Glass Wet was simulated in ANSYS for its similar anisotropic properties and base material composition.

To accommodate the 32-channel array in the structure (Fig. 1), 32 antenna-sized slots (250x50 mm²) were introduced with spacing of 28 mm (xy-plane) and 50 mm (z-axis). Load simulations accounted for a combined 2000 N load representing the patient, table, and dedicated receive array combined weight. Symmetric live loading was modeled with 1000 N applied per rail. Four fixed support regions (110 x 96 mm²) were defined using frictional constraints to prevent displacement or sliding. Adaptive mesh refinement was applied near high-strain regions to increase local accuracy.

Three designs were analyzed: original bore liner (no slots), a slotted version with sharp edges, and a slotted version including a 24 mm-radius edge rounding, positioned between the support rails. For all models, TD, as well as MPS and SvM were calculated to assess static structural response and identify stress concentrations.

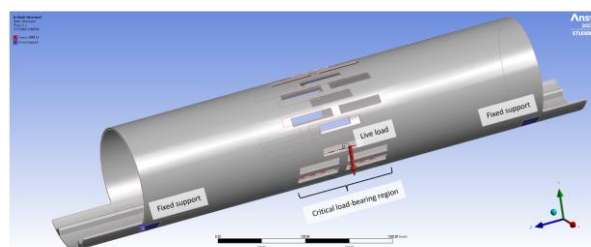


Fig. 1: 3D model of modified bore liner including loads (red) and fixed-supports (purple) in ANSYS Static Structural mode.

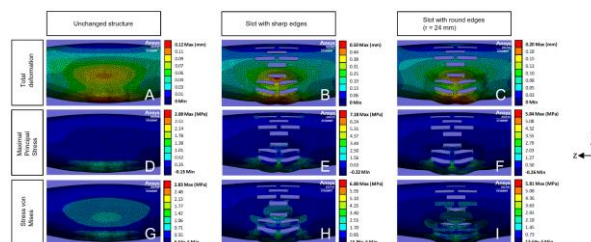


Fig. 2: Total deformation and stress distribution in bore liner for identical loading conditions in the zy-plane. (Note: deformation automatically exaggerated in post-processing by ANSYS Mechanical to highlight critical load effects.)

Results: Figures 2 and 3 show simulated deformation and stress distribution in the bore liner, viewed from lateral and base sections. Table 1 summarizes the maximum FEA values for each design.

TD was evaluated to assess structural deformation under a 2000 N load. The original bore liner (A) showed the lowest (maximal) value at 0.12 mm. Introducing 32 sharp-edged slots (B) increased the maximal total deformation nearly fourfold to 0.5 mm. Adding a 24 mm radius to the slot corners (C) reduced TD to 0.2 mm, significantly improving stability relative to the sharp-edged design. Maximum deformation in all models occurred near the support rail borders, while the rounded-slot design also showed severely reduced strain of 65% (from 0.4 mm to 0.14 mm) in the critical central region (Fig. 3-C).

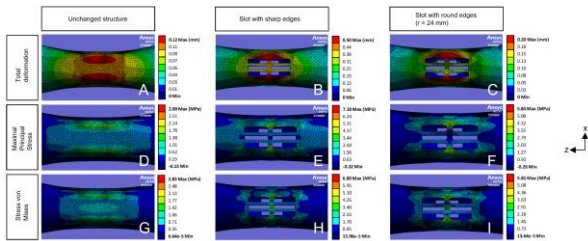


Fig. 3: Total deformation and stress distribution in the bore liner in the zx-plane for identical loading conditions. (Note: deformation automatically exaggerated in post-processing by ANSYS Mechanical to highlight critical load effects.)

Result type	Simulation case	Slots	Radius type	Maximal value	Unit
Total Deformation (εT)	A	0	-	0.12	mm
	B	32	sharp	0.5	mm
	C	32	round	0.2	mm
Maximal Principal stress (σ _{MPS})	D	0	-	2.89	MPa
	E	32	sharp	7.18	MPa
	F	32	round	5.84	MPa
Stress von Mises (σV)	G	0	-	2.83	MPa
	H	32	sharp	6.8	MPa
	I	32	round	5.81	MPa

Fig. 4: Maximum values of simulation results for total deformation, maximal principal stress, and von Mises stress corresponding to simulation cases A to I.

MPS and SvM results are summarized to support the deformation results. The original bore liner exhibited the lowest stresses (MPS: 2.89 MPa (D), SvM: 2.83 MPa (G)). The sharp-edged slotted design increased both values substantially (MPS: 7.18 MPa (E), SvM: 6.8 MPa (H)), while the rounded design reduced stress levels (MPS: 5.84 MPa (F), SvM: 5.81 MPa(I)), lowering both by approximately 1 MPa compared to the sharp-edged version.

All stress levels remained below IEC 61462 limits. Higher deformation and stress concentrations were consistently located near the support rail borders, with higher intensity in the central base region across all designs (Fig. 3 A–I).

Discussion: The original bore liner exhibited the lowest values across all failure metrics and served as the reference design. As the bore liner has a cylindrical shape, its mechanical behavior followed classical elasticity theory, where the sum of stresses is constant and their influence on the deformation along the cylinder's length is uniform⁸.

Geometric discontinuities such as sharp-edged notches or slot corners introduce stress concentrations and localized deformation⁷. In composite materials, where the matrix (epoxy) typically undergoes greater deformation than the fiber⁹, these effects are amplified. As a result, introducing square-edged slots increased total deformation (TD) nearly fourfold compared to the original configuration. These

findings are consistent with prior observations showing that deformation in composites tends to concentrate around openings⁹ (Fig. 2 B–C). Despite this, the maximum TD reached was half of a millimeter for a force of 2000 N, indicating a mechanically robust structure.

Applying a 24 mm radius to the slot edges reduced TD to 0.2 mm, improving deformation behavior and partially restoring performance toward the baseline design. The rounded-slot configuration redistributed deformation more uniformly and lowered peak stress in critical areas. This reduction in TD coincided with lower values of MPS and SvM, in line with established geometric strength strategies⁷.

Despite significant material removal, all stress values remained well below IEC 61462 limits. The upper region of the bore liner consistently exhibited low stress and deformation, identifying it as a promising area for RF integration under reduced mechanical loading.

Conclusion: High-channel RF arrays cannot be directly accommodated in the reduced internal space of newer Siemens 7 T MRI systems. To address this, modifications to the bore liner were assessed to enable array integration without compromising mechanical integrity. Finite element analysis showed that introducing sharp-edged slots led to a substantial increase of TD. Incorporating rounded slot corners significantly reduced TD and peak stress values, supporting previous results. These improvements are attributed to smoother load transfer and reduced stress concentration, reinforcing that optimizing slot geometry remains critical for stability. The mechanical response is further influenced by the anisotropic behavior of fiber-reinforced composites.

All stress values remained well within pre-established limits, insuring the structural stability and robustness. The modified design also allows to increase antennas-to-shield distance for future designs, enhancing transmission performance, while the structural sturdiness helps protect antenna elements from mechanical stress that could introduce malfunction of antennas.

Acknowledgements: The authors thank Reinhausen GmbH for providing the bore liner documentation, Siemens for supplying the bore liner models and the German Cancer Research Center (DKFZ) for providing the computational resources necessary for the mechanical simulations.

References:

1. Van de Moortele PF, Akgun C, Adriany G, Moeller S, Ritter J, Collins CM, Smith MB, Vaughan JT, Ugurbil K, B(1) destructive interferences and spatial phase patterns at 7 T with a head transceiver array coil, *Magn Reson Med.* 2005;54(6):1503-1518.
2. Mao W, Smith MB, Collins CM, Exploring the limits of RF shimming for high-field MRI of the human head, *Magn Reson Med.* 2006;56(4):918-922.
3. Orzada S, Solbach K, Gratz M, Brunheim S, Fiedler TM, Jahst S, Bitz AK, Shoostary S, Abuelhajja A, Voelker MN, Rietsch SHG, Kraff O, Maderwald S, Floser M, Oehmigen M, Quick HH, Ladd ME, A 32-channel parallel transmit system add-on for 7T MRI, *PLoS One.* 2019;14(9):e0222452.
4. Abuelhajja A, Solbach K, Orzada S, Comprehensive study on coupled meandered microstrip line RF coil elements for 7-Tesla Magnetic Resonance Imaging, 2015 9th European Conference on Antennas and Propagation (EuCAP), Lisbon, Portugal, 2015.
5. Pasca DP, Massaro FM, De Santis Y, Stamatopoulos H, Ljungdahl J, Aloisio A, Deformation Level and Specimen Geometry in Compression Perpendicular to the Grain of Solid Timber, *GLT and CLT Timber Products, Engineering Structures*, vol. 321, Dec. 2024.
6. Young W, Budynas R, Roark's formulas for stress and strain (7th ed.), McGraw-Hill. (2002)
7. Zheng J, Maharaj C, Liu J, Chai H, Liu H, Dear J, A Comparative Study on the Failure Criteria for Predicting the Damage Initiation in Fiber-Reinforced Composites, *Materials and Composite Mechanics*, vol. 2022, 2022, pp. 1–11.
8. Timoshenko, S., & Goodier, J. N., *Theory of Elasticity* (3rd ed.), McGraw-Hill, 1970.
9. Gupta S, Pal S, Ray B, An overview of mechanical properties and failure mechanism of FRP laminates with hole/cutout, *Journal of Applied Polymer Science* (2023), 140(20), e53862.

Real-Time Metabolic Profiling of Patient-Derived Human Midbrain-Like Organoids Using Hyperpolarized ¹³C-NMR Spectroscopy

Marta Pokotylo 1+2, Josh P. Peters 3, Franziska Rudolph 4, Farhad Haj Mohamad 3, Philip Seibler 4, Jan-Bernd Hövener 3, Andrey N. Pravdivtsev 3, Jannik Prasuhn 1+2+4+5+6

1 Department of Neurology, University Hospital Schleswig-Holstein, Campus Lübeck, Lübeck, Germany

2 Center for Brain, Behaviour, and Metabolism, University of Lübeck, Lübeck, Germany

3 Department of Radiology and Neuroradiology, Section Biomedical Imaging, University Hospital Schleswig-Holstein, Kiel University, Kiel, Germany

4 Institute of Neurogenetics, University of Lübeck, Lübeck, Germany

5 Department of Neurology, Johns Hopkins University School of Medicine, Baltimore, Maryland, USA

6 F.M. Kirby Research Center for Functional Brain Imaging, Kennedy Krieger Institute, Baltimore, Maryland, USA

Abstract: Neurological disorders are a leading global cause of disability, with mitochondrial dysfunction implicated as a prominent pathogenic factor. In this study, we utilized hyperpolarized ¹³C nuclear magnetic resonance (NMR) spectroscopy to monitor real-time metabolic dynamics in a human midbrain-like organoid (hMLOs) model, derived from a patient with a WDR45 mutation. With the help of dissolution dynamic nuclear polarization (dDNP) of [1-¹³C]pyruvate, we consistently observed reproducible pyruvate-to-lactate conversion, reflecting glycolytic activity. Our findings support the use of hMLOs as a platform for investigating metabolic dynamics, which can be utilized with various metabolic tracers to probe the metabolic pathway of interest.

Motivation: Neurological disorders are one of the leading causes of disability and the second most common cause of death worldwide. (1) The rising number of cases, the lack of disease-modifying treatments, and somewhat partially effective symptomatic therapies highlight the need for further research to improve patients' quality of life and reduce the healthcare system burden. Mitochondrial dysfunction is one of the most prominent pathogenic factors, potentially manifesting as dysfunctional adenosine triphosphate (ATP) synthesis (2–4). Emerging evidence suggests that a mitochondrial dysfunction-induced shift in other metabolic pathways, such as glycolysis, serves as a compensatory response to reduced ATP concentrations (5–7). A vast amount of supporting evidence highlights the need for further investigation of its underlying mechanism; however, our research utility in this regard remains limited due to the lack of readily available non-invasive techniques for real-time metabolic tracking, as well as disease models. Rodent animals are the most utilized models in neurological disorders research; however, ethical considerations, expenses, and the need for genetic or chemical manipulation to replicate the disease underscore the need for improved methodologies (8,9). To overcome these limitations, we investigated the feasibility of utilizing hMLOs derived from patient-specific induced pluripotent stem cells (iPSCs). Our model inherently carries the diseased genotype, and the use of genome editing tools such as the CRISPR/Cas9 system allows for precise correction of the genotype, generating an isogenic and fully matched control model. The hMLOs model reduces associated costs and ethical concerns and provides a relevant model for real-time metabolic dynamics investigation.

Materials & Methods: We obtained skin biopsies from a patient with beta-propeller protein-associated neurodegeneration (BPAN) with a known WDR45 mutation. One of the patient-derived iPSC lines was used for gene

editing. With the help of the CRISPR/Cas9 system, we corrected the mutation and generated an isogenic control line. Following gene editing, we generated hMLOs using a 60-day protocol designed by Jo et al. 2016 (10) (Figure 1). All measurements were performed using a cryogenic-free dDNP system (SpinAligner, Polarizer) (11). For the sample preparation, we polarized ~25 mg [1-¹³C]pyruvate at ~1.4 K and 6.7 T with trityl radical (AH111501, POLARIZE). Following ~25 s after dissolution with 3.6 mL superheated medium (DM), we obtained ¹³C signals using a 1 T 1H-¹³C benchtop NMR (Spinsolve, Magritek) and a 9.4 T WB NMR (Avance NEO, Bruker); the latter was used for metabolic assessment. The obtained spectra were quantified following manual phase correction, line broadening, and baseline correction (MestReNova 14.2.2, Masterlab Research S.L). We fitted functions based on first-order kinetics to the areas of each peak, resulting in analytical solutions for area under the curve, kPL, time-to-maximum-signal (t_{2m}), and others (NumPy, BFGS, Python).

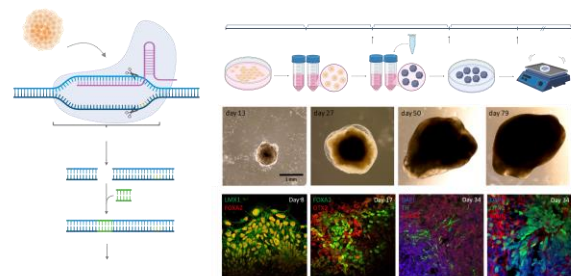


Fig. 1: Generation and characterization of hMLOs. A. The CRISPR/Cas9 system was used to correct the WDR45 mutation in patient-derived samples. B. Timeline and differentiation protocol overview. C. Morphology and D. neural/midbrain marker expression were assessed across multiple timepoints, confirming the successful hMLOs development and regional specification through immunostaining.

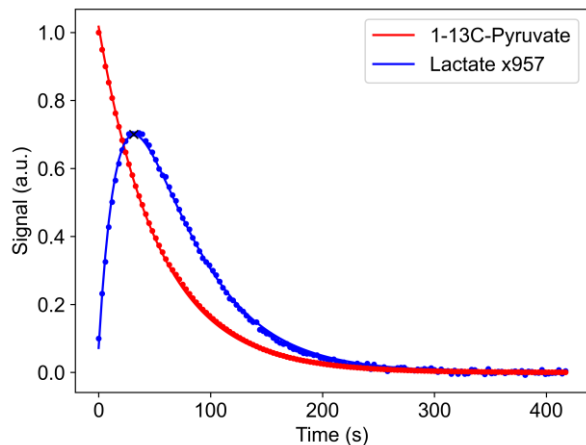


Fig. 2: Dynamic conversion of [1- ^{13}C] pyruvate to lactate in hMLOs. Measured data of hyperpolarized 1- ^{13}C pyruvate (red points) and its downstream metabolite, 1- ^{13}C lactate (blue points), and mono (red line) or biexponential (blue line) fit of the signals to extract the pyruvate-to-lactate-conversion-rate kPL.

Results: We performed 5 hyperpolarization NMR experiments ($n=2$ for control cell line, $n=3$ for WDR45-mutated cell line), to assess the metabolic conversion of [1- ^{13}C]pyruvate into its downstream metabolites. While we investigated the conversion of pyruvate into lactate, alanine, and bicarbonate, only lactate was detected. Following injection of the hyperpolarized pyruvate, its signal and exponential decay were observed in all cases (Figure 2). Due to the ongoing conversion of pyruvate to lactate, a lactate signal emerges and reaches a maximum after several seconds, before decaying with a shorter T_1 than pyruvate, following a characteristic biexponential profile. These temporal dynamics were reproducibly observed across both control and disease-model cell lines, supporting the reliability of the method, the hMLOs platform, and the conserved glycolytic flux.

Discussion: Our observations demonstrated the feasibility and reproducibility of utilizing hyperpolarized ^{13}C -NMR spectroscopy in real-time metabolomics investigation in a patient with BNAP-derived hMLOs. The consistently reproducible finding of lactate's signal buildup, followed by decay, demonstrates consistent conversion of pyruvate to lactate. This observation aligns with the expectation of lactate dehydrogenase activity during anaerobic glycolysis, and also has been implicated in cell death mechanisms observed in other WDR45-mutated in vitro models (12). While the small sample group size limits our ability to conduct statistical group comparisons, the replicability of these temporal dynamics supports the robustness of our methodology. The buildup of the lactate signal over time is indicative of enzymatic conversion and is not observed without organoids.

Conclusion: The findings of our study demonstrate the feasibility of utilizing hyperpolarized ^{13}C -NMR spectroscopy to investigate metabolic flux in real-time in patient-derived

hMLOs. Our methodology can be utilized for a more detailed investigation of glycolytic and other associated metabolic pathway reprogramming in disease models. A more advanced understanding of metabolic reprogramming in the context of disease physiology could fuel the development of novel tools for disease monitoring and progression, as well as personalized therapeutic approaches and the means for patients' stratification for existing therapies, improving their efficacy while reducing the side effects.

Acknowledgements: We gratefully acknowledge funding from the Else Kröner Fresenius Foundation for our project "In-vivo dysregulation of cerebral non-OXPHOS metabolism as a mitochondrial endophenotype of patients with Parkinson's disease." We acknowledge funding from the German Federal Ministry of Education and Research (BMBF) through the e:Med research and funding concept (01ZX1915C), and hyperquant consortium (BlueHealthTech, 03WIR6208A9), as well as the DFG (555951950, 527469039, 469366436, HO-4602/2-2, HO-4602/3, GRK2154-2019, EXC2167, FOR5042, TRR287). MOIN CC was supported by the European Regional Development Fund (ERDF) and the Zukunftsprogramm Wirtschaft of Schleswig-Holstein (Project no. 122-09-053). We also thank the patient who generously donated skin biopsies, which enabled the generation of the hMLO model in this study.

References:

- Gadhve DG, Sugandhi VV, Jha SK, Nangare SN, Gupta G, Singh SK, et al. Neurodegenerative disorders: Mechanisms of degeneration and therapeutic approaches with their clinical relevance. *Ageing Research Reviews*.
- Trombetta-Lima M, Sabogal-Guáqueta AM, Dolga AM. Mitochondrial dysfunction in neurodegenerative diseases: A focus on iPSC-derived neuronal models. *Cell Calcium*.
- Yang HM. Mitochondrial Dysfunction in Neurodegenerative Diseases. *Cells*.
- Zong Y, Li H, Liao P, Chen L, Pan Y, Zheng Y, et al. Mitochondrial dysfunction: mechanisms and advances in therapy. *Signal Transduction and Targeted Therapy*.
- Han R, Liang J, Zhou B. Glucose Metabolic Dysfunction in Neurodegenerative Diseases—New Mechanistic Insights and the Potential of Hypoxia as a Prospective Therapy Targeting Metabolic Reprogramming. *International Journal of Molecular Sciences*.
- Liu H, Wang S, Wang J, Guo X, Song Y, Fu K, et al. Energy metabolism in health and diseases. *Signal Transduction and Targeted Therapy*.
- Prasuhn J, Schiefen T, Güber T, Henkel J, Uter J, Steinhardt J, et al. Levodopa Impairs the Energy Metabolism of the Basal Ganglia IN VIVO. *Annals of Neurology*.
- Tello JA, Williams HE, Eppler RM, Steinhilb ML, Khanna M. Animal Models of Neurodegenerative Disease: Recent Advances in Fly Highlight Innovative Approaches to Drug Discovery. *Frontiers in Molecular Neuroscience*.
- Yin P, Li S, Li XJ, Yang W. New pathogenic insights from large animal models of neurodegenerative diseases. *Protein & Cell*.
- Jo J, Xiao Y, Sun AX, Cukuroglu E, Tran HD, Göke J, et al. Midbrain-like Organoids from Human Pluripotent Stem Cells Contain Functional Dopaminergic and Neuromelanin-Producing Neurons. *Cell Stem Cell*.
- Ferrari A, Peters J, Anikeeva M, Pravdivtsev A, Ellermann F, Them K, et al. Performance and reproducibility of ^{13}C and ^{15}N hyperpolarization using a cryogen-free DNP polarizer. *Scientific Reports*.
- Zhu Y, Fujimaki M, Snape L, Lopez A, Fleming A, Rubinsztein DC. Loss of WIP14 in neurodegeneration causes autophagy-independent ferroptosis. *Nature Cell Biology*.

3D spiral readouts for BOLD fMRI at 9.4T

Alejandro Monreal-Madrigal¹, Desmond H.Y.Tse², Denizhan Kurban¹, Nicolas Boulant³, Benedikt A Poser¹

¹ Maastricht Brain Imaging Centre, Faculty of Psychology and Neuroscience, Maastricht University, Maastricht, the Netherlands

² Scannexus BV, Maastricht, the Netherlands

³ University-Paris-Saclay, CEA, CNRS, BAOBAB, NeuroSpin, Gif-sur-Yvette, France

Abstract: In this work we explore the value of 3D stack or spiral readouts for BOLD functional MRI at 9.4T, targeting spatial resolutions that enable laminar fMRI analysis.

Motivation: Previous spiral BOLD fMRI studies have used a TE close to T_2^* [1,2], using a delay before excitation and signal acquisition. The deadtime before the readout results in a reduced sampling efficiency. Simulations of the BOLD point spread function (BOLD PSF) [3] show that a shorter TE can be used without compromising BOLD sensitivity. In this work, we aim to find a suitable TE for BOLD fMRI with spiral readouts at 9.4T by simulations and fMRI acquisitions. We also provide a pipeline for sequence, reconstruction and analysis tools for spiral fMRI data using freely available software.

Materials & Methods: Methods: Simulations of the BOLD PSF were performed to assess the optimal TE for BOLD fMRI with spiral readouts at 9.4T (Figure 1), following the approach described in [3], assuming a gray matter T_2^* of 20 ms. Following this, experiments were performed on a Siemens 9.4T scanner with a AC84-II gradient ($G_{max}=80$ mT, $SR=330$ T/m/s) and a 16Tx/31Rx custom RF coil from MR CoilTech Ltd. In previous experiments, we observed poor image quality at 9.4T for high-resolution (0.6 mm) single-shot readouts due to residual B0 artifacts; therefore, dual-shot readouts were chosen here. Five participants were scanned with different spiral BOLD protocols using dual-shot spiral-out (DS-SO) and dual-shot spiral-in (DS-SI) readouts while performing a visual task (12 min flickering checker-board, 30s on/off; two runs per participant). The imaging slab covered the visual cortex with a coronal orientation.

Sequence parameters: A 3D stack-of-spirals sequence was implemented in Pulseseq [4]. Both DS-SO and DS-SI sequences had the following common parameters: $FOV=140 \times 140 \times 24$ mm³ (40 kz partitions) with $res=0.55 \times 0.55 \times 0.60$ mm³, resulting in an effective isotropic resolution of 0.6 mm. Spiral readout duration of 27 ms with in-plane undersampling of $R_{xy}=3.3$, $G_{max}=50$ mT/m, $SR=250$ T/m/s and variable density of 1.3. Echo times were selected based on the BOLD PSF simulations (Figure 1): the DS-SO sequence had $TE=6$ ms and $TR_{vol}=3.11$ s, the DS-SI had a $TE=31$ ms (per shot) and $TR_{vol}=2.98$ s; both sequences used a fat saturation module before each excitation. The sequence diagrams can be found in Figure 2. Subjects S1/S2/S3/S4/S5 were scanned with the DS-SO approach, S2/S3/S5 with the DS-SI and S4 with the DS-SO approach with a $FOV_z=48$ mm. Functional data was reconstructed offline with the nominal trajectory using CG-SENSE [5] as implemented in MRIReco.jl including multifrequency interpolation off-resonance and DORK corrections as in [4].

Results: We found that for sub-millimeter resolutions the DS-SO approach provides sufficient sensitivity and tSNR when

$TE < T_2^*$ (Figure 3). The DS-SI with its long TE has a low tSNR and no significant activation was found (Figure 3). Percentage of active voxels, median z-score and mean effective tSNR results of all subjects can be found in Figure 4. Rotations between planes allowed to reduce the artifacts present in the DS-SO scan with $FOV_z=48$ mm, but some artifacts are still present.

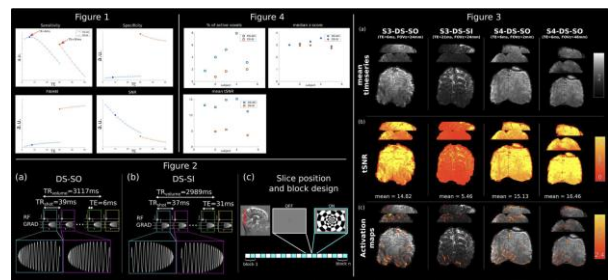


Fig. 1.: BOLD PSF simulations. Dual-shot spiral-out has highest sensitivity when $TE < T_2^*$; dual-shot spiral-in a larger FWHM than dual-shot spiral-out; dual-shot spiral-in provides higher specificity but lower tSNR than dual-shot spiral-out. Fig 2. Sequence diagrams. (a) dual-shot spiral-out, (b) dual-shot spiral-in and (c) slab positioning and stimuli of the block design. Fig 3. Functional run results for different subjects and acquisitions. (a) mean timeseries (b) tSNR and (c) activation maps. The dual-shot spiral-out approach has high tSNR and significant activation, dual-shot spiral-in has low tSNR and poor activation detection. Increasing the FOV_z and using a $rz=2$ produces images of good quality, although some artifacts are present. Fig 4. Multi-subject analysis. Dual-shot spiral-out outperforms dual-shot spiral-in in all metrics and for all subjects.

Discussion: In this work, we have shown that a TE shorter than T_2^* provides good sensitivity for BOLD fMRI when using spiral-out readouts for high-resolution BOLD fMRI at UHF.

Conclusion: We conclude that spiral-in approaches are only beneficial for lower resolutions (≥ 0.8 mm), where the readout duration is short. The higher tSNR of the DS-SO readouts is promising since it could allow reaching statistical significance with shorter functional runs. We have also shown the flexibility of the proposed framework to obtain images with a larger FOV. The use of a head-only high-performance gradient coil allowed for a reduction of 20% on TR_{vol} compared to what is achievable with conventional body gradients. Segmented spiral-out readouts are an important alternative to EPI for very high-resolution (< 0.8 mm) fMRI at UHF.

Acknowledgements: This work is funded by the H2020 FET-Open AROMA grant agreement no. 88587

References:

- [1] Glover, Gary. *Neuroimage* 62.2 (2012): 706-712.
- [2] Kasper, Lars, et al. *NeuroImage* 246 (2022): 118738.
- [3] Engel, Maria, et al. *ISMRM* (2022).
- [4] Monreal-Madrigal, Alejandro, et al. *Imaging Neuroscience 2* (2024): 1-14.
- [5] Pruessmann, Klaas P., et al. *MRM* 42.5 (1999): 952-962.

13C Hyperpolarization and 2H NMR enable real-time insights into the enzymatic activity of yeast and intestinal organoids

Josh P. Peters¹, Hang Xiang², Fatima Anum¹, Farhad Haj Mohamad¹, Charbel Assaf¹, Philip Rosenstiel², Stefan Schreiber², Jan-Bernd Hövener¹, Konrad Aden², Andrey N. Pravdivtsev^{1*}

Abstract: The low sensitivity of NMR has been a barrier to real-time metabolic imaging. Hyperpolarization and isotopic labeling (2H and 13C) have significantly improved matters, enabling detailed in vivo metabolic studies. In this study, we tested over 20 thermally polarized 2H-labeled tracers, as well as hyperpolarized [1-13C]pyruvate and [1,4-13C2]fumarate, using dissolution dynamic nuclear polarization (dDNP) to non-invasively monitor metabolism in yeast and organoids. We demonstrated that 13C hyperpolarized and 2H-labeled NMR are well-suited to probe enzymatic activity in vitro, longitudinally, and non-invasively.

Motivation: Cell cultures are used as models for investigating metabolism, but do not fully represent the complexity of an organism. Organoids, 3D clusters of multiple organ-specific cells, microplates, are more complex, contain multiple differentiated cell types (derived from an organ stem cell), and can undergo self-renewal. These features make organoids a more effective system for modeling diseases and exploring their mechanisms compared to traditional cellular models. However, current methods of tracking metabolism are limited to stable isotope labeling (e.g., 13C-tracing coupled with LC-MS), which require the breakdown of cellular integrity and, thereby, the interruption of the biological process and destruction of the sample. Here, we describe our methods for probing enzymatic activities and treatment responses using 2H and 13C NMR non-invasively and non-destructively in living constructs.

Materials & Methods: All 2H and 13C experiments were carried out at a 9.4 T NMR spectrometer (Bruker Avance NEO). 13C tracers were polarized using a cryogen-free dDNP system operating at ~1.4 K and 6.7 T, with samples ranging from 25 to 50 mg and containing the trityl radical (AH111501, SpinAligner, POLARIZE). 13C Hyperpolarized or 2H labeled compounds were injected into NMR tubes containing the cells or organoids inside the NMR. Intestinal organoids (which form spontaneous carcinogenesis in the Rnaseh2b/Xbp1ΔIEC mouse model, with or without targeted therapeutic mTOR inhibition by rapamycin) and baker's yeast were used as model systems.

Results: More than 22 thermally polarized 2H-labeled tracers were tested with yeast rapid metabolism of glucose, pyruvate, formate, nicotinamide, and acetone. The established protocol[1] was highly reproducible (Fig. 1, CV=8.5%, n=5).

Hyperpolarized experiments with [1-13C]pyruvate and [1,4-13C2]fumarate also showed metabolic conversions in yeast[2] and organoids[3] (Fig. 2). Hyperpolarized NMR revealed a 6.6-fold reduction in lactate production in rapamycin-treated intestine organoids (targeted therapeutic intervention by mTOR inhibition), indicating statistically significant suppression of metabolic activity (Fig. 2, p=0.016, n=3)[3].

Because the entire procedure was non-invasive, we were able to repeat the hyperpolarization experiment on the same organoids after another week of treatment.

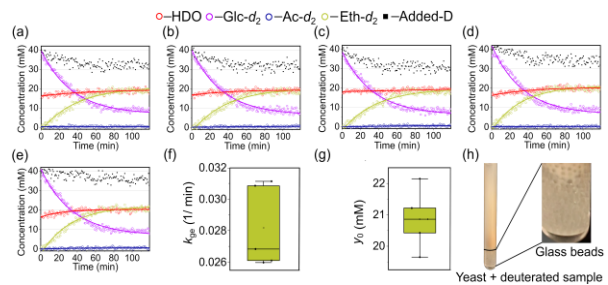


Fig. 1: Kinetics of [6,6'-2H2]glucose (Glc-d2) metabolism with fitted decay functions across five independent replicates showing consistent [2,2-2H2]ethanol (Eth-d2) production along with minor [2,2-2H2]acetate (Ac-d2) formation (a-e). Small standard deviations of fitted glucose-to-ethanol conversion rate constants, k_{ge} (f), and the final Eth-d2 concentrations, y_0 (g), confirm the method's reproducibility.

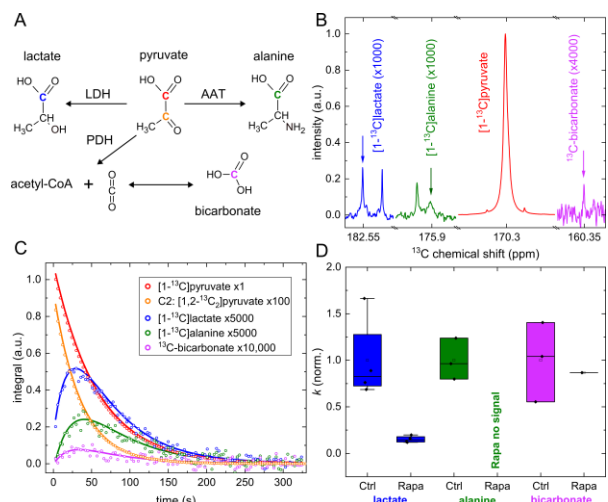


Fig. 2: Hyperpolarization-enhanced NMR revealed the strong metabolic effect of rapamycin treatment. (A) Chemical diagram of pyruvate metabolism. NMR spectra of hyperpolarized products (B) and corresponding kinetics (C) showed significant changes in conversion rate constants for the production of lactate ($p = 0.016$) and alanine (D).

Discussion: Bakers yeast cells proved to be a robust and easy-to-handle metabolic "factory" for pyruvate and fumarate metabolism, even for substrates with a 13C natural abundance[2] and thermally polarized 2H-tracers[1]. The protocol can be easily implemented in any lab that does not have access to dedicated cell culture facilities, biological safety standards, and whose primary focus is in vivo translation.

HMI and DMI both probe metabolism, but different aspects of it. HMI, because of its fast decaying but high signal, probes the

metabolic activity of enzymes “instantaneously”, within a few seconds, with relatively high sensitivity at 0.2 μ M tracer tissue concentration. DMI, on the other hand, provides less signal but allows averaging, accessing the metabolism over a timescale of many minutes with a sensitivity of ~ 10 mM tracer tissue concentration. The significance of these differences for understanding and assessing disease has yet to be understood.

A significant advantage of thermally and hyperpolarized metabolic MR is that it is non-destructive and repeatable, unlike traditional methods that destroy cellular integrity. The methods enable repetitive, non-invasive metabolic assessments, bridging the gap between preclinical and clinical applications and affirming the method's potential for targeted metabolic imaging as a novel diagnostic and treatment control approach in cancer medicine. In the future, intact samples of (human) tissue may further improve the applicability and translational potential of the methods.

Conclusion: Thermally and hyperpolarized MR/HMI and DMI are well suited to study different aspects of metabolism in selected pathways non-invasively in living yeast, cells, organelles, and organisms, with yeast being the easiest model to handle. The temporal and chemical resolutions of HMI and DMI vary: μ M tracer tissue concentration and seconds for HMI, and mM and minutes for DMI, whose meanings have yet to be interpreted. We demonstrated that the implementation

of in vitro ²H and hyperpolarized ¹³C NMR experiments is relatively straightforward, and baker's yeast is a robust and accessible initial test model. Using ¹³C-hyperpolarized pyruvate, a strong therapeutic response was observed in vitro, suggesting that the technology could be translated in vivo.

Acknowledgements: We acknowledge funding from the German Federal Ministry of Education and Research (BMBF) within the framework of the e: Med research and funding concept (01ZX1915C), and hyperquant consortium (BlueHealthTech, 03WIR6208A9), DFG (555951950, 527469039, 469366436, HO-4602/2-2, HO-4602/3, GRK2154-2019, EXC2167, FOR5042, TRR287). MOIN CC was founded by a grant from the European Regional Development Fund (ERDF) and the Zukunftsprogramm Wirtschaft of Schleswig-Holstein (Project no. 122-09-053).

References:

- [1] F. Anum, C. Assaf, F. H. Mohamad, M. Anikeeva, A. Brahms, J. Dey, S. Kaltenberger, E. Beitz, L. Welz, V. Annis, M. van Gemmeren, S. Duckett, J.-B. Hövener, A. N. Pravdivtsev, preprint 2024.
- [2] J. P. Peters, C. Assaf, F. H. Mohamad, E. Beitz, S. Tiwari, K. Aden, J.-B. Hövener, A. N. Pravdivtsev, *Anal. Chem.* 2024, 96, 17135–17144.
- [3] J. Peters, H. Xiang, C. Assaf, F. H. Mohamad, P. Rosenstiel, S. Schreiber, J.-B. Hövener, K. Aden, A. Pravdivtsev, preprint 2024, DOI 10.21203/rs.3.rs-5551528/v1.

4D-flow Derived Finite-Element-Method Analysis in Right Ventricle Differentiates Between Different Stages of Pulmonary Hypertension

Pascal Pretz 1 *†, Ali Nahardani 1 †, Verena Hoerr 1

Heart Center Bonn, Department of Internal Medicine II, University Hospital Bonn, Bonn, Germany; † Equal Contribution

Abstract: Pulmonary Arterial Hypertension (PAH) is a complex vascular disease that remains difficult to diagnose accurately using non-invasive imaging techniques. This study explores the potential of using fluid dynamics metrics derived from 4D-flow MRI to differentiate between various stages of PH. Particular emphasis was placed on analyzing relative pressure, vorticity, and helicity density. Notably, relative pressure was computed numerically using the Finite Element Method. Our findings indicate that each of these metrics demonstrates measurable differences across PH stages. These results suggest that 4D-flow MRI holds promise as a non-invasive tool for staging Pulmonary Hypertension.

Motivation: Pulmonary Hypertension (PH) is a progressive and life-threatening condition characterized by elevated pressure in the pulmonary arteries. This pressure overload imposes increased mechanical stress on the right ventricle, initiating both adaptive and maladaptive remodeling processes that can ultimately culminate in right ventricular failure. Although a range of imaging modalities can visualize the morphology and function of the right ventricle, the non-invasive assessment of spatially resolved intraventricular pressure remains a major challenge. Currently, right heart catheterization remains the clinical gold standard for accurate pressure measurement.

In contrast to conventional imaging techniques, 4D-flow MRI enables the quantification of time-resolved, three-dimensional blood flow velocities throughout the cardiac cycle. Velocity is a fundamental variable in fluid dynamics, as it is directly linked to pressure through the Poisson equation, which will be introduced in the Method section. From the acquired velocity fields, it is possible to compute relative pressure distributions numerically. Given the well-established correlation between PAH and intraventricular pressure, relative pressure derived from 4D-flow MRI may serve as a sensitive marker for disease staging.

Beyond pressure estimation, 4D-flow MRI also allows for the derivation of advanced hemodynamic parameters such as vorticity and helicity density, which characterize the rotational and helical features of blood flow, respectively. While these metrics are not directly related to pressure, they provide valuable insight into flow complexity and turbulence—phenomena that may also correlate with disease progression and serve as complementary markers for the staging of Pulmonary Hypertension.

Materials & Methods: Animal Study: A total of 9 male Sprague Dawley rats were included in the study and divided into three different experimental groups: (A) Baseline, n = 3; (B) Severe PAH, n = 3; and (C) Treated PAH, n = 3.

MRI: A prospectively gated stack-of-stars 4D-flow was performed on a 9.4T BioSpec 94/20 MRI (Bruker, Ettlingen, Germany). All the animals were examined by a 72mm-diameter quadrature volume resonator with the following sequence parameters: Flow encoding: HADAMARD; TR=10ms; TE=1.1ms;

FA=10°; BW=100kHz; undersampling factor=1.4–1.6; averages=1; resolution=(375×375×375) μm³; VENC=75–200cm/s.

Analysis: Relative pressure was computed during the systolic phase by solving the pressure Poisson equation, given by: $-\Delta p = \rho \nabla(v \cdot \nabla)v$, where v is velocity, p pressure and ρ density [1]. The equation was numerically solved using the Finite Element Method (FEM) [1]. No explicit inlet or outlet boundaries were defined in the computational domain. Dirichlet and homogeneous Neumann boundary conditions were enforced [1]. Blood was modeled as a Newtonian, incompressible fluid with a constant density of 1056 kg/m³ [2]. The right-hand side of the Poisson equation was discretized using finite differences, based on spatial derivatives of the velocity field evaluated on a uniform grid. In addition to relative pressure, helicity density ($h=v(\nabla \times v)$) [3] and vorticity ($\omega=\nabla \times v$) [1] were calculated using similar numerical differentiation schemes. These parameters, derived from the velocity field, provide insight into the rotational and helical nature of blood flow.

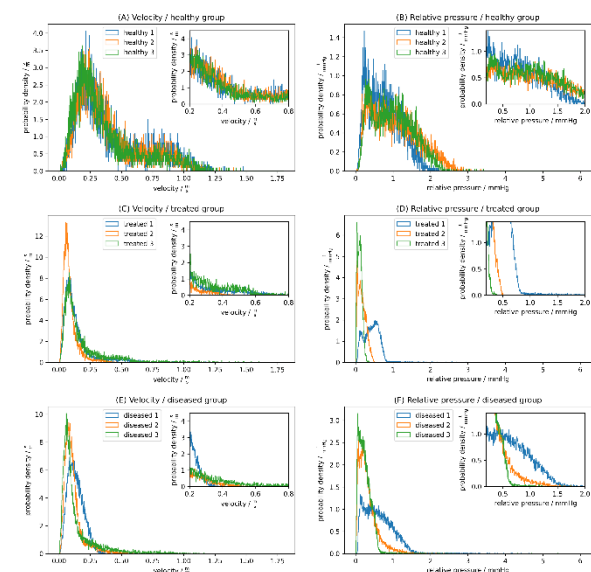


Fig. 1: Representative pressure maps of the right ventricle for a healthy (A, animal: healthy 2), treated (B, animal: treated 1) and diseased (C, animal: diseased 1) animal.

Results: In healthy animals, relative pressure was evenly distributed across the right ventricle, while treated animals exhibited a pronounced pressure buildup (approximately above 4mmHg) in the inferior ventricular region (fig.1). Both treated and diseased groups showed substantially reduced relative pressure near the right ventricular outflow tract compared to healthy controls.

Analysis of velocity magnitudes showed the lowest flow velocities in the diseased group and the highest in healthy animals. The most pronounced differences in velocity occurred in the superior region of the right ventricle (fig.2). These findings indicate a strong correlation between diseased and normal intraventricular flow dynamics.

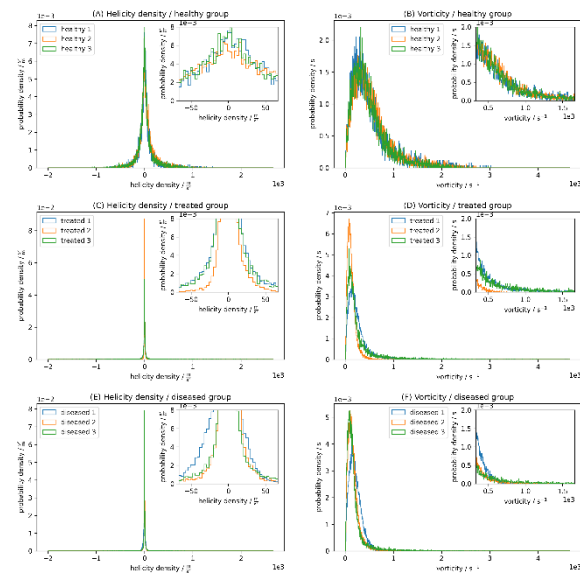


Fig. 2: Representative velocity maps of the right ventricle for a healthy (A, animal: healthy 2), treated (B, animal: treated 1) and diseased (C, animal: diseased 1) animal.

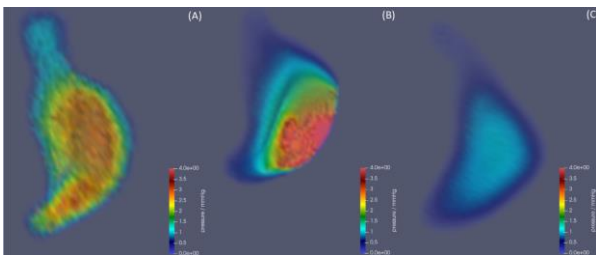


Fig. 3: Representative histograms showing velocity magnitude (A,C,E) and relative pressure (B,D,F) for healthy (A,B,n=3), treated (C,D,n=3) and diseased (E,F,n=3) animals.

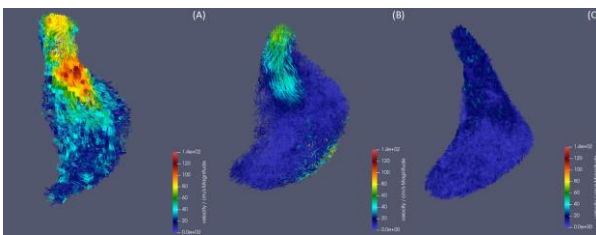


Fig. 4: Representative histograms showing helicity density (A,C,E) and vorticity magnitude (B,D,F) for healthy (A,B,n=3), treated (C,D,n=3) and diseased (E,F,n=3) animals.

To quantify these observations, voxel-wise histograms of relative pressure and velocity magnitude were generated. The distributions revealed consistent trends within each group. Descriptive statistics showed that both treated and diseased animals had substantially lower velocities and relative pressures than the healthy group. The range of the median values for velocity of healthy, treated, and diseased animals were 28–30cm/s, 7–11cm/s, and 8–13cm/s, respectively (fig.3). In addition, the relative pressures for each group were 1.24–1.75mmHg, 0.39–1.18mmHg, 0.24–0.53mmHg respectively (fig.3). Furthermore, hemodynamic characterization using vorticity showed consistently lower values in treated (107–194s⁻¹) and diseased (124–188s⁻¹) animals relative to healthy controls (403–442s⁻¹) (fig.4). The range of the helicity density

in healthy, treated, and diseased animals was 342–1150cm²/s², 10–19cm²/s², and –183–54cm²/s², respectively (fig.4). These reductions reflect decreased rotational and helical flow components in the presence of disease or following treatment.

Discussion: Within each experimental group, the distributions of velocity magnitude and relative pressure exhibited consistent patterns. In healthy animals, both histograms showed nearly identical, uniform profiles, indicating stable and homogeneous flow conditions. In contrast, diseased and treated animals displayed distributions with steeper decay in probability density toward higher velocities and pressures, suggesting an exponential-like trend. This rapid decline likely reflects reduced hemodynamic activity associated with disease-induced vascular remodeling. Some inter-animal variability within the diseased and treated groups is expected, given the differing progression of Pulmonary Hypertension across individuals.

Similar trends were observed for vorticity and helicity density. Vorticity distributions decayed more sharply in diseased and treated animals compared to healthy ones, indicating decreased rotational flow. Helicity density distributions appeared approximately Gaussian across all groups but with narrower peaks in diseased and treated animals, reflecting reduced helical flow complexity.

These findings suggest that 4D-flow MRI-derived metrics—particularly velocity, relative pressure, vorticity, and helicity density—can distinguish between healthy and pathological flow states. However, differentiation between treated and untreated diseased animals remains challenging due to overlapping disease stages and variable treatment response. Longitudinal studies are needed to clarify these effects.

Anatomical variability between animals presents further limitation, potentially confounding spatial comparisons. Moreover, while hemodynamic alterations were clearly identified, the direct relationship between these changes and the physiological consequences of Pulmonary Hypertension has to be fully understood. Further studies are required to link fluid dynamic biomarkers with disease mechanisms and outcomes.

Conclusion: In summary, 4D Flow MRI demonstrated distinct hemodynamic differences between diseased, treated, and healthy control animals within the framework of our PAH study. Velocity, relative pressure, vorticity, and helicity density appear to be parameters affected by Pulmonary Hypertension and may therefore serve as suitable markers for characterizing the disease.

However, more data are needed to strengthen the observations made here and to enable a clearer differentiation of the different phases of the disease.

Acknowledgements: This study was supported by the German Research Foundation (Deutsche Forschungsgemeinschaft/DFG, Project-ID: 468824876).

References:

- Rosales, R. R., Seibold, B., Shirokoff, D., & Zhou, D. (2021). High-order finite element methods for a pressure Poisson equation reformulation of the Navier–Stokes equations with electric boundary conditions. *Computer Methods in Applied Mechanics and Engineering*, 373, 113451. <https://doi.org/10.1016/j.cma.2020.113451>
- Everett, N. B., Simmons, B., & Lasher, E. P. (1956). Distribution of blood (Fe 59) and plasma (I 131) volumes of rats determined by liquid nitrogen freezing. *Circulation research*, 4(4), 419–424. <https://doi.org/10.1161/01.res.4.4.419>
- Moffatt, H. K. (1969). The degree of knottedness of tangled vortex lines. *Journal of Fluid Mechanics*, 35(1), 117–129. doi:10.1017/S0022112069000991

Effect of chemical exchange on T₁ and T₂ Spin Relaxation: succinate and pyruvate case studies

Ehtisham Rasool 1*, Josh P. Peters 1, Jan-Bernd Hövener 1, Andrey N. Pravdivtsev 1

1 Department of Radiology and Neuroradiology, Section Biomedical Imaging, University Hospital Schleswig-Holstein, Kiel University, Kiel, Germany,

Abstract: Nuclear spin relaxation is a critical property for NMR spectroscopy and magnetic resonance imaging. For hyperpolarized MRI, relaxation is the essential feature for success. Some molecules, in particular succinate and nicotinamide, have been reported to exhibit accelerated relaxation constants at specific pH levels and low magnetic fields. One hypothesis is that the accelerated relaxation in such conditions is caused by rapid chemical exchange. Here, we investigated the matter by analyzing the relaxation dispersion of T₂ (T₂RD). We measured T₂ as function of TE with a Carr-Purcell-Meiboom-Gill (CPMG) sequence and fitted the the Luz-Meiboom equation to T₂(TE), yielding exchange rates for succinate at pH 13.17, T₂-RD fitting yielded an exchange rate (k_{ex}) of $(122 \pm 24) s^{-1}$ and an amplitude term ($P_A P_B (\Delta\omega)^2 \tau_{ex}$) of $(41.0 \pm 10) s^{-1}$; at pH 2.80, k_{ex} was $(83.4 \pm 7.9) s^{-1}$ and the amplitude term was $(61.6 \pm 7.7) s^{-1}$. For ¹³C pyruvate at pH 7.62, k_{ex} was $(4184.2 \pm 1322.9) s^{-1}$ and the amplitude term $(384.8 \pm 133.2) s^{-1}$; for [¹⁻¹⁵N]nicotinamide at pH 8.27, k_{ex} was $(1207 \pm 2008) s^{-1}$ and the amplitude term $(1454.8 \pm 2564) s^{-1}$. Unlike 1D NMR, T₂-RD enables the assessment of chemical exchange when the chemical shifts of exchanging species are not different. The results provide quantitative insights into rapid molecular dynamics. By tuning the chemical environment, we plan to slow down the exchange rate, thereby decelerating relaxation and enabling better preservation of the hyperpolarization level.

Motivation: Increasing the alignment of nuclear spins drastically enhances the signal and sensitivity of magnetic resonance experiments. These hyperpolarization techniques allow for a thorough characterization of molecular dynamics and interactions. Here, the longitudinal (T₁) relaxation of hyperpolarized tracers is particularly important for storing and transferring the agents, while the transversal (T₂) relaxation is effective during detection. By methodically altering the echo spacing or echo time (TE), the Carr-Purcell-Meiboom-Gill (CPMG, Fig 1) pulse sequence can be used to obtain T₂ relaxation dispersion (T₂-RD), which offers a powerful means to investigate these relaxation processes. Analysis of T₂-RD can help disentangle intrinsic T₂ relaxation and the effect of chemical exchange. The rapid chemical exchange causes rapid T₁ relaxation at low magnetic fields, which is usually not accessible unless a high-resolution magnetic field cycling system is available, a technology that is not widely available. T₂-CPMG analysis would better characterize the relaxation of hyperpolarized species and serve as a practical tool in assessing exchange rates, thereby controlling the effect of the chemical environment on exchange and, consequently, T₂ and T₁ relaxation.

Materials & Methods: ¹³C and ¹⁵N NMR spectra were acquired with high-resolution NMR 9.4-T wide bore NMR (WB400, Avance NEO, Bruker) with a 5-mm BBFO probe and the following acquisition parameters: number of

accumulations for the ¹⁵N was 32 and for the ¹³C was 4, 90 pulse length (PL) for ¹⁵N was 20.75 μs, and for ¹³C was 10.65 μs with power of pulse for ¹³C was 78 W and for the ¹⁵N was 75 W, and relaxation delay before CPMG for ¹⁵N was 120 s and for ¹³C was 150 s. The echo time (TE) between two consecutive echoes was equal to $TE = 2 * (\tau + PL)$, where 2τ is the interpulse delay between two 180° pulses and PL the pulse length. A monoexponential decay function was fitted to the data to obtain T₂(TE), and the following Luz-Meiboom equation was fitted T₂(TE) to obtain the exchange rates, population and chemical shifts (eq 2 from ref 1) $1/T_2 = 1/T_2m + PAPB(\Delta\omega)2\tau_{ex}(1 - (2\tau_{ex}/TE) * \tanh(TE/2\tau_{ex}))$ (1). where T₂m is the relaxation time in the absence of chemical shift difference of species A and B, TE is the echo time, $\tau_{ex} = 1/k_{ex}$ is the characteristic exchange time, P_A and P_B are the populations of exchanging states, and the Δω is the chemical shift difference of species A and B.

Results: T₂ relaxation decay was found to be strongly influenced by TE (Figure 2, example of 1,4-¹³C2-succinate), where shorter TE (more frequent refocusing) yielded larger observed T₂ (slower observed T₂ relaxation), better compensating the slow dephasing mechanisms

The fitting of T₂-RD for succinate at pH of 13.17 (Figure 3A) yielded an exchange rate ($k_{ex} = 1/\tau_{ex}$) of $(122 \pm 24) s^{-1}$ and the amplitude term ($PAPB(\Delta\omega)2\tau_{ex}$) of $(41.0 \pm 10) s^{-1}$. At an acidic pH of 2.80 (Figure 3B), the exchange rate was determined to be $(83.4 \pm 7.9) s^{-1}$, and the amplitude term was $(61.6 \pm 7.7) s^{-1}$. We also studied ¹³C pyruvate at a neutral pH of 7.62; T₂-RD fitting yielded the exchange rate of $(4184.2 \pm 1322.9) s^{-1}$, and the amplitude term of $(384.8 \pm 133.2) s^{-1}$ (Figure 4A). The T₂-RD for [¹⁻¹⁵N]nicotinamide at pH of 8.27 yielded the exchange rate $(1207 \pm 2008) s^{-1}$ and the amplitude term of $(1454.8 \pm 2564) s^{-1}$ (Figure 4B).

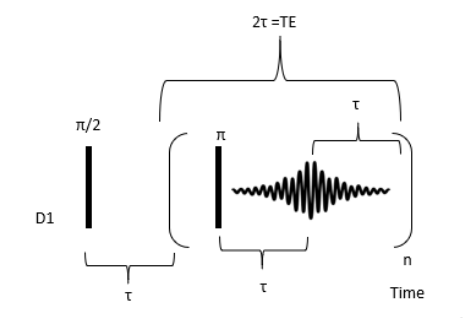


Fig. 1: Schematic representation of the CPMG pulse sequence used for T₂ relaxation measurements. The initial delay D1 allows for recovery of the thermal polarization, while TE denotes half of the echo time between refocusing pulses. The repetition of π pulses (n times) generates a train of spin echoes, allowing analysis of transverse relaxation behavior.

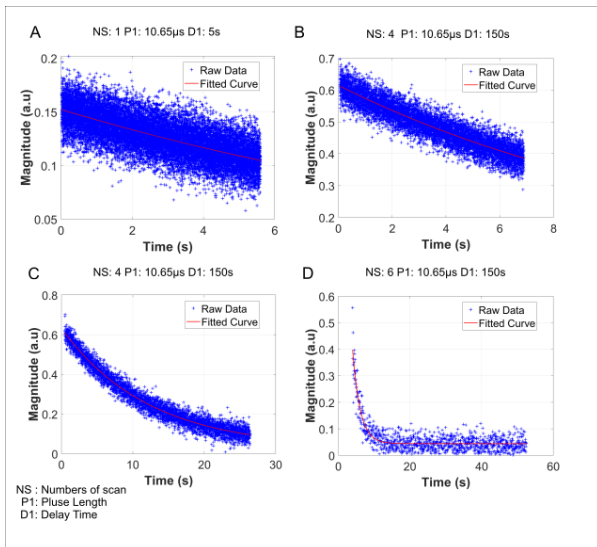


Fig. 2: T_2 relaxation decay of 1,4- $^{13}C_2$ -succinate during CPMG experiment: (A) $TE = 21.3003$ ms, number of echoes = 32768 (B) $TE = 21.3008$ ms, number of echoes = 16384, (C) $TE = 21.3064$ ms, number of echoes = 8192 and (D) $TE = 21.3512$ ms, number of echoes = 24590. The fitted function (red lines) was $M_0 \cdot \exp(-t/T_2)$.

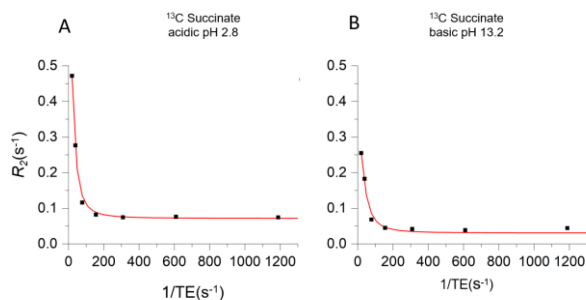


Fig. 3: T_2 -RD for [1,4- ^{13}C]succinate at pH of 2.80 (A) and 13.17 (B). R_2 initially decreases as $1/TE$ increases, then plateaus, showing suppressed chemical (shorter R_2) exchange at higher pulsing frequencies (larger $1/TE$). At pH 2.80, relaxation is much faster for long TE due to faster proton exchange near pK_a compared to pH 13.2 where the effect from TE variation is smaller. The fitted curves (red, eq1) match experimental data (black).

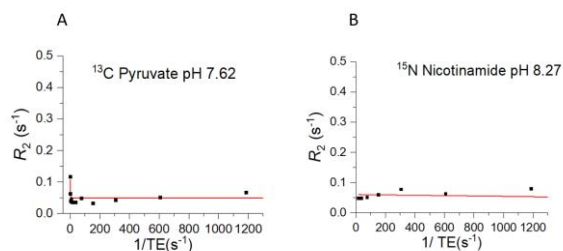


Fig. 4: T_2 -RD for [1,4- ^{13}C]pyruvate at pH 7.62 (A) and [1,4- ^{15}N]nicotinamide at pH 8.27. ^{13}C Pyruvate (pH 7.62) exhibits faster signal decay than ^{15}N Nicotinamide (pH 8.27), as shown by their respective relaxation rates ($1/TE$).

Discussion: The T_2 relaxation dispersion (T_2 RD) studies revealed distinct pH-dependent chemical exchange mechanisms across the systems. For succinate, under basic conditions, the slower exchange rate and smaller amplitude term indicate slow exchange with a limited chemical shift difference ($\Delta\omega$) between species. This only leads to mild T_2 shortening. In contrast, under acidic conditions, succinate showed an even slower exchange rate but a significantly larger amplitude term. This shows that, despite the slower kinetics, the much larger $\Delta\omega$ dominates the relaxation, leading to stronger exchange contributions and more noticeable T_2 relaxation. Pyruvate at neutral pH had a very high exchange rate along with a significant amplitude term, placing it firmly in the fast exchange regime ($k_{ex} \gg \Delta\omega$). Here, rapid interconversion leads to motional narrowing, averaging the chemical environment and resulting in a longer observed T_2 . Lastly, nicotinamide produced exceptionally high values for both the exchange rate and amplitude term, but considerable uncertainties prevent definitive conclusions. If these parameters are correct, they would suggest an intermediate exchange regime ($k_{ex} \approx \Delta\omega$), where T_2 shortening is maximized due to significant chemical shift differences and exchange kinetics occurring at the right timescale. Overall, the results show how pH affects both the exchange rate and the type of exchanging species, influencing the relaxation regime and its effect on T_2 .

Conclusion: Our study confirmed the effect of chemical exchange on relaxation time in pyruvate, succinate, and nicotinamide. By changing pH, one can control the impact of this relaxation source. The combination of CPMG and T_2 -RD provides a reliable framework for studying chemical exchange and its impact on spin relaxation. Further study of the contribution of additives to exchange parameters is necessary to explain a novel chemically induced deceleration of relaxation effect on the CIDER3 agents that observe in ^{15}N hyperpolarization of nicotinamide which will be the essential for enabling novel metabolic imaging.

Acknowledgements: We acknowledge funding from the German Federal Ministry of Education and Research (BMBF, 03WIR6208A hyperquant), DFG (555951950, 527469039, 469366436, HO-4602/2-2, HO-4602/3, GRK2154-2019, EXC2167, FOR5042, TRR287). MOIN CC was founded by a grant from the European Regional Development Fund (ERDF) and the Zukunftsprogramm Wirtschaft of Schleswig-Holstein (Project no. 122-09-053).

References:

- Zhong, J., Gore, J.C. and Armitage, I.M. (1989), Relative contributions of chemical exchange and other relaxation mechanisms in protein solutions and tissues. *Magn. Reson. Med.*, 11: 295-308. <https://doi.org/10.1002/mrm.1910110304>.
- Peters, J. P. et al. Nitrogen-15 dynamic nuclear polarization of nicotinamide derivatives in biocompatible solutions. *Sci. Adv.* 9, eadd3643 (2023).
- Peters, J. et al. Chemically induced deceleration of nuclear spin relaxation (CIDER) preserves hyperpolarization. Preprint at <https://doi.org/10.21203/rs.3.rs-4668036/v1> (2024).
- Peters, J. P., Assaf, C. D., Hövener, J.-B. & Pravdivtsev, A. N. Compact magnetic field cycling system with the range from nT to 9.4 T exemplified with ^{13}C relaxation dispersion and SABRE-SHEATH hyperpolarization. Preprint at <https://doi.org/10.48550/arXiv.2506.08711> (2025).

Quantitative characterization of lesional and normal-appearing deep brain structures in primary progressive multiple sclerosis at 7T

Renn Philipp 1*, Madsen Mads Alexander Just 1+2, Helms Gunther 3, Nygaard Sofus Alexander Drejer 1, Højsgaard Chow Helene 4, Blinkenberg Morten 4, Romme Christensen Jeppe 4, Sellebjerg Finn 3+4, Siebner Hartwig Roman 1+5+6, Wiggermann Vanessa 1

1 Danish Research Centre for Magnetic Resonance, Copenhagen University Hospital - Amager & Hvidovre, 2650 Hvidovre, Denmark

2 MS Center Amsterdam, Anatomy and Neurosciences, Amsterdam Neuroscience, Amsterdam University Medical Center, location VUmc, Vrije Universiteit Amsterdam, Amsterdam, the Netherlands

3 Max Planck Institute for Human Cognitive and Brain Sciences, 04103 Leipzig, Germany

4 Danish Multiple Sclerosis Center, Department of Neurology, Copenhagen University Hospital – Rigshospitalet, 2600 Glostrup, Denmark

5 Department of Clinical Medicine, University of Copenhagen, 2200 Copenhagen, Denmark

6 Department of Neurology, Copenhagen University Hospital - Bispebjerg & Frederiksberg, 2400 Copenhagen, Denmark

Abstract: This study investigates deep gray matter (DGM) pathology in primary progressive multiple sclerosis (PPMS) using structural imaging, quantitative susceptibility mapping (QSM), and magnetization transfer ratio (MTR) at ultra-high field 7T MRI. Twenty-eight PPMS patients and 18 healthy controls underwent multimodal imaging to assess lesion burden, atrophy, and microstructural changes across seven DGM structures. Lesions were symmetrically distributed, most frequently in the thalamus, caudate, and putamen, with significant volume loss in the thalamus and putamen. qMRI revealed reduced MTR and QSM in lesioned tissue and altered correlations between iron and microstructure in the thalamus and hippocampus, highlighting the sensitivity of 7T qMRI for detecting region-specific subtle DGM alterations in PPMS.

Motivation: Primary progressive multiple sclerosis (PPMS) is a less common but distinct phenotype of multiple sclerosis (MS), affecting approximately 10 to 15% of patients. It is characterized by continuous neurological decline from disease onset, differing from the relapsing-remitting pattern seen in most other MS patients [3]. Conventional MRI in MS typically assesses lesion burden and atrophy to track disease progression. However, these measures often miss subtle microstructural changes, particularly within deep gray matter (DGM) structures which are known to be involved in MS-related cognitive and motor dysfunction [2, 7].

DGM nuclei such as the thalamus, hippocampus, and basal ganglia show early signs of demyelination, neuronal loss, and iron dysregulation in MS [2, 7] Schwesinger. Ultra-high field MRI offers enhanced spatial resolution and contrast, enabling better visualization and segmentation of small structures and lesions. When combined with quantitative MRI (qMRI) techniques, this approach promises sensitive detection of pathological tissue alterations.

In this study, we employed a multimodal 7T qMRI framework in PPMS patients, using quantitative susceptibility mapping (QSM) as a marker of iron concentration and magnetization transfer ratio (MTR) as a proxy for macromolecular density and tissue integrity (see Figure 1). Our goal was to assess seven key DGM structures to characterize lesion burden and tissue changes, aiming to improve our understanding of microstructural pathology in PPMS and its role in disease progression.

Materials & Methods: Twenty-eight individuals with PPMS (EDSS range 2-6.5 median 4.0; time since diagnosis: 12.7 ± 6.6 years) and 18 age- and sex-matched healthy controls (HCs) underwent 7T MRI using a Philips Achieva scanner with a dual-transmit, 32-channel receive head coil. Each participant

completed two sessions acquiring structural (MP2RAGE, FLAIR, DIR) and quantitative (QSM, MTR) sequences. Structural images were bias field corrected and co-registered to FLAIR images. White matter lesions were automatically segmented using LST-AI [12]; T1- and T2-weighted images were lesion-filled to improve tissue segmentation.

DGM structures included the thalamus, caudate, putamen, globus pallidus, substantia nigra, hippocampus and the amygdala. These were segmented using a combined approach of FIRST [8], DBSegment [1], and the dual-contrast ANTs Joint Label Fusion pipeline [9]. Using FSLeves, DGM lesions were manually identified based on their characteristic contrast (hyperintense on FLAIR and DIR, hypointense on MP2RAGE) and size criteria (≥ six voxels across two slices). Lesion masks were overlaid on DGM segmentations in MATLAB to classify lesions by structure, hemisphere, and to identify whether they crossed structure's boundaries. For visualization, lesion masks were transformed to MNI space using ANTs [11].

Quantitative maps were processed with standardized pipelines and co-registered to FLAIR space. Structural volumes were normalized to intracranial volume. Normality was assessed via Kolmogorov-Smirnov tests. Group differences in volumes were analyzed using Welch's t-tests. For qMRI metrics, one-way ANOVA with Tukey's post-hoc correction compared HCs tissue to normal-appearing, and lesioned tissue in PPMS. Pearson correlations between qMRI measures were calculated separately for HCs and PPMS patients.

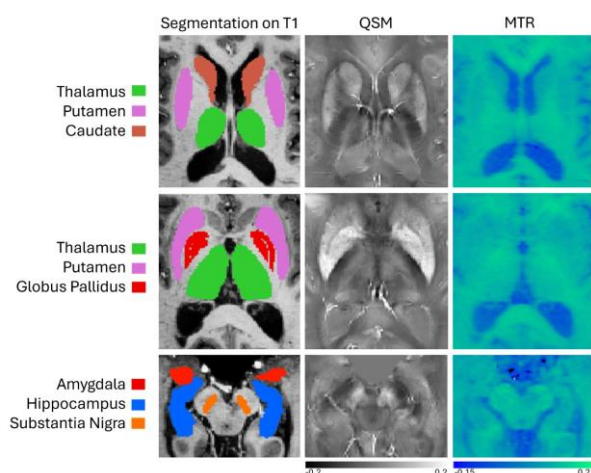


Fig. 1: Segmentations, QSM and MTR images from three axial slices each, showcasing an exemplary subject's DGM structures.

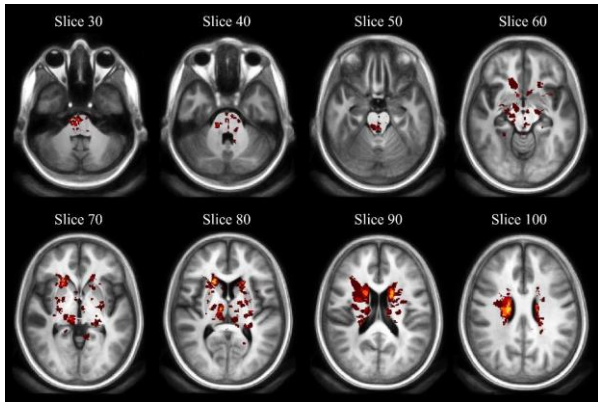


Fig. 2: Heatmap displaying the spatial distribution of lesions within the DGM region, projected onto MNI space for visualization.

	HC (n = 18)			QSM/MTR correlations	MS (n=28)			
	Affected Subjects	Lesions (crossing borders)	Volume mean (std)		Affected Subjects	Lesions (crossing borders)	Volume mean (std)	QSM/MTR correlations
Globus pallidus	1	2 (0)	0.1427 (0.022)	0.10	4	4 (3)	0.1372 (0.0162)	-0.23
Thalamus	2	7 (4)	0.9676 (0.0881)	-0.21	16	53 (31)	0.8599 (0.1332)	0.34
Caudate	2	2 (2)	0.4745 (0.0477)	0.36	16	41 (40)	0.4561 (0.0843)	0.12
Putamen	3	6 (3)	0.6186 (0.0676)	-0.07	9	19 (14)	0.5515 (0.1196)	-0.02
Hippocampus	0	0 (0)	0.4981 (0.0820)	-0.36	4	5 (5)	0.4576 (0.0631)	0.04
Amygdala	0	0 (0)	0.1393 (0.0299)	-0.58	1	1 (1)	0.1242 (0.0501)	-0.28
Substantia Nigra	1	1 (1)	0.0626 (0.0102)	-0.07	5	5 (5)	0.0626 (0.0099)	0.01

Fig. 3: Lesion counts (including border-crossing), affected subjects, structure volumes, and QSM–MTR Pearson correlations for HC vs. MS. Group differences in volumes were assessed using Welch’s t-test; significant values ($p < 0.05$) are highlighted in bold.

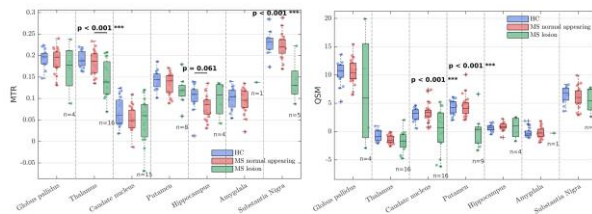


Fig. 4: Boxplots showing MTR and QSM values for healthy controls, MS normal-appearing tissue, and MS lesions across seven structures. Group differences were analyzed using one-way ANOVA with Tukey post-hoc tests.

Results: DGM lesions were symmetrically distributed, with 64 lesions identified in the left hemisphere and 82 in the right. The spatial distribution of lesions is illustrated in the lesion heatmap (Figure 2). Detailed lesion counts and volumetric measurements for each DGM structure are summarized in Table 1. The highest lesion burden was observed in the thalamus ($n = 60$; 35 crossing anatomical boundaries), followed by the caudate ($n = 43$; 42 crossing boundaries) and putamen ($n = 25$; 17 crossing boundaries). Volumetric analysis revealed significant atrophy in the thalamus ($p = 0.002$) and putamen ($p = 0.038$) of PPMS patients compared to HCs.

Boxplots depicting qMRI metrics across groups are presented in Figure 3. Compared to HCs, PPMS patients exhibited a trend toward reduced MTR in the hippocampus ($p = 0.061$). Lesioned tissue demonstrated significantly lower QSM values in the caudate ($p < 0.001$) and putamen ($p < 0.001$), and reduced MTR in the thalamus ($p < 0.001$) and substantia nigra ($p < 0.001$), relative to surrounding normal-appearing tissue in PPMS.

Pearson correlations between MTR and QSM differed markedly between PPMS and HCs in the thalamus (HC: -0.21; PPMS: 0.34) and hippocampus (HC: -0.36; PPMS: 0.04). In other DGM regions, correlation patterns remained relatively consistent across groups.

Discussion: Our findings reveal widespread involvement of DGM structures in primary progressive MS, including both focal lesions and microstructural abnormalities. Lesions were mainly symmetrically distributed, with a predominance in the thalamus, caudate, and putamen. The majority of these lesions crossed anatomical boundaries, suggesting diffuse pathology consistent with prior histological observations [4, 5].

Reduced thalamic and putamen volumes are in line with established evidence of DGM atrophy in MS [6]. While volume loss is a well-accepted marker of neurodegeneration, our qMRI results further highlight subtle tissue alterations. Lesioned areas showed reduced QSM and MTR, particularly in the caudate, putamen, thalamus, and substantia nigra, pointing toward local demyelination and disrupted iron homeostasis, as suggested by prior studies [4, 10].

Moreover, altered correlations between qMRI metrics in PPMS compared to HCs, particularly in the thalamus and hippocampus, indicate a decoupling of normal microstructural relationships. By contrast, structures such as the globus pallidus and caudate showed more stable cross-group associations, suggesting complex, region-specific mechanisms of injury and vulnerability across the DGM.

Conclusion: This study showed that PPMS affects DGM structures macroscopically, through lesions and atrophy, and microscopically, via altered iron and myelin-related states. Using ultra-high field 7T MRI combined with qMRI metrics, we identified widespread DGM lesions and significant volume loss, especially in the thalamus and putamen. qMRI revealed localized microstructural changes in lesions and distinct inter-metric correlations in PPMS versus HCs. In areas like the thalamus and hippocampus, altered relationships between qMRI measures suggest changes in how iron content relates to microstructure in PPMS.

These findings highlight the value of combining 7T MRI with quantitative imaging to detect subtle DGM changes in PPMS. While further research is needed to connect these markers with clinical outcomes, our results underscore the importance of DGM pathology in progressive MS and the usefulness of multimodal qMRI to characterize it.

Acknowledgements: We wish to thank all the participants in this project and acknowledge grant support from the Lundbeck Foundation and the Danish MS Society, without which this project would not have been possible.

References:

[1] Baniasadi, M., Petersen, M., Gocalves, J., Horn, A., Vlasov, V., Hertel, F., and Husch, A. Dbsegment: Fast and robust segmentation of deep brain structures considering domain generalization. *Human Brain Mapping* (2022).

[2] Damjanovic, D., Valsasina, P., Rocca, M. A., Stromillo, M. L., Gallo, A., Enzinger, C., Hulst, H. E., Rovira, A., Muhlert, N., DeStefano, N., Bisecco, A., Fazekas, F., Arevalo, M., Yousry, T. A., and Filippi, M. Hippocampal and deep gray matter nuclei atrophy is relevant for explaining cognitive

- impairment in ms: A multicenter study. *American Journal of Neuroradiology* (2017).
- [3] Dobson, R., and Giovannoni, G. Multiple sclerosis – a review. *European Journal of Neurology* (2019).
- [4] Lassmann H. Multiple Sclerosis Pathology. *Cold Spring Harb Perspect Med* (2018).
- [5] Mahad DH, Trapp BD, Lassmann H. Pathological mechanisms in progressive multiple sclerosis. *Lancet Neurol* (2015).
- [6] Minagar, A., Barnett, M., Benedict, R., Pelletier, D., Pirko, I., Sahaian, M., Frohman, E., and Zivadinov, R. The thalamus and multiple sclerosis. *Neurology* (2013).
- [7] Neema, M., Arora, A., Healy, B., Guss, Z., Brass, S., Duan, Y., Buckle, G., Glanz, B., Stazzone, L., Khoury, S., Weiner, H., Guttmann, C., and Bakshi, R. Deep gray matter involvement on brain mri scans is associated with clinical progression in multiple sclerosis. *Journal of Neuroimaging* (2009).
- [8] Patenaude, B., Smith, S., Kennedy, D., and Jenkinson, M. A bayesian model of shape and appearance for subcortical brain segmentation. *NeuroImage* (2011).
- [9] Salman, F., & Schweser, F., ANTs Joint Label Fusion Bi-parametric Segmentation Toolbox [Software]. Buffalo Neuroimaging Analysis Center, University at Buffalo. GitLab. https://gitlab.com/R01NS114227/antsjointlabelfusion_biparametric (2024).
- [10] Schweser, F., Martins, A., Hagemeyer, J., Lin, F., Hanspach, J., Weinstock-Guttman, B., Hametner, S., Bergsland, N., Dwyer, M., and Zivadinov, R. Mapping of thalamic magnetic susceptibility in multiple sclerosis indicates decreasing iron with disease duration: A proposed mechanistic relationship between inflammation and oligodendrocyte vitality. *NeuroImage* (2018).
- [11] Tustison, N., and Avants, B. Explicit b-spline regularization in diffeomorphic image registration. *Front Neuroinform* (2013).
- [12] Wiltgen, T., McGinnis, J., Schlaeger, S., Kofler, F., Voon, C., Berthele, A., Bischl, D., Grundl, L., Will, N., Metz, M., et al. Lst-ai: A deep learning ensemble for accurate ms lesion segmentation. *NeuroImage: Clinical* (2024).

Feasibility of Matrix Pencil Decomposition for Ventilation and Perfusion Mapping Using Low-Field MRI in Healthy Volunteers and Lung Tumor Patients

Laura Rozo Pardo^{1,2}, Rabea Klaar^{1,2}, Olaf Dietrich², Moritz Rabe³, Christopher Kurz³

¹ Comprehensive Pneumology Center (CPC-M), Member of the German Center for Lung Research (DZL), Munich, Germany

² Department of Radiology, University Hospital, LMU Munich, Munich, Germany

³ Department of Radiation Oncology, University Hospital, LMU Munich, Munich, Germany.

Abstract: Quantitative lung MRI enables safe, repeatable assessment of ventilation and perfusion without contrast agents or radiation, critical for early disease detection and adaptive radiotherapy. We investigate the feasibility of Matrix Pencil (MP) decomposition for functional mapping from free-breathing proton MRI on a 0.35T MR-Linac. Low-field MRI reduces susceptibility artifacts and significantly prolongs T2 and T2* relaxation times in lung tissue, improving signal detectability and image quality. MP decomposition reduces signal leakage and improves the separation of respiratory and cardiac components, particularly in patients with irregular or inconsistent breathing patterns. Our study in healthy volunteers and lung tumor patients demonstrates the potential of combining low-field MRI and MP for reliable, contrast-free pulmonary function assessment.

Motivation: Functional lung imaging has gained increasing attention in recent years for its potential role in early disease detection, treatment planning, and therapy monitoring, especially in chronic respiratory conditions. While CT remains the clinical gold standard for lung imaging due to its high spatial resolution and speed, its reliance on ionizing radiation poses risks particularly in pediatric, pregnant, or chronically ill patients.

In this context, proton MRI provides a radiation-free alternative, though it remains technically challenging due to low proton density, rapid signal decay, and motion-related artifacts. Low-field MRI systems may help mitigate some of these limitations. They offer reduced susceptibility effects and longer T2/T2* relaxation times in lung tissue, improving signal detection in the parenchyma, making them a promising for safe and reliable lung imaging.

To support broader clinical adaption, particularly for treatment monitoring and outcome prediction in MRI-guided adaptive radiotherapy, there is a need for robust, contrast-free methods to extract lung functional information from time-resolved MRI. Techniques such as PREFUL and Non-uniform Fourier Decomposition (NuFD) have shown promise. However, their reliance on peak detection in the Fourier spectrum is often unstable, particularly when signal components are not clearly separated, as can occur with irregular breathing or low temporal resolution (2).

In this context, MP decomposition offers a potentially more robust alternative. Unlike Fourier-based approaches, it models physiological signals as sums of exponentially damped sinusoids, enabling more accurate separation of respiratory and cardiac components. This study explores the feasibility of applying Matrix Pencil decomposition to free-breathing proton MRI on a 0.35 T MR-Linac.

Materials & Methods: Data acquired from three healthy volunteers, originally collected by Klaar *et al.* (1), were analyzed. Imaging was performed on a 0.35 T MR-Linac

(MRIdian, ViewRay Inc., Cleveland, Ohio) using an optimized 2D coronal cine balanced steady-state free precession (bSSFP) sequence (flip angle = 70°, TR/TE = 2.42/1.02 ms, FOV = 500×500×20 mm³, matrix = 128×128, frame rate = 3.68 images/s), resulting in 1:06 min total acquisition time per series. Additionally, one coronal slice at the tumor position was obtained for two lung cancer patients - one female (38 years old) and one male (29 years old) - during free-breathing immediately post- radiation treatment.

Using this data, prior to analysis, motion correction was performed via non-rigid registration (ANTs SyN), followed by manual segmentation of the lung parenchyma region of interest (ROI). Afterward, to separate physiological signals, the MP method was employed: first, a Total Least Squares Matrix Pencil (TLS-MPM) identified a basis set of dominant poles for ventilation and perfusion. Subsequently, to mitigate interference from the strong breathing signal, a sequential least squares estimation (LSE) fit was performed voxel-wise to isolate the weaker perfusion component. The ventilation component was fitted and subtracted, after which the perfusion component was fitted to the remaining residual signal. Final ventilation-weighted (Vw) and perfusion-weighted (Qw) maps were generated from the component amplitudes. For visualization, a Gaussian filter ($\sigma = 1.0$) was applied to improve smoothness.

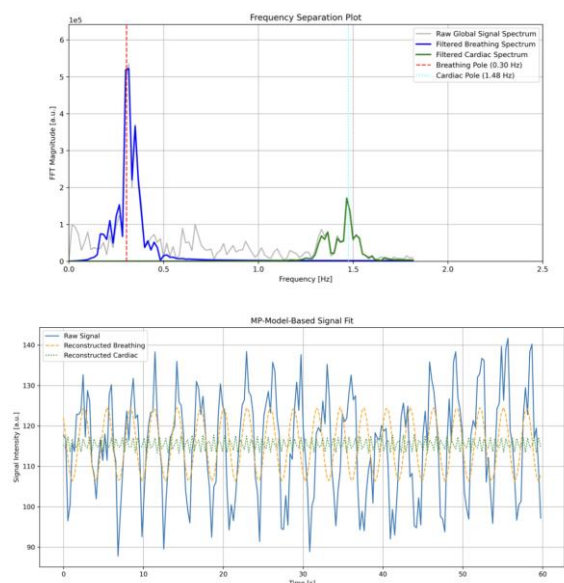


Fig. 1: Physiological MP signal decomposition. (A) The frequency spectrum of the global lung signal, showing distinct peaks for breathing and cardiac motion. The MP method identifies the dominant physiological poles from these peaks. (B) The resulting model-based fit for a representative voxel in the time domain. The raw signal intensity over time (solid blue line) is decomposed using the MP method into its breathing (dashed orange line) and cardiac (dotted green line) components.

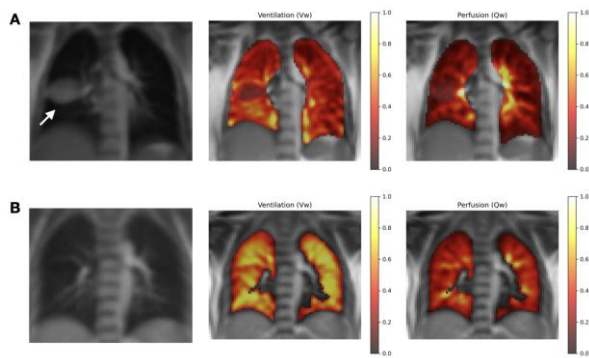


Fig. 2: Exemplary ventilation (V_w) and perfusion (Q_w) maps from two subjects. (A) Results from a patient with a tumor in the left lung (indicated by the white arrow on the anatomical reference image). The ventilation map shows a large, matched defect with low signal intensity corresponding to the tumor's location, and a corresponding perfusion defect is also visible. (B) In contrast, a healthy volunteer demonstrates relatively homogeneous distribution of both ventilation and perfusion throughout the lung parenchyma.

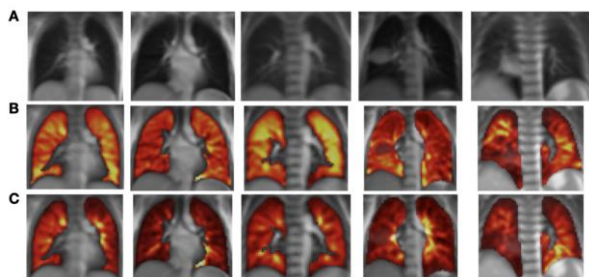


Fig. 3: Representative ventilation (V_w) and perfusion (Q_w) maps from all five subjects. The first three columns display results from healthy volunteers, while the final two columns show results from patients with lung tumors. For each subject, the anatomical reference image (A) is shown, along with the corresponding calculated ventilation (B) and perfusion (C) maps overlaid.

Results: The Matrix Pencil method successfully identified the dominant physiological poles from the raw signal data. Using this information, a clear separation of the signal components corresponding to breathing and cardiac frequencies was achieved for each voxel (Figure 1). This robust signal decomposition was consistently observed in scans from both healthy volunteers and patients.

To visually assess the method's feasibility, the separated components were used to generate ventilation (V_w) and perfusion (Q_w) maps, which were then normalized to the maximum (0-1). As demonstrated in Figure 2, this approach allowed for a clear depiction of lung function. The normalized maps revealed homogeneous ventilation and perfusion in healthy lungs of all volunteers, while pulmonary defects in patient scans were clearly identifiable as regions with reduced signal intensity.

Discussion: The analysis of the ventilation and perfusion maps in healthy volunteers and lung tumor patient demonstrated the feasibility of extending the Matrix Pencil decomposition method to low-field MR-Linac data. The MP approach improved the separation of overlapping physiological signals, producing perfusion maps with high contrast between pulmonary vessels and lung parenchyma. This improvement comes from the method's ability to target specific signal patterns defined by physiological poles. A key methodological insight was the robustness of the sequential least squares estimation (LSE). By first modeling and subtracting the ventilation signal, the subsequent fitting of the lower-amplitude perfusion signal became more accurate and stable, allowing the detection of peripheral perfusion components that may be suppressed by other methods.

Conclusion: We demonstrate that the Matrix Pencil method can be successfully applied to 0.35 T MRI-Linac data, providing reliable decomposition of ventilation and perfusion signals. The approach worked well in both healthy volunteers and lung tumor patients, offering enhanced separation of physiological components and improved functional mapping without the need for contrast agents or breath-holds.

Acknowledgements: RK and LRP acknowledge funding by the German Center for Lung Research (DZL).

References:

1. Klaar, R., Rabe, M., Gaass, T. *et al.* Ventilation and perfusion MRI at a 0.35 T MR-Linac: feasibility and reproducibility study. *Radiat Oncol* 18, 58 (2023). <https://doi.org/10.1186/s13014-023-02244-1>
2. Bauman G, Bieri O. Matrix pencil decomposition of time-resolved proton MRI for robust and improved assessment of pulmonary ventilation and perfusion. *Magn Reson Med* 77(1):336-342 (2017). doi: 10.1002/mrm.26096

Coregistration of Intraoral Optical Scan with Dental MRI for Visualization of Pulp Anatomy: A case report with CBCT comparison

Bennet Rzepka 1*, Jan-Bernd Hövener 1, Monika Huhndorf 1
1 Kiel, Klinik für Radiologie und Neuroradiologie

Abstract: This case report demonstrates the feasibility of coregistering intraoral optical scans with 3T dental MRI for visualizing pulp anatomy, supported by a CBCT comparison. A full-arch and single-tooth intraoral scan were aligned with MRI data using 3D Slicer and 3Shape Implant Studio. Due to the good soft tissue contrast of the MRI, the pulp and canal anatomy can be clearly seen without radiation. This workflow could demonstrate a possible step in endodontic toward safer and more precise diagnostics.

Motivation: Diagnostic imaging plays a key role in the field of endodontics. Accurate assessment of dental pulp anatomy is crucial in endodontics, trauma diagnosis, and minimally invasive treatment planning (1). Magnetic resonance imaging (MRI) is a non ionising radiation imaging modality which is currently being researched for use in dentistry (2). Intraoral optical scans provide detailed information about the surface morphology of teeth and MRI offers the capability to image internal structures such as the dental pulp and root canals in a non-invasive way (2). This case report presents the coregistration of a full-arch and a single tooth intraoral scan with 3T dental MRI. Furthermore it shows a comparison to cone beam computed tomography (CBCT). The aim is to explore the feasibility of combining these imaging modalities for dental diagnostics.

Materials & Methods: First, a full-arch intraoral scan is performed using the 3Shape TRIOS scanner. This is followed by 3T dental MRI (Cima.X, Siemens), acquired with a mandibular coil using SPACE and T2 TSE sequences. In addition, a cone-beam computed tomography (CBCT) scan of the same region is taken for comparison purposes. In a separate step, a single tooth is scanned with higher resolution using a MRI surface coil. Coregistration of the different imaging datasets is carried out using the open-source software 3D Slicer in combination with the 3Shape Implant Studio planning program. Landmarks and segmented surfaces are used to aid alignment. The pulp morphology is segmented from the MRI data and compared to the pulp visibility in the CBCT images.

Results: We expect successful coregistration of full-arch and single-tooth scans with greater anatomical detail in the single-tooth MRI dataset. MRI derived pulp volumes are expected to exhibit higher soft tissue contrast than CBCT images. This case report should enable three-dimensional visualization of the dental pulp within the optical scan and outline a new potential workflow for pulp imaging in the context of dentistry and endodontics.

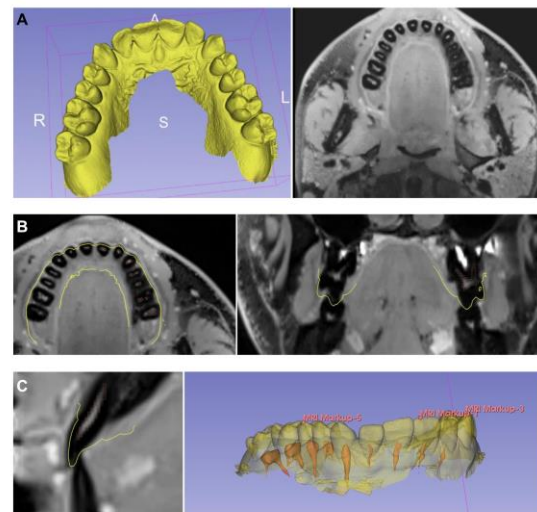
Discussion: This case demonstrates the diagnostic potential of combining intraoral scanning with 3T dental MRI. The MRI scan provided clear visualization of pulp tissue, especially in the single tooth scan. Knowledge of pulp and canal anatomy

is essential in endodontics to avoid treatment errors like perforations. This workflow could contribute to improving precision and safety. Compared to CBCT, MRI offers soft tissue contrast without radiation exposure, making it especially valuable in pediatric, trauma, or endodontic cases (3). Previous studies have also shown promising results using coregistration techniques in implant planning (4). Despite its advantages, clinical application remains challenging due to high costs, longer acquisition times, susceptibility to artifacts, and the need for specialized equipment (5). Nonetheless, this radiation free approach could represent a promising step toward safer and more precise diagnostics in endodontics

Coregistration of Intraoral Optical Scan with Dental MRI for Visualization of Pulp

Anatomy: A case report

1. Optical intraoral scan and 3T dental MRI (space, 0,7x0,7x0,7mm)
2. Coregistration and segmentation pulp and root canals (program: 3D slicer)
3. 3D-modell with visualization of the pulp tissue



Conclusion: The case illustrates that the integration of intraoral scanning with 3T dental MRI presents a promising method for dental diagnostics that does not involve radiation. It is possible to visualize and align internal and external tooth anatomy, which is crucial for effective endodontic treatment. Although there are still difficulties such as high costs, long scan times and artefact management. But improvements in MRI technology and coregistration methods could increase the clinical applicability. This workflow is especially advantageous for paediatric, trauma and endodontic cases where non-invasive imaging is desired, resulting in dental treatment that is safer, more precise and minimally invasive.

Acknowledgements: I would like to thank Prof. Hövener for the opportunity to conduct research in the field of dental MRI. I am also grateful to Dr. Huhndorf for her support during the

MRI scans, and to everyone who has kindly assisted me with their expertise and advice.

References:

1. Sarsam et al. (2025), *The role of imaging in endodontics*, *British dental journal*
2. Flügge et al. (2023), *Dental MRI—only a future vision or standard of care? A literature review on current indications and applications of MRI in dentistry*, *Dentomaxillofacial Radiolog*
3. Assaf et al. (2015), *Early detection of pulp necrosis and dental vitality after traumatic dental injuries in children and adolescents by 3-Tesla magnetic resonance imaging*, *Journal of Cranio-Maxillofacial Surgery*
4. Flügge et al. (2020), *Virtual implant planning and fully guided implant surgery using magnetic resonance imaging—Proof of principle*, *Clinical Oral Implants Research*
5. Candemil et al. (2024), *Accuracy of Magnetic Resonance Imaging in Clinical Endodontic Applications: A Systematic Review*, *Journal of endodontics*

Towards Reliable SABRE Hyperpolarization: Optimizing Stability of a [1-¹³C]Pyruvate polarizer

Martin Sandbrink 1*, Philip Saul 1, Julia Rosin 1, Jule Kuhn 1, Charbel Assaf 1, Ella Dieball 1, Yenel Gökpek 1, Josh Peters 1, Caspar Sax 1, Harriet Wulff 2, Stefan Petersen 3, Henri de Maissin 3+4, Andrey Pravdivtsev 1, Andreas Schmidt 3+4, Jan-Bernd Hövener 1

1 Department of Radiology and Neuroradiology, Section Biomedical Imaging, University Hospital Schleswig-Holstein, Kiel University, Kiel, Germany

2 Department of Physics, University College Cork, T12 CY82 Cork, Ireland

3 Department of Radiology, Medical Physics, Medical Center—University of Freiburg, Faculty of Medicine, University of Freiburg, Breisacherstrasse 60a, Freiburg 79106, Germany

4 German Cancer Consortium (DKTK), partner site Freiburg, a partnership between DKFZ and University Medical Center Freiburg, Germany

Abstract: In our SLIC-SABRE setup, we demonstrate that both polarization level and reproducibility can be significantly enhanced by controlling the magnetic environment during manual sample transfer. Magnetic field measurements revealed a field reversal inside the polarizer. Removing the outer μ -metal shields improved field stability. Experimentally, we show that optimized magnetic field handling increases the hyperpolarization level and reproducibility of [1-¹³C]pyruvate from (12 ± 2) % to (15.7 ± 0.3) %.

Motivation: Magnetic resonance imaging (MRI) is a widely used diagnostic tool but lacks sensitivity for detecting metabolic processes. Hyperpolarization (HP) techniques address this limitation by enhancing nuclear spin polarization, enabling real-time metabolic imaging with dramatically increased signal intensity.¹ For in vivo applications, dynamic nuclear polarization (DNP) remains the standard, though it is costly, time-consuming, and technically demanding. A novel technic, signal amplification by reversible exchange (SABRE), combined with spin-lock induced level anti-crossings (SLIC), enables rapid, cost-efficient hyperpolarization of biologically relevant molecules such as [1-¹³C]pyruvate, achieving polarization levels exceeding 20%.² However, no commercial equipment is available, and only few setups were reported in literature. Here, we present an implementation of SLIC-SABRE for hyperpolarizing [1-¹³C]pyruvate and evaluate key optimization parameters for the hyperpolarization process.

Materials & Methods: Critical parameters for high and reproducible polarization include B_0 homogeneity, B_1 homogeneity, B_0 power supply stability, shielding, and high-frequency (HF) amplifier noise. The major components include: (i) NMR unit (Fig. 1 A) consisting of a 4-layer μ -metal shield (Twinleaf, MS-2), a two-layer solenoid B_0 coil (360 mm length, 120 mm diameter) creating a magnetic field of $B_0 = 50 \mu\text{T}$, a power supply (Twinleaf, CSBA-30), a one-layer saddle shape B_1 coil (100 mm diameter), and an RF amplifier (Onkyo, TX8555), customized water bath supplied by a compact refrigerated circulating thermostat (Huber, Ministat 230) and reactor consisting of a high pressure 5 mm NMR tube (ii) homemade gas control unit supplying up to 10 bars of para-hydrogen (iii) a process control unit (PCU) consisting of a custom software and a digital-analogue converter (Matlab, National Instruments). The PCU was used to control the timing of the experiments and to generate the spin order transfer sequence (2 min, B1SLIC = 2 μT SLIC pulse + 2 s B1ad = 4 2 μT adiabatic pulse with a 50 Hz frequency modulation slope). The experiments were conducted using a solution containing sodium [1-¹³C]pyruvate (6.97 mM), [Ir(COD)(IMes)Cl] (7.15 mM), dimethylsulfoxide (DMSO

(45.57 mM) and Na₂-EDTA 1.24 mM) dissolved in 600 μL of a methanol-d₄. All magnetic field measurements have been performed using a magnetoresistive vector magnetometer (Twinleaf). Quantification of polarization has been done with a 1 T benchtop NRM-spectrometer (Spinsolve 60 MHz carbon, Magritek) after manual sample shuttling.

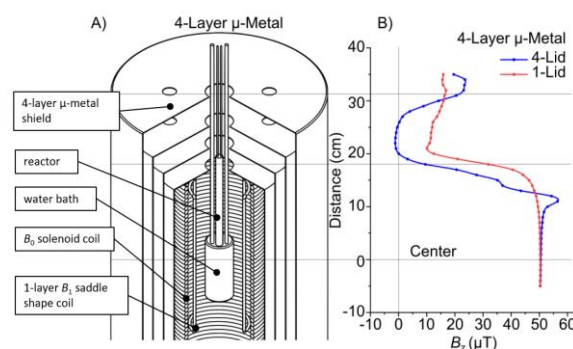


Fig. 1: Schematic view of the NMR unit of the SLIC-SABRE polarizer (A) and magnetic field profile along the z-axis with one lid closed (red) vs. four lids closed (blue)(B).

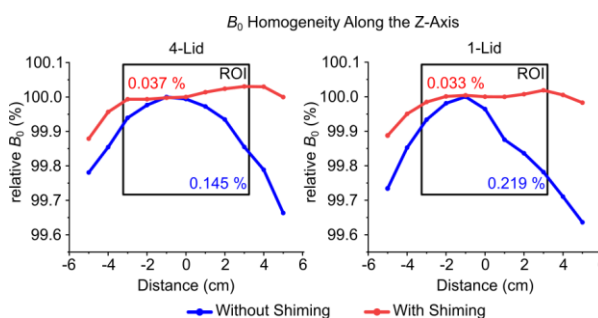


Fig. 2: B_0 Homogeneity of NMR unit along the Z-direction. Unshimed magnetic field in the polarization region showing a roughly parabolic profile with a deviation from maximum of 0.145 % vs. 0.22 %. Manual shimming reduced field deviation to 0.03% in both setups.

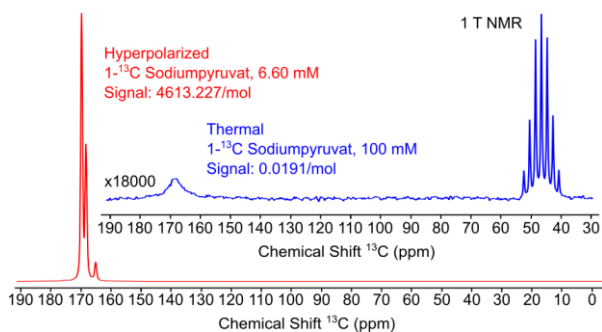


Fig. 3: ^{13}C NMR spectra of thermally and hyperpolarized pyruvate. A 15391-fold enhancement of the signal was observed, corresponding to a polarization of 21.47%. The multiplet in the thermal spectrum at 45 ppm is neat methanol at natural abundance (12.35 mmol).

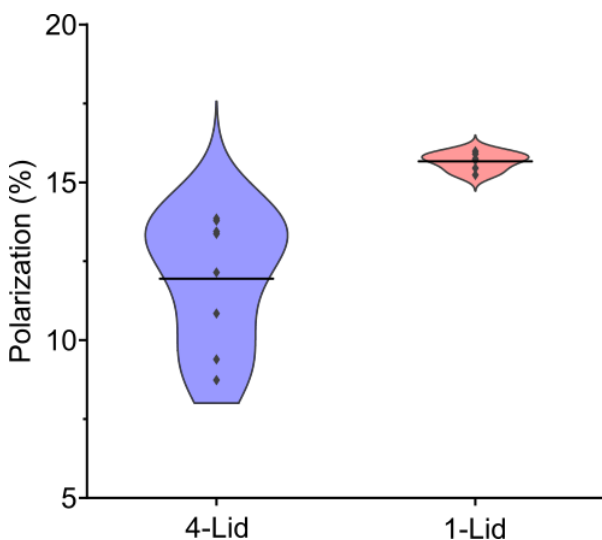


Fig. 4: The polarization of [1- ^{13}C]pyruvate was (11.9 ± 2.0) %, N=8, for four lids and (15.7 ± 0.3) % for one lid setup (N = 6).

Results: Using four magnetic shielding lids reduced the residual magnetic field to less than 0 T at a distance of approximately 5 cm, whereas using only one lid resulted in a minimum measurable field of 10 μT (Fig. 1B).

Removal of the outer mu-metal lids affected the magnetic field within the polarization area. The unshimed field showed a roughly parabolic maximum with a steeper increase for the

one lid setup. We obtained a deviation from the maximum of 0.145% for the four-lid setup and deviation of 0.22% for the setup using one lid. Manually shimming the field improved the homogeneity significantly to a maximum deviation of 0.03% for both setups. The hyperpolarization experiments have been carried out using the shimmed magnetic fields (Fig. 2).

Hyperpolarized [1- ^{13}C]pyruvate was polarized and quantified with respect to a thermally polarized reference (Fig. 3).

We conducted hyperpolarization experiments with the four-lid configuration and the one-lid configuration. On average, the polarization was (12 ± 2) % for the four-lid setup, and (15.7 ± 0.3) % for the one-lid setup (Fig. 4).

Discussion: Exposure of the hyperpolarized sample to near-zero magnetic fields resulted in a significant decrease in polarization levels accompanied by increased variability. This reduction suggests that maintaining a controlled magnetic environment is critical for preserving the enhanced spin polarization achieved during hyperpolarization. Our findings indicate that removing some of the μ -metal shielding lids partially mitigates this effect. However, residual fluctuations in the magnetic field remain, potentially affecting the hyperpolarization. Implementing an active magnetic field source, such as an electromagnet, may offer improved control and stabilization of the local magnetic field, thereby enhancing polarization retention and reproducibility. Additionally, integrating automated sample transfer systems could further minimize exposure to detrimental field variations during handling, reducing variability and preserving polarization.

Conclusion: Maintaining a controlled magnetic environment during transfer was critical to achieving both high polarization levels and reproducibility for [1- ^{13}C]pyruvate. With polarization reaching around 16%, SLIC-SABRE approaches the threshold for potential in vivo use.

References:

1. Nelson, S. J., et al. *Science Translational Medicine*. 2013. 10.1126/scitranslmed.3006070
2. de Maissin H et al. *Angew Chem*. 2023. 10.1002/ange.202306654

Investigating the link between glymphatic function and white matter microstructure in multiple sclerosis

Sascha D. Santaniello 1*, Gabriel Gonzalez-Escamilla 2+3, Markus Janko 1, Marc A. Brockmann 1, Sergiu Groppa 2+3, Ahmed E. Othman 1 & Andrea Kronfeld 1

1 Department of Neuroradiology, University Medical Center of the Johannes Gutenberg University Mainz, 55131 Mainz, Germany

2 Department of Neurology, University Medical Center of the Johannes Gutenberg University Mainz, 55131 Mainz, Germany

3 Department of Neurology, Saarland University Clinic, 66421 Homburg, Germany

Abstract: The glymphatic system (GS) supports brain waste clearance, and its dysfunction has been linked to multiple sclerosis (MS). We investigated the association between GS function, measured using the DTI-ALPS index, and white matter microstructure, assessed via fixel-based analysis (FBA), in 165 MS patients and 57 healthy controls. RRMS patients showed significantly reduced ALPS indices and widespread FBA alterations, particularly in the superior corona radiata, basal ganglia, and thalamus. Significant correlations between ALPS and FBA metrics suggest a link between impaired glymphatic function and microstructural degeneration in MS, supporting the hypothesis that GS dysfunction may contribute to MS-related white matter damage.

Motivation: The glymphatic system (GS) is a pathway that facilitates the movement of cerebrospinal fluid from the subarachnoid space into brain parenchyma, where it mixes with interstitial fluid to remove metabolic waste through the perivascular space[1]. GS dysfunction contributes to central nervous system pathology and it has been shown that neurological diseases like multiple sclerosis (MS) are linked to an abnormal accumulation of neurotoxic compounds. A non-invasive method to evaluate GS characteristics is the diffusion tensor image analysis along the perivascular space (DTI-ALPS)[2], where the ALPS index is computed from diffusion-weighted images in a region of interest (ROI) in the periventricular white matter (WM), providing a proxy for glymphatic activity and the efficiency of waste clearance from the brain. Despite its utility, traditional DTI-derived metrics have limitations in detecting microstructural changes, especially in regions with complex fiber architecture common to WM connections. Fixel-based analysis (FBA) overcomes these limitations by providing a more detailed estimate of microstructural changes within a population of fibers in a single voxel (fixel), yielding three metrics: fiber density (FD), fiber-bundle cross-section (FC), and their combined effect (FDC). These metrics allow for a more refined assessment of pathophysiological changes, such as fiber loss or atrophy, on a microscopic level, by capturing intra-axonal volume changes (FD) and macroscopic alterations in fiber bundle size (FC). In this study, we conducted and correlated DTI-ALPS and FBA to investigate the association between glymphatic function and WM microstructure integrity in healthy controls (HC), clinically isolated syndrome (CIS) and relapsing-remitting MS (RRMS) patients.

Materials & Methods: T1- and diffusion weighted image data of 165 adult MS patients (30 with clinically isolated syndrome; 17 of which female; and 135 relapsing-remitting MS, 91 female) and 57 healthy age- and sex-matched subjects (HC) were included in this retrospective study. Scanning was performed on a Magnetom Trio 3 T Siemens scanner. A T1-weighted MPRAGE was used with the following parameters:

Voxel size=1x1x1 mm, repetition time (TR)=1900 ms, echo time (TE)=2.52 ms, flip angle=9°, field of view (FOV)=256*256 mm. The T2-weighted echo-planar imaging sequence used to obtain the diffusion-weighted image data had the following parameters: Voxel size 2x2x2.5 mm, TR=9000 ms, TE=102 ms, flip angle=90°. 30 diffusion directions at b=900 s/mm² as well as one image at b=0 s/mm² were acquired. The DTI-ALPS index was calculated automatically for each individual using four spherical ROIs in standard space. FBA metrics (FD, FC, FDC) were computed using the MRtrix3 framework including preprocessing, response function estimation, and population template creation. Group comparisons were performed using connectivity-based fixel-enhancement with non-parametric permutation testing. In addition, correlations between mean FBA metrics and ALPS index values were assessed using Pearson correlation.

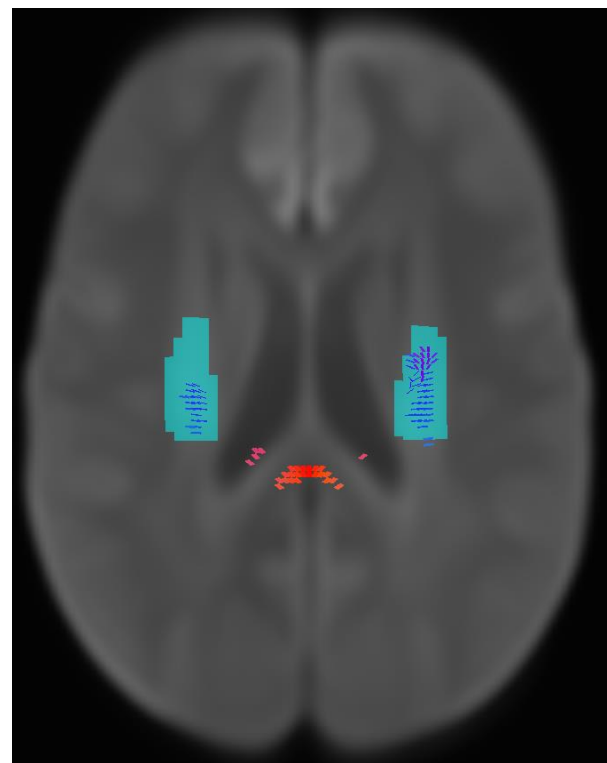


Fig. 1: Shown are the fixels that differ significantly between the healthy control group (HC) and the RRMS patient group (FEW corrected p-value <0.05) regarding fiber density and bundle cross-section (FDC). The blue ROI indicates the superior corona radiata - a region whose ROI is also used in the ALPS index calculation.

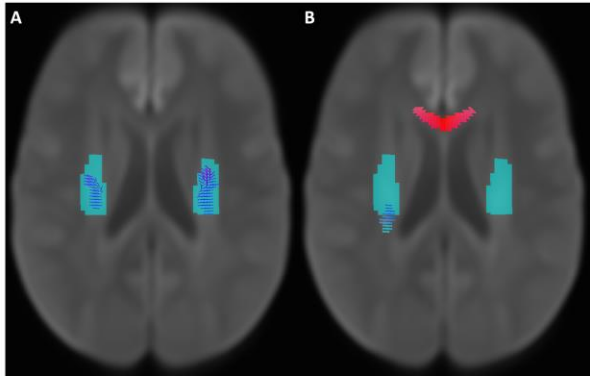


Fig. 2: A) Shown are fixels that differ significantly between the healthy control group (HC) and the RRMS patient group (FEW corrected p -value <0.05) regarding fiber bundle cross-section (FC). The blue ROI indicates the superior corona radiata shown in blue. B) Differences between CIS and RRMS group are shown, superior corona radiata shown in blue.

Results: A multiway ANOVA showed significant differences between the three groups regarding the left ($p=0.0047$), right ($p=0.0151$) and mean ALPS index ($p=0.0039$), and a post hoc test showed, that there was a statistically significant decrease of the ALPS index of RRMS patients compared to healthy controls for the left side ($p=0.0032$), the right side ($p=0.0115$) and as a mean ($p=0.0025$). Statistically significant differences between HC and RRMS groups were found for all FBA metrics. Especially regarding FC and FDC, the fixels that differ significantly (after FWE, $p<0.05$) between the two groups were located in the superior corona radiata (Fig. 1 & 2). Additionally, left, right and mean ALPS index values showed significant correlations with mean FD, FC and FDC in basal ganglia and thalamus ROIs.

Discussion: Our preliminary results indicate that glymphatic dysfunction, as reflected by a reduced ALPS index, may contribute to or reflect microstructural WM degeneration in MS. In particular, the frequent occurrence of significant fixels in the superior corona radiata, which also plays a role in

determining the ALPS index, suggests that there could be a connection between the state of the glymphatic system and the structural integrity of the WM microstructure in said area. The differences between groups found in the basal ganglia and thalamus, which are known to experience atrophic changes over the course of MS [3], may be associated with altered glymphatic function, supporting the hypothesis that axonal damage contributes to MS pathogenesis [4]. However, further work is needed to gain deeper insights into this context.

Conclusion: Our findings suggest a link between glymphatic dysfunction and WM degeneration in RRMS. Reduced ALPS index and FBA derived changes, particularly in the superior corona radiata, basal ganglia, and thalamus, indicate that impaired glymphatic function may contribute to MS-related microstructural damage or vice versa.

Acknowledgements: The work was supported by the Deutsche Forschungsgemeinschaft (DFG, grant agreement number 515302522 / SPP 2177). The funders had no role in method design, data selection and analysis, decision to publish, or preparation of the manuscript.

References:

1. Plog, B. A., & Nedergaard, M. (2018). "The glymphatic system in central nervous system health and disease: past, present, and future." *Annual Review of Pathology: Mechanisms of Disease*, 13, 379-394. <https://doi.org/10.1146/annurev-pathol-051217-111018>
2. Taoka, T., Masutani, Y., Kawai, H., et al. (2017). Evaluation of glymphatic system activity with the diffusion MR technique: diffusion tensor image analysis along the perivascular space (DTI-ALPS) in Alzheimer's disease cases. *Jpn J Radiol*, 35(4), 172-178. doi: 10.1007/s11604-017-0617-z.
3. Nishii, T., Hirata, A., Masaki, T., et al. (2000). [Reduced signal intensity of T2 weighted MR imaging of thalamus and putamen in multiple sclerosis in Japan]. *Rinsho Shinkeigaku*, 40: 677-682.
4. Carandini, T., Mancini, M., Bogdan, I., et al (2021). "Disruption of brainstem monoaminergic fibre tracts in multiple sclerosis as a putative mechanism for cognitive fatigue: a fixel-based analysis." *Neuroimage Clin*. 2021;30:102587. doi: 10.1016/j.nicl.2021.102587.

Hyperpolarization of Pyruvate using SLIC-SABRE and a Perfluorinated Catalyst

Philip Saul 1*, Martin Sandbrink 1, Jan-Bernd Hövener 1

Universitätsklinikum Schleswig-Holstein, Sektion Biomedizinische Bildgebung, Klinik für Radiologie und Neuroradiologie, Am Botanischen Garten 14, 24118 Kiel

Abstract: In this work, we show the hyperpolarization of 1-¹³C-pyruvate, an important metabolite for imaging of cancerous tissue, with a fluorinated catalyst. For polarization a signal amplification by reversible exchange (SABRE) experiment has been conducted, combined with spin lock induced crossing (SLIC). This combined SLIC-SABRE[1] approach allows for efficient polarization while used catalyst has favorable dissolution properties in water, allowing for a more efficient purification of the hyperpolarized pyruvate, thus taking an important step towards affordable and biocompatible hyperpolarized contrast agents for early cancer detection.

Motivation: Hyperpolarization is an important technique to significantly enhance the inherently low sensitivity of magnetic resonance experiments. In this context, magnetic resonance imaging (MRI) is of outstanding importance because hyperpolarization can allow for the direct observation of e.g. metabolic processes of compounds of interest. Pyruvate has gained quite some attention in the last years, mainly because of its altered metabolism in cancerous tissue, where it's converted to lactate. However, for direct application in the clinical context, some challenges have to be faced for different hyperpolarization techniques. While dynamic nuclear polarization (DNP) is the most reliable source of polarization to this day, it is very time consuming, taking up to several hours for a single batch of contrast agent. Additionally, the removal of organic radicals used for hyperpolarization, remains a challenge. Another source of polarization is para-hydrogen (pH₂). This isomer of hydrogen gas can be used to store magnetization and at a later point, transfer it to a molecule of interest, either through a chemical reaction (PHIP) or via a catalyst facilitating the transfer (SABRE). In both cases the hyperpolarization process can be finished within tens of seconds, making it significantly quicker than DNP. The remaining challenge, the removal of the used solvent (methanol) and the Iridium containing catalyst remains a challenge. This challenge, however can be solved by precipitation and filtration of the catalyst with the used

fluorinated catalyst being even less water soluble than the previously used ones.[2]

Materials & Methods: Polarization of 1-¹³C-pyruvate was conducted, using an in-house built SLIC-SABRE polarizer, with an automated bubbling setup. Furthermore, the polarizer consists of a μ -metal shield housing a copper coil as well as shim coils needed for field homogeneity. The sample solution consisted of methanol, the fluorinated catalyst, pyruvate and dimethyl sulfoxide (DMSO), while the para-hydrogen was supplied through a capillary at 8 bars of pressure. After the polarization in the aforementioned setup, the sample was manually transferred to a Magritek 1 T benchtop NMR for the detection of the hyperpolarized NMR signal.

Results: We were able to demonstrate the polarization of 1-¹³C-pyruvate to levels above 2% using a fluorinated catalyst which allows for efficient removal after the polarization experiment. The use of this novel catalyst was successfully implemented in our in-house built SLIC-SABRE setup, showing numbers comparable to our first attempts with other catalysts, allowing for a lot of improvement in the future.

Conclusion: This work paves the way for establishing the SLIC-SABRE method in combination with a new catalyst for hyperpolarized metabolic imaging. Further improvements, especially concerning the hardware, will allow for a cleaner path to an automated generator of hyperpolarized pyruvate.

References:

- [1] S. Knecht, A.S. Kiryutin, A.V. Yurkovskaya, K.L. Ivanov, *Molecular Physics* 2019, 117, 2762 – 2771.
- [2] J. Ettegui, B. Blackman, N. Raju, S.A. Kotler, E.Y. Chekmenev, B.M. Goodson, H. Merkle, C.C. Woodroffe, C.A. LeClair, M.C. Krishna, R.E. Swenson, *J. Am. Chem. Soc.* 2024, 146, 1, 946–953.

Higher levels of Lipoprotein (a), C-reactive protein and Interleukin-6 are associated with smaller hippocampal subfields

C. Schneider¹, Y. Tabi¹, O. Granert¹; A. Hanert¹, J. Rave¹, M. Heine¹, M. Manegold¹, L. Bonde¹, L. Erpenstein¹, M. Laudes³, C. Geisler³, J. Baines^{2,4}, T. Bartsch¹

¹ Neurology Department, University Medical Centre Kiel, Kiel University, Germany

² Institute for Experimental Medicine, Section Evolutionary Medicine, Kiel University, Germany

³ Institute of Diabetes and Clinical Metabolic Research, University Medical Center Schleswig-Holstein, Kiel, Germany

⁴ Evolutionary Medicine Group, Max Planck Institute for Evolutionary Biology, Plön, Germany

Abstract: The hippocampus plays a key role in cognitive processes such as learning and memory (Bartsch & Wulff, 2015). It can be structurally altered by neurological diseases such as Alzheimer’s or limbic encephalitis (Bartsch, 2012). Due to its characteristic neuroplasticity, it is especially vulnerable (Bartsch & Wulff, 2015). An obesity-related lifestyle can reduce adaptive cellular stress responses, promote oxidative stress and systemic inflammation, impairing neurogenesis and increasing neurodegeneration (Fontan-Lozano *et al.*, 2007; Stranahan, 2015). Here, Lipoprotein (a), a non-modifiable blood parameter, was associated with smaller hippocampal volumes. In addition, higher concentrations of IL-6 and CRP were linked to smaller hippocampal volumes.

Motivation: Obesity has been linked to a wide range of health complications such as cardiovascular diseases and Type 2 diabetes as well as depression and neuropathy (WHO, 2022). In Germany, 19% of adults are obese. It’s prevalence has continued to increase since 2012 for both women (+2.5%) and men (+2.1%). nearly 13 million adults in Germany are obese (Schienkiewitz *et al.*, 2022). Obesity is often accompanied by metabolic alterations as well as increased inflammation, which have both been observed to impact neuronal health (Ho *et al.*, 2013; Vafaei-Nezhad *et al.*, 2022, Sadeghi *et al.*, 2016; Strahanan, 2008; Erta *et al.*, 2012)

From a cognitive standpoint, the question arises, of how neurological function might be impacted by obesity. How do the metabolic changes manifest neurologically? Do lifestyle factors impact neuronal health more than genetic components?

In an attempt to better understand the potential impact of obesity on cognitive function, this master thesis delves into the influence of specific biological parameters and inflammatory markers on hippocampal structural integrity.

Materials & Methods: For this thesis MRI, blood parameters and biographical data of 94 participants (FOCUS/Cognifast study) were revisited. Two groups of 47 participants were analysed. The obese group with a BMI >30 kg/m² (43.61 years ± 11.61 years, 6 male) and a control group BMI >18 <25 kg/m² (43.99 years ± 10.37 years, 5 male). All examinations were performed on 3T MRI scanners. For the participants in the FoCUS study, the model Phillips Achiva with a 32-channel head coil (Dual coil) was used (Achieva; Phillips Medical Systems, Eindhoven, the Netherlands). The scans for the Cognifast study were done on the Phillips Ingenia CX using multi-coil. Volumetric data was generated using Freesurfer (version 7.2.0), data was then checked for correct segmentations using ITK-Snap (version 4.0.2) before all volumina were corrected for head size and age using a GLM.

Final statistical analysis was performed with IBM/SPSS (version 28.0.1.0) and JASP (version 0.18.3) as well as Python.

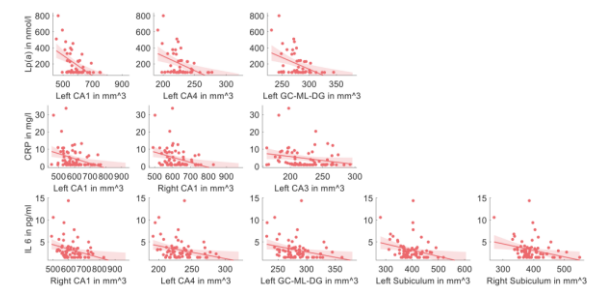


Fig. 1: Lipoprotein (a), C-reactive protein (CRP) and Interleukin 6 (IL 6) negatively correlated with hippocampal subfields. There was evidence for negative correlations between Lp (a) and left CA1, left CA4 and left GC-ML-DG. Further, biomarkers for inflammation, CRP and IL 6, were negatively associated with left CA1, right CA1 and left CA3; and right CA1, left CA4, left GC-ML-DG, left subiculum and right subiculum respectively.

	Left CA1	Left CA4	Left GC-ML-DG	Left CA3	Left subiculum	Right CA1	Right subiculum
Lp(a)	72.208	15.723	14.133	2.5885	0.4152	1.2082	1.0191
Lp(a) without flooring	4.887	2.052	2.456	/	/	/	/
CRP	17.783	1.3998	1.0625	4.306	0.3625	7.326	0.5450
IL-6	2.6045	3.7028	4.6935	0.3954	4.11	4.11	4.11

Fig. 2: Lipoprotein (a), C-reactive protein (CRP) and Interleukin 6 (IL-6) negatively correlated with hippocampal subfields.

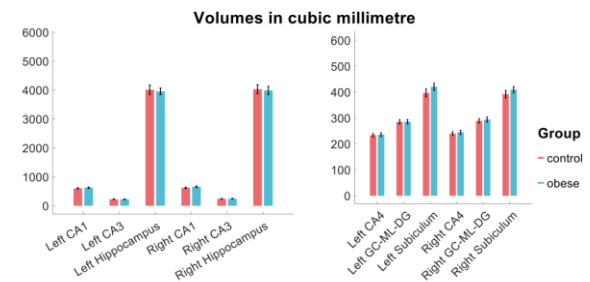


Fig. 3: Hippocampal volumes did not differ between groups. Bayesian U-test analysis did not provide evidence for a difference between controls and obese in hippocampal volumes and subfields.

Results: Bayesian correlation analysis using Kendall’s tau showed a negative correlation between Lp (a) and left hippocampal subfields CA1 ($r = -0.35$, $BF_{10} = 72.208$), CA4 ($r = -0.30$, $BF_{10} = 15.723$), and the granule cell layers of the dentate gyrus (GC-ML-DG; $r = -0.29$, $BF_{10} = 14.133$), suggesting that higher blood levels of Lp (a) are associated with lower hippocampal subvolumes (Fig. 1). When the

flooring effect for Lp(a) caused by the laboratory measurement method and observed in Figure 3 was accounted for by filtering out Lp(a) values under 100 nmol/l, the correlation with left CA1 proved to be robust ($r = -0.35$, $BF_{10} = 4.887$), while correlations with left CA4 ($r = -0.29$, $BF_{10} = 2.052$) and GC-ML-DG ($r = -0.30$, $BF_{10} = 2.456$) were henceforth anecdotal. CA1 was previously associated with retrieval of remote episodic memory and the autoegetic consciousness (Bartsch et al., 2011), and there is emerging evidence for its significance in the development of Alzheimer's disease (Khan et al, 2015; Shim et al., 2017).

Further, C-reactive protein and interleukin 6 showed a negative relationship with left CA1 ($r = -0.25$, $BF_{10} = 17.783$), right CA1 ($r = -0.23$, $BF_{10} = 7.326$) and left CA3 ($r = -0.21$, $BF_{10} = 4.306$); and – respectively – right CA1 ($r = -0.21$, $BF_{10} = 4.11$), left CA4 ($r = -0.21$, $BF_{10} = 3.703$), left GC-ML-DG ($r = -0.21$, $BF_{10} = 6.694$), left ($r = -0.21$, $BF_{10} = 4.11$) and right subiculum ($r = -0.21$, $BF_{10} = 4.11$). CA3, with its recurrent collateral connections, enables fast retrieval of spatial location and associations with objects (Cherubini & Miles, 2015).

Discussion: Despite a significant difference in BMI between the obese and non-obese cohorts, the anticipated direct association between obesity and reduced hippocampal volume was not observed in this study (Fig.2).

Our findings of Lp(a), CRP, and IL-6 association with lower volumes of hippocampal subfields are particularly relevant given the role of these biomarkers in systemic inflammation and their link to cognitive impairment and neurodegenerative diseases. While the association between Lp(a) and vascular disease is well documented (e.g., Lau & Giugliano, 2022), there is only little research on its direct impact on the hippocampus. The ischemic impact of Lp(a) may exacerbate the vulnerability of the hippocampus to neurodegenerative conditions. Lp(a)'s pro-inflammatory properties could provoke or worsen neuroinflammatory pathways in the brain, contributing to reduction in hippocampal volume and potential cognitive decline (Ridker et al., 2021; Stiekema et al., 2020; Simantiris et al., 2023)

Chronic low-grade inflammation, characterized by elevated levels of inflammatory markers like CRP and IL-6, was observed in patients with cognitive impairment and age-related cognitive decline (Ge et al., 2013; Weaver et al., 2002), as well as Alzheimer's patients (Erta et al., 2012). IL-6 specifically is linked to inflammation in the hippocampus of Alzheimer's patients, with higher levels found around amyloid plaques in both patients and animal models (Wang et al., 2015). High CRP levels are associated with lower overall hippocampal volume (Wang et al., 2022; Satizabal et al., 2012).

Conclusion: In conclusion, the implications of the findings presented here are significant for both clinical practice and future research. They suggest that interventions aimed at reducing levels of systemic inflammation in obese individuals may help mitigate some of the neurocognitive risks associated

with obesity. Furthermore, these results underscore the importance of considering a broader spectrum of factors when studying the impact of obesity on brain health, including detailed metabolic and inflammatory profiles. Future studies should aim to include a more extensive array of metabolic and inflammatory markers and consider longitudinal designs to better understand the temporal relationship between obesity, marker variability, and changes in brain structure and function.

Acknowledgements: I would like to thank Prof. Dr. med Thorsten Bartsch for his warm welcome in Kiel, his supervision, his patience, his invaluable expertise and personal advice. I would also like to thank Oliver Granert and Younes Tabi for their methodological support, advice and the time they invested in me.

References:

- Bartsch, T., & Wulff, P. (2015). The hippocampus in aging and disease: From plasticity to vulnerability. *Neuroscience*, 309, 1–16. <https://doi.org/10.1016/j.neuroscience.2015.07.084>
- Bartsch, T. (Hrsg.). (2012). *The clinical neurobiology of the hippocampus: An integrative view (First edition)*. Oxford University Press.
- Fontán-Lozano, Á., Sáez-Cassanelli, J. L., Inda, M. C., De Los Santos-Arteaga, M., Sierra-Dominguez, S. A., López-Lluch, G., Delgado-García, J. M., & Carrión, Á. M. (2007). Caloric Restriction Increases Learning Consolidation and Facilitates Synaptic Plasticity through Mechanisms Dependent on NR2B Subunits of the NMDA Receptor. *The Journal of Neuroscience*, 27(38), 10185–10195. <https://doi.org/10.1523/JNEUROSCI.2757-07.2007>
- Stranahan, A. M. (2015). Models and mechanisms for hippocampal dysfunction in obesity and diabetes. *Neuroscience*, 309, 125–139. <https://doi.org/10.1016/j.neuroscience.2015.04.045>
- WHO & Nutrition, Physical Activity & Obesity (NAO), Office for Prevention & Control of NCDs(MOS). (2022, 2. Mai). WHO European Regional Obesity Report 2022. <https://www.who.int/europe/publications/i/item/9789289057738>
- Schlenkewitz, A., Kuhnert, R., Blume, M., & Mensink, G. B. M. (2022b). Overweight and obesity among adults in Germany—Results from GEDA 2019/2020-EHIS. <https://doi.org/10.25646/10293>
- Ho, N., Sommers, M. S., & Lucki, I. (2013a). Effects of diabetes on hippocampal neurogenesis: Links to cognition and depression. *Neuroscience & Biobehavioral Reviews*, 37(8), 1346–1362. <https://doi.org/10.1016/j.neubiorev.2013.03.010>
- Vafaei-Nezhad, S., Vafaei-Nezhad, M., Shadi, M., & Ezi, S. (2022). The Impact of Diabetes on Hippocampus. In X. Zhang (Hrsg.), *Hippocampus—Cytoarchitecture and Diseases*. IntechOpen. <https://doi.org/10.5772/intechopen.99895>
- Sadeghi, A., Hami, J., Razavi, S., Esfandiary, E., & Hejazi, Z. (2016). The effect of diabetes mellitus on apoptosis in hippocampus: Cellular and molecular aspects. *International Journal of Preventive Medicine*, 7(1), 57. <https://doi.org/10.4103/2008-7802.178531>
- Stranahan, A. M., Arumugam, T. V., Cutler, R. G., Lee, K., Egan, J. M., & Mattson, M. P. (2008). Diabetes impairs hippocampal function through glucocorticoid-mediated effects on new and mature neurons. *Nature Neuroscience*, 11(3), 309–317. <https://doi.org/10.1038/nn2055>
- Erta, M., Quintana, A., & Hidalgo, J. (2012). Interleukin-6, a Major Cytokine in the Central Nervous System. *International Journal of Biological Sciences*, 8(9), 1254–1266. <https://doi.org/10.7150/ijbs.4679>
- Bartsch, T., Döhning, J., Rohr, A., Jansen, O., & Deuschl, G. (2011, September 9). PNAS 2011 Autobiographical memory.pdf.
- Khan, W., Westman, E., Jones, N., Wahlund, L.-O., Mecocci, P., Vellas, B., Tsolaki, M., Kloszewska, I., Soininen, H., Spenger, C., Lovestone, S., Muehlboeck, J.-S., & Simmons, A. (2015). Automated Hippocampal Subfield Measures as Predictors of Conversion from Mild Cognitive Impairment to Alzheimer's Disease in Two Independent Cohorts. *Brain Topography*, 28(5), 746–759. <https://doi.org/10.1007/s10548-014-0415-1>
- Shim, G., Choi, K., Kim, D., Suh, S., Lee, S., Jeong, H., & Jeong, B. (2017). Predicting neurocognitive function with hippocampal volumes and DTI metrics in patients with Alzheimer's dementia and mild cognitive impairment. *Brain and Behavior*, 7(9), e00766. <https://doi.org/10.1002/brb3.766>
- Cherubini, E., & Miles, R. (2015). The CA3 region of the hippocampus: How is it? What is it for? How does it do it? *Frontiers in Cellular Neuroscience*, 9. <https://doi.org/10.3389/fncel.2015.00019>
- Lau, F., & Giugliano, R. P. (2022). Lipoprotein(a) and its Significance in Cardiovascular Disease: A Review. *JAMA Cardiology*, 7(7), 760. <https://doi.org/10.1001/jamacardio.2022.0987>
- Ridker, P. M., Devalaraja, M., Baeres, F. M. M., Engelmann, M. D. M., Hovingh, G. K., Ivkovic, M., Lo, L., Kling, D., Pergola, P., Raj, D., Libby, P., & Davidson, M. (2021). IL-6 inhibition with ziltivekimab in patients at high atherosclerotic risk (RESCUE): A double-blind, randomised, placebo-controlled, phase 2 trial. *The Lancet*, 397(10289), 2060–

Comparison of Aortic Blood Flow in Rabbits using MRI: Physiological vs. Extracorporeal Circulation

Jonah S. Schrauder 1+2, Anna Kathrin Assmann 3, Sinje Reimers 3, Artur Lichtenberg 3, Alexander Assmann 3, Tor Rasmus Memhove 1+4, Amir Moussavi 1+4, Susann Boretius 1+2+4

1* Functional Imaging Laboratory, German Primate Center, Göttingen;
 2 Georg-August University of Göttingen;
 3 Department of Cardiac Surgery, Medical Faculty, Heinrich Heine University, Düsseldorf;
 4 DZHK (German Center for Cardiovascular Research), Partner Site Göttingen.

Abstract: Extracorporeal circulation (ECC) alters blood flow patterns compared to physiological perfusion, but its regional effects remain unclear. Using 9.4 T phase-contrast MRI, we compared aortic flow under physiological, antegrade ECC, and retrograde ECC conditions in rabbits. A triple-VENC approach enabled accurate velocity mapping during ECC, navigator-based retrospective gating was used for physiological flow.

Antegrade ECC most closely resembled physiological flow in proximal and distal aorta, while retrograde ECC showed distinct deviations. Supraaortic and visceral branches showed no significant differences. This study demonstrates a robust MRI framework for evaluating ECC strategies and informs future optimization of perfusion protocols.

Motivation: Extracorporeal circulation (ECC) is vital in cardiac surgery [1], yet its effects on flow dynamics and tissue perfusion are still debated. Comparing ECC with physiological blood flow is essential for understanding these effects. MR imaging of moving organs requires advanced tracking for reliable results [2]. In addition, the wide range of flow velocities during ECC present specific challenges for phase-contrast MRI.

To explore the impact of the different perfusion types, we compared aortic flow during ECC with physiological conditions in a rabbit model using MRI. Non-pulsatile flow was measured using an MR-compatible ECC set up [3], while physiological flow was assessed using navigator-guided, retrospectively gated imaging, both in anesthetized rabbits.

Materials & Methods: All MR data were acquired from healthy rabbits using a 9.4 T Bruker BioSpec equipped with a Tx/Rx birdcage coil. Rabbits were examined under 3 perfusion conditions —physiological, antegrade, and retrograde—each tested on 7 rabbits. Flow MRI covered the entire aorta and major branching vessels, divided into thoracic, abdominal, and pelvic segments, achieving an isotropic spatial resolution of 0.5 mm.

For the continuous ECC blood flow, a specialized MRI protocol utilized 3 Venc values (200, 50, and 20cm/s, TR/TE: 7.5/3.5ms) allowing for accurate reconstruction of a wide velocity range (Fig. 1). For physiological blood flow, Bruker’s FLOWMAP was adapted by adding a navigator, eliminating the need for complex physiological recording (TE/TR: 4/9.3ms, Venc: 100cm/s, 14 oversamplings), and retrospective gating was used to reconstruct pseudo-dynamic physiological flow (Fig. 2) [4]. All datasets were processed using ROMEO phase-unwrapping [5] and polynomial surface fitting on static tissue for background phase correction.

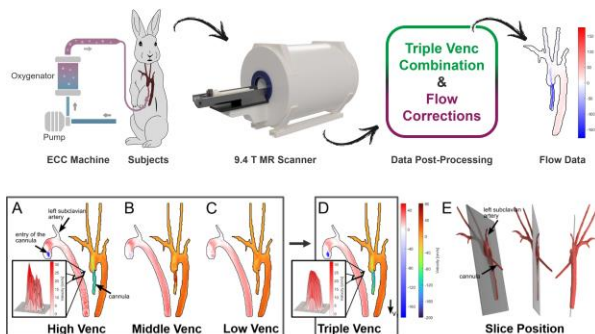


Fig. 1: Workflow of ECC measurement (top) and aortic blood flow analysis (bottom), illustrating noise reduction and elimination of phase aliasing. (A–C) High Venc (200cm/s) shows high noise; middle (50cm/s) and low (20cm/s) Venc reduce noise but introduce phase aliasing in the cannula. (D) Triple Venc combination reduces noise without aliasing.

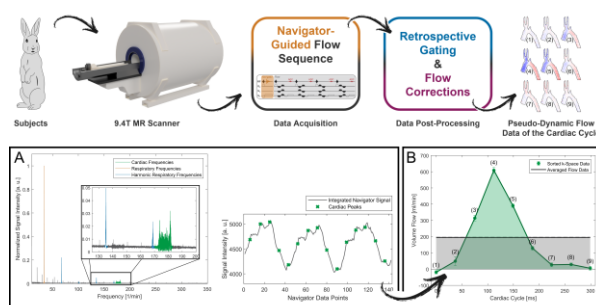


Fig. 2: Workflow of the measurement in anesthetized rabbits (top) and aortic blood flow analysis via retrospective gating (bottom). (A) The frequency spectrum shows minor artifacts. The integrated navigator signal (right) highlights peaks of cardiac activity. (B) Final output includes 9 retrospectively gated pseudo-phases (green) and data averaged over all oversamplings (gray).

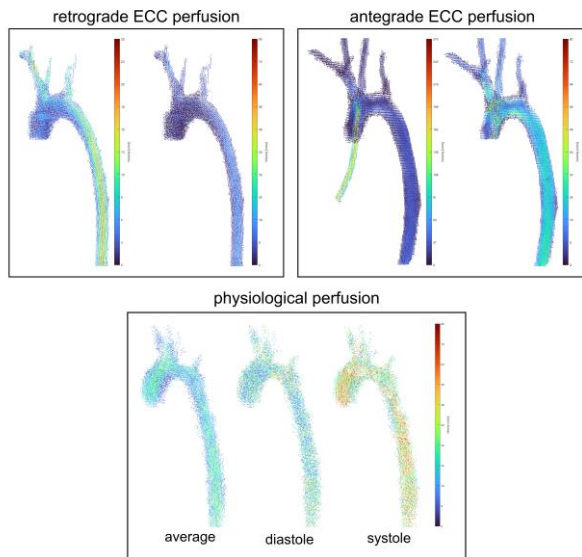


Fig. 3: ECC perfusion (top) are compared to physiological perfusion (bottom). ECC flow is shown with full scale (left) and scaled to 80cm/s without cannula (right). Aortic flow differs between ECC types, but supraaortic branches remain unchanged. Physiological flow is shown as cycle average (left), and during diastole (middle) and systole (right).

Results: Both types of perfusion during ECC were conducted using similar volumetric inflow rates, with only minor variations between individual measurements.

In the ascending aorta, significant differences in volume flow rates were noted between antegrade and retrograde perfusion, while antegrade perfusion and physiological perfusion yielded comparable results. In the biologically downstream segments of the aorta, including thoracic and abdominal areas, substantial differences in blood volume flow rates were observed among all three types of perfusion, with antegrade perfusion showing the highest volume flow rates. In the descending aorta, the volume flow rates for antegrade perfusion were three times higher than those for retrograde perfusion, while the value for physiological flow was intermediate between the two (Fig. 3). In the distal aorta,

volume flow rates were similar for physiological and antegrade perfusion, whereas retrograde perfusion exhibited significantly higher rates. Conversely, in the supraaortic and visceral branches, no significant differences were found among the three types of perfusion.

Discussion: Since ECC perfusion aims to replace cardiac function, it is preferable to achieve volume flow rates that are comparable to physiological conditions, even though pulsatility is absent. Evaluating perfusion conditions specific to the ECC scenario and comparing them to physiological conditions can provide valuable insights for developing optimal procedures for human applications.

Using the triple VENC technique employed here, it was possible to accurately quantify different flow velocities, particularly in the inflow region of the cannula as well as in peripheral areas. As expected, due to the varying flow directions, differences in flow rates between antegrade and retrograde perfusion could be quantified. Interestingly, rather than following a strict pattern, differences between the two ECC methods and the physiological condition varied across different vascular regions.

A significant challenge encountered was the segmentation of small peripheral vessels. For future studies, higher spatial resolution will be necessary to address this limitation.

Conclusion: Using a dedicated triple Venc approach for ECC and a navigator-based method for pseudo-dynamic physiological blood flow, different perfusion strategies could be systematically compared in a rabbit model. The presented methodology enables reliable evaluation of different ECC approaches in vivo, providing a robust foundation for future testing and optimization of new perfusion strategies intended for clinical application in humans.

Acknowledgements: Jonah S. Schrauder is member of the RTG 2824 funded by Deutsche Forschungsgemeinschaft (DFG)

Improving Image Resolution in Deuterium Metabolic Imaging with bSSFP for Clinical Translation at 3T

Rolf F. Schulte 1, Michael Vaeggemose 2+3, Esben SS Hansen 3, Christoffer Laustsen 3

1 GE HealthCare, Munich, Germany

2 GE HealthCare, Copenhagen, Denmark

3 MR Research Centre, Aarhus University, Aarhus, Denmark

Abstract: Motivation: Improve SNR and spatial resolution in deuterium metabolic imaging (DMI) on 3T in humans.

Goals: Implement and validate a bSSFP DMI sequence; investigate whether up-take alone can be a measure for DMI.

Approach: The DMI bSSFP sequence excite the whole volume with a block RF pulse, followed by 3D phase encoding, acquisition and a phase rewinder. Three spatial dimensions are density-weighted phase-encoded, while spectral encoding is insufficient for separating different metabolites but used for artefact reduction.

Results: Voxel size in human brain was improved from (2.4cm)³ for regular, spectrally-resolved MRSI to (1.5cm)³ for bSSFP MRSI in 10 minutes scan time with minor loss in SNR.

Impact (≤40 words)

DMI provides valuable clinical information, such as tumour-treatment response, and might complement or even partially substitute PET. The significant gain in spatial resolution demonstrated here could be the missing link to establish DMI clinically on 3T.

Motivation: Deuterium Metabolic Imaging (DMI) provides valuable dynamic metabolic information and has great clinical potential. Most commonly, [6,6'-2H₂]glucose is ingested and data is acquired with MR Spectroscopic Imaging (MRSI) [1]. Scanning deuterium on Ultra-High Field (B₀≥7T) is highly advantageous because of SNR gain and better spectral separation. However, these scanners are rare in clinical settings and DMI needs to run on clinical 3T scanners to facilitate clinical adoption. Challenges of DMI at 3T include spectral overlap and low SNR, limiting the achievable spatial resolution.

A balanced steady-state free precession (bSSFP) sequence implemented on a preclinical 15.2T scanner demonstrated a significant gain in SNR, while still resolving the spectral dimension sufficiently [2,3]. Unfortunately, this approach is not easily translatable to 3T, because the TR to encode the spectral dimension becomes too long, hence violating the bSSFP condition: TR<<T₂<T₁.

Spectral encoding might not be needed for glucose DMI, as the accumulation of HDO, glucose, glutamine/glutamate and lactate in tissue can be viewed as a surrogate marker for metabolism, similar to the sugar-analogue 18FDG in PET. Thus, DMI is potentially a non-radioactive alternative to 18FDG PET without requiring cyclotrons and hotlabs. Furthermore, imaging is sufficient for measuring 2H₂O perfusion [4] or long-term enrichment after administration of 2H₂O over multiple days/weeks [5,6] or after administration of [2H₇]glucose [7]. The goal of this work was to implement and validate a bSSFP sequence on 3T to improve resolution, image metabolic activity in human brain and abdomen after [6,6'-2H₂]glucose ingestion, and investigate whether up-take alone can be a measure for DMI.

Materials & Methods: Sequence

The proposed DMI bSSFP sequence excites the whole volume via a hardpulse, followed by 3D-spatial phase encoding, spectral acquisition and finishing with a phase rewinder (Fig.1) to return to the centre of k-space and fulfil the bSSFP condition. While the short acquisition time of 5.5ms is insufficient for resolving the different metabolites at 3T, spectral encoding (BW=15.6kHz, #pts=86) helps to reduce artefacts from coherent RF noise. Three spatial dimensions were encoded using density-weighted MRSI to improve the point-spread function. A long acquisition duration (here 10:58min, 12 repetitions) is required for signal averaging to obtain sufficient SNR, hence neither spectral encoding nor density-weighting has any negative impact on the required overall acquisition duration.

Reconstruction

Data was reconstructed via gridding the non-Cartesian k-space locations onto a Cartesian grid of 1.6-times the matrix size (mtx), spatial zero-filling to twice mtx, followed by 3D-spatial and 1D-spectral FFT. Maps of the overall metabolic activity were generated via selecting the central spectral point, hence excluding potential RF interference at Δf>182Hz. Signal intensity images for spectrally-resolved MRSI acquired for comparison were generated by averaging the 4 largest spectral signals.

Experimental

Four healthy volunteers were scanned on deuterium frequency (19.6MHz) before and after ingestion of 75g of [6,6'-2H₂]glucose both with regular spectrally-resolved density-weighted MRSI (mtx=103, BW=5kHz, #pts=700, #excitations=1678, TR=156ms, flip=70°, acquisition duration/average=4:22min) and bSSFP density-weighted MRSI (mtx=163, BW=15.6kHz, #pts=86, #excitations=6500, TR=8.4ms, flip=65°, acquisition duration/average=55sec). Data was acquired using a dual-tuned 1H/2H transmit-receive birdcage head coil (PulseTeq, Surrey, UK) on a 3T whole-body MRI (MR750, GE HealthCare, Milwaukee, WI, USA). Sequence and reconstruction were implemented in Matlab using the MNS Research Pack, a flexible sequence environment reading and playing RF, gradient waveforms and various modulations from file.

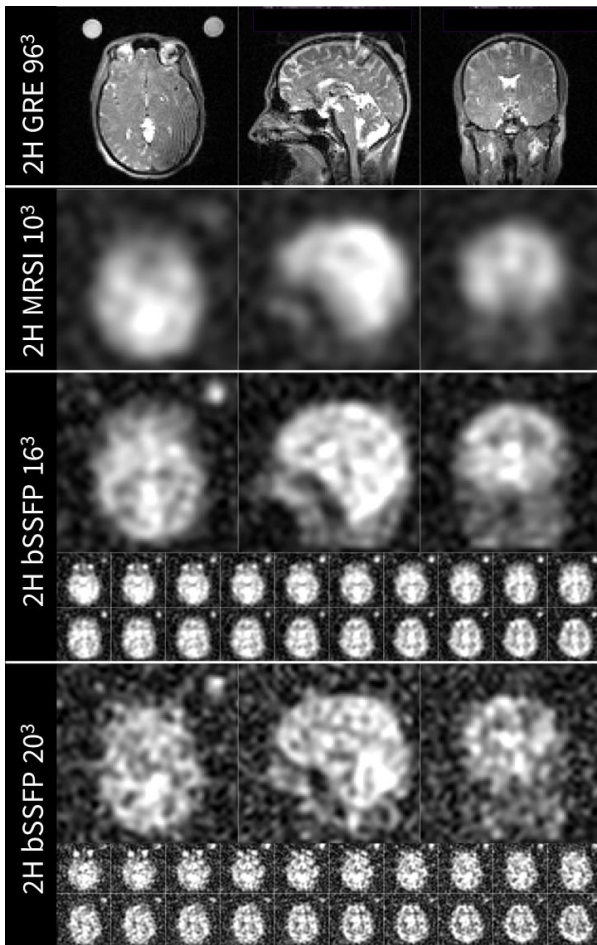


Fig. 1: Basic bSSP sequence: after a spatially non-selective hardpulse excitation, three spatial dimensions are phase encoded, followed by a short spectral acquisition period and a rewinding of the phase to be fully balanced. The first 138 excitations are dummy scans to reach the steady state.

Results: The bSSFP yields higher resolution and high-quality images, shown here in human brain (Fig. 2-4) and liver (Fig. 5). The metabolic rate can be extracted via the linear change in signal level (Fig. 4). Voxel volume in human brain was reduced fourfold from $(2.4\text{cm})^3$ for regular MRSI to $(1.5\text{cm})^3$ for bSSFP. Please note that throughout this work, the density-weighting implementation uses real=nominal resolution (width at 64%-height according to Rayleigh criterion), which is in contrast to most common implementations with normalised k-space (nominal= $1.6 \times$ real mtx), resulting in a reported mtx=283 instead of mtx=163.

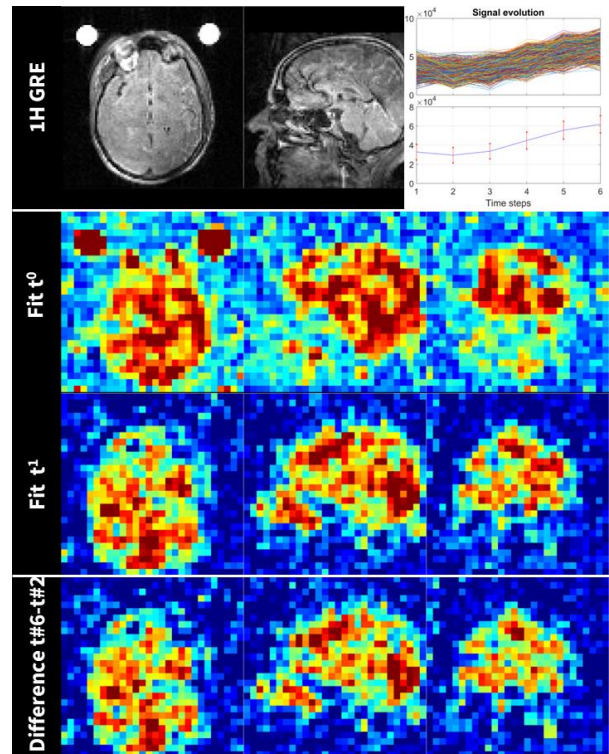


Fig. 2: Spectrally-resolved (second row, mtx=103, 8:43min, 2 averages) and bSSFP (lower rows: mtx=163, 10:58min, 12 averages and mtx=203, 10:06min, 6 averages) MRSI scans one hour after glucose ingestion in human brain (FOV=24cm).

Discussion: Spectrally separating the different metabolites with regular MRSI is challenging at 3T due to short T2* and heavy spectral overlap. Fitting the data is difficult, requiring good initial values and user interaction. Skipping this step greatly simplifies DMI.

We currently investigate if separating the different metabolites and water signal is required in various diseases for $[6,6'\text{-}^2\text{H}_2]\text{glucose}$ or if imaging the overall signal level is sufficient, like done in FDG-PET. For other deuterated compounds, imaging is sufficient, hence boosting the resolution with bSSFP is highly advantageous. The spatial resolution in FDG-PET images is typically 4-5 mm and with implementation of the bSSFP sequence we are getting closer to an equivalent metabolic imaging modality. Injecting instead of ingesting $[6,6'\text{-}^2\text{H}_2]\text{glucose}$ shortens scan time, further progressing to a clinical workflow.

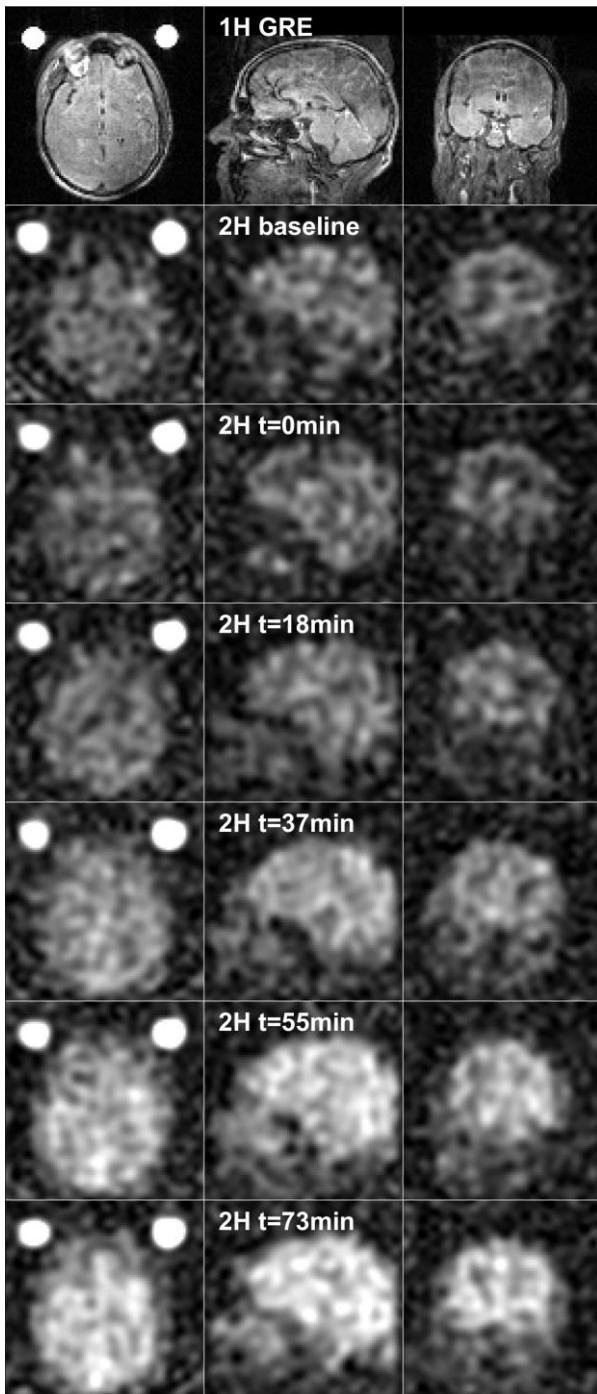


Fig. 3: Dynamic bSSFP scans before (baseline) and after glucose ingestion (t=0 to 73min) (FOV=24cm, mtx=163, 10:58min, 12averages).

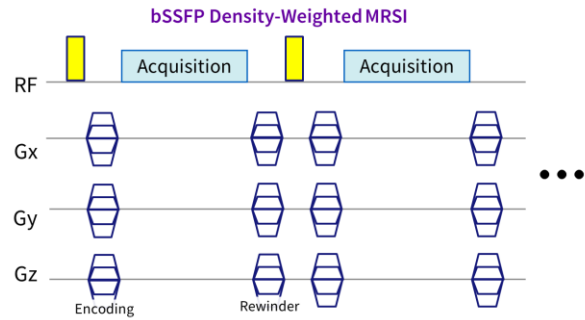


Fig. 4: Extraction of dynamic information from Fig. 3 (omitting zero-filling; matrix size=283). The line plot of signal evolution in a masked region shows the approximately linear increase over time. Fitting a first-order polynomial (linear regression) voxel-by-voxel for time steps 2 to 6 is shown in middle two rows. The linear increase is similar to the difference image between the 2nd and 6th time step. Differences in intermediate images look similar, although with decreased SNR.

Conclusion: DMI bSSFP can greatly improve spatial resolution at the cost of losing spectral separation.

Acknowledgements: This work has received funding from the European Innovation Council programme under the EU Horizon Europe programme, Project number 101185775, DDG-MRI.

References:

- [1] Deuterium metabolic imaging (DMI) for MRI-based 3D mapping of metabolism in vivo. De Feyter HM, Behar KL, Corbin ZA, Fulbright RK, Brown PB, McIntyre S, Nixon TW, Rothman DL, de Graaf RA. *Sci Adv.* 2018 Aug 22;4(8):eaat7314. doi: 10.1126/sciadv.aat7314.
- [2] Improving deuterium metabolic imaging (DMI) signal-to-noise ratio by spectroscopic multi-echo bSSFP: A pancreatic cancer investigation. Peters DC, Markovic S, Bao Q, Preise D, Sasson K, Agemy L, Scherz A, Frydman L. *Magn Reson Med.* 2021 Nov;86(5):2604-2617. doi: 10.1002/mrm.28906.
- [3] Deuterium imaging of the Warburg effect at sub-millimolar concentrations by joint processing of the kinetic and spectral dimensions. Montrazi ET, Bao Q, Martinho RP, Peters DC, Harris T, Sasson K, Agemy L, Scherz A, Frydman L. *NMR Biomed.* 2023 Nov;36(11):e4995. doi: 10.1002/nbm.4995.
- [4] Deuterium nuclear magnetic resonance measurements of blood flow and tissue perfusion employing 2H2O as a freely diffusible tracer. Ackerman JJ, Ewy CS, Becker NN, Shalwitz RA. *Proc Natl Acad Sci U S A.* 1987 Jun;84(12):4099-102. doi: 10.1073/pnas.84.12.4099.
- [5] Deuterium brain imaging at 7T during D2O dosing. Cocking D, Damion RA, Franks H, Jaconelli M, Wilkinson D, Brook M, Auer DP, Bowtell R. *Magn Reson Med.* 2023 Apr;89(4):1514-1521. doi: 10.1002/mrm.29539.
- [6] In vivo deuterium magnetic resonance imaging of xenografted tumors following systemic administration of deuterated water. Brender JR, Assmann JC, Farthing DE, Saito K, Kishimoto S, Warrick KA, Maglakelidze N, Larus TL, Merkle H, Gress RE, Krishna MC, Buxbaum NP. *Sci Rep.* 2023 Sep 7;13(1):14699. doi: 10.1038/s41598-023-41163-9.
- [7] Deuterated water imaging of the rat brain following metabolism of [2H]glucose. Mahar R, Zeng H, Giacalone A, Ragavan M, Mareci TH, Merritt ME. *Magn Reson Med.* 2021 Jun;85(6):3049-3059. doi: 10.1002/mrm.28700.

Towards GABA measurements in the human cervical spinal cord with MEGA-PRESS

Jonathan P. Schwardt 1*, Hanna Braaß 1, Jürgen Finsterbusch 1

1 Department of Systems Neuroscience, University Medical Center Hamburg-Eppendorf, Hamburg, Germany

Abstract: MEGA-PRESS was applied in the human cervical spinal cord after spurious echo artifacts were eliminated by increasing spoiler gradient moments. With a SNR of 9.5 ± 1.3 , the spectral quality allowed GABA+ detection in four out of seven examinations, each containing a total of 1920 averages, with a CRLB as low as 15 %, which was further reduced to 9 % in the average spectrum over all five volunteers. The concentration ratio of GABA+/tNAA in the average spectrum as estimated by LCModel was 0.305. Furthermore, the detection threshold was met in seven, five and six spectra for tNAA, Glx and Glx + GSH, respectively.

Motivation: Metabolite concentrations in the human body can be determined noninvasively with magnetic resonance spectroscopy (MRS) in vivo. The neurotransmitter γ -aminobutyric acid (GABA) is an interesting target in the central nervous system due to its inhibitory role. However, it has many peaks with low signal amplitudes and is obscured by metabolites with higher concentrations. The MEGA editing technique (1) can help identifying GABA by influencing the phase evolution caused by J-coupling such that subtracting the different editing conditions ideally removes some overlapping signals and is well established for applications in the human brain (2).

Neuroscientists' interest in the spinal cord has recently increased as it connects the brain with the peripheral nervous system (3,4). However, spectroscopy in the human spinal cord suffers from a low SNR caused by the small diameter of the spinal cord limiting the voxel size, strong susceptibility differences in surrounding tissue and low coil sensitivities (4). Editing of GABA requires an echo time of 68 ms further reducing the SNR compared to the typically shorter echo time of 30 ms.

The relative GABA concentration in the human spinal cord was reported by one study, which averaged unedited spectra of multiple volunteers, with CRLB of 28 % (4). Here, it is aimed to complement these data by acquiring MEGA-edited spectra in the human cervical spinal cord, as MEGA-editing is the gold standard to determine GABA in the brain at 3 T, but is more challenging in the spinal cord due to the low SNR.

Materials & Methods: All MR experiments were performed on a 3 T MR system (Magnetom PrismaFit, Siemens Healthineers) with a 64-channel head-neck coil. T1-weighted images were used to position a $9 \times 6 \times 35 \text{ mm}^3$ (R-L x A-P x F-H) voxel in the cervical spinal cord (Figure 1). An in-house shim algorithm shimmed an adjustment volume of $20 \times 20 \times 35 \text{ mm}^3$ followed by manually adjusting the linear shim terms in the voxel. The MEGA-PRESS sequence used for voxel localization and spectral editing is the MRS sequence provided by the vendor, extended by a spectral editing option (Figure 1).

Ten MRS measurements were acquired, each with 96 averages per editing condition and a TR of 2 s resulting in a duration of 6 min and 28 s. After each set of two measurements, new T1-weighted images were obtained, the voxel position updated if required, the shimming routine

repeated and a new water reference scan performed. If the MRS voxel was moved $<1 \text{ mm}$ in the transverse plane, only manual adjustment of the linear shim terms starting from the previous shim result was conducted. Whenever a lipid peak was observed on the inline display, the voxel position was updated, and the corresponding acquisition was removed from further analysis.

Five male volunteers (age 28 ± 6 years) were recruited, one of whom was invited for three scan sessions to assess reproducibility. The volunteers had experience with MRI and no contraindications to MRI. The local ethics committee approved the study. All volunteers gave written informed consent prior to the start of the experiment.

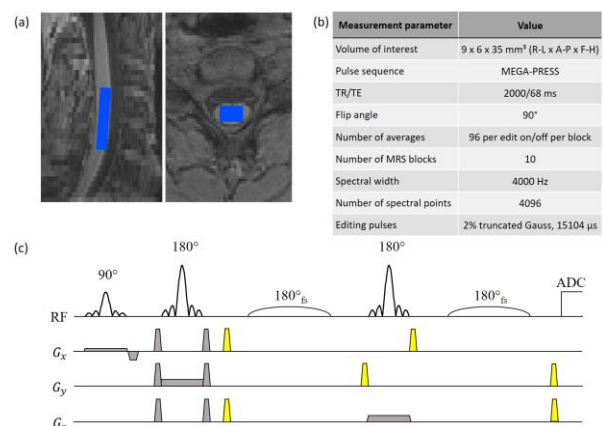


Fig. 1: Exemplary voxel positioning on sagittal and axial T1-weighted images (a), MRS sequence parameters for volunteer measurements (b) and MEGA-PRESS sequence used (c) with frequency selective MEGA pulses denoted as 180°fs and related spoiler gradients, which were increased in phantom measurements to reduce artifacts, marked in yellow.

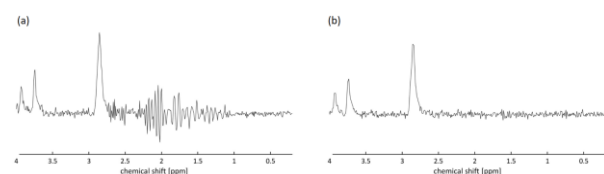


Fig. 2: EDIT ON spectra from phantom measurements with (a) small spoiler gradients show spurious artifacts, which are removed by (b) increasing the spoiler gradients.

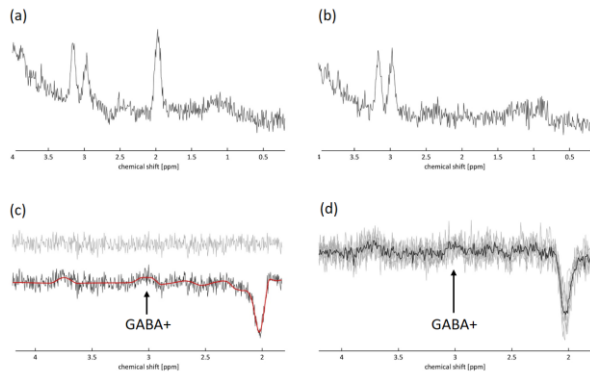


Fig. 3: EDIT OFF (a), EDIT ON (b) and resulting difference spectrum (c) with LCMoDel fit (red) and residual (grey) of spinal cord MEGA-PRESS data of the volunteer with best results. Difference spectra of all volunteers (grey) and average spectrum over these (black, total of 6718 averages) are shown in (d).

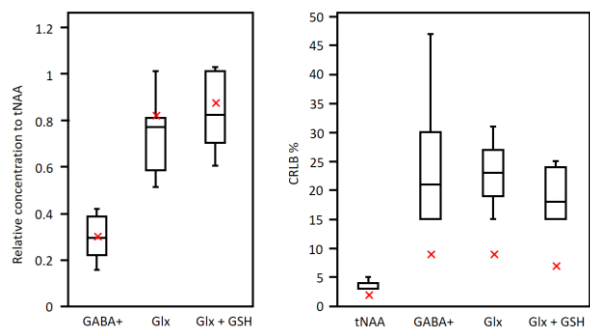


Fig. 4: The left boxplot shows the concentrations of GABA+, Glx and Glx + GSH relative to tNAA and the right boxplot shows the CRLB % of the metabolites in the individual difference spectra as reported by LCMoDel. The red crosses indicate the respective value of the average spectrum.

Results: While testing the sequence, brain spectra were artifact-free (data not shown), but spinal cord spectra showed spurious echo artifacts. The artifact was reproduced in EDIT ON spectra between 1.0 and 2.8 ppm in a phantom and eliminated by increasing spoiler gradient moments from 46 to 138 μ Ts/m (Figure 2).

The EDIT OFF, On and difference spectra from spinal cord spectroscopy of the best volunteer with CRLB of 15 % for GABA+ are depicted in Figure 3. The fit and residual obtained by LCMoDel are included for the difference spectrum, which shows a peak at 3 ppm, where GABA+ is expected. Finally, the difference spectra from all volunteers as well as the difference spectrum after averaging of all volunteer data are also shown in Figure 3.

The SNR was 9.5 ± 1.3 for the individual spectra and in all spectra, tNAA had CRLBs of ≤ 5 %. Four of the seven individual spectra show a CRLB of GABA+ ≤ 25 % and therefore pass the detection threshold of 25 %. For Glx, this condition was met in five spectra and for Glx + GSH in six spectra. The difference spectrum averaged over the volunteers had CRLBs of 2, 9, 9 and 7 % for tNAA, GABA+, Glx, and Glx + GSH, respectively. The concentration ratios to tNAA of the averaged spectrum are 0.305, 0.823, and 0.875 for GABA+, Glx, and Glx + GSH. Figure 4 shows boxplots of the relative concentrations and CRLBs of the individual volunteers and group average.

Discussion: Increasing the spoiler gradient moments eliminated spurious echo artifacts and allowed the application of MEGA-PRESS in the human spinal cord without artifacts overlapping the metabolites of interest.

Applying MEGA-PRESS in the human spinal cord suffers from small voxel sizes, field inhomogeneity and a relatively great distance to the coils, thus small SNR and therefore requires many averages for reliable concentration estimation resulting in a long measurement time. With 960 averages per editing condition however, the detection of GABA+ was successful with CRLB ≤ 25 % in four out of seven examinations, which showed the applicability of MEGA-PRESS in the human spinal cord and possibility to detect GABA+ in a single subject.

The measured relative GABA+/tNAA concentration of the average spectrum of 0.305 is higher than the previously reported value for GABA/tNAA of 0.18 (4), which was measured with PRESS. While the contribution of macromolecules to the estimated GABA+ concentration can be around 50 % for MEGA-PRESS in the human brain (2), this contribution is unknown for the spinal cord. On the other hand, estimating GABA with standard PRESS at 3 T is challenging due to overlap with more pronounced metabolites (2). The differences in reported concentrations might therefore result from using different measurement approaches.

One volunteer showed more motion than all other and had the highest CRLB for GABA+ with 47 %, but was not excluded. For studies, however, it might be necessary to exclude volunteers that showed larger motion from analysis.

Conclusion: The applicability of MEGA-PRESS for editing of GABA in the human spinal cord was shown and led to detection of tNAA, Glx + GSH, Glx and GABA+ in all seven, six, five and four spectra, respectively. However, long scan sessions of about two hours were required to compensate for the low SNR of spinal cord spectroscopy and the obtained concentration ratio of GABA+/tNAA is larger than previously reported with PRESS. Usability for spinal cord fMRS for neuroscientific research is questionable as spectral editing in the human cervical spinal cord remains a difficult task, requires a long measurement time and might require exclusion of volunteers that showed larger motion.

Acknowledgements: This study was funded by the European Research Council (grant agreement ID: 883892)

References:

1. M. Mescher, H. Merkle, J. Kirsch, M. Garwood, and R. Gruetter, "Simultaneous in vivo spectral editing and water suppression," *NMR in Biomedicine*
2. I.-Y. Choi, O. C. Andronesi, P. Barker, W. Bogner, R. A. E. Edden, L. G. Kaiser, P. Lee, M. Marjanska, M. Terpstra, and R. A. de Graaf, "Spectral editing in 1H magnetic resonance spectroscopy: Experts' consensus recommendations," *NMR in Biomedicine*
3. F. Eippert, J. Finsterbusch, U. Bingel, and C. Büchel, "Direct Evidence for Spinal Cord Involvement in Placebo Analgesia," *Science*
4. Hock, B. Wilm, G. Zandomenighi, G. Ampanozi, S. Franckenberg, N. Zoelch, P. O. Wyss, N. De Zanche, J. Nordmeyer-Maßner, T. Kraemer, M. Thali, M. Ernst, S. Kollias, and A. Henning, "Neurochemical profile of the human cervical spinal cord determined by MRS," *NMR in Biomedicine*

Metabolic characterization of hypoperfused brain tissue for stroke risk stratification in patients with recently symptomatic intracranial stenosis based on HP MRI - study protocol

Alexander Seiler¹, Olav Jansen², Jan-Bernd Hövener³

¹ Department of Neurology and Neurovascular Center, University Hospital Schleswig-Holstein, Kiel, Germany

² Department of Radiology and Neuroradiology, University Hospital Schleswig-Holstein, Kiel, Germany

³ Department of Radiology and Neuroradiology, Section Biomedical Imaging, University Hospital Schleswig-Holstein, Kiel University, Kiel, Germany

Motivation: Chronic compromise of cerebral perfusion due to atherosclerotic steno-occlusive disease of brain-supplying arteries is a well-established independent risk factor for ischemic stroke. Depending on demographic and other concomitant risk factors and comorbidities, the annual stroke risk may be increased dramatically and amount to up to 20%. Since “misery cerebral perfusion” with exhausted vascular reserve capacity is characterized by an increased cerebral oxygen extraction and a shift of intracellular pH towards alkaline values (the latter favoring enzymatic reactions of anaerobic glycolysis), an increase of intracellular lactate concentrations seems plausible as a metabolic cellular response in a state of chronic circulatory deficiency.

Materials & Methods: Building upon previous research and several years of experience with metabolic imaging in cerebrovascular disease, this project aims at characterizing local changes of cerebral energy metabolism in patients with recently symptomatic unilateral intracranial stenosis of a brain-supplying artery at high risk of recurrent ischemic stroke over a period of 4 years. To assess the clinical relevance of altered cellular metabolism, 40 patients with locally increased lactate concentrations on ¹³C HP MRI (Fig. 1) will be randomized to either revascularization with endovascular stenting or best medical treatment, with standardized outcome assessments 90 days and 1 year later. ¹³C HP MRI will be performed +/- 5 days before and after stenting. Another 40 symptomatic stenosis patients without altered cerebral energy metabolism on ¹³C HP MRI will serve as controls. Comprehensive cognitive testing will be performed (+/- 5 days, 90 days and 1 year after the index event) to evaluate clinical symptoms related to altered energy metabolism and their improvement after reperfusion.

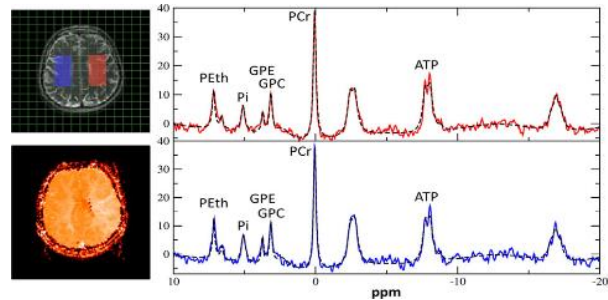


Fig. 1: ¹H MRI, perfusion map and ³¹P multi voxel spectroscopy from a previous study on cerebral energy metabolism in patients with carotid artery stenosis, where we used perfusion imaging (lower left image) to identify the region-of-interest for metabolic mapping and comparison to the contralateral area. We suggest to use a similar approach of using multiparametric MRI to guide HP metabolite mapping.

Results: An interim analysis for preliminary results will be performed after inclusion of the first 50% of all planned subjects in order to investigate trends regarding group differences in functional outcomes and cognitive function between patients treated with stenting and patients treated conservatively by best medical treatment.

Conclusion: The outlined will investigate whether ¹³C HP MRI allows for identifying patients at increased risk for recurrent stroke and substantial hemodynamic compromise, which may benefit from endovascular treatment.

Simulation of Liver Perfusion VSASL Towards Isolation of Hepatic Arterial Signal

Lena Sommer 1*, Mareike Buck 1, Jörn Huber 1, Daniel Hoinkiss 1, Matthias Günther 1+2+3

1 Fraunhofer Institute for Digital Medicine MEVIS, Bremen, Germany

2 mediri GmbH, Heidelberg, Germany

3 University of Bremen, Bremen, Germany

Abstract: The dual blood supply of the liver makes non-invasive perfusion measurement via Arterial Spin Labeling (ASL) a complex task. A distinction of hepatic arterial from portal venous perfusion signal could be helpful in determining the arterial perfusion of the liver. This could play a crucial role for tumor diagnostics or for the assessment of hepatic hemodynamics in cirrhosis [1]. This work uses a simulation model for perfusion data to determine a VSASL based approach on isolating arterial perfusion signal in liver perfusion measurements, by systematically varying key acquisition parameters such as the inflow time (TI) and the encoding velocity (venc) to investigate their effect on the resulting perfusion-weighted signal.

Motivation: Arterial Spin Labeling (ASL) offers a promising non-invasive alternative to contrast-agent based techniques for perfusion quantification by magnetically labeling the spins of the inflowing blood as an endogenous tracer. Several labeling approaches exist which label the blood based on its spatial origin, such as Pulsed ASL (PASL) or pseudo-Continuous ASL (pCASL). The perfusion assessment of the liver is particularly complex with these approaches due to the duality of its blood supply. Only approximately 25% of the liver's total blood flow is delivered via the hepatic (proper) artery, while the remaining 75% stem from the portal vein [2]. Differentiating these components could be beneficial for tumor diagnostics, since many hepatic tumors experience predominantly arterial blood supply [3]. Additionally, assessing variance of arterial compared to portal perfusion might give insights into hepatic hemodynamics in cirrhosis patients [1]. However, this distinction presents as challenging with the spatial labeling techniques. Velocity-Selective ASL (VSASL), on the other side, offers the opportunity to label blood based on its flow velocity [4]. The intrinsic velocity difference of arterial and venous blood makes VSASL a promising technique for isolating the hepatic arterial perfusion signal from the portal venous signal. Yet, optimal configurations of acquisition parameters that allow for the isolation of the arterial portion of the liver's perfusion signal, remain unclear. This work presents a simulation model for liver perfusion, that was created in order to determine suitable parameter settings.

Materials & Methods: In order to identify a combination of acquisition parameters allowing for isolation of the hepatic signal, a Python-based simulation model for perfusion was created (fig.1).

Initially, simulations were performed using 4 different vencs [2,5,10,15]cm/s and 5 different TIs [200,350,500,1000,1500]ms, both for the portal venous and the hepatic arterial model. The radius of the feeding vessel and the initial blood flow were set to 5mm and 1000mL/min for the portal vein and 2mm and 350mL/min for the hepatic artery, respectively.

The resulting data was analysed to determine the maximal mean intensity of the arterial signal. Additionally, the percentage of the arterial signal from the total signal (arterial+portal signal) was calculated to identify the parameter configuration, for which the arterial signal portion gets maximized.

A second dataset was simulated, where the arterial crusher velocity (vcrush) was decoupled from venc. While varying vcrush across [0.05,0.5,1,2,10]cm/s combined with TIs of [250,300,350]ms, venc was kept constant at 15cm/s.

This data was evaluated using the same criteria as the first dataset. For all simulations the post-labeling delay (PLD) was kept at 0ms.

Lastly, the influence of anatomical variability on the perfusion signal was investigated. For this, the radius of the feeding vessels and the initial blood flows were varied across ranges representative of physiological variability [5-8]. For the portal venous model, vessel radii 3.5mm and 7.5mm and the blood flows of 800mL/min and 1200mL/min were examined. Meanwhile for the hepatic artery, radii of 1.5mm and 2.5mm and initial blood flows of 250mL/min and 400mL/min were tested.

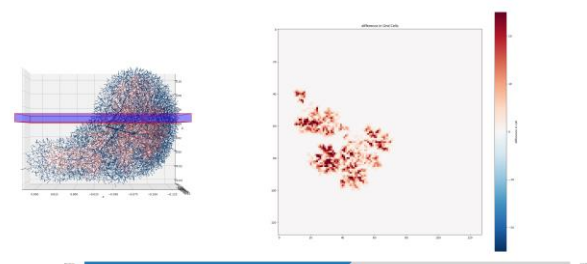


Fig. 1: This figure presents the Python-based simulation model for liver perfusion. On the left, the vascular tree model (based on .swc-file [9]) is visualized. Red segments symbolize the labeled blood (blue=unlabeled). The right side shows the perfusion-weighted signal in the respective slice, indicated in the tree visualization (left in blue).

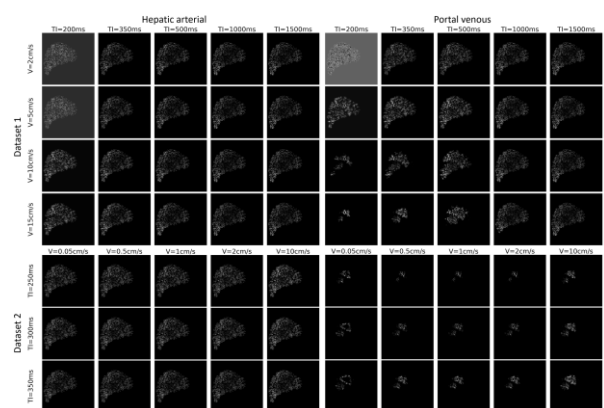


Fig. 2: This figure shows the visualization of the middle slice from the perfusion weighted signal. The left half of the images displays the hepatic arterial perfusion signal, the right half the portal venous signal. The upper images present the first dataset, lower images the second dataset.

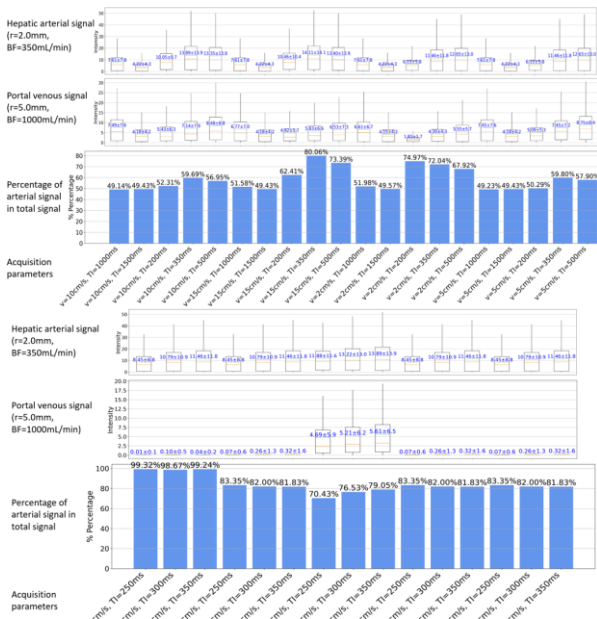


Fig. 3: This figure displays the first (upper half) and the second dataset (lower half). The boxplots present the mean intensity (\pm standard deviation) of the acquisition. The lines indicate the median signal (red) and average signal (dashed green + blue text). The bar chart visualizes the arterial percentage of the total signal.

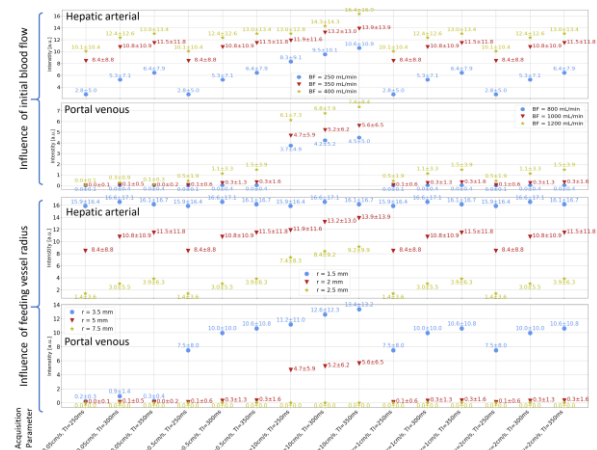


Fig. 4: This figure presents the influence anatomical parameters have on the perfusion weighted signal. For the upper two graphs, the initial blood flow through the feeding vessel was varied, while the lower two graphs show the signal with variance in the radius of the feeding vessel.

Results: A visual assessment (based on the middle slice of the image portraying the perfusion-weighted simulation output) of the first dataset reveals that for short TIs (200ms and 350ms) in combination with high vencs (10cm/s and 15cm/s) the labeled portal venous blood remains confined to the entrance of the vascular tree and neighboring segments (i.e. larger vessels), resulting in generally lower signal and an absence of signal in the capillary region, which is typically indicative of tissue-level perfusion, while for the hepatic arterial model the labeled blood has fully entered the vascular tree thus yielding strong perfusion-weighted signal (see figure 2). The arterial signal is maximal for $venc=15cm/s$ and $TI=350ms$ with an intensity of 14.11 ± 14.1 arbitrary units (a.u.). For these parameter settings, the arterial signal yields

also the highest percentage of the hepatic arterial signal from the total signal at 80.06%. This can be seen in figure 3.

For the second dataset, the maximum of the absolute arterial signal can be found for the parameter settings of $vcrush=10cm/s$ and $TI=350ms$, reaching $13.89\pm 13.9a.u.$. However, the portal signal for this setting lies relatively high at $5.61\pm 6.1a.u.$, reducing the hepatic percentage to 79.05%. Whereas the highest hepatic percentage was achieved with $vcrush=0.05cm/s$ and short TIs – highest at 99.32% for $TI=250ms$. This is displayed in figure 3.

The investigation of the anatomical influences demonstrated a signal increase for decreasing vessel radius and for increasing initial blood flow and reduced signal for increased radius and decreased blood flow. Figure 4 shows these results.

Discussion: For the first dataset, the low portal signal observed for high vencs and short TIs is physiologically plausible, given that due to the slower portal venous flow, blood is labeled primarily at the entrance of the vascular tree. The short TI doesn't allow the labeled blood to reach organ tissue. Whereas the faster arterial blood is labeled deeper within the tree, reaching the capillaries even at short TIs. This simultaneously explains the high arterial percentage for these parameters.

These results motivated the approach of the second data set of decoupling $venc$ and $vcrush$. The high $venc$ restricts portal labeling to larger vessels, while a low $vcrush$ only allows capillary-level signal contribution. Consequently, the portal signal approaches zero, yielding an arterial signal percentage near 100% at very low $vcrush$ ($v=0.05cm/s$), which is confirmed by the second dataset. Notably, the mean arterial signal intensity remained constant for $vcrush < 10cm/s$ – likely, due to the lowest arterial velocity before entering the capillaries in this model is around $7cm/s$, thus all $venc$ settings sample the same capillary regime. Similarly, the plateau of the portal signal for $vcrush=[0.5, 1, 2]cm/s$ can be explained with vessel-based velocity discretization, possibly placing these velocities within the interval.

The anatomical variability produced expected trends: decreased vessel radii and higher initial blood flows both increase flow velocity, enabling labeled blood to penetrate deeper and intensifying signal. Consequently, non-existent portal signal for increased radius is reasonable, since low velocity prohibits the labeled blood from reach the vascular tree.

Conclusion: A simulation model was created to simulate liver perfusion measurement techniques. It was specialized for VSASL. The model was used to find a combination of acquisition parameters, that allows for isolation of the hepatic arterial signal. The results showed, when decoupling the arterial crusher velocity from the encoding velocity and using low TIs, it was possible to nearly eliminate portal venous perfusion signal completely, thus isolating hepatic arterial signal. The parameter setting that delivered best results is an encoding velocity at $venc=15cm/s$, a crusher velocity at $vcrush=0.05cm/s$ and TIs between 250ms and 350ms. Next, these results need to be tested with real MRI data of healthy probands to confirm their relevance. If these parameter settings proof to work in a clinical setting, a baseline for arterial liver perfusion quantification could be determined.

References:

1. Yoshiki Asayama, Kengo Yoshimitsu, Yunosuke Nishihara *et al.*, *Arterial Blood Supply of Hepatocellular Carcinoma and Histologic Grading: Radiologic-Pathologic Correlation*, *American Journal of Roentgenology*
2. Arjun Kalra, Ekrem Yetiskul, Chase J. Wehrle *et al.*, *Physiology, Liver*, StatPearls Publishing
3. Natalia Rush, Hongliu Sun, Yukihiko Nakanishi *et al.*, *Hepatic arterial buffer response: pathologic evidence in non-cirrhotic human liver with extrahepatic portal vein thrombosis*, *Modern Pathology*
4. Eric C Wong, Matthew Cronin, Wen-Chau Wu *et al.*, *Velocity-selective arterial spin labeling*, *Magnetic Resonance in Medicine*
5. Gemechu Geleto, Wandim Getnet, Tsegaye Tewelde, *Mean Normal Portal Vein Diameter Using Sonography among Clients Coming to Radiology Department of Jimma University Hospital, Southwest Ethiopia*, *Ethopian Journal of Health Science*
6. Christian Eipel, Kerstin Abshagen, Brigitte Vollmar, *Regulation of hepatic blood flow: The hepatic arterial buffer response revisited*. *World Journal of Gastroenterology*
7. Dao-Bing Zeng, Chuan-Zhou Dai, Shi-Chun Lu *et al.*, *Abnormal splenic artery diameter/hepatic artery diameter ratio in cirrhosis-induced portal hypertension*, *World Journal of Gastroenterology*
8. Abdulkadir Bilir, Zeliha Fazliogullari, Mustafa Koplay *et al.*, *Diameter Measurements and Variations of the Hepatic Arterial System in Multidetector Computed Tomography Images*, *International Journal of Morphology*
9. Lars Ole Schwen, Arne Schenk, Clemens Kreutz *et al.*, *Representative Sinusoids for Hepatic Four-Scale Pharmacokinetics Simulations*, *PLOS one*

13C pyruvate drug compounding and terminal sterilization

Nicolas Spath 1, Farhad Haj Mohamad* 2, Jan-Bernd Hövener 2

1 Department of Hematology and Oncology, University Hospital Schleswig-Holstein, Kiel University, Kiel, Germany

2 Department of Radiology and Neuroradiology, Section Biomedical Imaging, University Hospital Schleswig-Holstein, Kiel University, Kiel, Germany

Abstract: Drug compounding and preparation for use in humans are a delicate process. The goal of this experiment was to test our manufacturing process for an injectable 13C Pyruvate drug product considering: (1) bacterial contamination, (2) unknown antimicrobial compounds and (3) the effectiveness of terminal sterilization with medical grade microbial filters for aqueous solutions. Drug compounding, subsequent growth promotion tests utilizing *Bacillus subtilis* ssp. *spizizenii* followed by microbial filtering showed a sufficiently sterile product.

Motivation: Injecting humans with non-sterile fluids risks severe bloodstream infections. Thus, preparing sterile drug products is of utmost importance. It is not feasible to use methods of sterilization utilizing high heat and/or pressure because pyruvate is unstable at higher temperatures. Therefore, we used medical grade filters as proposed by the European pharmacopeia and EU regulatory bodies to carry out terminal sterilization.

Materials & Methods: Sterility testing methods follow the European Pharmacopoeia [1]. Moreover, the EU Guidelines to Good Manufacturing Practice [2] were taken into consideration.

The product comprises an aqueous solution of TRIS (1089 mg), NaOH (648 mg), Na₂EDTA (9.0 mg), [1-13C]pyruvic acid (1.44 g) and 15 mM AH111501 sodium salt (27.7 mg).

Growth Promotion Tests

1. Portions of Fluid Thioglycollate Medium (FTM), Tryptic Soy Broth (TSB) and agar plates were inoculated with 100 CFU or less of *B. subtilis* (Sigma Aldrich ATCC 6633).
2. Then incubated at 5% CO₂ and 30-35°C (FTM, Agar) or 20-25°C (TSB) for 3 days.
3. The growth media were considered suitable if a clearly visible growth of the microorganisms occurred.
4. Positive and negative controls were conducted with terminal filter sterilization cultures.

Testing for Filter Terminal Sterilization Bacterial Growth:

1. Solutions of 500, 1100, and 50 000 CFU of *Bacillus subtilis* were added into the product solution.
2. *Bacillus subtilis* in solution was diluted and filled up to 60 ml with sterile water for injection (SWFI) and drawn into a 60ml syringe.

3. Sterility medical grade 0.2 µm production filters were attached to 60ml syringe and expelled through filter into sterile vials containing growth medium
4. Product solution was injected into growth media or on agar plate
5. Which were incubated at 5% CO₂ and 30-35°C (FTM, Agar) or 20-25°C (TSB).
6. Results were obtained in 7 days for agar plates and 14 days for TSB and FTM Tubes.

Results: The results show that our compounding process of the final drug product containing pyruvate, TRIS/EDTA, and sterile water does not have any relevant sources of contamination. Nor are there unknown components with antimicrobial activity that would interfere with growth and sterility testing.

No bacterial growth is detected at the highest concentration of 50 000 CFU after using sterile filters for aqueous solutions. Therefore, using sterile filters is sufficient to ensure terminal sterilization. The manufacturing process is safe and does not add a significant amount of micro bacterial contamination.

Discussion: A limitation was that AH111501 sodium salt (the electro hyperpolarizing agent, EPA) discolors the growth media with a green color, such that it is not possible to determine bacterial growth. We thus did not utilize EPA in this experiment.

Nonetheless, there is no reasonable physical explanation that EPA might disrupt the filtration process. Therefore, the setup of the experiment according to the Committee for Medicinal Products for Human Use (CHMP) and the European pharmacopeia guidelines, sufficiently shows that terminal sterilization with medical grade 0.2 µm filters for aqueous solutions is feasible and safe.

Conclusion: It is necessary to closely monitor the drug production process in the future and sample bacterial cultures from every compounded drug batch to monitor contamination.

References:

- [1] Committee for Medicinal Products for Human Use, 2008, European Pharmacopoeia 6.0, Chapter 2.6.1. Page 155
- [2] Committee for Medicinal Products for Human Use, 2022, EU Guidelines to Good Manufacturing Practice, Volume 4, Annex 1

Region of interest characteristics in diffusion MRI along perivascular space index

Carlotta Staats 1, Justus Christian Rudolf 1, Janina Kremer 1, Aileen Schmidt1+2, Peter Schramm 1, Patricia Ulloa 1

1 Department of Neuroradiology, University Hospital Schleswig-Holstein (UKSH) Campus Lübeck, Lübeck, Germany

2 Department of Diagnostic and Interventional Radiology, University Hospital Bonn, Bonn, Germany

Abstract: Diffusion-tensor imaging (DTI) and diffusion-weighted imaging (DWI) along perivascular spaces (ALPS) index are non-invasive methods to assess glymphatic function. However, variability in examination parameters - particularly ROI definition- limits inter-study comparability. This study evaluated 11 different ROI configurations in 13 healthy volunteers to determine which best supports consistent ALPS index analysis. Significant differences in ALPS values were found across ROI types. Squared ROIs yielded the highest consistency with excellent inter-method agreement (mean ICC = 0.83). No significant inter-method differences were observed. Standardizing ROI characteristics, especially shape, is essential for reliable ALPS index calculation.

Motivation: The glymphatic system enables the removal of neurotoxic substances via cerebrospinal fluid (CSF) and interstitial fluid out of the brain.(1)

To date, the glymphatic function has been assessed non-invasively, primarily using diffusion tensor imaging and the ALPS index calculated as described by Taoka et. al.(2) Changes in the ALPS index compared to healthy controls have been observed in neurodegenerative disorders, brain tumours and other diseases. The index is based on the measurable movement of ISF in the white matter near the lateral ventricles, parallel to the periventricular veins. The DTI-ALPS index is calculated based on diffusion only along the x, y and z axes. This means that DWI in three orthogonal gradient directions can also be used to calculate the DWI ALPS index. DWI is used more frequently in clinical practice and is also significantly faster than DTI.

However, considerable heterogeneity has been observed in DTI studies, indicating that standardised parameters are needed to obtain comparable clinical data. Therefore, the standardisation of region of interest (ROI) placement appears to be essential.(3) Different sizes and various shapes of the ROI like circular, spherical, cubic, squared or single voxel have been studied previously. This work aims to show how the size and shape of the ROI influence both the DTI and the DWI ALPS index.(4)

Materials & Methods: This study was approved by the ethical committee of the University of Luebeck. The thirteen volunteers provided consent before the scans.

The examinations were carried out using a 3T MRI scanner with 20-channel head coil in neutral position. The imaging parameters for DTI and DWI were: TE/TR = 92/4400 ms, FOV = 200x200 mm², voxel size = 2x2x2 mm³, and b-values = 0 and 1000 s/mm².

DTI used 64 diffusion directions, and DWI included three orthogonal directions along readout, phase-, and slice-encoding axes. The scan durations were 5:30 min for DTI and 1:30 min for DWI.

The DTI images were analysed by DSI Studio and the DWI images in ImageJ, as described in Taoka et al.

Eleven ROIs were evaluated, placed next to the lateral ventricle in projection and association areas (see Figure 1). Projection ROIs were positioned at least one voxel away from the ventricle or association areas. Likewise, association ROIs were set at least one voxel from projection and subcortical regions. All ROIs were placed in the same single slice per hemisphere for both DTI and DWI. Diffusivities along the x-, y-, and z-axes were extracted from the diffusion tensor to calculate the DTI-ALPS index using $\text{mean}(\text{DxProj}, \text{DxAssoc})/\text{mean}(\text{DyProj}, \text{DzAssoc})$; the same formula was applied to DWI using readout (x-), phase (y-), and slice-encoding (z-) directions instead.

The Wilcoxon signed-rank test was used to assess differences between ROI configurations. Method agreement between DTI and DWI was evaluated using the intraclass correlation coefficient (ICC) and Bland-Altman-Analysis.

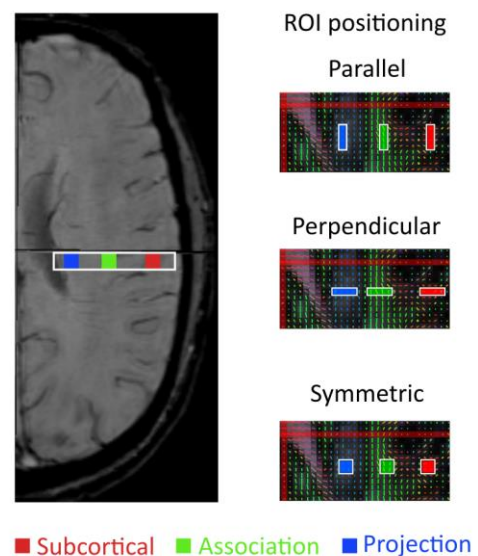


Fig. 1: Left: Susceptibility-weighted image showing the position of the projection (in blue) and association ROIs (in green). Subcortical regions are marked red.

Right: ROI configurations placed parallel or orthogonal to the lateral ventricle, as well as square ROI configurations. For simplicity, only the ROI placement on the left hemisphere is shown.

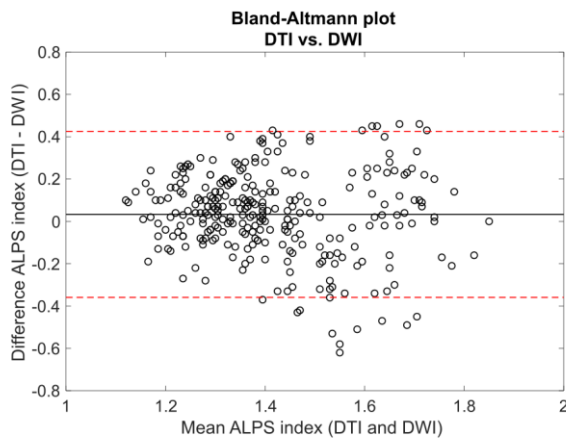


Fig. 2: Bland-Altman plots illustrating the comparison of DTI and DWI measurements

Results: Different methods led to differences in the results when comparing among ROIs with different size and shape. The DTI-ALPS index tended to have a higher mean (1.43) and median (1.40) than the DWI-ALPS index (1.40 mean, 1.36 median).

However, no significant differences were found when comparing the DTI and DWI ALPS indices with the same ROI size and shape, as shown by the Bland-Altman plots (mean bias 0.03, see Figure 2) and the Wilcoxon signed-rank test ($p < 0.04$)

The intraclass correlation coefficient (ICC) shows that 96.36% of inter-voxel configurations show good to excellent agreement for both DTI and DWI. The average ICC is 0.83. In particular, v9s with the highest ICC (0.80, $p < 0.001$) shows excellent reliability. The relatively wide 95% confidence interval (0.55, 1.04) indicates variability within the sample. However, poor agreement between the methods was found between different voxel configurations (mean ICC = 0.42).

Discussion: The effect of different ROI sizes and shapes was investigated, and their comparability was determined. Larger and square ROIs such as v4s and v9s are more stable and reliable because they compensate spatial inhomogeneities more effectively. In addition, asymmetrical ROIs should be avoided, as in particular orthogonal configurations should not be compared with others.

Since DWI does not require complex analysis, the software used for ROI placement is irrelevant. In contrast, the methodology of different software systems can vary for DTI, which could lead to differences in the ALPS index calculation. But the DWI-ALPS index is highly dependent on the planning and positioning of the study subject in the scanner, which can lead to deviations in the measurements.

Since manual ROI placement is very time-consuming, automated calculation tools are recommended, except for diseases with white matter lesions. To avoid the affected areas, manual placement of the ROI is necessary to deliver reproducible results.

It should be noted that the ALPS index in deep white matter should not be used to draw conclusions about complete glymphatic function. The ALPS index has therefore been questioned and should be further investigated and compared with other methods.

Conclusion: This study shows the importance of standardising ROI to enable reliable and comparable DTI and DWI measurements.

Squared or cubic ROIs are usually better for MRI image analysis. They have a better voxel grid alignment, are therefore simpler to implement, and are easier to use in statistical analysis.

If study results are to be compared with others, it is recommended to use squared ROIs, which compares well with other ROI shapes and sizes. Introducing the v4s ROI as a standardised method would enable the ALPS methods to be established in everyday clinical practice. Especially while using the DWI-ALPS, as DWI is available in all scanners, easier and faster than DTI.

A standardised ALPS index could be used as a potential biomarker for diffusion in the perivascular space and thus also for glymphatic function. Other methods should also be used in combination for further investigation of the glymphatic system.

Acknowledgements: The project was supported by the University of Luebeck in the form of a doctoral scholarship for Janina Kremer and Justus C. Rudolf

References:

1. Iliff JJ et al, Paravascular Pathway Facilitates CSF Flow Through the Brain Parenchyma and the Clearance of Interstitial Solutes, Including Amyloid β . *Sci Transl Med.* 2012;4(147):147ra111.
2. Taoka T et al, Evaluation of glymphatic system activity with the diffusion MR technique: diffusion tensor image analysis along the perivascular space (DTI-ALPS) in Alzheimer's disease cases. *Jpn J Radiol.* 2017;35(4):172-8.
3. Carotenuto A et al, Glymphatic system impairment in multiple sclerosis: relation with brain damage and disability. *Brain.* 2022;145(8):2785-95.
4. Ulloa P et al, Influence of orientation, size and shape of the region of interest in diffusion MRI along perivascular spaces index. *MAGMA*, 2025 <https://doi.org/10.1007/s10334-025-01248-0> (in press)
5. Taoka T et al, Reproducibility of diffusion tensor image analysis along the perivascular space (DTI-ALPS) for evaluating interstitial fluid diffusivity and glymphatic function: CHanges in Alps index on Multiple condition acqulsition eXperiment (CHAMONIX) study. *Jpn J Radiol.* 2022;40(2):147-58.

Application of the Segmented Monoexponential IVIM Model for Separating Diffusion and Perfusion Changes in Sepsis-Associated Acute Kidney Injury

Ronja Steiling 1 *†, Ali Nahardani 1†, Van Nhat Minh Vo 1†, Verena Hoerr 1

1 Heart Center Bonn, Department of Internal Medicine II, University Hospital Bonn, Bonn, Germany; † Shared Authorship

Abstract: Early-phase imaging of sepsis-associated acute kidney injury (S-AKI) remains a clinical challenge. This study investigates the potential of diffusion-weighted MRI (DWI), combined with a segmented monoexponential intravoxel incoherent motion (IVIM) model, for the early detection of S-AKI by quantitatively separating diffusion-driven (D) and perfusion-related (D*) components of the signal. In a murine model of sepsis, diffusion parameters were assessed six hours post-induction. A significant reduction in D was observed in both the renal cortex and medulla, indicating early microstructural alterations. Although dynamic contrast-enhanced (DCE) perfusion imaging revealed reduced renal perfusion, no significant change in D* was detected, suggesting limited sensitivity of D* to acute perfusion deficits in the kidney.

Motivation: Sepsis-associated acute kidney injury (S-AKI) is associated with high morbidity and mortality [1]. However, there is still a lack of sensitive imaging techniques capable of capturing pathological renal changes, while conventional biomarkers such as serum creatinine are known to exhibit delayed responses to functional kidney impairment [2]. This has led to growing interest in imaging-based methods for earlier detection. Among them, dynamic contrast-enhanced (DCE) perfusion MRI has demonstrated sensitivity to renal perfusion impairment [3]. Yet, its reliance on gadolinium-based contrast agents poses a significant limitation, which is contraindicated in patients with AKI.

Given that alterations in renal diffusion and perfusion play central roles in the pathogenesis of AKI, diffusion-weighted imaging (DWI) offers a noninvasive approach for assessing renal microstructural and functional changes [4]. The most commonly used DWI parameter – the apparent diffusion coefficient (ADC) – reflects both tissue microstructure and microvascular perfusion. However, this dual sensitivity limits its specificity as a biomarker.

In this study, we investigate whether the diffusion and perfusion components of the DWI signal can be separately quantified to serve as early biomarkers for S-AKI. We applied a segmented monoexponential intravoxel incoherent motion (IVIM) model to derive two key parameters: the true diffusion coefficient (D), indicative of microstructural alterations, and the perfusion-related pseudo-diffusion coefficient (D*), reflective of renal perfusion. These parameters were calculated using high and low b-values, respectively. Finally, D* measurements were compared with DCE perfusion imaging to evaluate their sensitivity to early microvascular alterations and potential as a contrast-free alternative.

Materials & Methods: Animal Preparation & Sepsis Model:

A total of 20 adult male C57BL6/J mice (aged 9–12 weeks) were divided into control and sepsis groups. Sepsis was induced using the Peritoneal Contamination and Infection (PCI) model via intraperitoneal injection of a standardized

fecal suspension [5]. MRI was performed 6 hours after sepsis induction.

DWI – MRI: All scans were performed on an 11.7 T Bruker BioSpec system using a 72 mm ¹H volume resonator and a 4-channel receiver coil with respiratory gating. DWI was acquired using a spin-echo sequence (TR/TE: 500/20 ms; 7 b-values: 0, 50, 100, 200, 300, 500, 700 s/mm²; matrix: 128×128; FOV: 35×35 mm²; slice thickness: 1 mm; number of slices: 11, averages: 2). Diffusion gradients were applied along the z-axis in axial slices covering both kidneys.

DWI – Analysis: Diffusion and perfusion parameters were estimated using the IVIM model with a segmented monoexponential fitting approach, enabling separation of the true tissue diffusion coefficient – D, from the pseudo-diffusion coefficient – D*, associated with microvascular perfusion.

The signal decay was modeled using two monoexponential functions as illustrated in Fig. 4.

To separate diffusion and perfusion effects, D was estimated from high b-values (>200 s/mm²), where perfusion influence is minimal, while D* was derived from low b-values (≤200 s/mm²), reflecting microvascular perfusion. ADC was calculated across the entire b-value range, capturing both diffusion and perfusion contributions. Region-of-interest analyses were performed in the cortex, medulla, and pelvis of the left kidney.

DCE-based Perfusion: A golden-angle 2D-UTE sequence was performed following the administration of gadobutrol at a dose of 0.13 μmol/g body weight. The raw data were regridded using an iterative sampling density compensation method and subsequently reconstructed via inverse Fourier transform. To enhance image quality, an iterative non-local means denoising algorithm was applied. Renal arterial blood flow (RABF) was determined from the perfusion curves after cubic spline interpolation [6].

Region	Parameter	× 10 ⁻³ mm ² /s	Control	Sepsis	p-value
Cortex	D		1.7 ± 0.3	1.4 ± 0.5	0.0229
	D*		3.1 ± 1.4	3.2 ± 1.5	0.4698
	ADC		1.7 ± 0.3	1.5 ± 0.5	0.1142
Medulla	D		2.0 ± 0.3	1.3 ± 0.5	0.0229
	D*		2.2 ± 1.2	3.5 ± 1.5	0.1447
	ADC		2.1 ± 0.4	1.5 ± 0.6	0.1416
Pelvis	D		2.0 ± 0.5	1.8 ± 0.5	0.1416
	ADC		2.1 ± 0.5	2.0 ± 0.5	0.3510

Fig. 1: D, D*, and ADC for the cortex, medulla, and pelvis regions in control and sepsis groups (mean ± SD).

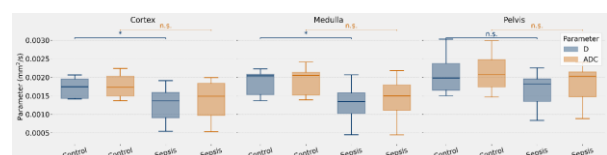


Fig. 2: Box plots of D and ADC in the cortex, medulla, and pelvis for control and sepsis groups.

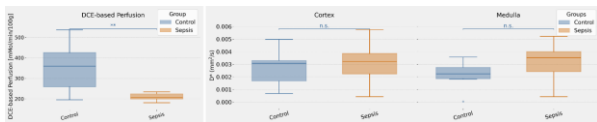


Fig. 3: Box plots of D^* and DCE-based perfusion in the cortex and medulla for control and sepsis groups.

$$S(b) = S_0 \cdot e^{-bD} \quad \text{s. t. } b > 200 \text{ s/mm}^2$$

$$S(b) = S_0 \cdot e^{-bD^*} \quad \text{s. t. } b \leq 200 \text{ s/mm}^2$$

Fig. 4: To separate diffusion and perfusion effects, signal decay $S(b)$ was modeled using two monoexponential functions. The diffusion coefficient D was estimated from high b -values ($b > 200 \text{ s/mm}^2$), where perfusion effects are minimal. In contrast, the pseudo-diffusion coefficient D^* was derived from low b -values ($b \leq 200 \text{ s/mm}^2$), reflecting microvascular perfusion.

Results: Alternations in D , D^* and ADC across renal regions:

In the renal cortex, the diffusion coefficient D was significantly reduced in the sepsis group compared to controls (median: $0.0014 \pm 0.0005 \text{ mm}^2/\text{s}$ vs. $0.0017 \pm 0.0003 \text{ mm}^2/\text{s}$, $p = 0.0229$). In contrast, ADC values, although lower under septic conditions ($0.0015 \pm 0.0005 \text{ mm}^2/\text{s}$ vs. $0.0017 \pm 0.0003 \text{ mm}^2/\text{s}$), did not reach significance ($p = 0.1142$). The perfusion-related parameter D^* also showed no significant difference between the groups ($0.0032 \pm 0.0015 \text{ mm}^2/\text{s}$ vs. $0.0031 \pm 0.0014 \text{ mm}^2/\text{s}$, $p = 0.4698$).

In the medulla, both D ($0.0013 \pm 0.0005 \text{ mm}^2/\text{s}$ vs. $0.0020 \pm 0.0003 \text{ mm}^2/\text{s}$, $p = 0.0229$) and ADC ($0.0015 \pm 0.0006 \text{ mm}^2/\text{s}$ vs. $0.0021 \pm 0.0004 \text{ mm}^2/\text{s}$, $p = 0.1416$) values were reduced in the sepsis group; however, only D reached statistical significance. D^* values did not differ significantly between the groups ($0.0035 \pm 0.0015 \text{ mm}^2/\text{s}$ vs. $0.0022 \pm 0.0012 \text{ mm}^2/\text{s}$, $p = 0.1447$).

In the pelvis, neither D ($0.0018 \pm 0.0005 \text{ mm}^2/\text{s}$ vs. $0.0020 \pm 0.0005 \text{ mm}^2/\text{s}$, $p = 0.1416$) nor ADC ($0.0020 \pm 0.0005 \text{ mm}^2/\text{s}$ vs. $0.0021 \pm 0.0005 \text{ mm}^2/\text{s}$, $p = 0.3510$) showed statistically significant differences. D^* was not assessed in this region due to the absence of a detectable perfusion signal.

Comparison of D and ADC across renal regions:

Across all anatomical regions, ADC values were consistently higher than the corresponding D values. Both parameters tended to decrease under septic conditions, with statistically significant reductions observed only for D in the cortex and medulla.

Comparison of D^* and DCE-based Perfusion across renal regions:

Despite a significant reduction in directly measured renal perfusion ($353.254 \pm 110.831 \text{ mL/min/100g}$ vs. $209.296 \pm 19.089 \text{ mL/min/100g}$, $p = 0.0014$, whole kidney) [6], D^* did not show significant changes in any anatomical region. Quantitative results are summarized in Figure 1.

Discussion: Our results demonstrated a significant reduction in the diffusion coefficient D in both the renal cortex and medulla six hours after sepsis induction, suggesting early structural alterations in renal tissue. Likely driven by inflammation and hypoxia, these changes cause cellular swelling, reduced extracellular space, and restricted diffusion. ADC values were consistently higher than D , reflecting the

combined influence of diffusion and microvascular perfusion, but group differences were not statistically significant. This underlines the role of D as a more specific and sensitive marker of microstructural changes, unaffected by perfusion-related effects.

In contrast, the perfusion-sensitive IVIM parameter D^* showed no significant differences between the sepsis and control groups, despite a clear reduction in renal perfusion confirmed by independent measurements [6]. This discrepancy suggests that D^* may lack the sensitivity required to detect acute microvascular changes in the early phase of S-AKI.

As previously reported, D^* primarily reflects intravascular water movement, which contributes relatively little to the overall MR signal – approximately 5% in the brain. Since most signals arise from extravascular tissue with limited perfusion effects, D^* must be derived from subtle fluctuations, making it highly susceptible to noise and motion [7]. Its narrow dynamic range limits its ability to discriminate between groups.

In summary, D appears to be a reliable biomarker of early microstructural damage, while D^* fails to capture acute perfusion deficits under current conditions. Future studies may benefit from technical improvements such as multi-directional diffusion encoding and increased signal averaging to enhance the sensitivity of perfusion-related IVIM parameters.

Conclusion: The separate analysis of diffusion and perfusion using a segmented IVIM approach demonstrates that the diffusion parameter D may serve as a reliable marker for early structural tissue alterations, particularly in the cortex and medulla, during the early phase of S-AKI. In contrast, the perfusion-sensitive parameter D^* showed no significant changes, despite a measurable reduction in renal perfusion, suggesting insufficient sensitivity of D^* for detecting acute microvascular alterations under the current conditions. These findings highlight the potential of D as a specific biomarker in the early phase of S-AKI, while the diagnostic value of D^* appears limited.

Acknowledgements: This work was supported by the Deutsche Forschungsgemeinschaft (German Research Foundation, Project-ID 431460824).

References:

- [1] D. Khadzhyrov u. a., „The Incidence of Acute Kidney Injury and Associated Hospital Mortality“, *Dtsch. Arztebl. Int.*, Mai 2019, doi: 10.3238/arztebl.2019.0397.
- [2] Z. H. Endre, J. W. Pickering, und R. J. Walker, „Clearance and beyond: the complementary roles of GFR measurement and injury biomarkers in acute kidney injury (AKI)“, *Am. J. Physiol.-Ren. Physiol.*, Bd. 301, Nr. 4, S. F697–F707, Okt. 2011, doi: 10.1152/ajprenal.00448.2010.
- [3] J. R. Privratsky u. a., „Dynamic contrast-enhanced MRI promotes early detection of toxin-induced acute kidney injury“, *Am. J. Physiol.-Ren. Physiol.*, Bd. 316, Nr. 2, S. F351–F359, Feb. 2019, doi: 10.1152/ajprenal.00416.2018.
- [4] H. C. Thoeny, F. De Keyser, R. H. Oyen, und R. R. Peeters, „Diffusion-weighted MR Imaging of Kidneys in Healthy Volunteers and Patients with Parenchymal Diseases: Initial Experience“, *Radiology*, Bd. 235, Nr. 3, S. 911–917, Juni 2005, doi: 10.1148/radiol.2353040554.
- [5] F. A. Gonnert u. a., „Characteristics of Clinical Sepsis Reflected in a Reliable and Reproducible Rodent Sepsis Model“, *J. Surg. Res.*, Bd. 170, Nr. 1, S. e123–e134, Sep. 2011, doi: 10.1016/j.jss.2011.05.019.
- [6] A. Nahardani, S. Moradi, V. N. M. Vo, und V. Hoerr, „23Na Magnetic Resonance Imaging in Sepsis-Induced Acute Kidney Injury: A Preclinical Study“, gehalten auf der 2024 ISMRM & ISMRT Annual Meeting, Toronto, ON, Canada, S. 0706. doi: 10.58530/2024/0706.
- [7] J. J. Neil, C. S. Bosch, und J. J. H. Ackerman, „The use of slice-selective inversion to improve the dynamic range for measurement of pseudodiffusion coefficient“, *J. Magn. Reson.* 1969, Bd. 98, Nr. 2, S. 436–442, Juni 1992, doi: 10.1016/0022-2364(92)90145-W.

Implementation of an automated purification protocol for a low field SABRE

Isadola Steinman ^{*1,2}, Martin Sandbrink ¹, Philip Saul ¹, Julia Rosin ¹, Yenel Gökpek ¹, Andrey N. Pravdivtsev ¹, and Jan-Bernd Hövener ¹

¹ Department of Radiology and Neuroradiology, Section Biomedical Imaging, University Hospital Schleswig-Holstein, Kiel University, Kiel, Germany

² Department of Physics and Astronomy, Amherst College, Amherst, MA, 01002–5000, USA

Abstract: Magnetic resonance imaging (MRI) is a non-invasive technique that offers superb soft tissue contrast but has limited ability to image metabolism. Hyperpolarizing (HP) nuclear spins permits a significant increase in sensitivity, allowing for direct observation of metabolic flux. Signal amplification by reversible exchange (SABRE) has drastically simplified the production of hyperpolarized tracers, but is most effective in methanol, so purification is needed before *in vivo* application. We present an automated setup for obtaining purified, aqueous solutions of hyperpolarized [1-¹³C]pyruvate, the most important metabolite for imaging cancer with HP. We were able to reduce the methanol content by over 98% in 15 seconds—an important step towards biocompatible hyperpolarization.

Motivation: Magnetic resonance imaging (MRI) is a powerful diagnostic tool in modern medicine, providing high-resolution imaging of soft tissue without the use of ionizing radiation. However, the ability of MRI to image metabolism is limited. Increasing the alignment of nuclear spins, *i.e.*, the polarization, permits the increase of the MR signal. Using stronger magnetic fields provides an increase that is approximately linear with the strength of the magnetic field. Going from 1.5 T to 3 T, for example, has about doubled the signal for all tissues. Moreover, techniques that involve hyperpolarization (HP), have been shown to boost the signal of MRI by several orders of magnitude, although only for selected molecules.² While dynamic nuclear polarization (DNP) produces hyperpolarized material reliably, it is a time consuming process. Parahydrogen-induced polarization (PHIP) is a quick alternative. However, adding parahydrogen (pH₂) to an unsaturated bond requires dedicated precursor molecules and requires one or two chemical reactions (hydrogenation, optional cleavage). Signal amplification by reversible exchange (SABRE) does not involve covalent chemical reactions for polarizing a substrate. SABRE, combined with spin-lock induced level anti-crossings (SLIC), enables HP of biologically relevant molecules such as [1-¹³C]pyruvate. This process was found to be most efficient using a metal-based catalyst [Ir(COD)(IMes)Cl] in methanol. Both the catalyst and the solvent are cytotoxic and must be removed before *in vivo* application. Here, we describe the implementation of a customized purification system to an existing experimental SLIC-SABRE setup and demonstrate the removal of methanol from [1-¹³C]pyruvate.

Materials & Methods: The purification system was described by Gökpek *et al.*¹ and consists of (i) two syringe pumps driven by stepper motors and a custom designed housing, (ii) a valve system consisting of three hand valves (P-783, IDEX H&S) made of high chemical resistance polymer (ETFE, PEEK) driven by servo motors. (iii) a vacuum pump (Welch CRV pro 6) with a vacuum valve (Nieruf GO2309313). (iv) a control box with customized code consisting of a MEGA2560 microcontroller, stepper, and servo motor driver. (v) a 60°C hot water bath.

The main components of the experimental SLIC-SABRE polarizer include an NMR unit, a hyperpolarizing reactor consisting of a 5 mm NMR tube, a homemade gas control unit, a process control unit featuring custom software (hypercontrol), and a digital-analog converter (MATLAB, National Instruments). The control unit controls the timing of the experiments.²

The SLIC-SABRE experiment was conducted using a 600 µL solution containing sodium [1-¹³C]pyruvate (4.82 mM), [Ir(COD)(IMes)Cl] (6.24 mM), dimethylsulfoxide (DMSO) (39.99 mM), and Na₂-EDTA 0.77 mM dissolved in methanol-d₄.

The purification protocol consisted of the following 4 steps:

1. Addition of 600 µL D₂O to the solution in an NMR tube, 5 seconds;
2. Manual transfer of NMR tube to 60°C hot water bath, 10 seconds
3. Evaporation of methanol by applying vacuuming, 15 seconds;
4. Extraction of the final aqueous solution, 10 seconds.

For quantification of the residual methanol content, we used a 9.4 T high-resolution NMR (Bruker Avance 400). We compared the water content and methanol content of the sample by integrating each of their NMR spectrum lines and taking the ratio of these integrals.

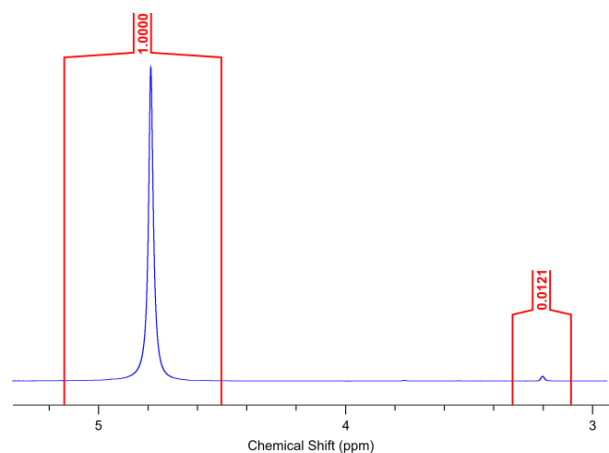


Fig. 1: ¹H NMR spectrum of a [1-¹³C]pyruvate solution after purification with 15 s evacuation (blue) and integrals (red). The signal intensity of methanol was 1.21% of the water intensity.

Results: We successfully implemented the purification system in the experimental SLIC-SABRE setup by integrating the purification system's electronics with the control unit of the SLIC-SABRE setup. The addition of liquid and valve actuation, and hence, the entire purification process, was automated. The whole process was controlled by the customized MATLAB software. We were able to perform the purification in the 5 mm NMR reactor.

The NMR integrals of the proton signals of water and methanol (both 99.5% deuteration level) have been compared, and the ratio was found to be 0.012 (methanol) to 1 (water) (Fig. 1). This led us to conclude, that after 15 s of evacuation of the tube, the methanol content was reduced to levels below 2%.

Discussion: The procedure described allowed us to remove 98% of methanol from the sample. Similar purification approaches showed similar results (99% of purification at 90°C in 15 s).³ However, as we started evaporation, the methanol in our sample started to overboil inside of the reactor. Further experiments are required to optimize the evaporation process. The filtration of the metal catalyst is pending, along with the experiments with hyperpolarization. An amount of methanol of about 1% may be acceptable for preclinical studies.³ More optimizing steps are required before we can use the hyperpolarized contrast agent for in vivo studies.

Conclusion: The purification protocol successfully removed over 98% of the methanol content in the [1-13C]pyruvate sample, approaching levels acceptable for preclinical studies. More optimization of the protocol is required before the hyperpolarized contrast agent can be used for these studies

and in vivo studies. Future steps include optimizing the filtration of the metal catalyst and preventing the sample from overboiling.

Acknowledgements: We wish to thank the Charles Hamilton Houston Program of the Amherst College Loeb Center for Career Exploration and Planning for funding this project's efforts. We also wish to thank the MOIN CC and the hyperquant from the program BlueHealthTech of the BMBF (Federal Ministry of Research, Technology and Space).

References:

1. Gökpek, *et al.* A parahydrogen polarizer for >30 bars hydrogenation and automated purification. 26th Ann. Meet. Ger. Chapter Int. Soc. Magn. Reson. Med. 2024, Tübingen
2. Sandbrink, *et al.* Implementation of SLIC-SABRE hyperpolarization of 1-13C pyruvate. 26th Ann. Meet. Ger. Chapter Int. Soc. Magn. Reson. Med. 2024, Tübingen
3. de Maissin, *et al.* In Vivo Metabolic Imaging of [1-13C]pyruvate-d3 Hyperpolarized by Reversible Exchange With Parahydrogen. *Angew. Chem. Int. Ed.* 2023; 62(36) e202306654. doi: 10.1002/anie.202306654
4. Hövener JB, Schwaderlapp N, Borowiak R, Lickert T, Duckett SB, Mewis RE, Adams RW, Burns MJ, Highton LA, Green GG, Olaru A, Hennig J, von Elverfeldt D. Toward biocompatible nuclear hyperpolarization using signal amplification by reversible exchange: quantitative in situ spectroscopy and high-field imaging. *Anal Chem.* 2014 Feb 4;86(3):1767-74. doi: 10.1021/ac403653q. Epub 2014 Jan 24. PMID: 24397559; PMCID: PMC3929132.

Preliminary In Vivo and Ex Vivo Assessment of MRI Artifacts from Biodegradable Mg-10Gd Implants: Implications for Alloy Design and Imaging Protocol Optimization.

Yu Sun 1†*, Aaron Diercks 2†, Olga Will 2, Heike Helmholtz 1, Berit Zeller-Plumhoff 1+3, Jan-Bernd Hövener 2, Regine Willumeit-Römer 1

1 Institute of Metallic Biomaterials, Helmholtz-Zentrum Hereon, Geesthacht, 21502, Germany

2 Section Biomedical Imaging, Department of Radiology and Neuroradiology, University Medical Center Kiel, Kiel University, Kiel, 24118, Germany

3 Data-Driven Analysis and Design of Materials, Faculty of Mechanical Engineering and Marine Technologies, University of Rostock, 18059, Germany

† equal contribution.

Abstract: Metallic artifacts in magnetic resonance imaging (MRI) significantly constrain the postoperative evaluation of orthopaedic implants, especially those made from conventional metallic materials like titanium or stainless steel. Recent evidence indicates that biodegradable magnesium (Mg)-based implants generate substantially fewer artifacts. The authors' preclinical and clinical studies also confirmed that pure Mg and certain Mg alloys allow reliable postoperative MRI monitoring of fracture healing. However, variability among alloying compositions may still induce localized artifacts under conventional imaging sequences. This study demonstrated the necessity for routine evaluation of artifact control and the exploration of novel sequences during the development of novel Mg-based materials.

Motivation: Magnetic resonance imaging (MRI) plays an important role for the preoperative evaluation of musculoskeletal diseases, and is promising for early diagnosis of severe postoperative complications such as fracture nonunion. Yet, metallic implants commonly used for bone fixation, particularly conventional inert metals, generate pronounced artifacts that impede quality imaging. Previous studies have demonstrated that biodegradable magnesium (Mg)-based materials induce far less artifacts in MRI than titanium implants, thereby supporting clearer insights into tissue-implant interfaces [1,2]. Nevertheless, some alloying components such as gadolinium (Gd), may present artifact susceptibility and require optimized sequences to ensure high image quality. The purpose of this preclinical study is to characterize artifact profiles of Mg-10Gd implants with different MRI sequences, through in vivo scans of cortical bone undergoing fracture healing process, as well as ex vivo scans of trabecular bone samples.

Materials & Methods: For preclinical validation, femoral shaft fractures were induced via osteotomy in female Sprague-Dawley rats under general anesthesia (n = 6; Ethical application via the local authority: V242-9462/2021). After intramedullary implantation of cylindrical Mg-10Gd pins (1.2 mm in diameter, 5.0 mm in length; prepared by permanent mold casting and extrusion procedures, followed by gamma-radiation sterilization), the femurs were stabilized with external fixation devices. At postoperative week 12, in vivo micro-CT was performed, followed by removal of fixators and in vivo MRI using T1-weighted rapid acquisition with relaxation enhancement (T1 RARE) sequence. To further assess MRI artifacts ex vivo, three types of hardware with similar dimensions were implanted transcortically into the humerus of chicken (*Gallus gallus domesticus*; n = 3), including pure Mg, Mg-10Gd and polyetheretherketone (PEEK). Ex vivo

MRI scans were conducted using a T2 RARE sequence. Micro-CT imaging served as a reference to qualitatively evaluate the impact of MRI artifacts on trabecular bone visualization. All MRI scans were performed using a 7 Tesla small animal MR system (BioSpec, Bruker BioSpin, Germany), and micro-CT scans were conducted with a vivaCT 80 scanner (Scanco Medical AG, Switzerland).

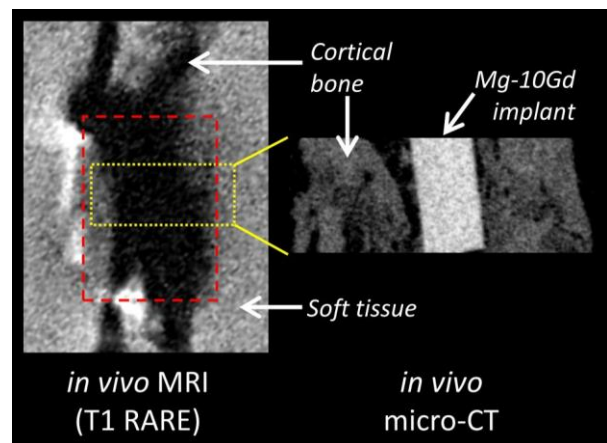


Fig. 1: In vivo MRI and micro-CT scans.

In vivo T1 RARE scan demonstrated the presence of signal voids surrounding the Mg-10Gd implant, indicating a localized magnetic-susceptibility artifact that masked the peri-implant cortical bone structure. In contrast, in vivo micro-CT scans provided clear visualization of both the cortical bone and the cylindrical implant at the level of osteotomy. (Note: MRI parameters: TR 477 ms, TE 11 ms, slice thickness 1 mm, pixel spacing 0.12 x 0.1 mm², acquisition duration 1193 sec; Micro-CT parameters: voltage 70 kVp, beam current 114 μA, isotropic voxel size 20 μm, integration time 300 ms; The red dotted box indicates the area affected by imaging artifacts; The yellow dotted box corresponds to the osteotomy site scanned by micro-CT.)

Results: In vivo T1 RARE scans revealed the existence of signal voids surrounding Mg-10Gd implants, indicative of localized magnetic susceptibility artifacts. The artifacts obscured the peri-implant cortical bone structure and resulted in signal loss in the adjacent tissue area (Figure 1). In contrast, the corresponding in vivo micro-CT scans provided clear rendering of both cortical bones and cylindrical implants. In ex vivo MRI, T2 RARE sequence allowed clear visualization of the cartilage tissue and the trabecular area in distal humeral region without hardware (Figure 2). The pure Mg and PEEK implants did not introduce severe artifacts, enabling clear visualization of the surrounding bone architecture. In comparison, Mg-10Gd implants induced more susceptibility artifacts, characterized by a region of signal distortion and loss, which obscured the adjacent trabecular structures.

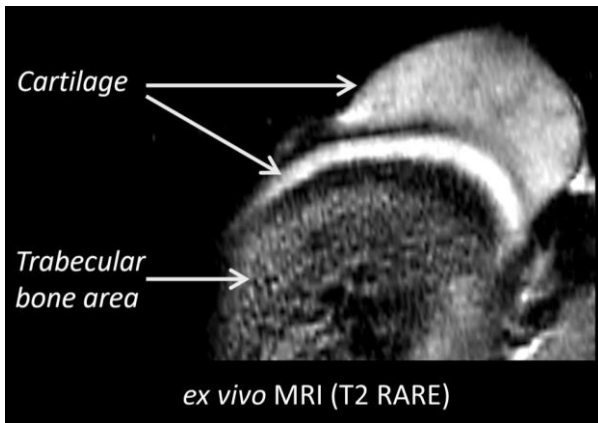


Fig. 2: Ex vivo MRI (T2 RARE) in an anatomical region without implants.

The soft tissue contrast provided by T2 RARE MRI enabled clear visualization of non-mineralized anatomical structures, that are typically challenging to assess using conventional CT imaging. Specifically, the articular cartilage is distinctly delineated as a hyperintense layer overlaying the subchondral bone, while the trabecular bone area reveals heterogeneous signal intensities representing both mineralized trabeculae and intertrabecular soft tissue components, such as marrow or connective tissue. (Note: MRI parameters: TR 3068 ms, TE 42 ms, slice thickness 1 mm, pixel spacing 0.086 x 0.086 mm², acquisition duration 660 sec.)

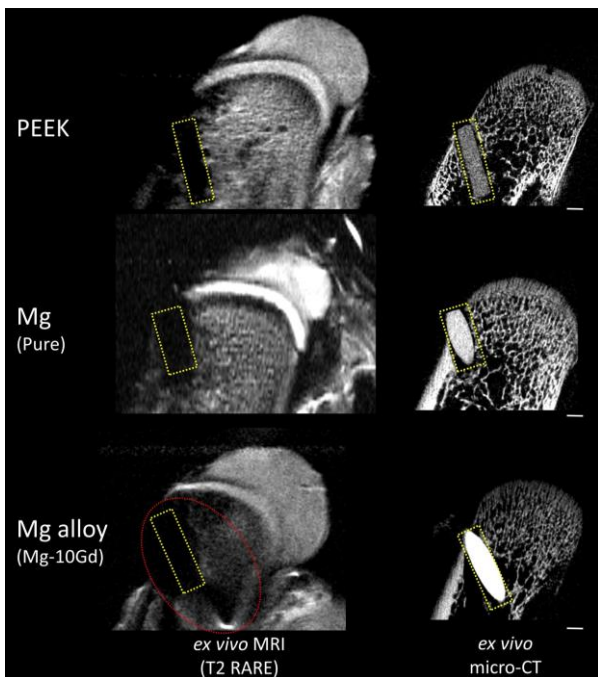


Fig. 3: Ex vivo MRI (T2 RARE) of transcortical hardware in the trabecular region.

The pure Mg and PEEK implants did not introduce severe artifacts, allowing clear visualization of the surrounding tissue architecture. In comparison, Mg-10Gd implant induced susceptibility artifacts, characterized by a region of signal distortion and signal loss, obscuring the adjacent trabecular structures (Note: The yellow dotted box corresponds to the implant region; The red dotted circle indicates the anatomical region affected by imaging artifacts; Scale bar: 1.0 mm).

Discussion: The magnetic susceptibility mismatch between the Mg-10Gd alloy and the surrounding tissue can lead to local magnetic field inhomogeneities, resulting in spatial misregistration and signal voids, especially in fast spin echo (FSE)-based sequences such as RARE. In preclinical and potential clinical contexts, such interference could compromise the assessment of osseointegration, bone remodeling and localized tissue responses. Sequence adjustments (e.g., increased bandwidth, shorter echo times, etc.) and validated strategies for titanium implants, such as multi-acquisition variable-resonance image combination (MAVRIC) and slice encoding for metal artifact correction (SEMAC), may help mitigate susceptibility effects [3,4]. To address the challenge, more imaging sequences will be tested by the authors to mitigate susceptibility effects, to realize comprehensive and artifact-resilient development of biodegradable metallic implants. Future research should also give attention to the radiofrequency-induced heating of Mg implants during MRI [5].

Conclusion: The presence of Mg-10Gd implants induced regional artifacts in MRI scans using T1 RARE and T2 RARE sequences, highlighting the necessity of alloy-specific artifact evaluation and the potential need for MRI protocol adaptation when using rare-earth containing alloys during translational research.

Acknowledgements: This work was supported by the IDIR-Project (Digital Implant Research), a cooperation financed by Kiel University, University Hospital Schleswig-Holstein and Helmholtz Zentrum Hereon. In vivo and ex vivo imaging were performed at Molecular Imaging North Competence Center (MOIN CC), which was founded by a grant from the European Regional Development Fund (ERDF) and the Zukunftsprogramm Wirtschaft of Schleswig-Holstein (project no. 122-09-053).

References:

1. Sun Y, Helmholtz H, Will O, Damm T, Wiese B, Luczak M, Peschke E, Luthringer-Feyerabend B, Ebel T, Hövener JB, Glüer CC, Willumeit-Römer R. Dynamic in vivo monitoring of fracture healing process in response to magnesium implant with multimodal imaging: pilot longitudinal study in a rat external fixation model. *Biomater Sci.* 2022;10(6):1532-1543.
2. Espiritu J, Berangi M, Yiannakou C, Silva E, Francischello R, Kuehne A, Niendorf T, Könniker S, Willumeit-Römer R, Seitz JM. Evaluating metallic artefact of biodegradable magnesium-based implants in magnetic resonance imaging. *Bioact Mater.* 2022;15:382-391.
3. Lu W, Pauly KB, Gold GE, Pauly JM, Hargreaves BA. SEMAC: Slice Encoding for Metal Artifact Correction in MRI. *Magn Reson Med.* 2009;62(1):66-76.
4. Filli L, Jud L, Luechinger R, Nanz D, Andreisek G, Runge VM, Kozerke S, Farshad-Amacker NA. Material-Dependent Implant Artifact Reduction Using SEMAC-VAT and MAVRIC: A Prospective MRI Phantom Study. *Invest Radiol.* 2017;52(6):381-387.
5. Espiritu J, Berangi M, Cwieka H, Iskhakova K, Kuehne A, Florian Wieland DC, Zeller-Plumhoff B, Niendorf T, Willumeit-Römer R, Seitz JM. Radiofrequency induced heating of biodegradable orthopaedic screw implants during magnetic resonance imaging. *Bioact Mater.* 2023;25:86-94.

Transfer agents for relaying parahydrogen-induced hyperpolarization.

Kolja Them 1*, Philip Saul 1, Andrey N. Pravdivstev 1, Jan-Bernd Hövener 1

1 Department of Radiology and Neuroradiology, Section Biomedical Imaging, University Hospital Schleswig-Holstein, Kiel University, Kiel, Germany

Abstract: Relaying hyperpolarization between molecules via proton exchange is a broadly applicable method to polarize various target molecules. We investigated different transfer agents using quantum spin dynamics simulations to identify efficient chemical and physical systems for parahydrogen-induced polarization relayed via proton exchange (PHIP-X). The influence of proton exchange rates, magnetic field cycling, relaxation times, and J-coupling networks was systematically evaluated. The simulations indicate that high polarization levels can be achieved under specific conditions: exchange rates around 200 s⁻¹, magnetic fields below 10 nT, labile proton T₁ relaxation times above 0.1 s, and matched J-couplings. Under these conditions, polarizations of up to 24% (¹³C) and 14% (¹⁵N) were calculated.

Motivation: Parahydrogen-induced hyperpolarization (PHIP) offers a promising approach to enhance MR sensitivity in a cost-effective and time-efficient manner. A key advantage of PHIP-X lies in its broad applicability: it can be used to hyperpolarize a wide range of molecules participating in proton exchange, including many biologically and chemically relevant compounds.

However, the polarization levels achieved with PHIP-X still require further improvement for practical applications. The underlying potential of PHIP-X is evident, as polarization levels exceeding 40% can be obtained on the transfer molecule itself. The key challenge lies in optimizing the polarization transfer mechanism to relay this high polarization to the target molecule efficiently.

In this work, we addressed this issue by using quantum spin dynamics simulations and explored how various physical and chemical parameters affect polarization transfer efficiency in PHIP-X. In particular, we investigated the roles of proton exchange rates, magnetic field, relaxation times of labile protons, and J-coupling networks. We aimed to provide a basis for the future design of more effective transfer agents and experimental protocols.

Materials & Methods: The transfer agent was approximated by using a 13C-1H spin system (two spins-1/2, #1 and #2). The target molecule was either a 1H-13C or a 1H-15N pair (total: 4-spin-1/2 system, #3 and #4, Fig. 1b, c). We assumed that the 13C spin of the transfer agent was initially polarized to 50% at t=0 (Fig. 1, red) and that the protons, #2 and #3, undergo chemical exchange with rate k. A three-step magnetic field cycling was applied, B1(t1), B2(t2) and B3(t3) as indicated in the figures. The transfer agent may be assumed to be produced by hydrogenation of 13C-labeled propargyl alcohol with pH₂ (Fig. 1a). The mathematical structure used for the simulations included exchange and relaxation superoperators (fig. 2).

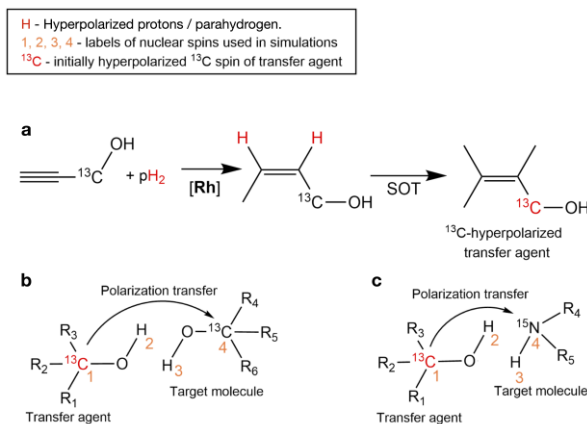


Fig. 1: Process of polarizing 13C of the transfer agent 1-13C allyl alcohol using PHIP (a). Spin systems of transfer and target molecule (b, c). Note that the transfer agent could also be polarized using DNP.

The spin dynamics were calculated by solving eq. (1):

$$\frac{d}{dt} \sigma(t) = \hat{G} \sigma(t), \text{ where } \hat{G} = \hat{L} + \hat{R} = \begin{pmatrix} L^X & 0 \\ 0 & \hat{Y} \end{pmatrix} + \begin{pmatrix} -K_1 & K_2 \\ K_1 & -K_2 \end{pmatrix} \quad (1)$$

We have $\hat{L}^A = -i\hat{H}_A + \hat{R}_A$, $A = X, Y$, where $\hat{H}_A = H_A \otimes \hat{1} - \hat{1} \otimes (H_A)^T$ and

$$H_X = 2\pi (J_{12}\vec{S}_1 \cdot \vec{S}_2 + J_{34}\vec{S}_3 \cdot \vec{S}_4) - \sum_{i=1}^4 \gamma_i (1 - \sigma_i) B_{ext}^X(t) S_i^z$$

$$H_Y = 2\pi (J_{13}\vec{S}_1 \cdot \vec{S}_3 + J_{24}\vec{S}_2 \cdot \vec{S}_4) - \sum_{i=1}^4 \gamma_i (1 - \sigma_i) B_{ext}^Y(t) S_i^z$$

J_{ij} are J-coupling constants and $\gamma_i (1 - \sigma_i) B_{ext}^X(t) S_i^z$ describes the interaction of spins with external magnetic fields. The relaxation superoperator was chosen to be

$$\hat{R} = \sum_{i=1}^4 1/T_{i1} \left(\sum_{a=x,y,z} S_i^a \otimes (S_i^a)^T \right) - 3/4 \sum_{i=1}^4 \hat{1} \otimes \hat{1}$$

The initial state $\sigma(t=0) \equiv \sigma_0$ was chosen to be by $\sigma_0 = \begin{pmatrix} \sigma_{x0} & 0 \\ 0 & \sigma_{y0} \end{pmatrix}$, where (for $A=X, Y$) $\sigma_{A0} = \sigma_{A1} \otimes \sigma_{A2}$,

$$\sigma_{A1} = \frac{1}{2} \begin{pmatrix} 1 + P_0 & 0 \\ 0 & 1 - P_0 \end{pmatrix}$$

and

$$\sigma_{A2} = \sigma_{A2U} / \text{Tr}(\sigma_{A2U}) \text{ with } \sigma_{A2U} = \exp(-\beta \sum_{i=2,3,4} \gamma_i (1 - \sigma_i) B_{ext}^X(t) S_i^z + J_{34}\vec{S}_3 \cdot \vec{S}_4)$$

With $P_0(13C) = 50\%$ of the transfer agent at t=0. J-couplings used in system X (if not stated otherwise): $J_{12} = -3$ Hz, $J_{13} = 0$, $J_{34} = 0$, $J_{34} = -3$ Hz for ¹³C and $J_{34} = 90$ Hz for ¹⁵N. System Y: $J_{12} = 0$, $J_{13} = -3$ Hz, $J_{34} = 0$, $J_{34} = -3$ Hz for ¹³C and $J_{34} = 90$ Hz for ¹⁵N.

Fig. 2: Mathematical structure used for the spin dynamic simulations.

Results: Maximum polarization (P) of the target was found for exchange rates of $k = 200$ s⁻¹ (fig. 3 a and b, blue lines). For 13C we found $P(\text{SzC}) \approx 19\%$ and for 15N we found $P(\text{SzN}) \approx 12\%$. Slower exchange rates ($k = 50, 10, 5, 1$ and 0.1 s⁻¹) significantly reduced polarization transfer. Exchange rates of 1 s⁻¹ still generated target polarizations of up to 4% (13C) or 3% (15N). Variations of B₂ during MFC provided maximum polarizations of $P(\text{SzC}) \approx 19\%$ and $P(\text{SzN}) \approx 12\%$ for fields $B_2 < 10$ nT (Fig. 3 c and d). Stronger magnetic fields ($B_2 = 50, 100, 500$ and 1000 nT) resulted generally in significantly reduced polarization yields. Not unexpectedly, the polarization of the target increased with T_{1L} of the labile proton (Fig. 3 e and f). For T_{1L} = 0.05 s, $P(13C/15N) > 2\%$, and maximum polarizations were $P(13C) \approx 24.8\%$ and $P(15N) \approx 14.1\%$ for T_{1L} = 4 s. For T_{1L} < 0.01 s, the 13C and 15N polarizations nearly vanished. Next, $P(13C / 15N)$ were calculated for different J-coupling networks (fig. 4). We varied J₁₂ from -1 Hz to -12 Hz, J₃₄ was kept fixed at -3 Hz (fig. 4 a), -6 Hz (fig. 4 b) and -9 Hz (fig. 4 c) for 13C and J₃₄ = 90 Hz (fig. 4 d) for 15N. For 13C, the

maximum polarization PM and the average polarization PA (calculated as the mean value between $t = 500$ ms and $t = 2500$ ms) had a common maximum if $J_{12} = J_{34}$. P(SzN) increased monotonously from $J_{12} = -1$ Hz to $J_{12} = -12$ Hz.

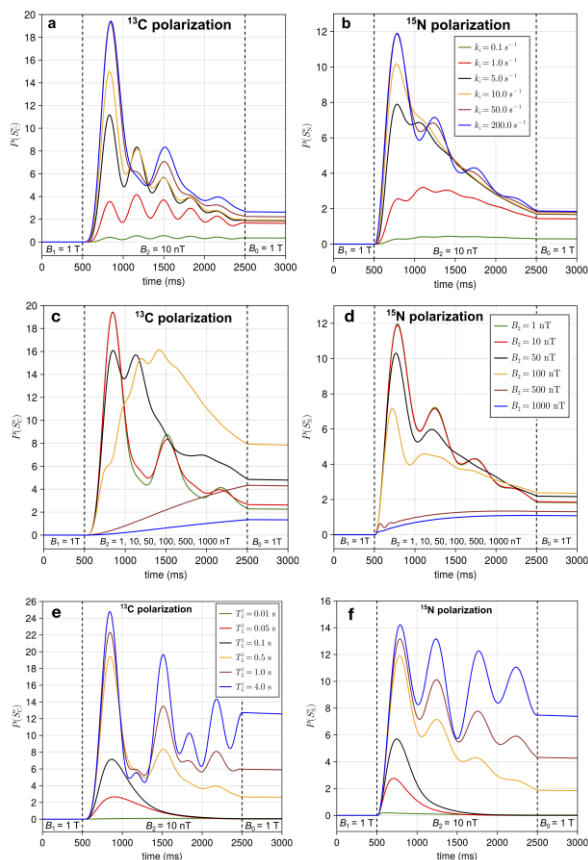


Fig. 3: ^{13}C (a) and ^{15}N (b) polarization of the target molecule for different exchange rates k . Maximum polarization was found at $k = 200 \text{ s}^{-1}$. Slower exchange rates ($k = 50, 10, 5, 1,$ and 0.1 s^{-1}) significantly reduced polarization yields. ^{13}C (c) and ^{15}N (d) target polarization as a function of the field strength B_2 during MFC. A maximum ^{13}C - and ^{15}N -target polarization was found for fields $B_2 < 10 \text{ nT}$. ^{13}C (e) and ^{15}N (f) target polarization as function of T_{1L} of the labile protons. Shorter relaxation times drastically decrease the polarization yield, making T_{1L} a critical parameter.

Discussion: Using an X nucleus in the transfer agent as a polarization storage is a promising approach for PHIP-X, where high target polarization may be achieved. The challenge remains to tailor novel transfer agents and solvent systems to fine-tune chemical exchange rates, labile protons' relaxation times, and J-coupling networks. When the correct conditions are met, ^{13}C polarizations of 24 % and ^{15}N polarizations of 14 % on various molecules may be achievable. The challenge remains that the spin system could be more complex experimentally, and valuable polarization will sink to other non-exchanging protons instead of direct transfer to the target via #3-#4 proton exchange.

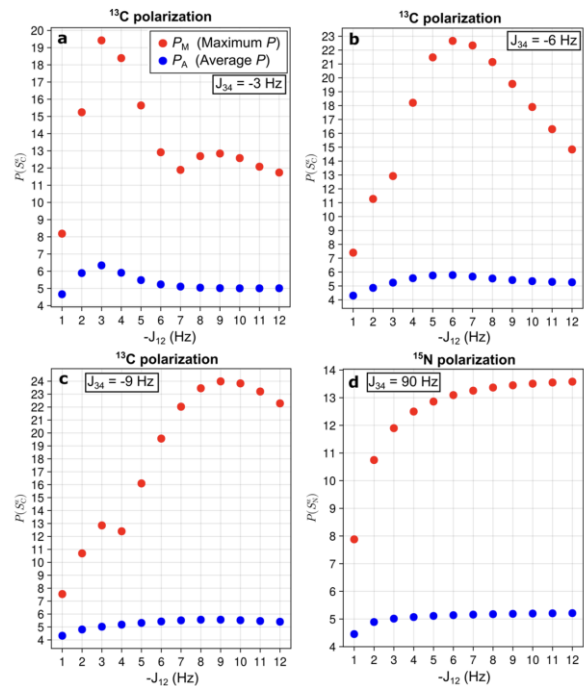


Fig. 4: ^{13}C / ^{15}N polarization as a function of J_{12} , while J_{34} was kept fixed at -3 Hz (a), -6 Hz (b), -9 Hz (c), and 90 Hz (d). For ^{13}C , the maximum polarization (PM) and the average polarization (PA) showed a maximum if $J_{12} = J_{34}$ (a, b, and c). P(SzN) increased monotonously from $J_{12} = -1$ Hz to $J_{12} = -12$ Hz.

Conclusion: The study shows that, for an initially ^{13}C -polarized transfer agent, the efficiency of polarization transfer via proton exchange depends on exchange rates, MFC, relaxation times of labile protons, and J-coupling networks. Fine-tuning these parameters to $k = 200 \text{ s}^{-1}$, $B_2 < 10 \text{ nT}$, $T_{1L} > 0.5 \text{ s}$, and $J_{12} = J_{34}$ by tailoring novel transfer agents and solvent systems can lead to a significant polarization gain in PHIP-X.

Acknowledgements: We acknowledge support from the German Federal Ministry of Education and Research (BMBF) (03WIR6208A hyperquant), DFG (555951950, 527469039, 469366436, HO-4602/2-2, HO-4602/3, HO-4602/4, EXC2167, FOR5042, TRR287). MOIN CC was founded by a grant from the European Regional Development Fund (ERDF) and the Zukunftsprogramm Wirtschaft of Schleswig-Holstein (Project no. 122-09-053).

References:

1. Adams, R. W. *et al.* Reversible Interactions with para-Hydrogen Enhance NMR Sensitivity by Polarization Transfer. *Science* 323, 1708–1711 (2009).
2. Cavallari, E., Carrera, C., Aime, S. & Reineri, F. Metabolic Studies of Tumor Cells Using [^{1-13}C] Pyruvate Hyperpolarized by Means of PHIP-Side Arm Hydrogenation. *ChemPhysChem* 20, 318–325 (2019).
3. Iali, W., Rayner, P. J. & Duckett, S. B. Using parahydrogen to hyperpolarize amines, amides, carboxylic acids, alcohols, phosphates, and carbonates. *Science Advances* 4, eaao6250 (2018).
4. Them, K. *et al.* Parahydrogen-Induced Polarization Relayed via Proton Exchange. *J. Am. Chem. Soc.* 143, 13694–13700 (2021).
5. Them, K., Kuhn, J., Pravdivtsev, A. N. & Hövener, J.-B. Nuclear spin polarization of lactic acid via exchange of parahydrogen-polarized protons. *Commun Chem* 7, 1–11 (2024).

Assessment of Hypoxia in a Glioblastoma Model by MRI, PET and Histopathological Analysis

Jesse Torija-Maximo^{1*}, Martin Grasheis¹, Carolin Kitzberger², Sandra Sühnel¹, Elisabeth Bliemsrieder¹, Peter J. Nelson², Rainer Glaß³, Wolfgang Weber¹, Christine Spitzweg², Franz Schilling¹

¹Technical University of Munich, TUM University Hospital, Klinikum rechts der Isar, School of Medicine, Department of Nuclear Medicine, Munich, Germany

²Department of Internal Medicine IV, LMU University Hospital, Ludwig-Maximilians-University Munich, Munich, Germany

³Neurosurgical Research University Clinics, Ludwig-Maximilians-University Munich, Munich, Germany and Walter-Brendel-Centre of Experimental Medicine

Abstract: Here we demonstrate the ability to characterize the microenvironment of bulk and individual glioblastoma subtypes (GBM2: highly invasive, and GBM14: more hypoxic and angiogenic) through hypoxia, vascularization and tissue density by PET, Histology and DWI, respectively. Hypoxia was confirmed with positive pimonidazole staining and correlated with [18F]FMISO PET ($r=0.49$, $p=0.035$). Vascularization was quantified through CD31 staining and had a negative correlation with [18F]FMISO ($r=-0.50$, $p=0.011$) but not with pimonidazole ($r=-0.13$, $p=0.56$). No correlation was observed between ADC and hypoxiaHC ($r=0.19$, $p=0.42$) or hypoxiaPET ($r=0.024$, $p=0.92$). Our results suggest that lack of vascularization is a stronger indicator of hypoxia than tissue density and highlights that angiogenesis functions differently across glioblastoma subtypes.

Motivation: Glioblastoma is among the most fatal brain tumors, in part due to contribution of hypoxia to therapy resistance (1). Furthermore, glioblastoma heterogeneity of the tumor has led glioblastoma into the classification of different subtypes (2). These heterogeneities create a microenvironment (Fig. 1a) with unique variations in hypoxia, vascularization and tissue density. Through the adaption of oxygen supply these alterations contribute to the invasiveness, angiogenesis and treatment outcome (3). Current methods involve characterizing hypoxia in glioblastomas through [18F]FMISO (in vivo) but the underlying principles on a microscale are often unclear (4). In this study we utilize two distinct glioblastoma models: GBM14, a more angiogenic and hypoxic proneural subtype and GBM2, a highly invasive mesenchymal-like model (5)(6). With the aim to unravel how the glioblastoma microenvironment drives hypoxia utilizing positron emission topography (PET), magnetic resonance imaging – diffusion weighted imaging (DWI) and histology to understand hypoxia formation in different glioblastoma subtypes.

Materials & Methods: Animal Study: Subcutaneous xenograft models were generated by injecting 1×10^6 patient derived glioblastoma cells (GBM2, $n = 16$; GBM14, $n = 22$) into the right flanks of 38 CD-1 nu/nu mice.

MR-Imaging: T2-weighted RARE-imaging was used to localize tumors, followed by diffusion weighted imaging (DWI) using a DWI-EPI-sequence with 16 b-values. Apparent diffusion coefficients (ADC) were derived by monoexponential fitting of the DWI data and analyzed in MATLAB.

PET-Imaging: Three hours prior to data acquisition mice were injected with 12.71 ± 0.78 MBq ([18F]FMISO). Standard uptake values (SUV) were calculated from activity concentration, decay rate, body weight and injected activity. Inveon research

workplace 4.2. was used to analyze the data, and mean SUV were obtained by drawing regions of interest (ROIs).

Immunohistochemistry: One hour prior to sacrifice, mice were intraperitoneally administered 60 mg/kg body weight pimonidazole. Tumors were extracted, paraffin embedded and sectioned in the same orientation as MR-images. Immunohistochemistry was performed for pimonidazole and cluster of differentiation 31 (CD31). Cell detection was performed in QuPath using a trained object classifier for pimonidazole detection, classifying cells as positive, negative or necrotic (7). With results reported as the percentage of positive pimonidazole detections relative to all classified cells. For CD31, a pixel classifier was trained to identify positive staining, and results were reported as the proportion of CD31 positive area relative to the total analyzed area.

Statistical Analyses: Data was analyzed in GraphPad Prism. Statistical significance was considered for $p \leq 0.05$. Correlation analyses were conducted using the Pearson R coefficient.

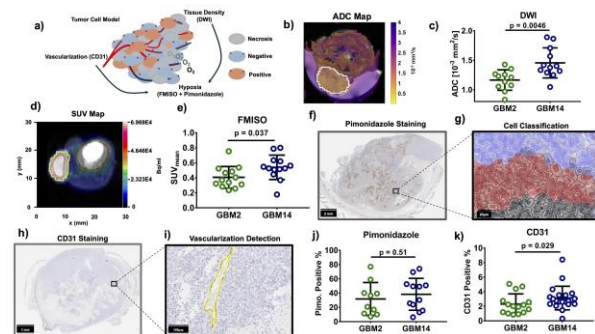


Fig. 1: Study overview. (a) Tumor model schematic. (b-c) ADC-map with tumor ROI; statistical difference in tissue density. (d-e) [18F]FMISO uptake with ROI; statistical difference in hypoxiaPET. (f-g) DAB staining for pimonidazole(hypoxiaHC) and cell classification. (h-i) DAB staining for CD31(vascularization) and pixel classification. (j-k) GBM2 and GBM14 compared for hypoxiaHC and vascularization.

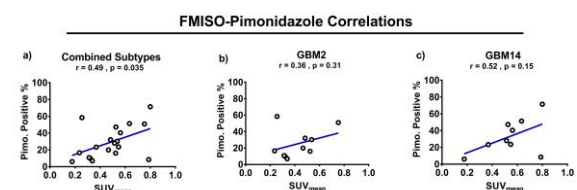


Fig. 2: Correlation of the hypoxia measures SUVmean for [18F]FMISO and positivity of pimonidazole. (a) Hypoxia assessed by PET and histology shows a strong linear correlation between both hypoxia measures. (b) Analysis of the GBM2 cohort only shows no significant correlation. (c) Analysis of the GBM14 cohort only shows no significant correlation.

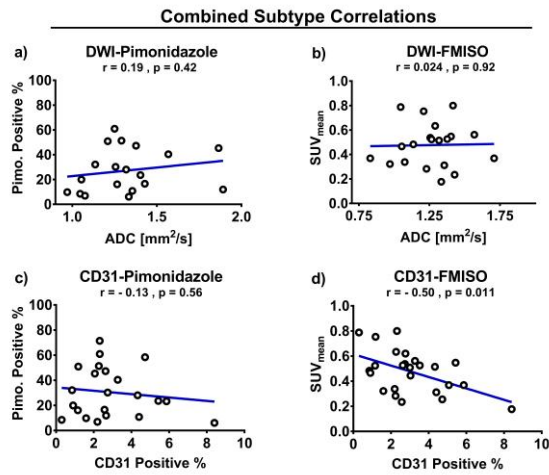


Fig. 3: Correlation plots of hypoxia with tissue parameters across collective subtypes. (a) ADCmean(tissue density) and pimonidazole(hypoxiaIHC) show no significant correlation. (b) ADCmean(tissue density) and SUVmean(hypoxiaPET) show no significant correlation. (c) CD31 (vascularization) and pimonidazole(hypoxiaIHC) show no significant correlation. (d) CD31 (vascularization) and SUVmean(hypoxiaPET) show a significant negative correlation.

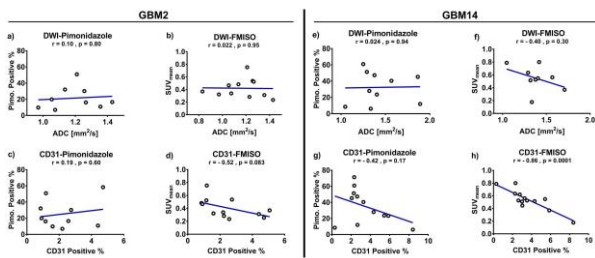


Fig. 4: Correlation plots of hypoxia with tissue parameters across subtypes. Parameters include ADCmean(tissue density), pimonidazole (hypoxiaIHC), SUVmean(hypoxiaPET) and CD31(vascularization) matched across tumor subtype. GBM2: (a-d) No significant correlations. GBM14: (e-g) No significant correlations; (h) CD31 (vascularization) and SUVmean(hypoxiaPET) show a significant negative correlation.

Results: ADC-maps (example in Fig. 1b) show GBM14 to have a significantly higher apparent diffusivity ($ADC_{mean} = (1.46 \pm 0.07) \cdot 10^{-3} \text{ [mm]}^2/\text{s}$, Fig. 1c) compared to GBM2 ($ADC_{mean} = (1.16 \pm 0.05) \cdot 10^{-3} \text{ [mm]}^2/\text{s}$, $p=0.005$). For $[18F]FMISO$ -PET (Fig. 1d), GBM14 exhibited a higher uptake with a $SUV_{mean} = 0.54 \pm 0.05$ significantly greater than GBM2 ($SUV_{mean} = 0.41 \pm 0.04$), $p=0.037$, Fig. 1e).

Pimonidazole stains (Fig. 1f) and detections (Fig. 1g) show relevant fractions of positive cells ($30.5\% \pm 0.04\%$). Vessel detection on CD31 stainings (Fig. 1h,i) exhibit $2.856\% \pm 0.003\%$ mean positive area. GBM2 show lower, but non-significant pimonidazole detections $31.8\% \pm 0.07\%$ compared to GBM14 ($38.3\% \pm 0.06\%$, $p=0.51$, Fig. 1j). For CD31, GBM14 exhibited a significantly higher vascularization $3.232\% \pm 0.004\%$ compared to GBM2 ($2.304\% \pm 0.004\%$, $p=0.03$, Fig. 1k).

Hypoxia detection appears valid as measurements from both PET (hypoxiaPET) and pimonidazole (hypoxiaIHC) correlate ($r=0.49$, $p=0.035$, Fig. 2a). However, individual subtypes show no correlation (GBM2: $r=0.36$, $p=0.31$, Fig. 2b; GBM14: $r=0.52$, $p=0.15$, Fig. 2c). Regarding its tissue density, no correlation with hypoxiaIHC ($r=0.19$, $p=0.42$, Fig. 3a) and hypoxiaPET ($r=0.024$, $p=0.92$, Fig. 3b) was found. For vascularization no

correlation was observed for hypoxiaIHC ($r=-0.13$, $p=0.56$, Fig. 3c) while it negatively correlates with hypoxiaPET ($r=-0.50$, $p=0.011$, Fig. 3d). When separated by glioblastoma subtype no correlation persisted neither for tissue density with hypoxiaIHC (Fig. 4a, e) and hypoxiaPET (Fig. 4b, f) nor vascularization correlation with hypoxiaIHC (Fig. 4c, g). Vascularization correlation persists with hypoxiaPET in GBM14 ($r=-0.86$, $p=0.0001$, Fig. 4h) but not in GBM2 ($r=-0.52$, $p=0.083$, Fig. 4d).

Discussion: Combined analysis across subtypes was used to assess whether the relationship between hypoxia and tissue microenvironment persists across glioblastoma subtypes of varying angiogenic and invasiveness. To account for variability in glioblastoma, that may influence the tumor microenvironment and therapeutic response, tumors were also analyzed by subtype.

Hypoxia was confirmed by demonstrating a correlation between pimonidazole and $[18F]FMISO$. The positive correlation between hypoxia markers was not maintained for each individual subtype, suggesting subtype specific differences in hypoxia dynamics. The lack of correlation may be an attribute of different pharmacodynamic behaviors of hypoxia tracers. $[18F]FMISO$ provides a whole tumor evaluation while pimonidazole assesses only a thin slice ($3 \mu\text{m}$) amplifying this discrepancy. Differences in hypoxia dynamics were confirmed by the significant uptake difference of $[18F]FMISO$ ($p=0.037$), suggesting that GBM14 may be more hypoxic than GBM2.

A correlation was observed between $[18F]FMISO$ and CD31 but not between pimonidazole and CD31. CD31 quantifies vessel density but not actual perfusion nor does it predict tissue oxygenation. Since $[18F]FMISO$ is delivered by the bloodstream, its accumulation into hypoxic regions is perfusion dependent. A closer look at CD31 revealed that the negative correlation with $[18F]FMISO$ in GBM14 but not in GBM2, indicating that angiogenesis as a response to or driver of hypoxia functions differently across glioblastoma subtypes.

Neither hypoxia marker correlated with tissue density, suggesting that oxygen availability is independent of cell density measured by ADC.

Conclusion: These results show that subtypes collectively reveal a close relation between angiogenesis and hypoxia but are not always preserved within individual subtypes. Our PET, MRI and histological analysis successfully distinguishes between glioblastoma models based on DWI, $[18F]FMISO$, pimonidazole, and CD31 suggesting subspecific differences. These findings highlight the complexity of the tumor microenvironment seen between the distinct patterns in hypoxia, vascularization and tissue density. Accurately measuring hypoxia and the underlying causes remains a complex field, even when integrating multimodal imaging with histology. To fully understand the tumor microenvironment further analysis is needed which might be able to bridge the gap in tissue coverage between PET and histology.

Acknowledgements: We acknowledge help from Sybille Reder, Markus Mittelhäuser and Hannes Rolbieski for help with PET-Acquisitions, Michael Herz for PET-Tracer Synthesis

and Marion Mielke, Olga Seelbach and Tanja Groll from pathology department (CeP) for help with histology. Further, we acknowledge support from the Deutsche Forschungsgemeinschaft (DFG, German Research Foundation – 391523415, SFB 824).

References:

1. Bar EE. Glioblastoma, cancer stem cells and hypoxia. *Brain Pathology*. 2011 Mar; 21(2):119-29.
2. Eisenbarth, D., Wang, Y.A. Glioblastoma heterogeneity at single cell resolution. *Oncogene* 42, 2155–2165 (2023).
3. Chen, Z., Han, F., Du, Y. et al. Hypoxic microenvironment in cancer: molecular mechanisms and therapeutic interventions. *Sig Transduct Target Ther* 8, 70 (2023).
4. Preibisch C, Shi K, Kluge A, Lukas M, Wiestler B, Göttler J, Gempt J, Ringel F, Al Jaber M, Schlegel J, Meyer B, Zimmer C, Pyka T, Förster S. Characterizing hypoxia in human glioma: A simultaneous multimodal MRI and PET study. *NMR Biomed*. 2017 Nov;30(11).
5. Giorgia Mastrella, Josefine Radke, Rainer Glass, Roland E. Kälin; Targeting APLN/APLN Improves Antiangiogenic Efficiency and Blunts Proinvasive Side Effects of VEGFA/VEGFR2 Blockade in Glioblastoma. *Cancer Res* 1 May 2019; 79 (9): 2298–2313.
6. Matthias Jürgen Schmitt, Massimo Squatrito, Michela Serresi, Gaetano Gargiulo; Phenotypic Mapping of Pathologic Cross-Talk between Glioblastoma and Innate Immune Cells by Synthetic Genetic Tracing. *Cancer Discov* 1 March 2021; 11 (3): 754–777.
7. Bankhead, P., Loughrey, M.B., Fernández, J.A. et al. QuPath: Open source software for digital pathology image analysis. *Sci Rep* 7, 16878 (2017).

StrokeCap: the mobile stroke diagnostics – a simulation study

Teresa Reichl 1, Johanna Günther 1+4, Martin A. Rückert 1, Thomas Kampf 1+2, Andreas Wörle 1, Mirko Pham 2, Moriz Herzberg 3+6, Volker C. Behr 1, Stefan Herz 3+5, Patrick Vogel 1+4

1 Department of Experimental Physics 5 (Biophysics), Julius-Maximilians University, Würzburg, Germany

2 Department of Diagnostic and Interventional Neuroradiology, University Hospital, Würzburg, Germany

3 Department of Diagnostic and Interventional Radiology, University Hospital, Würzburg, Germany

4 Phase VISION GmbH, Rimpf, Germany

5 Radiologie Augsburg Friedberg, Augsburg, Germany

6 KWM Juliusspital, Würzburg, Germany

Abstract: Stroke is a leading cause of death and disability worldwide resulting in high healthcare costs. Early detection of ischemic stroke, caused by vessel blockage, is critical for effective treatment.

This study introduces StrokeCap-project aiming to develop a portable, real-time diagnostic device based on Magnetic Particle Spectroscopy.

The cap-like system uses multiple transmit-receive coils to detect brain pathological perfusion abnormalities by inductively detecting administered MNP-tracer (magnetic nanoparticles).

To optimize the coil setup for a first StrokeCap-prototype, real CT-perfusion data from different stroke types are used to simulate an artificial MNP bolus distribution in the brain over time. Based on this simulation, the coil position and sequencing can be optimized enhancing the detection accuracy.

Motivation: Stroke poses a significant public health issue worldwide, affecting approximately 15 million individuals annually, with around 5 million resulting in death and another 5 million left permanently disabled [1]. Most strokes are ischemic, caused by blood clots in cerebral arteries, while hemorrhagic strokes account for a smaller percentage. Following the time is brain concept the start of treatment as early as possible is paramount for better outcome. However, reliable diagnostics is currently only widely available by clinic-based CT or MRI delaying the transport of patients to dedicated hospitals with stroke unit and, hence, start of treatment.

Recent advancements in measurement methods based on nonlinear magnetic behavior, particularly Magnetic Particle Imaging (MPI) [2,3], and Magnetic Particle spectroscopy (MPS) [4], offer promising new pathways for developing mobile stroke diagnostics [5]. Unlike conventional imaging modalities such as CT and MRI, MPI and MPS utilize magnetic nanoparticles (MNPs) as a tracer to provide sensitive measurement of blood flow in the brain in real-time. While MPI has demonstrated high sensitivity and temporal resolution in preclinical models, existing MPI scanners remain stationary and cumbersome, limiting their clinical application compared to established imaging settings.

In this context, we introduce the StrokeCap, a portable brain scanner-array concept based on MPS to address the urgent need for early on-site stroke diagnosis by detecting areas of reduced blood supply in the brain in real-time.

Materials & Methods: The StrokeCap aims to detect ischemic stroke using MPS technology [6] by monitoring an intravenously injected bolus of magnetic nanoparticles (MNPs), e.g., Resotran® [7]. Time-varying magnetic fields

(~15–20 kHz, 5–20 mT) are used to generate a non-linear magnetization response of the MNPs resulting in higher harmonics detectable via inductive receive coils (fig.2 a,b).

Cerebral perfusion is divided across two hemispheres, each supplied by three main arteries (see fig.1). To provide the necessary localized information, the StrokeCap consists of a flexible, cap-like array of at least six transmit-receive coils forming multiple individual MPS sensors. Each sensor detects MNP concentrations within its sensitivity zone, allowing localized, time-resolved perfusion monitoring (fig.2 b,c). This concept is similar to MREG known from MRI [9].

The MNP concentration is tracked over time to identify perfusion delays or absence, indicating arterial occlusion (fig.2 d). Perfusion signals can be analyzed and visualized via parameters such as time-to-peak (TTP), enabling fast assessment of perfusion dynamics (fig.2 e).

To optimize coil placement and system sensitivity, simulated MNP bolus propagation through the brain based on real CT-perfusion data from stroke patients is used within a home-built simulation framework [8]. These datasets were preprocessed to extract clean tracer dynamics and used to generate synthetic MNP perfusion signals across vascular territories.

Results: For initial simulation studies, six CT perfusion data sets from stroke patients have been processed to provide the 3D time-dependent distribution of the injected tracer. Data preparation consists of multiple steps: time ordering, pre-filtering as well as re-gridding to provide isotropic spatial resolution. To overcome undesired signal-spikes due to slightly displacements between time-resolved slices, volumes are co-registered at all time-steps. Finally, all information of non-brain tissue was removed before calculating a DSA-like tracer-perfusion signal.

Within a specific MPI simulation framework [8] different transmit-receive coil setups as well as different generation methods have been implemented and compared for their performance. The coil distribution over the head follows a hexagonal structure to reduce crosstalk between adjacent coils. Four different approaches for signal generation and acquisition have been compared:

1. Multi-MPS approach: multiple small coils ($R_{\text{small}}=40$ mm) act as independent MPS sensors with local excitation and acquisition.
2. RXtx approach: a large solenoid coil (headband; $R_{\text{large}}=110$ mm) is used as receive coil in combination with multiple small coils as excitation coils.
3. TXrx approach: a large solenoid coil (headband) acts as global excitation coil while multiple small coils are used for local signal acquisition.

4. TXRXoffset approach: two large solenoid coils (headband) operate as a large MPS sensor covering the entire brain. Multiple small coils generate successively static offset fields resulting in a local generation of even higher harmonics.

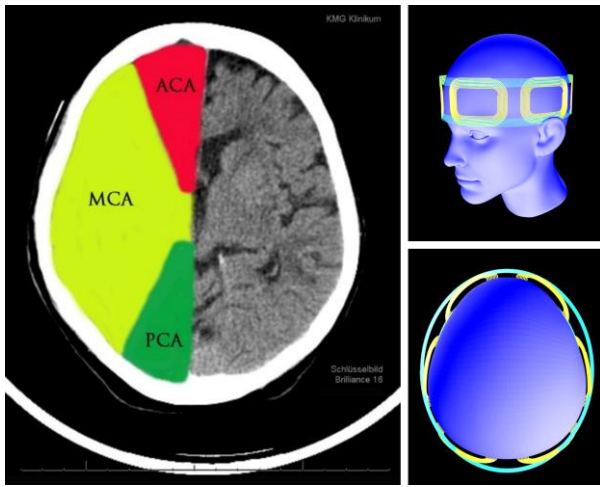


Fig. 1: Left: In case of arterial ischemic stroke, it is important to know the affected area within the brain depending on the supplying artery: Anterior (ACA), Middle (MCA), and Posterior Cerebral Arteries (PCA). Right: Simulated coil concept for MPS-based brain scanner.

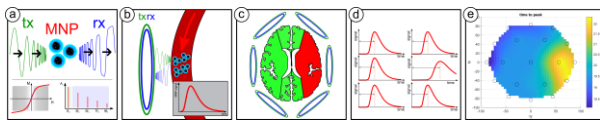


Fig. 2: (a) MPS basics: nonlinear magnetization response of MNPs to sinusoidal magnetic fields. (b) Single-sided MPS sensors provide spatio-temporal detection of MNPs using an array of MPS sensors (c). The MPS signals of each MPS sensor (d) can be visualized in different ways, e.g., as time-to-peak representation (e).

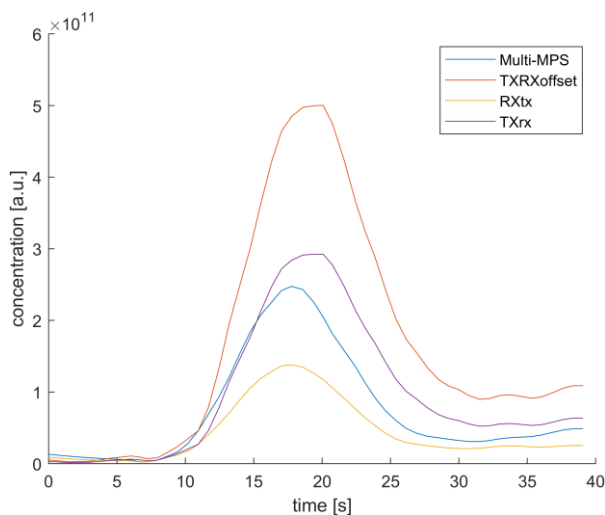


Fig. 3: Comparison of the received signal for different operation methods. A large transmit and receive coil system combined with local offset field generators provide 65% higher signal. For comparison similar coils have been used.

Comparing the different signal generation methods revealed that in principle all approaches allowed the time-resolved measurement of the tracer-bolus through the brain.

However, Fig 3. shows a comparison of the signal generation for all four approaches. The sensitivity of the TXRXoffset approach is about 65% higher than other methods.

Discussion: The goal of this study is to use real perfusion data from CT and MRI within a home-built simulation framework [8] to optimize the number and positioning as well as the signal generation of the tx-rx system for the StrokeCap. The preparation of real perfusion data from CT datasets requires multiple steps and is limited due to CT's low temporal resolution. Furthermore, standard CTA procedure does not cover the complete brain. Hence, a part of the signal generating MNP-tracer bolus is not covered in the simulation leading to deviations in the simulated signals.

Besides the principal ability to detect the time course of the tracer bolus the tested hardware setting also have to be implemented in a point of care setting. This requires robust hardware design with reduced complexity. From the tested hardware configuration, this goal is best achieved by the TXRXoffset configuration. Furthermore, the offset approach also changes the receive-frequency range: instead of using odd higher harmonics of the excitation frequency, the signal also occurs at even higher harmonics due to the fact of an asymmetric magnetization behavior through the additional offset field.

Conclusion: With the aim of developing a portable MPS-based stroke diagnostic system, this study investigated different coil configurations and signal generation strategies within a simulation framework based on real patient CT perfusion data to assess the feasibility of this approach. The results identified one promising coil setup, which combines sensitivity for detecting regional perfusion deficits with reduced complexity of hardware requirements. These findings directly informed the design of a first functional StrokeCap prototype, which is currently under development. The prototype aims to enable spatially resolved, real-time detection of ischemic stroke at the point of care. This represents a key step toward a portable, fast, and non-invasive diagnostic tool that could significantly reduce time-to-treatment in emergency scenarios.

Acknowledgements: We thank Dr. Michael Angerer from Kliniken Nordoberpfalz AG Weiden for providing CT perfusion datasets for simulations.

References:

1. Feigin V.L. et al. Global, regional, and national burden of stroke and its risk factors, 1990–2019: a systematic analysis for the Global Burden of Disease Study. *The Lancet Neurology*. 20(10):795-820 (2019).
2. M. Graeser et al. Human-sized magnetic particle imaging for brain applications, *Nat Commun*. 10:1936 (2019).
3. P. Vogel et al. iMPI: portable human-sized magnetic particle imaging scanner for real-time endovascular interventions. *Sci Rep*. 13:10472 (2023).
4. P. Vogel et al. Critical Offset Magnetic Particle Spectroscopy for rapid and highly sensitive medical point-of-care diagnostics *Nature comm*. 13:7230 (2022).
5. J. Guenther et al. Human-Sized Lightweight Head-Scanner Design. *Int J Magn Part Imag*. 8(1):2203064 (2022).
6. S. Biederer et al. Magnetization response spectroscopy of superparamagnetic nanoparticles for magnetic particle imaging. *J Phys D: Appl Phys*. 42:25007 (2009).
7. Mohn F. et al. Characterization of the Clinically Approved MRI Tracer Resotran for Magnetic Particle Imaging in a Comparison Study. *Phys Med Biol*. 69(13) (2024).
8. Vogel P. et al. Modular Simulation Framework for Magnetic Particle Imaging. *Int J Magn Part Imag*. 9(1):2303081 (2022).
9. Hennig J. et al. 15 years MR-encephalograph. *Magn Reson Mater Phys*. 35, 85-108 (2021).

Correction of FID artifacts in TSE-based sequences using deep learning methods

Hanna Wichtel 1+2+3*, Dominik Paul 2, Hans-Peter Fautz 2+3, Florian Putz 4, Jana Hutter 1

1 Friedrich-Alexander Universität Erlangen-Nürnberg
2 Siemens Healthineers
3 Imaging Science Institute
4 Universitätsklinikum Erlangen

Abstract: Turbo spin echo (TSE) based MRI with a single average can produce FID (free-induction decay) artifacts caused by residual FID signals. These artifacts can be suppressed by acquiring two averages with phase cycling doubling the scan time. Deep learning-based correction enables artifact removal using only a single average and thus half the acquisition time. A U-Net was trained to predict the artifact itself, which is subtracted from the input to generate a corrected image. Training was performed on 6776 phantom slices acquired on a 1.5T clinical Magnetom Sola scanner from Siemens Healthineers using a SPACE sequence protocol. Results show effective artifact removal, demonstrating the potential for faster, artifact-free TSE imaging.

Motivation: FID artifacts, also called fineline artifacts, commonly occur in the SPACE (Sampling Perfection with Application optimized Contrast using different flip angle Evolution) sequence. This single-slab three-dimensional turbo spin echo (TSE) sequence is susceptible to such artifacts due to incomplete refocusing or gradient spoiling [1]. These artifacts occur due to residual longitudinal magnetization that is converted into transverse magnetization by refocusing pulses with flip angles less than 180 degrees. If the gradient crushing, intended to dephase this unwanted transverse component, is insufficient, it leads to artifactual FIDs that bleed into subsequent echoes of the echo train, as illustrated in Figure 1. A conventional solution involves acquiring two signal averages in combination with phase cycling. Inverting the phase of the refocusing pulses on the second excitation inverts the phase of the FID signals, while the echoes remain. Summing these averages cancels the artifact while adding the echoes, as shown in Figure 1. However, this also doubles the scan time, which is a major drawback in clinical workflow. Previous work [2] focused on removing this artifact by adapting end-to-end deep learning reconstruction networks, initially designed for reconstructing undersampled MRI data, so that artifact suppression was integrated into the reconstruction process. In contrast, the approach presented here employs a deep learning-based method that operates directly in k-space to remove FID artifacts. The method outputs corrected raw data that can be processed by conventional reconstruction pipelines, enabling artifact correction in half the time compared to the conventional method and preserving compatibility with existing workflows.

Materials & Methods: MRI data were acquired on a 1.5T clinical Magnetom Sola scanner from Siemens Healthineers using the Siemens SPACE sequence. The dataset consists of 9680 image slices from water phantom scans acquired with two averages, chosen to isolate artifact characteristics in a controlled setting. 6776 slices were used for training, 1452 slices for validation, and 1452 slices for testing. A basic U-Net architecture [3] was trained to directly predict the FID artifact from images acquired with one average. The network was trained for 70 epochs using the Adam optimizer (learning rate

= $5e-4$) and a mean squared error loss in combination with a regularizer, that avoids values close to 0 and 1. Rather than using artifact-free images as targets, the training labels consisted of isolated artifact images obtained by subtracting one average from the other and dividing the result by two to preserve intensity consistency with the input data. This subtraction cancels the true signal but retains the artifact, due to the phase cycling properties of the sequence. The predicted artifact is subtracted from the input image to obtain a corrected output. To restore the final image to its original intensity scale, a small auxiliary CNN (Convolutional Neural Network) was trained to predict denormalization parameters from the complex-valued input data. The artifact removal pipeline is illustrated in Figure 2.

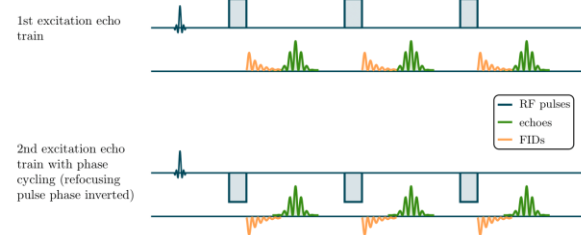


Fig. 1: Illustration of artifact correction by two average acquisition with phase cycling.

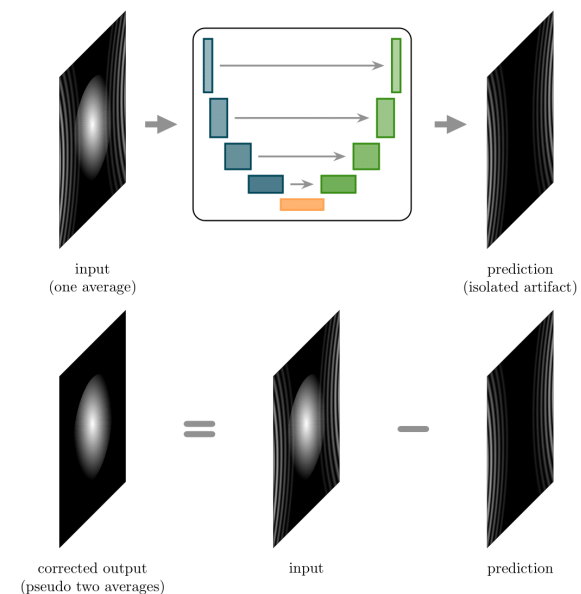


Fig. 2: Artifact removal pipeline: The U-Net predicts the isolated artifact from a single average input. Subtracting the prediction from the input yields a corrected image approximating a two average acquisition.

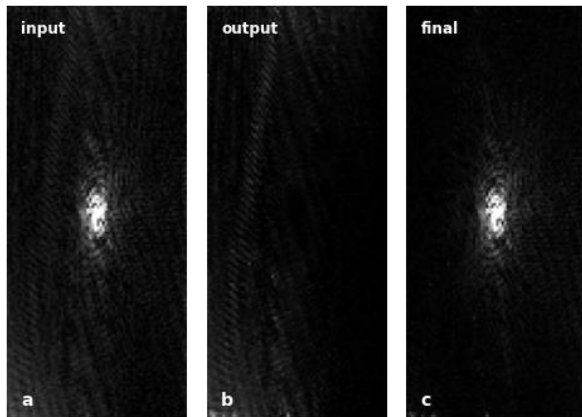


Fig. 3: Representative example illustrating the FID artifact in k-space, shown for one slice from a single channel: (a) input to the network (single-average acquisition), (b) output of the network (isolated artifact), and (c) final corrected k-space obtained by subtracting the output from the input.

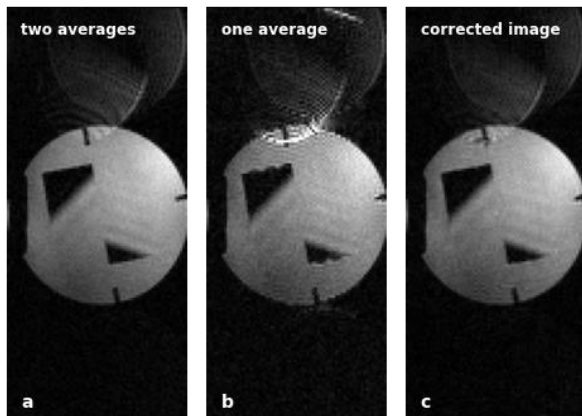


Fig. 4: Representative example demonstrating the FID artifact correction, shown for one slice of a single channel: (a) Two average acquisition with suppressed FID artifacts due to phase cycling, (b) single-average acquisition showing prominent FID artifacts, and (c) single-average acquisition after network correction, with visibly reduced artifacts.

Results: Figure 3 shows the k-space of a representative example, illustrating one slice from a single channel, including the input (single-average), the output (isolated artifact), and the final corrected result. The correction is achieved by subtracting the output from the input, effectively simulating a measurement with two averages. The presence of additional signal due to the FID artifact is evident, as it can be eliminated by acquiring two averages with phase cycling. Figure 4 shows the same representative example as in Figure 3, but in image space. It depicts a two-average acquisition, the single-average input, and the final corrected image, each corresponding to the same slice and channel. The artifact appears as rippling along the edges of the phantom, predominantly in the readout direction (top to bottom in this case), and is most prominent along the aliasing edge at the top of the phantom. The trained U-Net predicts the isolated FID artifact from single-average acquisitions. Subtracting this

prediction from the input results in a corrected image with visibly reduced artifacts. The visual comparison shows that the artifact suppression is nearly comparable to that of a two-average acquisition. This is also reflected in the quantitative results, with a structural similarity index (SSIM) of 0.83 and a peak signal-to-noise ratio (PSNR) of 32.41 dB.

Discussion: This work demonstrates that a deep learning-based approach can effectively correct FID artifacts in turbo spin echo MRI images, enabling reliable artifact suppression with only a single average. Initial results on phantom data show that the network can reliably identify and remove the FID artifact. The SSIM and PSNR values achieved by the corrected image indicate a high degree of structural preservation and effective artifact suppression, with the extent of artifact removal being comparable to that of a two-average acquisition. The approach operates directly in k-space and preserves compatibility with conventional reconstruction pipelines, making it suitable for integration into existing workflows. Importantly, it avoids the need for additional averages, which reduces scan time and potentially increases patient comfort and scanner throughput. Future research will extend the approach to in vivo data to validate clinical applicability and robustness across anatomies and contrasts.

Conclusion: The proposed method demonstrates the feasibility of using deep learning for targeted correction of FID artifacts in turbo spin echo MRI, enabling artifact-free reconstruction from single-average acquisitions. By isolating and subtracting the predicted artifact, the approach achieves comparable results to conventional two-average scans while reducing scan time. The method is compatible with existing reconstruction workflows and has the potential to improve clinical efficiency without sacrificing diagnostic reliability. Future work will validate this approach on in vivo data and explore generalizability and clinical applicability to assess its robustness and broader applicability in routine diagnostic practice.

Acknowledgements: Valuable input and support were provided by the Strahlenklinik of the Universitätsklinikum Erlangen.

References:

1. Mugler III, John P., "Optimized three-dimensional fast-spin-echo MRI.", *Journal of magnetic resonance imaging* 39.4 (2014): 745-767.
2. Ahn, Sangtae, Anne Menini, and Christopher J. Hardy, "A deep network for reconstruction of undersampled fast-spin-echo MR images with suppressed fine-line artifact."
3. O. Ronneberger, P. Fischer, and T. Brox, "U-Net: Convolutional networks for biomedical image segmentation", *Proc. Medical Image Computing and Computer-Assisted Intervention (MICCAI)*, 2015, pp. 234-241. doi:10.1007/978-3-319-24574-4_28

Assessing the Reliability of Volumetric Thermometry for Coil Modeling Uncertainty at 7T

Saskia Wildenberg 1+2, Nico Egger 2, Judith Schirmer 2, Ralph Kimmlingen 3, Titus Lanz 4, Armin Nagel 2+5, Andreas K. Bitz 1

1* Electrical Engineering and Information Technology, University of Applied Sciences – FH Aachen, Aachen, Germany

2* Institute of Radiology, Friedrich-Alexander-Universität Erlangen-Nürnberg (FAU), Erlangen, Germany

3 Siemens Healthcare GmbH, Erlangen, Germany

4 RAPID Biomedical GmbH, Rimpf, Germany

5 Division of Medical Physics in Radiology, German Cancer Research Center (DKFZ), Heidelberg, Germany

Abstract: With increasing B0 field strengths, the calculation of quantitative safety factors based on thermometry data gets more important, as B1p deviations no longer reliably reflect SAR variations. In this work, we evaluate the suitability of thermometry data for the quantitative determination of coil modeling uncertainty (CMU) at 7T. Thermometry is performed on a phantom with the Proton Resonance Frequency Shift method, multiple oil references and three excitation vectors. Thermometry-based SAR maps showed high sensitivity to the location of the oil references, with CMU_SAR_individ values fluctuating by up to 80%. The reliability of CMU_SAR values is further decreased, as a reduced accuracy of thermometry data compared to B1p maps was revealed.

Motivation: To ensure patient safety at ultra-high fields (UHF), Specific Absorption Rate (SAR) hotspots are predicted from simulations with generic human body models. As a digital coil model is used for these simulations, a safety factor for coil modeling uncertainty must be considered. This safety factor is usually determined from the deviations between simulated and measured B1p maps, relying on the linear relationship between B1p2 and SAR anticipated by the quasistatic approximation of Maxwell's equations. While this relationship is in fact linear at low field strengths, this cannot be assumed for 7T UHF imaging, due to complex wave effects [1]. Therefore, thermometry has been applied as an additional method to validate SAR simulations where B1p mapping alone may not suffice [2]. In this work we evaluate the suitability of thermometry-based SAR maps for the quantitative determination of a safety factor for coil modeling uncertainty at 7T. The evaluation includes an analysis of typical sources of inaccuracy, with special focus on the B0 field and its impact on measurement reproducibility.

Materials & Methods: Experiments were performed on a SIEMENS Magnetom Terra.X using a phantom stack consisting of four cylindrical discs with viscous filling. Two of these discs were equipped with a pair of fiber-optic sensors [3] mounted to a fiberglass rod (see Fig.1b). The setup is completed by an 8Tx/16Rx torso array [4] (see Fig.1a) and two/three spherical containers filled with oil for B0 drift correction.

During the experiment, the temperature rise was measured locally using fiber-optic sensors, and volumetric via the proton resonance frequency shift (PRFS) method [5]. This method relies on the linear relationship between temperature rise ΔT and phase shift $\Delta\phi$, with ΔT being calculated according to $\Delta T = \Delta\phi / (TE \cdot B_0 \cdot \gamma \cdot \alpha)$. Three excitation vectors with different locations of temperature hotspots were used, with maximum transmit power limited by hardware. Subsequently, B0 shimming was performed, and GRE B0 phase maps (45min,

55s temporal resolution, 1mm² in-plane, 4 coronal slices within each sensor disc) were measured.

After the experiments, phase wrapping and B0 drift were corrected, the latter by applying averaged values from all oil-references per measurement. The material-specific PRFS constant α was derived utilizing the sensor temperatures to substitute ΔT in the equation mentioned above. Finally, the SAR distributions were derived according to $SAR = C \cdot (\partial T / \partial t)$, where $C = 4186 J / (kg \cdot K)$ is the specific heat capacity of the phantom.

B1p maps were gathered with the AFI method [6] at 4mm isotropic resolution. The coil modeling uncertainty based on SAR and B1p maps was calculated according to Steensma et al. [2].

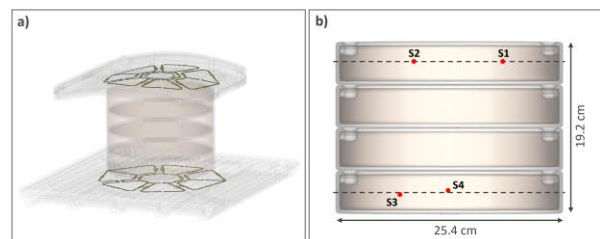


Fig. 1: a) The torso coil consists of a ventral and dorsal array, each containing 8 loops combined into 4 transmit channels. b) Schematic representation of the sensor positions (S1 – S4) within the phantom. The discs can be rotated and reordered to adjust the locations of the sensors.

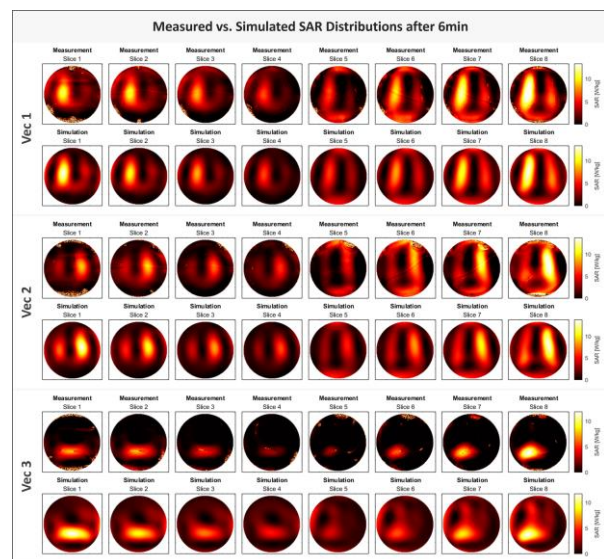


Fig. 2: Comparison of simulated and measured SAR distributions after a heating period of 6min for all excitation vectors. The maps show high qualitative agreement for both upper (slice 1-4) and lower disc (slice 5-8). As peak SAR values emerge at the surface, SAR maps were only evaluated in the outer discs.

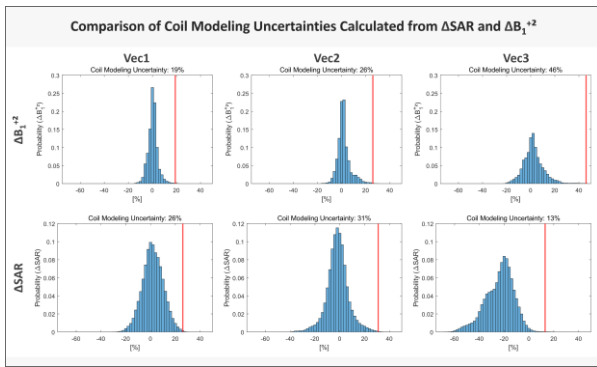


Fig. 3: Coil modeling uncertainties calculated from SAR and B1p maps following the model of Steensma *et al.*, with $\Delta B1p^2 = (|B1p_{meas}|^2 - |B1p_{sim}|^2) / |B1p_{sim_max}|^2$ and $\Delta SAR = (SAR_{meas} - SAR_{sim}) / SAR_{sim_max}$. The values of $B1p_{sim_max}$ and SAR_{sim_max} denote the disc-specific maxima of each distribution.

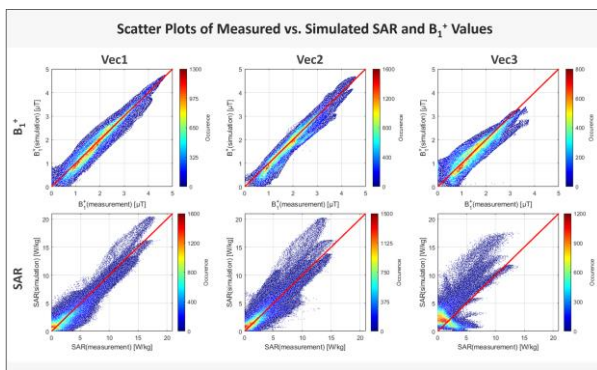


Fig. 4: Comparison of simulated and measured B1p and SAR maps for all measured excitation vectors. The lobe-shaped clusters in the SAR comparison indicate layer dependent variations between simulated and measured values. This layer-dependent effect is absent in the B1p maps, indicating higher robustness to simulation deviations.

Results: SAR distributions were calculated for the duration of linear temperature rise (6min) and an average PRFS constant of $\alpha = -0.063$ ppm/°C. The resulting measured SAR maps showed high qualitative agreement with the simulations (see Fig.2), even though there appears to be a consistently reduced signal intensity throughout the area for Vec3. This discrepancy can be explained by larger spatial variations in the B0 drift: While the average phase drifts across different oil references varied by up to 6° for Vec1 and Vec2, deviations of up to 13° were observed in the measurement of Vec3.

Subsequently, SAR and B1p maps were used to calculate the coil modeling uncertainty (CMU), with unreliable pixels excluded from the calculation (see Fig.3). CMU values calculated from B1p maps (CMU_B1p), and SAR maps (CMU_SAR_avg) showed good agreement. However, to highlight the impact of B0 drift variations, CMU values were also calculated for B0 drift corrections based on each reference individually. The results of CMU_SAR_individ are 9%/50%/23% for Vec1, 16%/47% for Vec2, and 57%/–28% for Vec3. CMU_SAR_individ values undergo huge variations depending on the position of the oil reference.

Figure 4 illustrates a pixelwise comparison of simulated and measured SAR and B1p values. B1p maps show high agreement. In contrast, SAR maps show increased variability,

and the formation of lobe-shaped clusters can be observed. These clusters indicate slice dependent variations between simulated and measured data, that do not occur for the B1p maps.

Discussion: The results in Fig.3 confirm that variations between simulated and measured B1p maps do not necessarily lead to the same variations in SAR maps. This emphasizes the relevance of thermometry as a supplementary validation method for coil modeling uncertainty at UHF. The qualitative comparison of Vec1 and Vec2 in Fig.2 demonstrates the potential of thermometry to capture small temperature changes. However, it also illustrates the systematic underestimation of measured data for Vec3, caused by B0 drift inhomogeneities. The effect of B0 drift correction on the validation results is further investigated by calculating CMU_SAR values for individual oil references, with CMU_SAR_individ values fluctuating by up to 85%. A possible explanation for this discrepancy is that Vec1 and Vec2 were the first measurements of the day, while Vec3 was measured after the scanner was already in use. This may have caused preheating of the hardware, resulting in more significant B0 drift inhomogeneities.

These findings demonstrate the sensitivity of thermometry to system imperfections. To improve the reliability of the results and allow for a more detailed error analysis, thermometry should be performed with multiple oil references and excitation vectors. Furthermore, imaging parameters should be chosen to maximize temperature rise to reduce the influence of B0 drift. Since the overall accuracy of the method is reduced compared to B1p maps, as shown in Fig.4, a qualitative evaluation of thermometry data should be considered instead of a potentially overly conservative safety factor.

Conclusion: In this work, we evaluated the suitability of thermometry data for the quantitative determination of a safety factor for coil modeling uncertainty at 7T. Thermometry-based SAR maps revealed high sensitivity to the position of the oil reference used for B0 drift correction. These fluctuations undermine the reliability of quantitative CMU assessment, as the robustness of the measurements is limited due to the B0 drift dependence. Calculating CMU values based on the most conservative drift is an option, but this would overestimate safety margins. To improve robustness and reproducibility, multiple oil references and excitation vectors should be used, and imaging parameters should be optimized to maximize temperature rise. Future work should focus on developing methods that enable volumetric B0 drift measurements or effectively mitigate its influence.

References:

1. Fiedler TM, Ladd ME, Bitz AK. SAR Simulations & Safety. *Neuroimage*.
2. Steensma BR *et al.* Tier-based formalism for safety assessment of custom-built radio-frequency transmit coils. *NMR Biomed*.
3. Polytec GmbH, Fiber Optic Temperature Sensor, Type TS4.
4. RAPID Biomedical GmbH, Rimpar, Germany.
5. Rieke V, Butts Pauly K. MR thermometry. *Journal of Magnetic Resonance Imaging*.
6. Yarnykh VL. Actual flip-angle imaging in the pulsed steady state: a method for rapid three-dimensional mapping of the transmitted radiofrequency field. *Magn Reson Med*.

Initial experience of one-click Cardiac Magnetic Resonance Imaging: a comparison in 122 patients

Amelie Wüllner* 1, Jens Wetzl 2, Michaela Schmidt 2, Lynn Johann Frohwein 1, Jonas Ströder 3, Alexandra Weißgerber 3, Susanne Puls 3, Jörg Barkhausen 3, Alex Frydrychowicz 3

1 Siemens Healthineers AG

2 Research & Clinical Translation, Magnetic Resonance, Siemens Healthineers AG, Erlangen, Germany

3 Universitätsklinikum Schleswig-Holstein, Campus Lübeck, Lübeck, Germany

Abstract: Cardiovascular Magnetic Resonance Imaging (CMRI) is the gold standard for assessing heart disease [1]. To increase access to CMRI, a higher degree of automation and standardization are needed. The AI Cardiac Scan Companion (AICSC) offers AI-based suggestions for iso-centering, slice positioning and optimal Inversion Time post-contrast, enabling one-click scanning. An AICSC-based protocol was applied in 61 CMR patients; comparable non-AICSC cases were retrospectively identified. Total scan time and time to clinically relevant images were evaluated.

Mean scan time was (40.6 ± 10.6) min for the clinical protocol and (39.9 ± 7.1) min for AICSC, with no significant mean difference, but a significant reduction of standard deviation ($p < 0.003$).

Motivation: Cardiovascular Magnetic Resonance Imaging (CMR) has become the gold standard for the assessment of cardiac function and is essential for the diagnosis of cardiovascular disease [1] [2]. However, there is a shortage of MR technicians, even more so technicians trained in CMRI. To overcome this, assisting technology is warranted. The research software package AI Cardiac Scan Companion (“AICSC”) provides an AI-based approach for iso-centering, slice positioning and Inversion Time (TI) determination for late gadolinium enhancement (LGE) [3]. It adds to the commercially available CMRI assistance tool “myExam Cardiac Assist” for automated detection of cardiac orientations and parameter propagation. In doing so, technician input for scan planning is reduced to a minimum, allowing more time for image quality control, patient monitoring and communication. Therefore, it was the aim of this work to compare an AICSC-based CMRI protocol in conjunction with Assist (“AICSC+Assist”) with an Assist-only approach (“Assist”) in a routine clinical CMRI setting in patients scheduled for typical indications such as myocarditis, fibrosis and post myocardial infarction scar determination. The total scan time, time intervals from scan start to clinically relevant timestamps, time for planning and preparation steps, quality of imaging planes, and percentage of the Field of View (FoV) covered by the heart were evaluated to ensure a standardized image acquisition.

Materials & Methods: 61 patients referred for CMR were scanned using the AICSC+Assist protocol on a 1.5 T clinical MRI system (MAGNETOM Sola, Siemens Healthineers, Forchheim, Germany). 61 patients scanned with the comparable Assist protocol were retrospectively selected. Data were evaluated under an existing Institutional Review Board (IRB) protocol. Scans were performed by radiographers with over 5 years’ CMRI experience. Patients with scan gaps over 30 min were excluded and replaced with comparable cases.

AICSC was used to set up a CMR protocol with AutoPositioning and AutoTI [4]. AutoPositioning performs automated isocen-

tering and slice positioning in standard orientations. AutoTI suggests the optimal Inversion Time (TI) for late gadolinium enhancement (LGE). AutoAlign from the myExam Cardiac Assist workflow was used in both protocols for automated planning of cardiac views. In the clinical protocol, TI was manually selected. Cine, T1 mapping, and phase-sensitive Inversion Recovery (PSIR) LGE were acquired in both protocols per clinical standard and imaging recommendations.

A 3–6 min respiratory-gated 3D MRA was added to the AICSC+Assist protocol between contrast administration and LGE (Fig. 4), the Assist cases did not contain this sequence.

Total scan time and time to key images were compared between protocols. AutoAlign-based FoV placement was verified. An elliptical estimate of heart size in the cine sequences was compared to the chosen FoV.

Data processing and statistics were done in Python (version 3.13, Python Software Foundation). Unpaired Student's t-test assessed significance for mean differences, F-test for variance differences (significance limit $p < 0.05$).

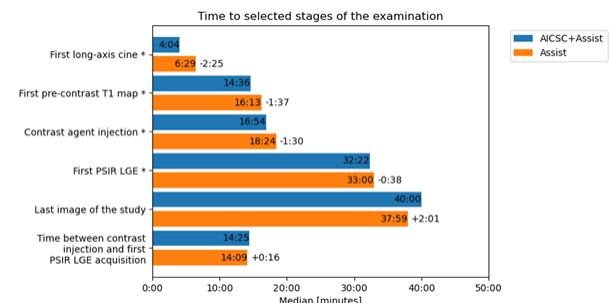


Fig. 1: Median in min until selected stages of the examination for the AICSC+Assist and Assist protocol. The difference between the medians is displayed on the right of the bars. All stages denoted with an asterisk show a statistically significant median difference with $p < 0.05$.

Results: In the AICSC+Assist protocol cohort, five exams were aborted and conducted as manually planned protocols due to largely deviating anatomic conditions and these scans were excluded from further analysis. The total scan time was 40.6 ± 10.6 min (median 38.0 min) for the Assist protocol and 39.9 ± 7.1 (median 40.0 min) for the AICSC+Assist protocol. Mean differences showed no statistical difference ($p = 0.67$), but the reduction in standard deviation was significant ($F = 2.2$, $p < 0.003$). Fig. 1 shows the median times to reach specific time stamps, including the difference between Assist and AICSC+Assist protocol. The time points marked with an asterisk show a statistically significant time reduction between the AICSC+Assist and Assist protocol. Fig. 2 and 3 shows the wait times in between sequences for one patient with AICSC+Assist protocol and Assist protocol. The 3D MRA sequence was used in 87% of all AICSC+Assist protocol cases.

None of the imaging planes were rejected in the Assist protocol group, two were in the AICSC+Assist protocol group (1 %). The average percentage of the Field of View (FoV) covered by the heart using the AICSC+Assist protocol were: (0.37 ± 0.07), (0.54 ± 0.11), (0.53 ± 0.11), (0.33 ± 0.08). For the patients scanned with Assist protocol: (0.35 ± 0.10), (0.46 ± 0.13), (0.53 ± 0.13), (0.30 ± 0.09). The students t-test showed no significant deviation in between the value sets.

Patient ANONYM-MJYCG9: Planning and preparation time between sequences (total scan time: 33:24)

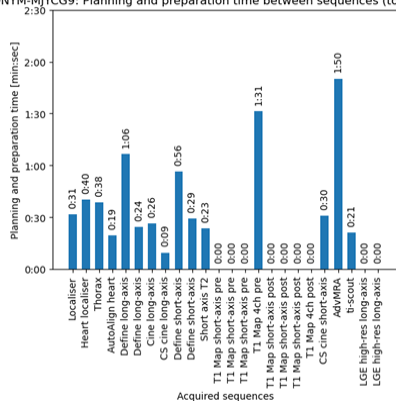


Fig. 2: Planning and preparation times between sequences for a patient scanned with the AICSC+Assist protocol.

Patient ANONYM-1FVSDX: Planning and preparation time between sequences (total scan time: 39:25)

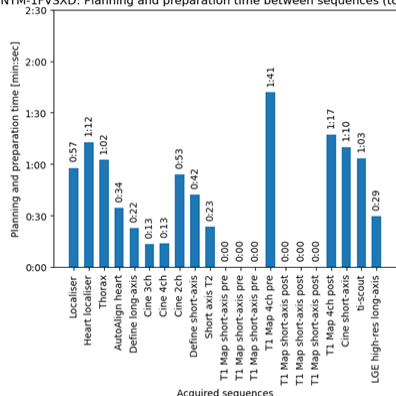


Fig. 3: Planning and preparation times between sequences for a patient scanned with the Assist protocol.

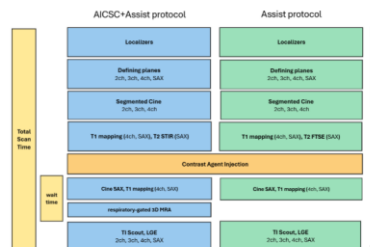


Fig. 4: Timeline of both protocols. Left column: total scan time includes contrast agent injection time, wait time and all sequences. 2ch: 2-chamber view, 3ch: 3-chamber view, 4ch: 4-chamber view, SAX: short-axis stack, STIR: Short-TI Inversion Recovery, FTSE: Fast Turbo Spin Echo, MRA: Advanced Magnetic Resonance Angiography, LGE: Late Gadolinium Enhancement.

Discussion: We successfully tested an AI-based research software package for CMR scan automation. As the AICSC+Assist protocol contained an additional 3D MRA

protocol, no reduction in scan time could be demonstrated compared to the Assist protocol. However, the increased automation and standardization can be demonstrated by a significantly reduced standard deviation of scan times. The effect of increased planning automation can be observed quantitatively in the reduced median time until the first long-axis cine (4:04 min for AICSC+Assist, 6:29 min for Assist) in Fig. 1. This can also be observed qualitatively in the wait times shown in Fig. 2 (AICSC+Assist case) and 3 (Assist case), with wait times for the planning steps (“Localizer” to “AutoAlign heart”) are shorter. Additionally, the effect of AutoTI can be observed in the wait time for the “ti-scout” step (0:21 min for AutoTI, 1:03 min for manual TI selection).

More than 99% of imaging planes in the AICSC+Assist protocol group were considered acceptable which reflects solid performance for an automated system. Even so, the user always has the option to intervene and correct suggestions. While five patients had to be excluded due to large anatomic deviations, overall results indicate AICSC successfully enabling a “one- click” cardiac exam for standard clinical cardiac MR exams. Hence, this complex exam will become available in sites with technicians at different training levels or in remote supervision situations.

Future work will investigate the possibility of enabling less experienced operators to perform successful CMR imaging and improving reproducibility and standardization for operators of different experience levels. Overall time savings could be more conclusively demonstrated through a prospective study applying a fully matched protocol across both methods and larger patient sample.

Conclusion: The AICSC+Assist protocol significantly reduced variability in total scan time compared to the Assist protocol, resulting in more consistent and predictable exam durations. Although no significant difference was found in overall scan time, specific workflow steps such as initial planning and TI-scouting were completed faster. This highlights the potential of automation to streamline the acquisition process. These findings suggest that AI-based automation can enhance standardization, reduce operator dependency, and improve access to CMRI by enabling more consistent examinations, even in settings with less experienced staff or under remote supervision. Future studies with larger samples and fully matched protocols are needed to further assess overall time savings and validate clinical benefits.

Acknowledgements: The authors would like to acknowledge the continuous support of Alexandra Weißgerber and Susanne Puls.

References:
 [1] Wang, YR., Yang, K., Wen, Y. *et al.* Screening and diagnosis of cardiovascular disease using artificial intelligence-enabled cardiac magnetic resonance imaging. *Nat Med* 30, 1471–1480 (2024). <https://doi.org/10.1038/s41591-024-02971-2>
 [2] T Emrich, K Emrich, N Abegunewardene, K Oberholzer, C Dueber, T Muenzel, K-F Kreitner, Cardiac MR enables diagnosis in 90% of patients with acute chest pain, elevated biomarkers and unobstructed coronary arteries, *British Journal of Radiology*, Volume 88, Issue 1049, 1 May 2015, 20150025, <https://doi.org/10.1259/bjr.20150025>
 [3] Budde S, Soriano BD, Powell AJ. Survey of centers performing cardiovascular magnetic resonance in pediatric and congenital heart disease: a report of the Society for Cardiovascular Magnetic Resonance. *J Cardiovasc Magn Reson*. 2022 Feb 3;24(1):10. doi: 10.1186/s12968-021-00830-4. PMID: 35109865; PMCID: PMC8812017.
 [4] Cardiac Dot Engine: Significant Time Reduction at Cardiac Magnetic Resonance Imaging, Jesús Ciro Pueyo, M.D., Ph.D., Paula García-Barquín, M.D., Laura Romina Zalazar, M.D., José Miguel Madrid, M.D., Jon Etxano, M.D., Efrén Ojeda, M.Sc., Óscar Fernández, *MAGNETOM Flash*, Issue Number 60 · 5

Poster

Presenter

- P1 Ali Ajouz
Multi nuclear MR imaging and spectroscopy using a whole body, 3T human MR system with 200 mT/m gradients
- P2 Fatima Anum
Comparison of the robustness of manual spectral line integration and automated spectral line fitting for deuterium-labeled metabolomics
- P3 Lisa Artmann
Deep learning-based velocity anti-aliasing of 4D-flow MRI for intracranial vasculature
- P4 Charbel Assaf
J-coupling interactions and Hydrogen/Ligand Exchange in SABRE-pyruvate Systems
- P5 Alper Atici
Open-Source, Modular 4D-Flow MRI Pre-Processing Pipeline for research applications
- P6 Laura Bauer
Implementation, and Assessment of Methods for Improved Temperature Mapping
- P7 Lucas Bolster by Mariya Pravdivtseva
Evaluation of Various Cross-Linking Agents for Tunable MRI Relaxation Times in Multimodal Phantoms
- P8 Lukas Bönsel by Frederik Testud
The importance of RF-pulse-timing for B0- and B1-insensitivity in a T2-prep module
- P9 Dario Bosch
Liberating pTx from Vendor Lock-in: Open-Source Cross-Vendor Parallel Transmit MRI Sequences by extending pTx-Pulseq to Siemens UHF Scanners
- P10 Petr Bulanov
Measuring liver and kidney relaxation times at 7 T
- P11 Aaron Diercks
Metabolic imaging with deuterated Glucose and Lactate
- P12 Ali El Ahmar
Feasibility of 4D Flow MRI for Flow Diverter Assessment Using a Custom-Built Phantom
- P13 Francisco J. Fritz
Quantitative MRI study of excised brain tissue in drug-resistant epilepsy patient: from in-vivo to ex-vivo
- P14 Dominik Gabbert
Anatomy of neo-aorta can cause abnormal flow patterns related to dilatation
- P15 Julius Glaser
A deep nonlinear subspace modelling and reconstruction for diffusion-weighted imaging using variational auto-encoder
- P16 Yenal Gökpek
PHIP-SAH polarizer with increased sample volume and hydrogen diffuser
- P17 Farhad Haj Mohamad
Tracing metabolic flux of hyperpolarized [1-13C]pyruvate in Escherichia coli K12
- P18 Majd Helo
Characterizing reproducibility of fat/iron quantification in phantom across 0.55T, 1.5T, and 3T
- P19 Ruben Hernandez-Vega
Hyperpolarized 13C metabolic MRI of tumor xenografts in fertilized chicken eggs with a tailored surface RF coil
- P20 Niklas Himburg
Improving the Quantification Accuracy of Long T1 Times in Magnetic Resonance Fingerprinting
- P21 Annika Hofmann
Assessing the Repeatability of SMS accelerated QTI Imaging at 7T

- P22 Ville Iso-Kouvola
Impact of sequence parameters, parallel imaging and reduced FOW DWI techniques on ADC values
- P23 Maryam Kargaran
Accelerated Phase-Cycled bSSFP Imaging Joint Reconstruction with Improved Profile Estimation
- P24 Benedict Korzekwa by Marc Jonuscheit
Assessing scanner specific correction factors for calculation of fatty acid composition with 1H-MRS
- P25 Franziska Lohrengel
Investigating Reproducibility Issues of the 1⁻³ 3⁻¹ Excitation Pulse During wbNAA Sequence Implementation
- P26 Ameya Ajit Markale
Dual Approach to Artifact Detection and Classification in High b-Value Breast DWI: A Deep Learning Perspective
- P27 Kai Meinerz
Super-resolution in vitro 4D Flow MRI for intracranial aneurysms assessment
- P28 Siawoosh Mohammadi
Assessing the microstructure of drug-resistant temporal lobe epilepsy patients using the fingerprint of in vivo histology MRI
- P29 Lion H. Mücke
Quantitative Susceptibility Mapping (QSM) of kidney stones: an ex-vivo investigation of the effect of masking the low-signal kidney stone regions
- P30 Konstantin Müller
Phasor analysis enables unsupervised k-means-based metabolic segmentation of Hyperpolarized 13C-CSI data
- P31 Angela Osenberg by Pavel Povolni
Age-Related Changes in Myelin and Iron on MR Parameters Through Cortical Layers at 9.4T.
- P32 Stefan Petersen
Scaling Up SABRE: Development of a Hyperpolarizer for Large-Animal Studies and Human-Dose Production
- P33 Andrea Pino
Assessment of structural response of FRP bore liner for a high-count UHF transmission array
- P34 Marta Pokotylo
Real-Time Metabolic Profiling of Patient-Derived Human Midbrain-Like Organoids Using Hyperpolarized 13C-NMR Spectroscopy
- P35 Benedikt A. Poser
3D spiral readouts for BOLD fMRI at 9.4T
- P36 Andrey Pravdivtsev
13C Hyperpolarization and 2H NMR enable real-time insights into the enzymatic activity of yeast and intestinal organoids
- P37 Pascal Pretz
4D-flow Derived Finite-Element-Method Analysis in Right Ventricle Differentiates Between Different Stages of Pulmonary Hypertension
- P38 Ehtisham Rasool
Effect of chemical exchange on T₁ and T₂ Spin Relaxation: succinate and pyruvate case studies
- P39 Philipp Renn
Quantitative characterization of lesional and normal-appearing deep brain structures in primary progressive multiple sclerosis at 7T
- P40 Laura Rozo Pardo
Feasibility of Matrix Pencil Decomposition for Ventilation and Perfusion Mapping Using Low-Field MRI in Healthy Volunteers and Lung Tumor Patients

- P41 Bennet Rzepka
Coregistration of Intraoral Optical Scan with Dental MRI for Visualization of Pulp Anatomy: A case report with CBCT comparison
- P42 Martin Sandbrink
Towards Reliable SABRE Hyperpolarization: Optimizing Stability of a [1-13C]Pyruvate polarizer
- P43 Sascha Santaniello
Investigating the link between glymphatic function and white matter microstructure in multiple sclerosis
- P44 Philip Saul
Hyperpolarization of Pyruvate using SLIC-SABRE and a Perfluorinated Catalyst
- P45 Jonah Schrauder
Comparison of Aortic Blood Flow in Rabbits using MRI: Physiological vs. Extracorporeal Circulation
- P46 Rolf Schulte
Improving Image Resolution in Deuterium Metabolic Imaging with bSSFP for Clinical Translation at 3T
- P47 Jonathan Patrick Schwardt
Towards GABA measurements in the human cervical spinal cord with MEGA-PRESS
- P48 Andreas Seiler by Naomi Larsen
Metabolic characterization of hypoperfused brain tissue for stroke risk stratification in patients with recently symptomatic intracranial stenosis based on HP MRI - study protocol
- P49 Lena Sommer
Simulation of Liver Perfusion VSASL Towards Isolation of Hepatic Arterial Signal
- P50 Nicolas Spath by Farhad Haj-Mohamad
13C pyruvate drug compounding and terminal sterilization
- P51 Carlotta Staats
Region of interest characteristics in diffusion MRI along perivascular space index
- P52 Ronja Steiling
Application of the Segmented Monoexponential IVIM Model for Separating Diffusion and Perfusion Changes in Sepsis-Associated Acute Kidney Injury
- P53 Isadola Steinman
Implementation of an automated purification protocol for a low field SABRE
- P54 Yu Sun
Preliminary In Vivo and Ex Vivo Assessment of MRI Artifacts from Biodegradable Mg-10Gd Implants: Implications for Alloy Design and Imaging Protocol Optimization.
- P55 Kolja Them
Transfer agents for relaying parahydrogen-induced hyperpolarization.
- P56 Jesse Torija Maximo
Assessment of Hypoxia in a Glioblastoma Model by MRI, PET and Histopathological Analysis
- P57 Patrick Vogel
StrokeCap: the mobile stroke diagnostics – a simulation study
- P58 Hanna Wichtel
Correction of FID artifacts in TSE-based sequences using deep learning methods
- P59 Saskia Wildenberg
Assessing the Reliability of Volumetric Thermometry for Coil Modeling Uncertainty at 7T
- P60 Amelie Wüllner
Initial experience of one-click Cardiac Magnetic Resonance Imaging: a comparison in 122 patients